NOAA | CREST

EDUCATION & SCIENCE FORUM 2004

Research & Education Advancements in Oceanic & Atmospheric Sciences

Editors:

Reza Khanbilvardi, PhD., P.E.

Shakila Merchant, PhD.

Proceedings of Papers and Abstracts of NOAA Educational Partnership Program, Education and Science Forum. City College of New York, October 21-23, 2004

CREST PUBLICATION SERIES

NO: 02-2004

NOAA CREST

Research & Education Advancements in Oceanic and Atmospheric Sciences

CREST Publication Series
No: 02-2004

Edited by:
Reza Khanbilvardi, Ph.D., P.E.
City College of City University of New York &
NOAA-Cooperative Remote Sensing Science & Technology Center

Shakila Merchant, Ph.D.
NOAA-Cooperative Remote Sensing Science & Technology Center

Proceedings of Abstracts and Papers (also available on CD-ROM) of the NOAA Educational Partnership Programs' "Education & Science Forum", 2004, City College of CUNY, October 21-23, 2004

Admiral Conrad Lautenbacher Jr.

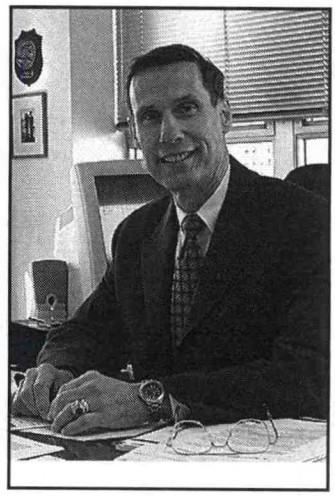

In hosting this Science and Education Forum, the NOAA Educational Partnership Program and the NOAA Cooperative Remote Sensing Science and Technology Center (CREST) at the City University of New York (CUNY) are providing a number of vital services. I am especially pleased that research being conducted by the Centers is central to NOAA's mission of science and service, and that this conference serves to nurture young talent in science and engineering.

This important conference brings scientific, academic and government communities together to address advancements and opportunities in NOAA-related sciences. It gives students the chance to explore interests in NOAA and interact with scientists, academicians and professionals in marine and atmospheric research and remote sensing technologies.

I am grateful for the co-sponsorship NASA-Goddard Institute for Space Studies, Columbia University and Raytheon. Their support for this conference is advancing opportunities essential to building America's environmental and economic health.

Vice Admiral USN (Ret) Conrad C. Lautenbacher, Jr., Ph.D.
Under Secretary of Commerce for Oceans and Atmosphere
and Administrator of the National Oceanic and Atmospheric
Administration (NOAA)

EDITORIAL FOREWORD

The "Research & Education Advancements in Oceanic and Atmospheric Sciences" is the Proceedings of the "Education and Science Forum" held in City College of The City University of New York, October 21 to 23, 2004. It is sponsored by National Oceanic and Atmospheric Administration and co-sponsored by CREST, City College of New York, Raytheon, Columbia University and NASA-Goddard Institute for Space Studies.

It includes 206 papers and abstracts covering oral and poster presentations. Keeping in view NOAA's Mission and Research domain, the themes selected for the technical presentations were: Atmospheric Sciences; Satellite Remote Sensing; Coastal and Ocean Sciences; Fisheries; Marine Resource Management; Climate & Weather; Environmental Sciences and Education & Outreach. The proceeding is also available on the CD-ROM. Table of Contents will help quickly access the paper of interest to the readers. All papers except those invited have been reviewed and changed in layouts based on the requirements of the publication.

The Editors wish to express their thanks to all the authors for submitting the papers on their recent or ongoing research findings to be included in this proceeding.

To edit a Proceeding of 206 papers/extended abstracts within an extremely limited period of time was indeed a challenge ahead of the team working on it. The editors also wish to thank the professional team who accepted the challenge and time constraints for typesetting and designing the proceedings and brought to the present form.

Reza Khanbilvardi, Ph.D., P.E, and

Shakila Merchant, Ph.D.

ACKNOWLEDGEMENTS

The members of the Organizing Committee would like to express their gratitude to NOAA and all co-sponsors who helped in making the Education and Science Forum 2004, a success.

Special thanks go to all the invited speakers for accepting our invitation to participate in the forum and speak at the plenary sessions.

Thanks also go to all the participants from various academia, universities, industries, scientists and engineers for their participation and contributions to the Forum.

The Committee also wishes to thanks all the presenters for their oral and poster presentations.

All the Cooperative Centers of NOAA Educational Partnership Program and their other university partners need a special mention on their contribution in the Forum 2004.

The organizing committee also wishes to thank all the Chairs of the technical sessions for concurring on facilitating the technical sessions, as also the oral and poster presenters who took time and patience to put their research work together for presentation at the Forum.

The organizing committee is also thankful to all the judges of the poster session & review, for agreeing to judge for the poster recognition awards.

All the research students involved in the NOAA-related sciences deserve a special note of appreciation and encouragement for being a part of the Cooperative Centers and exhibiting keen interests in NOAA research and careers.

Thanks are also due to the staff of City College of New York and NOAA-CREST for making all possible efforts to accomplish this event.

A special thanks to the Ms. Jacqueline Rousseau, EPP Program Director, Linda Belton, Outreach Coordinator, EPP, Dr. Meka Laster, EPP, and all other staff of NOAA EPP for giving all support and guidance in the publication of this proceedings and through out all events of the Education & Science Forum, 2004.

INVITED PARTICIPANTS

Dr. Richard Rosen, Assistant Administrator, NOAA
Congressman Jose Serrano
Congressman Charles Rangel
Dr. Gregory Williams, President, City College of New York
Dr. Selma Botman, Executive Vice-Chancellor for Academic Affairs, City University of New York
Dr. Ghassem Asrar, Deputy Associate Administrator, NASA
Mr. Paul Thompson, Vice President, Raytheon, Information Solutions
Dr. Colleen Hartman, Deputy Assistant Administrator, NOAA-Satellite and Information Services
Dr. Jim Hanson, NASA-GISS
Mr. John Jones, Deputy Assistant Administrator, NOAA -Weather Services
Dr. Steve Murawski, NOAA/Fisheries
Dr. Marie Colton, Director, NOAA/NESDIS
Dr. Phil Ardanuy, Director, Raytheon Information Solutions
Dr. Roberta Balstad Miller, CIESIN, Columbia University
Dr. Robert Chen, CIESIN, Columbia University
Dr. Ron Birk, Director, Science Applications, NASA Science Mission Directorate
Dr. Steve Klosko, Raytheon Information Solutions
Mr. Carroll Hood, GOES Architect
Dr. Dan Durett, Danhiko International
Ms. Margaret Spring, Senior Counsel Senate, Commerce Committee
Dr. Joseph Barba, Dean School of Engineering, City College of New York
Dr. Jeffery Puschell, Raytheon
Mr. Steve Drescher, NOAA Grants Management Division
Chairs of the Technical Session

Session A1: Ocean & Coastal
Prof. Sam Ahmed, CUNY/CREST
Dr. Eric Bayler, NOAA/NESDIS

Session A2: Marine Resources Management
Prof. Mark Harwell, FAMU/ECSC
Dr. David Johnson, NOAA/NOS

Session A3: Environmental Sciences
Prof. Larry Robinson, FAMU/ECSC
Mr. Gary Matlock, NOAA/NOS

Session A4: Atmospheric Sciences
Prof. Emanuel Glakpe, HU/NCAS
Dr. Paul Menzel, NOAA/NESDIS

Session B1: Atmospheric Sciences
Prof. Vernon Morris, HU/NCAS
Dr. Mitch Goldberg, NOAA/NESDIS

Session B2: Marine & Fisheries Sciences
Prof. Eirc May, UMES/LMRCSC
Dr. Laura Oremland, NOAA/Fisheries

Session B3: Fostering the Entrepreneurial Spirit

Prof. Victoria Cooper, CCCU/Wright College
Ms. Jewel Griffins-Linzey

Session C1: Satellite Remote Sensing
Prof. Fred Moshary, CUNY/CREST
Mr. Gerald Dittberner, NOAA/NESDIS

Session C2: Climate & Weather
Prof. Ramon Vasquez, UPRM/CREST
Mr. Daivd Kitzmiller, NOAA/NWS

Session C3: Education & Outreach
Prof. Reid Strieby, CUNY/CREST
Ms. Jana Goldman

Session C4: Environmental Entrepreneurship Activities
Prof. Conrad Ingram, Clark Atlanta University
Mr. Clement Lewsey, NOAA

Session D1: Atmospheric Sciences
Prof. Dr. Everette Joseph, HU/NCAS
Dr. Pablo Clemente-Colon, NOAA/NESDIS

Session D2: Fisheries
Prof. Joseph Okoh, UMES/LMRCSC
Ms. Laura Oremland, NOAA/Fisheries

Session D3: Satellite Remote Sensing
Prof. Ray Hoff, UMBC/CREST
Ms. Shobha Kondragunta, NOAA/NESDIS

Judges for the Poster Recognition Award:

Meka Laster, NOAA/EPP
Jewel Griffins-Linsey, NOAA/EPP
Kimani Kimbrough, NOAA/NWS
David Kitzmiller, NOAA/NWS
Priti Brahma, NOAA/NWS
Randy Chambers, NOAA/NWS
Terry McTigue, NOAA/NOS
Robert Ziobro, NOAA/NMFS
Jana Goldman, NOAA
Jacek Chowdhary, NASA-GISS
Juliana Maantay, CUNY/CREST
Jeffery Steiner, CUNY/CREST
Hamed Parsiani, UPRM/CREST
Everette Joseph, HU/NCAS
Dionne Hoskins, SSU/LMRCSC
Robert Gragg, FAMU/ECSC

SPONSOR:

National Oceanic and Atmospheric Administration, Education Partnership Program

CO-SPONSORS:

Cooperative Remote Sensing Science & Technology Center (CREST)
City College of City University of New York
Raytheon
NASA-Goddard Institute of Space Studies
Columbia University

TABLE OF CONTENTS

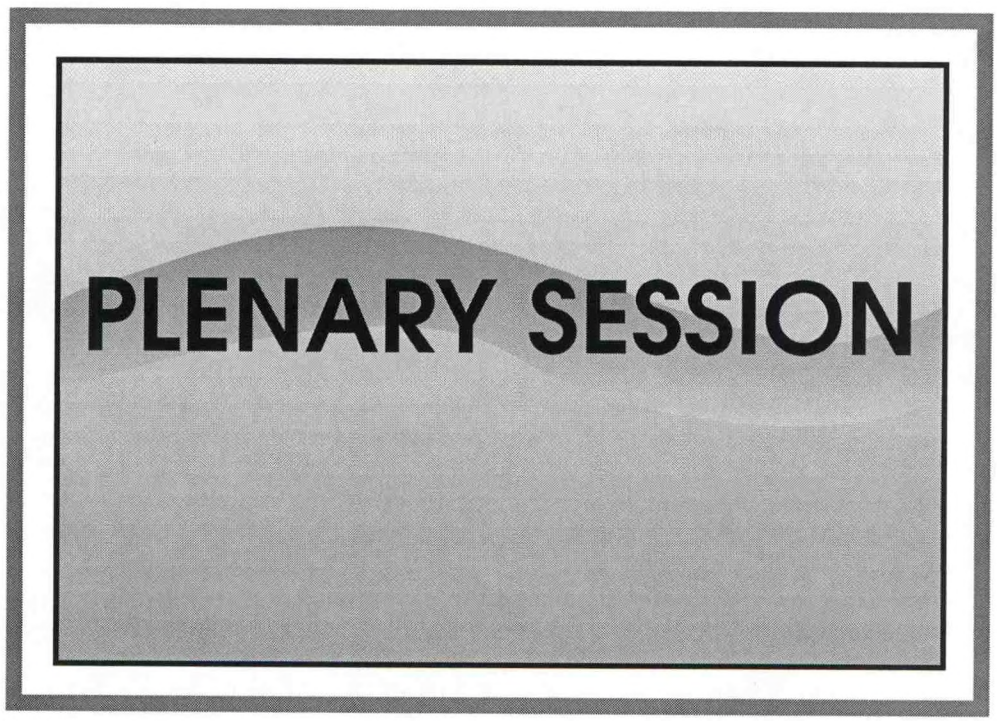
PLENARY SESSION

New Sensors and Old Questions: Studying Ice Sheet Mass Balance and the State of the Hydrological System Using ICESat and GRACE

Steve Klosko
Raytheon ITSS

Abstract

A major goal of the NASA Oceans and Ice Program is to investigate and monitor ice sheet mass balance on scales that significantly affect sea level. NASA has developed and deployed two new sensors that are providing measurements that are directly applicable to this goal: (a) The Geosciences Laser Altimeter System (GLAS) on board ICESat is acquiring surface height measurements with a focus on polar regions, while (b) ultra-precise inter-satellite range and range rate measurements from the GRACE tandem satellite mission provide a complementary form of remote sensing with its ability to detect gravity (mass) change. The promise of using these satellite missions to improve our estimates of ice sheet mass flux over regional (e.g. large glaciers, ablation zones, etc.) and basin-wide scales is discussed. GRACE observations, by sensing mass flux, can also provide a unique form of remote sensing to monitor the state of the continental hydrological system and the replenishment of major aquifers. Results will be shown based on the work of our team at NASA/GSFC and others working with these unique data sets now being coincidently acquired by these missions.

The Gravity Recovery and Climate Exper-iment (GRACE) Mission (Tapley and Reigber, 2001) is dedicated to providing an improved understanding of the Earth's gravity field both as a uniform mean field with better than 2 degree resolution along with highly resolved (to 400 km) estimates of the global mass flux about the mean field on a monthly basis. When met, these mission goals will improve gravity modeling accuracies from one to three orders of magnitude depending on wavenumber over previous gravity models, like EGM96 (Lemoine et al, 1998), which were derived from tracking data of opportunity. Models produced to date from GRACE are at least an order of magnitude better than any former modeling effort (c.f. Tapley et al, 2003, 2004; Reigber et al, 2004) and will continue to improve with refinements in data analysis strategies driving towards fulfillment of pre-launch goals. The fundamental GRACE measurement system is a highly accurate K-band microwave range rate measurement made between two co-orbiting satellites separated by approximately 250km. The intersatellite line-of-sight measurement precision delivered by GRACE is below the 1_m/s level giving GRACE unique observational sensitivity to the accelerations induced on low Earth orbiting satellites.

The Ice, Cloud and Land Elevation Satellite (ICESat) mission (Zwally et al, 2002) measures changes in elevation on the Earth's surface with a focus on Greenland and Antarctic ice sheets as part of NASA's Earth Observing System (EOS) of satellites. Time-series of elevation changes contribute to our understanding of the present-day mass balance of the ice sheets, polar climate, and estimation of the present and future contributions of the ice sheets to global sea level rise. The Geoscience Laser Altimeter System (GLAS) on ICESat has a 1064 nm laser channel for surface altimetry and a 532 nm lidar channel for the vertical distribution of clouds and aerosols. The accuracy for the surface-elevation measurements being achieved is better than 15 cm with, for example, tracks over flat lakes having noise levels which are below 5 cm.

By its very nature, temporally varying surface height, dh/dt, obtained from altimetry is a boundary condition that has a somewhat ambiguous relationship to the underlying mass flux. In over ice investigations, one must understand melting, snow fall, compaction, sublimation, wind erosion and transport, and

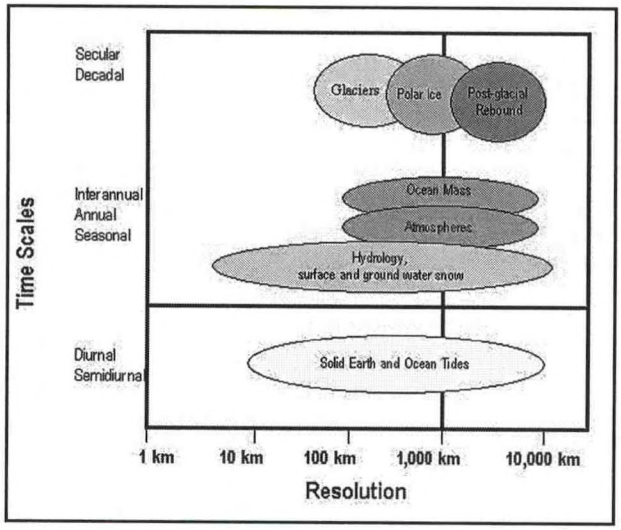

Figure 1. Mass flux within the Earth Systems occurs at various spatial and temporal scales

other effects which change the density of the ice column to accurately relate surface height change to mass flux. The contribution of Post Glacial Rebound (PGR) to dh/dt measured by ICESat is comprised of solid earth material having approximately 5 times the density of ice. However, there is no comparable ambiguity in the mass change sensed by GRACE. Thereby, improving PGR modeling is an integral part of the challenge when combining GRACE and ICESat observables.

These missions are designed to improve our overall understanding of key questions remaining in the Earth Sciences which have both surface height and mass transport manifestations:

- Hydrological cycle of the continents and in the ice regions,
- Ice mass balance and as a consequence the variation of sea level,
- Mass transport in the oceans and the ocean currents transport of heat
- The melting of the large ice covers and the resulting isostatic adjustment,
- Mass changes within the Earth, caused by various forces within the Earth

At GSFC, we have developed a capability to recover local/regional gravity changes using non-global functional representations (i.e. surface anomalies vs. global spherical harmonics) from the GRACE data. Our approach takes irregularly shaped regions, populate them with surface anomaly blocks of suitable area, and solve for the resulting mass flux with respect to a mean field. The surface mass or gravity anomalies benefits from both spatial and temporal constraints to add stability to the solution. These results will be integrated with the dh/dt changes coincidently observed by altimetry and those predicted by hydrological models.

This presentation will review some of the current work ongoing at NASA/GSFC in the use of GRACE data to better understand dh/dt.

REFERENCES

Chao, B.F., W. O'Connor, A. Chang, D. Hall, J. Foster, *Snow load effects on the Earth's rotation and gravitational field, 1979-1985*, **JGR**, 92, B9, 9415-9422, 1987.

Chen, J.L., C.R.Wilson, X.G. Hu, B.D. Tapley, *Large-scale mass redistribution in the oceans, 1993-2001*, **GRL**, 30, 20, OCE 1-1, 2003.

Han,S.C., C.Jekeli, C.K. Shum, *Time variable effects of ocean tides, atmosphere, and continental water mass on monthly mean GRACE gravity fields*, **JGR**, 109, B04403, 2004.

Lemoine, et al., *The Development of the Joint NASA GSFC and National Imagery and Mapping Agencey (NIMA) Geoptoential Model EGM96*, NASA/TP-1998-206861, July, 1998.

Rowlands, D.D., R.D. Ray, D.S. Chinn, F.F. Lemoine, *Short-arc analysis of intersatellite tracking data in a gravity mapping mission*, **J. Geodesy**, 76,307-316, 2002.

Swenson, S. and J. Wahr, *Methods for inferring regional surface-mass anomalies from Gravity Recovery and*

Climate Experiment (GRACE) measurement of time-variable gravity, **JGR**, 107, B9, ETG 3-1, 2002.

Tapley, B.D., Ch. Reigber, *The GRACE Mission: Status and future plans, EOS Trans.* **AGU**, 82(47), Fall Meeting Suppl., G41, C-02, 2001.

Tapley, B.D., D.P. Chambers, S. Bettadpur, J.C. Ries, *Large scale ocean circulation from the GRACE GGM01 Geoid*, **GRL**, 30, 22, OCE 6-1, 2003.

Tapley, B.D., S. Bettadpur, M. Watkins, Ch. Reigber, *The Gravity Recovery and Climate Experiment: Mission Overview and Early Results*, **GRL**, in press, 2004.

Thompson, P.F., S. Bettadpur, B.D. Tapley, *Impact of short period, non-tidal, temporal mass variability on GRACE gravity estimates*, **GRL**, 31, L06619, 2004.

Velicogna, I. and J. Wahr, *A method for separating Antarctic postglacial rebound and ice mass balance using future ICESat Geoscience laser Altimeter System, Gravity Recovery and Climate Experiment, and GPS satellite data*, **JGR**, 107, B10, ETG 20-1, 2002.

Wahr, J., M. Molenaar, F. Bryan, *Time variability of the Earth's gravity field: Hydrological and oceanic effects and their possible detection using GRACE*, **JGR**, 103, B12, 30,205-30,229, 1998.

Wahr, J., D. Wingham, C. Bentley, *A method of combing ICESat and GRACE satellite data to constrain Antarctic mass balance*, **JGR**, 105, B7, 16,279-16,294, 2000.

Zwally et. al., *ICESat's Laser Measurements of Polar Ice, Atmosphere, Ocean, and Land*, **J of Geodynamics**, Vol. 34, No. 3-4, pp. 405-445, 2002.

ORAL SESSION A1
Ocean & Coastal

NOAA's Current Interest in Satellite Ocean Remote Sensing

Eric Bayler

Chief, Oceanic Research and Applications Division (ORAD)
Office of Research and Applications (ORA)
National Environmental Satellite, Data, and Information Service (NESDIS)
National Oceanic and Atmospheric Administration (NOAA)
NOAA/NESDIS/ORA/ORAD
NOAA Science Center, Room 601, 5200 Auth Road
Camp Springs, MD 20746

Satellite oceanography within the Center for Satellite Applications and Research (STAR) in National Oceanic and Atmospheric Administration's (NOAA) National Environmental Satellite, Data, and Information Service (NESDIS) focuses on observation retrievals and applications to address the NOAA missions of environmental assessment, prediction, and stewardship. Satellite oceanography within NOAA/NESDIS is an end-to-end process, addressing user requirements, sensor design support, observation retrieval research and development, calibration, applications and product research and development, the transition of research to operations, continuing product validation, and operational user support. The breadth of scientific investigation encompasses three functional areas: satellite ocean sensors, ocean dynamics/ data assimilation, and marine ecosystems/climate. A cross-cutting science team from these functional areas has been established for each core subject: sea-surface temperature, sea-surface height, sea-surface roughness, ocean color, ocean surface winds, and sea ice. These science teams pursue the science and issues end to end within the core subject, with the primary objective being the transition of research to operations. Data fusion opportunities between science teams are also pursued. Each science team area addresses the common themes of calibration/validation, data assimilation, climate, and operational oceanography. Experimental and operational products, as well as user support, are provided to the user community via the NOAA OceanWatch/CoastWatch program.

Separation of Overlapping Elastic Scattering and Fluorescence from Algae in Seawater through Polarization Discrimination

A. Gilerson, A. Gill, B.M. Gross, F. Moshary, J. Zhou and S. Ahmed

Optical Remote Sensing Laboratory, Department of Electrical Engineering

Abstract

In this presentation, we discuss the development of a polarization discrimination technique to separate elastic reflectance and fluorescence components resulting from white light illumination of algae. Two types of algae were tested: *Isochrysis sp* and *Tetraselmis striata*. Preliminary results under laboratory settings show that this technique is capable of simultaneously separating fluorescence and scattering spectra which agrees with laser induced fluorescence measurements. This approach has been validated both for polarized and unpolarized illumination sources. Issues such as particulate sizes, solar angle and surface waves will also be discussed. While these experiments were carried out in the laboratory, with both artificial and sunlight sources, the simplicity of the technique should permit its application to a variety of field conditions.

Introduction

Separating the fluorescence and elastic scatter/reflection components of fluorescing materials illuminated by white light (or sunlight) is of interest for a variety of environmental remote sensing, medical diagnostics, and colorimetry applications. These include the study of upwelling radiation from algae in sea water, where the magnitude of the fluorescence peak can be considered as a measure of chlorophyll concentration and photosynthetic activity, and the examination of coral reefs containing fluorescing pigments (Fuchs 2001, Gower *et al.* 1999, Gitelson *et al.* 2000, Szekielda *et al.* 2003). Separation of fluorescence and elastic scatter under white light illumination has been approached by a variety of techniques. These include dual monochromator techniques utilizing sources and detectors selectively tuned in tandem over appropriate spectral ranges to measure true elastic reflectance (Grum 1980). Band pass filters in wavelength sequences have also been used to separate elastic and inelastic components (Fuchs 2001). Polarization methods have also been widely used alone and in combination with other different methods for the improvement of the image visibility and separation of optical signals in turbid media (Scmitt *et al.* 1992, Demos, Alfano 1996, Morgan *et al.* 1997, Schilders *et al.*1998, Cunningham *et al.* 2002).

The new polarization discrimination technique recently developed by our group (Ahmed *et al.* 2002) makes use of the polarization properties of elastically scattered light and the unpolarized nature of excited fluorescence to separate the two components and thus extract the fluorescence component from the total reflectance spectra of algae in sea water excited by white light, including sunlight. The validity of the technique is confirmed by the excellent match between the spectral shape of fluorescence extracted in this manner and laser induced fluorescence of the same species. The technique is applicable to many situations of practical interest, with both polarized and unpolarized light sources, making it applicable for passive remote sensing with sunlight illumination.

We reported (Ahmed *et al.* 2004, Zhou *et al.* 2004, Gilerson *et al.* 2004) that the technique was successfully applied in the laboratory to four types of algae with different particle shapes (spheres, ellipsoids, plates) and different sizes (5-18μk), and concentrations up to 4x106 cells/ml. It was also shown that the approach had been tested with in-situ field measurements along eastern Long Island. The technique allows the extraction of fluorescence for the whole range of angles of illumination from 0o from zenith to 90o for polarized light sources (probe vertical) and up to 45o for unpolarized light and sunlight (Gilerson *et al.* 2004). In laboratory experiments this was found to holds true even with

surface waves when signal averaging of the detected signal is used. Comparison of our technique for polarized and unpolarized illumination with the other methods of the estimation of Chl concentration showed very good correlation with the calculation of fluorescence height over baseline (Abbott, Letelier, 1999).

In the work reported here, we include consideration of the efficacy of the technique for the extraction of fluorescence in the presence of additional scatterers.

Basic Features of the Polarization Discrimination Technique

The essential premise of the technique is based on the fact that light elastically scattered by the algae in water in a given direction will show greater or lesser degrees of linear polarization when illuminated by white light, depending on the incident polarization and angle of the illumination (Bohren, Huffman 1998), whereas fluorescence excited and emitted by these same algae is always unpolarized. This is also true for unpolarized light illumination, except for 180 degree backscatter or complete forward scatter. Thus if an analyzer is placed in front of a detector situated to detect the scattered light, Fig. 1, rotation of this analyzer will cause the detected light to vary from a minimum to a maximum depending on the degree of polarization of the scattered light. The respective spectra for maximum and minimum detected light, $R_{max}(\lambda)$ and $R_{min}(\lambda)$ obtained by rotating the analyzer consist of $R_{||}(\lambda)$ and $R_{\perp}(\lambda)$, the components of elastic scattering respectively parallel and perpendicular to the scattering plane, plus half the fluorescence $0.5Fl(\lambda)$ spectra due to the chlorophyll band in the algae (with a peak at 685 nm and a width at half maximum of 25 nm), which remains unchanged as the detector is rotated. These maximum and minimum detected signals may be expressed as:

$$R_{max}(\lambda) = R_{\perp}(\lambda) + 0.5Fl(\lambda), \qquad (1)$$

$$R_{min}(\lambda) = R_{||}(\lambda) + 0.5Fl(\lambda). \qquad (2)$$

The total signal $R(\lambda)$, is then given by

$$R(\lambda) = R_{max}(\lambda) + R_{min}(\lambda) =$$
$$= R_{\perp}(\lambda) + R_{||}(\lambda) + Fl(\lambda) \qquad (3)$$

and the total elastically scattered component is given by $R_s(\lambda) = R_{\perp}(\lambda) + R_{||}(\lambda)$. (4)

We will next examine how these relationships may be used to separate and extract the fluorescence component from the total signal, and hence separately obtain the fluorescent and elastically scattered components.

Polarized Illumination

To facilitate the discussion, we first examine the special case shown in the experimental arrangement of Fig. 2 with $i_1 = 90°$ and $i_2 = 0$ where the illumination is horizontally polarized (i.e. direction of polarization is perpendicular to the scattering plane formed by the axis of illumination and detection). Again we will have expressions for $R_{max}(\lambda)$, $R_{min}(\lambda)$ and $R(\lambda)$ given by equations (1)-(3). For this case single scattering theory (Bohren, Huffman 1998) shows (for particles large compared to the wavelength) the elastically scattered light will be polarized in the perpendicular direction and $R_{||}(\lambda)$ will be zero (when any depolarization caused by the finite numerical aperture and collection geometry limitations is negligible). Under these conditions, (2) reduces to: $Fl(\lambda) \approx 2R_{min}(\lambda)$ (5). We can obtain the total elastically scattered component $R_s(\lambda)$ subtracting the fluorescence $Fl(\lambda)$ from the total reflectance, thus, $R_s(\lambda) = R(\lambda) - Fl(\lambda)$. In this case of horizontally polarized illumination $R_s(\lambda)$ is the elastically scattered light that is polarized in the direction perpendicular to the scattering plane.

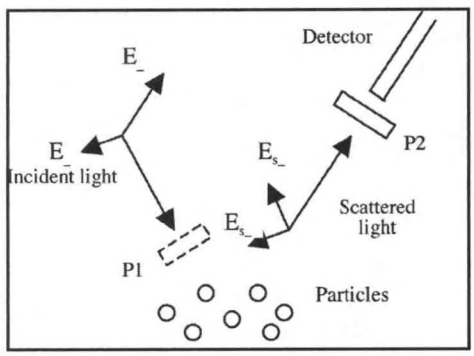

Fig.1. Scattering of the light on the particle. P1 – polarizer, P2 – analyzer.

Unpolarized Illumination

We now consider the more general case of unpolarized illumination. If the initial illumination is unpolarized, the resulting equation (3) would, along with a component $R_{\perp}(\lambda)$, now also have a significant non-zero component $R_{\parallel}(\lambda)$. In our previous work (Ahmed *et al.* 2004) , (explanation discussed below) it was found that a strong linear correlation exists between the difference signal

$$R_D(\lambda) = R_{max}(\lambda) - R_{min}(\lambda) = \\ = R_{\perp}(\lambda) - R_{\parallel}(\lambda) \qquad (6)$$

(which has had fluorescence components eliminated in the subtraction process) and the sum signal outside the fluorescence zone (4) $R_s(\lambda) = R_{\perp}(\lambda) + R_{\parallel}(\lambda)$.

If the correlation between the sum and difference spectra extends into the fluorescence zone, then, the fluorescence can be easily extracted, so that $Fl(\lambda) = R(\lambda) - R_s(\lambda)$ (7). Making use of the assumption that $R_D(\lambda)$ and $R_s(\lambda)$ for the elastic scattering are linearly correlated throughout the spectral range, linear regression is performed to fit the function $R_D(\lambda)$ in the 450 - 670 nm range (outside the fluorescence spectral region) into $R(\lambda)$. The regression parameters were then used to calculate the scattering spectrum $R_s(\lambda) = AR_D(\lambda) + B$ for the whole wavelength range 450 – 750 nm. The fluorescence $Fl(\lambda)$ component in the total spectrum $R(\lambda)$ can then be obtained from equation (7). The validity of the near linearity assumption between $R_D(\lambda)$ and $R_s(\lambda)$ and appears borne out by experimental results and can be understood in terms of Kramers-Kronig analysis (Ahmed *et al.* 1989) and the simulation model described (Ahmed *et al.* 2004) for scattering by particles with complex refractive index where the real part n' relative to the water is small (less than 1.06) and the elastic scattering process is dominated by the imaginary, absorptive component, and hence largely independent of polarization. Under these conditions, the spectral dependence of both $R_{\parallel}(\lambda)$ and $R_{\perp}(\lambda)$ will be essentially the same, and the two will be linearly related.

Experimental Results

Experiments were carried out with both polarized and unpolarized sources, including sunlight, both in the laboratory and in the field. The basic laboratory experimental set-up is that shown in Fig. 2. The details of this set-up were explained before (Ahmed *et al.* 2004, Gilerson *et al.* 2004). Experiments were carried out with pure algae as well as with additions of different concentrations of 2 types of clay: Na-Montmorillonite and Ca- Montmorillonite. The algae Isochrysis sp. are largely spherical with approximately 5 μm diameter. Concentrations tested were approximately 106 cells/ml. Both types of clay additives: Na-Montmorillonite and Ca-Montmorillonite have particulates with diameters in the range 2-6 μm. The concentration of clay was varied from 10 mg/L to 1000 mg/L.

To examine the impact of additional scattering on the application of the polarization discrimination fluorescence measurement technique, clay particles were added to a constant concentration of algae in seawater. Addition of the clay particles is found to lead to both an increase of scattering/reflections as well as a change of the shape of the total scattering/reflectance spectrum. Scattering and fluorescence from the mixture was investigated using both polarized and unpolarized light sources. With clay concentrations ranging from 10 mg/L to 500 mg/L the fluorescence magnitude and shape extracted by the technique remained almost the same as with pure algae. Angle of illumination i_1 (Fig.2) was 90°. There were no significant differences in results in using the technique with either 2 polarizers or 1 polarizer. Fig. 3 shows the total scatter/fluorescence signal, $R(\lambda)$, , obtained

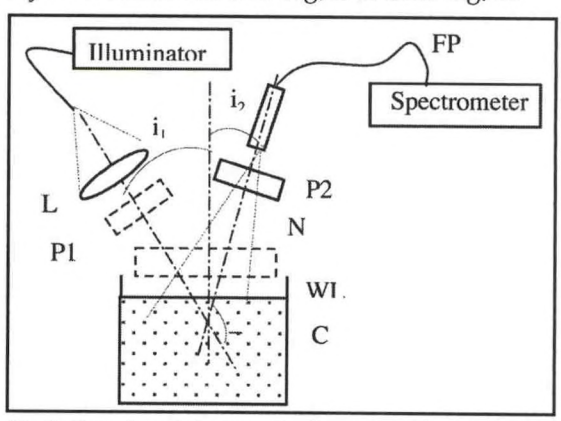

Fig.2. Experimental set-up. L – lens, FP – fiber probe, A – aperture, P1, P2 – polarizer and analyzer, C – cuvette with algae, WL – water level, N – air nozzle for creation water surface roughness.

for different concentrations of clay while keeping the algae concentration constant. Comparison of extracted fluorescence for pure algae and for high concentration of clay with the algae is also shown in Fig. 3.

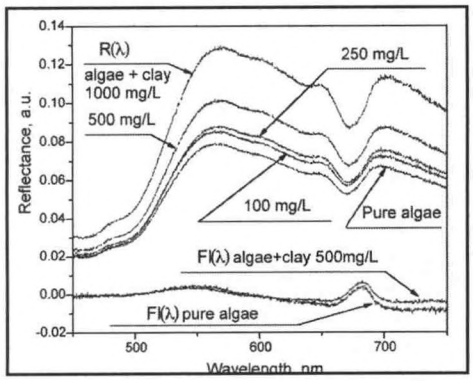

Fig.3. Reflectance curves and extracted fluorescence for different concentrations of clay with the algae. Algae Isochrysis sp, clay Na-Montmorillonite.

It is interesting to note that even at the high clay concentrations, in the multiple scattering regime, the extracted fluorescence was a very good match with the pure algae case, confirming applicability of the technique in these conditions. Application of the proposed technique in the multiple scattering regime needs further investigation.

To understand the range of possible applicability of technique with different types of clays we measured reflectance spectra of the pure clays in seawater for polarized and unpolarized illumination and 2 mutually perpendicular positions of polarizer in front of detector. Concentrations of clay for both types of clay Na-Montmorillonite and Ca-Montmorillonite varied from 50 mg/L to 500 mg/L. One pair of the spectra for unpolarized light source is shown in Fig. 4. Application of the regression procedure explained in Section 2 for these spectra showed very good fit of $R_D(\lambda) = R_{max}(\lambda) - R_{min}(\lambda)$ into $R_s(\lambda) = R_{\perp}(\lambda) + R_{||}(\lambda)$. Correlation coefficient for spectra in Fig.4 was 0.9867. Similar numbers have been obtained for other conditions for both types of clay. This explains successful retrieval of fluorescence presented in Fig. 3 as well as gives the possibility of the usage of technique in different conditions with additional scatterers.

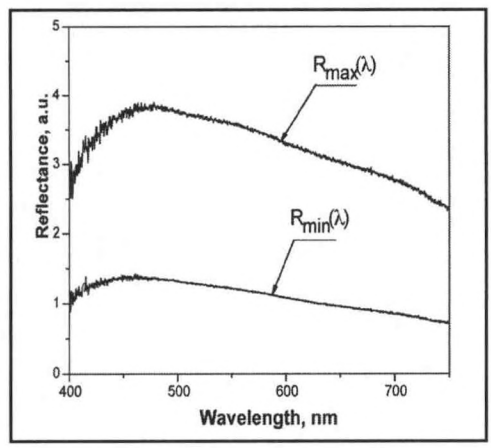

Fig.4. Spectra for the pure clay Na-Montmorillonite in seawater with unpolarized light source and different positions of polarizer in front of the detector. Concentration of clay 500 mg/L.

Conclusions

The results of recent experiments and analysis on the polarization discrimination technique developed by us to separate elastic reflectance and fluorescence components resulting from white light illumination of algae in seawater was successfully applied to measurements of algae of different sizes and shapes in the laboratory. It is shown that fluorescence can be effectively extracted for any angle of illumination with a polarized light source, and less accurately but still reliably with unpolarized light in certain ranges of illumination angles. Magnitudes of the fluorescence peak extracted through polarization discrimination correlate very well with the peaks of the reflectance curves over the baseline for different concentrations of algae. The results of experiments on the impact of surface roughness on the efficacy of the technique show that even in presence of appreciable surface roughness the fluorescence can be accurately extracted with appropriate time averaging during the spectral acquisition process.

Fluorescence also can be successfully retrieved from the algae with different concentrations of clays like Na-Montmorillonite and Ca-Montmorillonite with polarized and unpolarized light sources.

ACKNOWLEDGEMENTS

This work is supported by grant from NOAA #NA17AE1625.

REFERENCES

Abbott, M.R., and R.M. Letelier, 1999: Chlorophyll fluorescence. ATBD-MOD-22.

Ahmed, S., M.A. Ali, K. Mitwally, and M. El-Massry, 1989: Optical refractive and reflective properties of resonantly absorbing media. J. Chem. Phys. **91**, 3838-3845.

Ahmed S., A. Gilerson, A. Gill, B. M. Gross, F. Moshary, and J. Zhou, 2004: Separation of Fluorescence and Elastic Scattering from Algae in Seawater Using Polarization Discrimination. Opt. Comm., **235**, 23-30.

Bohren, C.F., and D.R. Huffman, 1998: Absorption and Scattering of Light, Wiley, John & Sons.

Cunningham, A., P. Wood, and D. McKee, 2002: Brewster-angle measurements of sea-surface reflectance using a high resolution spectroradiometer. J. Opt. A: Pure Apl. Opt. **4**, S29-S33.

Demos, S.G., and R.R. Alfano, 1996: Temporal gating in highly scattering media by the degree of optical polarization. Opt. Lett., **21**,161-163.

Fuchs, E., 2001: Separating the fluorescence and reflectance components of coral spectra. Appl. Opt., **40**, 3614-3621.

Gilerson, A., J. Zhou, A. Gill, B.M. Gross, F. Moshary and S. Ahmed, 2004: Properties and Potential of a Polarization Technique for the Separation of the Overlapping Fluorescence and Elastic Scattering Applied to Algae in Seawater. Proceedings of SPIE, **5569** (In press).

Gitelson, A.A., Y.Z. Yacobi, D.C. Rundquist, R.Stark, L.Han, and D. Etzion, 2000: Remote estimation of chlorophyll concentration in productive waters: Principals, algorithm development and validation. Proc. of **NWQMC**, 149-160.

Gower, J.F.R., R. Doerffer, and G.A. Borstad, 1999: Interpretation of the 685 nm peak in water-leaving radiance spectra in terms of fluorescence, absorption and scattering, and its observation by MERIS. Int. J. Rem. Sens. **20**, 1771-1786.

Grum, F., 1980: Colorimetry of fluorescent materials in *Optical Radiation Measurements*, Chap. 6, vol. 2, Academic, New York.

Morgan, S.P., M.P. Khong, and M.G. Somekh, 1997: Effects of polarization state and scatterer concentration on optical imaging through scattering media. Appl. Opt., **36**, 1560-1565.

Schilders, S.P., X.S. Gan, and Min Gu, 1998: Effects of scatterer size on microscopic imaging through turbid media based on differential polarization-gating. Opt. Comm., **157**, 238-248.

Schmitt, J.M., A.H. Gandjbakhche, and R.F. Bonner, 1992: Use of polarized light to discriminate short-path photons in the multiply scattering medium. Appl. Opt., **31**, 6535-6546.

Szekielda K.H., C .Gobler, B. Gross, F. Moshary, and S. Ahmed, 2003: Spectral reflectance measurements of estuarine waters. Ocean Dynamics, **53**, 98-102.

Zhou, J., A. Gilerson, A. Gill, B. M. Gross, F. Moshary and S. Ahmed, 2004: Polarization discrimination technique to separate overlapping fluorescence and elastic scattering applied to algae in seawater. Proceedings of SPIE, **5544** (In press).

REMOTE CHLOROPHYLL ESTIMATION IN COASTAL WATERS WITH TRIPTON AND CDOM INTERFERENCES

Christine Hladik[1], John F. Schalles[1], and Kevin Dillon[2]

[1]Department of Environmental and Atmospheric Science, Creighton University, Omaha, NE 68178 USA
[2]Environmental Sciences Institute, Florida A&M University, Tallahassee, FL 32307

We are testing variants of semi analytic algorithms for estimating chlorophyll pigment. Our approach attempts to adjust for the signal amplification effects of tripton particles and the signal dampening effects of CDOM in turbid, Case 2 waters. As part of a larger NOAA-ECSC remote sensing project, we've made close range measurements since 2002 at five coastal sites (Delaware, South Carolina, Georgia, Florida, and Mississippi) with diverse optical properties. A dual Ocean Optics USB2000 system was used to simultaneously measure solar downwelling and upwelling radiance or water-leaving radiance (below surface and above surface data were collected at each station). Sampling was designed to capture the upriver and coastal water mixing gradients in each estuary. Additionally, blue water stations in the Western Caribbean (Roatan Island) were measured as a Case 1 benchmark and contrast. Our algorithms utilize chlorophyll absorption and phytoplankton cell scattering and fluorescence features in the red and lower NIR regions, with interference adjustments using bands in the blue and green regions. These data, in turn, will also be used to calibrate airborne water data from an AISA imaging spectrometer flown at or near the time of our close range sampling.

Bio-Optical Properties and Remote Sensing of Mayaguez Bay

Fernando Gilbes, Ph.D.

Geological and Environmental Remote Sensing Laboratory
Department of Geology, University of Puerto Rico at Mayagüez

The application of remote sensing in coastal environments has been very difficult because of the optical complexity of these waters. Seasonal river discharge and land run-off increase the concentration of phytoplankton biomass along with colored dissolved organic matter and suspended sediments. Such conditions make that conventional remote sensing techniques do not work properly. Therefore, in order to estimate these water quality parameters in coastal waters is necessary a new approach where all sources responsible for the optical variability are considered in the interpretation of the remote sensing signal. In Puerto Rico, a large effort has been done during several years in order to better understand the bio-optical properties of Mayagüez Bay. This semi-enclosed bay in the west coast of Puerto Rico suffers spatial and temporal variations in phytoplankton pigments and suspended sediments due to seasonal discharge of local rivers. Several years ago a joint project with researchers from NASA Stennis Space Center and the University of Puerto Rico at Mayagüez intended to use remote sensing for a better understanding of the land-sea interface in this bay. However, the complexity of bay's optical properties and certain limitations of the technology at that time made it very difficult. New efforts using improved methods and better instruments are accomplishing the original objectives. Here we summarized some of the research work in Mayagüez Bay toward a better understanding of the bio-optical properties and the application of digital imagery in coastal waters. The work also involves the development of new site-specific bio-optical algorithms. These efforts are extremely relevant with several NOAA programs related to remote sensing of coastal waters, like the Coast Watch Program. This research has been partially supported by the NOAA CREST project from the University of Puerto Rico at Mayagüez.

HYPERSPECTRAL SENSING OF COASTAL WATERS: THE GOES-R COASTAL WATER IMAGER

Marco Vargas, Barry Gross Fred Moshary, Samir Ahmed
Optical Remote Sensing Laboratory, NOAA CREST Center, City College of New York

Abstract

The Hyperspectral Environmental Suite (HES) on GOES-R offers the possibility of well calibrated hyperspectral coverage with threshold footprints on the order of 1km making this instrument the prototype for hyperspectral sensing (with continuous 10nm coverage) of coastal waters. Unlike deep ocean (case I) waters, coastal waters (case II) are more complex and besides the organic algae signifying productive waters, case II waters also contain inorganic particulates (TSS) as well as dissolved organic matter (CDOM) making quantification of Chlorophyll (CHL) concentrations much more complex. In this presentation, we first illustrate that chlorophyll in deep turbid waters can be related to band ratios in the red portion of the spectrum. However, when shallow waters are present, we show first that hyperspectral sensor configurations are required to obtain simultaneously ocean water parameters and ocean bottom parameters in turbid shallow waters.

Introduction

Satellite retrieval algorithms are generally only suitable for type I (ocean water) systems. Water near coastal regions is far more complex including a host of organic and inorganic materials which makes the water signal far more complicated. The research to date has looked at the feasibility of using reflectance spectra near the absorption feature of the second absorption band instead of the fluorescence regime in the blue. In this regime, closely separated sensors on MODIS are available and can be used. Other advantages include the far simpler atmospheric corrections that are required. However, disadvantages include the lower S/N at these wavelengths so obvious trade off studies need to be explored. Besides the Modis sensor, the Hyperspectral Environmental Suite (HES) on GOES-R offers the possibility of well calibrated hyperspectral coverage with threshold footprints on the order of 1km making this instrument the prototype for hyperspectral sensing (with continuous 10nm coverage) of coastal waters. Unlike deep ocean (case I) waters, coastal waters (case II) are more complex and besides the organic algae signifying productive waters, case II waters also contain inorganic particulates (TSS) as well as dissolved organic matter (CDOM) making quantification of Chlorophyll (CHL) concentrations much more complex. However, with hyperspectral coverage near both the absorption and fluorescence bands of CHL, hyperspectral algorithms which are less sensitive to both water contaminants and atmospheric corrections can be implemented.

Ratio Algorithms

The conventional algorithms for the retrieval of the sea water constituents such as the chlorophyll concentration are usually based on the ratio of radiance or reflectance measured in the blue and green spectral bands. A polynomial is usually used to represent the relation between the logarithm of the band ratios and the logarithm of chlorophyll concentration. The coefficients of the polynomial are found by regression between the band ratios and the sea-truth value of chlorophyll concentration measured from water samples taken at various places. This method based on band ratios works reasonably well in open ocean waters (case I waters), where chlorophyll and covarying substances such as detritus determine the optical properties. Case II waters are characterized by high concentrations of chlorophyll, CDOM, and suspended matter. The scattering and absorption characteristics are now determined not only by chlorophyll, but also by CDOM and non-chlorophyllous suspended matter. Coastal sea waters are typically case II waters. The simple band ratio algorithms that work in deep

ocean waters do not work well for this category of waters and other "hyperspectral" band algorithms are needed. In particular, we investigate the use of differential signal ratios where both wavelengths lie in the 2nd absorption band of Chlorophyll.

Procedure

Reflection Measurements taken with a fiber spectrometer in Long Island Sound along with simultaneous measurements of Chlorophyll content taken at LIU and NASA were used to study the correlation between chlorophyll A concen eflectance. In particular, the most important aspect was to examine the impr made by looking at the correlation between band ratios and chlorophyll co ary results show that correlations between chlorophyll ratios defined as have a higher correlation than the

$$R_{rat}(\lambda) = \frac{R(\lambda)}{R(\lambda = 670)}$$

reflectance spectrum alone as long as the ratios are taken within the absorption feature. The correlation between concentration and reflection ratios defined as above are shown below. Note in particular, the marked improvement when ratio bands are used.

Figure 1. Chlorophyll vs Reflection

To obtain preliminary assessment of the remote sensing capabilities, we will begin by examining parameterized bio-optical models which depend on a small number of regression estimated parameters including TSS, CHL and ABSCDOM. The model may be briefly defined as

$$b_{tot}(\lambda) = \frac{b_w(\lambda)}{2} + b1 \times b2 + b_{TSS}$$

$$b1 = \left[0.002 + 0.02(1/2 - 1/4\log(CHL))\left(\frac{550}{\lambda}\right)\right]$$

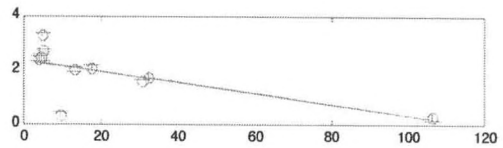

$$a_{total}(\lambda) = \left[a_{cdom}(\lambda) + a_{det}(\lambda) + a_{phyt}(\lambda) + a_{water}(\lambda)\right] m^{-1}$$

where the data has been processed with correction procedures to help account for variability of the illumination geometry, b represents the total volume backscatter coefficient and a is the total attenuation.The backscatter is comprised of an empirical model including the background water, the chlorophyll scattering model component and a TSS mode:

$$a_{cdom}(\lambda) = a_y(\lambda_0)\exp[-0.014(\lambda - \lambda_0)] m^{-1}$$

$$a_{phyt}(\lambda) = P_0 a_0(\lambda) + P_1 a_1(\lambda)$$

$$P_1 = P_0 \times \ln\left(\frac{P_0}{1055}\right) m^{-1}$$

$$P_0 = 0.02062[CHL]^{1.291} m^{-1}$$

$$a_{det}(\lambda) = a_{det}(\lambda_0)\exp[-0.011(\lambda - \lambda_0)] m^{-1}$$

Recent work suggests modeling of the TSS backscatter trough a total surface area parameter X and a λ^{-1} wavelength dependence.

Preliminary calculations will focus on determination of the best optical data ratios that yield high correlations and linearity which are robust against CDOM and TSS parameters As an example, for all combinations of ratio spectra $R_{ij} \equiv \frac{R(\lambda_i)}{R(\lambda_j)}$ ı the 390nm to 730nm range, the first panel shows regions

where the ratio $R_{ij}(CHL, B_{TSS}, \alpha_g, \alpha_{\det})$ deviation between case I (all turbidity and CDOM parameters =0) and turbid (parameters set to largest values) is small while the second panel shows for the case of small deviations, which band ratios have the highest dynamic range. It is clear that the 710/680nm and nearby bands are most suitable combining large dynamic range with low perturbations.

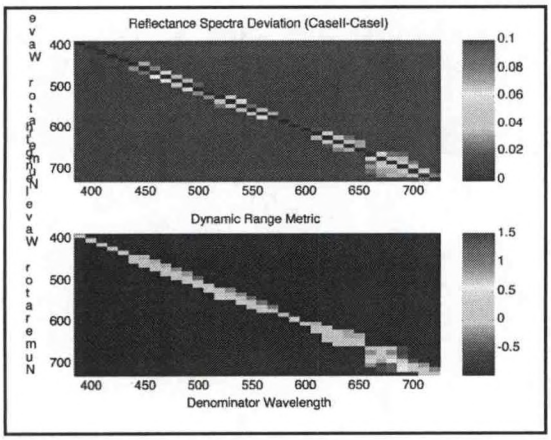

Figure 2. Optimized ratios

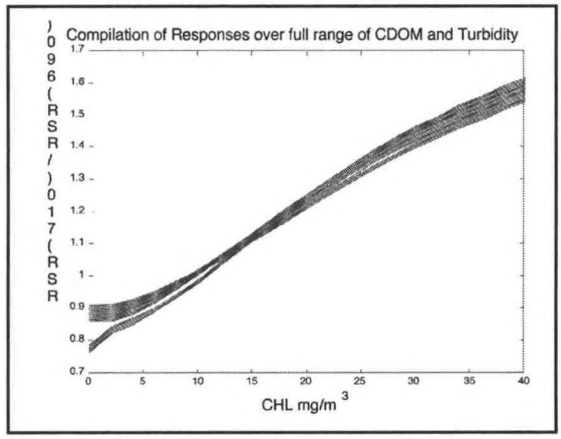

Figure 3. Rsr vs Chlorophyll

Magnitudes of the deviations of the selected band ratios between over the entire range of reasonable case II parameters shows clearly the suitability of this ratio against both water impurities and atmospheric correction for CHL concentrations > 10mg/m3. To begin an analysis of channel sensitivity, we explore the RSR (case I) with 1% uncorrelated gaussian noise which is shown in the graph below. From this graph, we can see that over the entire range of CHL concentrations, errors on the order of $\Delta CHL \approx 1\, mg/m^3$ are obtained.

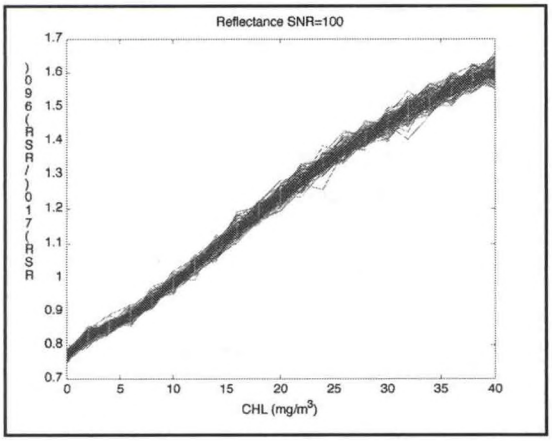

Figure 4. Rsr sensitivity to noise

Hyperspectral Sensing by Optimization

Hyperspectral sensors are required to perform quantitative analysis of coastal waters. Case II waters such as coastal waters with a high sediment load usually have a higher reflectance in the visible wavelength region than the clear case I waters in the open oceans. Hence, the signal to noise ratio of hyperspectral sensors over coastal waters may be sufficiently high, such that meaningful measurements of the optical properties of the coastal waters may be possible.The engine of calculation uses a coastal type bio-optical model existing in the literature (Lee et all 1999) that provides simultaneous retrieval of depth, surface albedo intensity, and inherent optical properties of absorption and

backscatter. The model is defined as: $R_{RS}(\lambda) = \frac{0.5 r_{rs}}{1 - 1.5 r_{rs}}$

R_{RS} = Above water r_{rs} = Below wate.

$r_{rs} = r_{rs}^{c} + r_{rs}^{B}$

$b_b(\lambda)$= total backscatter $a(\lambda)$= total extinction

$a_{total}(\lambda) = a_w(\lambda) + a_{\varphi}(\lambda) + a_g(\lambda) m^{-1}$

$a_w(\lambda)$ is the absorption coefficient due to water.

$a_j(\lambda)$ is the absorption coefficient due to phytoplankton.

$a_g(\lambda)$ is the absorption coefficient due to gelbstoff.

$b_{tot}(\lambda) = b_{bw}(\lambda) + b_{bp}(\lambda)$

$b_{bw}(\lambda)$ is the backscattering of water.

$b_{bp}(\lambda)$ is the backscattering of particulate matters.

$a_g(\lambda) = G \exp(-S(\lambda - 440))$

G is the gelbstoff absorption at 440 nm.

$a_{\varphi}(\lambda) = [a_0(\lambda) + a_1(\lambda) \ln(P)]P$

$a_0(\lambda) and a_1(\lambda)$

taken from tabulated values in lee et al.

$$b_{bp}(\lambda) = X\left[\frac{440}{\lambda}\right]^{Y}$$

X is the backscattering coefficient of particulates at 440 nm. Y gives an indication of the size particles H is the bottom depth and B is the bottom albedo value at 550 nm. defined as $\rho_B = B\rho_{sd}(\lambda)$ where water bottom (lambertian). using sand based normalized spectral response.

The parameters in the shallow reflectance model (case II) to be retrieved are: P,G,X,Y,H,B. For open ocean waters (case I) the model reduces to a four parameter model, and the parameters retrieved

$$r_{rs}^{c} = r_{rs}^{dp}\left(1 - \exp\left\{-\left[\frac{1}{\cos(\theta_w)} + D_u^{c}\right]\kappa H\right\}\right)$$

$$r_{rs}^{B} = \frac{1}{\pi}\rho_B \exp\left\{-\left[\frac{1}{\cos(\theta_w)} + D_u^{B}\right]\kappa H\right\}$$

$$r_{rs}^{dp} = (0.084 + .170u)u \quad D_u^{c} = 1.03(1 + 2.4u)^{0.5}$$

$$D_u^{B} = 1.04(1 + 5.4u)^{0.5} \quad u \equiv \frac{b_b}{a + b_b} \quad \kappa \equiv a + b_b$$

are: P,G,X,Y. The spectral bands used in the multispectral simulation are: 412,443, 477,490,510,530, 550, 645, 667, and 678 nm. corresponding to the Multispectral specification of GOES-R. For the hyperspectral case 37 bands are used corresponding to GOES-R

Results

The following plots show the comparison (Hyperspectral vs. Multispectral) of the retrieved parameters. Notice that for the hyperspectral case a significant level of improvement is obtained .

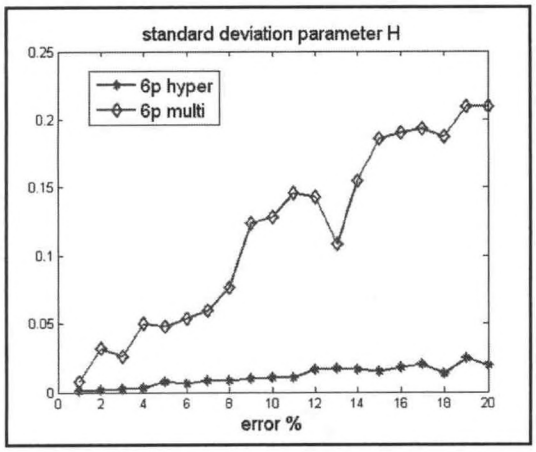

Figure 5. Parameter H

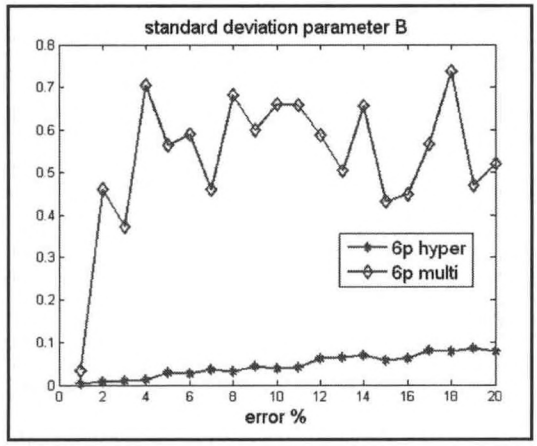

Figure 6. Parameter B

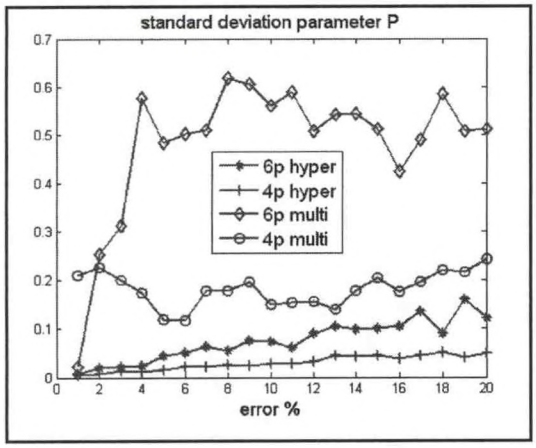

Figure 7. Parameter P

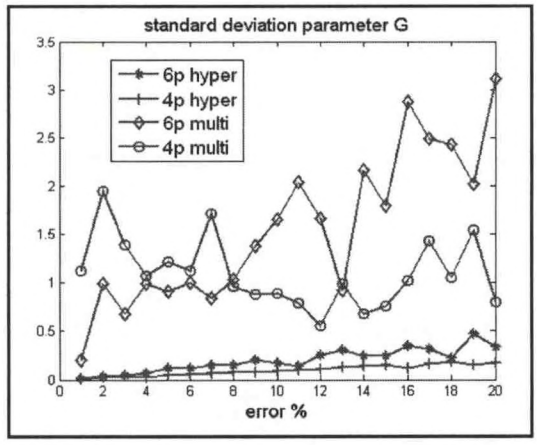

Figure 8. Parameter G

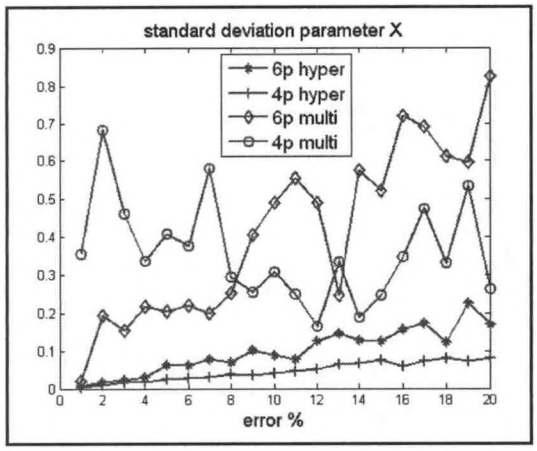

Figure 9. Parameter X

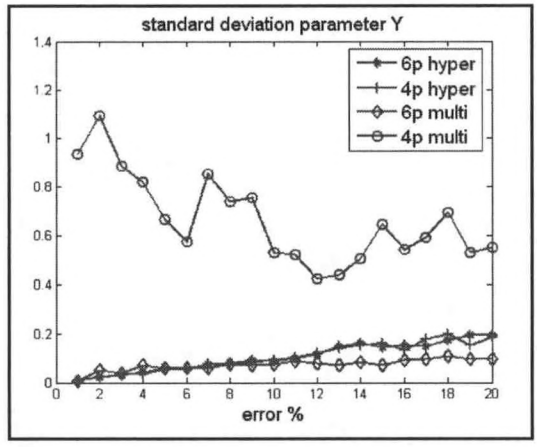

Figure 10. Parameter Y

Conclusions

Preliminary analysis of a shallow water bio-optical model show that Hyperspectral channels are needed to reduce errors in shallow bottom heights and reflectance. In addition, ocean column parameters are also much better retrieved using Hyperspectal configuration except for spectral slope of backscatter parameter which makes sense since this parameter caused only broad modification of the reflectance spectra. Furthermore, there a factor of two degradation in retrieving water column parameters between shallow and deep waters except for the spectral slope which seems to be recoverable with the same accuracy

Future work

Due to the wide spectral coverage of HES, spectral inversion of bio-optical model parameters appears feasible. Research will focus on the inversion information content between bio-optical models over the 390-730nm band and preliminary inversion of field Reflectance spectra taken with the GER spectrometer. In particular, we are interested in matching up insitu spectral data directly with the full spectral reflectance measurments to test the validity of other bio-optical models. Finally, controlled experiments in the lab will be performed to better quantify the remote sensing on particulate parameters such as total scattering volume, optical scattering volume and improved bio-optical models for TSS.

Future work involves the simultaneous retrieval capabilities of hyperspectral sensors of atmosphere and water parameters using a simplified decoupled atmosphere ocean model initially and then assessing the need to consider more realistic ocean-atmosphere models.

ACKNOWLEDGEMENTS

This work is supported by grant from NOAA #NA17AE1625. We would also like to thank Raytheon for their support of this project.

REFERENCES

Lee Zhongping, Kendall L. Carder, Curtis D. Mobley, Robert G. Steward, and Patch, J. S. *"Hyperspectral remote sensing for shallow waters. I. A semi analytical model," Applied Optics*, vol. 37, No. 27, 6329-6338 (1998).

Lee, Z. K.l.Carder,C.D.Mobley,R.Steward, and J.Patch, *Hyperspectral remote sensing for shallow waters: 2. Deriving bottom depths and water properties by optimization. Applied Optics*, 38, 3831-3843 (1999)

ORAL SESSION A2

Marine Resources Managemen

MICROBIAL EXTRACELLULAR POLYMERS (EPS) FROM A COASTAL GEORGIA MUDFLAT: THEIR ABUNDANCE AND AVAILABILITY TO THE BENTHOS

D. L. Hoskins

DOC/NOAA/NMFS and Marine Science Program, Savannah State University, Savannah, Georgia, USA 31404

Research on bacterial extracellular polymers (EPS) has shown that soluble EPS can be utilized by several deposit-feeders and that bioavailability depends on the composition and structure of the polymer (Decho & Moriarty 1993; Hoskins et al. 2001 & 2002). However, feeding studies have most often used laboratory-cultured EPS that is not representative of EPS found in naturally occurring biofilms. Before the nutritional role of these exudates in marine sediments can be determined it is necessary to characterize their occurrence. The objective of this research was to examine the EPS found in sediments on a mudflat in coastal Georgia. The study site was characterized by a cyanobacterial mat that dominated the microbial community in the winter and shifted to a diatom film in the summer. An additional goal was to assess whether the carbohydrates present were in a form or quantity trophically important for the deposit- feeders present.

Monthly cores (10 intertidal, 10 subtidal) were taken from December 2001-2002. Twenty small cores (3x15cm) were extracted for EPS and 20 large cores (7x15cm) were sorted for macrofauna. Large cores were fixed in 10 % formalin & Rose Bengal, sieved on a 500 mm sieve, and sorted to the lowest taxa. For EPS measurement, small cores were fixed in 10 % formalin then suspended 1:1 in deionized water (by sediment weight) to dissolve soluble EPS modifying a method by Decho (1990). The water was decanted and centrifuged and the supernatant was precipitated three times in cold 70% ethanol. The precipitated EPS was dialyzed 24 hours, lyophilized, then weighed. Compositional analysis was performed on hydrolyzed samples by the Complex Carbohydrate Research Center (University of Georgia) using a gas chromatograph with a Supelco column (Supelco Incorporated). Differences in EPS concentration, its composition, and the associated macrofaunal community were compared seasonally as the dominant microbial community shifted.

Polychaetes and nematodes were the dominant fauna followed by *Nebalia spp.* shrimp and juvenile crabs, each varying significantly by month ($p<0.051$). Capitellid worms were most consistently present. Carbohydrate analysis detected seven sugar monomers (arabinose, rhamnose, mannose, glucose, xylose, fucose, and galactose) and two uronic acids, glucuronic and galacturonic acid. The most abundant sugars were mannose galactose and glucose, but varied widely with other sugars like fucose and xylose. The mixture of sugars was likely due to microbial diversity, the presence of adsorbed compounds, and the mixed physiological state of community. When considered per unit sediment mass, total EPS at this site is very small and an order of magnitude lower than published values (Underwood et al. 1995). This data suggests that the diatom and cyanobacterial EPS in this community may be very similar in composition and that EPS exists in quantities that may be very important to for meiofauna. However, for the macrofaunal deposit feeders, the importance of EPS is probably episodic.

Literature Cited

Decho A. W., and D. J. W. Moriarty. 1990. Bacterial exopolymer utilization by a harpacticoid copepod: a methodology and results. Limnol. Oceanogr., 35(5), 1039-1049

Decho A. W., 1993: Methods for the observation and use in feeding experiments of microbial exopolymers. In: PF Kemp, BF Sherr, EB Sherr, and JJ Cole (eds) *Handbook of Methods in Aquatic Microbial Ecology*. Lewis Pub. Ann Arbor, Michigan p. 685-694.

Hoskins D. L., S. E. Stancyk, A. W. Decho, 2002: Utilization of algal and bacterial extracellular polymeric secretions by the deposit-feeding brittlestar *Amphipholis gracillima* (Stimpson). Mar. Ecol. Prog. Ser., 247, 93-101

Hoskins D. L., S. E. Stancyk, A. W. Decho, V. P. Lewis, J. Baynes, 2001: Digestion of Biofilm Carbohydrates by the Deposit-Feeding Brittlestar *Amphipholis gracillima* (Stimpson) (*Ophiuroidea: Amphiuridae*). Proc.10th Int. Echin. Conf., Dunedin, NZ (ed: M. F. Barker. Balkema, Rotterdam)

Underwood GJC, Paterson DM and Parkes RJ. 1995. The measurement of microbial carbohydrate exopolymers from intertidal sediments. Limnol. Oceanogr. 40(7):1243-1253.

Applications of Moderate Spectral Resolution Sensor Data in National Estuarine Research Reserves

Katherine Milla

Director, Laboratory for Remote Sensing and Spatial Analysis Environmental Cooperative Sciences Center, Florida A&M University

Multispectral digital imagery collected from airborne and satellite platforms are commonly used for characterizing water quality and delineating aquatic and wetland vegetation on a regional scale. Reflectance data from distinct spectral bands in the visible and infrared portions of the spectrum have enabled the quantification of spectral characteristics that can be used to distinguish features on the surface of the Earth.

Most multispectral images consist of a small number of spectral bands, in the range of 3 to 10. Recent advances in sensor technology have resulted in the ability to acquire images of moderate (tens of bands) to very high (hundreds of bands) spectral resolutions. This increased resolution makes it possible to distinguish features with greater detail. Potential applications in coastal environments include the possibility of distinguishing different species of vegetation (for example, native vs. introduced invasive species) and deriving more detailed water quality parameters from a remote platform.

The Environmental Cooperative Sciences Center (ECSC) has acquired digital imagery using the AISA sensor over four National Estuarine Research Reserve (NERR) sites: Apalachicola NERR in north Florida, ACE Basin NERR in South Carolina, Grand Bay NERR in Mississippi, and Delaware Bay NERR in Delaware. AISA is an airborne sensor capable of acquiring data of both high spatial and moderate to high spectral resolution. Data at the NERR sites was collected at spatial resolutions of 1.5 to 3 meters, and spectral configurations of 20 to 31 bands in the spectral range of 440 to 900 nm. This presentation will discuss some of the current ECSC research projects using AISA data collected at NERR sites.

METAL CONCENTRATIONS IN LOGGERHEAD SEA TURTLE EGGS FROM THE FLORIDA GULF AND ATLANTIC COASTS

Aaron J. White [1]*, Mark Harwell[1], Dragosloav Marcovich[2]

1 Florida A&M University, Environmental Sciences Institute, Tallahassee FL, 32307

2 U.S. Environmental Protection Agency, Gulf Ecology Division, Gulf Breeze, FL, 32561

Introduction

Loggerhead sea turtles are known to nest along the Florida Coast (Alam and Brim 2000). These nesting sites have been relatively protected, but these and all other species of sea turtles are still being affected by human perturbations. There are several federal and local measures in effect to protect sea turtles, e.g. the Federal Endangered Species Act (1973) and Florida's Marine Turtle Protection Act, Section 370.12 of Florida Statutes; however, they are incapable of protecting the entire migratory range of the turtle (Wold 2002). Therefore indirect influences may still be harming them. Non-point as well as point sources of pollution load coastal rivers with excess contaminants, including metals. Eventually these metals end up in the larger bodies of water, e.g. the Gulf of Mexico and the Atlantic Ocean. In the Gulf of Mexico alone, there are over 3,700 point source discharges. This is higher than any other US coastal region (Lewis et al. 2002). Once in the ecosystem, many metal contaminants become available for bioaccumulation to higher trophic level species.

Of the seven species of sea turtles, the loggerhead (*Caretta caretta*) is the most prevalent to nest on the Florida peninsula and panhandle. They are known to nest in most of the coastline counties in the state. Tagging data since the late fifties have shown that females can travel over 1000 miles away from the nesting beach before returning (Caldwell et. al. 1959).

Loggerhead turtles have been known to live for over one hundred years, become sexually mature in about 15 years, and the females tend to nest several times a season (Alam and Brim 2000). They are generally omnivorous during their first stage of life, or pelagic phase feeding on mainly cephalopods, plankton, and zooplankton (Alam and Brim 2000). As they get older, the turtles become more carnivorous, feeding on benthic invertebrates like mollusks and crustaceans (Alam and Brim 2000; Caurant et al. 1999).

Catching live turtles for research purposes is problematic since killing live turtles is illegal. One way for determining metal body burdens is to use turtles that have died and washed onshore. However, Saki et al. (1995) stated the best method for monitoring metal accumulation is through eggs; see also Alam and Brim 2000, Clark and Krynitsky1980, Stoneburner et al. 1980.

The main objective of this study was to measure metal accumulations in sea turtle eggs collected along two beaches of the Florida peninsula and panhandle. Eggs collected from the beaches of St. George Island in Franklin County, on the Gulf Coast of northwest Florida, and from the beaches of Flagler County on the Atlantic coast of northeast Florida. Supplementary objectives were to compare intraclutch variation in eggshells and egg yolks from a single sea turtle nest; and determine if there has been an increase in the amount of metals found in eggs collected from St. George Island since the study by Alam and Brim (2000).

Method

The first stage of the study consisted of the sample collection during the sea turtle hatching season, which begins in July and continues until mid-October. The next stage was the sample preparation phase. During this stage the egg yolks were separated from the eggshells and placed into 50ml

Falcon® conical tubes. Once in the conical tubes, the samples were lyophilized and digested. Finally, the last stage included the sample analysis and statistics.

Study Sites

The sites sampled in this study were located in Flagler and Franklin Counties in Florida, see Figure 1. Sea turtle nests have been found along a 27.4 km span of Flagler County's beaches. In 2001, this area alone had 278 loggerhead nests (FMRI 2002).

Turtle nests in Franklin County were sampled once before in the study published by Alam and Brim (2000). This area is of interest because it is the central location of the Apalachicola National Estuarine Research Reserve (ANERR). Franklin County is near the center of the panhandle in Florida, between Tallahassee and Pensacola, FL. The beach's survey length consists of 19.3 km; in 2001, there were 315 nests.

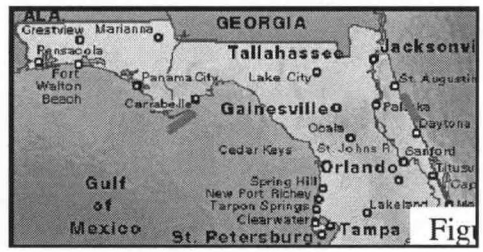

The marks indicate the sampling location, to the west is St. George Island to the east is Flagler County.

Egg Sampling

The methods used were similar to those followed by Alam and Brim (2000). Sample collection began during the late summer of 2003. The sample collection consisted of five nests from each site. Within four nests from each site, up to 4 eggs and several pieces of eggshells from hatched eggs were removed from four sections separated during the excavation of the nest. The four sections were also used for the intra-clutch variation. They were labeled by Roman Numerals beginning with section I at the top of the nest indicating the last eggs lain and section IV at the bottom indicating the first. For the intra-clutch variation one nest from each site was sampled completely. All samples were placed on dry ice then transported to the lab.

Yolk Separation

Once in the lab, the whole eggs separated as abated, unfertilized, or partially developed. The yolk separation began with a four-hour thawing process under a ventilated hood. The egg whites were emptied and discarded, and the yolks were poured into Falcon® conical tubes. The shells were rinsed with deionized water, placed into a separate conical tube and returned to the freezer until digestion.

Lyophilization and digestion

The second stage of the sample preparation consisted of lyophilization and microwave digestion. During lyophilization, the frozen samples were placed into insulated freeze dry vessels with their lids loosened and wrapped with foil for 48-50 hours or until dryness was verified. 0.3 grams of the sample were digested for the metal analysis. Trace metal grade nitric acid (10ml) was added to samples before digestion in the microwave (CEM Corp. Matthews, NC). Microwave digestion followed the USEPA Method 3052 (1996), digestion for organic tissues and siliceous matrices.

Metal Analysis

Yolk and eggshell samples were analyzed for Al, Cr, Fe, Co, Ni, Cu, Zn, As, Se, Rb, Sr, Mn, Cd, Cs, Ba, Pb, and Hg following USEPA method 6020 (1994). Trace element analysis was performed by ICP-MS (Perkin Elmer, Norwalk, CT) on samples diluted 1:1 with double-deionized water. Blanks were included in the digestion and analysis procedure for quality control purposes. Furthermore, series of spike recoveries, instrument duplicates and triplicates, batch duplicates, sample duplicates

and triplicates, as well as the use of standard reference material and standard additions were all apart of the quality control procedures.

Results

Intra-clutch Variation

The data from the eggshell concentrations had a wide variation. One-way repeated measures ANOVA with Tukey shows there were no similarities between the two sample sites. The Franklin County eggshell data did show variation within the clutch for Al, Cr, Mn, Fe, Sr, Co, Cs, Ba. These metals had significantly higher concentrations in nests sections II and III ($p<.05$). Figures 2 and 3 illustrate the concentrations for the eggshells. Figures 3 and 5 show Fe and Sr separate because of their high concentrations.

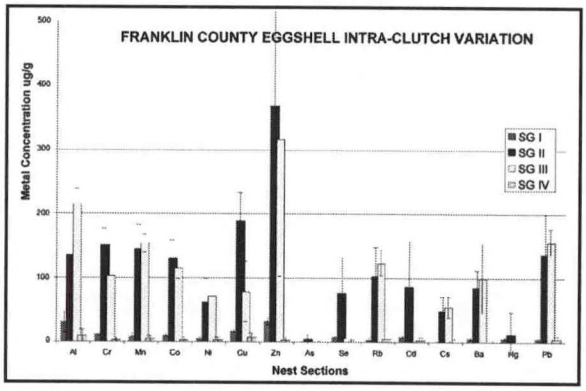

Figure 2

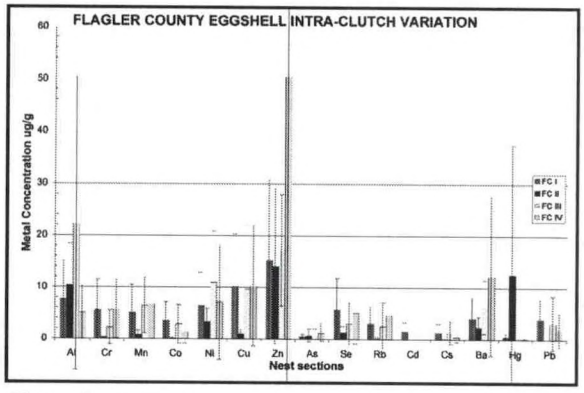

Figure 3

Overall, variation within the eggshells from Flagler County, Figures 4 and 5, had no significant differences amongst any of the metals for each nest section. The variation within the nest masked any visible trend.

Figure 4

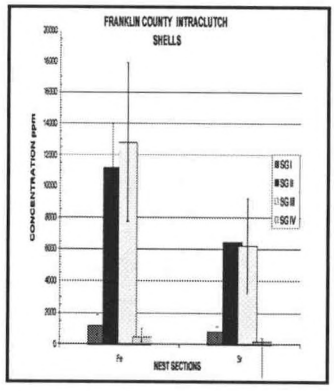

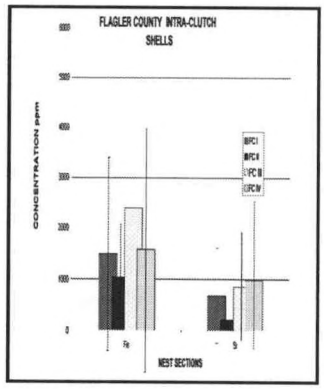

Figure 5

Figures represent intra-clutch variation data for the eggshells and yolks for both Franklin and Flagler Counties. Concentrations are in µg/g dry weight.

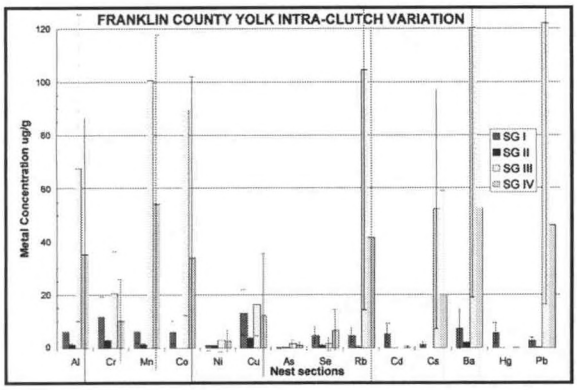

Figure 6

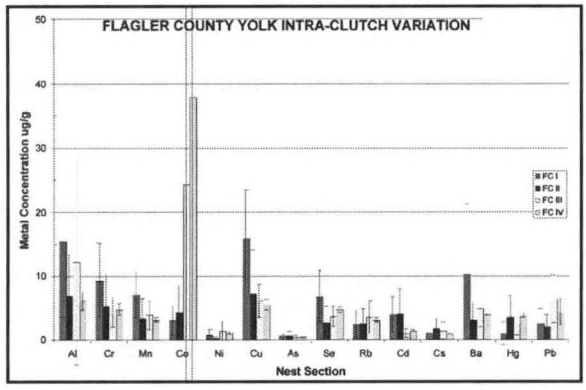

Figure 7

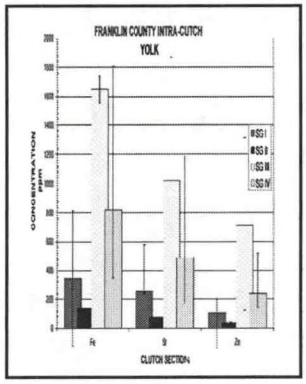

Figure 2

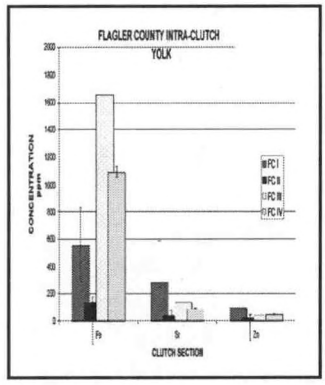

Figure 3

The egg yolk intra-clutch variation, seen in Figures 6 and 7, shows a decrease in metal accumulation through laying period. Section I and II contain the last-lain eggs, in both sample sites there appeared to be a slight decrease, followed by a sharp increase in section III following a decrease in Section IV. This pattern was consistent for both sample sites. For the Franklin County egg yolk data, the only significant difference between sections was for section III ($p<.05$). Figure 4 also illustrated this between metals from Franklin County. Similar analyses for Flagler County samples show a similar composition. Although as a group, the only significant difference between the nest sections was between sections I and II Figure 3 also shows a comparable metal relationship.

County Comparison

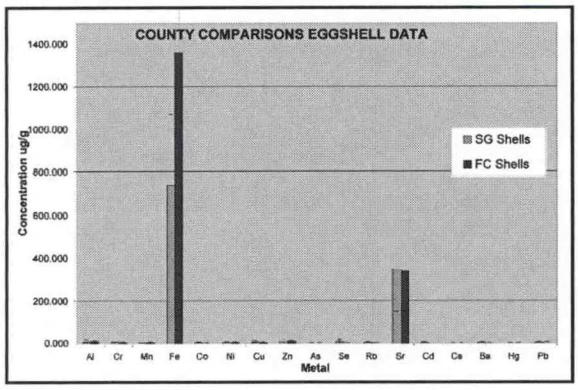

Figure 6

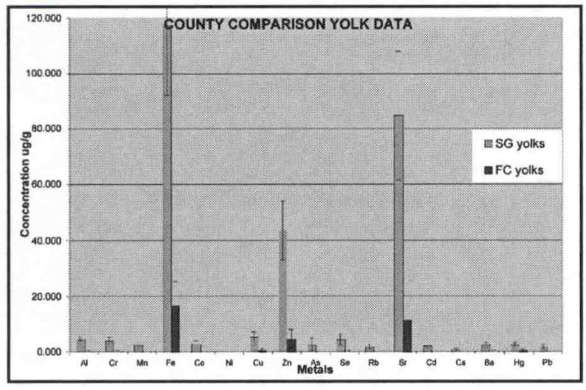

Figure 7

In Figure 6, an unpaired, one-tailed t test proved no difference between the two sites from the eggshell data. The only metal with a significant difference between sites was Cd.

However in Figure 7 a different story was seen. Every metal had different concentrations between the two sites, $p<.05$ except Ni. The samples from Franklin County had significantly higher concentrations, $p<.05$, for all metals in yolk material.

St. George Island Site Comparison

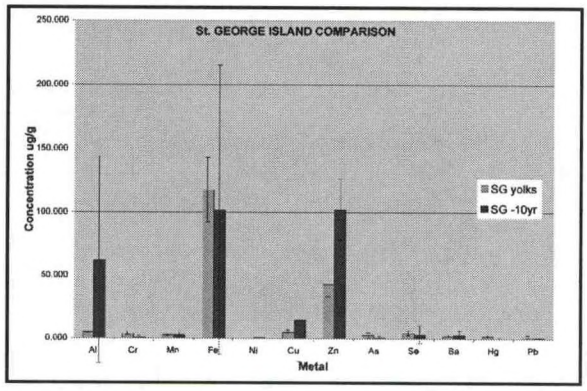

Figure 8

When comparing the St. George Island site to the concentrations reported by Alam and Brim (2002), few metals show different concentrations, and overall there was no significant difference between the two sample sets. When comparing each individual metal to each other in an unpaired t-test, for an estimated 8 eggs at the site for Alam and Brim (2002). Ni, As, Pb and Hg have all significantly increased since 1992, the date the initial sample collection. Zn has actually reduced in concentration ($p<.05$).

Discussion

When comparing the intra-clutch variation data for the Franklin County eggshells an interesting, but non significant, trend was observed. A similar conclusion can be derived for the Flagler County eggshell samples. Metal concentration for both sites changed proportionally for each section of the nest. Iron (Fe) and Strontium (Sr) were significantly higher then the rest of the metals in every data set.

In Figures 4 and 5 the difference within nest sections was more distinct. Section III had significantly higher concentrations of Fe and Sr with Zn having a close relation. As seen with the eggshells the change in concentration within the nest was similar for each metal.

The purpose of the intra-clutch variation data was to determine if laying order plays a role in the concentration of metals within a clutch. The four nest sections were separated qualitatively to counteract the effect the fall would cause on the position of the egg within the nest. The lack of a significant difference within the nest for both the eggshells and egg yolks, justifies sampling from the clutch.

With the clutch sampling justified by a complete excavation and examination of a single nest at both sites, a county comparison was made with several other nests from each site. When comparing the eggshell concentrations of the abated eggs, no difference was seen between the two sites. As seen in the intra-clutch variation data for the eggshells, the sample variances were high and Fe and Sr were significantly higher than the other metals. Cd was the only metal with differing concentrations between the two sites. Unpolluted coastal waters generally have less then .1 µg/l and the concentration for Flagler County was less then that (Elinder, 1992).

The yolk concentrations for the two counties demonstrated a greater difference between sample sites. 16 of the 17 metals observed had different concentrations, with every metal, except Ni, hav-

ing higher concentrations in the Flagler County sites. The Franklin County site had Cu, As, Hg, Cd, Pb, Al, Cr, Se which were all above the levels found in ambient sea water listed in the ASTDR. Hg, Pb, Al, Se, and Cu were also above the average levels for Flagler County.

The increase of metal concentrations since 1992 at St. George Island, in Franklin County, for the heavy metals As, Hg, and Pb has brought their concentrations to levels which might be of concern at 2.6, 2.5, and 1.7µg/g respectively. The remaining metal concentrations did not change enough to show a significant difference. Unfortunately there is little information for which to determine if these concentrations were toxic. Therefore, this study is also justified as an exposure assessment for marine turtles.

Conclusion

Overall the differences between the concentrations for the egg yolks from Franklin and Flagler Counties might be attributed to the diet of the female sea turtle. As to the use of eggshells as an alternative to unhatched and abated eggs, no difference was seen between the sites.

The most interesting result of this study was the evidence of an increase of the heavy metals As, Hg, and Pb, since 1992. These metals have various anthropogenic sources throughout the Gulf Coast. Futures studies are needed to explore the toxicokinetics for these and other metals in sea turtles and the loggerhead specifically.

REFERENCES

Alam, S.K. and M.S. Brim, 2000: Organochlorine, PCB, PAH and metal concentrations in eggs of Loggerhead sea turtles (Caretta caretta) from Northwest Florida, USA. *Journal of Environmental Science and Health*, **B35** (6), 705-724.

Caldwell, D,K, A. Carr, L.H. Ogren, 1959: "Nesting and Migration of the Atlantic Loggerhead Turtle," The Atlantic Loggerhead sea turtle, Caretta caretta (L.), in America. *Bulletin of the Florida State Museum Biological Sciences*, **4** (10).

Caurant, F., P. Bustamante, M. Bordes, and P. Miramand, 1999: Bioaccumulation of cadmium, copper and zinc in some tissues of three species of marine turtles stranded along the French Atlantic Coasts. Marine Pollution Bulletin, **38** (12), 1085-1091.

Clark, D.R. and A.J. Krynitsky, 1980: Organochlorine residues in eggs of loggerhead and green sea turtles nesting at Merritt Island, Florida- July and August 1976. *Journal of Pesticide Monitoring*, **14**, 7-10.

Elinder, C.G, 1992: Cadmium as an environmental hazard. *IARC Sci. Pub.* **1118**, 123-132.

Lewis, M., G.I. Scott, D.W. Bearden, R.L. Quarles, J. Moore, E.D. Strozier. S.K. Sivertsen, A.R. Dias, and M. Sanders, 2002: Fish tissue quality in near-coastal areas of the Gulf of Mexico receiving point source discharges. *The Science of the Total Environment*, **284**, 249-261.

Sakai, H., H. Ichihashi, H. Suganuma, and R. Tatsukawa, 1995: Heavy metal monitoring in sea turtles using eggs. *Marine Pollution Bulletin*, **30** (5), 347-353.

Stoneburner, D.L, M.N. Nicora, and E.R. Blood, 1980: Heavy metals in loggerhead sea turtle eggs (Caretta caretta): Evidence to support the hypothesis that demes exist in the western Atlantic population. *Journal of Herpetology*, **14** (2), 171-175.

United States Environmental Protection Agency (USEPA), 1996: Method 3052 Microwave assisted digestion of siliceous and organically based matrices. Washington, D.C.

United States Environmental Protection Agency (USEPA), 1994: Method 6020 Inductively Coupled Plasma Mass Spectrometry. Washington D.C.

Witkowski, S. A. and J.G. Frazier, 1982: Heavy metals in sea turtles. *Marine Pollution Bulletin*, **13** (7), 254-255.

Wold, Chris, 2002: The Status of Sea Turtles under International Environmental Law and International Environmental Agreements. *Journal of International Wildlife Law and Policy*, **5**, 11-48.

Using Visual Quality Assessments as an Integral Environmental Planning Tool for Coastal Habitats

Professor Yasmin Fozard, MLA.

Morgan State University, Institute of Architecture and Planning, Baltimore, MD 21251

yfozard@moac.morgan.edu

Abstract

Designers and architects have long known that the quality of form and appearance of any environment – built or natural – can influence the behavioral patterns and interactions of the people within the particular environment. This can imply important connections to the issues of sustainability in the coastal zone community. For the Critical Bay area in Maryland, the visual appearance of the environment can indicate the first signs of stress to the Bay or negative impacts from the surrounding uses. This research explores the idea of using enhanced Visual Quality as a catalyst for economic revitalization in coastal communities. It explores the relationships that exist among the coastal communities within the Critical Bay Area, the City of Baltimore Planning Department, and NOAA. It involves using visual quality surveys within two sets of communities and allied or interested municipal and private groups to assess negative and positive visual qualities within the particular community as it relates to the environment, the economy, and place attachment. The Visual Quality was assessed by using a Visual Impact Assessment (VIA). It is a method of predicting and judging the effects that development may have on landscape resources/characters and visual amenities.

The two coastal communities are Middle Branch located in Baltimore City watershed area in Baltimore City and the Edgewood community located in Bush River watershed area in Harford County, Maryland. In each community, visual quality was assessed through the survey. The survey focused on the participant's familiarity with particular images and their preferences for a variety of visual qualities for different environments. These differences are to be assessed on both the individual level and, more importantly, on the community level. This research project is following the urban design model of The Heritage State Park Program in Massachusetts. It was a unique state effort that was seeking to meet two major public concerns: environmental enhancement (improved visual quality) and economic revitalization. The Massachusetts legislature approved $35 million in 1979 for eight downtown parks in needed older industrial cities across the commonwealth. Implementation was a joint effort between the state, municipalities and community residents. Today these State Parks have economic successful.

CHRONOLOGY OF THE APALACHICOLA BAY GEOCHEMISTRY: AN ANALYSIS OF NUTRIENT TRENDS AT THREE SITES IN THE APALACHICOLA BAY

Donatto Surratt[1], Jennifer Cherrier[1], Larry L. Robinson[1], Jaye Cable[2]

1 Environmental Sciences Institute – Florida A&M University 1520 S. Bronough St, Tallahassee, FL 32310

2 Department of Oceanography and Coastal Sciences, Coastal Ecology Institute – Louisiana State University

Apalachicola Bay is one of the most productive oyster nurseries in the nation, accounting for ~90% of Florida's and ~10% of the nation's annual oyster yields (HUANG et al, 2002). Historically, the bay has a strong dependence on the freshwater discharge (HUANG and SPAULDING, 2002) and terrestrial nutrient flux (LIVINGSTON, 1997) from the Apalachicola-Chattahoochee-Flint (ACF) River Basin. The bay is presently in danger of degradation due to upstream freshwater reduction, wastewater intrusion, and probable contamination, which is one premise for the ACF water wars (RITCHIE, 2001). A historic analysis of the bay was performed to understand the trends in alterations for the bay following activities such as channeling, dredging, and damming carried out by the Corp of Engineer within the Apalachicola Drainage Basin since the early 1950's. Sediment cores were collected at three sites in the bay (near the river mouth, an oyster bar, and at an additional site northeast of the river mouth - East Bay) and analyzed for organic carbon (OC), total nitrogen (TN), and total phosphorous (TP); 13C and 15N isotopic abundances; and atomic C/N, C/P, and N/P ratios. Significant spikes in bulk concentrations of OC (5.1%, $t(4)=5.9$, $p<0.0025$), TN (0.35%, $t(4)=6.7$, $p<0.0025$), and TP (110 _g TP/g, $t(4)=2.79$, $p<0.01$) were observed for sediments cores dated to the 1950s near the river mouth. These spikes indicate disturbances that correlate to the introduction of Jim Woodruff dam in 1954 as well as dredging activities for Gulf Intracoastal Waterway (GIWW) maintenance. For sediments dated to the late 1970s at this site, spikes in bulk OC (2.2%) and TN (0.2%) were observed, but these spikes were not significant with respect to the average core concentration. However, significantly heavier _13C (-21.33‰, $t(3)=2.35$, $p<0.0025$) values were observed for these sediments indicating a marine source input, which corresponds to the introduction of breakwater islands in 1977. The OC, TN, and TP concentrations and C/P and N/P ratios for the oyster bar follow normal diagenetic patterns with little variability downcore. No significant shifts in isotopic abundances (_13C and _15N) were observed. In contrast we did observe a significant ($t(5)=-4.99$, $p<0.0025$) shift in the C/N ratios near the oyster bar from 16.3±0.25 in the late 1950s to 13.84±0.31 in 2002 indicating a shift to a more marine nitrogen source. In East Bay OC (1.73%±0.09%), TN (0.105%±0.003%), and TP (123_g TP/g±12_g TP/g) concentrations, _13C (-24.73‰±0.20‰) values, and C/P (146±19) and N/P (8.74±0.95) ratios had little variability downcore. The values in East Bay shift significantly ($t(6)=4.17$, $p<0.0025$) from 7.69‰±0.47‰ in 1960 to a heavier nitrogen signature of 10.61‰±0.55‰ in 2002 indicating a shift to a more marine source. The observed shift to a more marine source as indicated by the _15N signatures was supported by the core C/N ratios, which also showed a significant shift ($t(6)=-2$, $p<0.05$) from 23.82±1.36 in ~1952 to 15.27±0.76 in 2002. The noted shifts suggest a decrease in terrestrial nutrient input to East Bay from the 1950s to 2002. Overall, the observed alterations to bulk nutrient concentrations, stable isotopic signatures, and nutrient ratios suggest that the bay is shifting to a more marine nutrient source. This shift is most likely a function of decreased freshwater discharge to the bay resulting from alteration to the hydrology of the ACF river basin. Independently the bulk nutrient concentrations, stable isotopic signatures, and nutrient ratios can act as indicators for a discrete assessment of historic sediment trends. However, our results have shown that this suite of geochemical tracers when used concurrently can be a powerful tool for assessing natural and anthropogenic geochronological alteration to estuarine systems.

TOWARD UNDERSTANDING THE LIFE CYCLE OF THE ETIOLOGIC AGENT OF DAMSELFISH NEUROFIBROMATOSIS: INSIGHTS USING *IN VITRO* TECHNIQUES

Cinda P. Scott

University of Miami, Rosenstiel School of Marine and Atmospheric Science
4600 Rickenbacker Causeway, Miami, FL 33139

Introduction

Damselfish Neurofibromatosis (DNF) is a disease affecting populations of bicolor damselfish, Stegastes partitus, on Florida and Caribbean reefs. DNF was first described in bicolor damselfish in 1983 as a disease which manifests as visible external tumors on the body surface of the fish, including hyperpigmented nodules, and deep, unpigmented, fibrous nodules (Schmale et. al., 1983) (Fig. 1). A small, DNA virus-like agent was discovered and is thought to be the etiologic agent of DNF (Campbell et. al., 2001). The damselfish virus-like agent (DVLA) is associated with tumors found in bicolor damselfish, and has prompted the investigation of this agent in order to characterize, localize and understand its replication and life cycle. Ultimately, the goal of this research is to understand how DVLA induces cellular transformation.

DVLA affects the peripheral nervous system (PNS) and chromatophores of the bicolor damselfish. It is the only known naturally occurring, transmissible disease affecting cells of neuroectodermal origin including Schwann cells and chromatophores (Schmale et. al., 2002). DNF is characterized by neurofibromas, chromatophoromas and malignant peripheral nerve sheath tumors (MPNSTs). Upon infection with the disease, the life span of the afflicted fish is greatly reduced.

The human disease, Neurofibromatosis Type 1 (NF1), is an autosomal dominant disease affecting tissues of neuroectodermal origin. NF1 affects approximately 1/3500 individuals (Viskochil et. al., 1993). Patients with NF1 have several abnormalities including café-au-lait spots, neurofibromas and optic nerve gliomas (Gutmann and Collins, 1992). Individuals with NF1 carry one normal copy and one mutant copy of the NF1 gene. NF1 presents itself in the individual when the normal copy of the NF1 gene is mutated. This loss of heterozygosity (LOH) leaves the patient with two mutant copies of the NF1 gene. The NF1 gene encodes a protein known as neurofibromin. When LOH of the NF1 gene occurs, neurofibromin cannot be produced. The NF1 gene is a tumor suppressor gene. Neurofibromin acts as a tumor suppressor protein and is thought to be involved with cell growth and signaling for proliferation via proteins such as ras. Cellular transformation is thought to occur when, in the absence of neurofibromin, ras becomes overexpressed and cells are allowed to proceed through the cell cycle without regulation (Gutmann and Collins, 1992).

Although the human disease, NF1, and the fish disease, DNF, result in similar phenotypes, the initial events that occur which eventually cause disease are different. NF1 is a genetic disorder and DNF is caused by a virus-like agent. However, the mechanism of cellular transformation that governs how healthy cells are turned into cancerous cells in NF1 and DNF may be related. Therefore, the study of DVLA infection and replication and host cell interaction are of extreme importance.

DVLA was first discovered in the Florida Keys National Marine Sanctuary (FKNMS). Accessibility to the FKNMS is essential for ongoing studies of diseased fish. Studies of prevalence and distribution patterns of tumors in bicolor damselfish showed that reefs located in the FKNMS with high population densities also have high prevalence rates of DNF (Schmale, 1991). In general, the fish are very aggressive and will defend their territory by biting if boundaries are not respected. Due to this territorial behavior, DVLA can be passed via fish to fish contact resulting in DNF.

Cell free tumor homogenates from infected fish administered to healthy fish in the laboratory via intramuscular injection (IM) resulted in the growth and dissemination of tumors. In addition, IM of DVLA infected cells grown in culture into healthy fish also resulted in the formation of tumors. This suggested that DNF is caused by a sub-cellular, transmissible, infectious agent (Schmale et. al., 2002).

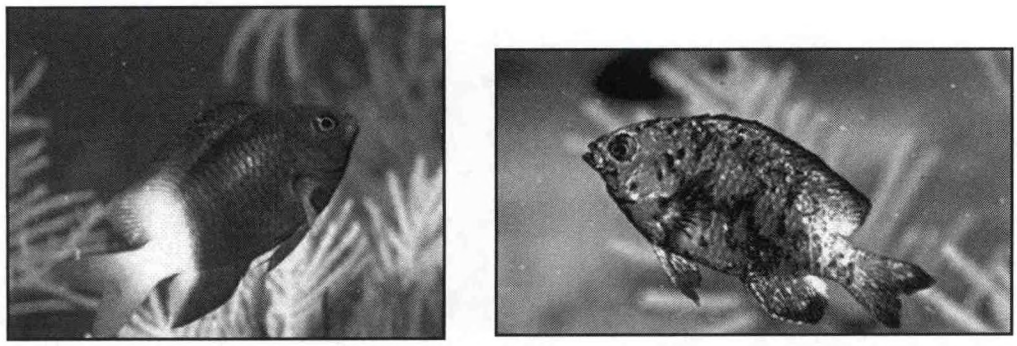

1a. *1b.*

Fig. 1a. Healthy bicolor damselfish, Stegastes partitus, has black and white pigmentation on the body and bright yellow fins. b. Bicolor damselfish with DNF displaying hyperpigmented tumors.

DVLA was first discovered as an extrachromosomal DNA (eDNA) associated with fish and cell cultures affected by DNF. Detection of this eDNA was accomplished by ethidium bromide staining of agarose gels containing samples of undigested genomic DNA from the 92-16 tumor derived cell culture in our laboratory (Schmale et. al., 2002). Faint, but distinct 1.4 and 2.6 kb DNA fragments were visible under UV light.

The 1.4 kb fragment from the 92-16 cell line was excised, cloned and purified and used as a probe to detect homologous sequences of the eDNA in other cell cultures on a Southern Blot (Fig. 2). When the 1.4 kb fragment was used as a probe on a southern blot, all tumor derived cell lines were positive for the eDNA and all cell lines derived from healthy damselfish tissue were negative (Schmale, 2002). This indicated that the eDNA was indeed associated with the disease due to the presence of the DVLA in infected cell lines and its absence in healthy cell lines.

To test whether the eDNA was associated with actual fish tissue, the 1.4 kb DVLA fragment was used as a probe on a southern blot to see whether DNA from tumored fish and DNA from healthy fish tissue would be positive for the eDNA fragments. All DNA samples from tumored fish were positive for the eDNA and all healthy fish DNA samples were negative (Schmale et. al., 2002). However, when healthy fish DNA samples were subjected to PCR using DVLA specific primers, low levels of DVLA were detected. This suggested that DVLA may have an incubation period before resulting in DNF (Campbell and Schmale, 2001).

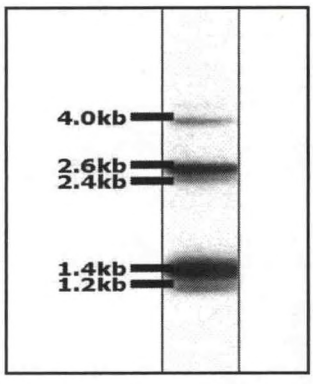

Fig. 2. Typical pattern of DVLA DNA fragments on a southern blot.

The identification of the 1.4 kb DNA fragment enabled the design of primers to amplify regions of the DVLA. A partial sequence of PCR products was deposited into GenBank (accession no. AY043182). DVLA has no homology to any sequences including viral sequences published in GenBank (Schmale, 2002). This lack of homology strongly suggests that DVLA is a novel infectious agent.

The total size of the DVLA genome is approximately 2.4 kb and has a circular secondary structure with DNA southern blot fragments ranging in size from 1.2 to 7 kb (Campbell, 2001). Due to the circular, super-coiled nature of DVLA, it is possible to have concatamers with mobility on agarose gels greater than 2.4 kb. Fig. 2 illustrates the presence of one of these possible concatamers as a 4 kb fragment.

The circular genome of DVLA is thought to be protected by an envelope

or a capsid. This conclusion was drawn from experimental data showing that when DNase was added to fractionated cell homogenates from conditioned media, approximately 5 out of 6 tumor derived cell cultures were resistant to the DNase treatment (Schmale, 2002). Based on these results, it was speculated that the viral genome should be present and detectable as viral particles. To date, no viral particles have been detected by electron microscopy in fish tissue or in cell culture.

The lack of viral particles has made understanding the viral life cycle of DVLA difficult. In comparison to known viruses, DVLA is a small virus. Viruses of this size usually do not carry their own polymerase genes and therefore cannot encode their own DNA polymerases, which would allow them, for example, to exist in the cytoplasm and replicate. The small size of DVLA therefore, renders it completely dependent on cellular machinery in order to replicate. Of all known viruses, only six families of virsuses are considered tumorigenic. These include the retroviridae (ssRNA), adenoviridae (dsDNA), hepadnaviridae (dsDNA), herpesviridae (dsDNA), papovaviridae (dsDNA) and poxviridae (dsDNA). The only known virus to replicate in the cytoplasm is the enveloped, dsDNA pox virus.

The large pox virus, with a genome size of approximately 130-350 kb, enables the virus to encode its own DNA polymerase and live outside of the nucleus without the aid of cellular components. The smallest known viruses, which are not known to be tumorigenic, are the circoviruses. The circoviruses have a ssDNA genome size of 1.8-2.3 kb and replicate in the nucleus with the help of cellular DNA polymerase. Due to the small genome size of the circovirus, it is forced to use alternative splicing methods to produce a significant number mRNAs for translation to protein (Okamoto et. al., 2002). All of the aforementioned tumorigenic viruses replicate in either the nucleus or the cytoplasm and are dependent on cellular machinery for replication except for the large pox virus.

If DVLA is to propagate and replicate successfully, it must either use its own DNA polymerase, the host cells DNA polymerase or a helper virus polymerase. Considering that DVLA is as small as the smallest known DNA virus, it is difficult to imagine that DVLA is able to produce its own DNA polymerse. Therefore, DVLA replication may be limited to cellular compartments where DNA polymerase is available, specifically either the mitochondria or the nucleus. There are no DNA viruses known to replicate in the mitochondria. However, initial experiments focused on DVLA replication suggest that unlike the other known tumorigenic viruses, DVLA is associated with the mitochondria.

Fractionation experiments have shown that the virus separates with the cytoplasmic and mitochondrial fractions rather than the nuclear fraction. This suggests that DVLA may not be dependent on nuclear machinery for replication. Therefore, location for DVLA replication may be limited to the cytoplasm and the mitochondria. However, as previously discussed, it is highly unlikely that DVLA would be able to exist in the cytoplasm without the aid of cellular machinery. To address this problem, experiments using established bicolor damselfish cell cultures infected with DVLA were manipulated with various chemical agents to study the effects of these chemicals on DVLA DNA patterns. These experiments were carried out with the intention of gathering more information about the unique and peculiar life cycle of DVLA.

Methods and Materials

Preliminary studies involved the use of four chemical agents. Aphidicolin is a tetracyclic diterpenoid molecule produced by fungus that stops nuclear DNA synthesis. The drug acts directly on DNA polymerase-_ to stop nuclear DNA synthesis (Spadari et. al., 1982). If DVLA is associated with the nucleus, then any affect on nuclear DNA polymerase should also have an affect on DVLA copy number. 8-Bromo-cyclic-GMP (8-Br-cGMP), a drug which triggers mitochondrial biogenesis via nitric oxide cGMP dependent signaling, was used to stimulate the growth of mitochondria (Nisoli et. al., 2003). Therefore, if 8-Br-cGMP is able to stimulate mitochondrial DNA content via biogenesis, then an increase in DVLA copy number should occur if DVLA is dependent on mitochondrial DNA polymerase.

The chemical agent, dideoxycytidine (ddC), also known as the AIDS drug, zalcitabine, is a nucleoside analog used to treat patients suffering from AIDS. Many AIDS drugs including zalcitabine (ddC), zidovudine (AZT) and didanosine (ddI) are toxic to the mitochondria (Benbrik et. al., 1997).

Nucleoside analog AIDS drugs terminate DNA synthesis by not leaving an available 3' end that is able to have additional nucleotides added. Therefore, the DNA chain is terminated and DNA synthesis cannot occur. If there is a decrease of mitochondrial DNA polymerase activity due to the chain terminating characteristics of ddC, then there may also be a decrease in the amount of DVLA DNA.

Lastly, the DNA intercalating acridine dye ethidium bromide which acts on circular DNAs, was used to try and deplete cells of their mitochondrial DNA. Ethidium bromide functions by interfering with nucleic acid synthesis via intercalation between base-pairs in the DNA double helix (Aktipis and Martz, 1970).

Established cell cultures, derived from healthy and tumored tissues from fish collected in the Florida Keys National Marine Sanctuary, were maintained in incubators in the laboratory. Cells were fed L-15 media supplemented with fetal bovine serum (BioWhitaker) containing varying concentrations of aphidicolin (6.5 µM), 8-Br-cGMP (1mM), ddC (10µM and 100µM) or ethidium bromide (50nM, 100nM and 1µM) over a period of 1 to 2 weeks depending on cell viability. All control flasks were fed media without any chemical agents. Cells were harvested from all experimental cell cultures and genomic DNA was extracted by Proteinase K/SDS/EDTA digestion at 55°C followed by a phenol, chloroform, isoamyl alcohol extraction and precipitation in isopropanol (Sambrook et. al., 1989).

Five micro-grams (µg) of genomic DNA from each experimental cell culture were loaded onto an ethidium bromide stained 1% agarose gel. Southern blotting was performed using Hybond-N+ membrane (Amersham) in sodium saline citrate buffer by capillary action (Schmale et. al., 2002). Probe DNA was a radioactively labeled 1.3 kb PCR product made from fish culture cell lines and DVLA specific primers.

Results

The results showed that treatment of the DVLA infected 88-503 cell culture with the chemical agents previously mentioned had little effect on the viral DNA pattern in comparison to the control (Fig. 3). DNA harvested from 88-503 cell cultures treated with 10µM ddC and 100µM ddC appeared to have a weaker signal than the control, 8-Br-cGMP and Aphidicolin lanes. The 88-503 ethidium bromide treated lane appears to have the same DVLA signal strength as the ddC lanes.

The DVLA DNA pattern of the 86-583 and 89-05 cell lines appeared to be affected by ethidium bromide treatment. Treatment of the 86-583 cell line with 100nM ethidium bromide showed a complete loss of the 1.2 and 1.4 kb fragments. A large decrease in signal of the 1.2 and 1.4 kb fragments in the 89-05 cell line treated with 50nM and 100nM EtBr was also observed. However, treatment of the 89-05 cell line with 1µM concentration of ethidium bromide showed a decrease in DVLA signal of the 2.6 kb fragment (Fig. 3).

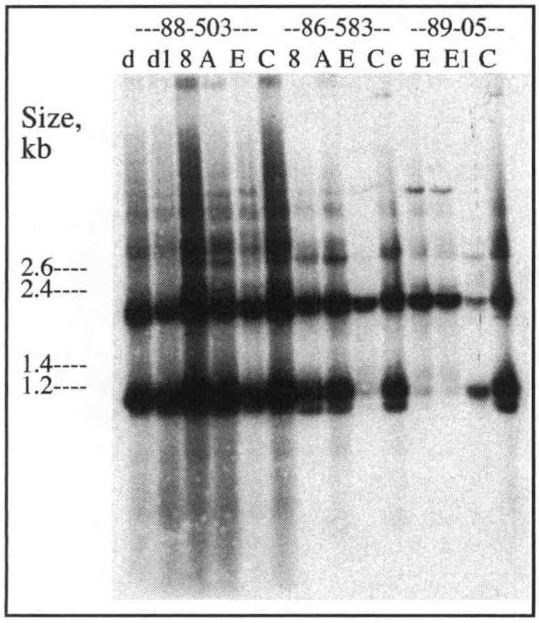

Fig. 3. Southern blot of uncut genomic DNA from harvested DVLA infected cell cultures (88-503, 86-583, 89-05) treated with either aphidicolin (A), 8-Br-GMP (8), ddC (d=10µM, d1=100µM) or ethidium bromide (e= 50nM, E=100nM, E1= 1µM), C=control.

Intrigued by the affect of ethidium bromide on DVLA, experiments were completed to monitor the affects of EtBr on three additional cell lines. In total, six cell lines were treated with a low concentration (50 nM) and a high concentration (1 µM) of ethidium bromide. Genomic DNA was extracted using the previously mentioned phenol, chloroform method. A total of 5 µg of genomic DNA was loaded onto an ethidium bromide stained 1% agarose gel. The gel was then southern blotted and probed using a radioactively labeled DVLA PCR product.

Results showed that three of the six cell lines were

greatly influenced by treatment with the low concentration of ethidium bromide (50 nM) (Fig. 4). The 86-583 cells treated with 1 µM ethidium bromide results were inconclusive due to loss of the DNA sample. Similar to the 89-05 cell line treated with 1 µM ethidium bromide (Fig. 3), there was an overall decrease in DVLA signal strength, but not a complete loss of any of the signals. The 89-734, 86-583 and 89-05 cell lines treated with 50 nM ethidium bromide all showed complete loss of the 1.2 and 1.4 kb DVLA fragments.

Further experiments involving the treatment of cell cultures with ethidium bromide were completed in which cells were treated with concentrations of ethidium bromide ranging from 10 nM to 2 µM. Again, southern blot results showed that at the lower concentrations, 10nM to 250 nM ethidium bromide, the 1.2 and 1.4 kb DVLA signal was greatly reduced (Fig. 5a). This southern blot was stripped and re-probed using a PCR product with homology to the mitochondrial cytochrome b region (Fig. 5b). Results indicated that the mitochondrial DNA may be affected by treatment with ethidium bromide due to a decrease in mitochondrial signal strength (Fig. 5b).

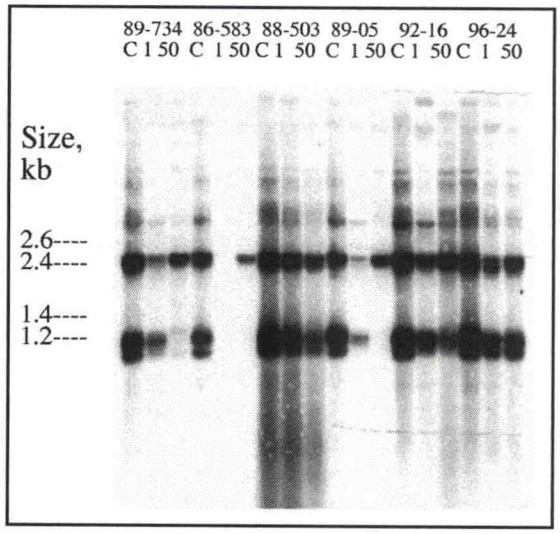

Fig. 4. Southern blot of uncut genomic DNA from harvested cells treated with low (50nM) and high (1µM) concentrations of ethidium bromide. C=control, 1= 1µM ethidium bromide, 50= 50 nM ethidium bromide.

As previously mentioned, ethidium bromide is an intercalating dye that works by wedging its phenanthridinium ring between DNA base-pairs (Aktipis and Martz, 1970). Though treatment of cell lines with ethidium bromide has provided some interesting results regarding DVLA fragments, whether or not there is a relationship between DVLA and the mitochondria has yet to be answered. Since ethidium bromide is an intercalating dye that is preferentially taken up by small circular DNAs, it is possible that DVLA is affected by ethidium bromide by this mechanism. Therefore, it would be dif-

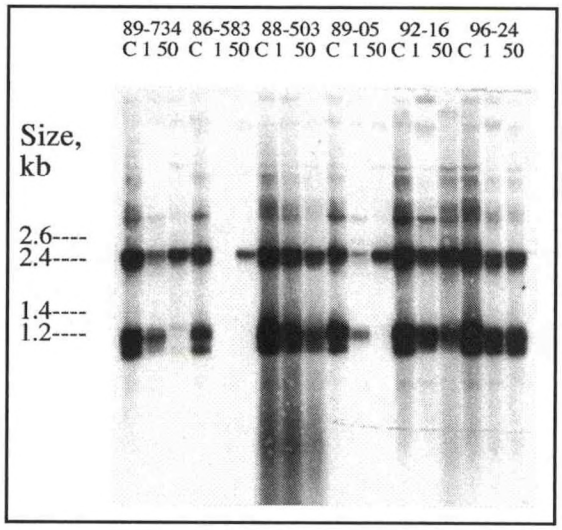

Fig. 5a.

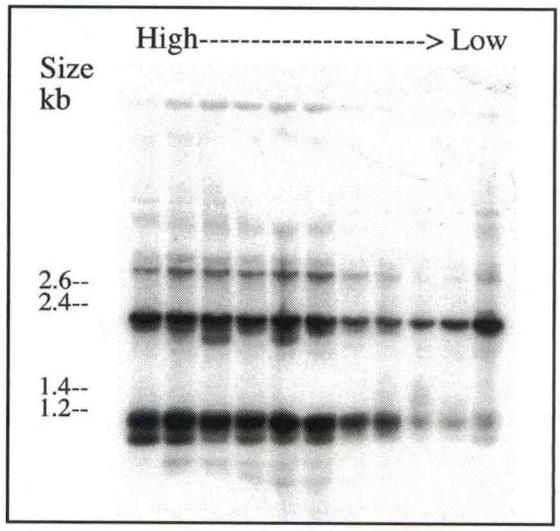

Fig. 5b.

Fig. 5. a. Southern blot showing the effects of high to low concentrations of ethidium bromide on the 89-734 DVLA infected cell line (2 µM-10nM). b. Southern blot showing the effects of high to low concentrations of ethidium bromide on the 89-734 mitochondria.

ficult to conclude that DVLA is solely associated with the mitochondria. A better way to infer a relationship between DVLA and the mitochondria would be to completely deplete cells of their mitochondrial DNA or block mitochondrial DNA polymerase-_. If mitochondrial DNA is not present in the cell and DVLA is dependent upon mitochondrial DNA _-polymerase for replication, then total DVLA copy number should be little to none.

Discussion

Preliminary experiments have involved the use of ethidium bromide to deplete cells of their mitochondria. Cells were grown in L-15 supplemented with serum supreme (BioWhitaker), glucose (2mg/ml), pyruvate (100µg/ml) and uridine (50µg/ml) (King and Attardi, 1996). Cells were treated with 100nM and 250 nM ethidium bromide for an average of 18 days or until cells could no longer survive. Upon harvesting the cells, the cells appeared small with an uneven shrunken surface. Little to no DNA was retrieved from tumor derived cell lines, however healthy cell lines treated with ethidium bromide had robust cells and a healthy sized DNA pellet was obtained.

One problem with using ethidium bromide to deplete cells of their mitochondrial DNA is that ethidium bromide also has an affect on DVLA (Figs. 3 and 4). Therefore, if cell cultures are unable to be completely depleted of mitochondrial DNA (mtDNA) and a decrease in DVLA signal is observed, then it cannot be concluded that DVLA is associated with the mitochondria. The use of nucleoside analogs is a better way to deplete cells of mtDNA because nucleoside analogs do not appear to have an outright effect on DVLA DNA (Fig. 3). Perhaps, if mtDNA is depleted using, for example, AZT, then a decrease in DVLA DNA would only be seen once the mtDNA polymerase has been affected.

Currently, experiments are in progress to create mitochondrial DNA-less cells (_0) to see whether DVLA is able to replicate without the use of mitochondrial enzymes. Cell lines are treated with AZT at a concentration of .5mM and 1mM. Due to the inherent toxic nature of this nucleoside analog drug, the cells began to die; therefore the concentrations were lowered to .25 mM and .5 mM respectively. These cells are currently still in culture and appear robust and healthy, however it is unknown whether these cells are in a _0 state.

Creating a stable line of _0 cells in culture has proven to be difficult. However, altering the concentrations of glucose, uridine and pyruvate may aid cells during the process of cellular respiration without mitochondria. Future work will involve doing more southern blots using mitochondrial probes to detect whether or not ethidium bromide or AZT is able to deplete fish cells of mitochondrial DNA. Though ethidium bromide and AZT function in different ways to lower the amount of total mitochondrial DNA in the cell, it is important to note that the ability to block mitochondrial DNA polymerase-_ is of greater imporatance than depletion of mitochondrial DNA to infer any relationship between DVLA and the mitochondria. One way to look at whether or not ethidium bromide or AZT is truly affecting the total amount of mitochondrial DNA is to use quantitative PCR.

The use of quantitative PCR (QPCR) in determining copy number per cell of DVLA in comparison to mitochondrial and nuclear DNA will provide useful information as to whether or not the use of chemical agents are able to affect mitochondria and in turn DVLA. QPCR is a more sensitive technique that can be used to see if DVLA copy numbers are decreased as a result of ethidium bromide or AZT treatment. In addition, QPCR can quantify copy number per cell of mitochondrial and nuclear DNA. This will allow for the comparison and establishment of a ratio of DNA copy numbers of the nucleus, mitochondria and DVLA. The development of primers and probes specific to DVLA and damselfish mitochondrial and nuclear DNA for use with a probe-based QPCR protocol is currently underway.

The ultimate objective of this research is to better understand replication and the life cycle of DVLA. Preliminary experiments that focused on chemical manipulation of cell cultures revealed that the 1.2 and 1.4 kb DVLA fragments are susceptible to ethidium bromide at low concentrations. The fact that ethidium bromide is preferentially incorporated into circular DNAs does not allow for the establishment of a relationship between DVLA and the mitochondria since DVLA is also circular. However, it is interesting that only the 1.2 and 1.4 kb DVLA DNA fragments are completely removed by ethidium bromide at low concentrations. Perhaps these low molecular weight DNA fragments are an intermediate step in DVLA replication. The 1.2 and 1.4 kb DVLA species could be more vulnerable to ethidium bromide inter-

calation because they are intermediate forms of DVLA and have a high turnover rate.

Establishing the ratio of mitochondrial DNA to DVLA DNA to nuclear DNA using QPCR will help to determine how the use of chemical agents on cell cultures affects this ratio. QPCR alone will not determine if DVLA and the mitochondria are associated. However, understanding the mt:DVLA:nuclear ratio, will help in the design of experiments which will utilize chemical agents more precisely targeted to reduce mitochondrial DNA polymerase-_. Studies will continue to be focused on cell culture manipulations and QPCR.

ACKNOWLEDGEMENTS

This research was partially funded by the NOAA Educational Partnership Program. Additional funding was provided by the Alfred P. Sloan Foundation. Special thanks are extended to the Florida Keys National Marine Sanctuary, the University of Miami and my academic advisory committee. Extended thanks to my advisor, Dr. Michael C. Schmale and to Dr. Mark Harwell, Dr. David Die and Dr. David Letson.

REFERENCES

Aktipis, S. and W.W. Martz, 1970: Circular dichroism properties of ethidium bromide-seoxyribonucleic acid complexes. *Biochem. Biophys. Res.* Commun., **39**, 307-313.

Benbrick et. al., 1997: Cellular and mitochondrial toxicity of zidovudine (AZT), didanosine (ddI) and zalcitabine (ddC) on cultured human muscle cells. *J. Neurol. Sci.*, **149**, 19-25.

Campbell, C.E., Gibbs, P.D.L. and M.C. Schmale, 2001: Progression of infection and tumor development in damselfish. *Mar. Biotechnol.*, **3**, S107-S114.

Campbell, C.E. and M.C. Schmale, 2001: Distribution of a novel infectious agent in healthy and diseased bicolor damselfish in Florida and the Caribbean. *Mar. Biol.*, **139**, 777-786.

Gutmann, D.H. and F.S. Collins, 1992: Recent progress toward understanding the molecular biology of Von Recklinghausen neurofibromatosis. *Ann. Neurol.*, **31**, 555-561.

King, M.P. and G. Attardi, 1996: Isolation of human cell lines lacking mitochondrial DNA. *Meth. Enzymol.*, **264**, 304-313.

Nisoli, E. et. al., 2003: Mitochondrial biogenesis in mammals: the role of endogenous nitric oxide. *Science*, **299**, 896-899.

Okamoto, H., Takahashi, M., Nishizawa, T., Tawara, A., Fukai, K., Muramatsu, U., Naito, Y. and A. Yoshikawa, 2002: Genomic characterization of TT viruses (TTVs) in pigs, cats and dogs and their relatedness with species-specific TTVs in primates and tupaias. *J. Virol.*, **83**, 1291-1297.

Sambrook, J., Fritsch, E.F., and T. Maniatis, 1989: Molecular cloning, a laboratory manual. *Cold Spring Harbor Laboratory Press.*

Schmale, M.C., 1991: Prevalence and distribution patterns of tumors in bicolor damselfish (*Pomacentrus partitus*) on South Florida reefs. *Mar. Biol.*, **109**, 203-212.

Schmale, M.C., Hensley, G. and L.R. Udey, 1983: Multiple schwannomas in the bicolor damselfish, *Pomacentrus partitus*; a possible model of von Recklinghausen neurofibromatosis. *Am. J. Pathol.*, **112**, 283-241.

Schmale, M.C., Gibbs, P.D.L., and C.E. Campbell, 2002: A virus-like agent associated with neurofibromatosis in damselfish. Dis. Aquat. Org., 49, 107-115.

Spadari, S., Francesco, S. and G. Pedrali-Noy, 1982: Aphidicolin: a specific inhibitor or nuclear DNA replication in eukaryotes. *Trends Biochem. Sci.*, 29-32.

Viskochil, D., White, R. and R. Cawthon, 1993: The neurofibromatosis type 1 gene. *Annu. Rev. Neurosci.*, **16**, 183-205.

ORAL SESSION A3
Environmental Sciences

SOIL WATER DYNAMICS MODEL

A. Suleiman

Center for Atmospheric Sciences, Hampton University, VA

ayman.suleiman@hamptonu.edu

Abstract

Water balance is an essential component of crop simulation and hydrological models. Soil Water Dynamic Model (SWDM) is an application being developed in a user-friendly platform to simulate the daily soil water redistribution. It estimates the change of soil water content due to vertical drainage, soil water evaporation, and infiltration separately. It uses easily measured soil physical properties such as sand and clay contents to estimate various hydraulic properties of a soil such as field capacity, saturated hydraulic conductivity, and bulk density. Field capacity is the soil water content at an end of a drainage cycle; saturated hydraulic conductivity is the speed at which water travels within a saturated soil profile; and bulk density is the ratio of soil mass to its bulk volume. These hydraulic properties are needed to run the SWDM along with some weather inputs namely daily or hourly rainfall amounts, maximum and minimum air temperatures, and daily solar radiation.

Introduction

Water balance is an essential component of crop simulation and hydrological models. A water balance would simulate the soil water contents, drainage, evapotranspiration, and water stress factors. Accurate modeling of soil water dynamics at the surface and the deeper layers plays a critical role in natural resource management decisions, and in investigating the impact of climate change, such as global warming, on these natural resources.

Soil moisture sensing is progressing rapidly, with ambitious field experiments ongoing (e.g., the Soil Moisture Experiments in 2002 (SMEX02 Experiment Plan Summary, *http://hydrolab.arsusda.gov/smex02/smex02.htm*) (Suleiman and Crago, 2004). However, remotely sensed soil moisture content data are not always available or accurate, especially for dense vegetation. Moreover, remotely sensed soil moisture does not represent the entire soil water profile but rather the first 1-2 cm of the soil profile. Therefore, other means of modeling soil moisture are needed to simulate soil moisture for soil profiles with multi-layers.

Modeling soil water dynamics under field conditions faces many challenges. Youngs (1995) mentioned seven factors that complicate the soil water dynamics modeling in field conditions. These factors are: the influence of air phase on the soil water movement, the effect of soil heterogeneity, cracks/soil swelling, the hysteresis in soil water relationships, thermal effects, deviation from Darcy's Law, and soil aggregation and instability. Numerical models have been used for decades to describe soil water dynamics with some simplifying assumptions to deal with these factors. These models are physically sound and require a hydraulic conductivity function and characteristic curve for each soil layer (Jacques et al., 2002; Suleiman and Ritchie, 2003). For field studies, these hydraulic properties are often estimated from easily measured soil physical properties because they are not readily available most of the time (Suleiman and Ritchie, 2001). The accuracy of the numerical models depends on the accuracy of the estimation of the input data and on their simplifying assumptions (Panigrahi and Panda, 2003).

The purpose for creating SWDM is to provide a simple accurate way to estimate daily soil water dynamics for any number of soil layers. The soil profile can be divided into a number of layers of at least 1 cm. This facilitates the assimilation of remotely sensed soil moisture into the SWDM. In SWDM, the user has the option to choose from two drainage models, three evaporation models, and

one infiltration model. So far the field capacity, bulk density, and saturated hydraulic conductivity calculators and the drainage and evaporation parts have been completed. It is anticipated to have SWDM completed by the end of 2004. Since the SWDM can be used as a tool for research, education and outreach, the user will have an option to run the whole SWDM or just some parts of it. For instance, if a student wants to run only a drainage model or an evaporation model they can do that. That makes it simple to understand the different processes involved in water dynamics modeling.

Models Description

Soil water Dynamic Model (SWDM) is an application being developed in a user-friendly platform to simulate the daily soil water redistribution. It estimates the change of soil water content due to vertical drainage, soil water evaporation, and infiltration separately.

2.1 Vertical Drainage

A soil loses water during vertical drainage due to gravitational forces. The change of water content for a particular soil layer, during free drainage, depends on its initial soil water content, its hydraulic properties, and its position in the soil profile. For a surface layer, the initial soil water content and hydraulic properties determine the rate of drainage. However, for a layer in the middle of a soil profile the position of this layer in the profile has a significant role as well.

Two vertical drainage models are included in the SWDM. First, the vertical drainage model of the water balance of DSSAT (Decision Support System for Agrotechnology Transfer) family crop models (Boote et. al, 1998). Within this model, the change of soil water content, due to vertical drainage, is calculated by multiplying the drainable soil water (initial Ø- drained upper limit Ø ($Ø_{dul}$)) by a coefficient (SWCON, the fraction of drainable soil water that can be drained in a day). Ritchie et al. (1986) introduced a procedure to determine SWCON from soil porosity. Ritchie (1998) suggested that SWCON maybe assumed 0.55 d^{-1} for different soils. Suleiman and Ritchie (2004) developed a new method to determine SWCON. The user has the option of using any of those three methods of SWCON calculations to use in the DSSAT drainage model. Second, the Suleiman (2004) vertical drainage model. Within this model, the change of soil water content, due to vertical drainage, is calculated from the ratio of the drainable soil water to $Ø_{dul}$. The user has the option of using the incoming flow function developed by Suleiman and Ritchie (2004) to adjust the change of soil water content. The incoming flow to a particular layer is equal to the cumulative drainage (from the layers above that layer), which can be calculated by summing the change of soil water content for all the soil layers.

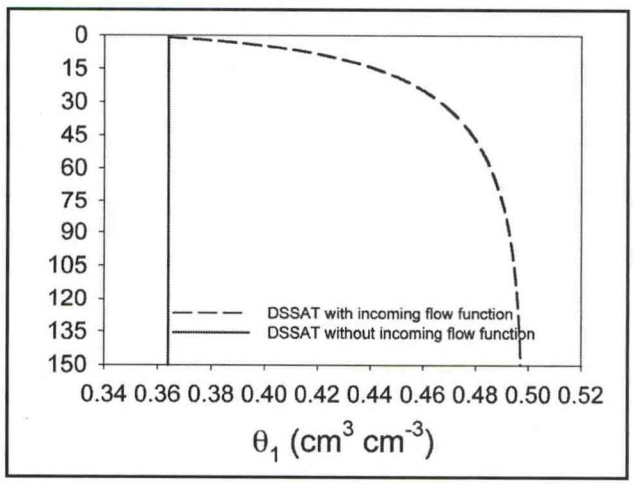

Figure 1. Calculated soil water content profiles after one day of drainage using DSSAT drainage model with or without the use of the incoming flow function.

Figure 1 shows the significant improvement that can be obtained by using the incoming flow function. The curvy line represents the DSSAT soil water content profile after one day of drainage using the incoming flow function while the straight line represents the DSSAT soil water profile after one day of drainage (without the incoming flow function). It is pretty obvious that the DSSAT line without the incoming flow function neither capture the value nor the trend of the soil water profile

during drainage.

2.2 Soil Water Evaporation

Soil water evaporation is a large component of the water balance (Ritchie 1972) and accurate modeling of soil water evaporation (Es) is highly needed to enable researchers find management strategies that may minimize water losses. The water evaporation from a soil surface can be divided into two stages: (1) the constant rate stage in which Es is limited only by the supply of energy to the surface and (2) the falling rate stage in which water movement to the evaporation sites near the surface is controlled by the hydraulic properties of the soil (Ritchie, 1972). The constant rate stage of evaporation vary not only with the prevailing atmospheric environment, but also with soil surface features such as soil surface color, aerodynamic roughness (Mcllroy, 1984). The falling rate stage of evaporation requires an internal movement of water to the regions where vaporization is actually occurring (near-soil surface) (Mcllroy, 1984).

Three soil water evaporation models are available in the SWDM. First, the DSSAT soil water evaporation model (Ritchie et al. (1986)). Within this model, the upward flow of water is calculated to account for the movement of water toward the soil surface during evaporation using Darcy's Law with many simplifying assumptions. Second, the Suleiman and Ritchie (2003) soil water evaporation model. This model was developed based on the diffusivity theory and it uses three parameters that are highly correlated to field capacity.

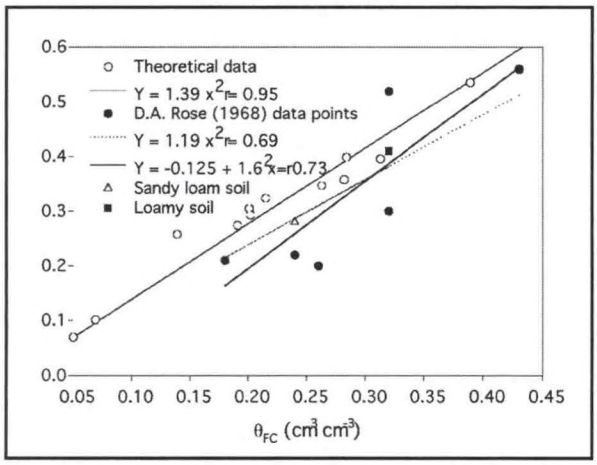

Figure 2. Relationships between _ and _FC of theoretical and laboratory soils (8 soils: Loamy and Sandy loam soils and 6 soils from D.A. Rose (1968)) and mean soils.

Figure 2 shows the relationship between $Ø_{FC}$ and one of those three parameters (*a*). The correlation (r_2) between a and $Ø_{FC}$ was 0.95 and 0.73 for the theoretical and laboratory soils, respectively.

Third, the Suleiman (2004, unpublished) soil evaporation model. This model is based on Darcy's Law and uses average daily soil water contents to drive the upward water flow. It is a promising approach since it is simple and reasonably accurate.

2.3 Infiltration

Water infiltration is the process by which a soil profile gains water through rainfall or irrigation. Only one infiltration model will be used in the SWDM. This model is based on the time-to-ponding (TP) concept. It is used to replace the infiltration curve numbers approach. The runoff curve number approach was found to be inadequate in representing variation in infiltration characteristics associated with differences in tillage and residue management. Time-to-ponding curves relate rainfall intensity to infiltration rate and define the point at which cumulative rainfall intensity exceeds the infiltration capacity of the soil, at which time water ponding in micro-depressions in the soil surface occurs. After ponding begins, infiltration is equal to the amount predicted by the TP curve as long as rainfall rate exceeds the infiltration capacity. When rainfall rate becomes less than the infiltration capacity, rainfall plus surface ponded water are infiltrated until the amount ponded is depleted. The main management-influenced parameter controlling the TP curve is the saturated hydraulic conductivity at the soil surface. The TP approach requires information regarding rainfall intensity. When only daily rainfall is known, a relatively simple disaggregation function may be used to derive rainfall intensities. The disaggregation function is defined for relatively large regions based on data from meteorological stations in the region, which have records of storm intensities.

2.3 Soil Bulk Density

Soil bulk density (BD) is a measure of the total soil porosity, which determines the saturated water content ($Ø_s$). In the SWDM, BD is estimated using a digitized data from Figure 1 of Rawls and Brakensiek (1985). A user needs the sand and clay contents of a soil in order to be able to calculate BD.

2.4 Field Capacity

Knowledge of the capacity soil water reservoir is useful in irrigation scheduling, watershed management, land use evaluation, and land planning. Field capacity ($Ø_{FC}$) is the soil water content after two days of drainage after thorough wetting. The Ritchie et al. (1999) approach is used to estimate $Ø_{FC}$ from bulk density and soil texture (sand and clay content).

2.5 Saturated Hydraulic Conductivity

Saturated Hydraulic conductivity (K_s) is one of the most important hydraulic properties of soils because it directly affects surface water runoff, soil erosion, and deep percolation. Suleiman and Ritchie (2001) developed a power function between K_s and relative effective porosity (= ($Ø_s$-$Ø_{FC}$)/$Ø_{FC}$) utilizing the Brutsaert (1967) Ks theoretical equation. Their K_s model worked well in estimating field-measured Ks for more than sixty soil profiles (Figure 3).

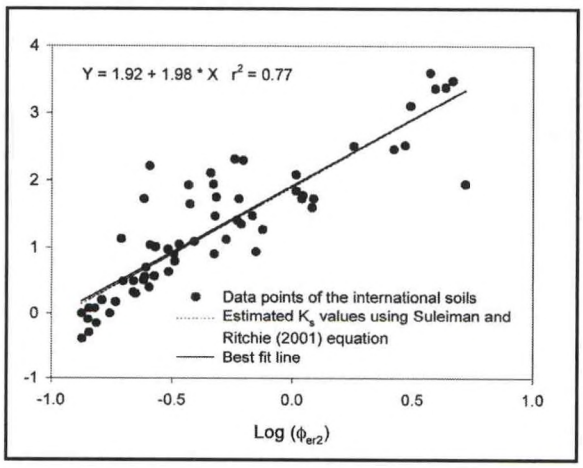

Figure 3. Log-log relationship of saturated hydraulic conductivity (K_s) and 2 d relative effective porosity (2) for the international soils (Reichardt and Nielsen, 1984).

Model Requirements

The SWDM has been developed in Visual Basic within a Visual Studio.net framework. In order to use this progarm the windows operating system with the microsoft .net framework is needed. If the computer does not have the microsoft .net framework one needs to run windows update and apply the patches needed. To run the program one needs to install the SWDM into hard drive. This will create a bin directory. Inside the bin directory gui.exe can be found. Once it is clicked on the SWDM application will lunch the program. Under help menu directions on how to run the models can be found. When a model is run an save dialog box will appear to save the results. The SWDM does not have an option to create graphs.

Summary

An overview of the soil water dynamics model (SWDM) has been given in this paper. More details about each of the models can be found in the literature cited above. Many copies of the beta version of SWDM (partially completed) have been distributed worldwide responding to demand from many national and international requests. In the future, the SWDM may be linked to a GIS to enable the SWDM to model the interaction between different cells such as lateral water flow from one soil profile to an adjacent soil profile.

ACKNOWLEDGEMENT

The author would like to extend his thanks to Mr. Edward Coleman who wrote the SWDM code.

REFERENCES

Boote, K.J., J.W. Jones, G. Hoogenboom, and N.B. Pickering. 1998: The CROPGRO model for grain legumes. p. 99-128. In G. Y. Tsuji et al. (ed.) Understanding options for agricultural production. Kluwer Academic Publisher, Dordrecht.

Jacques, D., J. Simunek, A. Timmerman, and J. Feyen. 2002: Calibration of Richards' and convection-dispersion equations to field-scale water flow and solute transport under rainfall conditions. J. Hydrol. 259:15-31.

Mcllroy, I.C. 1984: Terminology and concepts in natural evaporation. Elsevier Science Publishers B.V., Amsterdam, Agricultural Water Management, 8:77-98.

Panigrahi, B., and N.S. Panda. 2003: Field test of a soil water balance simulation model. Agric. Water Manage. 58:223-240.

Rawls, W.J., Brakensiek, D.L., 1985: Prediction of soil water properties for hydrologic modeling. In: Jones, E.B., Ward, T.J., (Eds.), Proceedings of a Symposium Watershed Management in the Eighties. April 30/ May 1, Denver, CO. Am. Soc. Civil Eng., New York, NY. pp. 293/ 299.

Reichardt, K., and Nielsen, D.R., 1984: Field soil-water properties measured through radiation techniques. IAEA-TECDOC-312. Joint FAO/IAEA Div. Isotope Radiat. Appl. Atomic Energy Food Agric. Dev. Vienna.

Ritchie, J.T. 1972: Model for predicting evaporation from a row crop with incomplete cover. Water Resources Res. 8:1204-1213

Ritchie, J.T., 1998: Soil Water Balance and Plant Water Stress. pp. 45-58. In Tsuji Y., Gordon Y.Tsuji, Gerrit Hoogenboom, Philip K. Thornton (Ed.) Understanding options for agricultural production. Kluwer Academic Publishers, Dordrecht. ISBN 0-7923-4833-8.

Ritchie, J.T., A. Gerakis, and A.A. Suleiman. 1999: Simple model to estimate field-measured soil water limits. Trans. ASAE 42(6): 1609-1614.

Ritchie, J.T., Kiniry, J.R., Jones, C.A., and Dyke, P.T., 1986: Model inputs. pp. 37-48. In C.A. Jones and J.R. Kiniry (Ed.) CERES-Maize, A simulation model of maize growth and development. Texas A&M Press, College Station, TX.

Suleiman, A.A. 2004: Modeling Daily Soil Water Dynamics During Vertical Drainage Using the incoming flow concept. Vadoze Zone J. (In review).

Suleiman, A.A., and R. Crago. 2004: Hourly and daytime evapotranspiration using radiometric surface temperatures. Agronomy J. 96: 384-390.

Suleiman, A.A., and J.T. Ritchie. 2004: Modifications to the DSSAT Vertical Drainage Model for More Accurate Soil Water Dynamics Estimation. Soil Sci. (In press)

Suleiman, A.A., and J.T. Ritchie. 2003: Modeling soil water redistribution under second stage evaporation. Soil Sci. Soc. Am. J. 67(2): 377-386.

Suleiman, A.A., and J.T. Ritchie. 2001: Estimating saturated hydraulic conductivity from soil porosity. Trans. ASAE 44(2): 235-239.

Youngs, E.G. 1995: Developments in the physics of infiltration. Soil Sci. Soc. Am. J. 59 (2):307-313.

MATERIAL CHARACTERISTICS IN FOURIER DOMAIN (MCFD) THE KEY TO MOISTURE CONTENT, VEGETATION HEALTH AND MATERIAL TYPE DETERMINATION

Maritza Torres (Graduate Student), Enrico Mattei (Graduate Student)
Advisor: Dr. Hamed Parsiani
University of Puerto Rico, Mayagüez Campus, Department of Electrical and Computer Engineering

Key words : Radar, Material Characteristics, Neural Network, Fourier Transform

Abstract

It is possible to determine the characteristics of the media by using the wavelet of the electromagnetic signal before and after it is reflected from the media. That is, the incident wave that is reflected from a material undergoes some transformation due to the characteristics of the material. A material characteristic in Fourier domain (MCFD) is defined and calculated at every reflection. An algorithm was developed which calculates the MCFD and it is used to train a two-layer Back-propagation Neural Network (NN). This NN was trained to determine the moisture content of the material: sand, loam or clay, successfully.

It was also found that by using the MCFD, vegetation could be classified according to its health using the GPR. The experiment was done using plantain leaves at different stages of health. The NDVI and MCFD were calculated for different vegetation levels, using a handheld spectral radiometer, and a GPR, respectively. Good results were obtained for NDVI greater than 0.5.

Material type can be determined irregardless of the layer at which the object is buried (limited to GPR reflection intensity level), object size, or if an extended subsurface layer is present. Another NN was developed and trained in order to determine the material type: sand, loam or clay. The NN has been tested with good results on sand.

Introduction:

The Material Characteristics in Frequency Domain (MCFD) can be obtained for a material buried at any layer. Figure 1.1 depicts a cross section of the ground where three different layers are visible. Figure 1.1 shows transmitted, S_{t_n}, reflected, S_{r_n}, and scattered waves, S_{s_n}, for each layer. In this development, it is assumed that there is no scattering. Let S_{t_0} be the incident wave, S_{t_n} the transmitted wave into the n^{th} layer and S_{r_n} be the reflected wave from the n^{th} layer. The reflected signal at any layer is a convolution of the transmitted signal with the material characteristics at that layer. Figure 1.2 demonstrates the system representation of the material characteristics, the transmitted wave is the input and the reflected wave is the output. In frequency domain the system is represented by equation 1. $S_{r_n}(u) = S_{t_{n-1}}(u) \cdot H_n(u)$ (1)

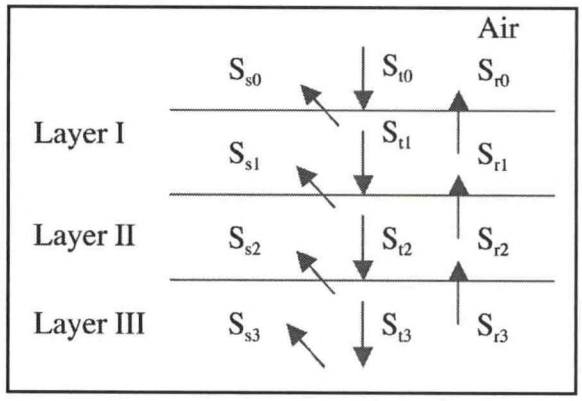

FIGURE 1.1: Cross section of the ground

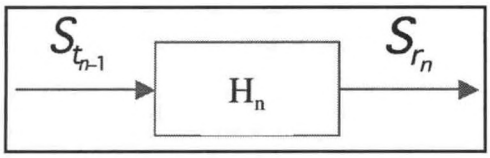

FIGURE 1.2: System representation of the layer characteristics, the transmitted and reflected waves

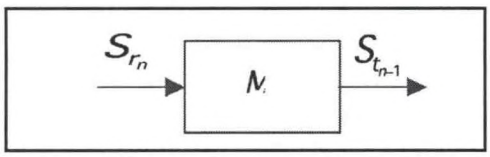

FIGURE 1.3: System representation of the new layer c characteristics, the transmitted, and reflected waves

Because this is a convolution operation, S_{r_n} has to be longer than $S_{t_{n-1}}$ but this is not the case, compression takes place and S_{r_n} is shorter in length than $S_{t_{n-1}}$. We developed MCFD by taking S_{r_n} as input to the system and $S_{t_{n-1}}$ as the output. Figure 1.3 shows the new system where M_n is the defined MCFD.

From figure 1.1 we see that $S_{tn-1}(u)=M_1(u)\cdot S_r(u)$ and $S_{t_1} = S_{t_0} - S_{r_1}$, consequently we obtain the following relationship

$$M_n(u) = \frac{\left[M_{n-1}(u)-1\right] * S_{r_{n-1}}(u)}{S_{r_n}(u)} \qquad (2)$$

where $S_{r_0} = S_{t_0}$, $n \geq 1$ and $SNR>>A$, where A is an acceptable measure. Equation (2) gives us the characteristics of the material at the n^{th} layer in terms of the material characteristics at the previous layer. We can also obtain the material characteristics at the n^{th} layer in terms of the material characteristics at the first layer.

From (2) we see that in order to obtain the material characteristics at the n^{th} layer, one must have knowledge of the previous' layer material characteristics. The MCFD for the n^{th} layer in terms of the previous layer can be obtained by the following equation.

$$(u) = \frac{\left[M_1(u)-1\right]\cdot S_{r_1}(u) - \sum_{i=2}^{n-1} S_{r_i}(u)}{S_{r_n}(u)} \qquad (3)$$

The MCFD was also calculated for LOAM and CLAY and Matlab's Neural Network was trained for the respective MCFDs. Loam moisture content values of 8.4, 10.2, and 23 percentages were calculated, as shown in Fig.2.2, and a NN was trained accordingly.

The Neural Network successfully classified an unknown loam sample, which had an average moisture content of 24.2% (measured by a Theta probe), as 23.41%.

Soil Moisture Determination

A method was developed by which the electromagnetic reflection of a Ground Penetrating Radar (GPR) can become an indicator of the moisture level of different soils. It was found that by analyzing the GPR wavelet of the air-soil boundary reflection one can identify near surface soil moisture content.

The dielectric constant is a function of both the frequency and the actual soil moisture content. The equipment that uses active measurements of the soil moisture such as Time Domain Reflectometer, or Theta Probe give different moisture measurements based on their frequency of operation. An algorithm is developed which uses Neural Network (NN) method to determine the moisture content based on the MCFD calculated for the material. A NN was developed for this experiment using Matlab. The training of the NN method can be based on any desired method of moisture measurements such as the usage of a theta probe or a gravimetric method.

2.1 Experimental Setup

Sand, Loam and Clay were used to test the NN developed in Matlab. Each soil type was placed in a box suspended in the air. The soil was evenly dampened and the moisture was increased gradually. Its moisture content was measured with the theta probe, five measurements, and the GPR at each level. The five measurements of the theta probe are averaged, in order to have one value corresponding to each wavelet. A table was created with these values.

2.2 Experimental Results

The wavelet was analyzed and the MCFD calculated at each moisture level. Using these values Matlab's NN was trained. One of the tests of the trained NN was to see if it was able to recognize

sand moisture (as an unknown) which was obtained from the field. The result of this test showed that the algorithm was able to recognize sand moisture approximately, as shown in Figure 2.1.

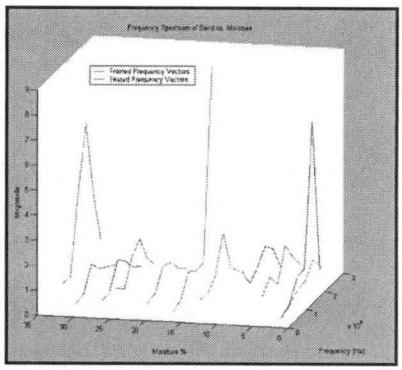

FIGURE 2.1: Moisture MCFDs of trained NN and tested results for sand

Vegetation

Using the MCFD, vegetation could be classified according to its health using GPR, as an extension of the moisture determination experiment. This is a great advantage in terms of higher resolution achievable by active as opposed to passive satellites in the measurements of vegetation health index.

The Normalized Difference Vegetation Index (NDVI) was defined to measure vegetation health; it is measured using passive sensors (radiometers). Satellite radiometers have low range resolution, depending on light and do not penetrate clouds. In areas like the tropics where there is a lot of continuous cloud coverage, radiometers cannot be as effective. On the other hand, radar can penetrate clouds and rain and does not depend on sunlight. Using the MCFD it is possible to measure vegetation health and compare it to the NDVI. The results obtained from the GPR and the Spectrometer demonstrates a linear relationship between the active and passive vegetation health index measurements.

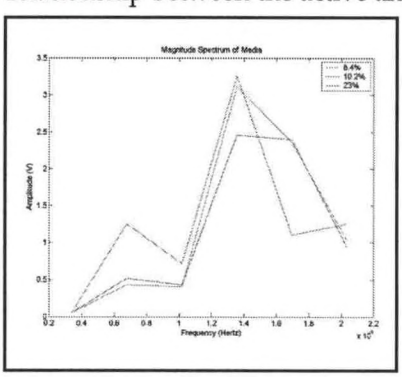

FIGURE 2.2: MCFD of loam for moisture content of 8.4%,10.2% and 23%

Testing of plantain with two different background materials was achieved. The two background materials used were wood and air.

After obtaining the MCFD, the average power of the frequency spectrum is calculated, using equation 4,

$$P_{ave} = \frac{\sum A(f)^2}{N} \tag{4}$$

where A is the amplitude of the MCFD at different frequencies, and N is the number of frequencies chosen. The average MCFD power is then correlated with the NDVI obtained from the spectroradiometer.

Experimental Setup

The measurements, in this research, took place at the near ground level over vegetations from dry to green conditions, using a Ground Penetrating Radar, and a handheld Spectrometer. Both measurements took place one right after the other, to allow an accurate comparison.

The MCFD power and NDVI data for plantain with two different backgrounds of wood and air obtained are shown in table II.

The correlation between the NDVI and MCFD Power was calculated, and plotted, as depicted in Figures 3.1, and 3.2.

Values of NDVI above 0.5 were chosen due to problems at lower values and a new technique must be adopted for the lower range. There is a good correlation of 0.9336, however, there are missing values of NDVI from 0.75 to 0.53. More measurements are needed in order to cover that area.

Material Type

The GPR was used to obtain the reflection wavelets from two layers defined by different materials at each layer (e.g. clay, loam, sand, rock, ceramic, etc.). In every file saved during these measurements there as two reflections: Air/Material-I and Material-I/ Material-II. Examples of GPR electromagnetic reflections data in time domain for various material types are presented in Table III..

After obtaining the signals described above and applying Fourier transform to them, the MCFD can

	NDVI	MCFD Average Power
Vegetation with Wood as Background	0.3	0.2
	0.43	0.1611
	0.62	0.1183
	0.83	0.017
	0.85	0.0168
Vegetation with air as Background	0.86	0.1409
	0.852	0.0598
	0.819	0.1052
	0.7908	0.1498
	0.4343	0.2611
	0.3165	0.2416
	0.9	0.0797
	0.86	0.1019
	0.81	0.1508
	0.75	0.2665
	0.53	0.4796
	0.13	0.2021

TABLE II. Data obtained from GPR and Spectrometer

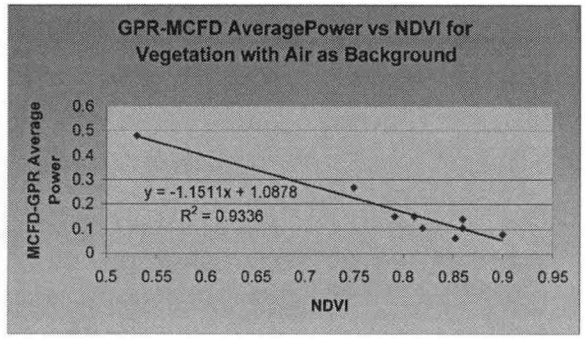

FIGURE 3.2: GPR-MCFD Power vs. NDVI for Vegetation with air as background

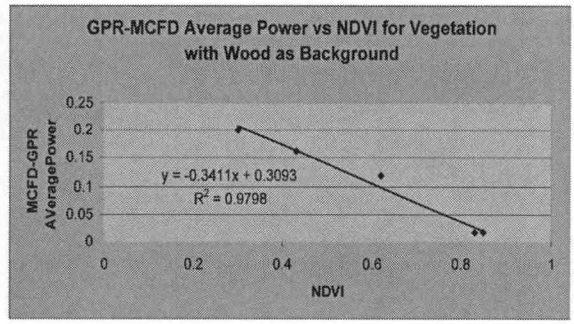

FIGURE 3.1. GPR-MCFD Power vs. NDVI for Plantain Vegetation using wood as background

File nam	Material I	Material II	Reflection: Air/ Material I (Magnitude vs. Time)	Reflection: Material I / Material II (Magnitude vs. Time)
LO-CO_001	Loam dry	Clay dry	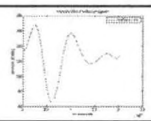	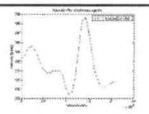
SO-Rock_00	Sand dr	Rock	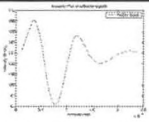	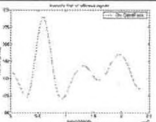
LO-Alum_0C	Loam dry	Aluminum	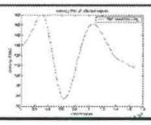	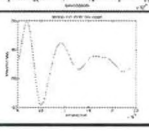

TABLE III: Example of intensity reflection obtained in the different boundary layers.

be obtained by equation (5), using the transmitted and reflected signals.

$$M_1(u) = \frac{S_{t_0}(u)}{S_{r_1}(u)}. \qquad (5)$$

A Neural Network (NN) was created to recognize the first layer of material in each combination of soils and objects that were measured. This NN was trained to recognize sand, loam and clay, based on their MCFD, $M_i(f)$, for $i=1$. The measurements were obtained from the boundary between the air and material I. This MCFD defines the signature of the particular material to be recognized.

The reflection of the signal transmitted by the GPR in the air (S_{t_0}) that was used in equation 1, is shown in Fig. 4.1.

The Neural Network (NN), Fig. 4.2 was used for the training of the material, based on their MCFD.

Experimental Setup

Each measurement was made with the GPR in the air at zero height from material I. Both reflections at air/material I and material I / material II are obtained for the three examples. Different combinations of material were used.

Experimental Results

The MCFD of the different samples which were used for training can be seen in figure 4.3. One of the tests of the trained NN was to see if it was able to recognize sand (as an unknown) which was obtained from the field. The result, Fig. 4.4, showed that the algorithm was able to recognize sand with a two percent error And, the material characteristic of the test material (as indicated) matches the sand characteristics.

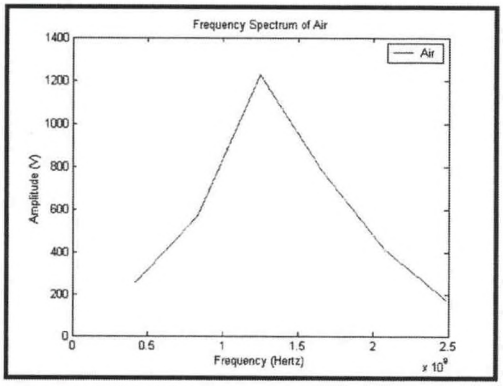

FIGURE 4.1: Frequency Spectrum of Air

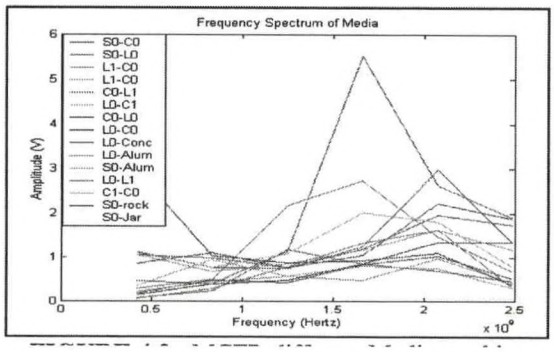

FIGURE 4.3: MCFD different Media used in training of NN.

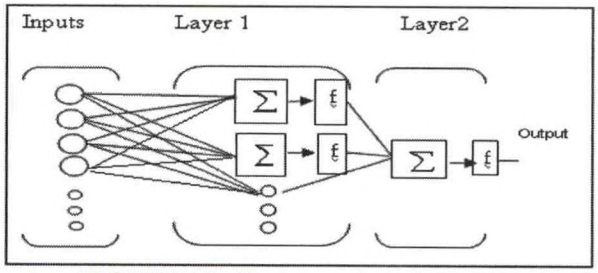

FIGURE 4.2: Representation of a two layer Neural Network.

Experimental Results

The MCFD of the different samples which were used for training can be seen in figure4.3. One of the tests of the trained NN was to see if it was able to recognize sand (as an unknown) which was obtained from the field. The result, Fig. 4.4, showed that the algorithm was able to recognize sand with a two percent error. And, the material characteristic of the test material (as indicated) matches the sand characteristics.

Conclusion

The block diagram of applications of MCFD is presented in Figure 4.1. MCFD/NN method has been shown to be a new method which is able to characterize soil moisture, and material type. Also, the same method has produced good preliminary results for determination of vegetation health. In this research the testing of material type determination was limited to the first layer.

However, more work is in progress to test the MCFD/NN concept with more unknown samples of soil moisture, and with variations of moist soil types. The MCFD/NN recognition of soil type will also need to be extended to consider other soil types, such as variations of sand, loam, and clay. Extension of MCFD/NN to other materials and to other layers will require calculations of MCFD for GPR wavelet information from different layers, and corresponding training of the Neural Network.

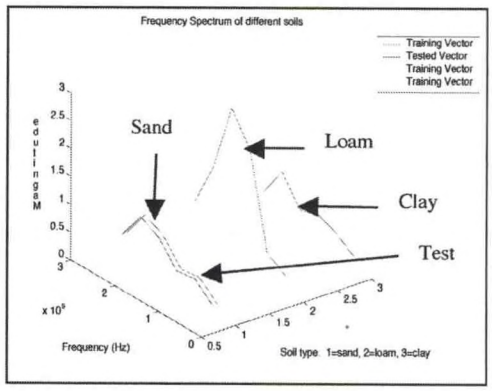

FIGURE. 4.4: Frequency Spectrum of trained and tested vectors.

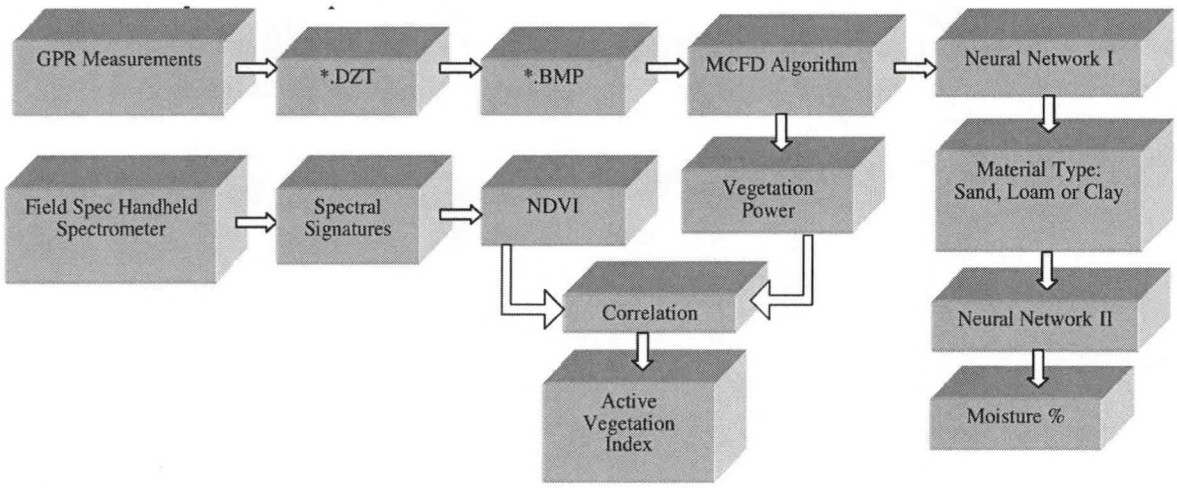

FIGURE 5.1: Block Diagram of the Application of MCFD

ACKNOWLEDGEMENT

The authors gratefully acknowledge the combined support of NOAA-CREST grant NA17AE1625, and NASA grant NCC5-252.

REFERENCES

D. J. Daniels,1996. Surface Penetrating, *Radar IEE Press*.

Hamed Parsiani, Pedro Rodriguez, 2004. Subsurface Material, Type Determination from ground Penetrating Radar Signatures. *SPIE 2004*, Spain.

Hamed Parsiani, Maritza Torres, Pedro Rodriguez,2004: High Resolution Vegetation Index as Measured by Radar and its Validation with Spectrometer *SPIE 2004*, Spain.

Hamed Parsiani, Maritza Torres, Pedro Rodriguez, 2004. Material Characteristics In Fourier Domain (MCFD) Formulation, A Signature To Determine Soil Type, Moisture, And Vegetation Health, Based On Multilayer Ground Penetrating Radar Reflection. SIP 2004, Hawaii.

Maritza Torres, Hamed Parsiani,2004. Non-linearity of Soil Dielectric as a Function of Radar Frequency and Soil Moisture Content. *A peer review, Proc. CRC'2004*, April 2, 2004, Mayaguez, P.R.

M. Tokunaga, T.Thuy Vu, 2002: Finding the Relationship Between Vegetation Index And Coherence Signature To Utilize The Product Of Radar Interferometry In Land Cover Application. *Asian Conference on Remote Sensing*.

Pedro Rodriguez, Hamed Parsiani, 2004: Moisture Determination Based on Ground Penetrating Radar Measurements. *A peer review, Proc. CRC'2004*, Mayaguez, P.R.

Pedro Rodriguez, Hamed Parsiani,2004. Moisture Determination Based on Ground Penetrating Radar Measurements. *A peer review, Proc. CRC'2004*, April 2, 2004, Mayaguez, P.R.

S. Cardimona, D.J. Webb and T, Lippincott, 2000. *Ground Penetrating Radar Geophysics.*

S. Kingpaiboon,2002. Microwave Remote Sensing for Land Cover Identification. *Land Use/Land Cover, Asian Conference on Remote Sensing.*

On Developing a Protocol for Assessing Estuarine Health I: Organic Compounds GC/MS Characterization of Terrestrial Lipid Biomarkers in Recent Sediments of a Fresh Water River (Pocomoke River, MD)

Gerald Kananen[1], Nianhong Chen[2], and Eric May[1]

1 University of Maryland Eastern Shore; Princess Anne, Maryland

2 Old Dominion University; Norfolk, Virginia

As part of an ongoing program for assessing the chemical health of the coastal bays, periodic surveys have been conducted over the past 5 years. Target analytes have included metals, nutrients and organics. In some cases there are demands for specific organic analytes such as methyturtbutylether (MTBE) or endocrine disruptors. Results of these surveys have been used by state agencies in determining development plans for the estuarine areas including the Coastal Bays. In addition to target analytes, general surveys are of value in determining a broader environmental picture from which to evaluate natural and anthropogenic influences and select methodology. It is the purpose of this paper to review some approaches to organic analyte characterization done at the University of Maryland Eastern Shore. Depending on the analyte, methodology can include headspace combined with capillary GC/MS for aqueous samples (MTBE), or capillary GC with electron capture detection for DNT degradation and semi-automated instrumentation for sediment characterization. Although the latter approach targeted outlying river areas, the developed protocols serve as a template to selecting methods suitable for comprehensive studies of the Coastal Bay areas.

An Interdisciplinary "Four-Component" Modeling Methodology for Resource Management: Design and Application

Michael A. Reiter

Dept. of Agriculture and Natural Resources, Delaware State University, Dover, DE 19901-2277

An integrated, interdisciplinary conceptual model was developed for the St. Jones River watershed, Delaware for use as a management and research tool. The model utilizes the "two-component" approach of the Environmental Cooperative Science Center methodology and expands upon it to include a third (valued ecosystem components-services) and fourth (services-drivers) component. The four-component model has the potential to more clearly link human activities not only to significant ecological impacts within a habitat, but to possible social and economic impacts on human services including feedbacks upon the initiating drivers. However, it can be difficult to analyze such models given the wide range of scales and units present in the model's components. Fuzzy logic, a rule-based approach using relative or linguistic variables (such as "high" and "low", or relative coefficients of "strength" from 0 to 1), can be used to analyze four-component integrated conceptual models despite the complexities of the different types of inputs, outputs, and components. The analysis identified several habitat components as being more or less significant than suggested by the Level One model. Using fuzzy logic analysis to sort the number of links and components appears to be a useful way to identify a strongly connected subset of model components simplified enough for use in monitoring and management. See Reiter in review for the full manuscript.

Expanded Summary

Estuaries and related coastal ecosystems are important to the nation's economy and recreation, and are an integral part of the environment as a whole. Understanding and protecting estuarine resources has become increasingly important due to unsound land use practices and increasing population in coastal areas, which can contribute to the degradation of estuaries (for example, wetlands of the 1600s were estimated to cover 89.5 million hectares, but by the 1980s wetland coverage was reduced to about 41.7 million hectares; Fretwell et al., 1996). The interdisciplinary conceptual modeling methodology utilized by the Environmental Cooperative Science Center (ECSC) is one attempt to integrate social and environmental factors into a unified picture of key interactions between activities in the watershed and important components of the watershed's habitats.

The purpose of many such environmental modeling efforts is to link changes in ecological indicators ("valued ecosystem components"; VECs) to both natural and anthropogenic "stressors" (measurable changes in the system that can be related to some activity or occurrence in the system). More complete studies incorporate the link between stressors and their origin (the actual activities or occurrences that lead to them: "drivers"). Once completed, such a "two-component" model (drivers ‡ stressors ‡ VECs) can directly identify the actions causing environmental deterioration (see Harwell et al 1996, Harwell et al in prep).

There is a logical extension to this process: identifying the ties between changes in environmental parameters and changes in the benefits humans derive from the environment ("services"). Service flows from nature include any tangible/quantifiable (ex. lumber) or less tangible/quantifiable (ex. pollution absorption) benefits of value to humans that depend upon the ecosystem for their pro-

vision. Models that include this third component provide a framework within which the value of environmental change can be investigated and/or quantified. Since many of these altered service flows impact drivers in turn (for example, depleted fish populations negatively impacting local fishing activity; "feedbacks"), a fourth step can be added in which the model loop closes and future impacts on drivers can be predicted (creating a "Four-Component" model; Figure 1). By describing the adverse environmental changes in terms of lost or foregone benefits to humans in addition to altered ecological components or functions, the political decision-making process can be more fully informed of the consequences of its actions (or lack thereof) in readily understandable terms (see Reiter et al in prep for a description of the four-component process).

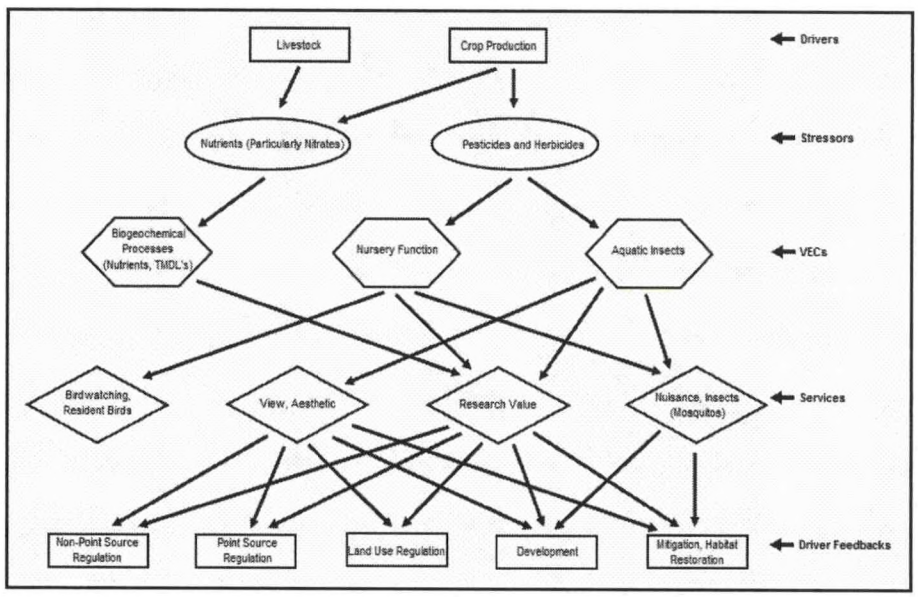

Figure 1. An example submodel extracted from a full four-component Saltmarsh habitat model, showing only the impacts linked to agricultural drivers (Reiter et al in press).

One potential difficulty with these models is that they can contain numerous drivers, stressors, VECs, etc. that are difficult to quantify, rank, and/or reduce to a workable number of items to measure and monitor. Forming a "Level 1" model (including only those components shown in the matrices to have at least one "high" link to another component) can reduce the numbers of drivers, stressors, etc., and it is also possible to use similar patterns of "High" and "Low" links to lump drivers, stressors, etc. wherever possible, but both approaches can increase subjectivity while still resulting in a complex model with more components than can be effectively ranked or utilized. Another significant issue with the Level 1 approach is that, by focusing only on major connections ("High" links) and pathways, the model can miss potentially significant impacts that could result from the collective influence of a large number of relatively weaker links.

One possible way to attempt to address these issues is to utilize fuzzy logic. Fuzzy logic, a rule-based approach designed to address imprecisely defined systems and applicable to relative or linguistic variables, allows for the conversion and analysis of four-component integrated conceptual models despite the different types of inputs, outputs, and components. To summarize the methodology as applied to this analysis, the linguistic and/or relative categories are converted into rule-based numerical representations that are then manipulated in simplified equations or studied using mathematical and statistical procedures including Monte Carlo simulations of potential outcome distributions. The resulting values are then interpreted based on the rules and categories used to generate them, and the Monte Carlo distributions used to eliminate components in the Level 1 model that have less connectivity. While the numerical process maintains the relativistic quality of the original cate-

gories, the results allow for a more detailed or nuanced interpretation of the system than would be possible based solely on the original linguistic or graphic representations of that system (see Ruspini et al 1998 and/or Pal and Mitra 1999 for details on fuzzy logic methodology). This methodology can potentially be used to both analyze a model and to simplify otherwise complex Level 1 models to make them more useful for monitoring and management decisions.

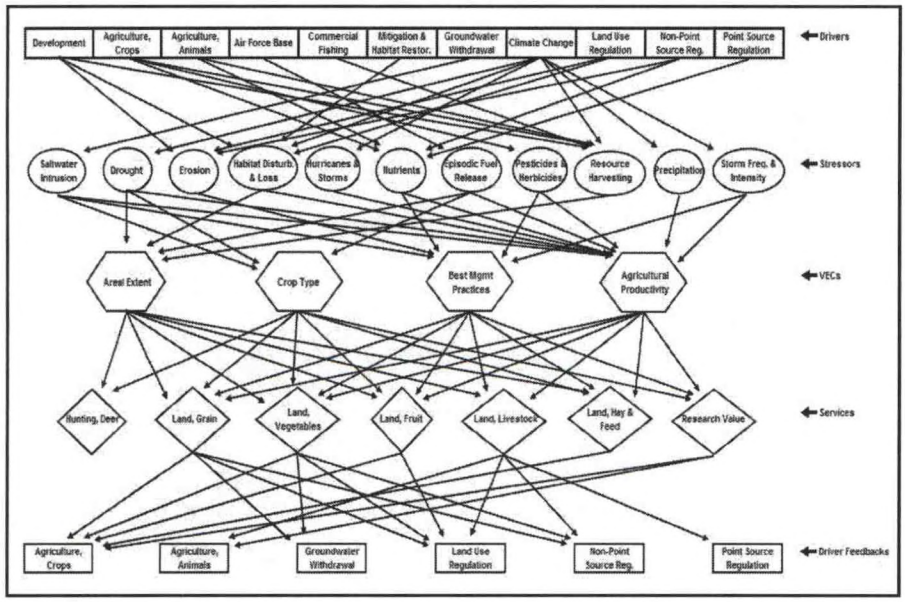

Figure 2. Example Level 1 model, Agriculture habitat, St. Jones River watershed.

As an example result, figure 2 shows a sample habitat (Agriculture) from the Level 1model, the starting point for the analysis. The Level 1 Agriculture model is still very complex, with 11 of 15 possible drivers, 11 of 21 possible stressors, 4 of 6 possible VECs, all 7 services, and 6 of 15 possible feedbacks figuring into the model. The model does not give a feeling for the relative importance of the numerous components in the model, except indirectly byconsidering the number of links coming into or leaving any particular point in the model.

Figure 3 illustrates the result of using the fuzzy logic and Monte Carlo process to narrow the Level 1 Agriculture model. The driver ‡ stressor and stressor ‡ VEC sections are notably simplified, with the remaining components weighted to allow for decisions to be made based on potential interaction strength. While in this example case the services and feedbacks were not reduced, reductions did occur in other habitat models to the extent that some habitats had no strong pathways to services or feedbacks remaining.

Conclusions

Using simple fuzzy logic analysis to narrow a Level 1 model appears to identify a connected set of potentially important components workable for resource management purposes in terms of complexity and scale. While the narrowed version does not include all potentially important impacts, it does appear to provide a subset that has enough connectivity to be potentially useful for monitoring.

Since the primary goal was to find a means of narrowing the existing Level 1 models based on connectivity, the equations and analysis were very simple (discreet choices, equal probabilities, and linear and additive equations). Since it is unlikely that linear relationships, purely additive impacts, and discreet levels of interaction strength are dominant in nature, this approach should be seen only as a first step and approximation to achieve a specific goal: a limited, connected set of rela-

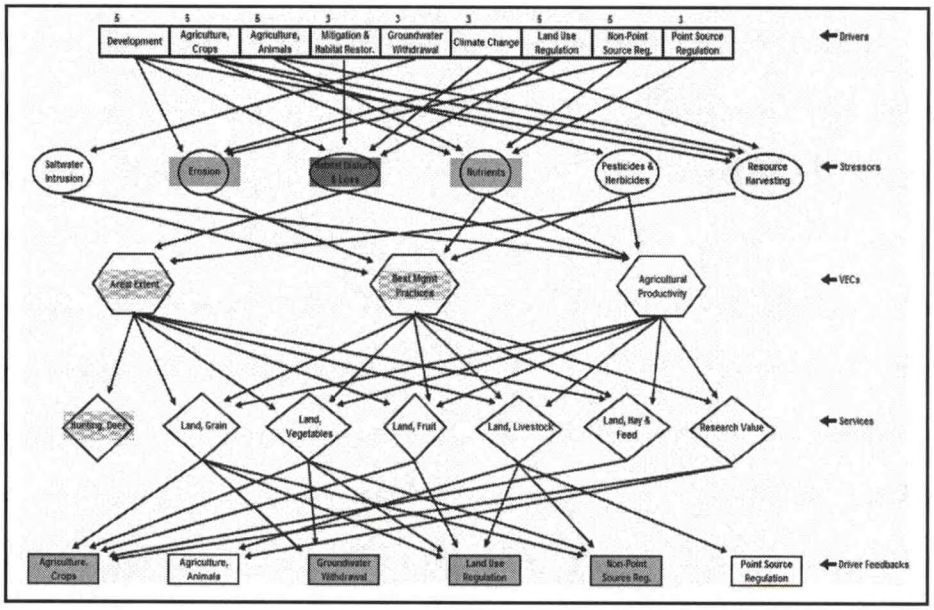

Figure 3. Example of a narrowed Level 1 model, Agriculture habitat, St. Jones River watershed. Dark: >2SD above mean; Light: >1SD above mean; Stippled: <1SD below mean.

tively important components for use in resource management. More sophisticated equations and interaction calculations based on existing data or more complex theoretical relationships could potentially improve the strength of the models, particularly if a part or the entire model is to be eventually quantified. See Reiter (in review) for the full manuscript on this topic.

ACKNOWLEDGEMENT

This work was supported by NOAA Grant #NA17AE1624 to the Environmental Cooperative Science Center.

REFERENCES

Harwell, M., J. Long, A. Bartuska, J. Gentile, C. Harwell, V. Myers, and J. Ogden, 1996: Ecosystem management to achieve ecological sustainability: The case of South Florida. *Environ. Manag.* **20**(4):497-521.

Harwell, M., J. Gentile, M. Reiter, J. Schalles, M. Thomas, D. Letson, and C. Forthman, In prep: Development and utility of conceptual models of coupled human-ecological systems. *Urban. Ecosys.*

Pal, S. and, S. Mitra, 1999: Neuro-Fuzzy Pattern Recognition: Methods in Soft Computing. Wiley-Interscience, NY.

Reiter, M. A, In review: A simple fuzzy logic approach to analyze integrated interdisciplinary "four-component" conceptual resource management models. Interdisc. Environ. Rev.

Reiter, M., G. Parsons, R. Scarborough, C. Fan, and S. Thur, In prep: An interdisciplinary conceptual metamodel for the St. Jones River watershed, Delaware: development, results, and implications. *Urban Ecosys.*

Ruspini, E., P. Bonissone, and W. Pedrycz, 1998: Handbook of Fuzzy Computation. Institute of Physics Publishing, NY.

Characterization of Biomass Burning: Fourier Transform Infrared Analysis of Wood and Vegetation Combustion Products

Diomaris Padilla and Dr. Jeffrey Steiner

Dept. of Earth and Environmental Sciences and Engineering, City College of New York, CUNY

Abstract

Fourier transform infrared examination of the combustion products of a selection of forest products has been undertaken in order to guide future detection of biomass burning by satellite sensing. Combustion of pine, cherry, maple, sweet gum and various oak wood blocks in a Meeker burner flame at about 1100 degrees Fahrenheit produces a broad relatively flat signal with a few distinct peaks at the upper and lower end of the wavenumber spectra (400 to 4000 cm-1). The distinct bands at about 450 to 660 wavenumber vary with species with the most pronounced differences occurring in the cherry and oak samples. Band differences are used to help distinguish vegetation type involved with recent wildfire propagation studies. Similar study of leaves and branches at combustion temperatures produces a similar set of spectra indicating that a forest canopy blaze spectrum may not be distinguishable from a fire involving primarily tree trunks.

Introduction

Aerosols exist in our atmosphere as a gaseous suspension of fine solid, liquid, gel-like and composite materials. The sources are copious, including volcanic emissions, sea spray from the marine environment, windborne dust, biomass burning, diesel emissions and numerous other points of origin. Smoke is the result of the incomplete combustion of fossil fuels, whereas soot is an agglomeration of carbon compounds impregnated with tar (see Seinfeld, 1998 for a more detailed account). Numerous studies (Tyson 2001) and models (Menon 2002) have agreed that certain aerosol types, such as soot and smoke, are creating problems on a localized basis affecting regions such as Africa and China. These conditions, however, tend to have a domino affect in the climate and may in turn aide in generating more atmospheric aerosols, such as dust, which is seen in the growth of dust storms generated in the Sahara desert (Schmidt 2002). It is due to the far reaching effects of aerosols that the role of monitoring different types of particulates comes into play. Distinguishing varying aerosol compositions remotely may make it viable to predict and possibly counter the negative influences of aerosols in our atmosphere.

The purpose of this research is three-fold: (1) to characterize soot originating from different sources (i.e. Wood soot from diesel soot or pine soot from cherry wood soot); (2) to distinguish between high temperature and low temperature soot; (3) and to observe heavy-metal-bearing dust particles using infrared sensing in order to improve the characterization of known constituents, such as chlorides and sulfates, with an emphasis on the characterization of new organic and heavy metal aerosols. Fourier Transform Infrared Spectrometry (FTIR) will be used to analyze absorption intensities of aerosol particles. The absorption spectra generated will aid in the identification of the compounds found within the dust, soot or smoke. A focus will be placed on how the FTIR results compare with other chemical characterization procedures, such as x-ray fluorescence and atomic absorption.

Background and Previous Works

Aerosols are a permanent fixture in our environment, serving both as useful additions and

hazards. The unique flexibility of the aerosol to affect both large scale systems, such as climatic changes, and small scale systems, human health, is seen in its size variations. An aerosol can range from 0.1 micrometers to slightly less than 100 micrometers (Pitts 2000), easily affecting cloud formation or human lung tissue development.

At its smallest size, 0.1 micrometers, an aerosol can play a deadly role in the human respiratory system. Although scientists still do not know the workings of the aerosol mechanism in the human lung or heart tissues, research has shown that aerosols such as soot, ozone and smog are damaging and at times fatal (Journal of Environmental Health 2004). In the United States alone there has been an increase in respiratory and heart related deaths of up to 17%, reaching numbers of up to 60,000 deaths a year due to over-exposure to smog and other aerosols (Journal of Environmental Health 2004). Asthma in other regions of the globe is also causing concern and being connected to aerosol chemistry and concentration. In the Caribbean scientists have found that asthma rates are on the rise and may be due to windborne dust traveling from Africa's Sahara desert (Schmidt 2002).

Climatically speaking, the affects of massive amounts of smoke, another type of aerosol, originating from wild fires and entering the atmosphere is seen by many observers as creating a significant degree of ongoing climatic change. Changes are evident through studies of satellite imagery, e.g. Very High Resolution Radiometer (AVHRR), where it is evident that the formation of large thunderstorms is related to nucleation by smoke particulates (Lyons 1998). Although nucleation is one manner in which smoke can alter thundercloud formation, the influx of particulate matter can influence the absorption/reflectance characteristics of an entire atmospheric system (Lyons, 1998). These effects are normally not localized to the outer edges of the system, but seen throughout the entire storm structure. Thunderstorms generated in this manner form uncommonly high amounts of positively polarized lightning, an occurrence typically observed in colder systems and normally leading to stronger storm cloud systems (Lyons 1998). Mesospheric red sprites, which are common in high positive polarized environments, are also more abundant with these smoke induced thunderstorms (Lyons 1998).

Fourier Transform Infrared (FTIR) Methods

Although previous studies have not used FTIR for distinguishing various types of soot, studies on diesel and other gas generated soot have been made. A recent study (Andoh 2004) uses the infrared spectra of live tree cuttings for the purpose of distinguishing wood grades by using FTIR however the study is done only on maple trees. Other studies using the infrared spectra of woods, while remaining in the forest products industry, have been done for the purpose of wood quality in tree movement programs (So 2004). So's research focused on the near infrared spectrum, but was basically similar to Andoh's work in that they were looking at living species of trees in order to compare a healthy specimen's (near) infrared spectra with an unhealthy specimen's (near) infrared spectra.

In either of the above cases the samples used were solid. Therefore the methodology used was a basic widely used technique of dispersing the sample in potassium bromide and pressing them into pellets. Since it is uncommon to use solid-state FTIR for aerosols, a method for capturing both soot and heavy metal particles directly onto a potassium bromide soft pellet has been the recent focus of this

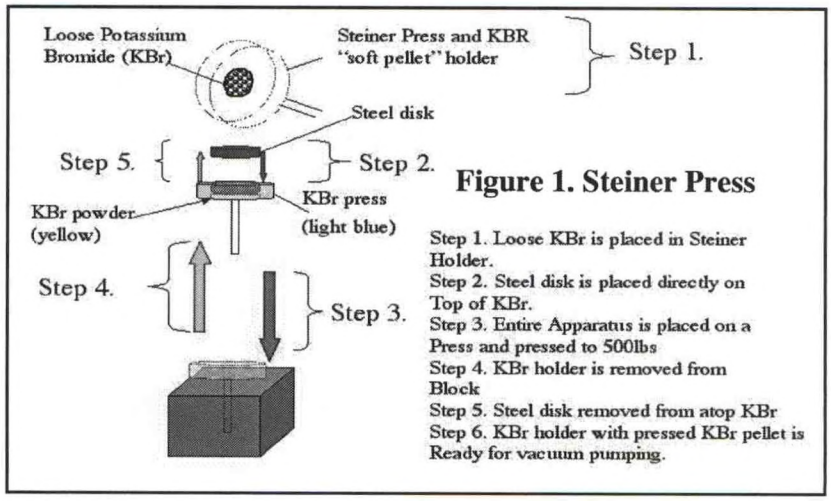

Figure 1. Steiner Press

Step 1. Loose KBr is placed in Steiner Holder.
Step 2. Steel disk is placed directly on Top of KBr.
Step 3. Entire Apparatus is placed on a Press and pressed to 500lbs
Step 4. KBr holder is removed from Block
Step 5. Steel disk removed from atop KBr
Step 6. KBr holder with pressed KBr pellet is Ready for vacuum pumping.

research. Potassium bromide, KBr, is a type of salt that is transparent in the infrared spectrum up to 400 cm-1, 25microns, (Mass 1972). By directly collecting aerosols onto KBr media, aerosol samples are then capable of being analyzed via a solid state FTIR. KBr 'soft' pellets were created for this specific purpose. A 'soft' KBr pellet is a pellet pressed to any amount less than the 1100lbs it takes to pressurize powdered KBr into glass. These pellets are produced on the "Steiner Press," a steel press designed by Dr. Steiner (Figure 1.) The Steiner press was designed to allow for the KBr to be pressed and held in the same container that is used for aerating. This method should minimize the loss of potassium bromide as the vacuuming, via the vacuum pump, takes place. Testing of this capturing technique has been performed in a controlled experiment using soot and smoke aerosols generated by the low temperature burning of various lumber. The woods used were: White Oak (Quercus alba), Maple (Acer rubrum), Pine (Pinus Strobus), Cherry Wood (Prunus serotina) Ash (Fraxinus excelsior) and Red Oak (Quercus borealis). The purpose of this phase of the experiment is as follows: (1) To find a standardized method of collecting aerosols directly onto KBr; (2) To find the spectra generated by varying wood species and; (3) To be able to match the spectra of the direct (mixing of soot directly into the KBr to create a standard pellet) and indirect (using the soft pellet as an air filter to capture the soot aerosols as they are generated) soot sampling methods.

Since aerosols are typically not analyzed directly by the FTIR spectrometer, methods have been implemented to aid aerosol characterization. In the present study, a solid state potassium bromide impactor (Steiner Press) is used for collection and the product is pressed into pellets at approximately 1100lbs (Smith 2000). The Steiner press was designed to allow for the KBr to be pressed and held in the same container for aerating, which is done in a sealed compartment (Figure 2.) The airflow rates through the vacuum pumps were found to be 0.1 liters per second for both 500lb and 250 lb pellets.

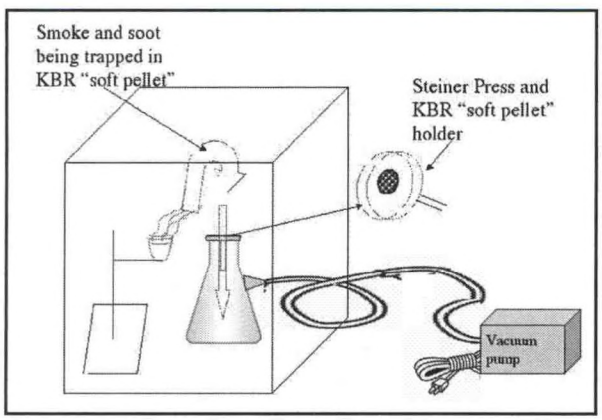

Figure 2. Collection chamber

Soot is collected by burning woods of various types in an enclosed chamber (Figure 3.) Before initiating combustion a potassium bromide pellet is placed on the mouth of a 1000ml flask which is attached to a vacuum pump. The wood is then held with tongs over a flame in order to initiate combustion. At the onset of flames the vacuum pump is turned on and the wood allowed to burn in a porcelain crucible. The tube connecting the vacuum pump to the flask is fitted through a hole on the side of the box and sealed to minimize smoke escape. The smoke and soot created is subsequently vacuumed onto the pellet and through it. The vacuum pump works at a rate of 4 cm Hg throughout the proceedings. After the aerosol samples are collected onto the KBr pellet, the holder and KBr pellet are reweighed and the pellet scraped off of the holder and placed into a glass dish. The soft pellet remains covered in an oven, which is maintained at a temperature of 100 degrees Celsius, for 24 hours and is then reground into powder for analysis. The new sample is treated like any other FTIR powdered sample and diluted to about 1% in powdered potassium bromide.

The manual press in the laboratory increases by steps of 500lbs; 500 lbs is used to create an initial seal, and then the compressed product is pressurized in one additional step just to analysis. Pressure comparisons of Potassium Bromide (KBr) soft pellets at: 250lbs, 500lbs and 750lbs clearly show that the highest concentration of materials is being collected at the 500lb pressure (seen in yellow in Figure 3.) Possible reasons for low collection concentrations at 250lbs may be due to the lack of cohesion of the potassium bromide grains allowing for airflow to pass right through the media without properly capturing aerosol particles. At 750lbs, shown in purple, the reverse is true. The high pressure of the 750lbs, purple line, has brought the potassium bromide grains so close together that the tight weaving of the

grains does not allow for easy airflow, thereby restricting aerosol capture within the soft pellet. At 500lbs of pressure, shown here in yellow, the grains are tightly enough woven to sustain an environment where aerosol capture is maximized. With this in mind flow rates for the two pressures falling under 750lbs, 250 and 500lbs, were taken. The 250lb press had a flow rate of 0.09 L/s (liters per second) and the 500lb press had a flow rate of 0.106 L/s, and so 500lbs of pressure was chosen for future pressing.

Experimental Results

Using a Nicolet Fourier Transform Infrared Spectrometer (FTIR) the spectra of plain potassium bromide and a soft pellet were obtained and compared to note any differences arising from applying pressure to create the pellets. Since the spectra of the pressed potassium bromide exhibits a significant difference in water and carbon dioxide levels the spectra will be used as a background to the wood spectra and will be subtracted from any spectra obtained through this method.

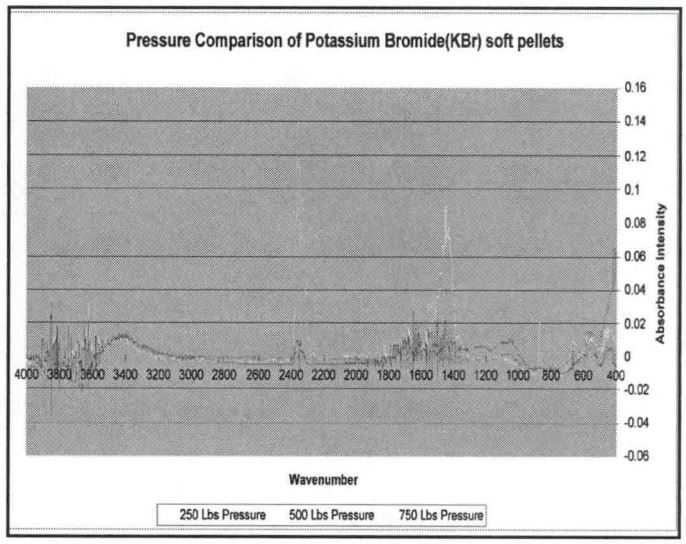

Figure 3. Pressure comparison of Potassium Bromide (KBr) soft pellets at: 250lbs, 500lbs and 750lbs. The comparison clearly shows that the highest concentration of materials is being collected at the 500lb pressure (seen in pale grey.)

Spectra generated via the direct and indirect capture method had a calculated variance of 0.0012, indicating adequate impaction on the KBr pellets. Our findings also show that each wood is displaying a group of different spectral bands and intensities, the actual variations, leading us to believe that each wood soot species has its own infrared signature. However there are common bands in each of the woods tested, those peaks appear specifically at 3300-3500 cm-1, sharp peaks at 3500-3900cm-1 and 1870-1339 cm-1 (due to water vapor- moisture in air), some medium peaks at 2362, 2345 and 2331 cm-1 and finally a clustering of medium to small peaks from 669-408 cm-1. Possible peak differences below 600cm-1 may be indicative of a fingerprint region for specific tree species, cherry, oak etc.

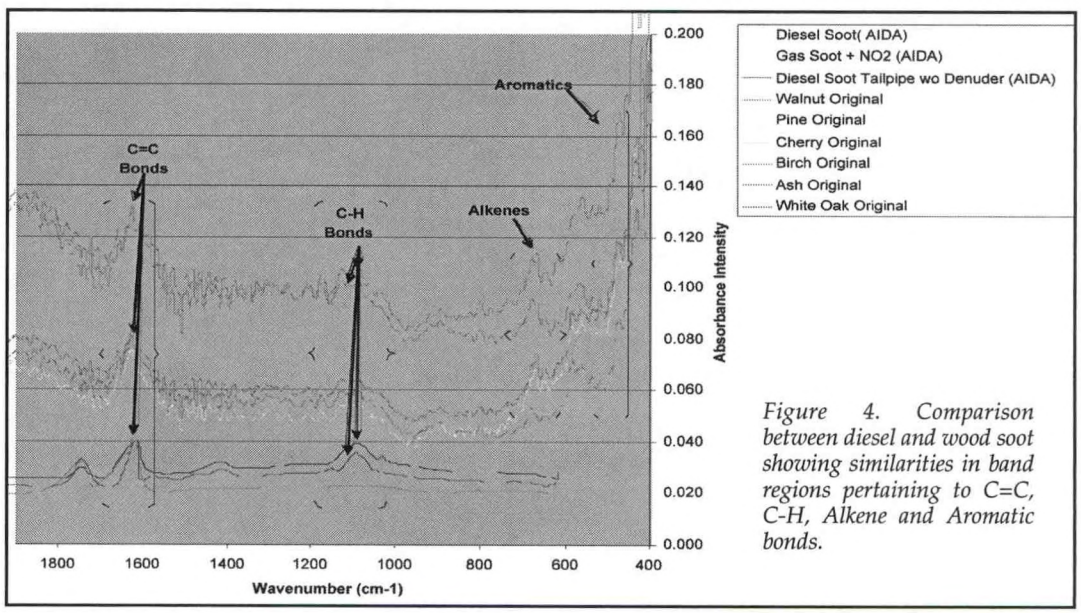

Figure 4. Comparison between diesel and wood soot showing similarities in band regions pertaining to C=C, C-H, Alkene and Aromatic bonds.

Through spectral subtraction some of the original bands did disappear during the process of spectral subtractions yielding new common peaks for the wood soot. The resulting peaks appeared at 3300-3500, 2300-2400, 1580-1630, 1380, 500-700 and 400-500 cm1. Comparing these peaks to infrared correlation charts we find that these spectral regions pertain to N-H bonding, at 3300-3500 and 2300-2400, C=C bonding at 1580-1630, C-H bonding at 1380 while the spectra at the lower regions, 500-700 and 400-500cm-1 , pertain to Alkenes and Aromatics.

When comparing lumber soot to other soot such as diesel soot we found there to be a similarity in the C=C bonding at 1580-1630 and in the C-H bonding at 1380 cm1 (Figure 4.) Differences seen throughout the rest of the soot spectra, however, may be indicative of a fingerprint for varying soot sources.

Future work will focus on more soot collection via the soft pellet filter method, with use of green trees, oils and gases being implemented. Atomic absorption and possibly X-ray diffraction will be utilized in conjunction with the FTIR technique to see how the concentrations found in the lab correlate with the aerosols found outside.

REFERENCES

Andoh, Benjamin E. "Infrared and Colorimetric Characterization of Discolored kiln-dried hard maple lumber." *Forest Products Journal*, Vol. 54 No. 1.

Chaffin, C.T. & T.L. Marshall. "An Introduction to Open path Fourier Transform Infrared Atmospheric Monitoring." *Aeroservey Inc.* 2002

Dixon, G.J.. "Compact FTIR Spectrometers address real world problems." *Laser World Focus*, Vol. 34 Issue 2, p111-117, Feb 1998

Fateley, W.G. & R.M. Hammacker. "Open Path FTIR." Kansas State University. 1994

Oros, Daniel, Bernd R.T. Simoneit. "Identification and emission factors of molecular tracers in organic aerosols from biomass burning, Part 1. Temperate climate conifers." *Applied Geochemistry*, 2001, Vol. 16, pp 1513-1544.

"Ozone at officially acceptable levels still affects asthmatic children." *Journal of Environmental Health*, Apr. 2004, Vol. 66, Issue 8, p51, 2/5p.

Pavia, Donald, Gary Lampman & George Peden, David B."Pollutants and Asthma." *Environmental Health Perspectives Supplements* Aug. 2002, Vol. 110, Issue Suppl. 4, p565, 4p

Russwurm, George M.. "FTIR Spectrometers perform Environmental Monitoring." *Laser Focus World*, April 1995, Vol. 32, Issue 4, p 79-84.

Santilllo, D.. "Investigation of the Distribution of Organic Compounds and Heavy Metals in Wastes associated with the Bely Island Incinerator, St. Petersburg area, Russia." GRL Technical Note. 2001

Schmidt, Laurie. "When the Dust Settles." Accessed through the web: http://earthobservatory.nasa.gov/study/dust. 2002

Sin, Su Ying. "Application of FT-Raman and FTIR measurements using a novel spectral reconstruction algorithm." *Journal of Raman Spectroscopy*. 2003,

Smith, Brian C. . *Infrared Spectral Interpretation, A Systematic Approach.* CRC Press. 1999

So, Cho-Leung. "NIR in the Forest Products Industry." *Forest Products Journal*, March 2004, Vol. 54, No. 3, p6-16.

Spoor, S. M. "Generation of ultra fine carbonaceous particle aerosols." *Journal of Aerosol Sciences*, 1996, Vol. 27, Suppl. 1, ppS397-S398.

"Urban air pollution Linked to Birth Defects." *Journal of Environmental Health*, Sep. 2002, Vol. 65, Issue 2, p47, 2p.

APPLICATION OF AVHHR-BASED VEGETATION HEALTH INDICES FOR MALARIA VECTOR ASSESSMENT OF CHITTAGONG DIVISION, BANGLADESH.

Atiqur Rahman , Felix Kogan and Leonid Roytman

The City College of New York, 138th Street & Convent Avenue, New York, NY 10031, USA
Tel: (212) 650 7000, E-mail: *fmatiq@yahoo.com* • NOAA/NESDIS, 5200 Auth Rd. Camp Spring MD 20746, USA

An epidemiological data of malaria cases were correlated with satellite-based vegetation health (VH) indices to investigate if these indices can be used as a proxy for monitoring the number of malaria cases. Mosquitoes, which spread malaria in Bangladesh, are very sensitive to environmental conditions, especially to changes in weather (Pampana 1969, Rosenberg 1982). Therefore, VH indices, which characterize weather conditions, were tested as indicators of mosquito development and activities.

The area of study was Chittagong division (Fig.1) in Bangladesh which has 60-80 percent of all country's malaria cases. Similar to the entire Bangladesh, Chittagong division has subtropical warm, wet and humid climate (Rosenberg and Maheswary 1982).

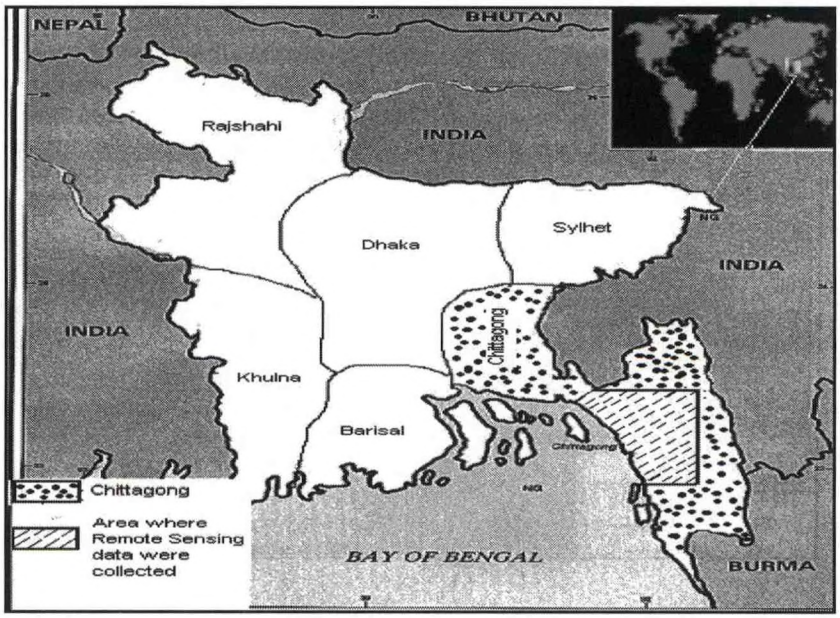

Fig. 1. Bangladesh, divisions including Chittagong and area of satellite data collection.

Malaria statistics, satellite data and meteorological data were used in this study. Figure 2 shows annual number of malaria cases in Chittagong division during 1992-2001 (Y) and trend (Yt), which was approximated by linear equation (1). The weather-related variations around the trend were expressed as a ration (%) of actual cases to the estimated from the trend (equation 2).

$$Yt = a0 + a1 * Y \quad (1)$$

$$DY = (Y/Yt) * 100 \quad (2)$$

Remote sensing data were presented by vegetation health indices (Vegetation Condition Index (VCI), Temperature Condition Index (TCI) and Vegetation Health Index (VHI)). They were derived from radiances measured by the Advanced Very High Resolution Radiometer (AVHRR) flown on NOAA afternoon polar orbiting satellites (Kogan 2001).

The number of annual malaria cases deviation from trend (DY) were correlated with weekly VCI and TCI data to investigate the most sensitive period. Figure 3 shows correlation dynamics of DY versus VCI and TCI. The results indicate that the strongest correlation with the indices occurs around the end of June. The correlation with TCI is stronger than with VCI indicating that in the wet climate of the area, thermal conditions are slightly stronger predictor. The TCI correlates positively indicating that DY increases from below trend values (fewer malaria cases) for smaller TCI (hotter conditions) to above trend (larger

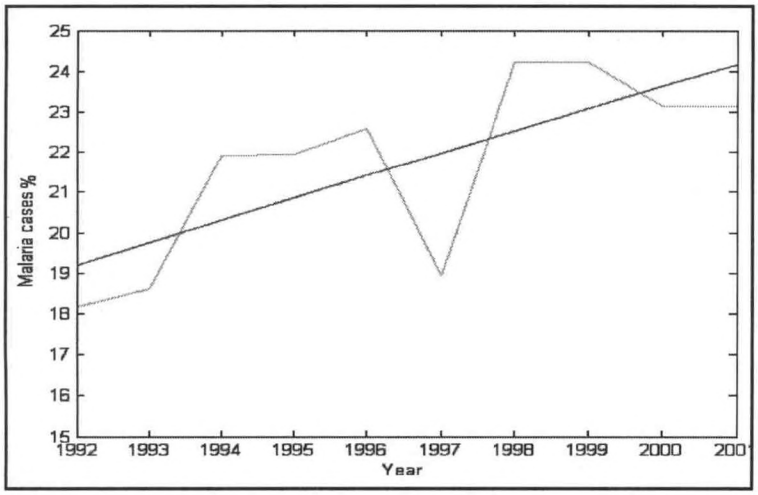

Fig. 2. Annual malaria cases in Chittagong division and trend line, 1992-2001.

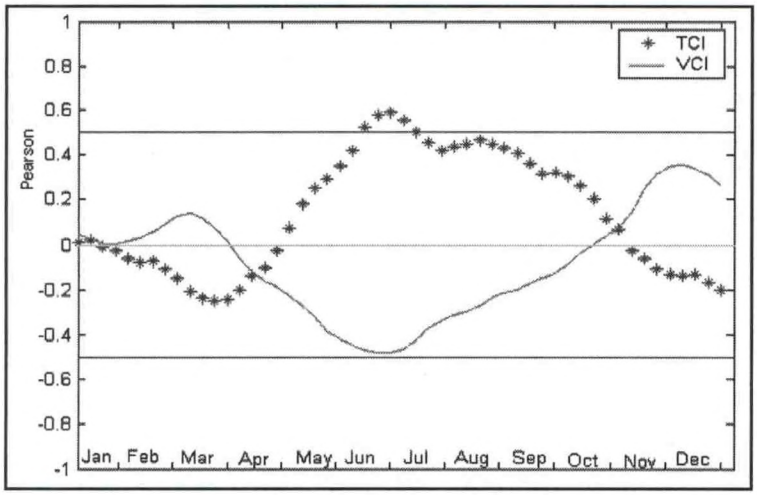

Fig. 3. Correlation coefficient dynamics of DY (percent deviation of malaria cases from trend) versus TCI and VCI.

malaria cases) for larger TCI (cooler conditions)and VCI has opposite correlation. These results are in line with references indicating limiting effect of hot weather on mosquito activity and malaria transmission (Russel et al., 1963). The VCI correlates negatively emphasizing opposite principal of the impact.

The results of correlation analysis in Fig. 3 were used to develop regression equation. Two options were investigated: using TCI only and using both TCI and VCI for the week of highest correlation. They are written below:

$$DY=89.96 + 0.24\ TCI_{26}$$
$$R=0.56;\ E=6.68\%$$
$$DY=96.49 + 0.201\ TCI_{26} - 0.096\ VCI_{26}$$
$$R=0.60;\ E=6.5\%$$

Where R is multiple correlation coefficient and E is the error of estimation.

The results of regression show that R increases slightly when both TCI and VCI are used, although regression coefficients indicate larger contribution of TCI (0.201) versus VCI (0.096).

This study indicates goal VH indices can be used for detection, surveillance and numerical estimate of malaria development in Chittagong division of Bangladesh.

REFERENCES

Kogan, F., 2001, Operational space technology for global assessment, Bulletin of the American Meteorological Society, 82, 1949-1964.

Pampana, E., 1969, A Text Book of Malaria Eradication, Oxford University Press, London, UK, 17-63.

Rosenberg, R., and Maheswary, N., 1982, Forest Malaria in Bangladesh, I. Parasitology, American Journal of Tropical Medicine and Hygiene, 31, 175-201.

ORAL SESSION A4
Atmospheric Sciences

Organic and Organo-Sulfate Aerosols: New Microanalytic and Thermogravimetric Information

Marc Cesaire, Jeffrey Steiner, Elizabeth Rudolph, and Aparna Lakhankar

Department of Earth and Atmospheric Sciences, City College of New York

138th and Convent Ave., NYC, NY 10031

Abstract

Recent investigations indicate that ambient polluted air over New York City often contains a significant fraction of a heavy-metal-bearing organo-sulfate aerosol component. An ongoing thermogravimetric (TGA) study demonstrates that the gas-absorbed fraction of these particulates is consistent with an aerosol comprising 10 – 60 percent organo-sulfate. The TGA record is inconsistent with the simple loss of ambient absorbed water, degassing of interstitial fluid, or the loss of loosely bonded water molecules. The TGA results support a model for the decomposition of metal-bearing organo-sulfate or carbonate compounds with decomposition temperatures ranging to six hundred degrees Centigrade. Scanning electron microscope analyses of both the original aerosol and the thermally decomposed products agree with a model that involves the single-step destruction of carbon- and sulfur-bonded material and the concomitant production of metal oxides in the reaction products. The decomposed material in particular includes a significant percentage of iron, zinc and copper oxides as residue from the decomposition reactions.

Introduction

The suite of heavy metals reported by numerous investigators as common pollution elements (see for example, Spurny, 2000), are not in many cases clearly linked to specific industrial pollutants, particularly with respect to heavy elements such as iron. However, recent studies of the effluents emitted by diesel engines and similar sources by Kirchner, et al. (2003) show that soot particles include a complex admixture of light and heavy trace metals, including sodium, potassium and iron. These are bonded to carbonaceous, nitrogen and sulfate fragments (C_2H_3O-, NO_2-, NO_3-, and HSO_4-) supporting the observation of Steiner et al. (2004) that, for example, iron-bearing organo-sulfate aerosols comprise a significant fraction of the PM2.5 micron aerosols in polluted New York City air masses. However, there is still only a limited survey of the chemistry of these particulates or their structural characteristics.

Recent scanning electron microscope and energy dispersive study (SEM/EDS) of $PM_{2.5}$ aerosols collected using a MetOne Environmental Beta Attenuation Measurement (E-BAM) shows that the composition of complex organo-sulfate aerosol can approximate to that of an evolved Fe-S particle formed by diesel emission, and that certain classes of aerosols seem to have simple mineral equivalents. A thermogravimetric study of these aerosol particles shows that particles decompose at temperatures comparable to those expected of heavy-metal carbonates and sulfates.

Scanning Electron Miscroscope Analyses

A recent studies of fossil fuel emissions demonstrates that alkali metals, sulfur, carbon and heavier metals, such as iron, are produced as solid nano-particle aerosols during the combustion of diesel fuels. Single particle mass spectra of diesel soot analyzed by Kirchner, et al. (2003) shows that individual soot particles comprise a complex admixture of sodium, potassium and iron ions bonded to carbonaceous, nitrogen compounds, sulfate fragments and silica fractions, SiO_2-, and SiO_3- (see Figures 1-2 for Fe and S analyses).

The Kirchner study illustrates the fractionation of Fe-particles into the larger aerosol size fraction, and that Fe-bearing aerosol appear to undergo recrystallize with aging, possibly exchanging sulfur complexes for nitrogen and carbon fragments. The micron-sized fraction has a clear analogy with compounds recovered with the PM2.5 E-BAM fraction as shown by SEM/EDS spectroscopy (Figures 3-4).

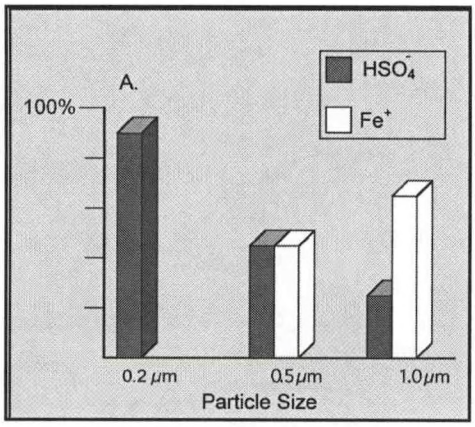

Figure 1. Demonstration of the production of fragmented iron-sulfate species by diesel engines and the variability of soot products over time by single particle mass spectrometry; spectra obtained from direct/raw emissions (after Kirchner, et al.,

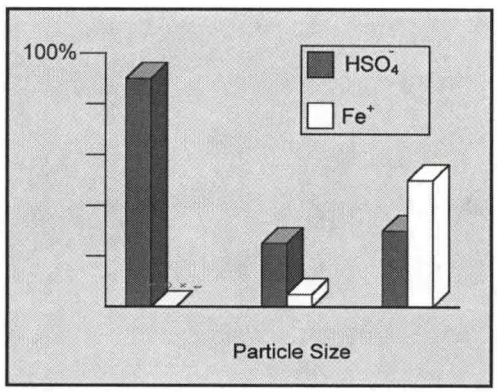

Figure 2. Result of 1 day of aging (After Kirchner, 2003)

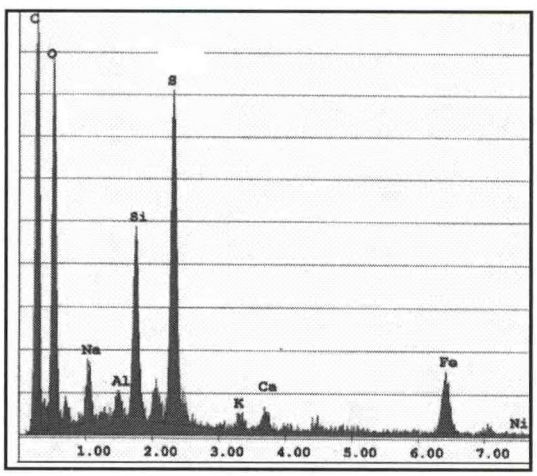

Figure 3. SEM/EDS analysis of Fe-organo-sulfate showing Fe associated with S and C background filters produce Na-Al-Si-K-Ca.

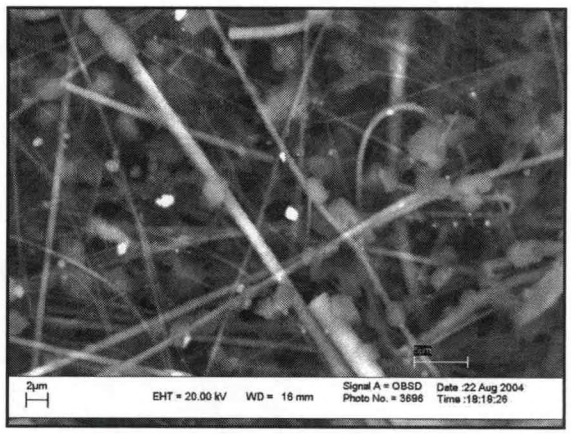

Figure 4. SEM backscatter image of organo-sulfate particle in Figure 3; small bright particulates comprise Fe-, Zn-, and Ba-organo-sulfates; lighter colored particles include alkali metal and ammonium nitrates and carbonates. The heavier-metal-bearing particulates also include significant fractions of nearly pure calcium-organo-sulfates that occur as small discrete particles and occasionally as sites immersed in lighter-element aggregates (Figure 5). These latter appear to be created during impactions, as discussed by Wittmaack (2002) and Wittmaack and Menzel (2002,).

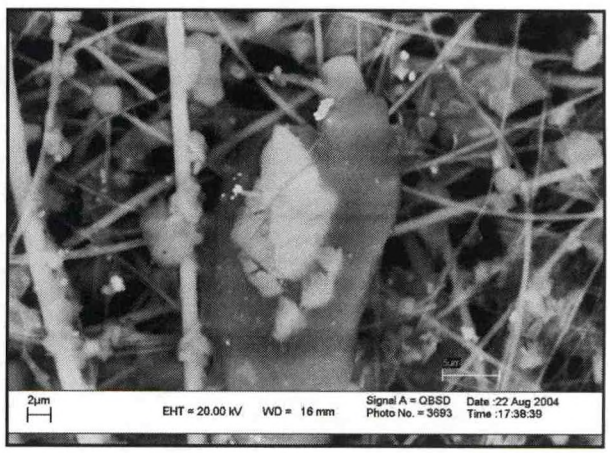

Figure 5. Irregular calcium sulfate crystal (center) embedded in ammonium nitrate and carbonate.

The heavier-metal-bearing particulates also include significant fractions of nearly pure calcium-organo-sulfates that occur as small discrete particles and occasionally as sites immersed in lighter-element aggregates (Figure 5). These latter appear to be created during impactions, as discussed by Wittmaack (2002) and Wittmaack and Menzel (2002,).

A significant fraction of calcium-sulfur particulates approximate compositionally to gypsum (CaSO4-2H2O), and fail to show a significant car-

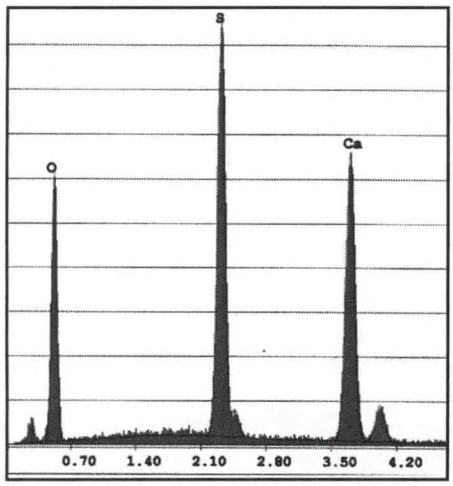

Figure 6. SEM/EDS analysis of calcium organo-sulfate with minimal carbon (top) relative to a gypsum standard (bottom). nergy dispersive microanalysis of a standard gypsum crystal.

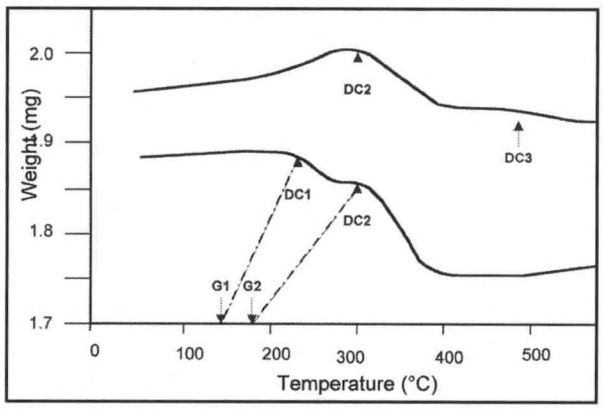

Figure 7. Thermogravimetric analysis of aerosol particles accumulated on an E-BAM ribbon showing thermal properties similar to those predicted for hydrated metal sulfates.

bon signal (Figures 6). This class of aerosol, and associated Fe-, Zn, and Ba-particles exhibit a thermo-gravimetric (TGA) profiles similar to those obtained for hydrated carbonates and sulfates.

The E-BAM silica glass ribbons resist thermal decomposition to approximately 600°C and can therefore be used directly as a platform for TGA analysis (Figure 7; drop in weight at points of structural degassing or decomposition).

Each class of S-N-C compounds has a distinctive dehydration or decarbonation signature. The structure of organo-carbonate-sulfate aerosols is yet to be determined, but it is instructive to compare the TGA breakdown of metal organo sulfates to the thermal decomposition of gypsum (Figure 7).

Gypsum is dehydrated in two steps. The first step results from the loss of 1.5 water molecules at approximately 130°C and the loss of the remaining 0.5 molecules at approximately 163°C (points G1 and G2). The substitution of iron (II), zinc (II) and possibly barium (II) for calcium will raise the dehydration points as indicated for the decomposition of an E-BAM aggregate with a strong SEM/EDS signature for an Ca-Fe-Zn-S aerosol (Figure 7). Other aerosols decompose in two steps (top, Figure 7) indicating a more catastrophic loss (one-setp dehydration) coupled with

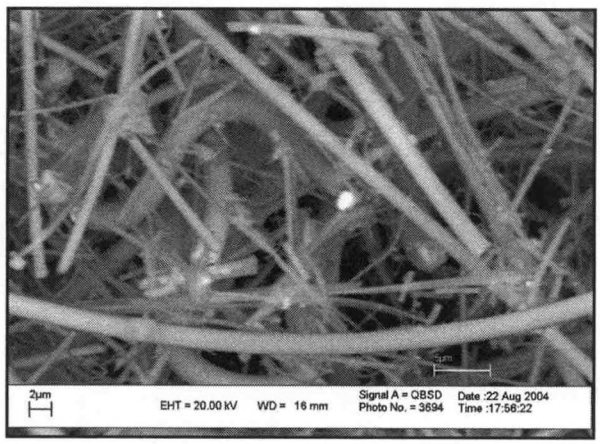

Figure 7. E-BAM ribbon after TGA firing to 600°C showing destruction of the light-element impactor-generated particles and a majority of the fine particles.

Figure 8. Fe-Cr particle embedded on an E-BAM silica ribbon filter (bright, center).

the possible compound dissociation at about 500° C. In addition to metal-sulfates, a significant fraction of PM2.5 particulates are metallic with only minor sulfur (Figure 8-9).

Conclusions

SEM/EDS evidence suggests that the 1-micron Fe-S fragmented particles produced by diesel emission recrystallize to Fe-S organo-sulfates in the ambient air in an industrial setting.

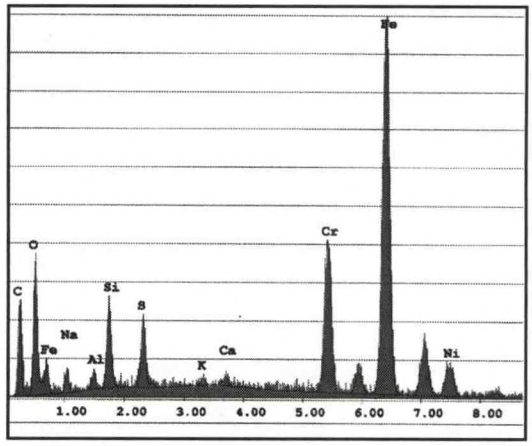

Figure 9. SEM/EDS analysis of the Fe-Cr particle in Figure 8.

BIBLIOGRAPHY

Kirchner, U., Vogt, R., Natzeck, C.

Goschnick, J., "Single particle MS,

SNMS, SIMS, XPS, and FTIR spectroscopic analysis of soot articles during the AIDA Campaign". Journal of Aerosol Science, 2003, Vol. 34, p. 1323-1346

Spurny, K. R., 2000, Aerosol Chemical Processes in the Environment. Lewis Publishers, New York, 615pp.

Steiner, J. C., Rudolph, E., Katz, A., Alimova, A., 2004, PM2.5 sourcing a multi-system geochemical approach for improving aerosol tracking algorithm, NOAA Crest Conference on Modeling and Measuring Aerosols, JUNE 14-16.

Wittmaack, K. Menzel, N., Wehnes, H.,

Heinzmann, U., "Phase separation and regrowth of aerosol matter collected after size fractionation in an impactor". Atmospheric Environment, 2002, Vol. 36, p. 5877-5886.

Wittmaack, K., "Impact and growth phenomena observed with sub-micrometer atmospheric aerosol particles collected on polished silicon at low coverage". Atmospheric Environment, 2002, Vol. 36, 3963-3971.

Is the Earth's Climate Changing and Affecting Fires and Air Quality? Investigations into the Effect of Climate Change on Fires and Air Quality

L. Mtetwa and P. M. McCormick

Center for Atmospheric Sciences, Hampton University, Hampton, Virginia

Abstract

The significance of biomass burning and its impact on the composition and chemistry of the lower atmosphere (troposphere and stratosphere), the earth's radiative balance and general air quality is gaining forefront recognition in studies of the atmosphere (Colarco et. al., 2004). Burning produces agents for depletion of the ozone layer, and contributes to global warming, deforestation, acid precipitation, and production of chemically and radiatively active species, carbon dioxide, methane, nitric oxide, tropospheric ozone (Goode et al., 2000), methyl chloride and elemental carbon particulates (Levine et al., 1995). For these reasons, fires are likely to have a noticeable impact on atmospheric chemistry, surface temperatures, hydrological processes, and climate change and air quality. Changes in climatic patterns are expected to proliferate throughout global issues such as fires, biogenic emissions and air quality. We will be undertaking research to provide a complete analysis of how pollutant emissions related to tropospheric ozone and particulate matter formation may be altered by future climate changes. We propose to provide new insights into the complex interactions of fire, climate and air quality and biogenic emissions and reduce the major uncertainties that exist in this area. We will accomplish this goal by a three step process involving: (a) Estimation (to understand Variability and forcing), (b) Assimilation (to improve/advance earth systems climate knowledge) and (c) Prediction (to establish feedback consequence and impact). By estimating emissions from biomass burning and biogenic source we will develop inventories of trace gases and particulates for the United States for utilization in the assimilation and prediction steps. This research will provide the first comprehensive emissions inventory for wild-land fires. The emissions inventories will be utilized in two very significant ways: (i) These data can be used in tools that predict air quality or in tools that study life-cycles of emissions and chemical and transport processes and (ii) To provide realistic scenarios for which a better understanding of future changes in primary forcing factors. We will assimilate aerosol and ozone results into the EPA's Community Multi-scale Air Quality (CMAQ) and provide data to the NOAA/NESDIS air quality team. Our team will develop predictive models for fires, the Fire Prediction Model (FPM), and will improve the NOAA geophysical Fluid Dynamics Laboratory GCM -Biogenic emissions model. The FPM can be coupled with General Circulation model (GCMs), and the Community Climate System Models (CCSM). These models will be used to predict the impact of climate change on fires and air quality.

Introduction

The role of vegetation fires in global and climate change, air quality studies, preservation of ecosystems and sustenance of ecosystem diversity is of paramount importance. Available evidence increasingly indicates that biomass burning in its various forms represents a major perturbation of atmospheric chemistry, comparable in magnitude to the effects of fossil fuel combustion (Crutzen and Andrea, 1990).

The world is witnessing profound changes in climate (temperature, precipitation, drought and clouds) with unclear implications for wildfires and subsequently air quality. Many of these changes can be directly linked to anthropogenic activities. Population increases are being reflected by increased demand for food and energy, which in turn is being reflected by increased agricultural production, changes in land use patterns, increased use of fertilizer and pesticides and depletion of fresh water resources. It is very clear that an increase or change in one climatic or global parameter has the potential for affecting others.

Changes in temperature may result in anomalous hydrological conditions, with direct consequences on agriculture, forestry, water supply, ecosystem diversity and stability and many others. Temperature also drives the earth's climate system, controls the earth's circulatory patterns, which in turn drive precipitation and evaporation patterns, storms, and other large scale climatic patterns (IPCC, 1998).

NASA's earth science enterprise research strategy for 2000-2010 executive summary wrote the following to define a feedback process; " one of the most important and intellectual challenges of the study of the Earth system- that most responses the earth system makes to a forcing (either natural or human-induced) can in turn become a forcing factors themselves. We can no longer address environmental issues in isolation. A better understanding of the linkages among these different issues is necessary if we are to avoid making decisions that simply benefit one environmental issue at the expense of others.

Science Goals

The primary goal of this proposed research is to provide a complete analysis of how pollutant emissions related to tropospheric ozone and particulate matter formation may be altered by future climate changes.

Objectives

Our team proposes to address the following primary areas of research:

a. We propose to give results on the effects predicted changes in climate (e.g. temperature, precipitation, drought, soil moisture content, sea change level, and clouds) will have on wildfires and consequently U.S. air quality;

b. We intend to develop methods that can be used to credibly project changes in biogenic emissions resulting from land-cover shifts over long-time frames (e.g., to 2050 and beyond) due to fires, fire management and changes in fires due to climate change; and

c. We propose to develop a database for emissions significant to ozone and particulate matter (PM) concentrations (e.g. primary PM, secondary PM precursors, ozone precursors) within the U.S. This database will include critical information on estimates of location, time, frequency, and fuel characteristics.

Strategic Questions

The overall goals and objectives of this proposal will be achieved by addressing five specific science questions. Each of the five questions directly corresponds to the number assigned to the corresponding linkage we propose to study. These linkages have been numbered a-f.

a) What effects might predicted changes in climate have on wildfires?

b) How will air quality change with a changing climate?

c) What will be the consequences of predicted changes in climate for biogenic emissions?

d) What impact will the resulting changes in fires have on US air quality?

e) How will Biogenic emissions respond to Fires induced by climate change?

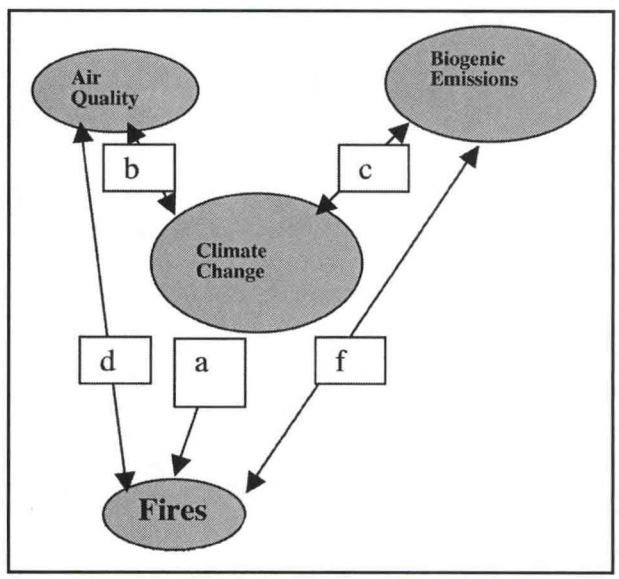

Fig. 1. Linkages among climate change-Fires-Air Quality and Biogenic Emissions.

Approach

This research will take an integrated, multi disciplinary approach to provide answers to the burning questions above. This research will be performed in three steps: (I) Estimation (to understand Variability and forcing), (II) Assimilation (to

improve/advance earth systems climate knowledge) and (III) Prediction (to establish feedback consequence and impact)

We will obtain data from satellites such as Calipso.

Figure 2 shows an example of biomass smoke in South America form The Lidar in Space Technology Experiment which flew on shuttle for 10 days in September 1994.The green, yellow, gold, and red represents scattering from biomass smoke plumes. Calipso will use three channels 1064 nm and 532 nm, plus depolarization at 532 nm to paint these pictures of biomass smoke plumes, which will be used in our research.

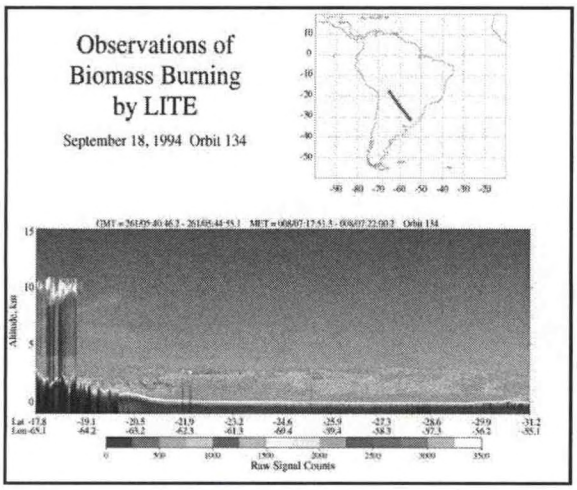

Fig. 2. Observations of Biomass burning by Lite.

Estimation

This section will deal with providing estimates of pollutant emissions related to tropospheric ozone and particulate matter formation from wildland fires and Biogenic emissions.

Wildland Fire Emissions

We will utilize the Mtetwa and Levine Biomass Burning Estimation algorithm algorithm in providing estimates of trace gases and particulates from biomass burning and establishing geographic distribution of species and their importance for regional and global budgets.

Assimilation

The next step after estimation is the assimilation of results;

We intend to use Global Circulation Models (GCM's), to help us predict future levels of emissions with new methods that or team will develop. Our team will assess the effect of emissions from fires on regional and global climate by initializing chemical transport models (CTM'S) using the improved emission rates we will develop from this study. The CTM"s will provide us with life-cycle information on emissions, and ultimate sinks of the species studied, and give some estimate on the net effects of emissions from fires in the United states on the composition, chemistry, climate, and general air quality on both regional and global scales. Specifically we intend to use the global coupled climate model (CCM) produced by the CCSM community. The Community Climate System Model (CCSM) is a fully coupled, global climate model that provides state-of-the-art computer simulations of the Earth's past, present, and future climate states (http://www.ccsm.ucar.edu/index.html)

Prediction

The prediction step of our research will cover the two areas of significance we have addressed throughout this proposal and highlighted in the EPA solicitation. The areas of research we propose to provide significant results and advance method development are (I) predict the impact of changes in climate (e.g. temperature, precipitation, drought, clouds) on wildfires and consequently U.S. air quality; (II) develop methods can be used to credibly project changes in biogenic emissions resulting from land-cover shifts over long-time frames (e.g., to 2050 and beyond) due to fires, fire management and changes in fires due to climate change.

To address the first area, we propose to develop a Fire Prediction Model (FPM) that can be coupled with Geographical Information Systems (GIS), General Circulation model (GCM), and The Community Climate System Model (CCSM). To address the later area of concern, we propose to improve and develop a new Biogenic emissions model based on the existing Levy and Yienger biogenic soil NOx emissions model.

Fire Prediction Model

We propose to develop a model which we will call the Fire Prediction Model (FPM). Prediction will involve the selection of appropriate software to link the model to GIS, GCM, and CCM, and develop-

ment of ideal protocol. We will develop this model by following the steps below:

a. Deriving diagnostic relationships between fire Characteristics and Climatic parameters.

b. We will assume that fire characteristics will be dependent on the following climatic variables; (i) ecosystem type, (ii) precipitation, (iii) wind speeds, (iv) cloud cover, (v) surface temperature, (vi) soil moisture, (vii) humidity and any others that might become important during the model description (which will influence fire characteristics such as fuel load, burning efficiency, combustion factors etc).

c. Use field and Laboratory studies to derive relationships between burning and associated chemistry.

d. Model will use historical and current fire data to develop an input of Area burned, number of fires, dates, geographic location and climatic conditions at the time of fire incidence.

e. Applying different future climate scenarios consistent with the continental scale emissions scenarios from the Intergovernmental Panel on Climate Change (IPCC), Special Report Emissions Scenarios (SRES) (http://www.ipcc.ch/pub/sres-e.pdf).

f. Model output parameters will be: Changes in Area burned; Frequency of fires; Rate of spread of fires; Changes in ecosystem vegetation types; Geographic distribution of future fires, and spatial and temporal distribution of fires.

REFERENCES

Colarco, P.R., M. R. Schoeberl, B.G. Dooddridge, L.T. Marufu, O. Torres, E. L. Welton., 2004: Transport of smoke from Canadian forest fires to the surface near Washington D.C.: Injection height, entrainment, and optical properties, Journal Geophysical Research., 109, D06203, doi:10.1029/2003JD004248.

Crutzen, P. J. and M. O. Andreae, Biomass burning in the tropics., 1990: Impact on atmospheric chemistry and biogeochemical cycles. Science, 250: p. 1669-1678.

Goode, J. G., R.J. Yokelson, D.E. Ward, R.A. Susott, R. E. Babbitt, M.A. Davies, and W.M. Hao., 2000: Measurements of excess O3, CO2, CO, CH4, C2H4, C2H2, HCN, NO, NH3, HCOOH, CH3COOH, HCHO, and CH3OH in 1997 Alaskan biomass burning plumes by airborne Fourier transform infrared spectroscopy (AFTIR), Journal Geophysical Research., 105, 2147- 2166.

Guenther, A., et al., 1995:A global model of natural volatile organic compound emissions, Journal Geophysical Research., 100, 8873-8892.

Intergovernmental Panel on Climate Change (IPCC), Greenhouse Gas Inventory workbook., 1995: Guidelines For National Greenhouse Inventories, Vol.3.

Levine, J.S., E.L. W.R. Cofer III, D.I. Sebacher, R.P. Rhinehart, E.L Winstead, S. Sebacher, C.R. Hinkie, P.A. Schmalzer, and A.M. Koller Jr., 1990: The Effects of Fire on Biogenic Emmisions of Methane and Nitric Oxide from Wetlands, Journal Geophysical Research., 95, 1853-1864.

Levine J.S, D.R. Cahoon, Jr., J.A. McAdoo, D.M. Robinson, W.A. Sasamoto, R.T. Sherrill, and K.D. Smith., 1996: FireSat and the Global Monitoring of Biomass Burning, *in Biomass Buring Global Change*, Vol. 1, J.S. Levine, ed., MIT Press, 107-132.

Levine, J.S, Cofer, R, Cahoon D.R, Winstead E.L., 1995: Biomass Burning, A Driver for Global Change, *Environmental science and technology*, Vol.29, no. 3.

Levine, J. S., W. R. Cofer, D. R. Cahoon, E. L. Winstead, B. J. Stocks, V. A. Krasovich and L. Mtetwa., 1998: Gaseous and Particulate Emissions from Burning in the Boreal Forest, in Disturbances in Boreal Forest Ecosystems: Human Impacts and Natural Processes, S.G. Conard, ed., U.S. Forest Service, Washington D.C.

Mtetwa L., 1998: Africa as a Regional and Global Source Of Atmospheric Gases and Particulates., Ph.D. Dissertation, College of William and Mary.

Yienger, J. J., and H. Levy., 1995: Empirical Model of Soil- Biogenic NOx Emissions, Journal Geophysical Research., 100, 11447-11464.

ON FIRST GASP

Raymond Rogers[1], Kevin McCann[1], Ana Prados[3], Raymond Hoff[1],
Jill Engel-Cox[1,2], Nikisa Jordan[1], Kamonayi Mubenga[1], Shobha Kondragunta[3]

[1]CREST, Joint Cneter for Earth Systems Technology, University of Maryland Baltimore County, 1000 Hilltop Circle, Baltimore, MD 21250 email: *rrogers@umbc.edu*

[2] Battelle Memorial Institute, 2101 Wilson Boulevard, Suite 800, Arlington, VA 22201 email: *engelcox@battelle.org*

[3]NOAA NESDIS, Camp Springs, MD

ABSTRACT

UMBC has been evaluating the GOES Aerosol and Smoke Product (GASP) in cooperation with NESDIS for approximately six months. NESDIS has been providing real-time GASP feeds to UMBC for analysis and interpretation. Time animations of the GASP data are being posted to the USAQ weblog and have been used in the flight planning for the INTEX/NE and NEAQS studies this summer. While the direct intercomparison of GASP optical depths are preliminary, a comparison with the Elastic Lidar Facility was performed for July 2004 and August 2004. Some immediate critical observations of the GASP product are possible. GASP time animations have the potential to lead to determination of mean wind speeds of aerosol features. GASP's AOD product is generally consistent with MODIS except that cloud screening appears different. MODIS has less of a "silver lining" effect where AOD increases near cloud edges. GASP has a strong diurnal bias in the retrieved AOD due to increased afternoon cloudiness in summer. GASP's early morning and afternoon AOD's were overestimated and now a more limited range of Airmass values are being treated as valid data. GASP shows great potential, especially when the product is applied to GOES-R spectral channels in the future.

INTRODUCTION

The GOES Aerosol and Smoke Product (GASP) has much to offer for the study of aerosol emissions and their transport across the continental US with much better temporal resolution than either the Moderate Resolution Spectroradiometer (MODIS) or the Multiangle Imaging Spectroradiometer (MISR) aboard NASA's AQUA and TERRA satellites (Knapp et al., 2002). The GASP product provides aerosol optical depth (AOD) at 4 km spatial resolution and with a 30 minute update interval, which allows GASP AOD time animations and the potential for mean wind speed determination. The GASP product is limited spectrally, however, with only a single visible channel (0.52-0.72 μm FWHM) that is used to determine AOD The four remaining channels in the IR and near IR are used to distinguish clouds from aerosols.

The Elastic Lidar Facility (ELF) uses a Continuum Surelite II ND-YAG laser, doubled to 532 nm. A Celestron 14" Schmidt-Cassegrain telescope collects the backscattered light and two Hamamatsu H6780 Photomultiplier Tubes (PMT) detect the light. One PMT measures backscattered signal in the same polarization of the laser while the other PMT measures backscattered signal perpendicular to the polarization of the laser.

ELF OPTICAL DEPTH

The calculation of aerosol optical depth for the ELF system is based on a simple numerical integration technique. The elastic lidar equation for the aerosol

backscatter coefficient, β_A is given by equation 1:

$$\beta_A(z)=\beta_R(z)\cdot\left(\frac{z^2P(z)}{K\cdot\beta_R(z)\cdot\exp[-2\int_0^z(\alpha_R(z)+\alpha_A(z))dz]}-1\right) \quad (1)$$

P(z) is the power measured by the PMT after background subtraction, K represents all range independent parameters, $\beta_A(z)$ and $\beta_R(z)$ are the aerosol and Rayleigh backscatter coefficients respectively, $\alpha_A(z)$ and $\alpha_R(z)$, respectively, represent the aerosol and Rayleigh extinction coefficients.

A constitutive relationship is assumed between the extinction coefficient and the backscatter coefficient:

$$\alpha = S_a \cdot \beta \quad (2)$$

where S_a is a constant, and depends on the size and shape distribution of the aerosols. For continental aerosols at 532 nm, S_a ranges between 50 sr and 80 sr (Ackerman, 1998). An iterative solution for backscatter coefficient is then employed (Hoff and Froude (1979); Comer, 2003).

$$\beta_A^{i+1}=\beta_R^{i+1}\left(\frac{z_{i+1}^2P(z_{i+1})}{K\beta_R^{i+1}\exp(2\sum_{k=0}^{i}(\alpha_R^k+S_a\beta_A^k)\Delta z)}-1\right) \quad (3)$$

Optical depth is determined by using equations 2 and 3 to obtain the extinction profile $\alpha(z)$ which is then integrated in the vertical to yield AOD.

$$\tau=\sum_{i=z\,\min}^{i=z\,\max}S_a\cdot\beta_A^i\Delta z \quad (4)$$

For the comparison to GASP optical depth, z_{min} was approximately 150 m and z_{max} was chosen to be the height at which the noise dominates the signal. For heights less than 150 m a constant extinction was assumed. The daytime value of z_{max} ranged from 4 km to 7 km.

GASP OPTICAL DEPTH

The calculation of the GASP AOD consists of three steps. First, a composite background image is obtained by finding the second darkest pixel from a 28 day time series of images at each observation time. This takes full advantage of the unchanging geometry of the satellite. The surface reflectance is then obtained from the background image by using look-up tables calculated with the 6S Radiative Transfer model. Finally, AOD is estimated using look-up tables from the 6S Radiative Transfer model, using the estimated surface reflectance and assuming a continental aerosol model and a lambertian surface. A more detailed description of the GASP product is presented by Knapp et al (2002).

RESULTS AND DISCUSSION

Figure 1 shows a plot of the GASP product at 11:45 UTC and at 15:45 UTC on July 27, 2004; two of the twenty images that were used to create a time animation of the GASP AOD on that day. In this figure there is a smoke plume that is moving across Canada and into the Northeast US, which is under cloud cover. These animations are posted on the US Air Quality weblog (Jordan et al., 2004) and have been used in the flight planning for the INTEX/NE and NEAQS (Singh, 2001) studies this summer. In addition to this, the GASP animations have the potential for the study of aerosol transport in conjunction with vertical profiles from the REALM lidar network (Hoff et al., 2003). The temporal resolution of GASP may also allow the determination of mean wind speeds of aerosol features, such as the smoke event in Figure 1.

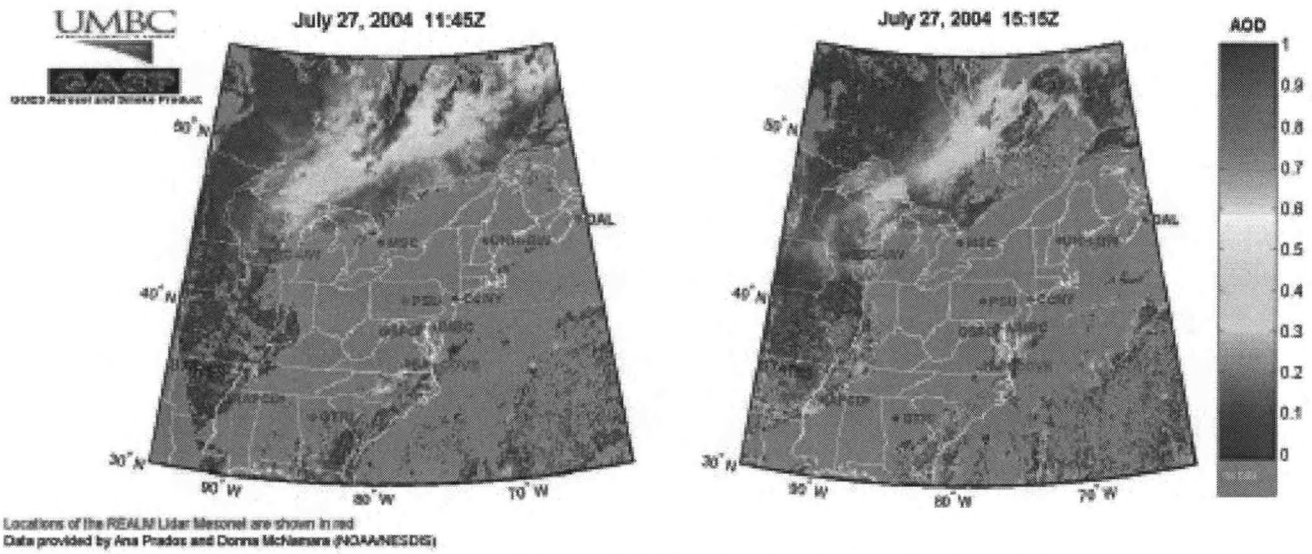

Figure 1 – The GASP product at 11:45 UTC and 15:15 UTC on July 24, 2004.

Some critical comments must also be made after evaluating the GASP product. Near the edges of clouds there is a pronounced "silver lining", where AOD increases as the cloud edge is approached. This is seen in Figure 1 above the US border from the Great Lakes up to Maine.

We have found that GASP has a strong diurnal bias in the retrieved AOD that is due to increased afternoon cloudiness in summer. GASP's early morning and late afternoon AOD's tended to be consistently larger than the noon AOD's. Recently, a more limited range of airmass values are being considered as valid data.

The preliminary AOD comparison of ELF and GASP shows fair agreement between the instruments. GASP tends to consistently underestimate the optical depth. A comparison case is presented in Figure 2, for July 21, 2004. The optical depth on this day was between 0.7 and 1 with good agreement between ELF, MODIS, and AERONET. GASP produces a much lower optical depth, with the highest values of AOD in the early morning and late afternoon and a minimum value at approximately local noon. The behavior of the GASP optical depth suggests that the solar angle may have an effect in the GASP optical depth.

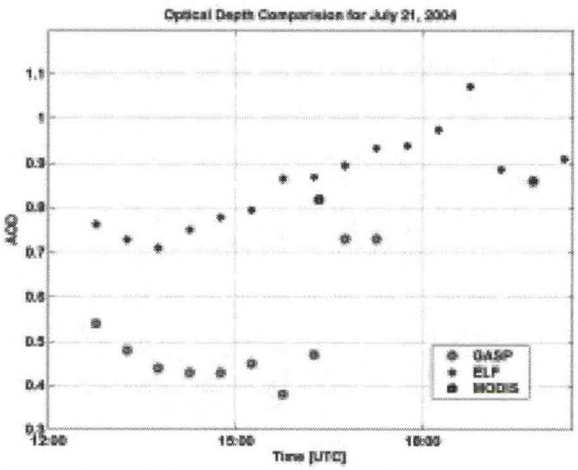

Figure 2 – ELF and GASP AOD time series comparison for July 21, 2004.

CONCLUSIONS

The preliminary GASP product has been used to create high-resolution time animations that have already proven useful for air quality applications and field mission planning. GASP has several problems such as higher AOD near clouds, diurnal

variations of AOD, and effects of airmass and solar angle on AOD. Additionally, comparisons with ELF show fair agreement for July 2004 and August 2004. We are continuing to examine these issues with the intent to improve GASP and to prepare for future multi-wavelength geostationary sensors.

REFERENCES

Ackerman, Jorg, 1998: The Extinction to Backscatter Ratio of Tropospheric Aerosol: A Numerical Study, *J. Atmos Oceanic Tech*, **15**, 1043 – 1050.

Comer, J, UMBC Elastic Backscatter Lidar Facility (ELF): Subvisible Cirrus Cloud and Aerosol Measurements during ABOVE 2002, Masters Thesis, University of Maryland, Baltimore County, 2003.

Hoff, R. M. and F. A. Froude, 1979: Lidar observation of plume dispersion in northern Alberta, *Atmos. Env.*, **13**, 35-43.

Hoff, Raymond M., Kevin J. McCann, Jens Reichardt, Belay Demoz, David N. Whiteman, Tom McGee, M. Patrick McCormick, C. Russell Philbrick, Kevin Strawbridge, Fred Moshary, Barry Gross, Sam Ahmed, Demetrius Venable, Everette Joseph, Thomas Duck, Ivan Dors, 2003: Regional East Atmospheric LIDAR Mesonet,REALM, *NOAA-CREST/NASA-EPSCoR Joint Symposium for Climate Studies University of Puerto Rico - Mayaguez Campus*.

Jordan, Nikisa, Jill A. Engel-Cox, Raymond Rogers, Kevin J. McCann, and Raymond M. Hoff, 2004: U.S. Air Quality Multi-Sensor Fusion for Air Quality Applications, *NOAA/NESDIS Symposium on Measuring and Modeling Aerosols*, Baltimore, MD.

Knapp, K. R., T. H. Vonder Haar, and Y. J. Kaufman, 2002: Aerosol optical depth retrieval from GOES-8: Uncertainty study and retrieval validation over South America, *J. Geophys. Res.*, **107** (**D7**), 4055, doi:10.1029/2001JD000505.

Singh, H. B., D. Jacob, and L. Pfister, INTEX-NA: Intercontinental Chemical Transport Experiment-North America, NASA 2001

ACKNOWLEGEMENTS

This work was sponsored by the Center for Remote Sensing of Science and Technology (CREST) through a grant to UMBC from the City University of New York Research Foundation (49866-00-02/C)

AEROSOL MEASUREMENTS DURING THE NCAS TRANS-ATLANTIC SAHARAN DUST AEROSOL AND OCEANOGRAPHIC SCIENCE EXPEDITION (AEROSE)

Lizette Roldán[a], Vernon R. Morrisa[b], Everette Joseph[c]

[a]Atmospheric Sciences, Howard University, Washington, DC 20059

[b]Department of Chemistry Howard University Washington, DC 20059

[c]Department of Physics and Astronomy Howard University Washington, DC 20059

ORAL and Atmospheric Sciences

The NOAA Center for Atmospheric Sciences (NCAS) at Howard University recently conducted a 27-day mission to characterize the evolution of chemical and physical properties of Saharan Dust during its spring time trans-Atlantic transport. The mission was designed to perform integrated atmospheric, oceanographic and satellite-based science in support of a large-scale study a single scientific phenomenon - Saharan Dust. A large suite of aerosol and chemical measurements were performed. The primary aerosol measurements were total black carbon aerosol, total condensation nuclei, PM10, size-fractionated aerosol mass distributions, and size-fractionated number distributions. Aerosol filter sampling for chemical, mycological, biological, and microphysical analysis was also performed. An overview of the preliminary results from the study will be presented.

A GLOBAL OZONE CLIMATOLOGY

Mike Hill, M. Patrick McCormick, and John Anderson

Center for Atmospheric Sciences, Hampton University, Hampton, Virginia 23668

Abstract

Stratospheric ozone concentrations determine the intensity of ultraviolet radiation from space that reaches the surface of the earth, which is important for life on earth. Solar irradiance, chemical reactions, and various dynamic processes influence the distribution of ozone in the stratosphere. The purpose of this research is to develop a stratospheric ozone climatology based on version 6.20 of the SAGE II ozone data product, and to conduct a trend analysis, in the equivalent latitude / potential temperature coordinate system. Since potential vorticity and potential temperature are conserved quantities of fluid motion under adiabatic conditions, averaging the ozone distribution in this coordinate system removes some of the short-term transport effects and reduces the dynamic variability in ozone unaccounted for in the model. The ozone regression model includes mean and trend terms, annual and semiannual fluctuations due to the seasonally varying solar intensity, a solar proxy (10.7 cm solar radio flux) to account for the effects of the sunspot cycle on solar output at wavelengths that produce photoionization, and a QBO phase representation using principal components derived from the Singapore zonal wind data. Potential vorticity and equivalent latitude figures are calculated from daily UKMO wind data.

SAGE II Ozone Data

SAGE II (Stratospheric Aerosol and Gas Experiment) is a nearly self-calibrating, remote-sensing solar occultation instrument consisting of a seven-channel sun photometer. It is mounted aboard the Earth Radiation Budget Satellite (ERBS), which was launched in October 1984, and has been collecting data for the last twenty years. SAGE II orbits the earth every 96.8 minutes at an altitude of 650 km. Its orbital inclination of 57° provides SAGE II with 15 sunrise and 15 sunset daily measurement events with near-global coverage. From solar transmission data that are acquired during each event and normalized to exoatmospheric measurements, vertical profiles of ozone are inferred at a resolution better than 1 km. In addition, SAGE II retrieves profiles of NO2, H2O, and aerosol extinction at four wavelengths. For more information on SAGE II see McCormick (1987).

The typical annual coverage of SAGE II by latitude prior to 2000 is illustrated in Fig. 1, which shows the measurement locations for 1999. In late 2000, SAGE II was forced to reduce its measurement frequency to compensate for an instrument problem that occurred earlier that year. Consequently, after 2000 the annual coverage is reduced by roughly half. Trend analyses extending through 1999 and 2002 have been conducted in order to assess the effects of this reduction in data on the fitted model.

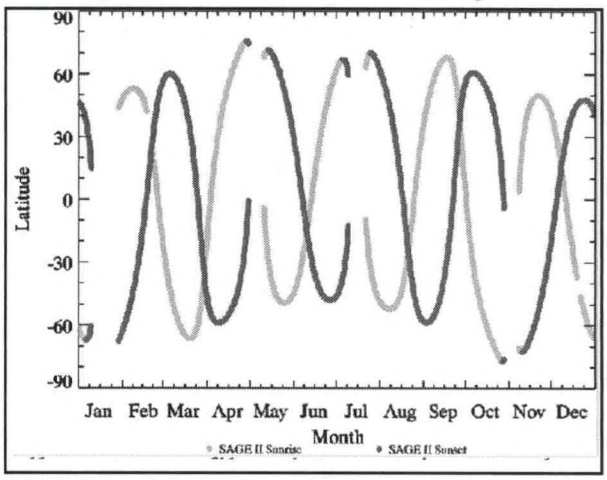

Fig. 1. SAGE II sunset (red) & sunrise (green) measurement locations for 1999.

Version 6.20 of the SAGE II ozone data product, which was released in the fall of 2003, is used exclusively throughout this study. The removal of artifacts and "contaminated" profiles from the ozone dataset is important in preparing the data for modeling and trend analyses. The following identified artifacts and corresponding filtering techniques were suggested by Wang et al. (2002). In addition to these recommendations, all ozone profiles that con-

tain error bars greater than 300% between 30 and 55 km were discarded. This eliminated a few remaining dubious profiles.

In order to reduce power consumption after a problem with its battery in 1993, SAGE II was constrained to make fewer exoatmospheric measurements during the following year. Several of these "short events", in which vertical transmission profiles terminated early near the top, resulted in atypical ozone values. These events were screened by eliminating any profiles retrieved between 1993 and 1994 in which the error bars between 30 and 50 km exceeded 10%.

The eruption of Mt. Pinatubo in June 1991 injected large quantities of aerosols into the stratosphere, which severely limited the ability of SAGE II to measure ozone concentrations in the tropics below 30 km (McCormick et al., 1995). Significant changes in the aerosol size distribution altered the wavelength dependence of aerosol extinction and subsequently affected the ozone retrievals. In addition, large aerosol extinctions due to the presence of clouds can affect ozone retrievals at all latitudes. Ozone data that have been influenced by these extremely high values of aerosol extinction can be removed by setting an extinction threshold value above which ozone retrievals are considered unreliable. A consensus of various studies suggests that an aerosol extinction of 6x10-3 km^{-1} is a sufficient limit.

To account for cloud interference and aerosol size distribution discrepancies in situations where the aerosol extinction level has not reached $6x10^{-3}$ km^{-1}, but is greater than $1x10^{-3}$ km^{-1}, the ratio of aerosol extinction at 0.525 _m to aerosol extinction at 1.02 _m can be examined (Kent et al., 1991 and Kent et al., 1993). While the extinction at a given wavelength can vary significantly, under normal aerosol conditions this extinction ratio maintains a value between 2 and 5. Clouds tend to reflect light at all wavelengths uniformly, resulting in an extinction ratio closer to 1. The final filter applied to the SAGE II dataset removes ozone retrievals that coincide with aerosol extinction values between 1x10-3 km^{-1} and $6x10^{-3}$ km^{-1} in which the 0.525 _m : 1.02 _m extinction ratio is less than 1.4.

UKMO Wind Velocity Data

Average daily wind velocity vector field data from 1991-2002 with a grid resolution of 2.5° latitude x 3.75° longitude over 22 pressure levels were obtained from the United Kingdom Meteorological Office (UKMO). Altitude and temperature data were also included on an interlaced grid. The potential vorticity values used in this study are calculated using the meridianal and zonal wind velocity data, as well as the supplied altitude and temperature data interpolated to the wind velocity grid, with the formula:

Here, $_^{R}$ is the local relative vorticity of the atmosphere, 2_ is the planetary vorticity, _ is the atmospheric density, and _ is the potential temperature.

Equivalent latitude values are then obtained in a manner similar to the one explained in Nash *et al.* (1996). The potential vorticity data are first interpolated onto potential temperature surfaces, after which potential vorticity isolines are identified and the surface areas enclosed by these isolines are calculated. The boundaries are then altered so that they fall on lines of constant latitude while the total enclosed areas remain constant. These latitude values are the equivalent latitudes. The procedure essentially amounts to finding those latitude values that subtend the same solid angles as the vorticity isolines. The equivalent latitude fields are interpolated onto the altitude grid of each of the ozone profiles retrieved by SAGE II using a trilinear interpolation.

The Model

The ozone distribution undergoes a seasonal cycle that is related to regional solar luminosity. To account for this mechanism, the model used in this climatology includes four sinusoidal terms, two with a one-year period and two with a six-month period, that describe the amplitude and phase of the annual and any semiannual variability. In addition, monthly averaged 10.7 cm solar radio flux data are used as a proxy for changing solar source conditions at wavelengths that stimulate photoionization and ozone production.

Ozone distribution is also affected by local dynamic atmospheric conditions. The quasi-biennial oscillation (QBO) is the dominant dynamic factor in the tropical stratosphere. It is characterized by a shift-

ing mean zonal wind flow that propagates downward with a period of approximately 28 months. It is driven by momentum fluxes from various atmospheric waves, including Rossby-gravity waves and Kelvin waves, and in turn influences meridianal circulation. For more on the QBO see Baldwin et al. (2001). Fig. 2 illustrates the evolution of the QBO at various pressure levels over Singapore for the last twenty years. Positive wind velocities indicate westerly winds and negative values indicate easterly winds. To account for the effects of the QBO on ozone distribution a linear principal component analysis (PCA) is applied to the wind data at all seven standard pressure levels over Singapore (Wallace et al., 1993). After subtracting the mean of the data and any linear trends and seasonal patterns in order to reduce the chance of multicollinearity with other terms in the model, the seven principal components (PCs) are calculated as linear combinations of the wind data. An inspection of the eigenvalues of the data covariance matrix shows that the two leading PCs collectively capture over 92% of the total variance in the data, and thus effectively represent the most prominent features of the QBO. These two linearly independent PCs constitute the two QBO terms ([QBO]0i, [QBO]1i) in the model.

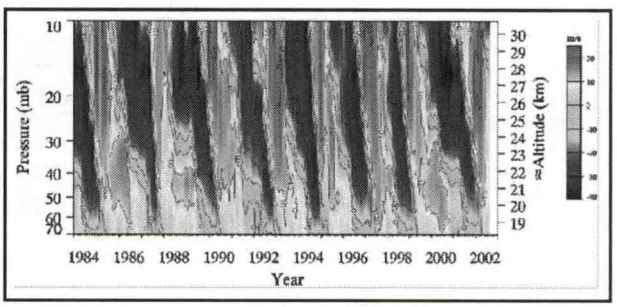

Fig. 2. Singapore monthly mean zonal wind velocities on seven pressure levels.

Finally, the model includes a mean ozone concentration term and a linear trend term. The model is summarized by the following formula:

The times (ti) are measured in years since the beginning of the time series record and the solar term is actually the offset from the mean solar flux. The coefficients (ai) are determined by fitting the model to the filtered monthly averaged SAGE II ozone data (yi) using singular value decomposition to minimize the sum of the squares of the error terms (errori). The Durbin-Watson test statistic is used to detect serial correlation in the time series data and, if present, an iterated modified Cochrane-Orcutt approach is used to estimate the autocorrelation parameter and correct the model by transforming the data based on the assumption that the error terms follow a first-order 1-month lag autoregressive process.

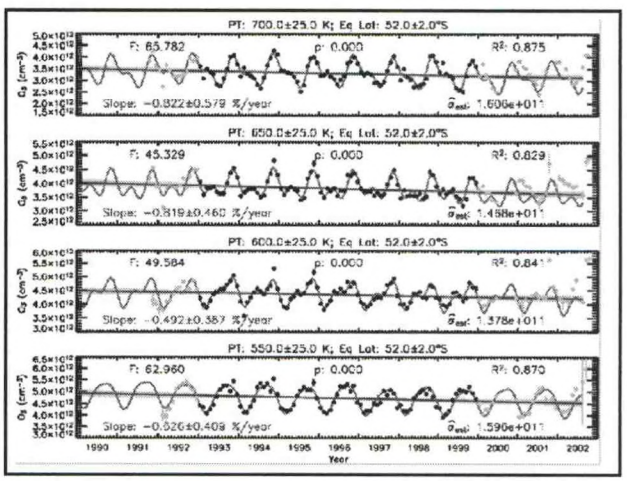

Fig. 3. SAGE II mean O3 data at 52°S EqL (550-700 K) and trends (1993-1999).

Results

The monthly averaged filtered SAGE II ozone number density data are regressed on the ozone model described above in 4° wide equivalent latitude (EqL) bins centered on the equator and 50 K wide potential temperature (PT) bins throughout the stratosphere. Figs. 3 and 4 show the SAGE II ozone time series data (black dots) and the derived best-fit models (red curves) at 52°S EqL for four PT bins from 550 K to 700 K (≈ 22-28 km). The estimated standard deviations in the ozonemonthly means are shown as vertical bars and the linear trend lines, as determined by the model, are shown in dark blue. The hyperbolic regions colored light blue (cyan) indicate the 95% confidence bands for the trend lines. The slopes of the trend lines, expressed as percentage gains or losses per year, are tabulated at the bottom left of each plot window with their associated 95% confidence intervals. Also shown are the F-values and p-values from the goodness-of-fit tests performed on the models, as well as the coefficients of multiple determination (R2) and estimated standard deviations of the data about the model. Green dots represent ozone data from SAGE II that were not included in the fitting of the model.

Equivalent latitude values based on the UKMO data are only calculated for SAGE II ozone profiles after 1991 since the UKMO dataset begins in 1991. However, to avoid starting the time series data with possibly biased ozone retrievals that were contaminated by the eruption of Mt. Pinatubo in 1991 the model was fit to data retrieved after 1993. Biased data at the endpoints of a time series have more of a tendency to skew the shape of the fitted model and, in particular, the slope of the trend line than do erroneous data in the middle of a time series. Fig. 3 shows the result of fitting the model to data between 1993 and 1999, while Fig. 4 shows the result of extending the time series through 2002.

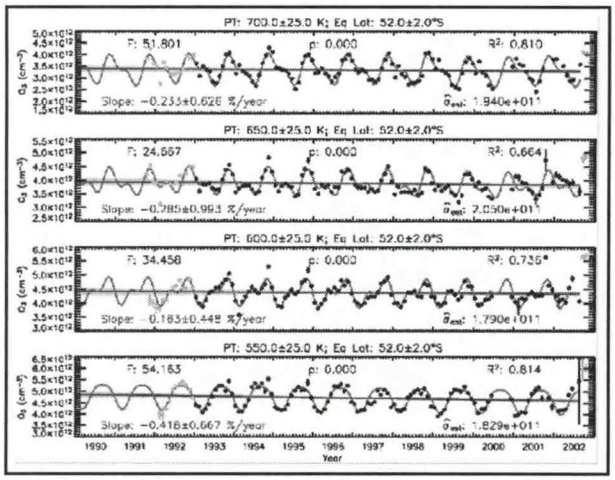

Fig. 4. SAGE II mean O3 data at 52°S EqL (550-700 K) and trends (1993-2002).

At these latitudes the model is dominated by the seasonal variations and the presence of the QBO is less discernible. It is interesting to note the secondary peaks that form annually around April or May and are most visible at 650 K in Fig. 3. This could be the result of the Brewer-Dobson circulation, which transports ozone from the tropics to higher latitudes during the winter in both hemispheres. Note also that the trend line tends to follow these secondary peaks as they decrease in magnitude from 1993 to 1998 where they reach a minimum. In fact, the trends for all four PT bins in Fig. 3 are negative within the 95% confidence interval. However, the model seems to underestimate the ozone concentrations after 2000, especially above 600 K. On the other hand, Fig. 4, which includes the data after 2000 in the model fit, indicates that the trends from 1993 to 2002 are less negative everywhere and are not statistically different from 0 at the 95% confidence level. The smaller value of R2 (0.664) at 650 K and the higher value of the estimated standard deviation about the model (2.05x1011) suggest that a linear trend term does not completely characterize the behavior of the ozone after 2000 and that perhaps the addition of a quadratic term to the model would yield a better fit. In any case, an examination of the error bars reveals that estimated monthly mean values for the data after 2000 generally have higher uncertainties associated with them. This is partly due to the reduced coverage of SAGE II during this period.

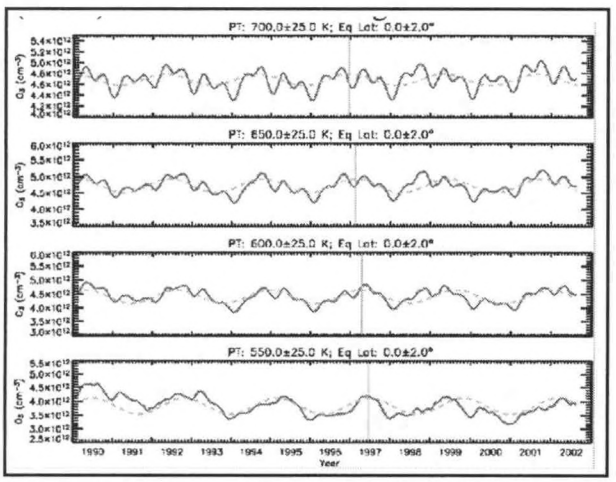

Fig. 5. SAGE II mean O3 data at 0° EqL (550-700 K) and trends (1993-2002).

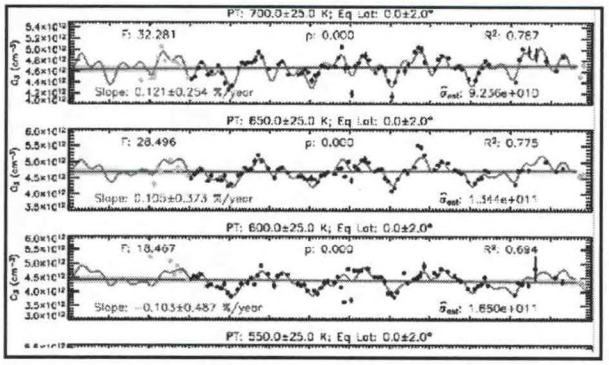

Fig. 6. O3 models from Fig. 5 with 28-month period sinusoids superimposed.

Fig. 5 shows the outcome of a similar regression analysis at 0° EqL for the same four PT bins. The effect of Mt. Pinatubo on the ozone data, especially in early 1992 below 650 K, is more evident here. Also more evident is the signature of the QBO. Although some annual and semiannual features can be seen,

the large-scale oscillations seem to occur with a period of about 2-2_ years. The average period of the QBO is about 28.2 months. A comparison with Fig. 2 reveals that the buildup in ozone coincides with the easterly phase of the QBO and the decrease in ozone occurs during the westerly phase. The modeled ozone behavior from these plots is redisplayed in Fig. 6 without the trend information, statistics, and SAGE II ozone data. A sinusoidal function with a 28-month period was fit to the model in each PT bin and is superimposed on the model as a dashed green curve. The vertical solid green lines designate the peaks in the fourth cycle of the sinusoidal curves at the four PT levels. Inspection of the time interval between the occurrence of the peaks at successively lower PT levels indicates that the rate of descent of the average QBO cycle, reflected in the rate of descent of the ozone cycle, is approximately 50 K (≈ 2 km) every 2 months. This concurs with the estimated rate of descent of the QBO of about 1 km/month.

Conclusion

An analysis of the residuals, the reasonable values of R2, and the good F-values for the goodness-of-fit tests indicate that this model adequately captures the main features in the behavior of the SAGE II ozone data in much of the lower stratosphere. Results in the upper stratosphere are less promising, probably because accurate wind velocity measurements at such altitudes are difficult to obtain. Also, the comparison with known characteristics of the QBO shows that the model accurately predicts the effects of the QBO on ozone distribution. To more fully exploit the long-term SAGE II ozone dataset for a study of stratospheric ozone trends it is necessary to have a record of wind velocity data extending back to 1984. Recently, pre-processed NCEP (National Centers for Environmental Prediction) equivalent latitude data interpolated onto the SAGE II altitude grid for each profile from 1984 to 2002 were acquired, and these data will be used to construct a global stratospheric ozone climatology in the EqL/PT coordinate system from 1984 to 2002.

ACKNOWLEDGEMENTS

I would like to acknowledge the NASA Langley Research Center for supplying the SAGE II ozone data that were used in this study and the UKMO for providing the wind velocity vector field data that were used to calculate potential vorticity and equivalent latitude values.

REFERENCES

Baldwin, M. P., et al., 2001: The Quasi-biennial Oscillation. *Reviews of Geophysics*, **39**, 179-230.

Kent, G. S., and M. P. McCormick, 1991: Separation of Cloud and Aerosol in Two-Wavelength Satellite Occultation Data. *Geophys. Res. Lett.*, **18**, 428-431.

Kent, G. S., D. M. Winker, M. T. Osborn, and K. M. Skeens, 1993: A Model for the Separation of Cloud and Aerosol in SAGE II Occultation Data. J. *Geophys. Res.*, **98**, 20725-20735.

McCormick, M. P., 1987: SAGE II: An Overview. *Adv. Space Res.*, **7**.

McCormick, M. P., L. W. Thomason, and C. R. Trepte, 1995: Atmospheric effects of the Mt. Pinatubo eruption. *Nature*, **373**, 399-404.

Nash, Eric R., Paul A. Newman, Joan E. Rosenfield, and Mark R. Schoeberl, 1996: An objective determination of the polar vortex using Ertel's potential vorticity. J. *Geophys. Res.*, **101**, 9471-9478.

Wallace, John M., R. Lee Panetta, and Jerry Estberg, 1993: Representation of the Equatorial Stratospheric Quasi-Biennial Oscillation in EOF Phase Space. *Journal of the Atmospheric Sciences*, **50**, 1751-1762.

Wang, Hsiang J., Derek M. Cunnold, Larry W. Thomason, Joseph M. Zawodny, and Greg E. Bodeker, 2002: Assessment of SAGE version 6.1 ozone data quality. J. *Geophys. Res.*, **107**, 4691.

MODIS Retrieval of Surface Temperatures in Puerto Rico for the ATLAS Field Campaign

Ana J. Picón[1], Ramón Vásquez[1], Jorge González[2], Jeff Luvall[3], and Douglas Rickman[3]

[1]Department of Electrical and Computer Engineering, UPRM
[2]Department of Mechanical Engineering, Santa Clara University,
[3]NASA Global Hydrology and Climate Center, Huntsville, AL

Abstract

The Airborne Thermal and Land Applications Sensor (ATLAS) from NASA/Stennis that operates in the visual and IR bands was used as the main sensor for a field campaign in San Juan, Puerto Rico with the main objective of investigating the Urban Heat Island (UHI) in tropical cities. The UHI represents the temperature difference between urban areas and surrounding vegetated areas and is a good indicator of the impact of the land use in the climate. The sensor was flown over Puerto Rico in a Lear 23 jet plane during February 2004. One of the efforts to support the data gathered by the ATLAS sensor was the acquisition of remote sensing observations for the flight period. A temporal analysis of this complementary data for the Atlas San Juan Mission is presented with the objectives of calibrating the response of satellite sensors such as MODIS(Moderate Resolution Imaging Spectroradiometer) to study the UHI effect in tropical and subtropical regions.

An analysis of the surface temperature variation was performed using remote sensing images from MODIS for the same days of the ATLAS field campaign. Surface temperatures were estimated for San Juan using the land surface temperature product MOD11_L2 distributed by Land Process Distributed Active Archive Center (LP DAAC). These results show the maximum, minimum and averages temperatures in San Juan and in the rest of the Island of Puerto Rico as measured by MODIS. A comparison of temperatures between El Yunque rain forest and San Juan reflects a tendency of higher temperatures for the San Juan area, an indication of the presence of a UHI.

The information retrieved from MODIS for land surface temperatures was compared with weather stations temperature measurements spread over San Juan reflecting similar temporal and spatial variations with absolute offsets of about 3.71°C due to the differences between surface and air temperatures. Observations from the weather stations and MODIS suggest an increase in temperature in urban areas during daytime over rural areas. Overall temperature variations estimated with the MODIS sensor for urban and rural areas agree with the expected temperature variations that characterize the UHI. Some differences between MODIS and other field sensors may be related to the total retrieval for Puerto Rico which in most cases was about 50%. Based on the available data from the MODIS product and the comparisons with other instrument measurements, some suggestions about the current algorithm will be made for applications in tropical regions.

Introduction

Remote sensing measurements can provide land surface temperatures at the regional scale. A brief review of relevant works is provided in this section followed by a calibration exercise under the San Juan Atlas mission. Landsat 7 has been used in urban heat island studies in the city of Atlanta [1]. This sensor has a spatial resolution of 60 m in the spectral range of 10.40 to 12.5 μm. One constraint of the instrument is the temporal variation due to overpasses through Puerto Rico which is every 16 days. Fukui [2] presented a study based on the surface temperature distribution and the urban structure in Tokyo using the Advanced Spaceborne Thermal Emission and Reflection Radiometer (ASTER) and LIDAR data. ASTER has a spatial resolution of 90m in the spectral range of 8.125 to 8.825μm, 8.925 to 9.275μm and 10.25

to 11.65μm. In this study, two different scenes from ASTER were used to calculate the surface temperature. The correlation of the surface temperature and the urban structure shows the impact of green areas on the urban heat environment and the falling of surface temperature in tall buildings during daytime and increasing of surface temperature during nighttime. Furthermore, NOAA Advanced Very High Resolution Radiometer (AVHRR) thermal IR images have been studied to understand the urban microclimates of cities such as Paris and Los Angeles [3]. This radiometer has a spatial resolution of 1km and two thermal bands in the spectral range of 10.3 to 11.3μm and 11.5 to 12.5μm. MODIS has the same resolution as NOAA AVHRR but has the capability of acquiring data over 36 spectral bands. McCabe [4] compared MODIS and NOAA AVHRR land surface temperatures with ground based infrared thermometry measurements made in Tomago, Sandbeds, north of Newcastle, Australia. Comparisons show good agreement between MODIS, NOAA AVHRR and the infrared thermometer. No major research has been reported where remote sensing images are used to estimate surface temperatures in tropical and subtropical regions.

A calibration exercise was conducted for the MODIS sensor using information gathered during the San Juan Atlas mission with the intention of verifying the ability of this sensor in observing surface temperatures in tropical regions. The land surface temperature (LST) product from MODIS (MOD11 from level 2) has been developed to get LSTs at a resolution of 1km and was used for this study. The theoretical basis of the LST algorithm is described in Wan [5]. The author presents two algorithms: the generalized split-window LST algorithm and the day/night algorithm. The generalized split-window LST algorithm uses the information from the spectral bands 31 and 32 (10.78 to 11.28μm and 11.77 to 12.77μm). Some of the constraints of the MODIS LST product are discussed in Wan [6]. One important concern about the day/night algorithm is to apply it to tropical regions because of the less clear-sky days. The author concludes that the algorithm can be used globally even in tropical regions. This LST product has been used in the evaluation of forest fire risk at Northeast China. Guangmeng [7] suggests the use of LST for this type of fire studies.

Different images were collected for the ATLAS campaign period and were analyzed to assess the accuracy of the MODIS sensor for tropical locations. Table 1 shows the date and time for every image collected from MODIS during the days of the San Juan ATLAS mission. For every day, there are two periods in which MODIS captures Puerto Rico. For some days, MODIS captures only half of the Island of Puerto Rico. That means that the day image will include half of the Island, most likely western Puerto Rico, while the night image will include eastern Puerto Rico. For the ATLAS period, this case occurred once.

Table1. Date and time for MODIS images

Date	Time
2004-02-11 (Day 042)	02:00 , 15:50
2004-02-12 (Day 043)	02:40 , 14:55
2004-02-13 (Day 044)	03:25 , 15:35
2004-02-14 (Day 045)	02:30 , 14:40
2004-02-15 (Day 046)	03:15 , 15:25
2004-02-16 (Day 047)	02:20 , 14:30

Methodology

Temporal Analysis from MODIS LST Product

All the images from the ATLAS period were georeferenced. The San Juan region was extracted according to the coordinates defined by ATLAS. MODIS did not capture San Juan during the daytime of February 11, 2004 but it did capture the Island during the nighttime. The hours during daytime may vary from one day to another. Figure 1 shows the extracted San Juan region for the specified date and hour during daytime for the days of the ATLAS mission. One observation about the retrieval is the lack of identification of some pixels. The day when most pixels were recovered was February 16, 2004 which was the day that the ATLAS over passed San Juan at 10

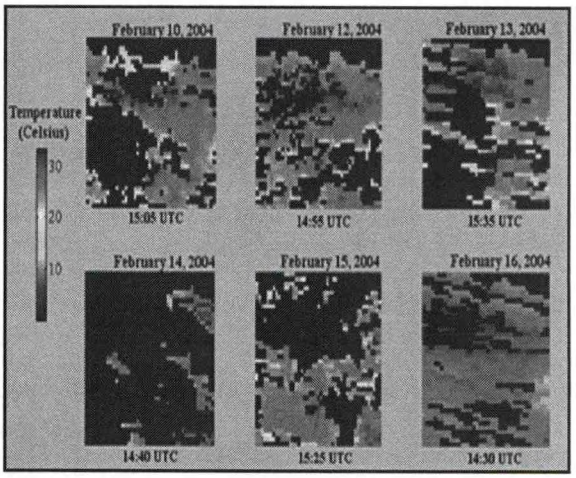

Figure 1: Extracted San Juan LSTs from MODIS during the ATLAS Mission period (Daytime).

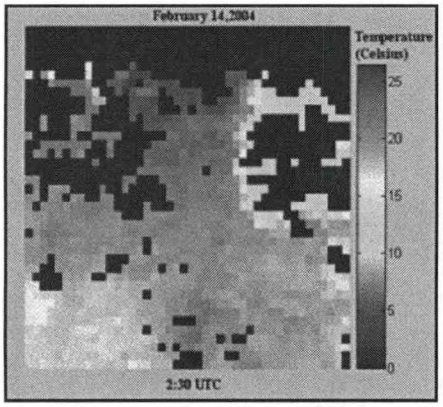

Figure 2. February 14,2004 02:30 UTC

meters resolution. The worst retrieval was February 14, 2004 which also corresponds to the largest precipitation activity during the mission.

Two important time intervals were not captured: February 11, 2004 at daytime and February 13, 2004 at nighttime. In February 14, 2004 at 2:30 UTC, there is a higher retrieval of LST measurements (see Figure 2). This observation is opposed to what was encountered during daytime when retrieval rates were lower.

Results for Remote Sensing Analysis

Three different tasks were performed as part of the temporal analysis using MODIS. The first one was to calculate the average temperature for San Juan and Puerto Rico during the time intervals mentioned before. To conduct this calculation, pixels that do not show retrieval were not taken into account. Figure 3 shows the

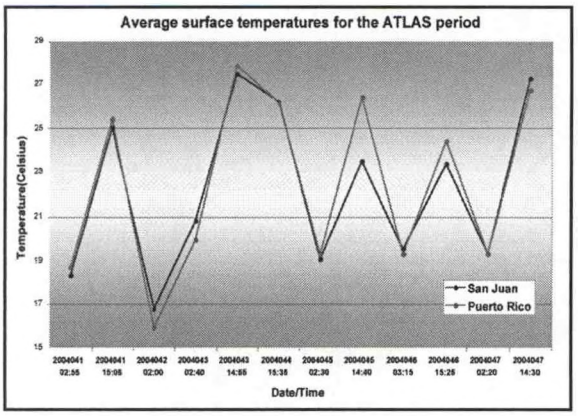

Figure 3. Average land surface temperatures

average temperature for the specified time intervals. The lowest average temperature occurred during February 11 at 2:00 UTC and it was 15.9 °C. The highest average temperature occurred during February 12 at 14:55 UTC and it was 27.85 °C. Both extreme averages temperatures were retrieved outside of San Juan.

The second task consisted of estimating the maximum temperature for San Juan and Puerto Rico. Table 2 shows the maximum temperatures for San Juan during the ATLAS period and the corresponding location. Maximum temperatures were encountered for more than one location for the same time interval. In February 11, 2004 at 2:00 UTC, for example, five different locations were identified with the highest temperature. These maximum temperatures were observed at 1km. Locations were near one to another, which means that an area of 4 km by 4 km was observed with 22.29°C at night during that particular day. Figure 4 shows the maximum temperatures for San Juan and Puerto Rico. The highest temperature observed was 37.87 °C during February 12, 2004 at 14:55 UTC and the lowest temperature was 22.29°C

Table 2 Identified maximum temperatures

Date/Time(UTC)	Temp(°C)	Geographic Coord(Lat/Lon)
2004-02-10/02:55	24.21	18°27'55.37" N / 66°6'49.79" W
2004-02-10/15:05	32.43	18°24'48.57" N / 66°9'43.14" W 18°24'16.06" N / 66°9'43.14" W
2004-02-11/02:00	22.29	18°30'1.57" N / 65°52'47.14" W 18°29'29.06" N / 65°54'31.96" W
		18°29'29.06" N / 65°53'57.02" W 18°29'29.06" N / 65°53'22.08" W 18°29'29.06" N / 65°52'47.14" W
2004-02-12/02:40	26.29	18°27'32.27" N / 66°7'47.47" W
2004-02-12/14:55	34.61	18°25'21.42" N / 66°3'23.50" W
2004-02-13/15:35	33.31	18°27'39.26" N / 66°4'37.30" W 18°27'37.66" N / 66°4'3.62" W 18°27'36.06" N / 66°3'29.94" W
2004-02-14/02:30	26.49	18°27'29.60" N / 66°7'45.74" W
2004-02-14/14:40	28.53	18°27'35.47" N / 65°53'24.15" W 18°27'35.47" N / 65°52'49.09" W
2004-02-15/03:15	24.45	18°28'6.74" N / 66°6'18.78" W 18°28'6.74" N / 66°5'43.00" W 18°27'34.24" N / 66°6'54.55" W 18°27'34.24" N / 66°6'18.78" W
2004-02-15/15:25	30.29	18°11'8.85" N / 65°50'28.20" W
2004-02-16/02:20	23.09	18°25'19.82" N / 66°5'56.96" W 18°25'19.82" N / 66°5'20.46" W
2004-02-16/14:30	32.35	18°26'37.02" N / 66°10'11.17" W 18°26'38.66" N / 66°9'37.51" W 18°26'40.30" N / 66°9'3.86" W

during February 11, 2004 at 2:00 UTC.

The third task consisted of a comparison of the available land surface temperatures from MODIS with surface temperatures from ground sensors located around San Juan during the ATLAS mission that were described before. The period observed occurred at 14:30 UTC in the same day of February 16, 2004. MODIS pattern seems to be more synchronized with the ground sensors for this case. Differences in temperatures are reasonable because ground sensors were measuring air temperature and not land surface temperatures. At rural areas, surface temperatures tend to decrease while urban areas will experience higher temperatures. MODIS resembles these expected trends, which relates well with the urban heat island effect. Figure 5 shows the temperatures measured by MODIS and the corresponding temperature sensors located at different points in San Juan. Table 4 below shows the geographic coordinates for MODIS pixels closer to the ground stations.

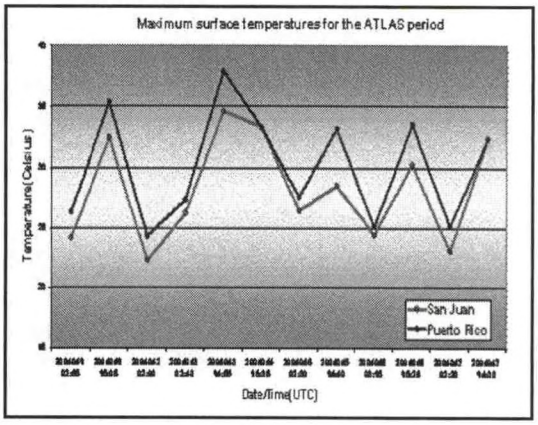

Figure 4. Maximum land surface temperatures

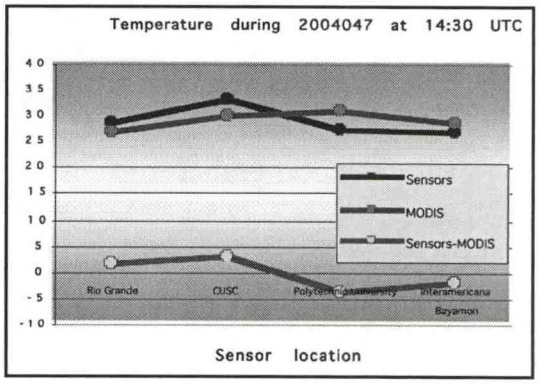

Figure 5. Comparison between weather stations and MODIS at daytime

Table 4 Locations of pixels nearest to the ground temperature sensors

Temperature sensor	Geographic location(Lat/Lon)
Rio Grande	18° 22'44.01"N / 65°45'22.07"W
NWS	18° 25'53.28"N / 65°59'29.00"W
CUSC	18° 26'29.02"N / 66°3'31.19"W
Polytechnic University	18° 25'19.06"N / 66°3'19.06"W
Interamericana Bayamón	18° 21'5.81"N / 66°11'0.6"W

Finally, a set of comparisons was made for El Yunque to observe the response of the MODIS sensor under a highly vegetated tropical zone. El Yunque is the only rainforest within US and is

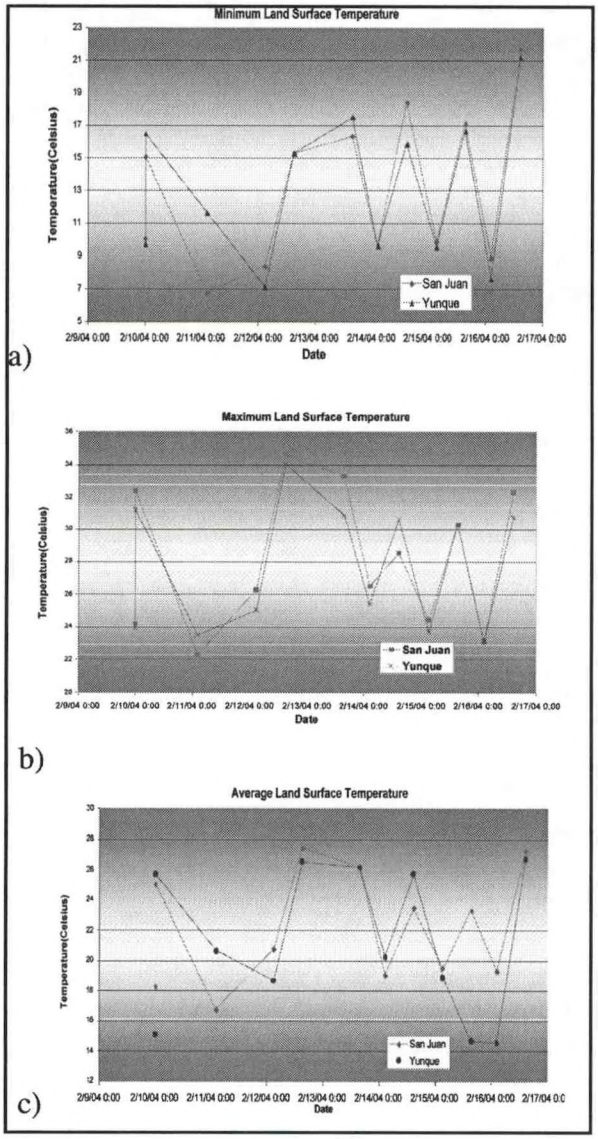

Figure 6. Minimum(a), maximum(b) and average(c) temperatures

located about 40 miles east of San Juan. Minimum, maximum and average land surface temperatures were calculated for El Yunque with MODIS. Figure 6(a) shows the minimum Land Surface Temperatures (LSTs) for El Yunque and San Juan. It can be observed that most of the time, El Yunque reported the lowest LSTs. On February 11, 2004, San Juan reported the lowest LST for the period of the ATLAS Mission, about 6.75 °C.

Figures 6(b) and 6(c) show the maximum and average LSTs for San Juan and El Yunque. It can clearly be observed that higher temperatures are frequent in San Juan. In general, MODIS maximum temperatures are in agreement with expected highest temperatures for urban areas.

Conclusions and Future Work

Higher temperatures were detected on February 12, 2004 at 14:55 UTC for San Juan and El Yunque when observed with the MODIS sensor. The lowest temperature detected by MODIS was on February 11, 2004 at 2:00 UTC. Temperatures tend to rise at 14:00 to 15:00 UTC which is about 10:00 a.m. to 11:00 a.m. in Puerto Rico. LST retrieval percent for MODIS reached about 60% in some cases. Cloud cover is one of the factors that may contribute to a low retrieval of LSTs from the MODIS sensor. Even if the retrieval rate is 60%, MODIS shows good agreement with the expected UHI pattern in San Juan. One suggestion to improve the retrieval rate is to combined other satellite land surface data with MODIS LSTs. McCabe et al. [4] suggest the combination of polar orbiters with similar characteristics to increase the confidence in predictions. In this case, NOAA AVHRR has similar characteristics to MODIS.

ACKNOWLEDGEMENTS

This research was sponsored by NOAA-CREST grant NA17AE1625. Thanks to the ATLAS mission campaign developer: the NASA Global Hydrology and Climate Center (NGHCC), Huntsville, AL. Special thanks to the EOS Data Gateway(EDG) and the Land Processes Distributed Active Archive Center(LP DAAC) for the distribution of MOD11_L2 Product data. Our appreciations also go to Dr. Sandra Cruz Pol (UPRM) for providing the ENVI software license.

REFERENCES

1. Poreh, M., 1996: Investigation of heat islands using small scale models, Atmospheric Environment, **30**, 467-474.

2. Fukui,Y., Hirose,Y., and N. Mushiake, 2002: A study on the surface temperature distribution and the urban structure in Tokyo with ASTER and LIDAR data. *Proceedings of Geoscience and Remote Sensing Symposium(IGARSS '02)*, **4**, 24-28.

3. Dousset, B., and F. Gourmelon, 2001: Remote sensing applications to the analysis of urban microclimates. *IEEE/ISPRS Joint Worshop Remote Sensing and Data Fusion over Urban Areas*, 168-172.

4. McCabe, M.F., Prata, A.J. and J.D. Kalma, 2001: The Effects of Scale on Predictions of Land Surface Temperature from a variety of Remote Sensing Platforms. *Proceedings of Geoscience and Remote Sensing Symposium(IGARSS '01)*, **3**, 9-13.

5. Wan, Z., 1999: MODIS Land-Surface Temperature Algorithm Theoretical Basis Document(LST ATBD). *http://modis-land.gsfc.nasa.gov/pdfs/atbd_mod11.pdf*

6. Wan, Z., 2003: Land Surface Temperature Measurements from EOS MODIS Data Report. *http://www.crseo.ucsb.edu/modis/wan2003_2.pdf*

7. Guangmeng, G. and Mei, Z, 2004: Using MODIS land surface temperature to evaluate forest fire risk of northeast China. *IEEE Geoscience and Remote Sensing Letters*, **1**, 98-100.

ORAL SESSION B1
Atmospheric Sciences

THE TRANS-ATLANTIC SAHARAN DUST AEROSOL AND OCEAN SCIENCE EXPEDITION (AEROSE)

Vernon Morris[a], Roy Armstrong[b], Pablo Clemente-Colon[c]

[a]NOAA Center for Atmospheric Sciences, Howard University, Washington, DC 20059
[b]University of Puerto Rico Mayaguez, Mayaguez, PR 00680
[c]NOAA/NESDIS, Office of Research and Applications, Camp Springs, MD

The Howard University NOAA Center in Atmospheric Sciences (NCAS) led a 27-day research cruise across the Atlantic Ocean during Feb-March 2004. The overall objective of the mission was to characterize the impacts of long-range transport of Saharan dust aerosol on the regional environment. During the Trans-Atlantic Saharan Dust AERosol and Ocean Science Expedition (AEROSE) comprehensive and integrated satellite, atmospheric, and oceanographic measurements were obtained by an international team of scientists and students from US, Spain, and Senegal. This presentation provides an overview of the scientific objectives and a summary of preliminary findings.

AEROSE website:

http://orbit-net.nesdis.noaa.gov/orad/sar/oceansar/AEROSE2004

Assessment of v6.2 Stratospheric Aerosol and Gas Experiment II Water Vapor Measurements

John Anderson, M. Patrick McCormick, and James M. Russell III

Center for Atmospheric Sciences, Hampton University, Hampton, Virginia

Abstract

The Stratospheric Aerosol and Gas Experiment (SAGE) II instrument has collected vertical profiles of stratospheric ozone, nitrogen dioxide, water vapor, and aerosol extinction at four wavelengths with high resolution since the program's inception in October, 1984. The previous version (v6.1) of SAGE II water vapor measurements in particular exhibit clear biases in comparisons with other instruments, notably the Halogen Occultation Experiment (HALOE), but were of sufficient quality to provide evidence of long-term stratospheric increases, in agreement with independent measurements. This bias has often been attributed to the inability to completely clear the effects of aerosols. In the latest version (v6.2), the SAGE II processing team has made great strides in characterizing stratospheric water vapor by performing a single wavelength-shift and increasing the channel-width by 10% from 1986-present. These advancements have significantly reduced this bias except in the proximity of heavy aerosol levels. We present results characterizing the geophysical variability in the new v6.2 water vapor retrievals. Analysis techniques include performing multiple linear regression analysis to reproduce the tropical tape recorder and near-global seasonal cycles. Comparisons with HALOE v19 data show dramatic improvements (compared to v6.1) in reproducing the near-global seasonal cycle patterns and the tropical tape-recorder.

Introduction

The Stratospheric Aerosol and Gas Experiment (SAGE) II instrument has collected vertical profiles of stratospheric ozone, nitrogen dioxide, water vapor, and aerosol extinction at four wavelengths with 1 km vertical resolution since the program's inception in October, 1984. The version 6.1 (v6.1) of SAGE II water vapor measurements in particular exhibit clear biases in comparisons with other instruments but were of sufficient quality to provide evidence of long-term stratospheric increases, in agreement with independent measurements. This bias has often been attributed to the inability to completely clear the effects of aerosols. The SAGE II processing team has made great strides in characterizing stratospheric water vapor. Recent advancements in the retrieval algorithm has significantly reduced this bias except in the proximity of heavy aerosol levels. These advancements include a single wavelength shift for 1986-present and the combination of 2 aerosol models. There exists a clear requirement for evaluating the water vapor's regular long-term behavior, and for extraction of information pertinent to broader studies of atmospheric radiation, dynamics, and chemistry. This data set becomes evermore valuable as time goes on due to its usefulness for global change studies.

We present results characterizing the seasonal variability in the new v6.2 water vapor retrievals (released October 24, 2003). Analysis techniques include fitting harmonic functions to reproduce the tropical tape recorder and seasonal cycles in the lower stratosphere [Randel et. al, 2001]. These results are compared to SAGE II v6.1 derived patterns to assess the changes due to the algorithm improvements and Halogen Occultation Experiment (HALOE) version 19 (v19) derived patterns to assess the quality of the new retrievals from a climatological point of view.

Data Sets and Methods

The SAGE II v6.1 and v6.2 water vapor data are first screened for short events and only cloud-free data are used when the 1.02 mm extinction value is less than 3×10^{-4} km^{-1} as recommended by Thomason et al. [2004] and an error bar filter of 50% [Taha et al., 2004].

The HALOE instrument on board the Upper Atmospheric Research Satellite (UARS) has been operating without flaw since it was activated on October 11, 1991. The experiment uses the instrumental methods of gas filter and broad-band radiometry and the solar occultation technique to measure vertical profiles of O_3, HCl, HF, CH_4, H_2O, NO, NO_2, extinction due to aerosols, and temperature versus pressure. The vertical resolution for the radiometer channels is approximately 2 km and 4 km for the gas filter channels. The HALOE H2O data in particular have been extensively used to examine transport and chemistry throughout the stratosphere and in the lower mesosphere, validation of other remote sensors, and also to infer how the circulation strength in the middle atmosphere has changed during the UARS time period. We use the 3rd public release (v19) from October 1991 through October 2003.

The HALOE H2O profiles are first averaged onto a SAGE II altitude grid over the 10-50 km range. HALOE data in the lower stratosphere were screened of cloud events using the method of Hervig and McHugh [1999]. Data were omitted in the lower stratosphere below 30 km from the beginning of the mission to August 1992 due to volcanic aerosol contamination. SAGE II v6.1 and HALOE data are averaged monthly in 10° latitude increments from 70°S to 70°N with centered latitude locations of 70oS, 60oS, and so on while monthly zonal medians were used for v6.2 in the same latitude ranges. Monthly zonal medians are used in v6.2 to filter out data points that are influenced by undetected clouds near the tropopause.

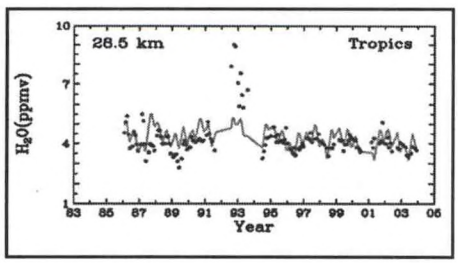

Fig. 1. Time series of SAGE II v6.2 unfiltered monthly zonal median water vapor measurements at 28.5 km, centered over the equator. The red line is a multiple linear regression fit to the time series.

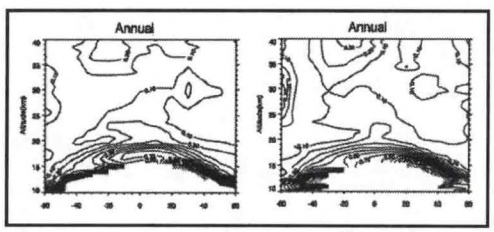

Fig. 2. Amplitudes of the annual and semi-annual cycles derived from SAGE II v6.2 (left column) and HALOE v19 (right column). Contour intervals are in .1 ppm increments.

Figure 1 shows the water vapor time series of the monthly-zonal-medians at 28.5 km and centered over the tropics. The red line is a fit to a model consisting of mean, trend, seasonal, and QBO terms. It is clear that there are still some additional anomalous points (especially after Pinatubo). Inspection of numerous latitude bands and altitudes showed similar patterns. The data between 1996-2003 were then averaged to obtain a mean and standard deviation. These were then used to filter out data points from 1986 through 1995 that were greater than 3 standard deviations from the calculated mean.

The screening process has filtered out most of the anomalous data points but missed some that may affect this analysis. We therefore use the more representative time series beginning in January 1996. The three water vapor climatologies are then derived from the time series of the monthly-zonal averages and medians. To examine the seasonal variability in H2O mixing ratios, multiple-linear-regression is used to fit the three time series to a seasonal model consisting of a mean, annual, and semi-annual terms. We also look for potential drifts between the SAGE II v6.2 and HALOE v19 water vapor channels by taking their time series that are at the same latitude band and altitude, deseasonalize them, then take the absolute difference of the two. The tropopause heights and isentropes used in this study were provided by NCEP in support of the SAGE II program.

Discussion

Figure 2 shows the amplitudes of the annual and semi-annual oscillations for the two data sets. Note the good agreement between v6.2 and HALOE for both the annual and semi-annual amplitudes. 'tape-recorder' pattern from SAGE II v6.2 (top figure), and HALOE v19 (bottom figure). The tape-recorder patterns depict how the amount of water vapor entering the stratosphere changes throughout the year as the tropical tropopause gets colder and warmer. The tape-recorder patterns show that the tropical region must be quite isolated from the rest of the stratosphere or these variations would be diluted [Mote et. al, 1996]. The v6.1 data have a very dry bias in the lower stratosphere but the tape-recorder pattern is evident from 16-25 km and possibly up to 27 km (not shown). The v6.2 data is much moister than v6.1 in the lower stratosphere with a very coherent tape-recorder pattern that extends from 16 to ~30 km. This enhancement

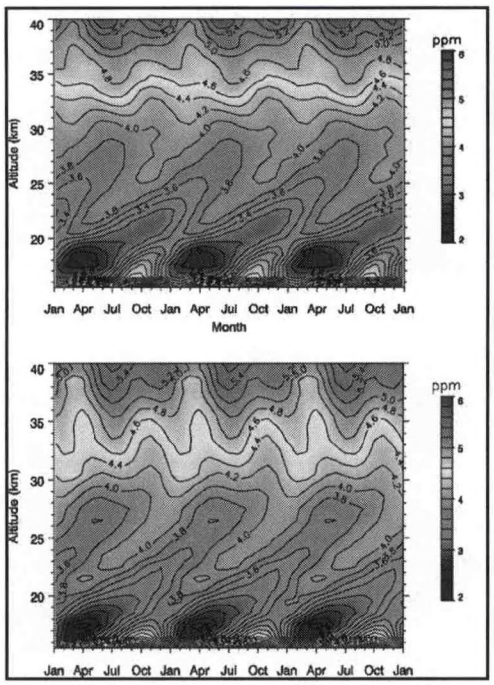

Fig. 3. Altitude time variations of equatorial (+/- 5°) water vapor mixing ratios derived from SAGE II v6.2 (top) and HALOE v19 (bottom) measurements. Contour intervals are in .2 ppm increments. Three seasonal cycles are shown in each panel.

probably due to the reduced sensitivity (by a factor of 10 or more) to aerosol of the newer version compared to v6.1 [Thomason et. al, 2004]. The v6.2 tape-recorder compares very well with the established HALOE v19 derived tropical pattern but there are some subtle differences above 30 km. Though v6.1 is very dry in the lowermost stratosphere, the data in this region show a reasonable seasonal cycle (not shown) showing fast, quasi-horizontal transport between tropics and midlatitudes [Randel et. al, 2001] but do not reproduce the vertical propagation above the equator as exhibited in HALOE v19 data (not shown).

The v6.2 data in Figure 4 do show the clear seasonal cycle in the lowermost stratosphere and the equatorial tape-recorder effects. The climatological structure in v6.2 compares very well with HALOE. The changes from v6.1 to v6.2 can be termed dramatic and though there is some subtle differences, the mutual consistency between v6.2 and HALOE v19 is phenomenal with respect to previous SAGE II versions.

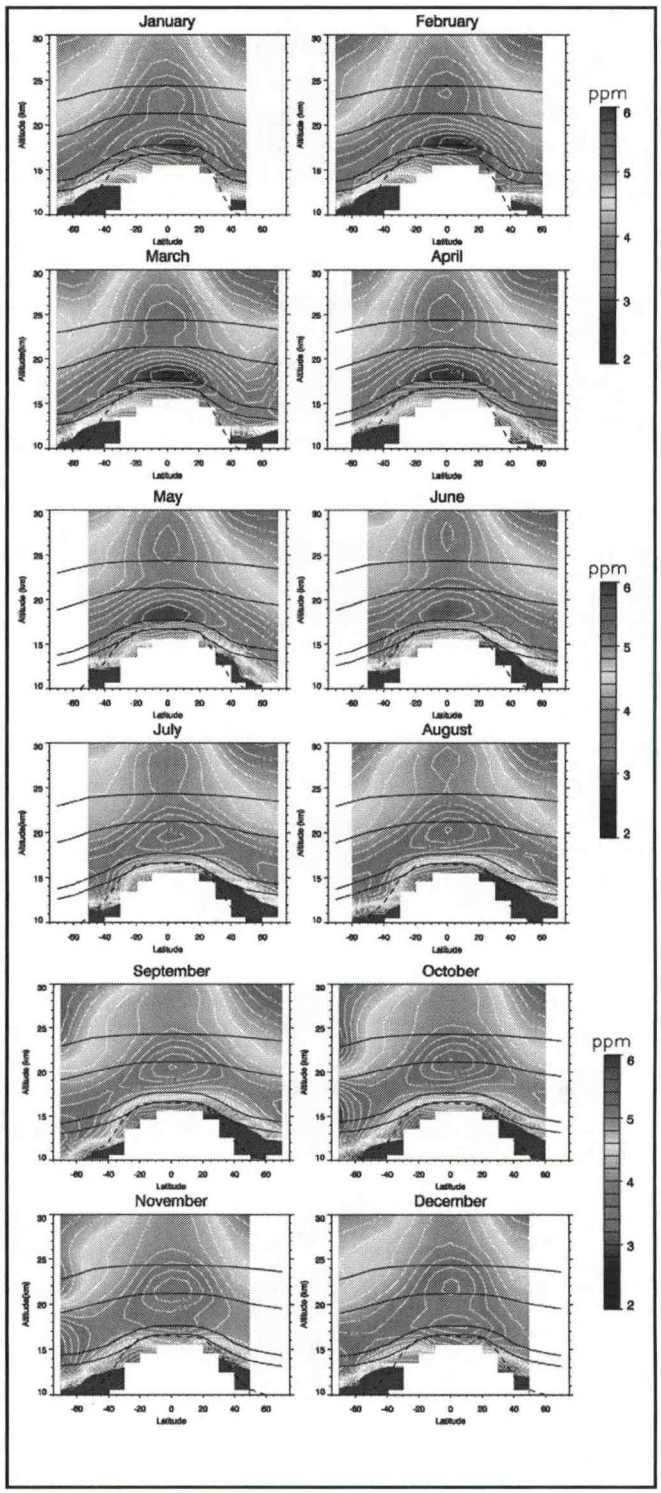

Fig. 4. Meridional cross sections of the derived monthly

Figure 5 shows the anomalies resulting from deseasonalizing the HALOE and SAGE II time series. There is a strong QBO in the tropics at 28.5 km for both data sets and the resulting difference time series appears to not have a significant slope. At 10oS and 32.5 km, there are some anomalous points in the SAGE II set near 1993 that are due to Pinatubo aerosol contamination. The difference time series also shows this and the apparent good agreement after 1995. At 40oN and 21.5 km, the agreement between the 2 is good.

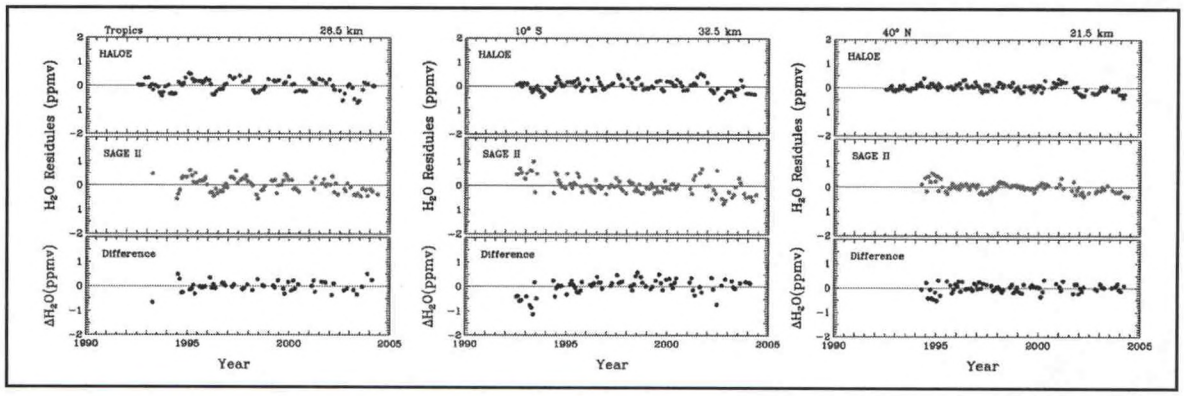

Fig. 5. De-seasonalised H2O time-series of HALOE v19 (top frames), SAGE II v6.2 (middles frames), and the absolute difference of the two (HALOE - SAGE II, bottom frames). The locations were at 28.5 km in the tropics (left), 32.5 km at 10oS (middle), and 21.5 km at 40oN (right). The green lines in each figure denotes zero ppmv.

Summary

Previous versions of the SAGE II water vapor measurements exhibited clear biases in comparisons with other instruments. This bias has often been attributed to the inability to completely clear the effects of aerosols. Recent advancements included a single wavelength shift of the primary water vaporsignificantly reduced this bias except in the proximity of heavy aerosol levels. Comparisons with HALOE v19 data show dramatic improvements (compared to v6.1) in reproducing the near-global seasonal cycle patterns and the tropical tape-recorder. The changes from v6.1 to v6.2 can be termed dramatic and though there is some subtle differences, the mutual consistency between v6.2 and HALOE v19 is phenomenal with respect to previous SAGE II versions. Future work will include tests to assess if the SAGE II water vapor channel does indeed have a significant drift with respect to HALOE.

ACKNOWLEDGEMENTS

The authors would like to thank the SAGE II and HALOE processing teams for producing high quality data sets.

REFERENCES

Hervig, M. and M. McHugh, 199: Cirrus Detection using HALOE Measurements, *Geophys. Res. Lett.*, **26**, 719-722.

Mote, P.W., K.H. Rosenlof, J.R. Holton, R.S. Harwood, J.W. Waters, 1996: An atmospheric tape recorder: The imprint of tropical tropopause temperatures on stratospheric water vapor, *J. Geophys. Res.*, **101**, 3989-4006.

Randel, W.J., F. Wu, A. Gettelman, J.M. Russell III, J.M. Zawodny, and S.J. Oltmans, 2001: Seasonal variations of water vapor in the lower stratosphere observed in HALOE data, *J. Geophys. Res.*, **106**, 14,313-14,325.

Thomason, Larry W., S.P. Burton, N. Iyer, J.M. Zawodny, and John Anderson, 2004: A revised water vapor product for the Stratospheric Aerosol and Gas Experiment (SAGE) II version 6.2 data set, *J. Geophys. Res.*, **109**, 6312 10.1029/2003JD004465.2004.

EXAMINATION OF THE SOLSE/LORE-2 LIMB SCATTERING DATA

Robert Loughman, Kristie V. Lee, and Michael Hill

Center for Atmospheric Sciences, Hampton University, Hampton, Virginia

David Flittner and Didier Rault

Radiation and Aerosol Branch, NASA Langley Research Center, Hampton, Virginia

Richard McPeters, Ernest Hilsenrath, Scott Janz, Tammy Brown, and P.K. Bhartia

Atmospheric Chemistry and Dynamics Branch, NASA Goddard Space Flight Center, Greenbelt, Maryland

Abstract

The Shuttle Ozone Limb Scattering Experiment (SOLSE) and Limb Ozone Retrieval Experiment (LORE) instruments were re-flown in January 2003 to test the potential of limb scattering ozone retrievals. In this paper, we discuss some remaining challenges associated with the SOLSE/LORE data set. Assigning the proper altitude scale to the data is complicated by the poor temporal sampling obtained from the LORE 350 nm channel, as well as frequent shuttle attitude adjustments and maneuvers during the measurements. Characterization of the stray light observed in the measured radiance profiles has also proven difficult. We outline the strategy pursued to overcome these obstacles and validate the measured ozone profiles, confirming the accuracy and robustness of the limb scattering ozone retrieval method.

Introduction

The limb scattering measurement and the SOLSE and LORE instruments are described in Lee and Loughman (2004). In this paper, we discuss the SOLSE data in greater detail, and describe the challenges associated with instrument pointing and stray light characterization for the measurements. The current validation strategy for the SOLSE ozone profile retrieval product is outlined, and comparisons to the ozone profiles retrieved from OSIRIS limb scattering and SAGE II solar occultation measurements are presented.

Instrument Pointing

The "RSAS method" (described in Janz et al., 1996) of tangent height registration for limb scattering data requires measurements near 350 nm. The LORE instrument provides these measurements, and the SOLSE pointing is derived from the LORE pointing estimate, providing for the relative alignment of the instrument boresights. But for the frequent cases when the SOLSE and LORE 350 nm observations are not synchronized, the issue of how to interpolate between LORE 350 nm pointing estimates to derive the SOLSE pointing becomes critical.

Two methods have been tried:

1. The shuttle maintains a record of its attitude in the form of Post-Flight Attitude and Trajectory History (PATH) data, recorded at 1 second intervals throughout the flight. The stated accuracy of this data is on the order of 20 km in tangent height, much worse than the 1 km accuracy obtained from the RSAS method. But we tried to assign pointing for SOLSE by using the variation of the PATH data as an interpolating function in time between the LORE 350 nm measurements.

2. We also tried simply assuming linear variation of the shuttle attitude with time between LORE 350 nm observations. Given the sporadic nature of the shuttle attitude adjustments (due to maneuvers or jets fired to keep the attitude within prescribed limits), method 2 clearly fails for cases in which adjustments occurred (see Fig. 1). But method 1 introduces the limitations of the PATH data product into our

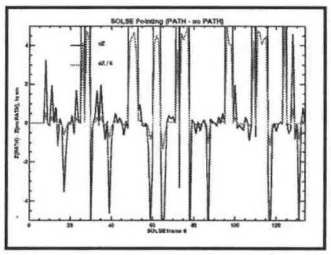

Fig. 1: Difference between the SOLSE pointing estimate obtained when the PATH data is used to interpolate and the SOLSE pointing estimate obtained with linear interpolation with time. The red line shows this difference divided by six, to illustrate the outliers that extend beyond the y-axis limits. The x-axis shows the SOLSE frame number.

SOLSE pointing estimate, which may introduce smaller (but more widespread) degradation in the quality of the estimate.

Neither method proved clearly superior, but method 2 was on average more effective. In this study, we have used method 2, and discarded a few cases for which the difference between the pointing estimates is particularly large.

Stray light

As measured during pre-flight characterization of the instrument, the SOLSE point spread function exhibits significant spatial and spectral variation across the detector. In addition, analysis of the measured data indicates significant "stray light" that is not captured in the measured point spread function. The stray light may be caused by diffuse scattering of light within the instrument, or may simply reflect the limitations of the detectable signal in the pre-flight laboratory measurements.

In addition, the SOLSE window features three neutral density filters (NDF) to flatten the overall signal at the detector. The most transparent filter is at the highest tangent heights (where the measured radiance is weakest), and the least transparent filter is at the brighter lowest tangent heights. The NDF greatly reduced the level of stray light relative to the initial SOLSE flight (see McPeters et al., 2000). But the NDF boundaries might also act as diffusers, introducing stray light and creating an unusable gap several pixels wide in the radiance profile. Efforts to characterize the radiance data continue, but constructing a continuous radiance profile across the NDF boundaries has posed a particular challenge.

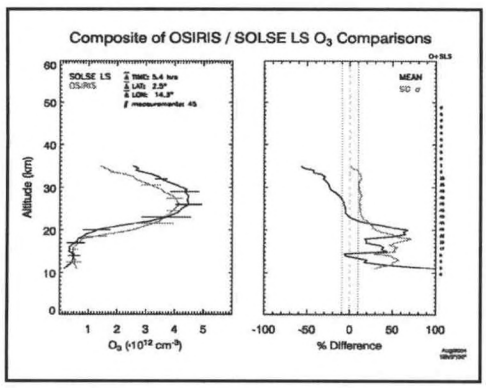

Fig. 2 The average ozone profile retrieved by SOLSE (black line) and OSIRIS (red line) for the coincident cases.

Validation procedure

The current SOLSE validation procedure uses only the middle NDF range for ozone retrieval, and we focus on cases for which that middle range includes the 15-35 km altitude range of primary interest. Only 50 frames pass that criterion. Excluding cases for which the ozone profile retrieval algorithm convergence is not satisfactory leaves only 25 frames for further analysis. (The reason why some frames converge well while others fail is under investigation.) We compare the remaining SOLSE ozone profiles to coincident data from independent sources: The OSIRIS (limb scattering, see Murtagh et al., 2002) and SAGE II (solar occultation, see Chu et al., 1989) data sets.

Comparison between SOLSE and OSIRIS ozone profiles is presented in Fig. 2. All coincidences within 12 hours in time, 5 deg in latitude and 30 deg in longitude contributed to the average ozone profiles shown in Fig. 2. The SOLSE profile tends to peak approximately 2 km higher than the OSIRIS profile, with approximately 10% more ozone at the peak. Given the difficulty of assigning the proper tangent height to the SOLSE data, a possible misregistration would not be surprising. But it is useful to note that, while the reported accuracy of the OSIRIS pointing is on the order of 200 m (von Savigny et al., 2003), early validation efforts have indicated possible systematic errors of 1 km or more for some of the months analyzed (Petelina et al., 2004), indicating that the OSIRIS pointing error may also contribute to the difference shown in Fig. 2.

Further evidence that the SOLSE pointing estimate contains little bias is displayed in Fig. 3, which compares the average SOLSE and SAGE II ozone profiles for the coincident measurements. The solar occultation measurement requires acquisition of a bright target against a dark background, and is therefore capable of producing very accurate pointing. We are therefore encouraged that Fig. 3 shows little

pointing offset between the two mean ozone profiles. Given the relative scarcity of solar occultation measurements, the coincident criteria were relaxed in this case to 24 hours, 5 deg in latitude, and 180 deg in longitude

Conclusions

Despite the challenges of unexplained stray light and uncertain pointing estimations, we have shown that the limb scattering ozone retrieval method can produce useful ozone profile information. Comparisons with OSIRIS limb scattering ozone profiles show that the two instruments produce a similar mean profile, with perhaps some tangent height offset between them. Agreement with the SAGE II solar occultation profile is better, with little apparent tangent height offset. Through further efforts to characterize the SOLSE data, we hope to expand this study to include more coincident cases. In the future, we hope to derive information on stratospheric aerosol profiles as well as ozone profiles. All of these efforts will prove useful for the Ozone Mapper Profiler Suite (OMPS) instrument, which will make limb scattering measurements as part of the ozone monitoring strategy to be administered by the Integrated Program Office (IPO) in the coming decade.

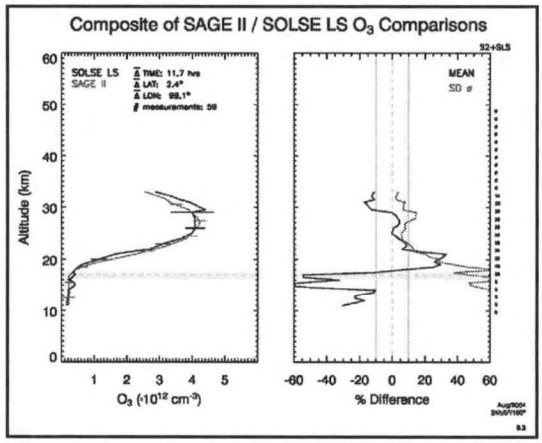

Fig. 3 The average ozone profile retrieved by SOLSE (black line) and SAGE II (red line) for the coincident cases.

ACKNOWLEDGEMENTS

We recognize the supreme sacrifice made by the crew of STS-107, and appreciate the opportunity to contribute to their legacy through analysis of the SOLSE/LORE-2 data. This work was made possible by the tireless efforts of the SOLSE/ LORE-2 instrument team, led by Scott Janz and Tammy Brown We received support from Ted Llewelyn in our OSIRIS data comparisons, and appreciate the OSIRIS and SAGE II teams' efforts to make their data available.

REFERENCES

Lee, K.V. and R. Loughman, 2004: this volume.

Janz, S. J., E. Hilsenrath, D. Flittner, and D. Heath, 1996: Rayleigh scattering attitude sensor. *Proc. SPIE Int. Soc. Opt. Eng.*, **2831**, 146-153.

McPeters, R.D. et al., 2000: The retrieval of ozone profiles from limb scatter measurements: Results from the shuttle ozone limb sounding experiment. *Geophys. Res. Lett.*, **27**, 2597-2600.

Murtagh, D. et al, 2002: An overview of the Odin atmospheric mission, *Can. J. Physics*, **80**, 309-319.

Chu, W., et al. 1989: SAGE II Inversion Algorithm, *J. Geophys. Res.*, **94**, 8339-8351.

Von Savigny, C., et al., 2003: Stratospheric ozone profiles retrieved from limb scattered sunlight radiance spectra measured by the OSIRIS instrument on the ODIN satellite: Methods and first results, *Geophys. Res. Lett.*, **30**, 1755-1758.

Petelina, S., et al., 2004: Comparison of the Odin/OSIRIS stratospheric ozone profiles with coincident POAM III and ozonesonde measurements. *Geophys. Res. Lett.* **31**, doi:10.1029/2003GL019299

ONE YEAR OF BLOGGING: SUCCESS OF THE U.S. AIR QUALITY WEBLOG

Nikisa Jordan[1], Jill Engel-Cox [2,1], Raymond Hoff[1], Shobha Kondragunta[3], Kevin McCann[1], Kamonayi Mibenga[1], Ana Prados[3], Ray Rogers[1]

[a]CREST, Joint Cneter for Earth Systems Technology, University of Maryland Baltimore County, 1000 Hilltop Circle, Baltimore, MD 21250 email: *rrogers@umbc.edu*

[2] Battelle Memorial Institute, 2101 Wilson Boulevard, Suite 800, Arlington, VA 22201 email: *engelcox@battelle.org*

[3]NOAA NESDIS, Camp Springs, MD

ABSTRACT

In September 2003, the U.S. Air Quality weblog (the "smog blog") was launched. Since that time daily observations of air quality events have been analyzed and posted daily. The site uses sources of data from NOAA, NASA, EPA and from UMBC observations. The intent of the log was to become a "one stop shop" for air quality information and to provide UMBC observations with some intelligent planning. Over the course of the year, events such as the fire plumes in North America, regional hazes and local air quality exceedences have been monitored. UMBC (and CREST partner) results have been web published and are being widely used by air quality managers across the nation (and the world). To date, over 250,000 hits of the site have been logged from over twenty countries. This site has to be considered a major success for CREST.

INTRODUCTION

Since the summer of 2003, the University of Maryland Baltimore County (UMBC) Atmospheric Lidar group has been operating a weblog called U.S. Air Quality. The weblog or blog, for short, enables multiple users to post daily images and text of analysis of U.S air quality. Data from multiple sources, including satellite sensors, ground-based air quality monitors, and UMBC lidar systems are used to evaluate daily air quality events. This effort is part of a parallel lidar network called the Regional East Atmospheric Lidar Mesonet (REALM) presented at last year's CREST Symposium [Hoff et al., 2003]. REALM is a lidar mesonet designed to monitor air quality in the vertical from multiple locations on the east coast. The URL for the USAQ blog is http://alg.umbc.edu/usaq.

DATA PRODUCTS USED

Imagery data from the MODIS instruments aboard the AQUA and TERRA satellites are examined daily. The data is obtained in near real time from a link to the University of Wisconsin MODIS direct downlink facility and the data granules are transferred to UMBC as part of a collaboration sponsored by NOAA CREST.

Data from EPA ground-based particulate matter monitors are also used to describe the air quality. These data are obtained from the

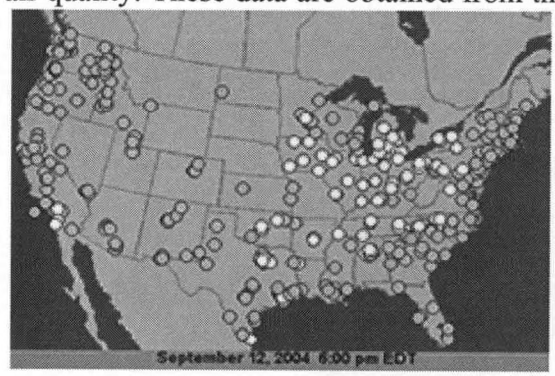

Figure 1 –EPA AIRNOW $PM_{2.5}$ Map http://www.epa.gov/airnow/

EPA AIRNOW website. $PM_{2.5}$ maps are posted on the blog to describe the possible affects of air quality on human health.

In collaboration with NOAA NESDIS, UMBC has developed a specialized GASP Aerosol Optical Depth (AOD) viewer that allows rapid scrolling through images, zooming, data-value retrieval, and animation. The GASP product, which is derived from GOES data, was originally developed by Ken Knapp [Knapp et al. 2002] and is being deployed by Ana Prados and Donna McNamara. UMBC GASP AOD animations are frequently posted on the weblog.

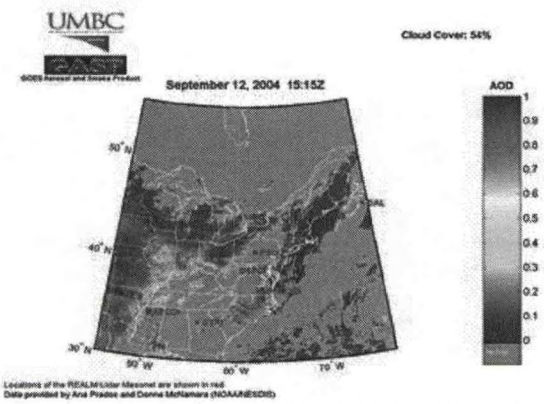

Figure 2 –UMBC GASP AOD Viewer

Data from the UMBC Elastic Lidar Facility (ELF) is posted daily. The ELF system operates in the visible at 532 nm, and can retrieve aerosol backscatter and extinction up to altitudes between 6-10 km in the daytime and 10-15 km at night. In addition, the ELF system can determine cloud bottoms up to an altitude of 15 km, and cloud tops when the cloud optical depth permits.

WEBLOG POST DESCRIPTION

The daily forecast by UMBC students is used to plan lidar-profiling sessions for either the elastic aerosol system or the water vapor profiling Raman lidar. UMBC cross-sectional lidar data are posted to the log daily [Hoff, et al., 2004a].

Posts are made daily by UMBC graduate students and take around 2-5 hrs. Each blogger reviews products from multiple sources, including satellite sensors, ground-based air quality monitors, and UMBC lidar systems. After careful analysis of each product, a logical analysis is made of the U.S air quality. Public posts are not allowed to assure the scientific quality/integrity of the information.

Many interesting events have been posted on the website. We have had several "hits" where this day-to-day attention to the environment in Baltimore, Maryland, has given us the ability to focus on air quality events, some which have long-range transport components. Local air pollution events have also been observed and described on the weblog.

LONG-RANGE TRANSPORT EVENTS

Fires in Alaska & British Columbia Canada

Fires were discovered in Alaska and northwestern Canada in early July, 2004. Lighting was responsible for triggering the fires and the damage was extensive. "As a matter of scale, Alaska had 25,000 km² in fire this year and the Taylor Complex fire alone was 5,260 km² in area, twice the area of all the 2003 Southern California fires combined. The Alaska fires comprised 86% the fire area of the US up to September 1." [Hoff et al., 2004b]

This major event was being monitored daily on the U.S Air quality smog blog. The smoke plumes progressed into the U.S and eventually arrived in the Northeast. The UMBC ELF Lidar system identified a

smoke plume at 4 km on July 9, 2004, which arrived around 1630 UT. The smoke plume is shown in Figure 3. We are fairly certain that this is a smoke plume due to the strong return in the depolarization channel, which indicates non-spherical particles. Researchers from the University of Wisconsin noticed smoke from the Alaska fires the previous day.

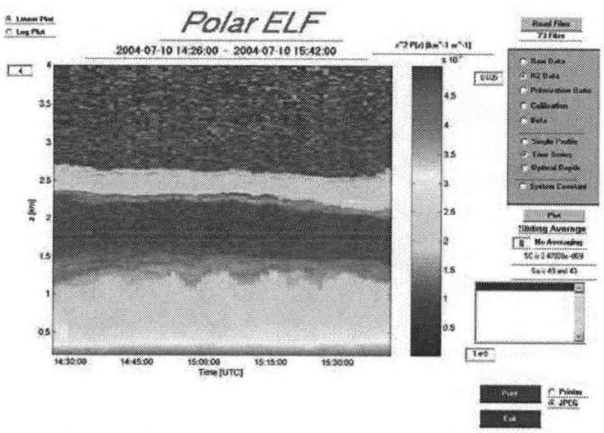

Figure 3 – AK/BC Smoke at UMBC July 10 2004

California Wildfires

We also detected fire plumes from the California wildfires over Maryland and the Northeast. The smoke arrived on November 2 of 2003 at high altitudes ranging between 7 and 12 km.

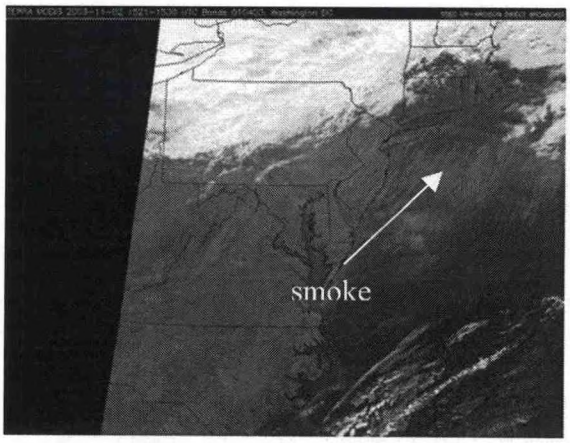

Figure 4 – California Smoke in Northeast U.S

OTHER EVENTS

Other unique events that could affect air-quality in the U.S. have been posted on the blog. One of these involved a sandstorm in New Mexico. Another showed a large ash plume near the South of Puerto Rico, which originated from the volcano on Montserrat.

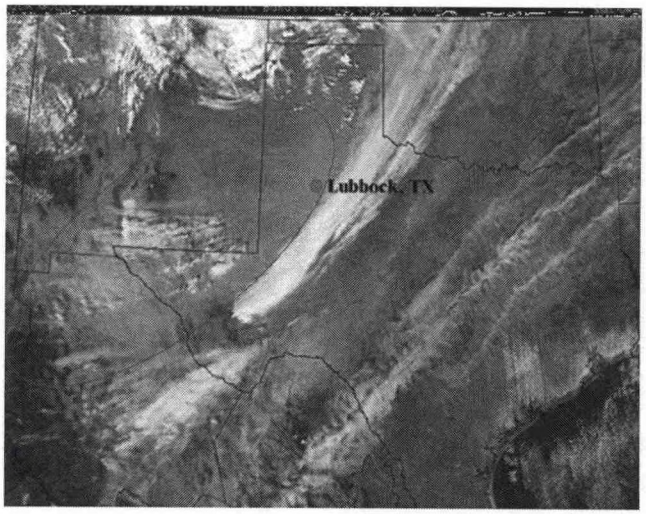

Figure 5 – Texas Dust storm (- MODIS Direct Broadcast University Wisconsin http://eosdb.ssec.wisc.edu/modisdirect/)

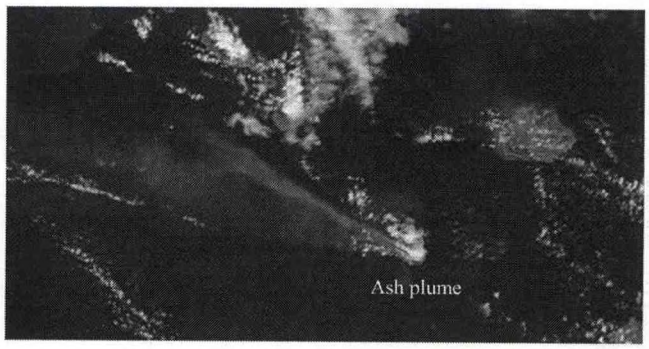

Figure 6 – Montserrat Ash plume (NASA MODIS Rapid Response System http://rapidfire.sci.gsfc.nasa.gov/realtime/)

GROWTH OF WEBLOG POPULARITY

The U.S Air Quality weblog has become increasingly popular. Our website statistics show that over 250,000 hits have been received since September 2003. More than 37,000 hits have been received for the first half of September. The "top level" domains accessing the site include U.S educational and government visitors.

Table 1 - "Top Level" Domains (Sep 12, 2004)

Hits	"Top Level" Domain
22,784	edu = US
5,885	net = US Network
4,926	com = US Commercial
800	it = Italy
1,336	ca = Canada
676	gov = US Government
448	us = United States
53	fr = France
63	pl = Poland
199	de = Germany
37	tw = Taiwan
54	org = US
46	jp = Japan
48	be = Belgium
39	in = India
10	nz = New Zealand
7	uk = United Kingdom
25	si = Slovenia
14	au = Australia
14	se = Sweden
6	il = Israel

ACKNOWLEDGEMENTS

This work was supported by grants from NOAA CREST (through the City College of New York Foundation) and from the Maryland Department of Environment.

REFERENCES

Hoff, Raymond M., Kevin J. McCann, Jens Reichardt, Belay Demoz, David N. Whiteman, Tom McGee, M. Patrick McCormick, C. Russell Philbrick, Kevin Strawbridge, Fred Moshary, Barry Gross, Sam Ahmed, Demetrius Venable, Everette Joseph, Thomas Duck, Ivan Dors, January 10-11, **2003**: Regional East Atmospheric LIDAR Mesonet, REALM, *NOAA-CREST/NASA-EPSCoR Joint Symposium for Climate Studies University of Puerto Rico - Mayaguez Campus*.

Hoff, R. M., K.McCann, B.Demoz, and D. N. Whiteman, **2004a**: Aerosol profiling in the Washington-Baltimore urban corridor: a REALM application. *Paper 1.12, 6th Symposium on Atmospheric Chemistry. Amer. Met. Soc. Annual Meeting, Seattle, WA*.

Hoff, Raymond M., Tom Duck, Ed Eloranta, Jill Engel-Cox, Nikisa Jordan, ShobhaKondragunta, Nick Krotkov, Kevin McCann, Fred Moshary, Kamonayi Mubenga, Steve Palm, Ana Prados, Ray Rogers, Lynn Sparling, James Spinhirne, KevinStrawbridge, Omar Torres, September **2004b**: Multisensor Observations of the Long-Range Transport of Three Large Forest Fire Plumes to the Northeastern U.S. *NOAA CREST- NOAA Educational Partnership Program Symposium, City College of New York CCNY campus.*

Knapp, K. R., T. H. Vonder Haar, and Y. J. Kaufman, 2002: Aerosol optical depth retrieval from GOES-8: Uncertainty study and retrieval validation over South America, *J. Geophys. Res.*, **107 (D7)**, 4055, doi:10.1029/2001JD000505.

BIOAEROSOL MEASUREMENTS ACROSS THE TROPICAL ATLANTIC OCEAN

Y. Detres, R. Armstrong, C. Betancourt, A. De La Mota, O. Rivera, J. Matta*, and E. Suarez*

NOAA Center for Atmospheric Sciences (NCAS), University of Puerto Rico at Mayagüez

* Ponce School of Medicine, Ponce, Puerto Rico

Global transport of dust provides an important means for dispersal of bioaerosols including microorganisms such as fungi and bacteria. Due to its proximity to northern African, the Canary Islands are frequently exposed to large amounts of dust originating in the Sahara and Sahel regions. During the summer, these African aerosols are also transported by the trade winds westward across the Atlantic Ocean into the Caribbean, Central America and southeastern United States. These microorganisms can cause diseases in plants and animals, and might be responsible for an increase incidence of asthma and respiratory diseases in the affected regions. This comparative study assessed the fungi species present in filtered air samples collected during Saharan dust events in the Canary Islands (2002-2003) and Dominica (Lesser Antilles) during the summer of 2002. Samples were also collected across the Atlantic Ocean during the AEROSE 2004 expedition aboard the NOAA Ship Ronald H. Brown. Microbiological characterization used the ITS region of the rDNA and primers ITS 1 and ITS 4. "Background" filters corresponding to days without dust influence were also examined for determination of the natural fungal population in the study areas. Samples from Dominica resulted in 14 species from the genera *Aspergillus, Penicillium, Fusarium, Cladosporium, Curvularia* and *Phanerochaete*. Some of these species are known to cause respiratory disorders in humans while others are plant pathogens affecting economically important crops. Preliminary analysis of samples from the Canary Islands resulted in the isolation of 29 fungal species. Although most of these species are considered opportunistic, primarily affecting immunocompromised hosts, they are environmental allergens, and agents of asthma and infection.

ORAL SESSION B2
Marine & Fisheries Sciences

Catch and Release – A Twenty Year Perspective on Research Investigating Angler Induced Mortalities in Striped Bass (*Morone saxatillis*) Populations Resident to the Chesapeake Bay

Dr. Eric B. May

NOAA Living Marine Cooperative Science Center; Department of Natural Sciences, University of Maryland Eastern Shore; Princess Anne, MD 21853

Through regulatory action or educational programs, resource agencies either force or advocate catch and release as a means of reducing harvest pressure on many commercially or recreationally important fish species. These actions often bring into focus the issue of "angler induced mortalities" and the significance of post release mortalities to the success of management programs.

Angler induced mortalities (AIMs), depending on species, occurs primarily as a consequence of physiological or traumatic harm to the fish during periods of extreme exertion or from damage due to terminal gear, respectively. This paper presents a review of research conducted during the past twenty years on striped bass, examining both environmental and physiological factors which influence survival among post release striped bass. The primary cause of AIMs appears to be primarily acidosis from increased lactic acid production, and in some cases reduced respiratory efficiency and minimally direct trauma due to terminal gear.

In addition, based on NOAA Fisheries recreational surveys, the body of work suggests that the 8% mortality rate used in harvest control models, and the 30% mortality rate suggested by other investigators are over-estimates of the true post release mortality rate.

THE INFLUENCE OF FEEDING ON SERUM CHEMISTRY OF STRIPED BASS *(MORONE SAXATILIS)*

Maria A. Richardson[1]* and John Jacobs[2]

[1]Living Marine Resources Cooperative Science Center, Department of Natural Sciences, University of Maryland Eastern Shore, Princess Anne, MD.

[2]Maryland Department of Natural Resources, Cooperative Oxford Laboratory, Oxford, MD

*Email address: *marichardson@umes.edu*

The objective of this experiment was to measure the effect of feeding of striped bass (*Morone saxatilis*) on blood chemistry variables (triglycerides, protein, glucose, chlorides, and osmolality), as well as the magnitude and duration of each variables' response. Traditionally, proximate composition is the gold standard for long term nutritional assessment. This technique, however, is highly invasive and leads to the death of the specimen. Analyzing serum chemistry, a less invasive technique, may be a preferred alternative to proximate composition. In this experiment, test fish were starved for a period of 4 weeks and then fed once. After reintroduction of food the fish were sampled at pre-assigned time intervals during a 96-hour duration. The fish had blood samples and fillets removed for the experiment. The serum was separated from the blood and tested to measure level concentrations of variables present within the serum. The fillets were used in the proximate composition technique to determine percent moisture and percent lipids. It was found that the triglycerides, glucose, and proteins increased dramatically after feeding, which is not reflective of long-term nutritional status. The time noted for initialization of the response after feeding is longer than other reported serum chemistry experiments. Ongoing studies are in progress to test other serum variables that could be linked to long-term nutritional assessment.

TOXIC EFFECTS OF HEAVY METALS AND ORGANICS ON WINTER FLOUNDER *(PSEUDOPLEURONECTES AMERICANUS)* EXPOSED TO MARINE SEDIMENTS IN THE CHESAPEAKE BAY

Bashiru Balogun[1]*, Andrew Draxler[2], Dan Wieczorek[2] and Yan Waguespack[1]

[1]Living Marine Resources Cooperative Science Center, Department of Natural Sciences, University of Maryland Eastern Shore, Princess Anne, MD.

[2]2NOAA/ NMFS, Howard Marine Sciences Laboratory, Highlands, NJ

*Email address: *bashirub@hotmail.com*

Sediment contaminants such as alkylated metals, polyaromatic hydrocarbons (PAHs), polychlorinated biphenyls (PCBs), and pesticides can enter young-of-the-year winter flounder (*Pseudopleuronectes americanus*) via respiration, ingestion, and transdermal uptake. Preliminary studies on winter flounder exposed to sediment from Newark Bay (New Jersey, U.S.A.) revealed an unexpectedly high mortality rate. Several sediment samples from Elizabeth River and York River (lower Chesapeake Bay) were analyzed for the following contaminants: copper, lead, zinc, fluoranthene and perylene. These contaminants were found to be significantly higher in sediments taken from Elizabeth River compared to York River. The effect of these contaminants on survival of winter flounder is currently being studied. Additional studies on the ecotoxicology of winter flounder will be conducted by exposing the sentinel, benthic fish to contaminated sediment (Elizabeth River and York River) at various time intervals.

FISHING GEAR INTERACTIONS WITH SEA TURTLES IN THE UNITED STATES VIRGIN ISLANDS

Kemit-Amon Lewis

Masters Student, Marine Science Program, Savannah State University

Assessing sea turtle interactions with the commercial fisheries industry is a mechanism by which information can be obtained to help continue the global conservation of sea turtle populations. In this preliminary study, fishermen on the islands of St. Croix and St. Thomas (U.S. Virgin Islands) were interviewed to determine the frequency at which sea turtles interacted with commercial fishing gear: traps, hook and line, and nets. Interaction was defined not specifically as capture, but as entanglements (trap buoy lines, nets) or impalements (hooks). Of the fishermen surveyed on St. Croix, 57% had never caught sea turtles in their fishing gear. Twenty five percent reported rare interactions, 7.1% reported occasional interactions, and 10.7% reported frequent interactions. On the island of St. Thomas, 45.5% never had any interactions with sea turtles, and 18.2%, 9.0%, and 27.3% reported rare, occasional or frequent interactions, respectively. Prevalent species of turtles observed on St. Croix were *Chelonia mydas*, the Green Sea Turtle (44.4%), *Dermochelys coriacea*, the Leatherback Sea Turtle (44.4%), and *Eretmochelys imbricata*, the Hawksbill Sea Turtle (1.1%). The Green and Hawksbill Sea Turtles (41.2%) were most commonly seen by fishermen on St. Thomas, followed by the Leatherback Sea Turtle (17.6%).

Although many fishermen overlap with the type of gear that they use, line and traps were the most often utilized. However, turtle interactions occurred more frequently with nets on both St. Croix and St. Thomas (83.3% and 87.5%, respectively). Fishers that used hook/line and rods accidentally hooked turtles approximately one-third of the time of the coasts of St. Croix and St. Thomas. On St. Croix there were no reported interactions with traps and sea turtles but 28.6% of the trap fishers reported having sea turtles tangled in their buoy lines.

In addition to survey data, local fishery- and boat-related sea turtle stranding data collected between 1994 and 2003 were analyzed. Only 57 reported cases of such sea turtle standings were reported for the territory. The few other cases were unknown or caused by stress or other complications associated with the Green Turtle FibroPapilloma. Of those fishery-related strandings, 5 turtles survived. Causes for the strandings were mainly boat strikes or propeller wounds and could also be attributed to entanglement, spearing, or other types of impalements. By assessing fishery- and boat-related impacts on turtles and their potential effect of strandings, management plans can be made that efficiently address the conservation issues of local species of sea turtles in the waters of the United States Virgin Islands.

TIDE-RELATED ACTIVITY PATTERNS IN GRASS SHRIMP *PALAEMONETES PUGIO*: DOES PARASITISM MAKE A DIFFERENCE?

Sue A. Chaplin-Ebanks and Mary Carla Curran

Marine Sciences Program, Department of Natural Sciences and Mathematics
Savannah State University, Savannah, GA

The grass shrimp *Palaemonetes pugio* is an important food source for many estuarine fish and crustaceans (Kneib and Knowlton, 1995; Manderson et al., 2000; Davis et al., 2003) and is parasitized by the bopyrid *Probopyrus pandalicola*, which is a parasitic isopod that negatively affects shrimp respiration, metabolic activity, and reproductive output (Anderson, 1972; Pike, 1960). The trematode *Microphallus turgidus* in its intermediate stage can also infect Palaemonetes pugio and usually encysts within the abdominal tissue. Kunz (2003) noted that cyst density had a positive effect on grass shrimp activity level thus increasing the probability that the shrimp would be eaten by the terminal host. The purpose of our study was to determine whether or not bopyrid infection played a role in grass shrimp activity levels. Additionally, we assessed whether shrimp maintain tidal rhythmicity in the laboratory and if so, whether tidal stage had an effect on grass shrimp activity levels.

Shrimp were collected and examined for length, number of trematode cysts, and the presence or absence of the bopyrid. Five bopyrid-parasitized and five bopyrid-unparasitized shrimp were selected with similar numbers of trematode cysts and randomly placed in individual aquaria with sand and filtered seawater. Small glass tanks were used for four trials and small plastic tanks were used for the other four trials since we suspected that reflection from the glass tanks was causing increased activity of the shrimp in the first four trials. Opaque dividers were placed between the tanks so that the shrimp could not see each other and lights were on from approximately 0630 until 2100. Shrimp were observed for activity beginning at high tide, with four trials starting at approximately 1800 and four trials at approximately 2400. Observations were completed every 3 h for 24 h and activity was divided into six behavioral categories: resting, floating, walking, swimming, diving, and darting.

The maximum numbers of shrimp were resting at the time periods associated with flood current (72% ± 7.6 SE) and the minimum numbers were resting at ebb current (20% ± 5.03 SE). Also, over the progression of the 24-h period, which consisted of two tidal cycles, there was a tendency for individuals to be more inactive regardless of tide stage (Figure 1). After preliminary statistical analysis, there appeared to be no effect of the bopyrid on grass shrimp activity.

Bass and Weis (1999) determined that bopyrid parasitism reduced grass shrimp activity levels; however, they used shrimp that had been acclimated in the laboratory for several days. The internal tidal rhythm may have diminished by that time and the effect of the parasite may have become the primary factor affecting shrimp behavior. Since the shrimp in our study were most active during observations corresponding with ebb currents, they would be more susceptible to predation by visual predators in the water column at this stage. Furthermore, they may be more susceptible to benthic predators during flood current when they were most inactive.

An Evaluation of Surgical Closure Techniques for Long-Term Retention of Telemetry Transmitters in American Eels (Anguilla rostrata)

Jessie C. Thomas, Dewayne A. Fox, and Michael A. Reiter

Department of Agriculture and Natural Resources, Delaware State University, Dover, DE 19901-2277

According to recent surveys, American eel (*Anguilla rostrata*) stocks are thought to be in decline. In an attempt to address these declines, there have been recent calls for an increased understanding of American eel habitat requirements. While telemetry has proven a powerful tool for gaining insights into habitat utilization in other species, low transmitter retention rates have limited its success in American eels. In fact, debate exists over the best method of transmitter placement for American eels. To address this problem, we are conducting research to identify the most appropriate method of implantation to maximize transmitter retention times. Individual eels (n=120) have been randomly assigned to one of four treatment groups (control, no closure, suture, and surgical adhesive with skin graft) to assess each technique's effect on transmitter retention. Contrary to published findings, preliminary results indicate that suturing of the incision is the most effective implantation method. A better understanding of transmitter implantation techniques will allow for increased utilization of resources and data collection in field projects utilizing telemetry.

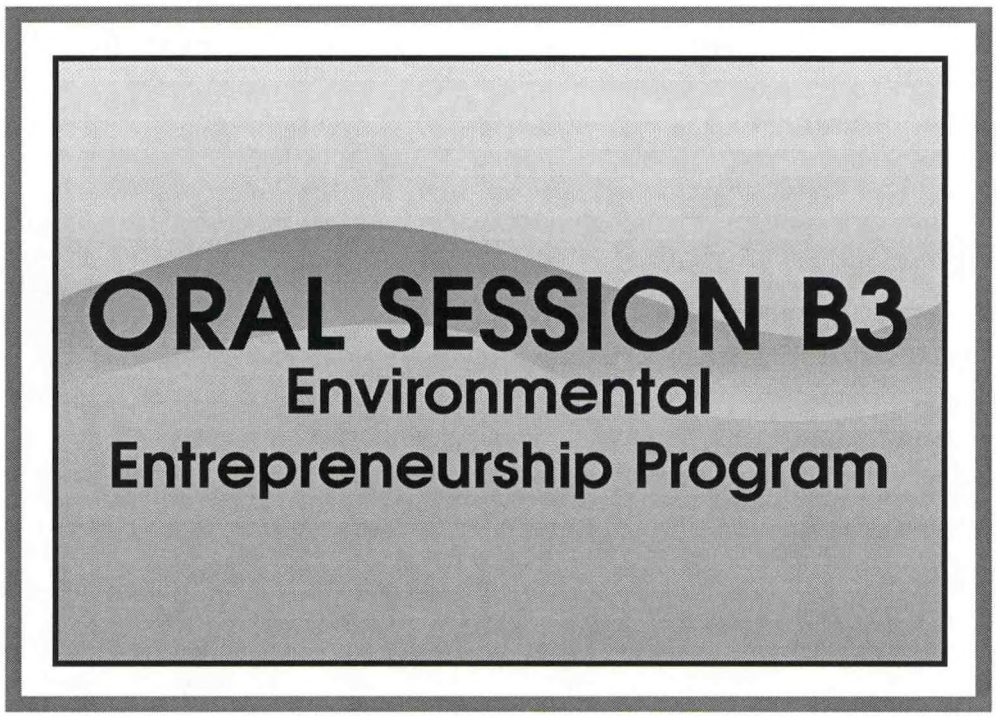
ORAL SESSION B3
Environmental
Entrepreneurship Program

Fostering the Entrepreneurial Spirit

Jewel Griffin-Linzey, NOAA/EPP, Clement Lewsey, NOAA,
Victoria Cooper, Wilbur Wright College, Arthur Allen, University of Maryland Eastern Shore
Conrad Ingram, Clark Atlanta University , Sis. John Karen Frei, Barry University
Frank Finley, Salish Kootenai College , Jonatan Jelen, The City College of CUNY

Abstract

The session is designed to provide insight and perspectives on entrepreneurship and will highlight the definition of entrepreneurship, illustrate examples, and discuss how to foster the entrepreneurial spirit through applied research, outreach and education, and partnerships that will promote commerce and economic development. There will be an opportunity to engage in open discussion to share perspectives on enhancing entrepreneurship through partnerships (between NOAA, MSIs and the public-private sector) and experiences that will allow students and faculty to gain the necessary entrepreneurial skills and training.

The objective of this session is to share perspectives on the concept of entrepreneurship and how it is achieved; to give insight on how to foster an entrepreneurial spirit among MSI students; to offer suggestions on how to engage students in a compliment of entrepreneurial training and technical skills that will promote commerce and economic development; and to discuss how to enhance the capacity of MSIs and partner's role in fostering entrepreneurship.

Topics in the session include: strategies on how to provide training for students on establishing Submerged Aquatic Vegetation (SAV) businesses; sharing of experiences on attracting and recruiting high school and undergraduate students into environmental and marine science careers; experiences on how-to train students with the necessary entrepreneurial skills and knowledge that will prepare them to plan and operate aquaculture businesses in collaboration with the private sector; perspectives on students' hands-on training and field based learning experiences at NOAA's Great Lakes Environmental Research Laboratory; and perspectives on increasing student's theory and practice of entrepreneurship through business plan development.

ORAL SESSION C1
Satellite Remote Sensing

LOSSLESS COMPRESSION OF AIRS DATA*

I. Gladkova[1], L. Roytman[1], M. Goldberg [2], M. Nash [3]

[1]NOAA-CREST City College of New York, New York, NY
[2]NOAA-NESDIS, Washington, DC
[3]Coalition School for Social Change, New York, NY

Abstract*

The proposed algorithm is based on adaptive clustering procedure that extracts the characteristic features of the sensor measurements. The clustering is performed recursively and at each iteration the set of features is modified so that the classification performance is maximized. The challenge is to derive an organic lossless compression scheme that is the most appropriate for the sounder data. Hence, the main objective of the project is to incorporate a priori knowledge of the physical characteristics of the sounder data into compression process in order to achieve an optimal compression ratio. Our overall strategy is to use the data itself as the prime driver in the search for the optimum solution.

Introduction

In this paper we present a lossless algorithm for compression of the signals from NOAA's environmental satellites. The project's aim is the design, analysis, and implementation of compression techniques that are suitable for the next-generation GOES-R instruments. We are using current spacecraft to simulate data from the upcoming GOES-R instrument and focusing on Aqua Spacecraft's AIRS instrument in our case study.

The AIRS is a high resolution instrument which measures infrared radiances at 2378 frequencies ranging from 3.74-15.4 _m. The AIRS takes 90 measurements as it scans 48.95 degrees perpendicular to the satellite's orbit every 2.667 seconds. We use Level 1A digital counts data granules, which represent 6 minutes (or 135 scans) of measurements. Therefore, our data set consists of a 90x135x2378 cube of integers ranging from 12-14 bits.

It should noted that noise in the channels introduce added complexity in compression. Therefore, in practice, we utilize only 1502 out of 2378 channels picked by NOAA/NASA for their favorable characteristics. Otherwise, we would need to add an additional step to detect these channels prior to running our compression algorithm.

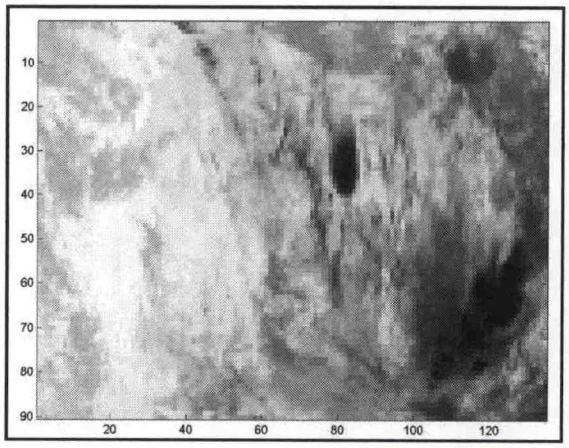

Fig.1: Image at channel index 600.

Compression Algorithm.

The algorithm consists of the following steps:

1. Channel Partitioning
2. Whitening
3. Projection
4. Estimated entropy coding of the residuals

In this paper we consider granule 60 (Asia, Daytime) as an example of the transformations that occur at each compression step. Below is the image from the considered granule for the channel index 600.

During the first stage, we partition the data into five units. The partitioning algorithm maximizes the

Sponsored by NOAA/NESDIS under Tim Schmit (ORA), Roger Heymann (OSD) HES Compression Group

continuity of each unit and takes into count that range of the digital counts varies (12, 13 and 14 bits) with respect to channel index. After this subdivision, each of the resulting 90x135xKn granules will be processed independently.

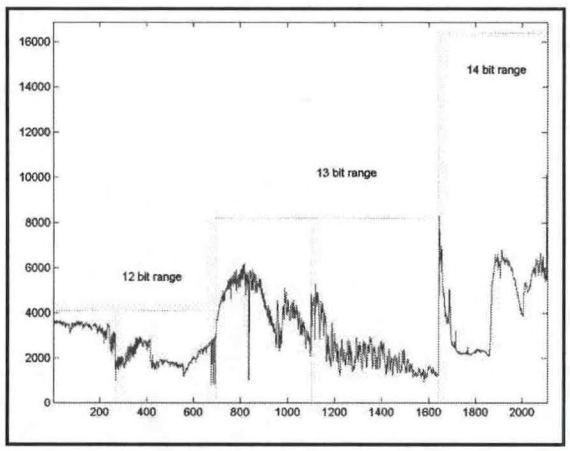

Fig.2: Change of digital counts values with channel index.

The purpose of the second (whitening) step of our algorithm is to transform the data so that its distribution is as close to normal as possible. Whitening is obtained via adaptive clustering as described in the following section.

Step 3 of our algorithm is a Karhunen-Loève transform that is known to be optimal (in some sense) provided a normal distribution of the data. For example, Karhunen-Loève transform is known to have the smallest average distortion when approximating a class of functions by their projection on L orthogonal vectors chosen a priori. Karhunen - Loève (also known as PCA) is a very well known transform used in compression as well as other applications and a set of theorems about optimal properties of this transform, for example, can be found in [3].

If the goal was to develop a lossy compression algorithm, our primary cost would be the error and we would have to define a notion of acceptable average error to determine the number L of projection vectors. Since we design a lossless compression algorithm, our primary cost is memory utilization and we need to define a notion of minimal memory space to save both projection vector coefficients and the residuals of the projection. The number L of the projection vectors is chosen to address this concern. Thus, during this step the global part of the information from each of the 5 bands is saved in L packets, where each packet contains a 90x135 image of the coefficients C(j) and a 1xKn projection vector v(j), resulting in L * (90*135 + Kn) elements in total. The residuals are saved separately through the last (approximated entropy coding) stage of our lossless compression algorithm.

Following are 8 out of 12 computed projection coefficients quantized and arranged in 2D arrays.

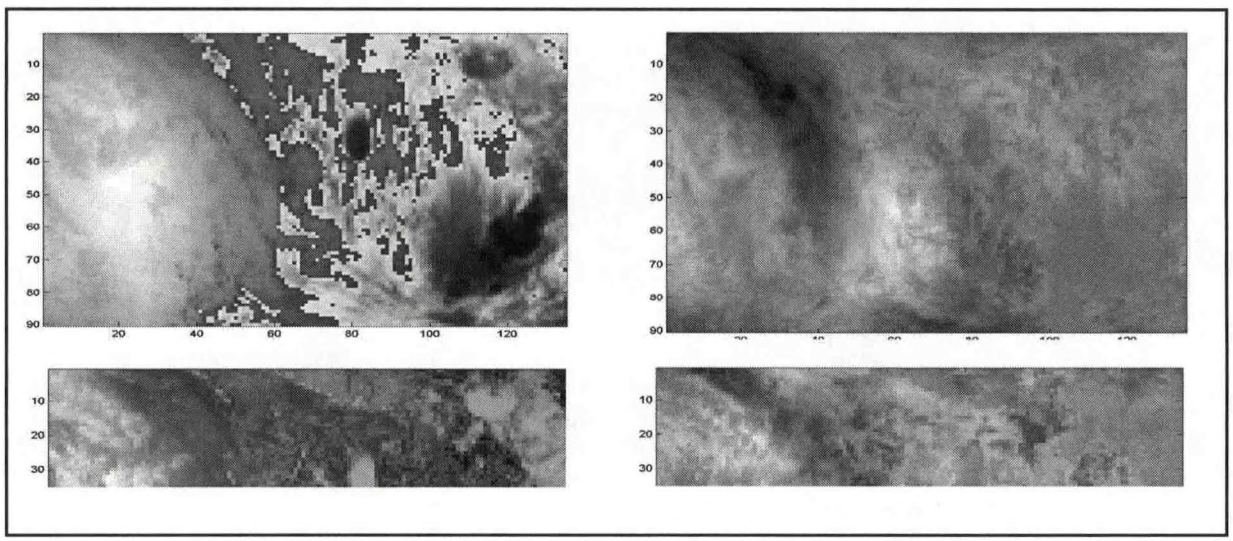

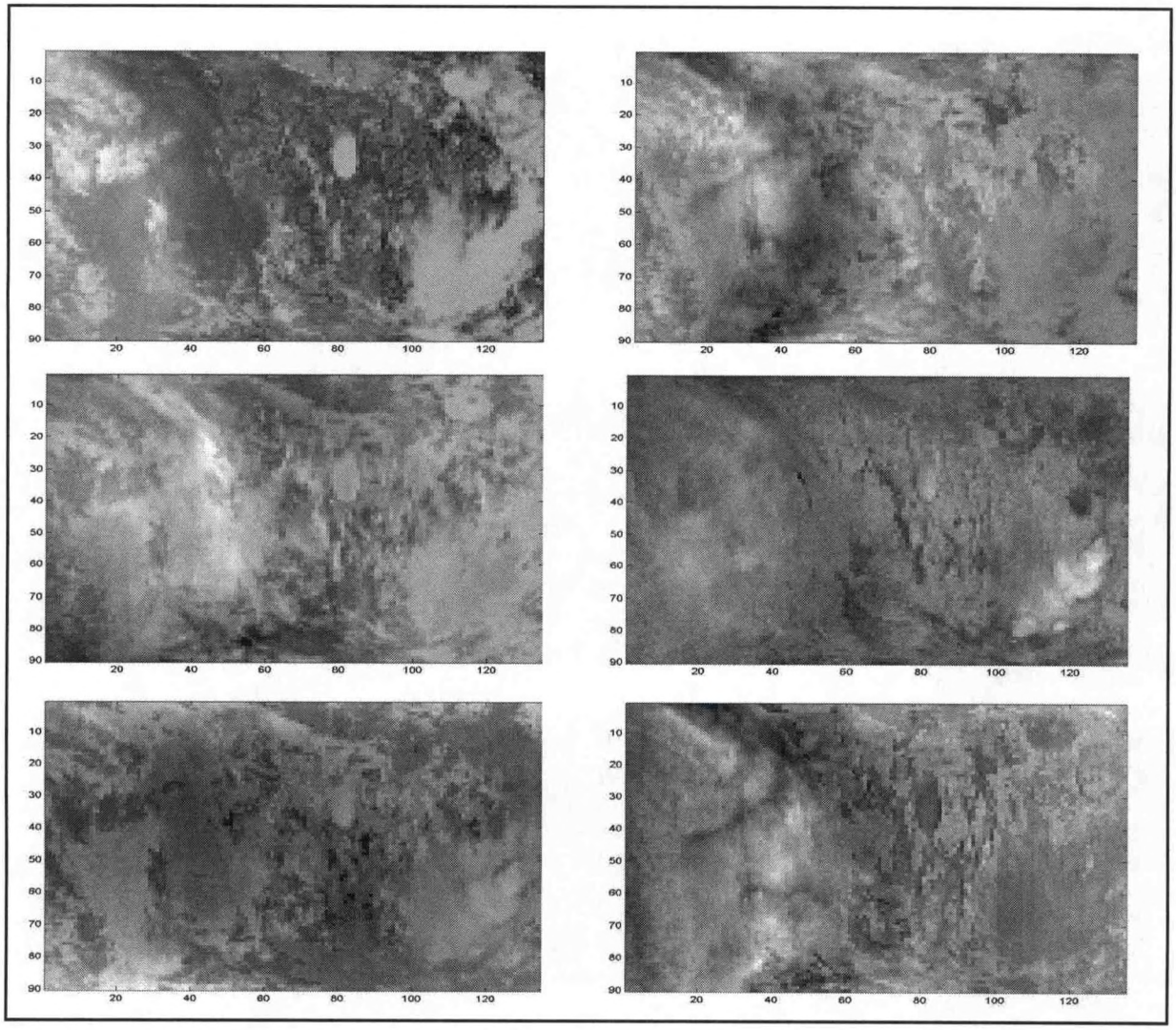

Fig.3: Images of first 8 quantized Karhunen-Loève coefficients

We should note at this point that arrays of the coefficients, as can be seen from the Fig. 3, comprise structured images that can be further compressed. The error propagation in the reconstructed granules due to a minor error (of even a single bit) in the compressed coefficient images could be quite significant. This further compression could be included if desired, and if properties of the communication medium allow, to further increase the compression ratio.

After third step, we have 90x135xKn granules of residuals that are approximately normally distributed but have a lower entropy (due to properties of Karhunen-Loève transform). In our computations, the entropy on the average decreased from 8.35 to 3.2 during step 3. Therefore, the lower bound on the number of bits per residual entry is 3.2 bits. We build our Huffman codebook [2] based on a normal distribution with variance computed from the residuals, rather than an actual codebook. This mitigates issues with errors during transmission, and also makes our program slightly more efficient.

Adaptive Clustering. We start with the observations about the nature of the correlation of data points between the consecutive satellite images that form a granule. Each point that appears in any given image can be considered one integer representation of a point in a multi-dimensional data space. As we

progress from one image to the next, as illustrated by Fig. 4 to Fig. 5 which display the satellite images for channel indexes 363 and 364 respectively, one find that they, like many other images in the granule, are visually similar.

To illustrate this relationship, one can plot the gray level values of pair of consecutive images as shown in Fig.6. Each dot represents a pixel in the image with horizontal coordinate being its gray value of the first image and the vertical coordinate being the gray level value of the second image. As they are highly correlated, the scatter plot in the Fig.6 shows points along the diagonal.

In the best case, one would find that the points are normally distributed about a line segment. In this case, projection on the principle directions will yield the best compression ratio.

As can be noted from the scatter plot in figure 6, the points of the actual data are concentrated in a non-linear manner. Moreover, the distribution of the points is skewed with varying concentrations. In this particular case, as can be seen in the figure, we can observe that there are at least three major concentration centers.

On figure 7 we have presented the frequency distributions of those points. As one can clearly see, there are multiple modes. The scatter plot of three consecutive images would result in a three dimensional cloud of points which also has a non-uniform distribution featuring multiple clusters.

Our clustering procedure is based on density estimation of this cloud of points in the Kn dimensional space. Dense regions (of Fig. 6) correspond to local maxima of the probability density function (see Fig. 7). Once the location of the local maxima is determined, a label is designated to represent all points in that dense region. Then every point in the labeled cluster is represented by (a quantized) value of the location of the associated local maxima. For example in the illustrated above case, there

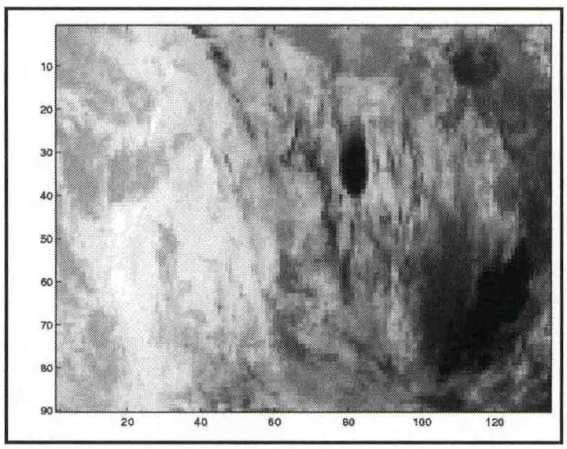

Fig.4: Image at channel index 363.

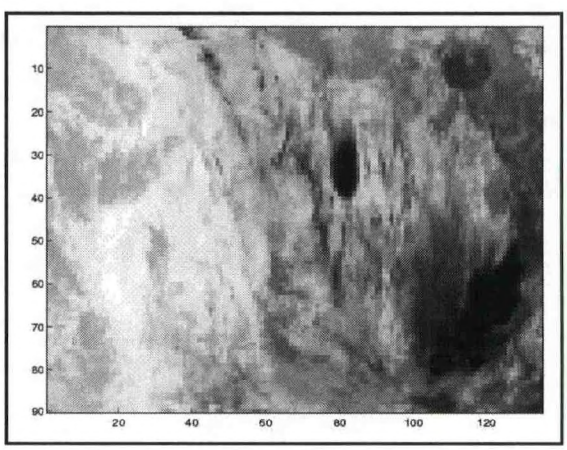

Fig.5: Image at channel index 364.

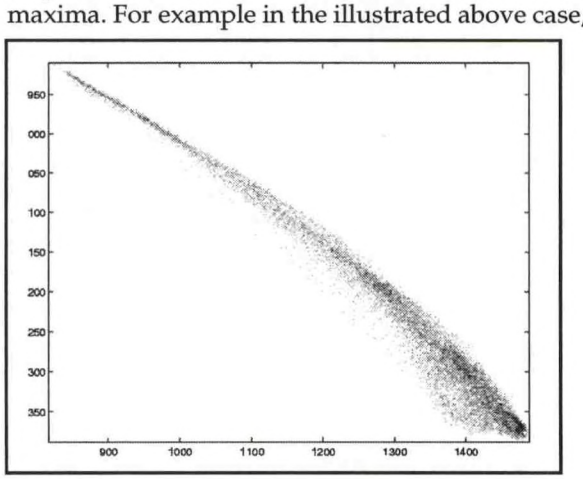

Fig.6: Scatter plot

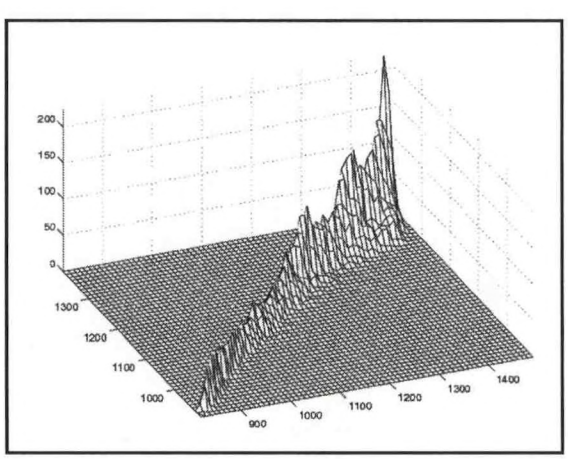

Fig.7: Frequency distribution

will be four labeled clusters and four two-dimensional vectors representing the modes of these clusters. After the modes are determined, they will be saved and subtracted from the values of the respective clusters identified in the images, resulting in a granule of residuals of the same dimensionality as the original one. As a result, the range of values in the residual granule is smaller.

We save the labeling of the clusters in order to undo the clustering subtractions during decompression. Labeling in the aforementioned example would be achieved using 2 bits (a binary representation of four distinct labeled clusters) for each of the 90*135 values of granule containing two considered images.

We should note that the previous example of a granule consisting of only two images was considered for illustrative purposes, so that one could visualize the frequency distribution function of a cloud of points in a low dimensional space. Considering our actual data, the numbers of clusters were 4, 5, 3 and 4 for the aforementioned considered bands 2, 3, 4 and 5 of the granule respectively. There was a similar range for the other nine considered granules. We have observed however that the first band (channel index from 1 to 256) never needed to be clustered.

As a result of clustering, the granule of residuals has a zero mean and is almost normally distributed. As was mentioned earlier, the purpose of the whitening stage is to transform the data so that its distribution is as close to normal as possible. The cost of the clustering is an increase in memory utilization (due primarily to record-keeping data structures needed for the decompression procedure). There are several theorems [3] which state an optimality of the Karhunen-Loève transform provided that the data is normally distributed. Therefore, if we know that the additional memory utilization introduced by clustering is negligible then the overall transformation is nearly optimal.

We have observed that the ratio of memory needed for step 2, with respect to the total memory occupied by the original granule, varied in the 10 considered granules but on average was approximately 0.02% of the memory used by the original granule. This negligible memory increase justifies the use of a known optimal approach.

In the following table, we give resulting ratios of lossless compression for our 10 test granules. One should note that these ratios are higher than those presented in previous work [1], where we have not used adaptive clustering in the second stage of the compression algorithm.

Granule	Location	Ratio
9	Pacific Ocean, Daytime	3.2424
16	Europe, Nighttime	3.2495
60	Asia, Daytime	3.1893
82	North America, Nighttime	3.2750
120	Antarctica, Nighttime	3.1947
126	Africa,	3.1769
129	Daytime Arctic, Daytime	3.2848
151	Australia, Nighttime	3.1367
182	Asia, Nighttime	3.0851
193	North America, Daytime	3.1563

References.

[1] I.Gladkova, L.Roytman,

M. Goldberg, J. Weber, 2004: Compression of AIRS data using Empirical Mode Decomposition, Proc. of SPIE,

[2] D. Huffman, 1952: A method for the construction of minimum redundancy codes, Proc. of IRE, 40:1098-1101.

[3] S. Mallat, 1998: A Wavelet Tour of Signal Processing, Academic Press.

[4] C. Shannon, 1949: Communications in the presence of noise, Proc. Of the IRE, vol.37, 10-21.

SPACEBORNE LIDAR, VALIDATION, AND THE REALM NETWORK

M. Patrick McCormick

Center for Atmospheric Sciences, Hampton University, Hampton, Virginia, 23668

Abstract

A long-duration spaceborne lidar called CALIPSO, now scheduled to be launched in Spring 2005, is the first such multi-wavelength and polarization-sensitive lidar specifically designed for the purpose of providing global aerosol and cloud data for reducing uncertainties in climate forcing. It will fly on the French-built Proteus Spacecraft. Further, it is the first lidar to be flown in formation with four other spacecraft that synergistically will produce fundamental improvements in climate prediction. Hampton University is integrally involved in this mission, providing science efforts, algorithm development, outreach leaderships and leadership in the quid-pro-quo validation effort. As part of that effort, and NOAA's CREST REALM lidar network, HU is developing a ground-based lidar that will operate at multiple wavelengths for elastic and inelastic backscatter retrievals, of aerosol and cloud characteristics and neutral density profiles. The system will operate during CALIPSO overpasses and during REALM campaigns to measure enhanced aerosol events as they transport off the eastern coast of the U.S. This paper will describe the new HU lidar that features a 48-inch diameter primary receiving telescope. It will also describe the CALIPSO spaceborne lidar program and set it into the context of past and future spaceborne missions. The so-called 'A-train' of five satellites flying in formation will also be described.

Introduction

The 48-inch lidar was developed by NASA LaRC in 1969-1970 as a state-of-the-art lidar for atmospheric measurements of aerosols and clouds. The system was integrated into a large trailer, and during the first few years, measurements were conducted at a number of remote sites like Boulder, Colorado and the NASA GSFC Wallops Flight Facility. Routine stratospheric aerosol measurements from the fixed position of NASA LaRC began in 1974 (McCormick and Fuller, 1975). Fig. 1 shows the long-term lidar data set from LaRC indicating that episodic volcanic aerosols drive the aerosol levels. The dates of volcanic eruptions that caused the aerosol enhancements are noted on the abscissa, the largest of which was the June 1991 eruption of Pinatuba in the Philippean Islands. It produced approximately 30 MT of new sulfate aerosol in the stratosphere. (McCormick et al., 1995)

Recently, Hampton University has obtained the 48-inch lidar as surplus property from NASA and installed it in an observatory refurbished for the lidar (fig. 2). It will be used initially for validation of the Cloud-Aerosol Lidar and Infrared Pathfinder Satellite Observations (CALIPSO) satellite lidar mission to be launched in April 2005 (Winker et al., 2002), and for measurements as part of the NOAA CREST Regional East Atmospheric Lidar Mesonet (REALM) network (Hoff et al., 2002).

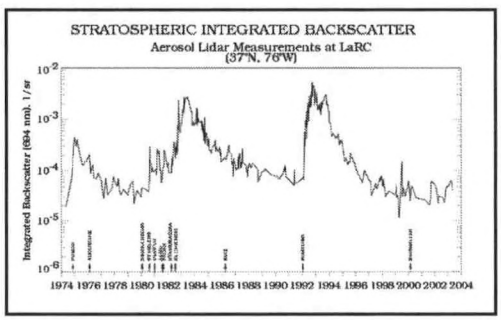

Fig. 1. Integrated backscatter from the tropopause upwards at the ruby wavelength of 0.6943 nm versus time is plotted. The data were taken at NASA LaRC, 37 N, 76 W. Annotated on the abscissa are the eruption dates for various volcanic eruptions that created stratospheric aerosol enhancements.

48-inch Lidar

The name comes from the atypically large f/2 receiving all metal primary mirror of 48-inches in diameter. The telescope has a 10-inch secondary mirror and is in an f/10 Cassegrainian configuration. Multiple photomultipliers are used to increase the dynamic range of the system and provide for multiple wavelength measurements. Initially, the system will be used for elastic and Raman backscattering, so a num-

ber of wavelength channels will be used. The bandpasses of each channel are controlled by interference filters. The return signal is analog-to-digitally converted and/or photon counted and stored on a hard disk. Two approximately 10-hz lasers are being mated to the telescope, both a ruby and a neodymium-YAG. An X-band radar is boresighted with the laser outputs to ensure safe operations. A picture of the lidar when it was originally used at LaRC is shown in fig. 3.

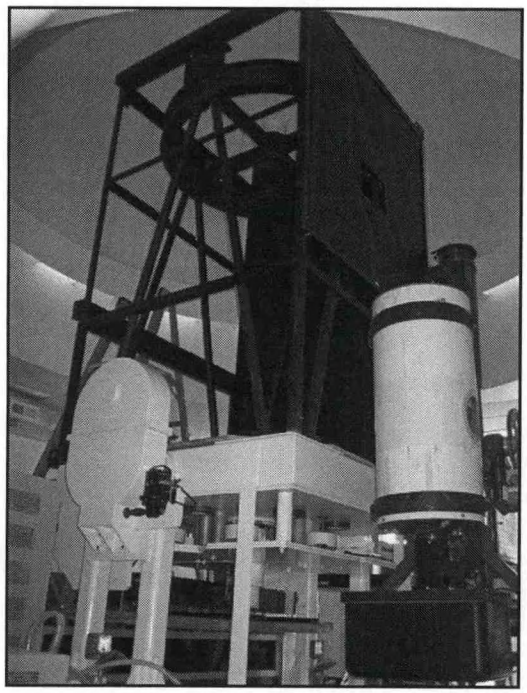

Fig. 2. The 48-inch lidar in the HU observatory.

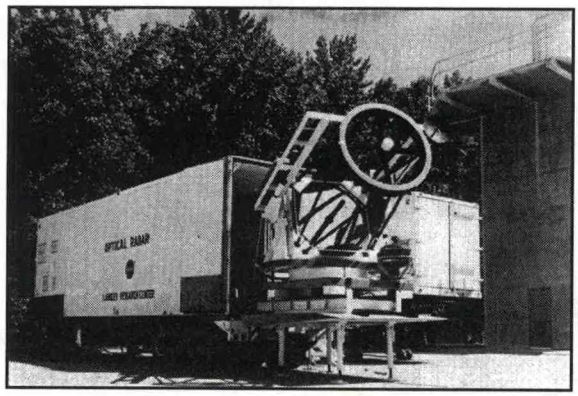

Fig. 3. The NASA LaRC 48-inch lidar in the 1970s.

CALIPSO

CALIPSO is a long -duration Earth orbiting satellite mission designed for continuous measurements for at least three years. CALIPSO will fly on the French satellite, Proteus. The CALIPSO lidar, which is the centerpiece instrument, is called CALIOP for the Cloud-Aerosol Lidar with Orthogonal Polarization. Also boresighted with CALIOP is a wide field-of-view camera for scene registration on the daylight side of the orbit, and a French Imaging Infrared Radiometer (IIR) instrument for characterizing primarily cirrus clouds. CALIOP is a three-channel lidar for 1064 nm measurements, and 532 nm parallel and perpendicular, measurements. A significant addition to the CALIPSO mission is the synergy that will be created by flying in formation with a number of other satellites in a 705-km circular orbit with ascending node equatorial crossing times ranging from 1330 to 1345 local time. CALIPSO will fly in formation with AQUA, AURA, CloudSat and PARASOL (see fig. 5). Combining data from the instruments on these spacecraft will allow a myriad of important characterizations of aerosols and clouds and their effects on radiation budget to be made.

The 48-inch lidar will make measurements while the A-train flies overhead. These data will be compared with the CALIPSO and other A-train data for validation of the satellite instruments. Likewise, the REALM data will be used for CALIPSO validation as well as in a coordinate manor to study air mass transport off the east coast. REALM will be challenged by the uses of the data from many diverse lidars and, therefore, intercomparisons and algorithm verifications will be performed early on in the REALM development.

Future Directions

In addition to hardware/technology issues, the challenges for spaceborne lidar in the near future include our ability to incorporate the data from the constellation of satellites flying in formation with CALIPSO, for example, into a more complete and understandable data set, and to use the data for various modeling studies and for a more complete understanding of various scientific studies including climate forcing. This effort, if successful, will serve as a paradigm for and, perhaps, justify future Earth-orbiting lidar missions.

The above improvements will enable future applications to be implemented in the subsequent decades like studies of the carbon cycle, circulation and forecasting through global tropospheric wind measurements, DIAL for constituent measurements, and elastic backscatter for aerosol and cloud measurements. The implementation of these lidars in space will greatly enhance our understanding of the Earth and other planet's atmospheric chemistry, climate and geophysical properties. The future is indeed

bright for spaceborne lidars, which are now taking their place alongside passive sensors, and fulfilling a myriad of measurement needs for the study of our solar system.

REFERENCES

McCormick, M. P., and W. H. Fuller, Jr., 1975: Lidar measurements of two intense stratospheric dust layers. *Applied Optics*, **14**, 4-5.

M. P. McCormick, L. W. Thomason, and C. R. Trepte, 1995: Atmospheric effects of the Mt. Pinatubo eruption, *Nature*, **373**, 399-404.

Hoff, R. M., Kevin McCann, Belay Demoz, Jens Reichardt, David N. Whiteman, Tom McGee, M. Patrick McCormick, C. Russell Philbrick, Kevin Strawbridge, Fred Moshary, Barry Gross, Sam Ahmed, Demetrius Venable, and Everette Joseph, 2002: Regional East Atmospheric Lidar Mesonet: REALM, 21st *International Laser Radar Conference Proceedings*, 281-284.

Winker, David M., Jacques Pelon, and M. P. McCormick, 2002:The CALIPSO mission: Aerosol and cloud observations from space, 21st *International Laser Radar Conference Proceedings*, 735-738.

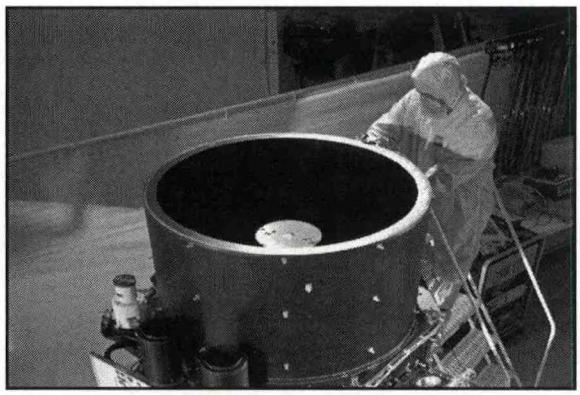

Fig. 4. CALIPSO during its final fabrication stages at Ball Aerospace and Technologies Corporation. (Courtesy of Ball)

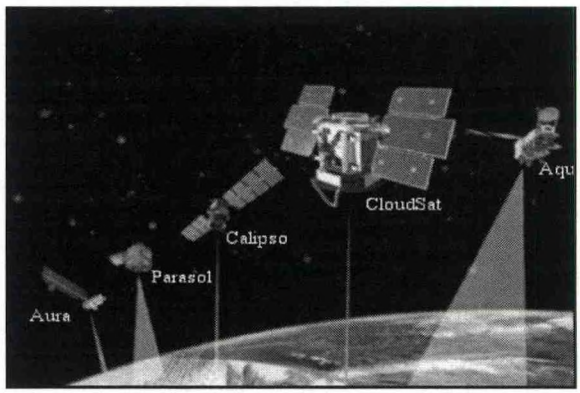

Fig. 5. Five satellites will fly in formation during the CALIPSO mission. This grouping is known as the EOS Aqua constellation or "A-train." The "A-train" name comes from the old jazz tune, "Take the A-Train" composed by Billy Strayhorn and made popular by Duke Ellington's band. It is an Afternoon constellation and has Aqua in the lead with Aura in the rear. (Courtesy of NASA GSFC)

LIDAR MEASURMENTS AT CCNY: SUPPORT OF THE NOAA-NEAQS AND NASA-INTEX-NA EXPERIMENTS

Yasser Hassebo , Badr El-Manuoii, Yu Zhao, Barry Gross, Fred Moshary, Sam Ahmed

Optical Remote Sensing Lab- City College of New York NOAA-CREST

Abstract

A description of the lidar system capabilities and processing algorithms used to process simultaneous backscatter lidar data with Aeronet CIMEL Optical Depth is presented. In addition, we discuss the measurements and analysis undertaken by our Lidar systems in support of the NOAA-NEAQS and NASA-INTEX-NA experiments. To focus discussions, we show results which identifies smoke plumes occurring over NYC on July 21 in support of MODIS imagery and validate the source using NOAA-HYSPLIT back trajectory analysis.

Introduction

The City College lidar system has two multiwavelength systems : a stationary or Lab based system and a mobile lidar system places on a truck. The specifications of these systems is given in the following tables.

Transmitter		Receiver	
Laser	Q-Switched Nd: YAG Continuum Surelite II-10	Telescope Aperture	CM_1400 Schmidt - Cassegrian telescope 14 " (35.56 mm)
Wavelength	1064, 532, 355, 266 nm	Focal length	153.9 " (3910 mm)
Energy/pulse	650 mJ at 1064 nm 300 mJ at 532 nm 100 mJ at 355 nm	Detectors 532 nm 355 nm 1064 nm	Hamamatsu PMT: R758 -10 PMT: R758 -10 APD
Pulse Duration	7 ns at 1064 nm	Data acquisition	LICEL TR 40 -160
Repetition rate	10 Hz	Photon Counter	LICEL TR 40 -160
Harmonic Generator	Surelite Double (SLD) Surelite Third Harmonic (SLF)		

Table 1a. Mobile Lidar Specifications

Transmitter		Receiver	
Laser	Q-Switched Nd: YAG Infinity 40 -100	Telescope Aperture	Newtonian telescope 20 " (50.8 mm)
Wavelength	1064, 532, 355 nm	Focal length	70 " (1778 mm)
Energy/pulse	500 mJ at 1064 nm 250 mJ at 532 nm 200 mJ at 355 nm	Detectors 532 nm 355 nm 1064 nm	Hamamatsu PMT: R758 -10 PMT: R758 -10 APD
Pulse Duration	3.5 ns at 1064 nm 3 ns at 532, 352 nm	Data acquisition	LICEL TR 40 -160
Repetition rate	0.1 – 50 Hz	Photon Counter	LICEL TR 40 -160
Harmonic Generators	Quanta_Ray HG -1		

Table 1b. Lab Based Lidar Specifications

Unlike radar, where the intervening medium is not that important, the backscatter signal from the lidar depends bopth on the scattering efficiency of the particulates at the range as well as the extinction from the intervening media and in the case of aerosols, the extinction and backscatter efficiencies are not related unambiguously. Therefore, we expect that some assumptions will be needed. Within the single scattering approximation valid for most atmospheric conditions, the received backscattered LIDAR signal for an atmosphere consisting of both molecules and aerosol particles is given (Fernauld) as where C is the Lidar calibration constant which

$$P_r(R,\lambda) = \frac{C P_0(\lambda) \beta_T(R,\lambda)}{R^2}$$

includes all geometrical and optical efficiencies, P_0 is the transmitted pulse power, R is the inline range from the instrument, $\beta_T \equiv \beta_a + \beta_m$ the total backscattering volume coefficent which includes both the molecular (Rayleigh) and the aerosol (Mie) contribution and $\alpha_T \equiv \alpha_a + \alpha_m$ is the total extinction coefficient. The R^2 term in the denominator accounts for the receiver FOV variations with range.

Under the assumption that the molecular components can be retrieved accurately, the LIDAR equation provides a single relationship between two independent quantities $\beta_a(R)$ and $\alpha_a(R)$ and in most LIDAR studies, it is assumed that the aerosol extinction to backscatter ratio $S_a = \dfrac{\alpha_a(R)}{\beta_a(R)}$ is a constant (homogeneous aerosol approximation) which can be estimated either from data tables or estimated from other data. Finally, the calibration constant is hard to determine directly from the physical geometry and instrumentation and therefore an absolute measure of one of the aerosol coefficients along the LIDAR path is needed.

A solution under the assumed conditions specified can be written (Fernauld)

$$\beta_a(R)+\beta_m(R)=\frac{P(R)\exp\left[-2(S_m-S_a)\int_R^{R_{max}}\beta_m(R')dR'\right]}{\left(\frac{P(R_{max})}{\beta_T(R_{max})}\right)+2S_a\int_R^{R_{max}}P(R')\exp\left[-2(S_m-S_a)\int_{R'}^{R_{max}}\beta_m(R'')dR''\right]dR'}$$

where R_{max} is chosen to be the highest point in the LIDAR range with sufficiently high SNR, and $\overline{P} \equiv PR^2$ is the range corrected backscattered power. Note that this solution fixes the boundary condition at the top of the LIDAR range and seeks a solution by backintegration that is more stable than the corresponding forward solution.

Therefore, given the following a-priori data set $\{S_a, \beta_a(R_{max})\}$, the LIDAR signal can be inverted to obtain both $\beta_a(R), \alpha_a(R)$.. Therefore, an estimate of the data set $\{S_a, \beta_a(R_{max})\}$ is required and the approach we use to analyze the LIDAR signals and estimate the optical coefficient error is outlined below.

1. A set of reasonable ratios $C \equiv \dfrac{\beta_a(R_{max})}{\beta_m(R_{max})}$

and a set of reasonable aerosol ratios $S_{min} < S_{aer} < S_{max}$ are generated. It should be noted that above the boundary layer, the aerosol concentration decreases substantially and the ratio can usually be bounded by some small number less than one with tighter constraints obtained by increasing the LIDAR range.

2. The aerosol profiles $\beta_a(R), \alpha_a(R)$ for each set of parameters, is calculated.

3. For each parameter set, the optical depth over the entire LIDAR range including the molecular contribution above the LIDAR range is calculated.

$$\tau_L(S,C) = \int_0^{R_{max}} (\alpha_a(R') + \alpha_m(R'))\, dR'$$

$$+ \int_{R_{max}}^{\infty} \alpha_m(R')dR'$$

4. The admissible profiles are those that simultaneously satisfy the constraints $C_{min} \le C \le C_{max}$ and $\tau_{min} \le \tau_L \le \tau_{max}$ estimated from sunphotometry measurements.

5. For each range R, a histogram can be constructed for both optical coefficients providing a reasonable estimate of both the aerosol extinction and backscatter profiles for each range.

While this procedure accounts for atmospheric variability, the effects of background and detector noise should also be included into the statistics. It should also be noted that in the body of this paper, only the mean value of the optical data coefficients are displayed. To verify the algorithm against other processing methods for consistency, we compare the Fernalud algorithm to an iterative algorithm (Russel et al) implemented at Langley and note the agreement between the two methodologies.

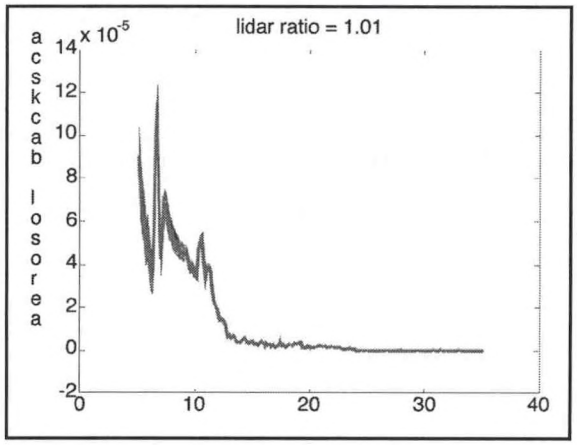

Figure 1: Aerosol Backscatter processed with CCNY algorithm I (Fernald) from S going from 10-100 (Langley used 50).

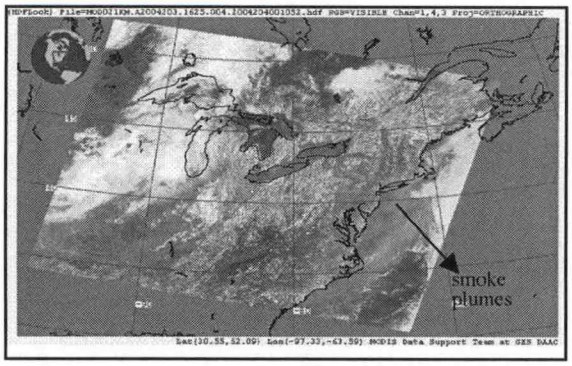

Fig.2 Smoke Plumes from MODIS satellite

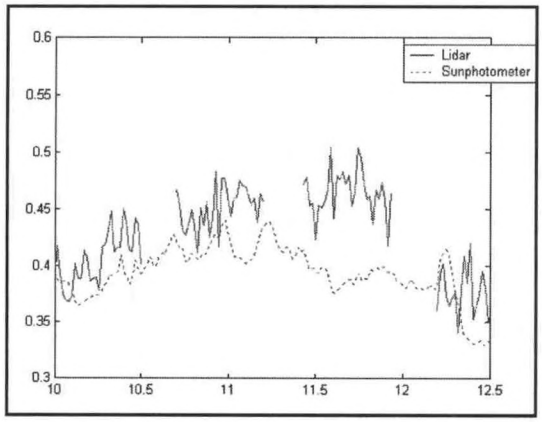

Fig. 3 Optical Depth Comparisons to validate choice of extinction to backscatter ratio for 532nm Sa~80.

Results

Much effort has been applied to obtaining larger continuous lidar data blocks to support both the NASA INTEX-NA and NOAA NEAQS experiment which is designed to study the transport of intercontinental chemical and aerosol transport. As an example, we were in position to track smoke plumes over the NYC area from the North West Canadian fires. Below, a MODIS image taken on July 21, 2004 clearly identifies the smoke regions. Below, in figure 2, we see clearly that smoke plumes are observed over the NYC area but of course, no knowledge of the vertical location or extent of the plume can be determined.

To obtain vertical information, analysis of a time sequence of lidar data is needed. Given this data, it is possible to apply the fernauld method to obtain the aerosol extinction and backscatter profiles. As mentioned in the introduction, to obtain separately the extinction / backscatter profile, knowledge of the optical depth is needed from other instrumentation. First, for a given point of time, we generate the Lidar optical depth measurement and compare to the CIMEL optical depth which is given as 0.4 at 532nm From this measurement, we estimate, we obtain Sa ~ 80. To see if this choice is valid over the entire time series, we compare in figure 3, the time series optical depths using Sa=80 resulting in good agreement in general. However, it is clear that the homogeneous model becomes more difficult to justify with a smoke plume and more sophisticated methods may be required.

With the choice of Sa=80, and assuming that the BC is determined by having nearly no aerosol contributions at 15 km $\beta_a/\beta_m = .01$, we plot the aerosol extinction coefficient profile In figure 4.

In particular, we note the existence of two very clear and stratified plume layers above the aerosol layer which by visual identification (and the low total extinction) were not clouds. To understand better their formation, we can examine these plumes by looking at their angstrom coefficient which is defined as

$$\gamma = \frac{\log\left(\beta^a_{532}/\beta^a_{355}\right)}{\log(355/532}.$$

If the vertical stratified structures were cloud particulates, the angstrom coefficient would be small ~0 independent of the cloud optical depth since clouds are always made up of large particle modes. On the other hand, smoke plumes can be made of very small absorbing particles which would have a high angstrom coefficient (O'Neill et al) However, when each channels backscatter is determined, it is possible to generate an estimate of the angstrom coefficient profile $\gamma(R)$ which is illustrated in figure 3 for 9:30 AM EDT which is the beginning of region 1 and the smoke plumes are weak.

The multiple plots are performed by varying significantly the far end BC and the S ratios from their expected value. While changes are evident, they are not significantly affecting the far end results. While it is tempting to exam-

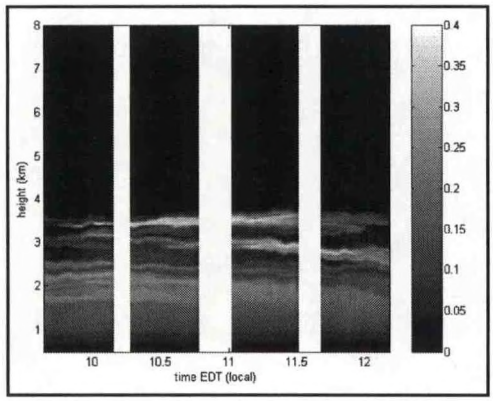

Fig.4 Lidar extinction profiles showing existence of plumes

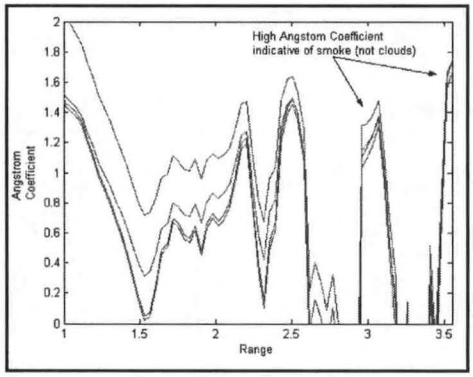

Fig.4a Angstrom Coefficient using 355-532nm lidar channels for weak plume at 9:30 AM EDT.

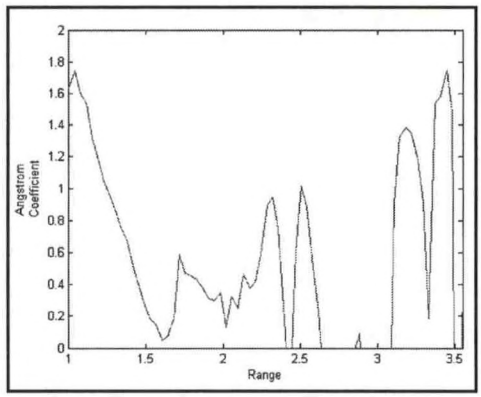

Fig.4b Angstrom Coefficient using 355-532nm lidar channels for weak plume at 10:10 AM EDT.

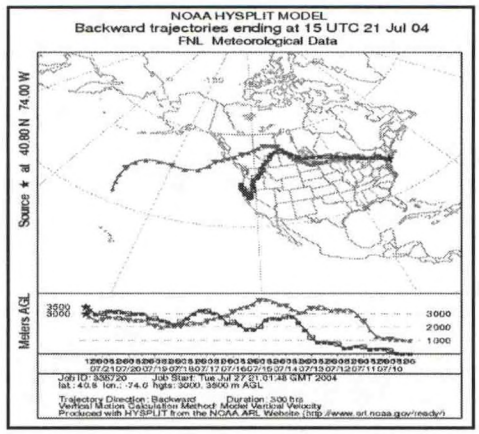

Fig. 5 Hysplit Backtrajectories showing source of smoke plumes

ine the angstrom coefficient as the plume intensifies, it must be remembered that the 355 channel is already some what noisy and with additional extinction due to the plume, processing of the angstrom coefficient which needs good estimates of the backscatter data at 355 nm (especially since it is in the denominator) becomes more suspect. In figure 4b, we see the angstrom coefficient profile but we see more regions where the coefficient is not positive (due to taking the log of negative numbers giving negative real part).

This problem gets more systemic as the plume depth increases and therefore, becomes more suspect with larger patches of unphysical values but the general observation of a large angstrom coefficient for the smoke plumes is still correct.

Finally, by locating the plume vertical heights, back trajectory analysis using NOAA-HYSPLIT can be used to examine the source regions. As seen below, the backtrajectories are consistent with the transport from the North West Canadian Fires.

Conclusions

Lidar measurements have been shown to support satellite measurements that identified transcontinental smoke plumes. In particular, by examining the angstrom coefficient calculated from the 355 – 532nm channels in the plume region, clouds which possess small angstrom coefficients near 0 were ruled out. In addition, backtrajectory analysis are consistent with satellite measurements. Unfortunately, an inherent weakness in looking at plumes with significant optical depth is the increased noise due to attenuation on the 355 channel making the results more suspect. Methods to improve the results including more temporal averaging are underway.

ACKNOWLEDGEMENTS

This work is supported by grant from NOAA #NA17AE1625.

REFERENCES

Fernald, F.G. Analysis of Atmospheric Lidar Observations: Some Comments. *Appl. Opt.*, **23**, 652. (1984).

Russell P. B., T. J. Swissler, and M. P. McCormick in "Methodology for error analysis and simulation of lidar aerosol measurements," Applied Optics, Vol 18, (1979).

O'Neill N. T., T. F. Eck, B. N. Holben, A. Smirnov, A. Royer and Z. Li "Optical properties of boreal forest fire smoke derived from Sun photometry JGR, 107, D11 AAC 6 – 1-21 (2002)

MULTISENSOR OBSERVATIONS OF THE LONG-RANGE TRANSPORT OF THREE LARGE FOREST FIRES LUMES TO THE NORTHEASTERN U.S.

Raymond Hoff[1], Tom Duck[2], Ed Eloranta[3], Jill Engel-Cox[4,1], Nikisa Jordan[1], Shobha Kondragunta[5],Nick Krotkov[6,7], Kevin McCann[1], Fred Moshary[8], Kamonayi Mubenga[1], Steve Palm[9,6], Ana Prados[5], Ray Rogers[1], Lynn Sparling[1], James Spinhirne[6], Kevin Strawbridge[10], Omar Torres[1,6]

[1]CREST, Joint Center for Earth Systems Technology, University of Maryland Baltimore County, 1000 Hilltop Circle, Baltimore, MD, 21250 email: hoff@umbc.edu
[2]Dalhousie University, Halifax, NS
[3] SSEC, University of Wisconsin, Madison, WI eloranta@ssec.uwisc.edu
[4]Battelle Memorial Institute, 2101 Wilson Boulevard, Suite 800, Arlington, VA 22201email: engelcoxj@battelle.org
[5]NOAA NESDIS, Camp Springs, MD
[6]Goddard Space Flight Center, Greenbelt, MD, 20771
[7]Goddard Earth Science and Technology Center(GEST), University of Maryland Baltimore County, 1000 Hilltop Circle, Baltimore, MD, 21250 email: krotkov@umbc.edu
[8]CREST, City College of New York, New York NY moshary@ee.ccny.cuny.edu
[9] Science Systems Applications International, GSFC, Greenbelt, MD 20771 email: steve.palm@gsfc.nasa.gov
[10]Meteorological Service of Canada, Egbert, ON, L0M 1T0, kevin.strawbridge@ec.gc.ca

ABSTRACT

Three large forest fires plumes, one from Russia, one from California, and one from Alaska/Yukon were observed in 2003 and 2004 over the east coast of the US using a wide suite of instruments including lidar on the ground, GLAS, MODIS, TOMS, AERONET and GOES-8. For the Russian fire plume, the smoke arrived in US mid-Atlantic states at a height of 3km. This same plume was seen in Europe at much higher altitudes. The California fires were higher (7-12km). The final fire plume from the northwestern part of NA (at 3-7 km) was noted on the USAirQuality weblog well in advance of its arrival in the US East. The coincident observation by several lidar systems is a good example of REALM observational capability. The heights of the plumes shows features of vertical plume transport which are governed by the shape of the isentropic surfaces north and south of the polar front.

1. INTRODUCTION

Recently, we have begun to fuse observations from passive remote sensing systems such as MODIS and lidar measurements from ground based sites such as REALM (Engel-Cox et al., 2004; Hoff et al, 2002). In the next few years, the use of active systems, such as the Geoscience Laser Altimetric Sensor (GLAS), its predecessor (the Lidar In-Space Technology Experiment), and its successor instrument (the Cloud and Aerosol Lidar for Pathfinder Spaceborne Observations, CALIPSO) will allow high resolution profiling of aerosols in the atmosphere. This paper describes several observations of smoke plumes which arrived at the US east coast from long range transport. The tools we used involved passive imaging instruments and lidars and this is a good example of the future of multi-instrument fusion in the EOS and NPOESS suite of instrumentation.

II THE SIBERIAN FIRES OF MAY 2003

In June, 2003, the UMBC elastic lidar system (ELF) was being operated in support of a validation experiment for the Advanced Infrared Radiometric Sounder (AIRS) at Chesapeake Lighthouse (36°54.6' N, 75°42.6' W) (McCann et al., 2003).

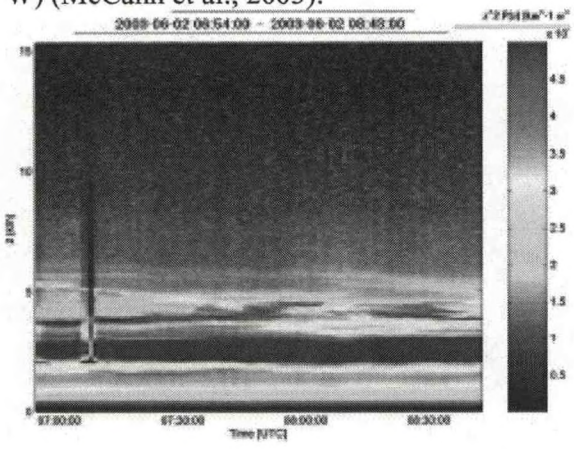

Fig. 1: 0700-0900 UTC June 2, 2003 Lidar range corrected signal

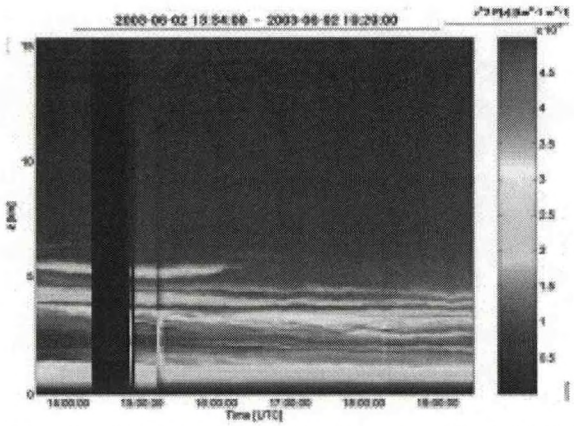

Fig. 2: 13:34-19:29 UTC June 2, 2003 Lidar range corrected signal at Chesapeake Light

Fig. 1 and 2 show the morning and afternoon ELF Lidar profiles for the two MODIS overpasses (TERRA and AQUA). AIRS is carried on the AQUA satellite. The color scale is proportional to the aerosol backscatter coefficient at 532 nm and the vertical extent of the sounding is 15 km. The layer of aerosol at 3 km persisted for most of the day on June 2 and was moderately hazy. Optical depths reported by the AERONET sunphotometer at the site were 0.34. Both MODIS and the Total Ozone Mapping Spectrometer (TOMS) saw a widespread haze layer over the Mid-Atlantic States. The MODIS aerosol optical depth is shown in Fig. 3.

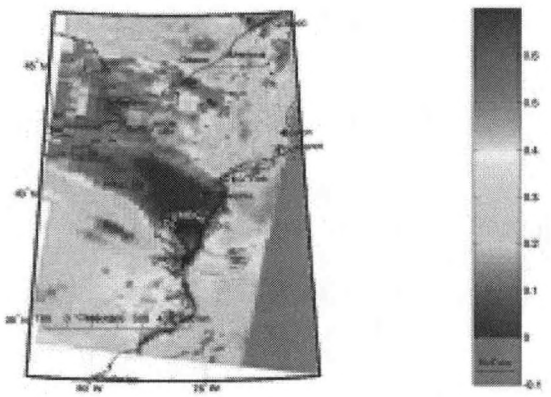

Fig. 3: MODIS Aerosol Optical depth product (MOD04) showing optical depths of >0.6 inland and ~0.3 over the water off Virginia.

It would be tempting at ascribe this event to another hazy day in Maryland but back trajectory information and MODIS images over the Arctic indicates that the source of the aerosols was distant. The haze plume seen in the Mid-Atlantic States can be tracked back to a position west of Hudson's Bay on May 29, 2003. Our conclusions is that this plume originated from a very large group of forest fires in Siberia in mid-May. There are other pieces of information from TOMS and from the lidar depolarization that support this conclusion and are shown in the conference version of this paper.

III. SOUTHERN CALIFORNIA FIRES OF 2003

In October 2003 a series of fires north and east of Los Angeles and east of San Diego, California, ravaged some 2750 km^2 of forest

and dry vegetation. Observation of these fires from space has been reported for CO using the Advanced Interferometric Radiometric Sensor (AIRS) (Datta et al., 2004) and for aerosols using the MODIS instrument and GLAS (Spinhirne et al, 2004).

At the same time as these studies, our group had been analyzing MODIS imagery in a national perspective to understand the occurrence of long range transport of pollutants. The MODIS imagery is obtained in real time from the University of Wisconsin direct broadcast receiving station in Madison. Recently, we have added the NESDIS Geostationary Observation Satellite Aerosol and Smoke Product (GASP) to these analyses. When images are analyzed which have a high probability of regional scale aerosols, we use these data to trigger observations in the Regional East Aerosol Lidar Mesonet (REALM) (Hoff et al., 2002).

As the fires developed in late October, we observed the transition from the Santa Ana westerly flows to a zonal flow in the MODIS imagery. By October 30, 2003, a noticeable brownish haze was seen in the MODIS Red-Green-Blue (RGB) product and was above the prevailing clouds in the US Midwest (Fig. 4).

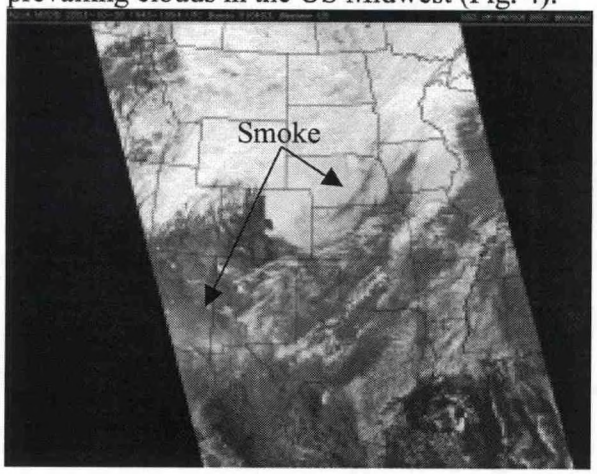

Fig. 4: MODIS RGB image from October 30, 2003, showing the smoke above clouds in Nebraska.

The path of the plume passed over Colorado, Nebraska, Kansas, Iowa, and Missouri. This plume was observed to pass high into the Great Lakes region and was previously reported to be in the Maine/Gulf of Maine region on October 31. The plume was quite close to a cloud system to the north of the Canadian border and made quantification of the optical depth of the plume difficult.

On the afternoon November 2, 2003, however, we observed a well-isolated plume of material in the MODIS images over the US mid-Atlantic states. Fig. 5 shows the highly striated structure in this plume. From the ground in Baltimore, the aerosol could have been easily confused with cirrostratus clouds. We noted visually, however, that there were extremely short aircraft contrails embedded in these spectacular clouds which led to the suspicion that they were not ice clouds. This led to a truly spectacular display of clouds at sundown.

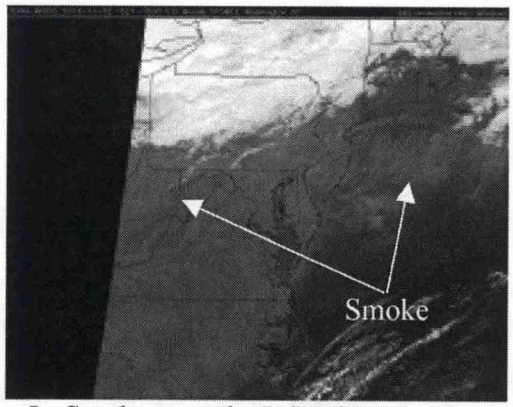

Fig. 5: Smoke over the US Mid-Atlantic states on the evening of November 2, 2003, in MODIS RGB.

Fortunately, during both the first observation of the plume over Oklahoma on November 1 and the mid-Atlantic observations of November 2, the GLAS sensor was operating and this provided the opportunity to discriminate between aerosols and clouds, both from spatial information and from spectral information from the GLAS sensor. Fig. 6 and 7 show the GLAS time-track cross sections for

the 532nm and 1064 nm channels. At the time of the production of these images, the GLAS sensor had only been calibrated for the 532nm channel.

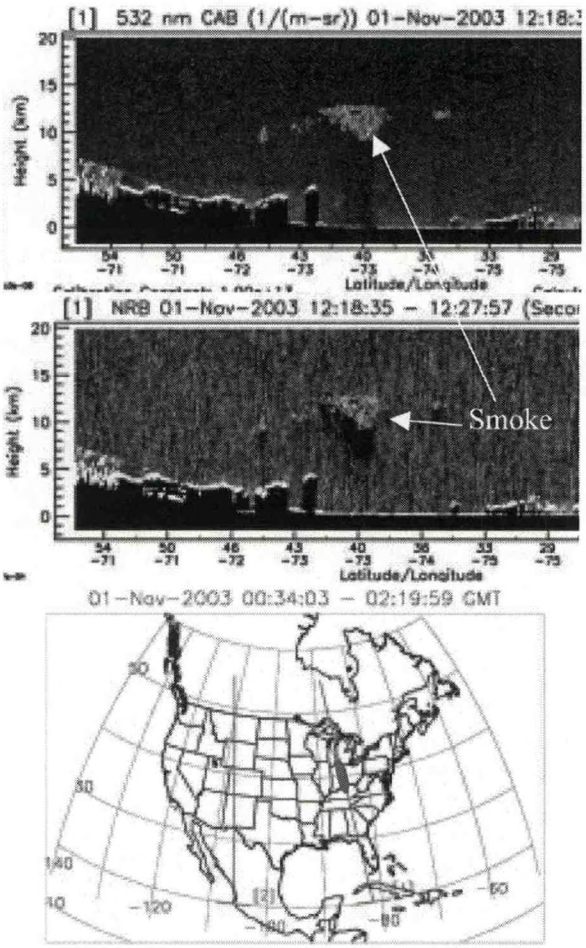

Figure 6: Smoke plume at 12km on November 1, 2003, over Oklahoma at 532 nm (a) and 1064 nm (b) showing the smoke layer at 12 km altitude. The signal to noise at 532 nm is significantly better than the IR channel. (c) GLAS flight track with red identifying smoke region.

In Fig. 6, the smoke plume is highly isolated in space within a clear area region from 38° to 42° latitude. The plume is remarkably high (10-12 km) and there is a widespread region of more tenuous aerosol throughout the troposphere. Fig. 7 is less clear but is easily

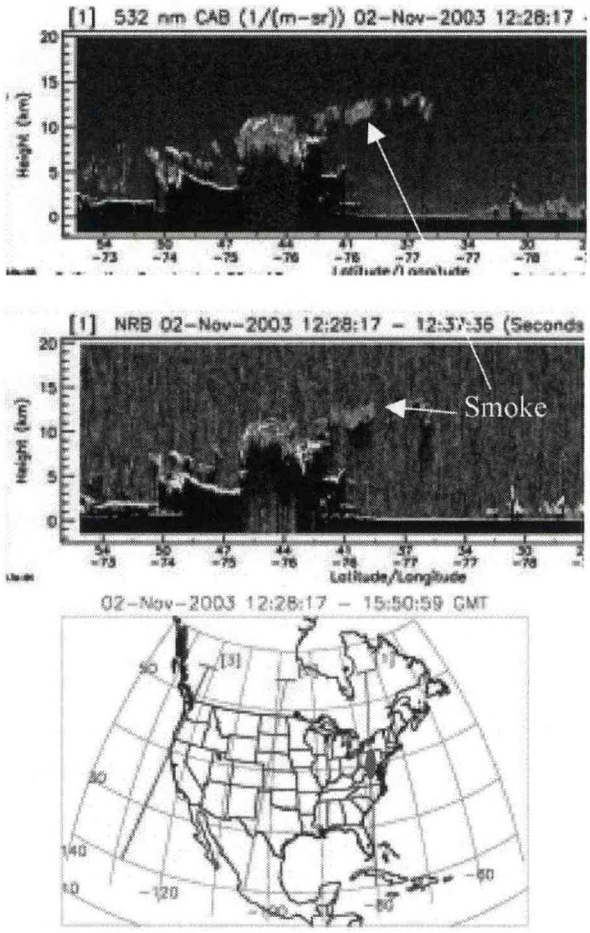

Fig. 7: November 2 GLAS cross-sections at 532 nm (a) and 1064 nm (b) showing the smoke layer at 12 km altitude. The smoke overlays a region of multiplayer cloud. (c) Ground track of GLAS.

interpreted with reference to Fig. 6. The layer of material marked in the figure as smoke lies above the layer of clouds to the north of the track of the plume. The altitude of the material is again very high (10-12 km).

IV. ALASKA/YUKON FIRES OF JUNE/JULY 2004

In June 2004, lightning strikes ignited severe fires in the areas around Kitimat, British Columbia, further north in the Yukon and through eastern Alaska. The fires near Fairbanks, Alaska, endangered wide areas of

populated areas, burned 50 homes and covered much of Fairbanks in deep ash (K. Sassen, private communication). As a matter of scale, Alaska had 25,000 km^2 in fire this year and the Taylor Complex fire alone was 5,260 km^2 in area, twice the area of all the 2003 Southern California fires combined. The Alaska fires comprised 86% the fire area of the US up to September 1. We followed the fire plumes from these fires for most of the month of June 15-August on the USAirQuality weblog. On July 21, the fires caused an increase of $PM_{2.5}$ in Baltimore which nearly put the city out of exceedence for $PM_{2.5}$. It was clear on July 9 that the correlation between $PM_{2.5}$ and MODIS aerosol optical depth was poor but was due to an elevated layer of smoke from the wildfires

The fires were tracked by lidar systems at the University of Wisconsin (Figure 10), Dalhousie University, City College of New York and UMBC. This is an example of the success of multiple lidar observations in the Regional East Atmospheric Lidar Mesonet (REALM).

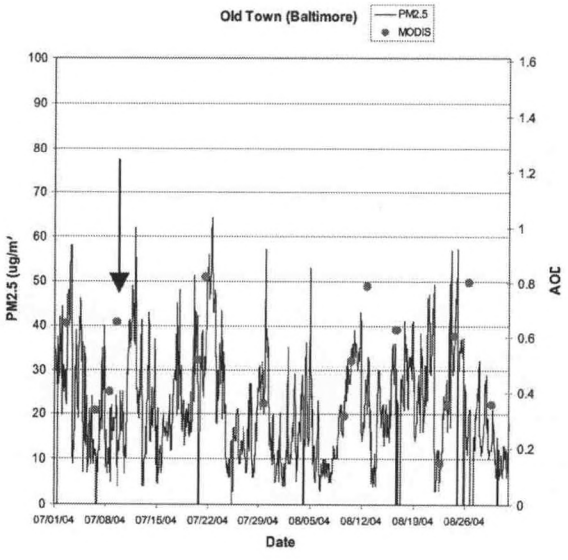

Fig. 8 - PM2.5 (line) and MODIS AOD from IDEA product (//idea.ssec.wisc.edu; red dots).. On July 9, poor correlation is due to smoke from Alaska (see Fig. 9) aloft.

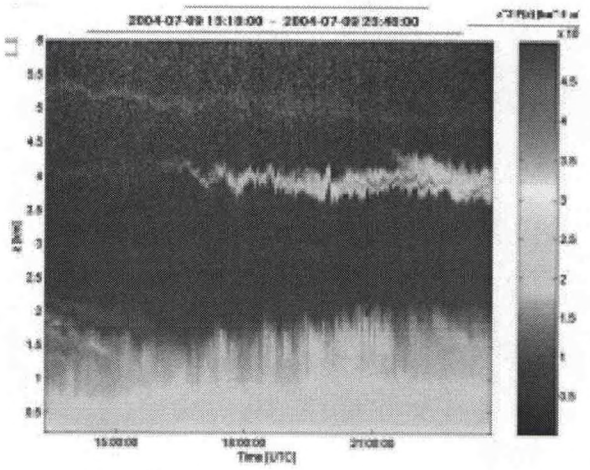

Fig. 9: Lidar image of the smoke plume at 4 km from Alaska fires over UMBC on July 9, 2004.

Both Figure 9 and Figure 10 show multilayer plumes at 4 and 7 kilometers with general descent from north to south. This descent is consistent with the plumes descending following isentropic surfaces as the air warms at lower latitudes..

V. IMPLICATIONS FOR FUTURE OBSERVATIONS

These observations show it would not have been possible to make a strong case for either the identification of these east coast observations without the synergy of these multiple sensor systems. This points out the importance of having multiple tools available to observe aerosols. The ability to use passive sensors, lidar from the ground and space and synthesizing tools such as our weblog, will bring out the full value of multisensor systems.

VI. REFERENCES

Balis, D. V. et al., 2003: Raman lidar and MFR measurements of aerosol optical properties during a biomass burning episode over Thessaloniki. Paper P6-10. *EARLINET Symposium*.

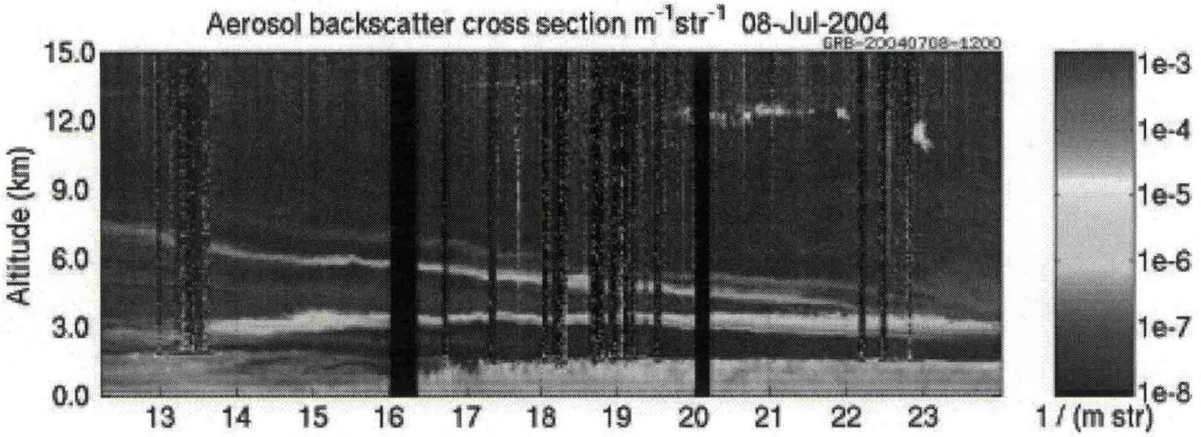

Figure 10: University of Wisconsin Arctic HSRL backscatter data from July 8, 2004, in Madison, WI. The elevated plumes at 3 and 4-7 km are believed to be the same layers as seen in Figure 9 in Maryland.

Chu, D.A. et al., 2002: Validation of MODIS aerosol optical depth retrieval over land. *GRL*, **29**, 1617.

Datta, S. et al., 2003: Retrieval of Carbon Trace Gases From AIRS Data, Paper 5758, American Geophysical Union Fall Meeting, San Francisco, CA.

Engel-Cox, J. A., C. H. Holloman, B. W. Coutant, and R. M. Hoff, 2004. Qualitative and quantitative evaluation of MODIS satellite sensor data for regional and urban scale air quality, *Atmos. Environ.* **38**, 16, 2495-2509; doi:10.1016/j.atmosenv.2004.01.039.

Hoff, R. M. et al., 2002: Regional East Atmospheric Lidar Mesonet: REALM, in *Lidar Remote Sensing in Atmospheric and Earth Sciences*, Luc Bissonette, Gilles Roy and Gilles Vallée, eds., Defence R&D Canada Valcartier, Val-Bélair, Québec, Canada, 281-284.

McCann, K. J. et al., 2003: A Comparison of Measurements of Cloud Optical Depth Made from the AIRS/AQUA Instrument and the UMBC Elastic LIDAR Facility (ELF), *International Symposium on Tropospheric Profiling: Needs and Technologies (ISTP-6)*, Leipzig, Germany.

Spinhirne, J. D. et al., 2004: The GLAS Polar Orbiting Lidar Experiment: First Year Results And Data Availability, *22nd International Laser Radar Conference*, ESA Special Publication SP-561 (2 volumes), European Space Agency, Nordvik, Holland, pp 411-414.

Wandinger, U. et al., 2002: Optical and microphysical characterization of biomass-burning and industrial-pollution aerosols from multiwavelength lidar and aircraft measurements. *J. Geophys. Res.*, **107**, 10.1029/2000JD000202.

Acknowledgements:
This work was sponsored by the Center for Remote Sensing of Science and Technology (CREST) through a grant to UMBC from the City University of New York Research Foundation (49866-00-O3). EE funding from the National Science Foundation is acknowledged. KM was supported by Bowie State University when this work was performed. NK, OT, SP, JS are supported by grants from NASA. Part of this work was previously published in ESA Special Publication SP-561.

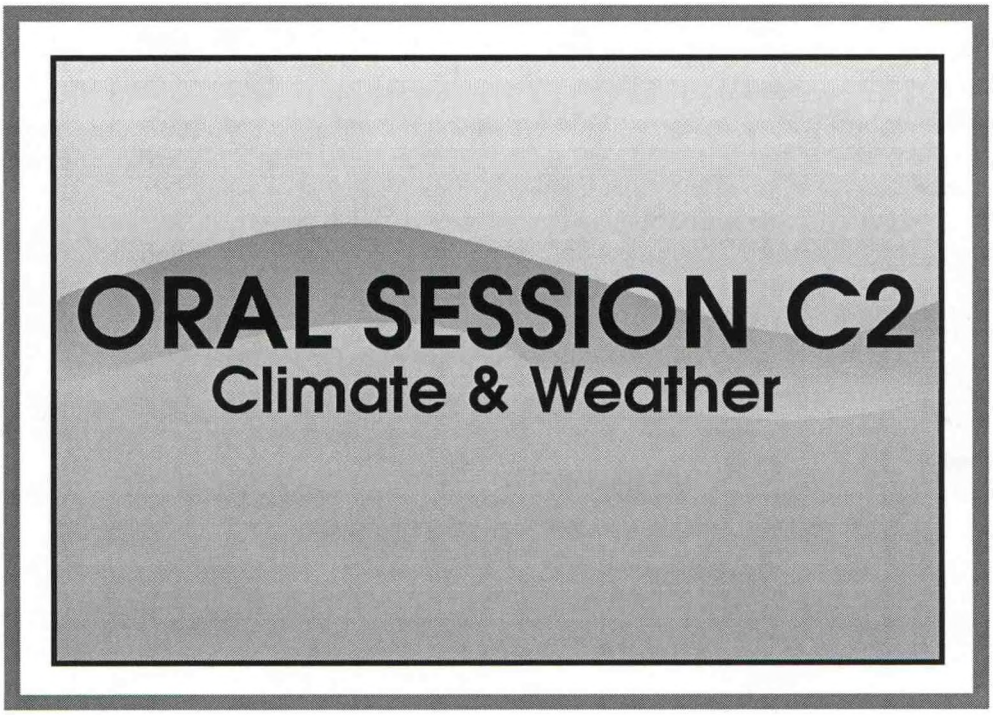
ORAL SESSION C2
Climate & Weather

Accuracy of Operational Gridded Precipitation Input to National Weather Service Hydrologic Models

David Kitzmiller, Chandra Kondragunta, Kiran Shrestha, and Dongjun Seo
Hydrology Laboratory, Office of Hydrologic Development, NOAA National Weather Service
Silver Spring, Maryland

Hydrologic forecasting operations in the NOAA National Weather Service (NWS) rely on estimates and forecasts of surface runoff, which is in turn largely dependent on estimates and forecasts of precipitation. Historically, precipitation input to the hydrologic forecast models has been in the form of 6-hour average areal precipitation accumulations for individual drainage basins, derived from rain gauge observations. However, advancing the state of operational hydrologic modeling requires precipitation input on much smaller spatial scales and more rapid update cycles, and precipitation analysis development efforts are focused on the production of gridded fields derived from a combination of rain gauge, radar, and satellite input.

This paper will briefly review the forms of precipitation input to operational hydrologic forecast models at NWS River Forecast Centers and Weather Forecast Offices, and will describe the quality of operational precipitation estimates in terms of absolute accuracy, statistical reliability, and detection of heavier precipitation events on short time scales. Future needs for remotely-sensed precipitation will be discussed.

SHARING NATIONAL WEATHER SERVICE DIGITAL DATA WITH XML AND A SOAP SERVICE

John L. Schattel Jr. and Timothy Boyer

John L. Schattel Jr. and Timothy Boyer, Meteorological Development Laboratory, Office of Science and Technology, National Weather Service, NOAA, Silver Spring, Maryland

Robert Bunge

Internet Services, Office of Chief Information Officer, National Weather Service, NOAA, Silver Spring, Maryland

Introduction

The National Oceanic and Atmospheric Administration's (NOAA) National Weather Service (NWS) is seeking to enhance the accessibility of its digital databases by exploiting existing technologies to enhance data dis-semination (NWS 2003a). To achieve that goal, the NWS is experimenting with eXtensible Markup Language (XML) and Simple Object Access Protocol (SOAP) services. These two World Wide Web (WWW) standards, allow scientists, academicians, the public, private sector companies, and governmental organizations to retrieve NWS data over the Internet. XML and web services also improve computer to computer transfer and automated processing. These traits should enhance the NWS's ability to share its data and to maximize the data's economic benefits to society.

This paper explores NWS XML products and SOAP services by first providing an overview of 1) the National Digital Forecast Database (NDFD; Glahn and Ruth, 2003), 2) XML including the dialects Common Alerting Protocol (CAP) and Really Simple Syndication (RSS), and 3) SOAP services. Next, we document NWS use of these technologies by describing the NDFD SOAP service, Watch, Warning, and Advisory CAP, and weather observation RSS products. Finally, this paper highlights the role that Student Career Experience Program (SCEP) and the NOAA Educational Partnership Program (EPP) students have played in developing NWS digital products and services

NDFD

The NDFD is one example of an experimental digital data source being made available with XML and web services. The NDFD contains a 7-day forecast of sensible weather elements. It is composed of grids created at 122 weather forecast offices (WFO) across the country. The grids contain forecasters' prediction of certain sensible weather elements at various time projections in the future. Table 1 lists the weather elements and forecast projections.

Weather Element	Projections
Max. Temperature	24 hourly to
Min. Temperature	24 hourly to
Prob. of Precip.	12 hourly to
Sky Cover	3 hourly to
Temperature	3 hourly to
Dew Point	3 hourly to
Wind Direction	3 hourly to
Wind Speed	3 hourly to
Weather	3 hourly to
Precip. Amount	6 hourly to
Snow Amount	6 hourly to
Wave Height	12 hourly to

Table 1. NDFD Weather Elements

NDFD grids are created at each WFO with the Interactive Forecast Preparation System (IFPS; Ruth et al. 1998; Peroutka et al. 1998). IFPS allows the forecaster to interact with the digital data and to automatically prepare a forecast product suite. Once the digital forecast is prepared, the grids are transferred (Fig. 1) to a central server located at NWS Headquarters in Silver Spring, Maryland, where they are combined to form the NDFD.

XML Basics

XML is a WWW Consortium (W3C) standard designed to improve upon the HyperText Markup Language (HTML) used commonly in WWW applications. XML addresses the

deficiencies of HTML (Morrison 2001) by removing presentation information from the document and by adopting the following rules:

- Tag names, characters between angle brackets (< and >) used to mark up a document, are case sensitive.
- Tags must come in opening and closing pairs.
- Tag pairs can not overlap.
- Attributes values must be quoted.
- An XML document can only have one root tag.

These strict rules promote the automated validation and processing of XML. As a result, XML is well suited for exchanging data.

Unlike HTML, XML does not have a predefined set of tags. Rather, XML allows each user community to define its own language complete with tags (its vocabulary) and rules for how those tags appear in the document (its grammar). An example of XML is the Digital Weather Markup Language (DWML) which is used to exchange NDFD data and is discussed more in Section 5.

An XML language's vocabulary and grammar are specified in a document called its schema. A schema is generally stored in a file and made available via the WWW. The schema is used by a validation program to ensure that any given instance adheres to the language's vocabulary and grammar. The schema, together with above rules, makes it possible for a user to process the data in an XML document.

RSS and CAP

Two XML based languages used by the NWS to disseminate digital data are RSS and CAP. RSS is used to exchange news-like information. An RSS document is posted to the WWW where it becomes a "channel" of information. The feed is composed of "items" which have a title, short description, and link to the complete source document. Once pub-lished to a website, the RSS feed is available for user client programs, called readers, to access and display.

CAP is an open standard for exchanging hazard warnings. This XML based language allows automatic multi-channel dissemination with a consistent content. Each CAP file contains information about the alert message itself, information about the hazard, and the location the alert applies to. Once a CAP document is received, an application running on a computer, personal data assistant (PDA), or cell phone can sound an alarm and display the hazard information.

SOAP Services Overview

A SOAP service is a protocol that enables two computers to request and exchange data across the WWW. One computer is designated as a server; the other computer is called the client. The communication process (Fig. 2) begins with the user's client software creating a data packet called a SOAP request which identifies the services' address and which piece (exposed function) of the service it wishes to access. The client also provides any input required by the exposed function. The request is then communicated over the Internet via the same HyperText Transfer Protocol (HTTP) used to communicate most web pages.

The SOAP server receives the request and runs the exposed function with the user supplied input. If the exposed function returns output, the SOAP server prepares a SOAP message containing that information. The message is communicated back to the client via HTTP. Once the client receives the SOAP reply, it can then extract the returned data with the help of the appropriate schema. The returned data are then ready to be displayed or further processed in some way.

The existence of a SOAP service is often announced with a Web Services Description Language (WSDL) document. The WSDL is an XML document generated by the data provider which assists the client in preparing the SOAP request. The WSDL provides the server's address, available functions, and the names and types of the functions' inputs and outputs. Software libraries are available that enable programs written in popular program-ming languages like PHP, Perl, C++, and Java to read the WSDL, to format the appropriate SOAP request, and to interpret the SOAP response.

NDFD Web Services

The NWS has deployed an experimental SOAP service to disseminate NDFD data. Technical information for accessing the ser-vice is available in the Service Description Document (NWS 2004a). The service cur-rently has a single exposed function named NDFDgen which takes the arguments in

Name	Description
latitude	The latitude of the grid point for which the user wants data.
longitude	The longitude of the grid point for which the user wants data.
product	time-series: returns selected weather elements.
	glance: returns max. and min. temperature, sky cover, weather, and weather icon links.
start_time	The beginning time for which the user wants data.
end_time	The ending time for which the user wants data.
parameters	The weather elements that the user wants from Table 1.

Table 2. NDFDgen Input.

Digital Weather Markup Language (NWS 2003c) is designed to accommodate the temporal, spatial, and weather parameter dimensions of NDFD data. DWML has metadata and forecast data sections as represented by the <head> and <data> tags. The <head> tag contains information about the product and the source of the DWML document. Within the <data> tag, the user will find <time-layout>, <location>, and <parameters> tags. There is one <time-layout> tag in a DWML document for each unique sequence of data valid times. The <location> tag contains a geographical type tag to specify the location where the data are valid. The <point> tag and its corresponding latitude and longitude attribute pair is currently the only geographical type tag. The <parameters> tag holds one or more NDFD elements tags such as <temperature> or <wind-speed>. These tags in turn hold the NDFD data in a <value> tag. Each <value> tag relates to a corresponding start time in the <time-layout> tag.

Together the SOAP service and DWML document provide a potent mechanism to disseminate NDFD data. The NWS first began using these technologies in an experimental service in June 2004. Since then, users have submitted 47 voluntary surveys, and this initial customer feedback indicates that the service is both easy to use and meets users' need for quality. The average response to a survey request to "rate [on a scale of 1 – 10 with 10 being the best] the technical quality of this service (e.g., forecast accuracy, timeliness, problems with display)" was 8.3. Similarly, users gave a 9.0 to the survey query "rate how easy you found the service to interpret and use." While the final word is not in, it is clear that the NWS is off to a good start in providing digital services for its NDFD.

Other digital data in XML

In addition to providing NDFD in XML, the NWS also makes its watches, warnings, and advisories available in CAP and RSS. Watches, warnings, and advisories are very perishable and need to reach the public as quickly as possible. By providing these life saving forecasts in CAP and RSS, the expec-tation is that third party software and wireless technologies like PDAs and mobile phones will allow the NWS to reach more customers more quickly. Technical information for accessing this service can be found in its Product Description Document (NWS 2003b).

Current weather observations are another type of data that the NWS provides in an XML format. This product makes Automated Surface Observation System (ASOS) data available in RSS and XML for about 1,800 locations across the United States and its ter-ritories. There is one RSS and XML docu-ment, updated hourly, for each state and territory. Technical information for accessing this product is contained in the Product Description Document (NWS 2004b).

Student Contributions

Creating and deploying NWS's suite of XML data feeds takes a team of software developers. Some team members were students participating in the Meteorological Development Laboratory (MDL) Student Career Expe-rience Program (SCEP) and the NOAA Educational Partnership Program (EPP).

SCEP
◦ Alternates full-time employment in Silver Spring, Maryland, with periods of study.
◦ Salary ranges from $24,600 – $41,800 per year based on years of education completed.
◦ Allows student a 120-day work period following graduation to look for permanent position.
◦ Provides for possible conversion to permanent position within NOAA.
EPP
◦ Work within NOAA during two 10-week Summer internships.
◦ Paid $650 per week during internship.
◦ Receive up to $4,000 per academic year in scholarship money toward tuition and books.

Table 3. SCEP and EPP Highlights.

Both of these programs allow students to learn what it is like to work for the federal government while gaining valuable work experience. Table 3 outlines the key features of the SCEP and EPP.

Students from the SCEP and EPP have made significant contributions to the NWS XML capabilities. These students have created the XML Schema that defines the vocabulary and grammar of NWS' observation and Watch, Warning, and Advisory XML. Other students have developed software that provides NWS customers with NDFD data summarized over a 24-h period. Still other SCEP and EPP participants developed the user interface for the NWS web page that animates NDFD images. These student contributions have enhanced the feature set of NWS digital products and services while providing valuable experience to the SCEP and EPP participants.

Future Plans

After a 6-month public comment period, the NWS will evaluate customer feedback and decide if its XML offerings should become official. Until that decision is made, the NWS will continue to enhance its XML services. MDL is developing a new NDFD "daily" XML forecast. This forecast, available from the NDFD SOAP service, will be valid for 24 h-periods and contain maximum and minimum temperature, probability of precipitation, a short phrase summarizing the weather, and a link to an associated icon.

Conclusion

As the NDFD becomes the NWS's pri-mary means of disseminating forecasts of sensible weather elements, XML encapsulated data are taking on an increasingly important roll. By using XML, the NWS is better able to meet the data needs of its customers and partners. With the positive feedback on its initial experimental suite of XML offerings, the NWS has evidence that it has made progress toward its goal of making its data more easily accessible to its customers. This success will probably lead to an increase in the quantity of data available in XML and via SOAP services.

REFERENCES

Glahn, H. R., and D. P. Ruth, 2003: The New Digital Forecast Database of the National Weather Service. *Bull. Amer. Meteor. Soc.*, **84**, 195-201.

Morrison, M., 2001: *Teaching Yourself XML.* SAMS, 483 pp.

NWS, 2003a: *Working Together to Save Lives, NWS Strategic Plan for FY 2003 – FY 2008,* NWS, 36 pp.

_____, 2003b: *Product Description Docu-ment: NWS Watches, Warnings, and Advisories Using RSS and CAP XML Based Formats,* NWS, 7 pp. [Available online at http://www.nws.noaa.gov/alerts/wwa_by_state_pdd.pdf.]

_____, 2003c: *Digital Weather Markup Language Specification (Version 1.0),* NWS, 68 pp. [Available online at http://www.nws.noaa.gov/mdl/XML/Design/MDL_XML_Design.doc]

NWS, 2004a: *Product/Service Description Document: National Digital Forecast Database Extensible Markup Language,* NWS, 7 pp. [Available online at http://products.weather.gov/PDD/Extensible_Markup_Language.pdf.]

_____, 2004b: *Product Description Docu-ment: NWS Current Observations Using RSS and XML Based Formats,* NWS, 5 pp. [Available online at http://products.weather.gov/PDD/NWS_Current_Observations_RSS_XML.pdf.]

Peroutka, M. R., R. K. Meiggs, and M. B. Romberg, 1998: The generation of products in interactive forecast preparation. Preprints, *14th Int. Conf. on Interactive Information and Processing Systems (IIPS) for Meteor., Oceanography, and Hydrology,* Phoenix, AZ, Amer. Meteor. Soc., 350-354.

Ruth, D. P., M. A. Mathewson, T. J. Le-Febvre, and P. K. Wu, 1998: Interpreta-tion and editing techniques for interactive forecast preparation. Preprints, *14th Int. Conf. on Interactive Information and Processing Systems (IIPS) for Meteor., Oceanography, and Hydrology,* Phoenix, AZ, Amer. Meteor. Soc., 321-326.

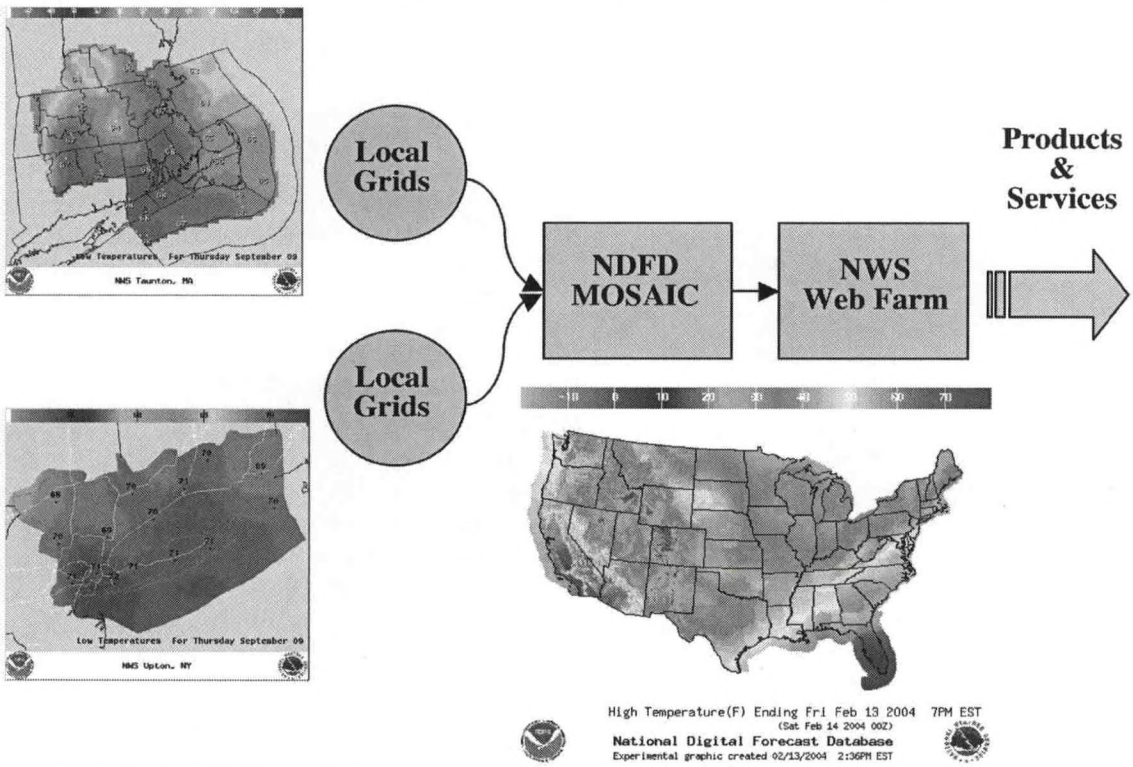

Fig. 1. The NDFD data flow.

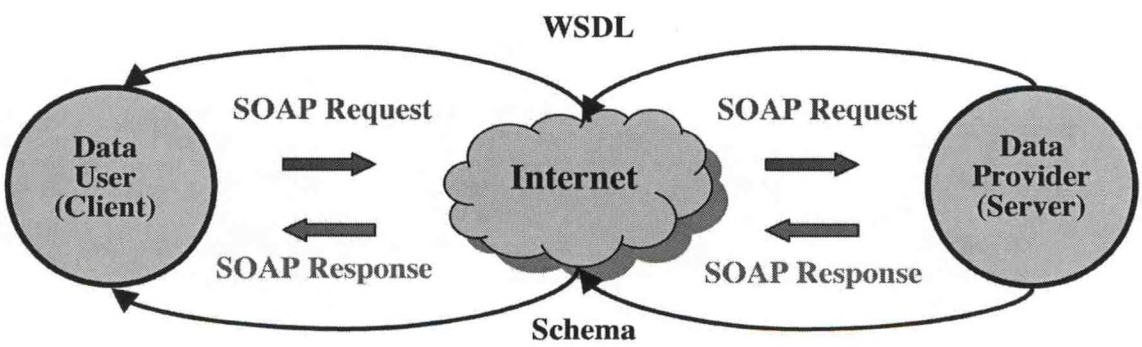

REMOTELY SENSED HIGH RESOLUTION PRECIPITATION ESTIMATION IN CONJUNCTION WITH NEXRAD, OVER THE MOUNTAINOUS REGIONS

Shayesteh Mahani and Reza Khanbilvardi

National Oceanic and Atmospheric Administration Cooperative Remote Sensing Science and Technology Center, NOAA-CREST Center, Steinman Hall, T-107 140th Street at Convent Avenue, New York, NY 10031, United States. (212-650-8440; *mahani@ce.ccny.cuny.edu*)

Abstract

This study focuses on coupling a rainfall retrieval model with a merging scheme to generate more accurate finer scale rainfall from multi-sources: satellite and ground-radar information. This approach is applied to generate rainfall over the mountainous regions where terrain radar beams leave behind but satellite imagery can cover. Estimating high resolution precipitation over high mountains, where the traditional ground-based radar and rain gauge observing techniques cannot cover, is still a challenging problem. Satellite imagery is the only source for acquiring information from the gap areas that radar beams cannot cover. Multi-Using multi-sensors: satellite VIS/IR (visible/infrared) and ground radar -based High resolution merged rainfall estimates from multi-sensors: remotely sensed infrared (IR) and ground-radar information have physical characteristics of both data sources, satellite and radar.

The merging technique is based on the method of successive correction (SCM), a weighting scheme. The satellite-based rainfall retrieval model is an artificial neural network based algorithm, PERSIANN (Precipitation Estimation from Remotely Sensed Information using an Artificial Neural Networks). This model is improved to estimate satellite IR-based rainfall at fine space and time scales to be match with high resolution NWS NEXRAD-Stage4, calibrated rainfall from radar reflectivity with the hourly rain gauge observation. Geostationary GOES satellite IR cloud-top brightness temperature (Tb) is used because of large spatial coverage and high space and time (half hourly, 4-km x 4-km) scales. In this study, hourly 12-km x 12-km, in latitude-longitude directions, satellite-based rainfall and NEXRAD are considered. Spatial resolution of merged product will be improved up to 4-km x 4-km in future. Hourly ground-based rain gauge data is used for validating the merged rainfall product.

The obtained results demonstrate improvement after applying the merging approach. Blended products higher correlated with the rain-gauge data rather than satellite estimates.

Introduction

Accurate high spatial and temporal resolution rainfall estimates are critically required for real time prediction, flood forecasting, severe weather monitoring, water resources management, and many other hydrological applications. Though, the contiguous United States is served by the WSR-88D (Doppler) radar network, the NEXRAD radar information is not available over high mountains, where the orography effect creates heavier storms, and also over remote regions. The terrain radar beams leave many effective coverage gaps, particularly, over mountainous regions, located west of 100∞W, and also large water bodies. There are usually very sparse or no real-time rain gauge networks, over the radar coverage gap areas.

Satellite-based remotely sensed observation provides a uniquely detailed view and information of hydrologically relevant variables, such as, precipitation beyond the traditional ground-based means (i.e., rain-gauge networks and radar). Therefore, satellite imagery is the only possible source of gathering information used for rainfall retrieval over the inaccessible regions. Infrared cloud-top brightness temperature, observed by geostationary GOES satellites, is used, as the basis to estimate precipitation, because of their

high temporal (30 minutes) and spatial (4-km) resolutions.

The satellite-based rainfall retrieval algorithm, PERSIANN, developed by Hsu, at the University of Arizona (Hsu et al., 1997; Hsu et al., 1999), is selected to be improved for producing high resolution precipitation. This model works based on the ANN (artificial Neural Network) system uses multivariate non-linear input-output relationship functions to fit local cloud-top temperature (Tb) to pixel rain rates (R). The functional relationship between cloud top pixel temperature and surface rainfall is complicated by many factors. To improve the resolution of rainfall product, model parameters must be adjusted, by optimizing relevant uncertainties, to derive more suitable input-output relationship. An important uncertainty is associated with different relationships between different cloud-types and their corresponding rainfall amounts. To improve model input-output relationship, a cloud classification scheme (CCS), developed by Yang at the University of Arizona (Yang, et al., 2004), based on cloud geometry and physics. The CCS scheme is applied to remove no-rainy cloud elements and also derive a suitable Tb-R relationship for every cloud category. Spatial displacement associated with cloud-top relief, wind speed, and other relevant uncertainties will be considered to be minimized for estimating satellite-based precipitation at higher space scale (4-km x 4-km). In order to generate rainfall products that are better suited to fine-scale distributed hydrologic simulation and also are better match with minimal bias with NEXRAD rainfall, model resolution must be improved.

To demonstrate the capability of the merging approach, a study area in the western United States has been selected, because of high mountains located west of the 100°W. Study site is in size: 10° (32°N to 42°N) by 12° (104°W to 116°W) in the latitude and longitude directions, respectively. Study time is at least two months during the warm season (June-September) and two month during the cold season (November-February).

Objective

The main objective of this study is to develop an approach for coupling an ANN-based rainfall retrieval model with a merging algorithm to estimate high resolution precipitation from multi-sources: satellite-IR and ground-radar information. The accuracy of model output will be improved suitable for fine space and time scales, up to hourly 4-km x 4-km resolutions. In the current study, hourly 12-km x 12-km resolutions are considered for rainfall estimation.

Methodology

To meet the objective of this study, following two procedures must be combined: (1) improving space and time scales of remotely sensed precipitation estimates, and (2) developing an algorithm to combine satellite-based precipitation estimates with ground-based NEXRAD rainfall measurements. The combined algorithm using multi-sources, satellite and ground-based radar, will be a promising technique which can produce continuous gridded precipitation, with the physics of both radar and satellite information systems, even over remote and mountainous regions. An artificial neural networks based model, PERSIANN, has been selected to retrieve rainfall. Model input is cloud-top IR brightness temperature (T_b) from geostationary satellites at half-hourly 4-km x 4-km resolutions. This algorithm designed to produce precipitation estimates with minimal bias relative to rainfall climatology, which is very important for hydrological applications. Therefore, to provide suitable rainfall estimates, the current operational PERISANN system is operated at lower resolution, a 6-hourly 0.25o x 0.25o latitude-longitude. Model parameters routinely are adjusted by microwave-based rainfall estimates from low- and also polar orbiting satellites such as: TRMM, NOAA-13 and -14, and DMSP (Sorooshian et al., 2000). Training the ANN model helps to adjust the connection weights between hidden and output layers for deriving the most fitted input-output relationship with a minimum matching error.

For improving resolutions and accuracy of model output, the effective relevant uncertainties on model input-output relationship must be optimized. Infrared-rainfall (IR-R) relationship varies significantly for different cloud types. And also, spatial relevant errors create displacement on cloud-pixel location and change the T_b-R relationship. In the current study, the cloud classification scheme (CCS) is applied to remove no-rainy parts of clouds and also derive an appropriate T_b-R relationship for every class of cloud. Cloud-top relief spatial displacement will be minimized when precipitation estimates are in finer

spatial (4-km x 4-km) resolution. An algorithm was developed by Mahani at the University of Arizona (Mahani, et al., 2000) for adjusting cloud-top relief spatial adjustment. Stereoscopic analysis over pairs of simultaneous images from two geostationary satellites, are used in this approach, to optimize parameters of the piecewise line identified the relationship between cloud-top T_b and height. Spatial displacement is estimated and adjusted using the formula that identifies the geometrical relationship between cloud-top height and associated displacement. A brief description for CCS and the merging approach are as following.

Cloud Classification Scheme (CCS)

A patch-based cloud classification algorithm in conjunction with pixel-based PERSIANN model is used to categorize different cloud types and to determine Tb-R relationship for every cloud type. Instead of using only the local pixel of cloud-top T_b, as in the PERSIANN system, CCS extracts both local pixel temperature textures and regional cloud patch features. This classifies cloud patches into various groups (Yang, et. al., 2004) with a specific T_b-R relationship for each group of clouds. Certain T_b-R relationship for every cloud type needs to be implied. For instance, cirrus, which is a high, cold, and thin cloud, produces no or very little rain but a thick convective cloud, with usually warmer pixels, produces a heavy storm. Therefore, removing no rainy parts of clouds and applying an appropriate T_b-R relationship will reduce errors significantly.

Several distinct stages are designed from separation of cloud patches to rainfall estimation in local pixels using specific functions, which are: (1) a segmentation scheme to separate cloud patches from an infrared image; (2) a feature extraction and classification schemes to process cloud patches into different categories; and (3) a set of T_b-R relationships for various cloud types. Identifying cloud types and T_b-R relationship for each cloud type is expected to be a promising solution for improving mostly spatial resolution of precipitation estimates.

Merging Approach

Merging multi-sources, satellite- and radar-based products is a challenge technique for reducing some of the errors and limitations associated to each source. Merging high resolution rainfall products can do better bias minimal, noise removal, and better suiting remotely sensed rainfall estimates with NEXRAD and climatology rainfall. In this study, the successive correction method (SCM), a weighting approach, is applied for combining multi-sources rainfall products. In SCM, with convergence properties, the objective analysis procedure is applied iteratively by making successive corrections to a background or first-guess field. In this project, a two-dimensional domain is considered for analysis of the variable: satellite-based rainfall estimates. (f_{SR}) with respect to the radar-based rainfall (f_{RR}). Satellite-based model output is identified as the background domain ($f_B = f_{SR}$), which is going to be analyzed using NEXRAD as observation domain (fO = fRR), for generating new analyzed (merged) data values (f_A). For analysis of every grid-point, pixel (k), a window centered at the pixel (k) is considered. Window size is selected with respect to the interest resolution, size of gap area, and accuracy for analyzed domain output. In the current study, where space scale is 0.12° x 0.12° lat-lon, window size varies from 9 x 9 to 17 x 17 pixels. The window moves in two directions where its center grid is placed on all pixels one by one. We need to assume that the background error is homogeneous and that consequently the expected background error variance $E_B^2 = \langle \varepsilon_B^2 \rangle$ is independent of location. And also to assume that the observation error is only a function of instrument (radar) type, and it is not correlated with the background error. The expected observation error variance at pixel (i) is denoted $E_{O(i)}^2 = \langle \varepsilon_{O(i)}^2 \rangle$.

- Calculating the weight factor with respect to the distances, from the following formula:

$$\text{If:} \quad r_i < R \Rightarrow \quad w_i = \frac{R^2 - r_i^2}{R^2 + r_i^2}$$

$$\text{If:} \quad r_i \geq R \Rightarrow w_i = 0$$

where: "w_i" is the weight factor relevant to any observation pixel (i), with available both satellite and radar rainfall amounts; "R" is the maximum distance from window center, pixel (k); and "r" is the distance between analysis center grid, pixel (k), and the observation pixel (i) inside window. If (x , y) is the grid

pixel coordinates, therefore: $r^2 = (x_i - x_k)2 + (y_i - y_k)^2$

- The merged value for center pixel (k), is calculated from the following equation:

$$f_{MR_k} = f_{SR_k} + \frac{\sum_{i=1}^{n} w_i (f_{RR_i} - f_{SR_i})}{\sum_{i=1}^{n} w_i + \varepsilon_{RR}^2}$$

where: $f_{MR(k)}$ and $f_{SR(k)}$ are the analyzed merged and satellite-based rainfall estimates for the center pixel (k); $f_{SR(i)}$, and $f_{RR(i)}$ are the satellite-based rainfall and NEXRAD rainfall for observation pixel (i) inside the window; and "n" is the number of tε_{RR})bservation pixels with available both radar and satellite rainfall inside the window; $(\varepsilon_{RR} = E_{RR}^2 / E_{SR}^2)$.) (observation instrument) error, that is equal to the constant expected observation error variance normalized by the constant expected background error variance:

Results and Conclusions

The developed merging scheme applied on satellite-IR PERSIANN-CCS algorithm at hourly 12km x 12km resolution for July 2002. Following figures demonstrate rainfall patterns comparison between rainfall images, for July 10,2002, at hour 01 UTC, after applying cloud classification scheme (Fig. 1-b) and also after merging with radar-based rainfall (Fig. 1-c) with NEXRAD observation image (Fig. 1-a). These images illustrate rainfall patterns after merging with radar-based data is better match with real rainfall. The no rainy parts of clouds are eliminated.

Following figures illustrate the relationship between ANN model rainfall estimates using CCS scheme (Fig. 2-a) and merged product (Fig.2-b) with respect to the NEXRAD observations. Statistical parameters indicate merging approach capable to improve model rainfall estimates. Correlation coefficient, root mean square error, and bias are improved from 0.50, 2.85 (mm), 0.28 (mm) to 0.88, 1.6 (mm), and 0.18 (mm) respectively.

For validating the quality of CCS scheme and merging model output, rainfall estimates from both algorithms compared with hourly rain-gauge observations. Figure 3, illustrate that satellite-radar merged rainfall estimates has higher correlation with rain gauge observation. Changing the merging criteria can improve accuracy of the merging products.

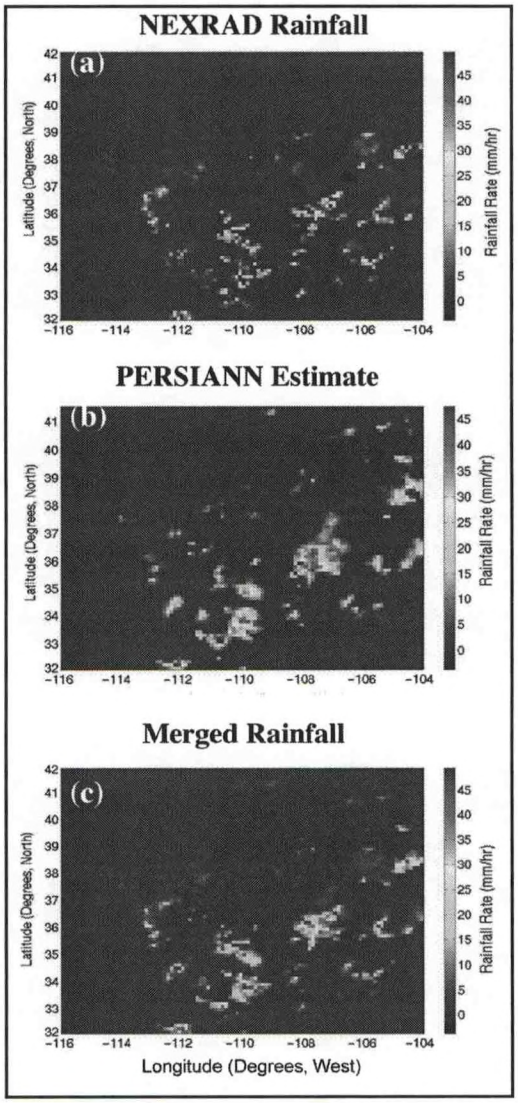

Figure 1: Comparing satellite-IR based rainfall using CCS scheme (b), and merged rainfall estimates (c), with the NEXRAD observation (a).

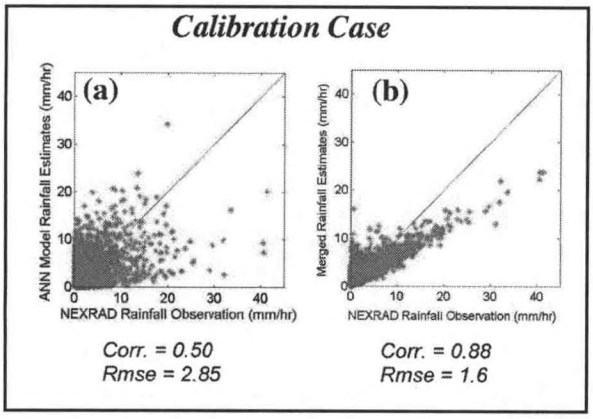

Figure 2: Comparing satellite-IR based rainfall using CCS scheme (a), and merged rainfall estimates (b) with respect to the NEXRAD observation.

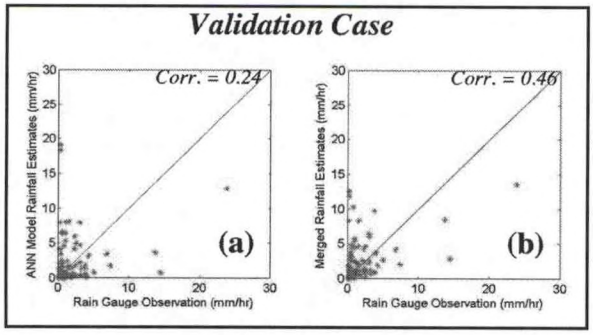

Figure 3: Comparing satellite-IR based rainfall using CCS scheme (a), and merged rainfall estimates (b) with respect to the hourly rain gauge observation.

REFERENCES

Hsu, K., X. Gao, S. Sorooshian, and H. Gupta, 1997; "Precipitation Estimation from Remotely Sensed Information using Artificial Neural Networks", *J. Appl. Meteo.*, V. 36 (9).

Hsu, K., H.V. Gupta, X. Gao, and S. Sorooshian, 1999; "Estimation of Physical Variables from Multiple Channel Remotely Sensed Imagery Using a Neural Network: Application to Rainfall Estimation," *Water Resources Research*, 35(5), 1605-1618.

Mahani, S.E., X. Gao, S. Sorooshian, and B. Imam, 2000; "Estimating Cloud-Top Height and Spatial Displacement from Scan-Synchronous GOES Images Using Simplified IR-Based Stereoscopic Analysis", *J. Geoph. Re.*, V. 105 (12).

Sorooshian, S., K. Hsu, X. Gao, H.V. Gupta, B. Imam, and Dan Braithwaite, 2000; "Evaluation of PERSIANN System Satellite-Based Estimates of Tropical Rainfall," *Bull. of the Amer. Meteo. Soc.*, Vol. 81, No. 9, 2035-2046.

Yang, H, K. Hsu, X. Gao, and S. Sorooshian, 2004: "Precipitation Estimation from Remotely Imagery Using an Artificial Neural Network – Cloud Classification System", *J. of Appl. Meteo.*,

EVALUATION OF NOAA'S RAINFALL ALGORITHM AGAINST SUMMER RAIN GAUGE DATA

Ismail Yucel

Hampton University, Center for Atmospheric Sciences, Hampton, VA 23668
Ismail.yucel@hamptonu.edu; 757-728 6729, Fax: 757-727 5090

Robert J. Kuligowski

NOAA-NESDIS, Camp Springs MD

David Gochis

NCAR

Abstract

This study investigates the performance of the NESDIS Hydro Estimator (HE) rainfall algorithm against observations taken from the North American Monsoon Experiment (NAME) program. A recent rainfall observation network established in NAME program provides precipitation measurements of convective origin over large complex topographical areas while comprehensive validations of the satellite-estimated precipitation characteristics such as the frequency, intensity, diurnal evaluation and its relation to the complex regional topography have been absent to date due to the unavailability of pre-existing dense observation network. The independence of the HE on radar data, on the other hand, makes its applicability appropriate for mountainous regions. The rainfall estimates are validated against the measurements obtained through Aug 2 to Sep 14, 2002 to report whether the results from the HE is capable of capturing terrain-induced precipitation characteristics. It seems that satellite estimates are able to capture main characteristics of terrain-induced precipitation during this comparison period.

Introduction

Visible and infrared (IR) imagery and passive microwave instruments are the satellite tools that have been used extensively to estimate stratiform and convective type of precipitation for a range of applications from climate-scale to instantaneous event. Although the microwave techniques with polar-orbiting sun-synchronous satellites are more physically direct while responding to precipitation-size hydrometeors within clouds rather than cloud-top temperature or albedo, the visible and IR based techniques are widely used in the depiction of the intensity and spatial extent of heavy precipitation due to their high frequency (15 min) and high spatial resolution (~ 4 km) measurements from Geostationary Operational Environmental Satellite (GOES). These satellites with their broad area coverage are therefore more suitable in operational use for estimation of extreme-precipitation events. Vicente et al. (2002) reported that it is possible to accurately observe rapidly developing thunderstorms at very high spatial and temporal resolutions with improved capabilities of the current geostationary satellites.

In support of the National Weather Service's (NWS) flash flood warnings and heavy precipitation forecasts efforts, the National Oceanic and Atmospheric Administration/National Environmental Satellite Data and Information Service (NOAA/NESDIS) Office of Research and Application (ORA) has been providing satellite precipitation estimates operationally since 1978. Operational satellite rainfall estimates are originated with the Interactive Flash Flood Analyzer (IFFA) (Scofield and Oliver 1977 and Scofield 1987) following the technique based on GOES longwave IR window (10.7 mm). To improve timeliness of the IFFA and to extend areal coverage of products, NESDIS developed an automatic algorithm called the Auto-Estimator (AE) (Vicente et al. 1998). In addition to IR window brightness temperature, the AE has the features of environmental moisture, cloud growth, cloud-top structure, orographic and parallax cor-

rections (Vicente et al. 2002), and a convective equilibrium level adjustment for warm-top events (Scofield 2001). As reported by Scofield (2001) and Scofield and Kuligowski (2003), the AE increased its productivity in terms of monitoring a greater number of heavy-rainfall and disseminating a greater number of satellite-precipitation-estimation messages in a more timely fashion. However, despite the use of temperature trends to distinguish cloud-tops between thick convective clouds and thin cirrus clouds in the AE, it still considerably overestimated the areal extent of rainfall reported in Rozumalski (2000) and Scofield and Kuligowski (2003). To overcome this problem, the AE algorithm uses 15-minute Weather Service Radar-1988 Doppler (WSR-99D) reflectivity data. As this addition alleviated the overestimation in spatial extent of rainfall, the dependence of the AE on radar makes its applicability inappropriate for regions with inadequate rainfall information from radar and/or rain gauges. In response to these concerns, NESDIS developed another version of the AE, called the Hydro-Estimator (HE), which is following a different approach for discriminating raining areas from non-raining without usage of radar as well as new adjustments for moisture availability effects. The statistical analysis of Scofield and Kuligowski (2003) showed that both the HE and AE with radar data have the similar performance, making the HE more preferable in operational use. Consequently, over mountainous regions lacking radars and dense networks of rain gauges, the HE algorithm offers operational rainfall data with high spatial and temporal resolution, which is crucial in flash flood forecasting as weather conditions can very greatly over short distances and cause weather-related hazards.

Although large-scale atmospheric motions control the general stability or instability in the atmosphere, local topographic effects are critical to the spatial and temporal distribution of convective activity because of the characteristics of the flow disturbances created by the mountains (Adams and Comrie, 1997 and Vicente et al., 2002). In general, precipitation amounts tend to increase with height as the greater amount of rainfall is located windward of the orographic crest. Vicente et al. (2002) showed that orographic correction of the AE algorithm enhanced precipitation distribution over the US west coast when comparing the results from the AE without correction. In their study, however, a thorough validation of this correction procedure was not carried out due to the lack of dense network of surface rainfall measurements. Furthermore, comprehensive validations of the satellite-estimated precipitation character such as the hourly frequency, intensity, diurnal evaluation and its relation to the complex local topography have been absent to date due to the unavailability of pre-existing dense observation network in mountainous regions. However, as part of the North American Monsoon Experiment (NAME) program, which has been developed to aim at improving both understanding and predictability of warm season precipitation in southwest US, a recent technical note (Gochis et al. 2003b) documented the establishment of a new event-based rain gauge network, known as the NAME Event Rain gauge Network (NERN), in northwest Mexico. Results presented in Gochis et al. (2003b and 2004) demonstrated the ability of the new network to capture high-resolution temporal aspects and general physiographic aspects of North American Monsoon (NAM) precipitation as these features are critical for the validation of remotely sensed and modeled precipitation estimates.

The primary goal of the research in this study was to investigate the HE algorithm's performance in documenting surface precipitation on topographically complex region of NAME and thus to report whether the HE is capable of capturing the aspects of terrain-induced rainfall and to define where algorithm improvement may be required. The 50 gauges of NERN sampled according to the temporal aspects of precipitation with respect to topography were used to compare with the 4-km rainfall estimates of the HE for the period of 2 Aug–14 Sep 2002, this being the period of NAM. It is envisaged that such evaluation will also be helpful to users of mesoscale atmosphere modelers as these models have the severe uncertainty in predicting convective systems at high spatial resolution due to the strong insolation and the presence of elevated heat sources associated with the complex topography over the US southwest (Yucel et al., 2002 and 2003).

Description of study area and rainfall algorithm

Observational arrays

In support of coordinated field activities of the NAME, a new event-based surface rain gauge network was installed in two phases corresponding to the 2002 and 2003. A network of the 50 tipping-bucket

rain gauges installed over the month of July and the first days of August 2002 was shown in Fig. 1. The 48 of these total rain gauges providing data for the entire selected comparison period from 2 Aug–14 Sep 2002 was used in this study. As seen from Fig. 1, the network configuration used in this research consists of the 5 west-east transects through the formidable Sierra Madre Occidental (SMO) mountains. The network does not present the most favorable installment for measuring the spatial pattern of convective rainfall while it provides instantaneous precipitation effectively on longitudinal extend with respect to the distribution of terrain elevation. Gochis et al. (2003b and 2004) divided the elevation into six groups to show the rainfall sampling as a function of elevation. The same elevation breakdown is also used in the research here that validates satellite rainfall estimates. A map of the elevation bands overlain with the 50 rain gauges is shown in Fig. 1. The overall range in elevation sampled by the network is between 71 m and 2979 m with the mean value of 1226 m. This sampling possesses a well-matched distribution of rain gauges with respect to elevation to avoid a low-elevation bias with the regional topography. For example, there are 13 gauges located at over 2000-m elevation, which are also critical for analyzing temporal features of terrain-induced convective precipitation. The dearth of the gauges located in the 1000-1500-m (elevation band 3) is because there is comparatively little terrain in this elevation band along the western slope of the SMO as it is apparent from Fig. 1. Gochis et al. (2004) notes that the NERN configuration is adequate for sampling the variability in precipitation frequency and relative intensity as a function of regional topographic gradients while the typical distance between NERN gauges is on the order of several tens of kilometers along a transect and up to hundreds of kilometers between transects.

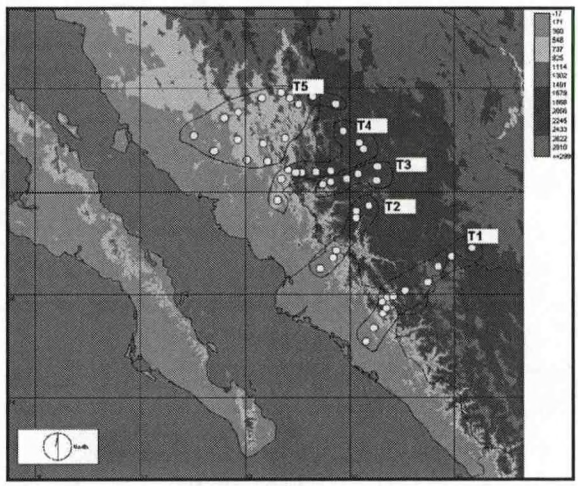

Figure 1: Shows the map of the elevation bands overlain with 50 rain gauges. Each color corresponds to an elevation band.

Rainfall Algorithm

Among several operational algorithms developed for quantitative precipitation estimation (QPE) at NESDIS, the HE from Scofield and Kuligowski (2003) is selected to use in this study because of its timeliness and applicability over mountainous areas. The HE computes real time estimates of instantaneous rain rate using 10.7-μm brightness temperatures based on a curve that was originally derived from 6800 pairs of collocated IR brightness temperatures and radar rainfall rates for the development of the AE algorithm.

Unlike the AE algorithm, the HE defines the raining pixels as "convective core" and "non-core" precipitation and assigns a rain rate that is a combination of the two depending on the spatial characteristics of the predetermined region surrounding the pixel of interest. This region can cover an area of interest up to a 50-pixel radius for cloud tops colder than 200 K, or up to 30-pixel radius for cloud tops warmer than 220 K depending on the minimum temperature determined using a 101x101-pixel box centered the interested pixel. The presence or absence of precipitation and the fraction of 'core" and "non-core" precipitation is determined based on a computed index value, which divides the difference of brightness temperatures between the mean of previously selected region and interested pixel to the mean standard deviation of selected region. The rain rate is set to zero if the pixel is warmer than the average of its surroundings (negative index) with the assumption that such pixels are cirrus or convectively inactive clouds. For positive index values constrained to be 1.5 or less, the "core" fraction is related to the index value and the "non-core" fraction is related to (1.5-index). The standard AE rain-rate curve is adjusted according to the difference between the pixel brightness temperature and the average value in the surrounding region. This approach has substantially reduced the exaggeration of rain area exhibited by the AE reported by Scofield and Kuligowski (2003).

A combined factor of precipitable water (PW) and relative humidity (RH) developed to adjust the tendency of precipitation overestimation in the AE (Vicente et al. 1998) was separated, with the PW value used to adjust the rain-rate curve based on moisture availability and the RH value used to derive an amount to be subtracted from the rain rate in the HE. The PW and RH are based on data from the Eta Model. These adjustments improved the handling of stratiform events with embedded convection, and also of wintertime precipitation, which is typically associated with low PW values (Scofield and Kuligowski, 2003). Other adjustment parameters incorporated in the HE are the convective equilibrium (Scofield 2001), the orography and parallax corrections (Vicente et al. 2002), and correction for satellite zenith angle.

Results

Spatial Patterns

Horizontal images of total rainfall for observations and satellite from 2 Aug–14 Sep 2002 are shown in Figure 2a and b, respectively. Observed values were generated by interpolating the station values to a grid using a linear interpolation algorithm. The maximum observed precipitation lies along the western slope of the SMO. The core region of maximum precipitation would exist as a more or less continuous band along the western slope according to the NERN configuration. These features are more or less followed by the satellite estimates with a tendency of overestimation over the lower elevation areas. Conversely, satellite retrievals significantly underestimate precipitation over high terrain areas as seen at southeastern part of the map.

Diurnal cycles

Figure 3 shows the diurnal cycle of hourly precipitation frequency for each of the 5 elevation bands along with the network-mean diurnal cycle. It is evident that precipitation initiates first and most frequently over the high terrain of the SMO. Precipitation frequency in elevation bands 5 and 6 increases beginning around 1200 local solar time following the diurnal minimum in frequency. Below bands 5 and 6, precipitation tends to occur later in the day and into the evening. The latest elevation bands to peak are the lowest elevation bands, 1 and 2. However, the highest elevation bands (5 and 6) represent the lowest frequency in satellite estimates even though they have the earliest peaks as in the observations. Bands 1 and 2 in satellite estimates also show the latest peak in frequency. However, all the bands reach their peak earlier than observations. Figure 4 shows the diurnal cycles of hourly mean precipitation intensity. They display increased hour to hour variability relative to the cycles of precipitation frequency. Both observation and satellite values show that intensity at the highest elevations is comparatively light and less than the network mean intensity.

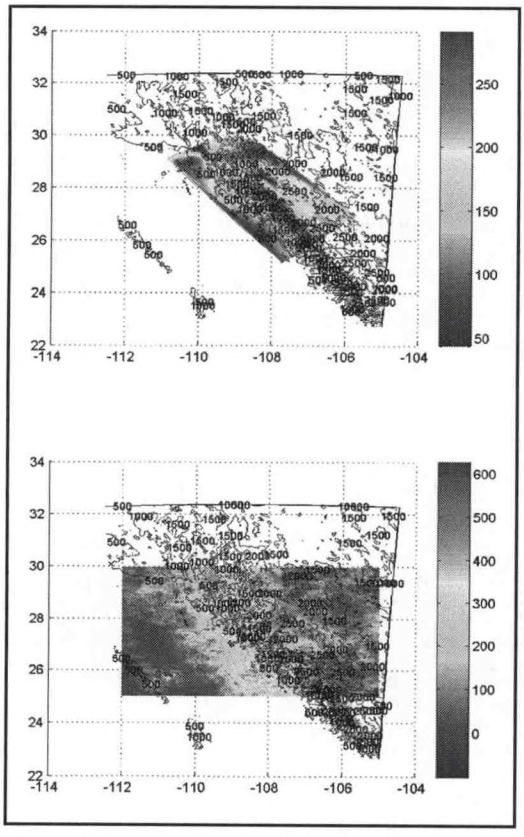

Figure 2: Total rainfall patters over the study site. Contour of topography is also provided at the background. Rain is in mm.

Discussions

NOAA-NESDIS rainfall estimates could play a critical role in replacing the poor rainfall estimates from mesoscale atmosphere models. Outcomes of this research will help us to determine future research directions, such as assimilation of satellite precipitation estimates into the mesoscale atmosphere model for making better predictions. We also plan to use these rainfall estimates in hydrological applications associated with flood risk analysis from extreme weather events.

REFERENCES

Gochis, D.G., J.-C. Leal, W. J. Shuttleworth, C. Watts, and J. Garatuza-Payan, 2003: Preliminary Diagnostics from a New Event-Based Precipitation Monitoring System in Support of NAME, J. Hydrometeorology, 4, 974-981.

Gochis, D.G., A. Jimenez, C. J. Watts, J. Garatuza-Payan, W. J. Shuttleworth, 2004: Analysis of 2002 and 2003 Warm Season Precipitation from the North American Monsoon Experiment (NAME) Event Rain gauge Network (NERN), Monthly Weather Review, (in press).

Scofield, R. A. and R. J. Kuligowski, 2003: Status and Outlook of Operational Satellite Precipitation algorithms for Extreme-Precipitation Events, Weather and Forecasting, 18, 1037-1051.

Vicente, G. A., J. C. Davenport, and R. A. Scofield, 2002: The role of orographic and parallax corrections on real time high resolution satellite rainfall rate distribution, Int. J. Remote Sensing, 23, 221-230.

Vicente, G. A, R. A. Scofield, and W. P. Menzel, 1998: The operational GOES Infrared Rainfall Estimation Technique, 79, 1883-1898.

Yucel, I., W. J. Shuttleworth, X. Gao, and S. Sorooshian, 2003: Short-Term Performance of MM5 with Cloud-Cover Assimilation from Satellite Observations, Monthly Weather Review, 131, 1797-1810.

Yucel, I., W.J. Shuttleworth, R. T. Pinker, L. Lu, and S. Sorooshian, 2002: Impact of Ingesting Satellite-Derived Cloud Cover into the Regional Atmospheric Modeling System, Monthly Weather Review, 130, 610-628.

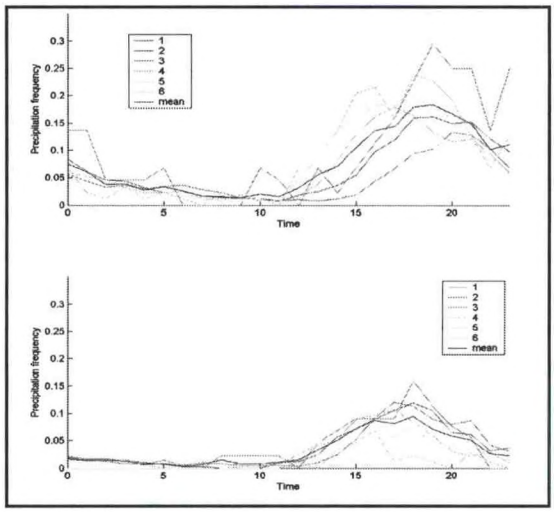

Figure 3: Diurnal cycles of precipitation frequency for each band (a) for observations and (b) for satellite estimates.

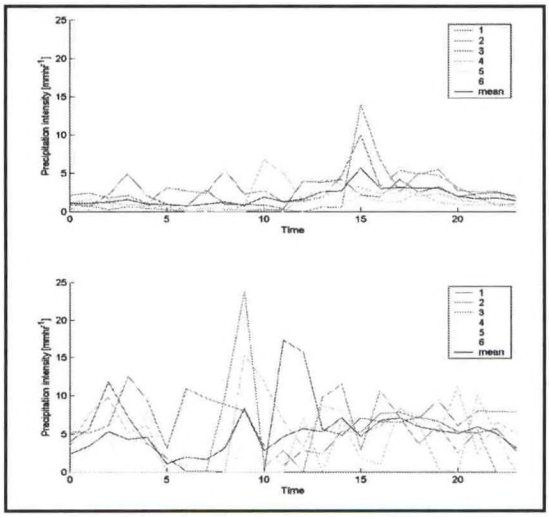

Figure 4: Diurnal cycles of precipitation intensity for each band (a) for observations and (b) for satellite estimates.

The Anomalous Intensification of Tropical Storm Allison (2001) over Land

Kwan-yin Kong and Stanley David Gedzelman

Department of Earth and Atmospheric Sciences and NOAA Cooperative Remote Sensing Science and Technology Center (CREST) , City College of New York, New York, NY 10031 USA

Abstract

The remnants of Tropical Storm Allison (2001) intensified over land in Louisiana without transforming to an extratropical cyclone. Allison's evolution is examined using observations and simulations by the fifth-generation Pennsylvania State University-NCAR Mesoscale Model Version 3 (MM5). MM5 was run using many combinations of physics options. Only one combination (Grell convective adjustment and MRF boundary layer) captured a portion of the intensification because it developed a convective line near storm center that enhanced the vorticity and vapor flux convergence and coupled with the storm's circulation to produce an eyelike feature seen on NEXRAD radar images. Replacing the cold bias of the NCEP objectively analyzed Sea Surface Temperatures (SST) near the Gulf of Mexico coast with measured warmer coastal waters produced a much more accurate simulation.

Introduction

Landfall usually spells rapid weakening for hurricanes and tropical storms although enormous rainfall totals can continue for several days. On occasion, tropical storms or marginal hurricanes intensify long after landfall when cold air is entrained on the western side and extratropical transformation (ET) takes place. This was the case for a number of storms, notably, Hurricane Hazel (1954), which deepened slightly as it approached Toronto (Anthes, 1990).

Allison (2001) belongs to a small class of tropical storms and marginal hurricanes that intensify after landfall without significant ET (Beven, et. al., 2003). In all these cases, intensification occurred while the storms were near enough to the ocean to obtain from it a substantial amount of water vapor, and significant portions of the lowlands were flooded. Much of Danny's record-breaking rainfall totals from Louisiana to Alabama occurred as the storm drifted aimlessly near the coast. Allison's torrential rains also soaked the swampy lands of the Mississippi River Delta region for five days prior to her arrival there.

Four general conditions are observed to accompany intensification of tropical storms and marginal typhoons over land in the vicinity of Taiwan. They are:

1. Large vapor flux convergence from ocean.
2. A mesoscale system to advect vorticity.
3. Cold upper troposphere with baroclinicity.
4. Upper level divergence.

Allison (2001) contained one additional feature that may have aided intensification. A convective rainband developed south of its center in the hours after landfall early on 11 June 2001. Allison deepened and became more organized when the northern part of the rainband wrapped around the storm center to form an eyelike core.

Outbreaks of towering convection in or near the center of tropical storms and hurricanes have been observed to precede or accompany intensification since at least the 1930's (Dunn, 1951). More recently the link has been made between deepening of the storm and convection that gets incorporated into the circulation to form or complete an eyewall. In this process of symmetrization the primary circulation strengthens, the eyewall becomes better defined, and the intense, local convection weakens or is replaced entirely by a more laminar and

stronger radial and vertical circulation. Using Hurricane Diana (1984) as an example, Hendricks, et. al., (2004) described hurricane formation as a two-stage process. During the first stage, isolated vortical convective towers generate small-scale potential vorticity maxima, which then merge into a larger axisymmetric vortex during the second stage.

In this article we employ the NCAR/Penn State Mesoscale Model Version 3 (MM5) to help diagnose the factors that caused Allison to intensify after landfall. The study focuses on three factors that potentially influenced intensification, namely 1: increasing SST, 2: flooding the land and, 3: the development of a convective rainband and its incorporation into Allison's circulation. Our approach follows the tradition of performing control numerical experiments on hurricanes using mesoscale models Anthes (1990) used to diagnose the extratropical transition of Hurricane Hazel.

MM5 has many parameterization schemes for microphysics, convective adjustment, and boundary layer physics. The general conditions under which each scheme is appropriate and performs best have been outlined (Grell, et. al., 1994). Nevertheless, because of the complexity of storm systems, it is seldom know a priori which combination of schemes will perform best when MM5 is applied to particular storms, and there are situations where only one combination will capture a critical storm feature. This uncertainty dictates a brute-force approach to determine key features and processes. In Section 2, observations of Allison are presented and analyzed. In section 3, MM5 simulations are presented, and results are summarized and discussed in Section 4.

Observations and Analysis

Tropical Storm Allison (2001) formed off the coast of Texas on 5 June and attained tropical storm status shortly before moving over land south of Houston. Despite weakening quickly into a depression and lingering over East Texas for the next four days, Allison's circulation remained intact. During this five-day period, two episodes of heavy rain caused massive flooding in and around Houston before the depression finally drifted back over the Gulf of Mexico early on 10 June. During this period, heavy rains also fell from Louisiana to Mississippi.

Once back over water, Allison appeared less organized. It then moved ENE toward the Louisiana coast. The Lake Charles (LCH) and Slidell (LIX) Doppler radars captured the evolution of a well-defined line of convection with an active nucleus near its northern end.

Allison's intensification can be linked to the evolution of the convective line. The line first developed on Allison's east flank. It extended over the Gulf of Mexico with a number of widely spaced thunderstorms strung out toward its southwestern terminus east of Brownsville, TX. The northern and most intense part of the convective line became incorporated into the storm's circulation and wrapped around the center to form a comma-shaped line (Fig. 1), which evolved into an eye-like feature over southern Mississippi. It appeared that this "squall line" was coupled with Allison's circulation.

Allison weakened a bit in the hours immediately after landfall but then intensified from about 0600 UTC to 1000 UTC, when the pressure reached a minimum of 1001.3 hPa. Maximum wind gusts (20 ms-1) were reported at nearby ground stations but the strongest sustained surface winds and wind gusts were reported just ahead of the squall line/rainband at the southern terminus of the Mississippi River delta, where a secondary low center or trough developed simultaneously. By 1030 UTC the eyelike feature was closed. Doppler radar at this time revealed a well-defined radius of maximum wind around 40 km from the center of the apparent eye with a maximum wind speed exceeding 33 ms-1 at about 175 to 350 m above ground level south of the storm center.

Infrared images indicated a hybrid nature for Allison. Cold cloud tops indicative of towering convection occurred initially over and to the east of the surface center while clouds with distinctly lower tops swirled westward to the north of the storm center. This aspect of Allison's cloud shield resembled the cold conveyer belt clouds more characteristic of extratropical cyclones. After 0900, the cirrus cloud shield expanded toward the north and east for about 18 hours. It exhibited anticyclonic motion and by 1700 UTC the outer edge of the cirrus assumed a banded, filamentary appearance, often seen emanating from hurricanes following a period of deepening.

Flow at 200 hPa at 1200 UTC had an open wave with anticyclonic flow and a sub-tropical jet streak just north and east of the surface low. Its entrance was marked by large horizontal divergence and strong

ageostrophic flow toward lower geopotential heights that accelerated downwind to a maximum exceeding 20 ms-1. A pool of warm air (T > -50°C) was centered over NE Texas, a feature more commonly observed in the tropopause structure of extratropical cyclones.

Spatial and temporal resolution of the constant pressure charts was too coarse to diagnose Allison's structure and determine if, for example, Allison developed a warm core. The charts indicated that temperature gradients were weak through the lower and mid troposphere. For example, no warm core could be discerned at 850 hPa and there was little gradient in the thickness from 850-500 hPa. As a result, the storm center did not tilt with height and the circulation remained closed. But above about 400 hPa, colder temperatures and drier air intruded from the NW and began to wrap around the storm center near the time of maximum intensity so that the flow regime was open.

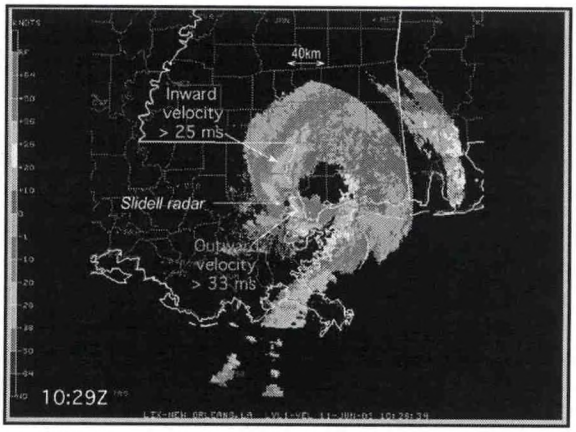

Fig. 1. Nexrad Doppler radial velocity at 1030 UTC at LIX showing large radius of maximum winds

MM5 Simulations

Numerical simulations using the fifth-generation Pennsylvania State University-NCAR Mesoscale Model Version 3 (MM5) were conducted to help diagnose Allison's anomalous intensification following landfall on 11 June 2001. Because model output is sensitive to a range of conditions and parameterizations that can be changed in the model, a large number of runs were made. All runs were initialized at 12 UTC 10 June 2001 and were integrated for 60 hours. For the first series of runs, the NCEP Reanalysis at 2.5° latitude resolution was applied without modification to provide initial and boundary conditions. Model resolution was set with two nested domains at 81 km and 27 km horizontal grid spacing, 23 vertical levels, and a time step of 240 s. Coarse resolution was considered to be adequate in this case since the central eye-like feature and scale of the convection were relatively large. One model run added a third nest with horizontal grid spacing 9 km, which is still too coarse for explicit convection. The inclusion of the inner mesh failed to produce any improvement in accuracy and furthermore, introduced spurious convective lines. In another run, horizontal grid spacing for the two nests was decreased to 45 km and 15 km respectively but the large spatial domain was retained. This run also produced spurious rainbands without any accompanying increase in accuracy.

About 30 combinations of precipitation physics, cumulus parameterizations, and boundary layer (PBL) options were attempted in the Allison simulations. Provided that ice was included, model simulations were least sensitive to further changes in the cloud microphysics options. Most runs used either the simple ice or mixed-phase schemes.

Model simulations were most sensitive to the choice of Cumulus and PBL schemes. The combination of the Grell Cumulus scheme and the MRF (Medium Range Forecast) PBL scheme produced the most accurate simulations. The Grell-MRF produced the most accurate track forecast although all simulated tracks were too slow and ultimately curved incorrectly northward into Alabama. The Grell-MRF was the only combination to deepen Allison over land although it produced the lowest pressure about 3 hours later than observed and only captured about 50% of the intensification (Fig. 2). It produced the strongest southerly surface winds ahead of the squall line and the greatest vapor flux into the storm and was the only combination that produced active convection in a squall line that wrapped around the storm center.

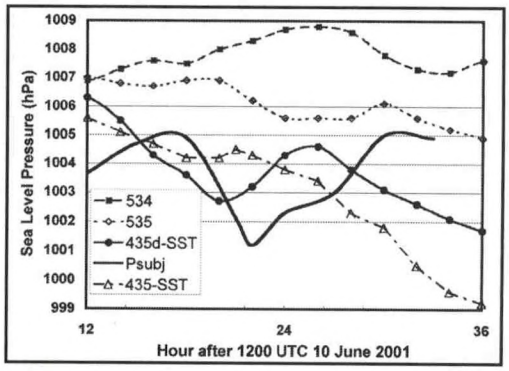

Fig. 2. Minimum surface pressure of Allison vs time for various model runs compared with subjective analysis. 435d-SST represents the run with corrected SST's and increased resolution near the tropopause.

By isolating the impact of the PBL schemes or the

Convective adjustment schemes on the simulation accuracy, the presence and location of convection was revealed to be a major factor in the deepening of Allison. Only the Grell MRF combination developed the region of strong convection near the storm center and the hook-shaped band of high rain mixing ratio on the southeast flank of a cyclone that closely resembled the squall line feature seen on Doppler radar. All the other schemes developed much weaker convection near the storm center while overdeveloping a mesoscale convective cell along the squall line at about 27° N latitude, far south of the storm center. In these simulations considerable flow of humid air was deflected into the outer convective cell, which weakened the southerly flow of humid air into the storm center.

Hendricks, et. al. (2004) used simulations of Hurricane Diana to demonstrate how convection generates vorticity in the lower troposphere as accelerating updrafts stretch vortex tubes and heat the larger scale vortex. The close link between convective updrafts and vorticity generation also occurred in the MM5 runs for Allison despite using a scale too coarse for explicit convection. Initially, the vorticity maxima were colocated with the convection and had similar scale. But in the hours leading up to the time of maximum intensity the scale of the vorticity maximum increased to storm size. Vorticity maxima also developed near storm center in the runs that developed convection far south of the storm center but they remained on a smaller scale, were less organized, and were compromised by other vorticity maxima further to the south.

The great sensitivity of hurricane intensification to Sea Surface Temperatures (SST's) combined with the inadequate simulation of Allison's intensification prompted us to consider the impact of checking SST's. The runs for Allison described above used SST's and surface reservoir temperatures based on the objective analysis of the NCEP data. This introduced a spurious cold strip along the Gulf Coast with values down to 296 K, while measured buoy temperatures remained an almost constant 299.8 for 10 and 11 June. When MM5 was run with manually corrected SST's and reservoir temperatures using the Grell-MRF scheme (435-SST), simulated deepening was more pronounced and occurred sooner and the pattern of convection with the eyelike feature wrapping around storm center at 1200 UTC matched observations most closely (Fig. 3). Simulated central pressure reached a relative minimum of 1004.2 hPa at about 0700 UTC about 3 hours too soon and then resumed falling after 0900. The continued deepening on 12 June was an unrealistic feature of most of the simulations (Fig. 2).

The simulations suggest that Allison's eyelike feature resulted from the wrapping of convection around the low center with a secondary contribution from compensating sinking motion of about 0.25 ms-1 centered at 275 hPa at the western edge of the most active convection. The eye only appears in the radar images and not in the satellite images because the sinking motion was too slow and occupied too small a region to clear the air. Horizontal advection of dry air from the west in the cross sections was also present but occurred too late to cause the eyelike feature. It did, however, ultimately lead to the formation of a dry slot a few hours later.

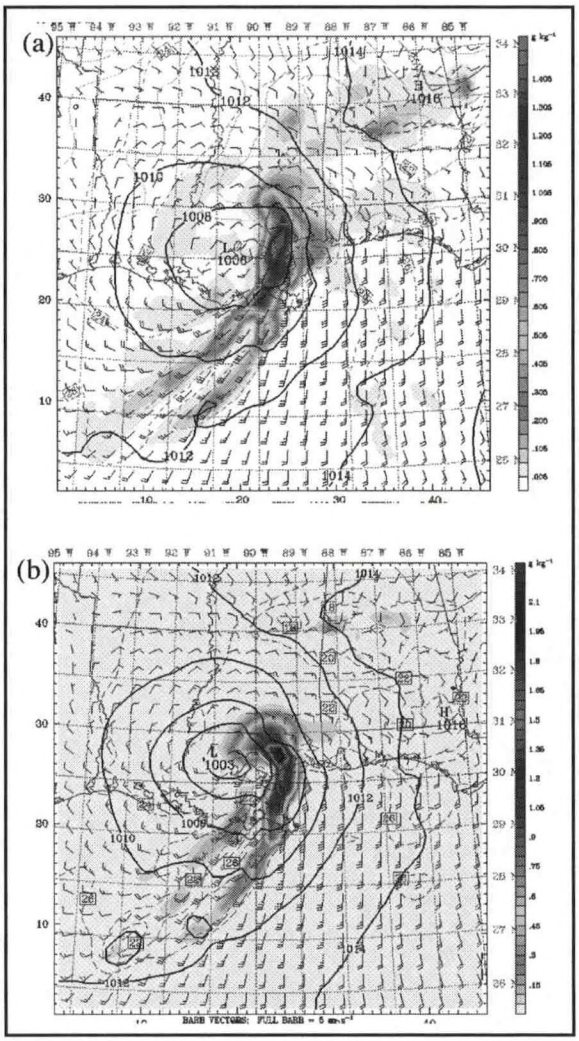

Fig. 3. Sea Level pressure and rain water content depictions of MM5 simulations at 1000 UTC 11 JUN 2001 using the Grell Convective adjustment and MRF Planetary Boundary Layer schemes with (a) objective (535) and (b) corrected SST analysis (Run 435d_SST).

A final experiment was performed to assess the impact of flooded land on Allison's evolution. Ten grid boxes with a total area of 7290 km2 were manually converted from land to sea and the higher SST's measured along the coast were retained. The change of land-use categories had surprisingly little impact on the simulated outcome. If this surprising result is general, it implies that the advection of humid air from a nearby warm sea surface is more important to storm development than vapor flux from wetted land.

Summary and Conclusions

The remnants of Tropical Storm Allison (2003), which produced torrential rains from Texas to Alabama, intensified after making a second landfall in Louisiana early on 11 June 2001. The intensification took place in a weakly baroclinic environment marked by the outbreak of organized convection near the storm center that became coupled to the storm's circulation and formed a feature that resembled an eye. Dry air was later entrained into the storm from the west at high levels and gave Allison a hybrid appearance and structure. As a result, Allison was classified as a subtropical storm.

The storm was analyzed with the help of computer simulations using the fifth-generation Pennsylvania State University-NCAR Mesoscale Model Version 3 (MM5). The model was run with relatively coarse resolution (outer grid 81 km, second grid, 27 km). Refining vertical resolution modestly and adding a third, inner grid with horizontal resolution 9 km had little impact on the simulations other than to add spurious fine scale features. The model was run using a wide range of physics options. Model results showed only small sensitivity to the cloud microphysics schemes provided ice was included. Much greater sensitivity was exhibited to the Cumulus Adjustment and Planetary Boundary Layer parameterization schemes.

The combination of the Grell Convective Adjustment and MRF PBL schemes produced the most accurate simulation because it was the only simulation to develop intense convection near the storm center that became coupled to the storm's circulation. It also generated several vorticity maxima that merged into a single region of maximum vorticity near time of maximum intensity in a manner described by Hendricks, et. al. (2004). The other runs developed a main convective cell far to the south of the storm center that reduced vapor flux into the storm center by deflecting the circulation and furthermore created satellite vorticity maxima. Comparison of the simulations strongly suggests that convection near storm center assists intensification while outer convection appears to be inimical to intensification.

Accuracy of the timing and amount of the simulated deepening were greatly improved by 1: replacing the cold bias of the objectively analyzed sea surface temperatures near the Gulf Coast with higher measured values, and 2: increasing vertical resolution near the tropopause. Simulated vapor flux into the storm's central region increased by over 30% and the central convective feature intensified. This suggests the importance of the proximity of warm ocean waters to storms that intensify over land. However, flooding the land by changing land use categories from swamp or forest to sea had little impact on the simulation. Thus, in the case of Allison at least, adequate moisture for storm development was provided by the nearby Gulf of Mexico waters.

REFERENCES

Anthes, R. A., 1990: Advances in the understanding and prediction of cyclone development with limited-area fine-mesh models. *Extratropical Cyclones: The Erik Palmén Memorial Volume*, C. W. Newton and E. O. Holopainen, eds. Amer. Meteor. Soc., 221-253.

Beven, J. L. II, S. R. Stewart, M. B. Lawrence, L. A. Avila, J. L. Franklin, and R. J. Pasch, 2003: Atlantic Hurricane season of 2001. *Mon. Wea. Rev.*, **131**, 1454-1484.

Dunn, G. E., 1951: Tropical Cyclones. **Compendium of Meteorology**, American Meteorological Society, 887-901.

Grell, G. A., J. Dudhia, and D. R. Stauffer, 1994: A description of the fifth-generation Penn State/NCAR Mesoscale Model (M5), NCAR Tech. Note NCAR/TN-398 + STR, 138 pp. (Available from National Canter for Atmospheric Research, P. O., Box 3000, Boulder, CO 80307.)

Hendricks, E. A., M. T. Montgomery, and C. A. Davis, 2004: The role of "vortical" hot towers in the formation of Tropical Cyclone Diana (1984). J. *Atmos. Sci.*, 61, 1209-1232.

A Transfer Function Model to Estimate Soil Moisture

Nazario D. Ramirez-Beltran[1], Ramon Vasquez[2], Harold Cruzado[2], and Eric Harmsen[3]

[1]Department of Industrial Engineering, University of Puerto Rico, Mayaguez PR, *nazario@ece.uprm.edu*
[2]Department of Electrical and Computer Engineering, University of Puerto Rico, Mayaguez Puerto Rico
[3]Department of Agricultural Engineering, University of Puerto Rico, Mayaguez Puerto Rico.

Abstract

The soil moisture process exhibits spatial and temporal variability. Spatial variability is mostly associated with climate, topography, soil and vegetation classes; where as, the temporal variability is closely related to rainfall and air temperature behavior. A transfer function model is proposed to express the spatial and temporal variability of the soil moisture. The spatial variability is modeled by identifying homogeneous vegetation classes and the time variability by correlating soil moisture with rainfall and temperature. At least one month of hourly observations of soil moisture, rainfall, and temperature is required to identify the structure of the model. Estimation of soil moisture for a selected region requires rainfall observation, which can be obtained either by rain gauges, radar, or satellite. The proposed method is a practical tool that can be used to create accurately initial conditions of soil moisture for regional numerical models such as the regional atmospheric modeling system (RAMS) and the mesoscale model (MM5). Cross-validation techniques show that the proposed algorithm is a reliable procedure for estimating soil moisture. The proposed methodology was successfully implemented to the climate conditions of Puerto Rico. This technique can easily be implemented in other climate conditions; although, it requires a set of few observations to calibrate the model.

Introduction

It is well established that performances of atmospheric numerical models are very sensitive to initial and boundary conditions. The regional atmospheric modeling system, which is being used to simulate the climate dynamics in Puerto Rico, is highly sensitive to soil moisture initial conditions (Comarazamy, 2001). Incorrect initial conditions will generate misleading modeling results, i.e., this article attempts to develop a reliable methodology for estimating soil moisture.

The stochastic behavior of the soil moisture exhibits spatial and temporal variability. The spatial variability is faced by identifying homogeneous vegetation classes across the island, and the temporal variability is attended by building a time series model. The inherent nature of the time series model takes in to account of the temporal variability by analyzing the auto- and cross-correlation functions among the variables of the soil moisture system.

The second section of this paper describes the observations studied in this research. Section three presents the proposed methodology to estimate soil moisture. Preliminary results are shown in section four and conclusions and recommendations are summarized in sections five.

Data

Data used in this study includes three variables: soil moisture, rainfall, and air temperature. These data were obtained from three sources: soil moisture stations, radar, and cooperative stations. Observation collected by soil moisture stations were used to identify the TF model, and data obtained from radar and cooperative stations were used to evaluate the TF model and to extrapolate the soil moisture into a large homogeneous region.

Observations of soil moisture were obtained from five portable stations that were placed in areas, whose spatial variability is homogeneous. Data were downloaded at the end of the month and the station was removed and placed in another location until a representative sample size was completed.

The soil sensor measures the dielectric constant of the soil to estimate its volumetric water content. Data loggers were programmed to record measurements every 10 minutes of the following parameters: soil moisture at one foot depth and at three different locations within a radius of 50 feet from the location of the data logger, air temperature and rainfall sensors were installed at about 3 and 4 feet from the floor, respectively.

Cumulative rainfall was estimated based on reflectance given on an hourly basis within spatial resolution of 5 Km. The empirical equation used to convert reflectance into inches per hour was developed by the Local Weather Forecast Office and has the following form (Roche and Vasquez, 2001):

$$L_{t,j} = 250 R_{t,j}^{1.2} \quad (1)$$

Where $R_{t,j}$ is the rainfall in inches at time t and at location j, $L_{t,j}$ is the reflectance measured at time t and at location j. Radar observations (NEXRAD) were provided by the National Weather Service and the nearest grid was used to estimate the required point location. Daily maximum and minimum air temperature were obtained from the National Climatic Data Center. Twenty two stations were used to interpolate temperature at the required grid location.

Soil Moisture Modeling

The soil moisture process may be better understood by studying the water balance system, which can be described as follows: Precipitation that falls in the land surface of Puerto Rico or in other tropical area can follow four major pathways: runoff, percolation, evapotranspiration, and soil moisture. The runoff is mostly related to the amount of precipitation, topography, vegetation, and soil types. Part of the precipitation that penetrates into the water table is called percolation. It should be noted that percolation rate is primarily dependent on the soil type. Essentially, evapotranspiration is the amount of precipitation that goes back into the atmosphere as a water vapor and this variable heavily depends on the air temperature, elevation, vegetations and soil types. Soil moisture is the remaining precipitation that is kept in the soil layer, and heavily depends on rainfall, temperature, elevation, soil type, and vegetation class. Based on the analysis of the water balance system and on the limitations of available data the following assumption was postulated. The soil moisture is a function of the following variables: the amount of instantaneous and cumulated precipitation, air temperature, elevation, vegetations and soil types. Thus, a stochastic behavior of the soil moisture can be represented by a transfer function model.

A TF model represents the interactions of the variables involved in the soil moisture process. The TF model pretends to express the spatial and temporal variability. The spatial variability is mostly characterized by the influence of the following variables: elevation, rainfall, air temperature, and vegetation and soil types. Spatial variability will be modeled by identifying homogeneous regions across the island and inside of each region the temporal variability will be model by using the TF model, which is an extension of the univariate time series model. The proposed methodology includes two major steps: 1) Identify the spatial variability. and 2) Model the temporal variability.

Identifying Spatial Variability.

One of the most comprehensive studies of vegetation in Puerto Rico (PR) was conducted by Helmer et al., (2002). They used a segmented and supervised classification method to identify 32 vegetations classes in PR. They used information from Landsat imagery, soil types, topography, rainfall and temperature to identify the vegetations classes in Puerto Rico during the period of 1991-92. They pointed out that in PR a single and the most extensive area is the pasture vegetation class and covers 36.7% of the island surface, 321,011 ha. It is well known that climatology, topography and soil type are highly correlated with vegetation classes, then the spatial variability of soil moisture is mostly expressed by the vegetations classes.

Modeling Temporal Variability

The stochastic interaction among soil moisture with rainfall and air temperature can be represented by a TF model. The concept of a TF model derives from the idea of cause and effect relationship among the input and output variables of a dynamic system (Box, and Jenkins 1976; Brockwell, and Davis, 2002). The input variables of the soil moisture system transfer into variations to the output variable of the system. Thus, the input variables are the air temperature and rainfall, and the system response (output) is the soil moisture. Sampling field observations show that the soil moisture is driven by the cumulated rainfall and air temperature when instantaneous rainfall event is not present. However, a significant response on the soil moisture is observed under the presence of an instantaneous precipitation event with large spell of no rainfall. On the other hand, if the soil is saturated (or reaches its hold capacity) with large spell of cumulated rainfall then the response of the soil moisture to the next rainfall event is marginal. Figure 1 shows sampling observations obtained during the period of June 16-23, 2004 where the sequence of dry spell and an instantaneous rainfall of 0.25 in/hour generates a large response on soil moisture. Figure 2 shows observation obtained from the same station during the period of July 3-16, 2004. This figure shows the cumulated rainfall increases so that the soil almost reaches its hold capacity and the response of the soil moisture is very small, even though the instantaneous rainfall event is very large, 1.25 in/hour. These observations show evidence that the dynamics of the soil moisture system can properly be modeled by a TF model.

On figures 1-2 the upper curve is air temperature (divided by a constant), in the middle the soil moisture is shown and on the bottom is the rainfall given.

The TF model that represents the soil moisture system for Puerto Rico has several input variables in addition of the noise component. However, because of data limitations only two input variables were considered: rainfall and air temperature. The sampling interval was 1 hour.

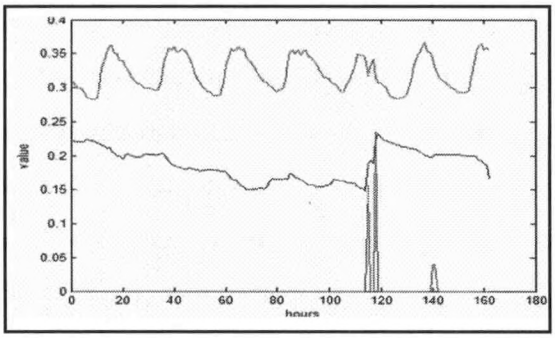

Figure 1. Sampling from June 16-23, 2004.

Temperature Model

The hourly air temperature model has three major components: periodic, impulse-response, and noise components. Thus, the introduced hourly air temperature can be written as follows:

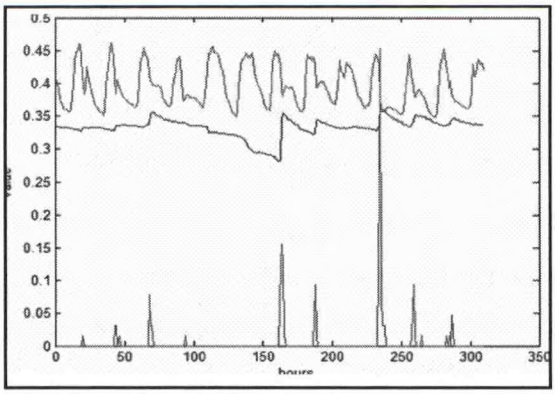

Figure 2. Sampling from July 3-16, 2004.

$$T_{t,j} = m_{t,j} + \nu_j(B)R_{t,j} + \alpha_{t,j} \quad (1)$$

Where

$$m_{t,j} = a_{0,j} + a_{1,j}d_{(i)t,j}\sin\left(\frac{2\pi t}{24}\right) + a_{2,j}d_{(i)t,j}\cos\left(\frac{2\pi t}{24}\right) \quad (2)$$

$$d_{(i)t,j} = T\max(i)_{t,j} - T\min(i)_{t,j} \quad (3)$$

$$\nu_j(B) = \frac{\omega_{0,j} - \omega_{1,j}B - \omega_{2,j}B^2 - \mathrm{L} - \omega_{r,j}B^{r_j}}{1 - \delta_{1,j}B - \delta_{2,j}B^2 - \mathrm{L} - \delta_{s,j}B^{s_j}} \quad (4)$$

$$\alpha_{t,j} = \frac{1 - \theta_{1,j}B - \theta_{2,j}B^2 - \mathrm{L} - \theta_{q,j}B^{q_j}}{1 - \phi_{1,j}B - \phi_{2,j}B^2 - \mathrm{L} - \phi_{p,j}B^{p_j}}Z_{t,j} \quad (5)$$

where the variable $m_{t,j}$ is the mean periodic component at time (hour) t, and at location j. The 24 hours periodic component is generated by the solar energy, and the amplitude of this component is modulated by the variations of the maximum and minimum daily temperatures, $d_{(i)t,j}$. $T\,max_{(i)t,j}$ and are the maximum and minimum air temperature for the ith day, at time t and at location j, and the $a_{i,j}$ are the specific

coefficients associated to the j location. The air temperature is significantly affected by the rainfall intervention, and especially if precipitation falls during the highest temperature of the day. The parameters ω_j's and δ_j's are the coefficients of the TF function at location j; this function is also known as the impulse response function, B is the back shift operator, and the variable $R_{t,j}$ is the hourly rainfall at time t and at location j. The rainfall variable is a pulse function which is greater than zero when rainfall occurs and zero when precipitation does not occur. The pulse function generates significant reduction of air temperature and disappears with and exponential decay of δ_j's values. There exists other factors that affect the behavior of the hourly temperature such as clouds and wind dynamics interaction; however, since these variables are very difficult to measure across the island on an hourly basis and since their effects on air temperature are marginal, they are considered as members of the noise component, $a_{t,j}$. The noise is expressed as an autoregressive and moving average process as shown by equation (5), where $z_{t,j}$ is a white noise process, i.e., it is a sequence of independent random variables with mean equal to zero and constant variance (Box and Jenkins, 1976).

Soil Moisture Model

The soil moisture process exhibits short and long term memory responses. The long term memory is the response of the soil moisture to a climate patterns, topography and soil types. The short term memory is the soil moisture response to current and temporary, and typically are the events that occurred during the last 24 hours and seriously impact the soil moisture.

In this article a model is proposed to estimate soil moisture and has four major sources: the trend component, rainfall intervention, temperature effects, and noise component. The model can be written as follows:

$$h_{t,j} = n_{t,j} + v_{1,j}(B)R_{t,j}e^{-y_{t,j}} + v_{2,j}(B)T_{t,j} + \varepsilon_{t,j} \quad (8)$$

Where

$$n_{t,j} = b_{0,j} + b_{1,j}d_{(i)t,j} + b_{2,j}Q_{t,j} + b_{3,j}\tau_{t,j} \quad (9)$$

$$Q_{t,j} = \begin{cases} \ln(y_{t,j}), & y_{t,j} > 0 \\ 0, & \text{otherwise} \end{cases} \quad (10)$$

$$y_{t,j} = \sum_{i=t-\rho}^{t} R_{i,j} \quad (11)$$

$$\tau_{t,j} = \frac{1}{\rho}\sum_{i=t-\rho}^{t} T_{i,j} \quad (12)$$

The $h_{t,j}$ variable is the soil moisture at time t over the j^{th} region. The variable $n_{t,j}$ represents the trend component and models the long term memory of the soil moisture. The trend component has four major sources: the average soil moisture from climatological and topographical patterns, the 24-hours gradient temperature, the cumulative rainfall during the last 4 days, and the average air temperature during the last 4 days. The variable $d_{(i)t,j}$ is the gradient temperature that occurred during the last 24 hours and was defined by equation (3). The 24-hours gradient temperature is essentially the result of the sun energy affected by cloud coverage and wind dynamics. This gradient provides a linear effect to the soil moisture, the larger the gradient the smaller the soil moisture. Equation (9) tries to model this linear relationship. The variable $Q_{t,j}$ is the cumulative rainfall during the last 4 days and increases the soil moisture in a logarithmic manner. Equations (9) and (10) try to express these relationships. The variable $\tau_{t,j}$ represents the moving averages air temperature during the last 4 days, and it is computed at time t and at the location j. This moving average varies linearly with the soil moisture, the larger the average the smaller the soil moisture. Equation (9) tries to represent this relationship. The parameter ρ represents part of the long term memory and in this case $\rho = 96$ hours. The ρ value was estimated by minimizing the sum of

square errors. The variable $\varepsilon_{t,j}$ is the noise component of the model.

Preliminary Results.

An arbitrary point was selected to implement the proposed methodology. Radar data were used to interpolate and obtain the hourly estimates of rainfall at selected gridded point, which is located on the pasture vegetation class at the following coordinates: La= 18o 3′ 14.6″, and Lo=-67o 3′ 31.6″. The nearest neighbor algorithm was used to estimate the rainfall. Figure 3 shows the estimated hourly rainfall for the November 2003. Temperature model equation (1) was used to estimate the hourly air temperatures for the same period of time and results are shown in Figure 4.

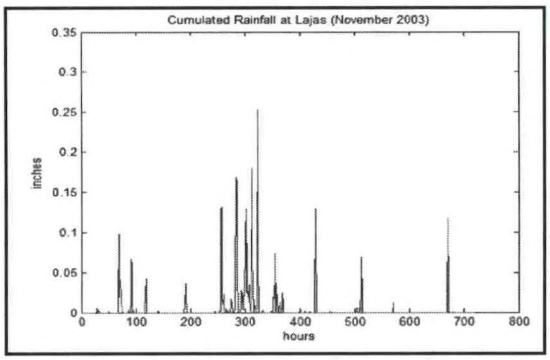

Figure 3. Rainfall on pasture vegetation class.

The identified model equation (8) was used to estimate the temporal variability of soil moisture using the estimated air temperature and rainfall process. The estimated soil moisture is shown in Figure 5.

Figure 6 shows the soil moisture estimates only for the pasture vegetation class, which cover about 40% of Puerto Rico surface. The map shows the average estimates of soil moisture for November 2003 at one km resolution. The average soil moisture varies from 12% to 55%. This Figure 5 shows the temporal variability for a single point while Figure 6 shows the spatial variability of soil moisture.

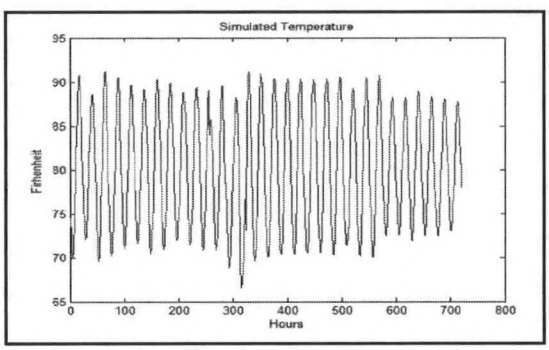

Figure 4. Hourly air temperature.

Conclusions

A new method is proposed to estimate soil moisture on an hourly basis. These estimates can be used to generate the initial condition of a regional atmosphere model. This methodology can easily be implemented into other climatic conditions, after properly performing model calibration.

The proposed soil moisture model exhibits short and long term memory. The long term memory is modeled by using climate and topography patterns, the gradient temperature that occurs during the last 24 hours and also the cumulated rainfall, as well as the average temperature during the last four days. The instantaneous rainfall and air temperature are used to model the short term memory. Air temperature model was also used to estimate the hourly temperature.

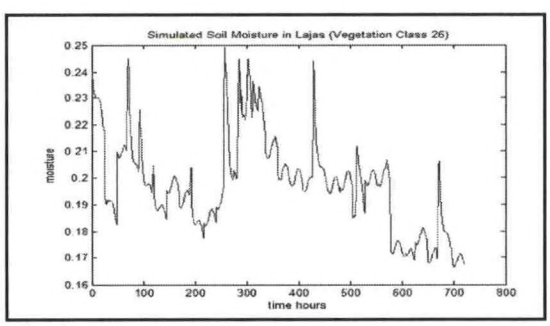

Figure 5. Estimation of soil moisture

Cross-validation technique shows that the proposed model is an appropriate method to estimate the soil moisture.

Elevation, soil and vegetation classes are inherent into the spatial variability of soil moisture, while precipitation and air temperature are mostly associated with time variability.

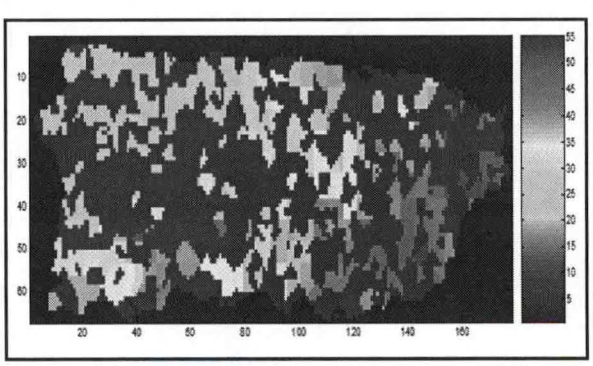

Figure 6. Estimation of soil moisture for the pasture vegetation class

ACKNOWLEDGMENTS

This project has been supported by NOAA-CREST grant number NA17AE1625. Authors appreciate and recognize the funding support this institution.

REFERENCES

Box, G.EP., and Jenkins, G.M., (1976). *Time Series Analysis: Forecasting and Control*, Holden-Day, Oakland, CA.

Brockwell, P.J., and Davis, R.A., (2002). *Introduction to Time Series and Forecasting*, Second Ed., Springer, New York.

Comarazamy, D.E., (2001). *Atmospheric Modeling of the Caribbean Region: Precipitation and Wind Analysis in Puerto Rico for April 1998*, Master Thesis, Department of Mechanical Engineering, University of Puerto Rico, Mayaguez, PR.

Helmer, E.H., Ramos, O., Lopez, T.D.M., Quiñónez, M., and Diaz, W. (2002). Mapping the Forest Type and Land Cover of Puerto Rico, a Component of the Caribbean Biodiversity Hotspot. *Caribbean Journal of Science*, Vol., 38, No., 3-4, 165-185.

Roche, A., and M. Vasquez, (2001). An Evaluation of WSR-88D Rainfall Estimates Across Puerto Rico During Hurricane Debbie. NEXRAD WFO-San Juan # 4000 Rd 190 Carolina, PR

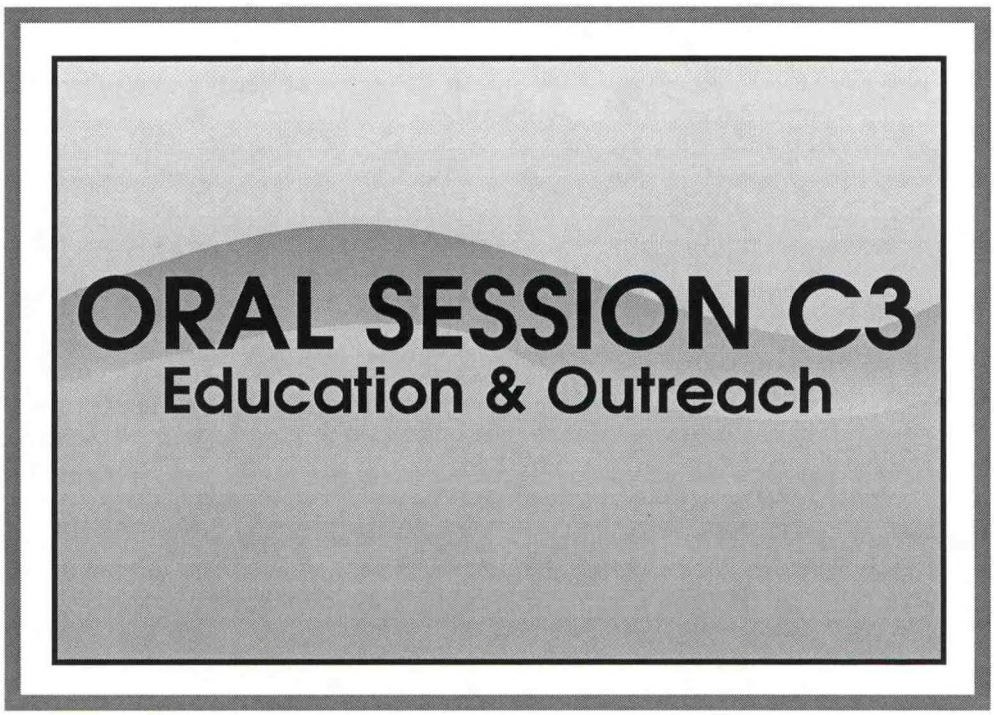
ORAL SESSION C3
Education & Outreach

EDUCATIONAL OUTREACH AND RECRUITMENT PROGRAMFOR MINORITY HIGH SCHOOL STUDENTS

Dr. Reid Strieby

Professor of Social Science, Director of the BCC Environmental Entrepreneurship Program
Faculty Member, NOAA CREST Program, CCNY

This presentation focuses upon a series of outreach and recruitment activities that faculty and staff from Bronx Community College's Environmental Entrepreneurship and Environmental Technology programs, as well as, faculty and staff of the NOAA CREST Center at CCNY have developed over the past two years. Our primary goal has been to increase the number of minority high school students interested in science and to create educational pathways that provide career direction and easy transferability for students to pursue careers in Environmental Science from high school, to college (both community and senior level), to graduate school.

To achieve this goal we have created a number of joint environmental research projects (with high school students/teachers and college faculty), established a team of high school science students and teachers at the Bronx High School of Science to compete in the NOAA Ocean Science Bowl, developed an enhanced education/training program for high school science instructors teaching Earth/Environmental Science classes to increase the teaching skills and research knowledge and made on site presentations related to the NOAA CREST Program at CCNY to large groups of students at BHSS interested in science.

In addition, we have created college level Advanced Standing courses in Chemistry, Math and Environmental Science at five Bronx high schools and linked our efforts to the Tech Prep and College Now Programs to significantly increase the number of students being prepared for college level study of science courses.

Fostering Entrepreneurship in Female Minority Marine Science Graduate Students

Burton V. Dean, SJSU; Asbjorn Osland, SJSU; Frederika Harmsen, Fresno State; H. Gary Greene, MLML[1]

Goal & Objectives

The goal of this three-year (2003-2006) project is to foster environmental entrepreneurship to engage minority marine science graduate students to promote economic development opportunities. The specific objectives are (1) to provide training and research opportunities to minority graduate students in the techniques and methodologies needed to map deep-water marine benthic habitats; and (2) to provide student entrepreneurship training, both in terms of coursework and complementary programs, to develop the necessary business and entrepreneurial skills, knowledge and practical experience to create and maintain a sustainable competitive advantage as entrepreneurs subsequent to graduation.

Mission

The mission of the project is the following:

- ***Education.*** Fresno State needs to prepare minority students in areas of scientific training and environmental entrepreneurship by providing them with skills, knowledge, and the necessary business acumen to create and maintain a sustainable competitive advantage.
- ***Capacity Building.*** Fresno State will build viable channels and mechanisms that ensure minority students enter and succeed in the sciences and environmental entrepreneurship.
- **Partnerships.** The project will build an institutional network with Fresno State, SJSU, MLML, CSUMB and private and public organizations. The MLML Center for Habitat Studies (CHS) has already served many public agencies and private organizations (foundations and companies). In particular, CHS has a long and productive history with various NOAA programs, laboratories and facilities. Specifically, CHS engages in deep-water marine habitat mapping for rockfish (Sebastes) and other bottom fish that address Essential Fish Habitat (EFH) and other mapping problems. Additionally, the CHS is working collaboratively with various NOAA National Marine Fisheries Service (NMFS) laboratories in Auke Bay, Alaska, Seattle, Washington, and Santa Cruz, California. These and other NOAA laboratories fund much of the habitat mapping work conducted at CHS.
- **Community Economic Development.** Economic development is envisioned at two levels: (1) MLML's industrial associates and (2) incubators. Contributions from industrial associates such as Thales Geosolutions (Pacific) of San Diego, CA and Triton-Elics of Watsonville, CA help support the MLML Habitat Center and provide technical assistance when needed. Such companies can serve as models and springboards for minority students. Local incubators, including the San Jose Software Business Cluster (SJSBC) and the Environmental Business Cluster (EBC), will partner with San Jose State University.
- ***Technical Training in "Deep-Water Marine Benthic Habitat Mapping Demonstration Project":*** MLML and Fresno State will train marine science undergraduate and graduate students about the techniques and methodologies needed to map deep-water marine benthic habitats; this entails geophysical data collection and interpretation.

Institutions Involved

Fresno State is a Minority Serving Institution and the grant's lead institution. Serving over 21,000 students in central California's San Joaquin Valley, Fresno State is one of the largest Hispanic-serving institutions in the California State University (CSU) system. The combined ethnic minority enrollment at

[1]SJSU refers to San Jose State University. MLML is Moss Landing Marine Laboratories, the graduate marine sciences program of CSU.

Fresno State is 53.3%, which includes Hispanic (32.7%), Asian (13.6%), African American (5.7%) and Native American (1.3%). Hispanic enrollment has increased 35.4% over a seven year period (1994-2001) and is projected to increase to nearly 40% of the student body in the next four years.

MLML's Center for Habitat Studies (CHS) was established as the geophysical institute of MLML in 1994 to focus on the research of characterizing marine benthic habitats and marine and coastal geo-hazards. Since that time, the CHS has grown into a geological and biological research facility that now leads in the field of deep-water marine benthic habitat mapping. The primary focus of the CHS is to characterize marine deep-water rockfish habitats for protecting recruitment stocks and sustaining demersal fisheries. The CHS is an interpretive institute that uses digital multi-beam bathymetric data (bathymetry xyz and backscatter data), analog and digital side-scan sonographs, seismic reflection profiles, and other geophysical data to construct various thematic maps. These include bathymetric artificial sun-shaded relief, geologic, geomorphic, geologic structure and hazards, habitat, slope inclination, roughness derivative and other specialty maps. Many of the maps produced at the CHS are used for managing marine fisheries.

SJSU and CSUMB will provide the project's entrepreneurship training. SJSU grants bachelor's and master's degrees in 134 areas. It is one of the 200 top research universities in the US with more than 30,000 undergraduate and graduate students in eight colleges. Silicon Valley companies employ more graduates of SJSU than from other universities. SJSU, in Fall 2002, had 30, 350 students of whom 54% were women and 59% minorities (32% Asian American, the largest minority group). CSUMB, a Minority Serving Institution, had 3,551 students in 2002, its 8th year of operation. 60% were women and 37% minorities (26% Hispanic, the largest minority group).

Mapping Marine Benthic Habitats

Students are to develop interpretive skills needed for mapping marine benthic habitats. Emphases will be on geophysical data interpretation and habitat characterization. Tools such as multi-beam bathymetry and backscatter, side-scan sonar, and seismic-reflection (sub-bottom) systems will be introduced and their application to mapping explained. Multi-beam and side-scan sonar processing techniques (i.e. Caris, MBSystem) and GIS software (TNTMIPS, ArcView) will also be introduced.

Hands-on, at sea data collection will occur, and the students will be involved in the production of habitat maps from data collection and interpretation to the printing of a map and construction of a digital GIS map with associated attribute codes. This project is interdisciplinary and will benefit interest in both geology and biology. Participation on active research projects will be offered.

The minimum expectations for a student completing the proposed training are as follows:

a) To design a marine benthic habitat mapping survey under specific cost limitations utilizing the latest technologies while addressing specific biologic criteria, such as focusing on a target species.

b) To evaluate various geophysical data sets in regard to the application of habitat mapping.

c) To process multibeam bathymetry/backscatter and side scan sonar data.

d) To scan and georeference maps of various projections.

e)To export georeferenced maps into a GIS using TNT Mips® or other software.

f) To edit line work and attribute polygons in a GIS for the purpose of producing marine benthic habitat maps.

Scientific and Educational Methodologies

Marine geophysics, geology and biology are the primary scientific and educational subjects to be addressed. In addition, participants will be introduced to the developing curriculum of marine benthic habitat mapping at Moss Landing Marine Laboratories.

Description of Entrepreneurship Curriculum

The basic entrepreneurship curriculum consists of five courses, one course per semester, spread over five semesters, leading to a Graduate Certificate in Entrepreneurship. Four will be taken at California State University Monterey Bay (CSUMB) since it is located only 12 miles from MLML where they take their

masters degree coursework in marine biology. SJSU is 55 miles from MLML and therefore too far for convenient commuting on a bi-weekly basis. The five courses are as follows:

- SJSU BUS 160 - Fundamentals of Management and Organizational Behavior: Provides a foundation for major topics in management and organizational behavior by surveying theories and practices relating to managerial roles, organizational cultures, fundamental strategic issues, planning, team building, communication, motivation, leadership, decision-making, control, structure and change. (Note: This course is a foundation course since the NOAA students do not have business backgrounds. It will be taken at a distance from SJSU). (3 credits) (Note: A comparable course may be offered at CSUMB, which would be more convenient for the graduate students)

- CSUMB BUS 310 - Entrepreneurship: Focus on the entrepreneurial process, opportunity recognition, entry strategies, market opportunities and marketing, creation of a successful business plan, financial projections, venture capital, debt and other forms of financing, external assistance for startups and small businesses, legal and tax issues, intellectual property, franchising, and entrepreneurship economics. Internet and eCommerce examples are provided. (4 credits)

- CSUMB BUS 322 Product Management and Marketing for Startups: Millions of products are launched each year, but the vast majority fail. Success requires not only effective personal skills but also effective management and marketing competence. This course focuses on the creation and development of innovative products and the necessary characteristics of businesses and markets associated with the success of such products. Investigates attributes of product success by scrutinizing the entire process of product creation, development, and launch. (4 credits)

- CSUMB BUS 651 Venture Formation and Financial Strategy: Prepares students from Business Administration or other academic programs to pursue technology-based new venture opportunities. Topics include opportunity, recognition and evaluation; new venture strategies and formation; marketing; financial management; entrepreneurial finance; and the process of sustaining organizational vision. Students prepare and defend a business plan, and identify sources of financing. If they have a promising opportunity, students receive assistance in approaching potential sources of capital and other resources. (4 credits)

- SJSU BUS 182 Business Plans for New Ventures: An integrative course involving teamwork to prepare complete plans for starting a new business. This will require analyzing the industry and potential market, the competitive advantage of the business proposition, human and financial resource requirements and the founders' skills. (3 credits). (Note: A comparable course may be offered at CSUMB, which would be more convenient for the graduate students).

The value proposition and initial marketing plan should be presented in the fall semester at the Neat Idea Fair and the formal business plan competition at SJSU. The student could go on and enter the Department of Commerce Minority Youth Business Plan Competition and others as well.

The entrepreneurship assignments will be integrated with the technical areas covered at MLML to the extent possible. The SJSU entrepreneurship Co-PIs will meet face to face with students at MLML for group discussions, to provide feedback, and also to provide time for individual meetings. Students will take the CSUMB courses either online or in class.

Complementary Support to Cohort

Students form an entrepreneurship cohort to enhance social support between students and to stimulate dialog on entrepreneurship. They would take the above mentioned courses and would participate in a variety of complementary activities designed to enhance their exposure to entrepreneurship. Such complements include: summer internships; Business Plan Competition; Entrepreneurship Corporate Classroom; Entrepreneurship Seminars by Practitioners; E-Teams, with technical service assistance and mentors and support for E-teams; incubators, including follow-up, all discussed below.

Summer Internships

Internships will be arranged with local companies and organizations with projects consistent with the interests and needs of the students.

Business Plan Competition

Students are given an opportunity to explore by merging theory and passion into a viable project. Competitions showcase the capabilities of students. Our competition would focus on utilizing new and innovative technologies to address environmental issues.

Entrepreneurship Corporate Classroom

Through the Entrepreneurship Corporate Classroom we will expose students to university-affiliated incubators and associated high tech start up companies and principals through plant tours and discussions with key executives. These visits provide students with first hand learning experiences, not available in the standard classroom learning experiences, even with guest lecturers. Typically the CEO addresses the students, providing background information. Afterwards, the students will interview a high tech startup firm's principals, including a Q & A session afterwards.

Entrepreneurship Seminars by Practitioners

The purpose of these activities is to give students and faculty exposure to real-life entrepreneurs who are invited to the campus. Seminars are planned for every other month in which an entrepreneur or panel of entrepreneurs discusses entrepreneurial issues.

E-Teams

E-teams are interdisciplinary, multicultural, and collaborative. The cohort will form one or two E-teams. E-team projects will be a required part of several courses, where students are to develop value propositions and marketing concepts and finally business plans, containing market analysis, financial projections and resource needs, implementation plans, and a schedule of important milestones. E-teams will make presentations of their business plans to review panels in the business plan competition comprised of faculty, entrepreneurs, and community mentors at several junctures during the process. The business plan competition concludes the process with a final review by a panel of industry executives, entrepreneurs, venture capitalists and technology experts. Winners receive monetary awards funded by the community.

Students are to learn the entrepreneurial process of invention, innovation and business creation through drafting a business plan as though they were going to launch a business.

Measurable learning objectives include:

- creativity and product/service development – creation of a viable product or service;
- teamwork and group problem solving - students will reflect on team process;
- effective communication – emphasis on writing and presentation skills;
- research and critical thinking – faculty will evaluate students' abilities at using published information as well as seeking out knowledgeable people to interview, and the students' ability to process the information; and
- business plan development – the review panel will assess the viability of the plan from technical, marketing, management, and financial perspectives.

Technical Service Assistance, Mentors and Support for E-teams

Some specific questions go beyond the expertise readily available from faculty with full teaching loads and volunteer mentors. Hence, technical service advisors are crucial to the success of the e-teams. The faculty mentors will seek out technical and business experts from Silicon Valley and Monterrey Bay and beyond that will provide consulting and technical support to the E-teams. Specific technical issues that may have to be addressed include access to market research studies only available commercially, financial projections and resource allocation, business plan review, consultation with cutting edge technical experts and the like.

Incubators

"The Marina Technology Cluster is a not-for-profit business accelerator assisting early-stage companies in the marine science, agriculture technology and information technology sectors through a com-

prehensive series of services and programs." It is sponsored by the City of Marina and the University of California's Monterey Bay Education, Science and Technology (MBEST) Center [www.ucmbest.edu]. Like other incubators, the Marina Technology Cluster works with startups or early-stage companies but focuses on marine science, agricultural technology and information technology sectors. Like other incubators, it provides guidance to build business skills and networks. The Cluster offers one-on-one coaching, an Executive Associates Program that provides business consulting on a pro bono basis, helps prepare companies to raise capital, hosts Brown Bag Lunches featuring speakers on relevant topics, a Monthly CEO Roundtable, varied Education and Training Programs, connections to regional institutions, and shared conference rooms and office resources.

The Environmental Business Cluster (EBC) and the Software Business Cluster (SBC) are incubators based in San Jose and affiliated with SJSU that could provide support for startups focused on environmental issues or software.

Career Planning and Placement

SJSU will work closely with MLML and CSUMB to follow up the demonstration project with career planning. The SJSU Career Planning and Placement Office offers a variety of services, including counseling on professional choices, coaching on resume writing and interviewing techniques, and hosts what have been very successful expositions where prospective employers meet students.

Graduate Students in Project

After a national search, five marine science graduate students were selected. All are women and have the following undergraduate majors (listed also is the college/university):Earth Systems Science and Policy from CSUMB; Biology from Bates College (Lewiston, Maine); Wildlife, Fish, and Conservation Biology, from UC Davis; Aquatic Biology, UC Santa Barbara; and Zoology, UC Santa Barbara. The students are all of minority ethnicity. Their accomplishments include interesting related work, research (e.g., Research Experiences for Undergraduates), presentations and even co-authored publications.

NCAS Oceanography and Remote Sensing Research and Educational Activities

Roy A. Armstrong, Yasmín Detrés, and Vernon Morris*

NOAA Center for Atmospheric Sciences (NCAS), University of Puerto Rico, Mayaguez Campus,
* Howard University, Washington, DC

Abstract

The main research objective of the NOAA Center for Atmospheric Sciences (NCAS) at the University of Puerto Rico, Mayaguez Campus (UPRM), has been the characterization of Saharan dust aerosols across the Atlantic Ocean. Sampling campaigns have been conducted in Puerto Rico, Dominica, Canary Islands, and in the open ocean during several oceanographic cruises. At-sea training in oceanographic and atmospheric measurements has taken place during short cruises aboard the R/V Chapman and during the AEROSE Trans Atlantic expedition aboard the NOAA Ship Ronald H. Brown. The main goal of AEROSE was to study the impacts and microphysical evolution of Saharan dust aerosols as they are transported across the Atlantic Ocean. The mission encompassed both atmospheric and oceanographic components presenting a unique opportunity to study the effects of dust on upper ocean biogeochemistry, water optics, and phytoplankton. Another leading research and education activity of NCAS has been the use of satellite remote sensing data to study possible links between aerosols and ocean color in the tropical western Atlantic Ocean. Time series analyses of AVHRR, SeaWiFS, and MODIS sensor data have been conducted to address these objectives. At-sea training in oceanographic and atmospheric measurements has taken place during the cruises. A series of seminars and two courses were organized and conducted during AEROSE for both UPRM and Howard University students. Remote sensing workshops have been offered at UPRM during the last three summers with the participation of NCAS partner institutions and other EPP/MSI centers. An advance remote sensing course was in the summer of 2004 and had the participation of 18 students from five institutions.

Introduction

The main research and educational goal of the NOAA Center for Atmospheric Sciences (NCAS) at the University of Puerto Rico, Mayaguez Campus (UPRM), involves the study of Saharan dust aerosols as they cross the Atlantic Ocean reaching the Caribbean Region. We conduct mass measurements at PM2.5 and PM10 size fractions, measure optical properties, and characterize bioaerosols. Field measurements are used to validate remote sensing estimates of aerosol optical thickness (AOT) and near-surface chlorophyll concentrations. Students are involved in all aspects of the research including field sampling, laboratory and data analysis, and image processing.

Several cruises aboard the UPRM's R/V Chapman to the eastern Caribbean have been conducted with the participation of UPRM and Howard University (HU) students and faculty. The March 2004 Aerosol and Ocean Science Expedition (AEROSE) aboard the NOAA Ship Ronald H. Brown (Figure 1) has been the most important cruise conducted so far. The AEROSE 2004 presented the unique opportunity of studying dust aerosols as they cross the Atlantic Ocean and their impact on atmospheric and oceanographic parameters. A series of seminars and two courses were organized and conducted during AEROSE for both UPRM and Howard University students.

Figure 1. The NOAA Ship Ronald H. Brown

We use satellite remote sensing data to study possible links between aerosols and ocean color in the tropical Western Atlantic Ocean. Time series analyses of AVHRR, SeaWiFS, and MODIS sensor data have been conducted to

address these objectives.

AEROSE 2004

The main mission of AEROSE was to provide a set of critical measurements to characterize the impacts and microphysical evolution of Saharan dust aerosol transport across the Atlantic Ocean. The 27 day mission on the NOAA Ship Ronald H. Brown began on February 29, 2004 in Bridgetown, Barbados and ended in San Juan, Puerto Rico on March 26. Over thirty-five scientists and students participated in the cruise, including ten students from UPRM and HU.

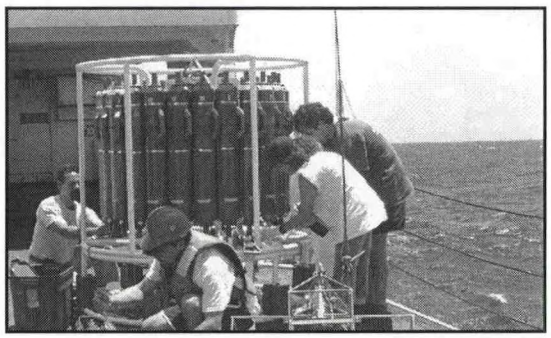

Figure 2. Scientists and students collecting water samples from the CTD/rosette system during AEROSE.

In conjunction with the efforts to characterize this dust plume emanating from the African continent, we carried out oceanographic and bio-optical observations to study the effects of the dust on the marine boundary layer, characterize water masses throughout the transect, and investigate upwelling conditions off the Northwest coast of Africa. Continuous near-surface sampling was conducted throughout the cruise track using the ship's flow-through system while depth profiles of physical, chemical and biological parameters were obtained at five oceanographic stations using a CTD/rosette system (Figure 2).

These measurements were used to test the hypothesis that deposition of iron and inorganic nutrients from atmospheric aerosols modulates biogeochemical processes in the ocean by fertilizing surface waters enhancing planktonic primary production.

AEROSE provided satellite validation experiments for three satellite instruments: the NOAA Advanced Very High Resolution Radiometer (AVHRR, measuring sea-surface temperature and column water) aboard the NOAA Polar Orbiter, the NASA Moderate Resolution Imaging Spectrometer (MODIS, measuring column water, temperature profile, and aerosol optical thickness) aboard the AQUA and TERRA satellites, and the Atmospheric Infrared Sounder (AIRS, measuring air temperature, surface temperature, and column water) also aboard the AQUA satellite. The validation experiments consisted of hourly sun photometer measurements, 3-hourly radiosonde launches, and sea-surface temperature (SST), skin temperature, and surface temperature measurements taken every minute throughout the cruise.

AEROSE Education and Outreach

AEROSE featured a strong educational and outreach component as well. On board the ship, the AEROSE science team organized and conducted a series of open seminars for participating students, crewmembers, and scientists during the cruise (Figure 3).

Over twenty separate presentations were delivered during the course of the mission. The cruise progress was followed by middle school students at St. Thomas More in Washington, DC and by two elementary schools from the cities of San German and Mayaguez, Puerto Rico. An interactive website maintained at NESDIS featured a daily log from the ship, location-tracking, satellite imagery, question-and-answer communications between scientists and students, and photos of the research activities. AEROSE scientists fielded questions from the schoolchildren as well as from the general public throughout the cruise.

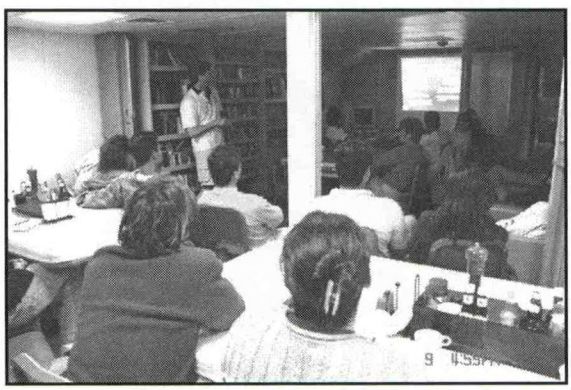

Figure 3. Lecture series during AEROSE.

Remote Sensing

MODIS Terra weekly images were analyzed to extract Tau 865 and Chlorophyll-a data for years 2002 – 2003. Data were acquired from 15 x 15 pixel boxes in the Caribbean Sea and Atlantic Ocean (Figure 4).

The selected regions differ in their water optics and biogeochemical characteristics. Station 1 is located

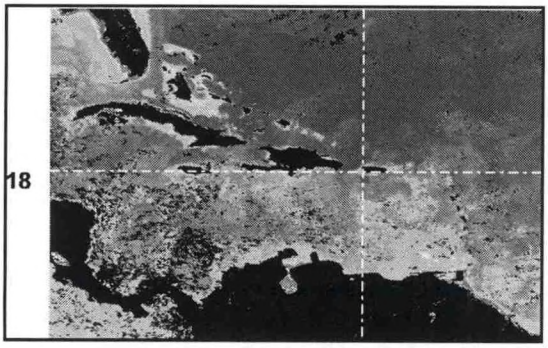

Figure 4. MODIS image showing the three sampling sites.

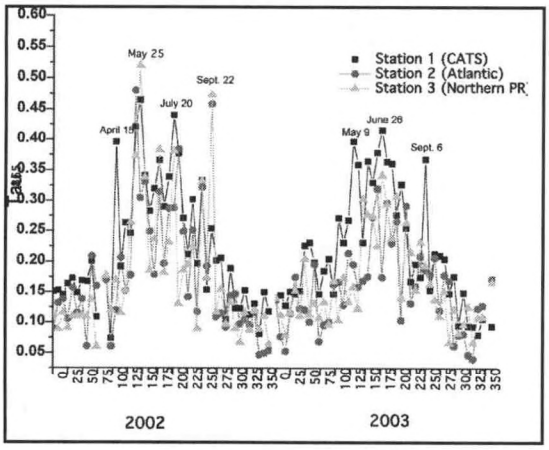

Figure 5. MODIS Tau 865 values for 2002-2003 for the three sampling sites.

approximately 26 miles south of Puerto Rico. This region is influenced by eddies and South American riverine intrusions that result in seasonal and inter-annual variability. Stations 2 and 3 are representative of more oligothrophic waters of the tropical Western Atlantic Ocean.

High seasonality of Tau 865 values were found at the three stations corresponding to the summer peak intrusions of Saharan dust in tropical Western Atlantic (Figure 5). A time series analysis of the dataset will be conducted to address possible correlations between Tau 865 and Chlorophyll-a.

We used the R/V Chapman for field validation of satellite remote sensing data. Profiles of apparent optical properties (AOT) and inherent optical properties (IOP) are obtained on a monthly basis at the Caribbean Time Series Station (CaTS). Students are trained in the various water optics measurement protocols (Figure 6).

Figure 6. Measuring sky radiance at CaTS.

Remote Sensing Summer Courses

The UPRM NCAS program has hosted three 2-week intensive summer remote sensing workshops. The summer 2002 workshop had the participation of eight students from Howard University (HU), City University of New York (CUNY), and UPRM. Ten students from HU, CUNY, FAMU, and University of Texas - El Paso (UTEP) participated in the 2003 workshop. The workshops were project oriented and included plenary lectures from distinguished scientists active in the remote sensing and GIS fields. The first two workshops consisted of one week of introduction to remote sensing data analysis and applications in oceanography and atmospheric sciences, and one week of intensive GIS training. During the summer of 2004, 18 students from HU, Hampton University, Jackson State University, Kutztown University, and UPRM participated in an advanced remote sensing workshop (Figure 7).

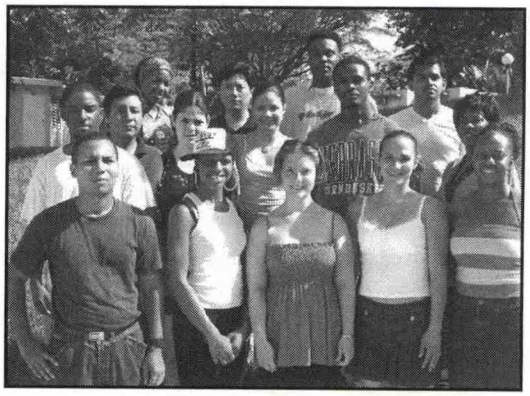

Figure 7. Participating students of the 2004 advanced remote sensing summer course.

ACKNOWLEDGEMENTS

Funding for UPRM/NCAS research and educational activities was provided by NOAA's Educational Partnership Program for Minority Serving Institutions. We thank Dr. Fernando Gilbes and the staff of CoHemis for their support and participation during the summer remote sensing courses.

LINKING UNDERGRADUATES AND SCIENCE: SAVANNAH STATE STUDENTS HELP ASSESS A RECENT MARSH-DIEBACK EVENT IN COASTAL GEORGIA

Mary Carla Curran and Benjamin F. Maher
Marine Sciences Program, Savannah State University

Reports of salt-marsh dieback in coastal Georgia began in the spring of 2002. These are areas of marsh with little or no live vegetation and both salt marsh cord grass (*Spartina alterniflora*) and black needle rush (*Juncus roemerianus*) have been affected. In Georgia, an excess of 600 acres of salt marsh have been affected, with dieback reported in all coastal counties. A variety of hypotheses have been put forward to explain the dieback including drought-related effects (increased soil salinity, decreased soil pH), sulfide toxicity, pathogens, snail herbivory, wrack, herbicides, pollution, heavy metal toxicity, and hydrologic manipulation. As part of a Marine Ecology course, students from Savannah State University started evaluating this phenomenon and the project has continued for the past two years. The purpose of the study was to provide an opportunity for students to collect data valuable to a topic of current ecological concern. To assess the marsh areas, we employed a modified version of the protocol designed by the Georgia Coastal Research Council (GCRC) in order to compete the monitoring within a two-hour laboratory session. More specific information can be obtained from the GCRC website at *www.marsci.uga.edu/coastal-council/*. In brief, the live and dead marsh was delineated with flags. Two 5-m transects were permanently positioned in the live and dead marsh and 0.5-m2 quadrats were placed at the 1, 3, and 5 m mark in each transect. Live and dead Spartina alterniflora stem densities were recorded in each transect and heights of live S. alterniflora were measured. Snails (Littoraria irrorata), mussels, and fiddler crab holes were counted in each quadrat. In addition to the GCRC protocol, sediment core samples were collected to determine meiofaunal abundance and were identified to major taxon (copepods, polychaetes, oligochaetes, nematodes, and ostracods). The major finding of our study was that stem densities and height changed over time. Mean live S. alterniflora stem density peaked in the fall. In the live marsh, values ranged from 85-221 stems per m2, whereas in the dead marsh values ranged from only 10-118 stems per m2. Mean live S. alterniflora height also peaked in the fall, and in the live marsh ranged from 30-128 cm, whereas in the dead marsh height ranged from only 22-76 cm. The predominant meiofaunal taxon was nematodes, and meiofaunal density was significantly higher in the dead marsh although variability was high. Mean snail densities generally ranged from 0-130 individuals per m2. Based on the relatively low snail densities we obtained, we do not believe that this was the initial cause of the dieback but instead believe that drought-related factors may be the most likely cause. In addition to the natural seasonal changes in the density and height of S. alterniflora in the live and dead marsh over time, we noted that the dieback area appears to be recovering slowly as indicated by the increased densities over the course of the study. Because students were trained adequately, they were able to collect accurate data that proved useful in monitoring the recovery of Georgia marshes. In the future, we hope to utilize this protocol to develop a lesson plan for K-12 students and encourage educators to include environmental monitoring in their science courses in order to encourage better stewardship of coastal areas.

TRAINING UNDERREPRESENTED STUDENTS THROUGH ATMOSPHERIC EXPERIMENTATION

Everette Joseph[1], Jose D Fuentes[3], Vernon Morris[2], Demetrius Venable[1], Belay Demoz[4], Paul Kucera[5], Gregory Jenkins[1], Fonya Nzeffe[1] , Miliaritiana Robjhon[1] Seygale Walford[1], and Rasheed Connell[1]

[1]Physics Department, Howard University, Washington, D.C.
[2]Chemistry Department, Howard University, Washington, D.C.
[3]Environmental Sciences, University of Virginia, Charlottesville, VA
[4]NASA Goddard Space Flight Center, Greenbelt, MD
[5]University of North Dakota

Introduction

The NOAA-Howard University Center for Atmospheric Sciences (NCAS) has developed a new state-of-the-art facility to conduct atmospheric measurements leading to better understanding of: cloud and aerosol impact on climate, regional air quality (ozone formation and deposition processes, and aerosol chemistry and physical characteristics), and atmosphere-surface interactions. An equally important purpose of this facility is to expose underrepresented students to experiential learning methods in atmospheric sciences. Two workshops have been conducted (24 – 26 June 2003, and 21 – 30 June 2004) towards that end, and in this paper we report on the experiences gained through these workshops. The principal goals of the workshops were (1) to introduce students to and facilitate student-interaction with leading atmospheric scientists, (2) to develop both horizontal and vertical mentoring strategies with graduate students and participating faculty members, and (3) to employ experiential methods of learning as a means to motivate students to pursue research and careers in atmospheric sciences. The unique features of the workshops included the participation of diverse faculty, and the different research interests among participating students and faculty members. Students assessed the workshop as a highly rewarding learning experience and recommended that similar efforts should be continued at both graduate and undergraduate levels in order to graduate well-rounded students

Instrument Workshops

The core elements of the workshops were research projects conducted by student teams, and scientific discussions facilitated by leading university and government scientists. The projects and seminars were developed within the context of the following workshop objectives:

- Study of regional atmospheric processes within an interdisciplinary framework
- Provide experience with state of the art observing systems, for example
- LIDARS and Radars
- Broadband and narrowband radiometers
- Trace gas analyzers (O3, NOx, H2O, CO2, and VOCs)
- Meteorological Sensors (Rawinsondes, Sonic Anemometers)
- Apply innovative methods of data interpretation

Approximately 31 students have participated in both workshops. Most were students at NCAS partner institutions, and were Hispanic or African American (64% African American, 22% Hispanic and 12% Caucasian). The student teams together with their graduate student mentor and faculty advisor developed projects requiring measurement and data analyses in one or more of the focus areas. A team approach was employed to complete the assigned projects and integrate databases from multiple observing systems. For

each research topic, the necessary scientific background was established through presentations and discussions. Leading scientists from NOAA's Air Resources Laboratory, NASA Goddard Space Flight Center, University of Virginia, Pennsylvania State University, and Howard University conducted the discussion sessions. During these sessions, students reviewed key measurement strategies and data analysis methods for each of the research areas as well as the significance of these areas in the larger context of understanding regional and global environmental change. In addition to the scientific content, the key attributes of becoming rigorous and meticulous scientists were sufficiently stressed. The discussions emphasized not only how to obtain reliable environmental datasets but also how to formulate research hypotheses or questions, evaluate hypotheses, and data interpretation and reporting. The scientists and faculty, most of whom come from underrepresented groups, served a second role of providing vertical mentoring to the participating students. Few graduate students, who worked at the research site and had familiarity with the instrumentation and data analysis protocols, provided horizontal mentorship. At the end of the weeklong workshop, each group made an oral presentation reporting the experiences learned in data acquisition, data analyses and interpretation, and scientific importance of results. Results from selected group projects are give in section 4 below.

The Howard Beltsville Field Site

The Howard University Beltsville Research Facility, where the workshops were held, is located approximately 12 miles NE of the main campus on 110 acres in suburban Maryland. The campus is in a rural setting and contains minimal development with not more than 5% of the land area occupied by building structures, making it an ideal environment for studying a range of surface-atmospheric interaction processes. A forest dominates the local landscape, with both deciduous and coniferous tree species. A comprehensive set of atmospheric observing systems have been or are under deployment at Beltsville. Table 1 below provides a list of these systems, and their measurement products, and Figure 1 is of the 31 m walk-up tower and its instrument package.

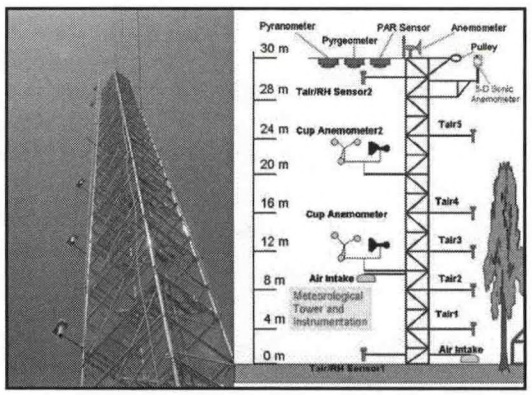

Figure 1. Actual and cartoon image of 31 m walk up tower at Beltsville instrumented for flux, radiation, and air quality observation

Surface Energy Balance

The surface flux group evaluated the diurnal variations in the surface energy balance at the tower site at Beltsville. These results and other presented below are useful for characterization of the site. The energy partition of the surface flux is given as follows: Rnet = H + LE + G, where Rnet is the net radiative flux at the surface, H is the sensible heat flux, LE is the latent heat flux and G is soil heat flux. For this case Rnet and H are determined from measurements and G and LE are derived. Figure 2 shows a strong diurnal variation of the surface energy fluxes for 26 June 2004, with a significant amount of the daytime radiative heating being balanced by the latent heating.

Intercomparison of Surface Radiation Budget Measurements

Among other studies, the radiation group conducted an intercomparison of the net surface radiation budget measured from 2 sets of instrument. The net radiation was calculated from measurements made by a Kipp & Zonen net radiometer own by the University of Virginia (UVa), and from measurements made by set of radiometers owned by Howard/NCAS. The Howard/NCAS instruments included up/down pointing Eppley PIR pyrgeometers measuring down/up IR fluxes, respectively; down pointing Eppley 8-48 measuring surface reflected shortwave flux; and an Eppley NIP and shaded 8-48 measuring direct and diffuse fluxes, respectively on a Kipp & Zonen gear driven tracker. Comparison of net surface radiative fluxes calculated from measurements made by the UVa and Howard/NCAS radiometers 27 – 29 June is shown in Figure 3. There is considerable discrepancy between the 2 calculations for fluxes greater than 400 Wm-2. This difference is speculated to be related to calibration, differences in the physical location of the instrument, and misalignment of the NIP. The former (calibration) is believed to be the main source of the difference, providing an important lesson to students of the critical need of performing regular and rigorous calibration of research

Core Instruments	Data Products
RSS (Rotating Shadowband Radiometer)	Measures direct, diffuse, and total irradiance: 300 – 1100 nm at 1024 resolution (CCD). Derived products: aerosol and cloud optical properties; ozone; NO2.
Multi-Filter Rotating Shadowband Radiometer (MFRSR)	Measures direct, diffuse and total 415, 500, 610, 665, 870, and 940. Derived products: cloud, aerosol optical properties ozone and water vapor.
MWR (Microwave Radiometer)	Measures microwave radiation from sky at 23.8 and 31.4 GHz. Derived products: cloud liquid water content and total column water vapor.
Total Sky Imager	Automated real-time panoramic image of sky
Broadband Radiometers (pyranometer, pyrgeometer, normal incidence pyrheliometer)	Direct up/down, diffuse and total solar irradiance; and Up/down infrared irradiance
Raman Lidar	Measures backscatter signals from molecular water vapor, molecular nitrogen, and combined Rayleigh and aerosol contributions. Derived products: high temporal and vertical resolution of water vapor and aerosols.
31m Meteorological Tower	Atmospheric fluxes, radiations, and standard meteorological variables
Balloon-Borne Sounding System	Pressure, Temperature, Relative Humidity, GPS Wind speed, and Wind direction
Tipping Bucket Rain Gauge Network	Rainfall
Commercial Doppler C-band Radar	Reflectivity and Rainfall. Fox Television is owner and primary uses (installation is in progress)
Thermo NOx Analyzer	Surface level NOx
Thermo Ozone Analyzer	Surface level Ozone
Thermo CO Analyzer	Surface level CO
R & P High-Volume Sampler	Large size-fractionated filter samples. 4 stages (0.3, 0.5, 1.0, 2.5 micron)
Quartz crystal microbalance cascade (QCM) impactor	Filter sampling for chemical and physical Mass fractionated sampling, Total suspended particulate mass, Size-fractionated samples
Climet Model CI-550 laser particle counter (LPC)	Size-fractionated number densities from 0.3 to 25 mm in seven size cuts

Table 1. List of instruments deployed at the Howard Belstville field site, and their data products

instruments.

Evolution of the Atmospheric Boundary Layer

Radiosonde launches were conducted approximately every three hours throughout the workshop using InterMet GPS radiosondes. The radiosonde measurements were conducted to observe the thermodynamics of the atmosphere, validate estimates of water vapor from the Howard/NCAS Raman Lidar (HRL), and for analysis with radiative transfer, and mesoscale models. Teams of 2-3 of all students in the workshop were formed to conduct the launches. The boundary layer group investigated the diurnal evolution of the convective boundary layer with data from the launches. The virtual potential temperature is plotted as function of height in Figure 4 for launches conducted 27 June at 0600, 0900, 1200, 1400, 1700, 2000, and 2300 hours local time. The 0600-hour launch exhibited a strong stable layer up to 0.25 km, a nocturnal boundary layer

from 0.2 km to 1.2 km, and a residual layer from 1.2 km to 2 km. The 0900-hour launch exhibited the development of a shallow convective boundary layer of 0.6 km depth. For this case study day the convective boundary reaches a maximum depth of 2.2 km as seen in the plot of the 1700-hour sounding. In the same plot an entrainments zone is evident between 2.2 and 2.6 km. By the 2000 hours launch a stable surface has developed with depth of 0.25 km.

As noted above boundary layer information derived from radiosonde measurements are being used to validate that derived from measurements of the HRL. The lidar group has conducted preliminary analysis of lidar measurements conducted for this day (27 June) and their results show reasonable agreement with boundary layer heights obtained from radiosonde measurements. For example lidar derived boundary layer hight for 1700 hour is approximately 2.6 km the same as shown in Figure 4 below. A more rigorous comparison of lidar and radiosonde measurements is done in a paper presented at the present conference: Connell et al 2004.

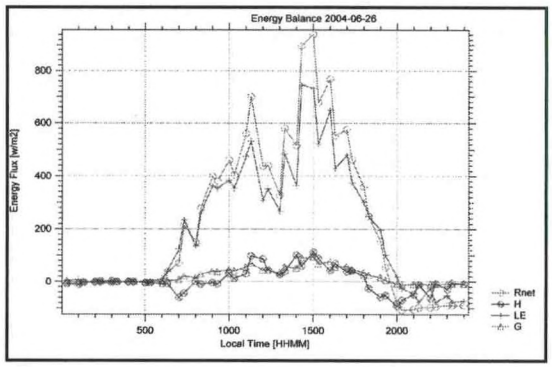

Figure 2. Surface energy balance calculated from measurements at Beltssville 26 June 2004

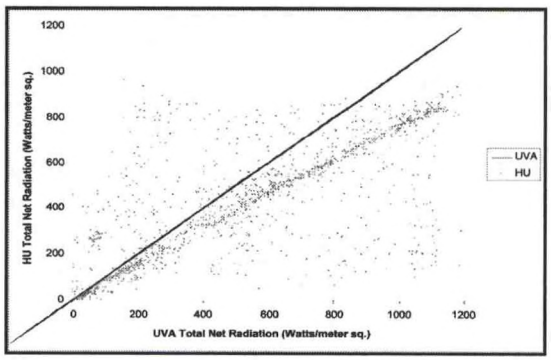

Figure 3. Comparison of net radiative flux calculated from measurements from 2 set of radiometers.

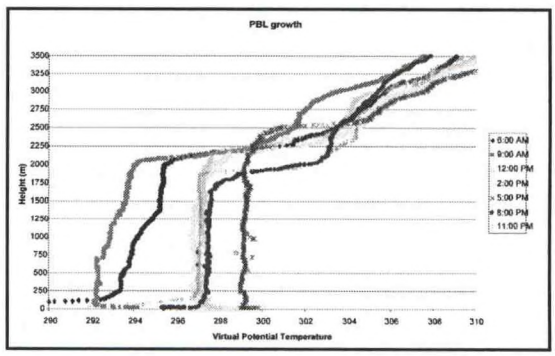

Figure 4. Virtual potential temperature derived from radiosondes launched during 27 June at Beltville

Summary and Conclusion

NCAS has developed a state of the art facility for investigating aerosol and cloud impact on climate, regional air quality, and atmosphere-surface processes through atmospheric observation. In addition to enabling advance research in these areas, the facility is also used to provide students from traditionally underrepresented groups experiential or hand-on training in atmospheric field studies. Experience and results from two NCAS instrumentation workshops are described.

Formally and informally students have judged the workshops to be a valuable learning experience that has reinforced concepts learned in class. They have obtained an appreciation for the challenge of obtaining and applying scientifically useful observations. They have recommended that the workshops be extended in length and conducted at the undergraduate as well as graduate levels.

ACKNOWLEDGEMENTS

NOAA Cooperative Agreement NA17AE1623 provided support for the workshops and to establish the NCAS field observation facility. Acknowledgement also goes to many NOAA, NASA, and university scientists without whose help the workshops, and facility would not have been possible.

REFERENCES

Connell, R., D. D. Venable, E. Joseph, 2004: Technical design considerations for a water vapor/aerosol Raman lidar system. Extended Abstracts, NOAA-EPP Education and Science Forum 2004, New York, NY.

Delivering Remote Sensing and GIS to a Graduate Ecology Instruction at Multiple Sites Using Distance- and in-PersonInstruction Methodologies

William Lawrence

(NOAA CREST Faculty), Natural Sciences, Bowie State University, Bowie State University, Bowie MD 20715

Phone 301 860-3338/Email ***wlawrence@bowiestate.edu***

Abstract

A graduate ecology course, ECOL596, is offered every spring at San Diego State University. This course has traditionally offered in-person instruction, with a one-week field excursion to a site in California. Recently the course has been expanded to include participation by students and faculty in Mexico at the Northwestern Center for Biological Investigations [CIBNOR] in La Paz, Baja California. The course has never had a remote sensing component, but through an invitation to the author, the remote sensing and GIS components are now provided by Bowie State University. This was made possible through NOAA CREST support to faculty time. Teleconferencing was used to bring traditional lecture material to the University and Lab sites, while in-person instruction was used in the field portion of the course, delivered in Puerto Lopez Mateos, Baja California. The focus of the course and field work was determination of local carbon flux in the mangrove fringe of the coastal areas.

Introduction

A graduate/upper division field course in Ecology, ECOL596 has historically been taught at San Diego State in the Spring semester of each year. The course includes lectures during the regular school term, and a field excursion during spring break.

In recent years the responsibility for the course has been taken over by Dr. Walter C. Oechel, head of the Global Change Research Group within the Biology Department. He was, coincidentally, my PhD advisor. Under Dr. Oechel's leadership the course has begun to focus on global carbon issues and has become a collaborative effort between San Diego State University and the Northern Center for Biological Investigations [CIBNOR] in La Paz, Baja California. CIBNOR is a Mexican National Laboratory with a focus on environmental issues. There are also collaborative research ties between SDSU and CIBNOR.

ECOL596 had alternated field work between San Diego and Mexico for a few years, but for now the decision has been made to continue the field portion of the course in Mexico, primarily to facilitate the inclusion of Mexican students, faculty and staff in the educational enterprise. It is much easier for the US participants to travel to Mexico than vice versa.

The strong participation of Mexican graduate and undergraduate students has been made possible, in great part, to the use of distance education tools to deliver content at all participating institutions.

Due to the use of distance education delivery tools, principally video teleconferencing, it was possible for the author to participate in this course for the first time Bowie State University in Maryland, synchronously with the other participants in San Diego and La Paz, Baja California. Travel was only required to join the course in the field exercise in Baja.

Methods

Lectures were delivered through synchrous teleconferencing, through the facilities at the three institutions. Experience proved that it was most successful if communication was inititated by San Diego State, with La Paz and Bowie State joining the Internet-based sessions. We were able to communicate, dur-

ing most lecture sessions, at 512 kbs, althought at times network congestion slowed our communication.

The original plan was to broadcast PowerPoint presentations with 'voice over' by the presenting faculty. This proved to lead to some problems with legibility and communication, so a new model was developed mid-semester. The second model broadcast the real-time image of the presenter in the conference center to the participating locations, with a 'local' copy of the PowerPoint presentation being shown, in full resolution, with a computer and projector. This did present some control and presentation problems, but proved to be much more successful.

After the conclusion of the lecture portion of the course, the students assembled in La Paz, Baja California and proceeded to the Pacific coast to the small town of Lopez Mateos for field work. The content of Lectures and Field Activities follows.

Lecture Materials Covered:

- Global Change and population growth- the large context: (Walter Oechel)
- Use of benthic invertebrates diversity to assess environmental change in coastal habitats (Irma Olguín).
- Natural and anthropogenic impacts in long-lived migratory species: Case Studies of gray whales and sea turtles in Magdalena Bay. (Susan Gardner)
- The Magdalena Bay Land-Sea Atmosphere system: horizontal and vertical fluxes and interactions. (Samuel Chavez
- Strategies, potentials, and challenges for Sustainability of Baja California in Terestrial and Agricultural Ecosystems. (Ricardo Rodríguez and Enrique Troyo)
- Weather systems of Baja California, forecasts for the future. (Luis Farfan)
- Cultural Eutrophication: Nutrient Sources to Coastal Zone (Carlos Lechuga)
- GIS, Remote Sensing for assessing and georeferencing data from the upper reaches of Magdalena Bay near San Mateo (Cesar Salinas and Bill Lawrence)
- Ecosystem gas exchange across a land-sea interface: cactus to algae. (Lipson)
- Regional vegetation, sampling techniques, endangered species and habitats. (Breceda); plus equipment and sampling technique overviews.

Field Schedule & Projects

Day One: Arrival and Orientation Session

Day Two: Travel to Puerto Lopez Mateo, Magdalena Bay; Whale watching trip and orientation to the area; Tour of terrestrial and marine habitats, ecosystems, and observation of behavior of gray whales; Discussion of field projects (15-20 students, 5 projects; 3-4 students each; 3 terrestrial, and 2 marine projects)

Terrestrial Projects:

- Soil processes and a comparison of arid environments to other ecosystems. (David Lipson)
- Estimating regional carbon balance (Walter Oechel)
- Use of Remote Sensing to Determine Surface Types and Productivity (Bill Lawrence)

Marine Projects:

- Mangrove forest structure and productivity (Samuel Chávez)
- Diversity of benthic invertebrates in coastal habitats. (Irma Olguín)
- Survey of nutrient sources to Lopez Mateos channels (Carlos Lechuga)

Days Three - Six: Field data collection for individual projects

Day Six: Field data collection and pack up; Travel to La Paz

Day Seven: Tour of CIBNOR; Data analysis and synthesis of results

Day Eight: Preparation of oral and written reports

Day Nine: Presentation of student projects and discussion; finish written reports

Day Ten: SDSU students return to San Diego

At the conclusion of the course, a web archive was set up to store and make available the data sets, research reports and presentations from the course work. Not surprisingly, a huge number of 'images' were collected by participants with their cameras during the field stage of the course. These pictures were also staged to the Web archive for all to enjoy.

Results & Discussion

This course proved to be exteemely effective in delivering content synchronously across the North American continent. It has been successful and greatly enjoyed by the students, faculty and staff involved. Some students even told us that it was the most memorable and impressive course they had taken in their University career. The research/field component even convinced some students to look for granduate school opportunities, so that they could continue studies along the lines of their ECOL596 expereince. The course will continue next year and will include Bowie State Univesity participation.

The few difficulties in delivering synchronous delivery of the materials will be improved. At Bowie State University we are looking at alternative technologies to 'teleconferencing' such as the multi-point internet capabilities in Microsoft Media Services [part of MS Server 2003] that would allow not only synchronous delivery, but later on-demand access to the lecture materials.

Conclusions

ECOL596 is an ideal model for multi-institution education. Its multi-national character also built diversity and a wider appreciation of science and education across borders. Future work will refine the multi-site content delivery portion of the course, and if the calendar coincides, students from NOAA CREST will also be able to participate.

ACKNOWLEDGEMENTS

The authors would like to thank the NOAA CREST Program for funding the author's time during this activity. I am also grateful to Dr. Walter C. Oechel of San Diego State and Dr. Irma Holguin of CIB-NOR for inviting me to participate in this couse and for supporting my travel costs to the field stage of instruction. I would also like to thank Bowie State University Office of Media Operations and the Telecommunications Office at San Diego State for getting me on-line in the teleconference lecture sessions.

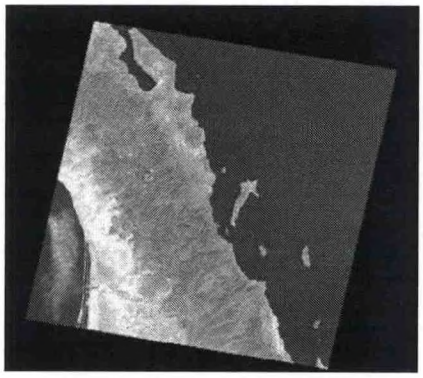

Landsat image of research area in Baja

ORAL SESSION C4

Environmental Entrepreneurship Activities

Tracing the Loss of Oxygen in the Bottom Waters of the Chesapeake Bay: the Intersection of Policy, Science, and Heritage

Benjamin Cuker

Department of Marine Science, Hampton University, Hampton, VA 23668

The MAST (Multicultural students At Sea Together) program is a NOAA supported effort that involves college students in marine science, policy, the heritage of African Americans and Native Americans on the Chesapeake Bay, and seamanship. The program includes a study of changing water quality in the main stem of Chesapeake Bay over time and space. We use a Seabird CTD to develop depth profiles of key parameters at circa 20 stations in early summer. We measure temperature, salinity, oxygen concentration, chlorophyll-a concentration, turbidity, pH and light penetration. Data collected from 2001-2004 reveal extensive anoxia in bottom waters 3 out of the four years. The Chesapeake is generally stratified in early summer, with estuarine circulation patters driving the entrainment and sublimation of marine waters moving in from the mouth of the Bay. We used salinity measurements to trace the sublimating surficial waters as they progressed up the Bay. By following the isohaline of this sinking water mass, we documented changes occurring in oxygen and chlorophyll concentrations. A general pattern emerged, with chlorophyll and oxygen levels initially increasing as the waters proceed up the Bay, but then declining as the water mass sank out of the photic zone. Eutrophication of the Bay appears linked to elevated levels of rainfall, and thus allocanthous nutrient input in 2003 and 2004.

The Chesapeake Bay is the largest estuary in North America. It supports important local commercial and sport fisheries, and provides essential habitat for other species that migrate to and from the Atlantic Ocean. An extensive maritime commerce uses the waterways and ports for the transportation of goods. The Chesapeake figures large in the history of the United States and the heritage of its people. Its shores witnessed many firsts, including; the first permanent English-speaking settlements, the first importation of African slaves to the English colonies, the first battle between iron-armored ships. Much of the American War of Independence, the War of 1812, and the Civil War were fought on its waterways and watershed.

African Americans and Native Americans played essential roles in the Bay's maritime history (Cuker 2003). Many of today's fishing techniques practiced on the Chesapeake trace to those developed by Native Americans, and then adopted by settlers. African Americans, both "free" and enslaved, provided much of the human power to run the local fisheries and maritime trade. Black participation in the maritime world of the Chesapeake Bay during the 18th and 19th Centuries including such trades as shipbuilders, caulkers, seafood processors, fishers, sail makers, able-bodied, seaman, pilots, and ships captains.

European encroachment on the Chesapeake all but wiped out the Native American population, leaving only a few disparate communities, and still fewer bands making a living from the water. The role of African Americans on the Bay waned during the 20th Century. Jim Crow racism, the shift to engine power for vessels, and increasing status for the waterman's trade all tended to marginalize the African American community. Yet still today Black watermen ply their trade in some areas, and populate seafood processing plants.

The heritage of people of color on the Chesapeake, and the greater maritime world in general, remains largely untold. Thus few ethnic minority students in the US consider careers on the water (Cuker 2001). The MAST program seeks to help today's students understand marine science and policy in con-

text of the heritage of people of color on the Bay. In particular, African Americans and Native American students can see themselves as the proud descendents of those who were essential members of the historic maritime world. As such, they learn of their "birthright" to pursue professions based upon the water (Cuker 2003). Through lectures, interactions with role models, readings, and museum visits, the MAST students rediscover the maritime heritage African and Native Americans.

MAST students explore marine policy and entrepreneurship through visits to governmental agencies (NOAA, USEPA), environmental advocates (The Chesapeake Bay Foundation), and the menhaden fishery. This provides the context for studying the Bay from a scientific perspective.

Visits to various laboratories (Virginia Institute of Marine Science, Chesapeake Biological Laboratory, The Horn Point Laboratory, The Smithsonian Environmental Research Center, The Center for Marine Biotechnology) expose MAST students to cutting edge research. In addition students conduct their own scientific study of the Chesapeake, focusing on changes in water-quality in the main-stem of the Bay. Eutrophication and the attendant depletion of oxygen in bottom waters during the summer months is the most important water-quality issue on the Bay. Hagy et al. (2004) document the progressive decline of oxygen in bottom waters since 1950, and show correlation to increasing nitrogen loads. Their work ends with 2001, corresponding to the start of the MAST sampling.

From 2001- 2004, MAST students sampled circa 20 stations in the main-stem of the Bay, in mid June of each summer. Using a Seabird SBE-25, we measured oxygen concentration, temperature, salinity, depth, and chlorophyll a concentration. The students analyzed the data to understand the water column dynamics, with emphasis on oxygen depletion of deeper waters.

Anoxia or hypoxia occurred in the bottom waters of the mid Bay in all four years (Fig.1). The size of the hypoxic region appeared to expand with each subsequent year, with the 2004 low oxygen zone being several times greater than for 2001. This trend follows the pattern of increasing chlorophyll concentrations over the years. Averaged over all of the stations, the oxygen concentrations (mg/l) were; 2001, 7.3; 2002, 4.5; 2003, 3.2; 2004, 2.6. Chlorophyll a concentrations (mg/l) were; 2001, 6.5; 2002, 8.7; 2003, 15.8; 2004, 12.8.

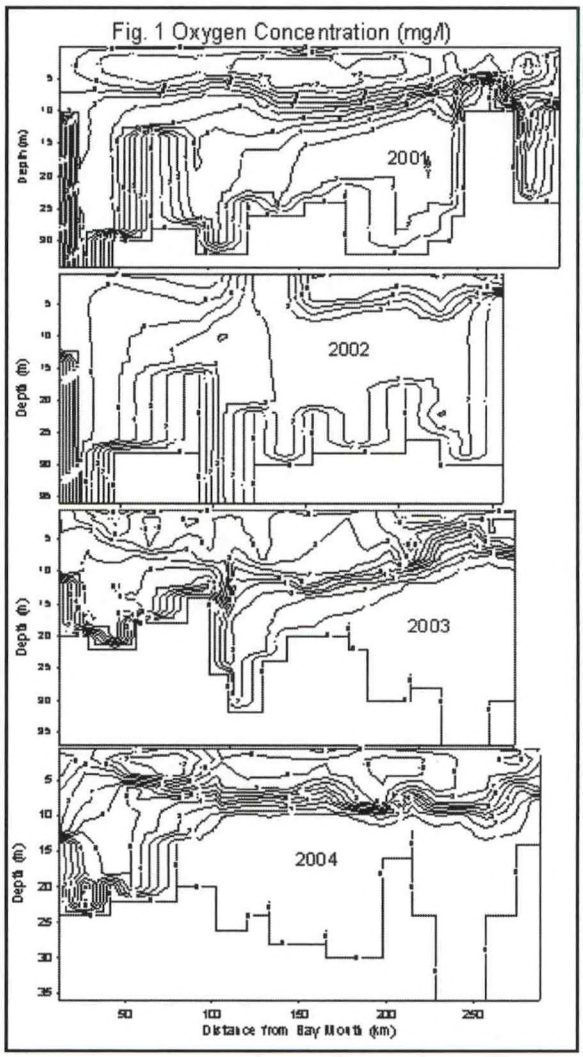

We determined the isohaline distribution of surface water from the Bay mouth as it progressed up the estuary (Example from 2004 shown in Fig. 2). Plotting the oxygen and chlorophyll concentrations along the isohaline revealed the fate of these two parameters as the water mass sank on its journey up the Bay. Generally, both oxygen and chlorophyll declined as the water mass sublimated. Oxygen concentration dropped at a rate of between 0.03 and 0.13 mg/l/km. In 2001 oxygen and chlorophyll both increased initially, until the mass reached a depth of circa 5 m, when both parameters declined with increasing depth and distance up the Bay.

In addition to the low oxygen levels observed below the photic zone, sub-saturated values appeared in surface waters in 2002 (Fig. 1). Oxygen concentrations of 3 and 4 mg/l (about 50% of satura-

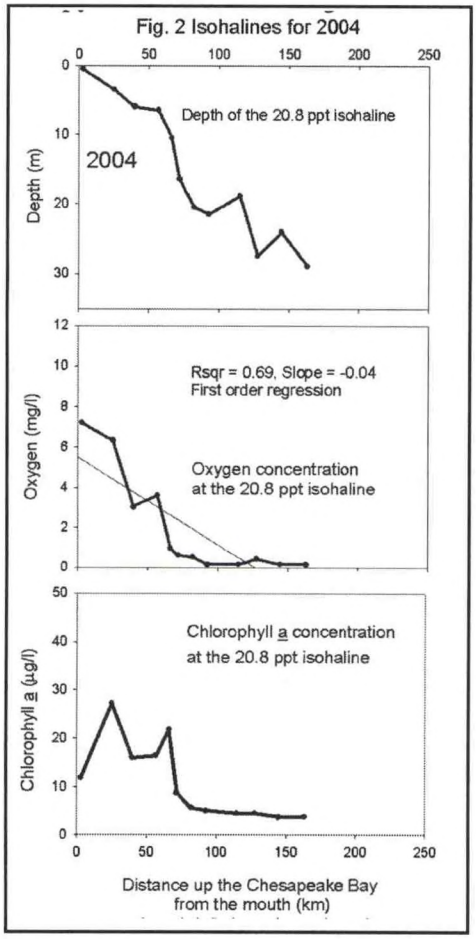

tion) occurred in a surface water mass in the vicinity of the mouth of the Potomac River. Salinity and chlorophyll data display corresponding signatures traceable to the Potomac. Low oxygen levels in surface waters may also trace to events that destabilize the pycnocline (Breitburg 2002).

Hagy et al. (2004) clearly document the eutrophication of the Chesapeake Bay since 1950. They correlate hypoxia with N loading and freshwater discharge While N loading is clearly the ultimate driver for eutrophication, the MAST data shows that phytoplankton is indeed the proximal cause.

The MAST students relate these findings to their studies of key species in the Bay. They learn about the historical declines in populations of oysters (Ostrea virginica), menhaden (Menidia menidia) and eel grass (Zostera mariana), and see how these shifts may relate at least in part to eutrophicaiton. This ecosystem approach helps the students better evaluate policies and restoration efforts aimed at these target species.

Fifty- seven students participated in the MAST program from 2000 – 2004. They were a diverse group, consisting of 60% African Americans, 21% Puerto Ricans, 12% Native Americans/Pacific Islanders, and 7% Hispanic Americans (not Puerto Rican). Thus far 13 of the students have gone on for advanced degrees.

LITERATURE CITED

Breitburg, D. 2002: Effects of hypoxia, and the balance between hypoxia and enrichment, on coastal fishes and fisheries. *Estuaries*, 25,767-781.

Cuker, B.E. 2001: Steps to increasing minority participation in the aquatic sciences: Catching up with shifting demographics. *Bulletin of the American Society of Limnology and Oceanography*, 10,17-21.

Cuker, B.E. 2003: Minorities At Sea Together (MAST): A model interdisciplinary program for minority college students. *Current, The Journal of Marine Education*, 18,45-51.

Hagy, J.D., W.R. Boynton, C.W. Keefe and K.V. Wood. 2004: Hypoxia in Chesapeake Bay, 195-2001: Long-term change in relation to nutrient loading and river flow. *Estuaries*, 27,634-658.

Characterizing Soil Hydraulic Properties under Varied Land Use in the Coles Creek Watershed

Alton B. Johnson, Peter Ampim, Rolanda Mayfield, Ella McCormick and Samuel Adu-Prah
Mississippi River Research Center, Alcorn State University

Land cover and land use impacts on soil quality may be characterized by changes in soil hydraulic properties. The Lower Loess in southwest Mississippi contains a dominant soil, Memphis silt loam (Typic Hypludalf) that is highly erodable and requires good management strategies to prevent sediment loading into streams after major rainfall events. Land use types are row crop production, tree farming, cattle production (pasture) and oil production. To understand runoff and erosion processes in this region, soil hydraulic conductivity, K(h) and water retention properties must be characterized. We measured hydraulic properties of the Memphis soil, which covers 50% of the Coles Creek watershed (1,300 km2). Unconfined infiltration measurements were made in a range of descending tensions (15, 10, 6, and 3 cm of water) using 20-cm disc tension infiltrometers. Land cover/land use types studied were hardwood, mixed and pine forests, pasture and fields with conventionally tilled corn-cotton and cotton-corn rotations. The Wooding's model for steady state water flow in soil was used to quantify K(h). Soil cores were extracted from the 0-15 cm depth to determine bulk density and the WP4 Potential Meter® was used to measure soil water retention. The van Genuchten-Maulem model was fitted to the experimental data using the optimization computer code, RETC. Results indicated that K(h) was highest near saturation (3 cm) in the hardwood forest followed by the mixed and pine forests ($p<0.05$). Water retention from 0 to –33 kPa was significantly lowest in the corn-cotton field followed by the cotton-corn filed and pasture ($p<0.05$). The van Genuchten-Maulem model showed good fit to the experimental water retention data for all land cover/land use types studied.

Acoustic Mapping of Shallow Benthic Habitat for Research & Education

Douglas R. Levin, PhD

Director, Earth Mapping Laboratory – AIT, University of Maryland – Eastern Shore, 6 Market Street, Pocomoke City, MD 21851 voice: 757.710.1631, email: *drlevin@umes.edu* web: *http://www.dougthegeologist.com*

Jeffrey P. Halka

Chief, Coastal and Estuarine Geology , Maryland Geological Survey , 2300 Saint Paul Street, Baltimore, MD 21218 voice: 410-554-5543 FAX: 410-554-5502 email: *jhalka@dnr.state.md.us,* web: *http://www.mgs.md.gov/coastal/index.html*

Abstract

In 2001 the Maryland Geological Survey (MGS) and The Earth Mapping Laboratory (EML) of the University of Maryland – Eastern Shore (UMES) joined forces to see how shallow water mapping technologies could aid area scientists with their resource management decisions. The resulting program aids ongoing research conducted at UMES and strengthens partnerships with NOAA, EPA, and other agencies. An inquiry based, experiential, educational component has also been integrated that introduces a diverse population of educators and students (K-12, undergrad/grad) to the Marine Sciences.

Using remote sensing equipment Chesapeake Bay and Coastal Bay Habitats are being imaged at high resolution (<1m). Survey boats are fitted with acoustic seafloor mapping devices tied to global positioning systems (DGPS). Side Scan Sonar creates an acoustic "photo-like" image of the bay floor. Seismic gear reveals antecedent topography of oyster reefs and other essential fisheries habitats. Depth data is collected to map nuances in the shallow portions of the bay area and to measure slope change. The acoustic signature returned by the substrate (QTC) determines sediment texture, such as sand, silty-sand, etc.

These mapping techniques can also be used to identify suitable sites for introduction of non-native oysters, submerged aquatic vegetation (SAV) bed restoration, and the evaluation of habitat for other fisheries related management decisions (Rubec, et al, 2001). Each of the data types is integrated into a GIS deliverable as a discrete layer. The remote data sets are, subsequently, visually inspected by diver and/or Remote Operated Vehicles (ROV). When all datasets are compiled into a GIS image, a complete, geo-referenced, interpretation of the bay bottom can be created and its ability to support candidate fisheries analyzed or evaluated for alternate environmental enhancement.

Shallow Water Mapping Institute

The Shallow Water Mapping Institute (SWMI) is an entity of The EML at UMES. It was created to refine mapping techniques in water depths less than 10 m. This is especially challenging in waters less than 2m deep because of difficulties in resolving detail from rapid acoustic returns. A dual mission of SWMI is to introduce sophisticated mapping technologies to K-16 students in a user-friendly environment with quiet water (to alleviate motion sickness as a detriment to learning).

SWMI's goal is to provide high-resolution map products of Chesapeake Bay and the Coastal Bays. Projects focus on the application of remote sensing technologies to Oyster Reef Restoration, Submerged Aquatic Vegetation, and Essential Fisheries Habitat studies. The applied technologies are routinely used by the Maryland Geologic Survey and the results are sought by agencies that envelope the Chesapeake Bay waters. SWMI will contribute to the building of a data archive and understanding of issues that tie directly to ongoing research efforts. For example, the Chesapeake Bay Foundation is calling for a 100,000+ acre increase in SAV (Submerged Aquatic Vegetation) coverage in the bay over the next ten years. Shallow

water mapping is required to determine where these plants will survive. The Oyster Recovery Partnership of Annapolis is just beginning to use shallow water mapping technologies to understand the architecture of Oyster Reef growth (Figure 1). The NOAA office of Chesapeake Bay has a goal to map every nuance of the Chesapeake Bay in an effort projected to take twenty years. In this activity the technologies that need to be applied to shallow water mapping will be researched and refined.

Deliverables designed into this program include a public accessible, web-housed, image-rich, database that allows images of the seafloor to be interactively viewed and analyzed both spatially and temporally. The archived data will follow the "Common Dataset" design developed by the University of New Hampshire, Joint Hydrographic Center, (Sea Technology, 2000). It will be accessible for active use and interrogation by the public, following internal review and permissions release. This electronic library will be developed in concert with the Maryland Geological Survey, ORP, and NOAA Chesapeake.

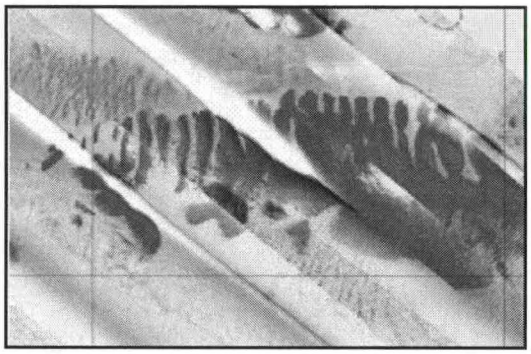

Figure 1. Acoustic Image of an Oyster Reef taken with Side Scan Sonar in 15m depth. The rough scale of the picture is 1cm = 100m.

"Sea-Links" is an impact educational program integrated into this initiative integrated into SWMI. A goal of this program is to give teachers expanded opportunities to work towards their Graduate Degree and improve the delivery of the Marine Sciences to their students. This program will create field-experienced teachers that instill a contagious excitement of the marine sciences on their students. Participants will plan, acquire, and analyze expedition data and will participate in outreach activities that will extend the data to the broader educational and scientific community, including the K-12 classroom. Graduate and undergraduate students will work shipboard, side by side, with the teachers. These students will become mentors to the teacher's K-12 students and may inspire some of the graduate students to become teachers themselves. SWMI has also adopted the MATE (Marine Advanced Technology Education) program through a NASA supported program "Robotics in the Classroom" that introduces middle and secondary school students to marine technology through the hands-on construction of Remotely Operated Vehicles (Figure 2) (Sullivan, et al, 2003).

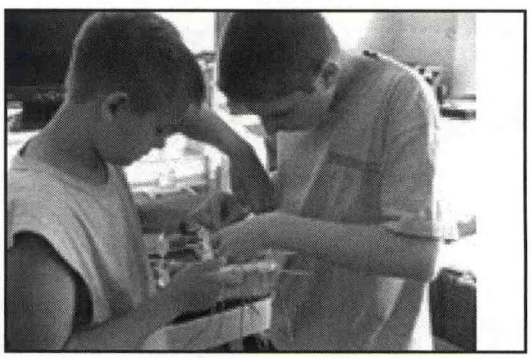

Figure 2: Middle School Students putting finishing touches on a Remote Operated Vehicle.

Shallow Water Mapping in the Chesapeake bay and Coastal Bays

Of primary interest to this program is the gathering of detailed data from the less navigated tributaries on the eastern side of Chesapeake Bay, especially those located along the western shoreline of Delmarva Peninsula. The Pocomoke River, for example, is described historically as a main waterway of the Pocomoke Indians and the site of the first American naval engagement of 1635 (Tunis, 1931). In addition, other rivers and tributaries of the Eastern Shore of the Chesapeake, such as the Wicomico, Nanticoke, Choptank, and Chester, although navigable, have not been systematically surveyed for artifacts of historical

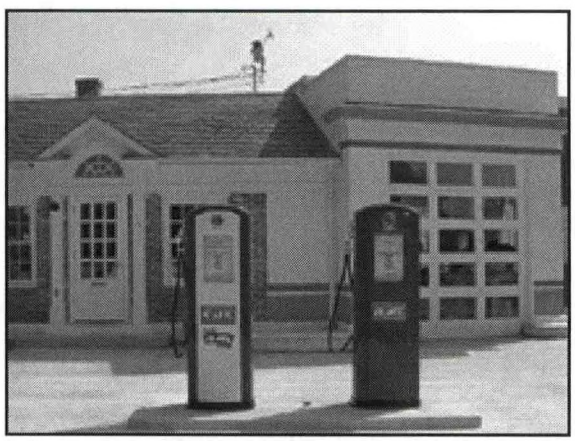

Figure 3: Home of the Shallow Water Mapping Institute

significance, resource habitat, or stratigraphic history. One of the many attractive features of this program lies in the fact that the target region is in "our own backyard". All of these Chesapeake Bay tributaries are located on the Eastern Shore within convenient travel distances from the UMES campus. This minimizes costs for mobilization and demobilization while concentrating the bulk of the investment on data collection, hands-on education, and deliverable preparation. There are innumerable theses opportunities within easy reach of UMES and the proposed Earth Mapping Lab facility.

The Shallow Water Institute for Mapping

The Pocomoke River Exploratory is located in a restored gas station in an area of the city where the population is extremely diverse and economically challenged (Fig 3). It is situated within 200 feet of the Pocomoke River. The Exploratory is the research and teaching arm of the Delmarva Discovery Center. The building's inside contains an Internet connected laboratory, classroom, and office. It offers a comfortable, non-traditional, unique, learning environment. A classroom, without walls or learning boundaries. Its equipment cache includes sophisticated mapping equipment that can be deployed from its resident research vessel.

Equipment

This effort requires equipment that can be conveniently installed and uninstalled on ships of opportunity. The Earth Mapping Laboratory already maintains a cache of mapping equipment. The existing program maintains side scan sonars, echosounders, DGPS, and a Remote Operated Vehicle. A sub bottom profiler, QTC benthic mapping system, Doppler current meters, and spectrophotometer will soon round out the "toy box". The data will be gathered using integrated navigation software packages with electronic charts, and acquisition computers specific to each piece of equipment. All of the deliverables generated from these expeditions will be presented with the aid of ArcView GIS or similar programs and posted on the Internet for review and community use.

SEA-LINKS, Partnering Expeditions with Educators and Their Students

Our science community has been seeking recruiting assistance. There is a real lack of "budding" scientists being developed (Walker, et al, 2000). The paucity of replacements occurs because there aren't enough experiential programs that launch contagious interest in the sciences at impressionable ages. The Institute for Exploration's Jason Project says that a student not engaged in science by the 8th grade, will not choose that path (Bob Ballard, personal communication). The Ocean Exploration edict includes a plea for more content about maritime cultural resources and heritage (McClean, 2000) and identifies education and outreach as important components. SWMI will work with teachers to integrate Marine Technologies and GIS applications into their classrooms as promoted by Audet and Ludwig, 2000.

For example, there are few topics that illicit a greater reaction than that of treasure hunting (Levin and Montvilo, 1998). Shipwreck searches are truly interdisciplinary (Levin and Montvilo, 1996). They integrate science, math, social studies, business, technology, science, history, governments, and the legal system.

Conclusion

The Shallow Water Mapping Institute, an entity of the Earth Mapping Laboratory will work with the Maryland Geological Survey to improve benthic mapping capabilities that assist fisheries habitat restoration programs and resource management decisions in the Chesapeake Bay, Coastal Bays and Mid-Atlantic near shore. The data collected using the equipment described in the equipment section of this proposal will be used to create web-based maps and add to a Chesapeake Bay Common Dataset.

Educators and their students will work shipboard using the sea floor mapping equipment to create benthic habitat maps. Each participant will be able to run this equipment, collect data, and perform a rudimentary analysis of the data. The hands-on, experiential approach is designed to infuse a new sense of excitement in the Sciences, and ultimately lead to mentored science/teacher/student relationships that encourage student inquiry into marine science career paths.

REFERENCES

Audet R. and G. Ludwig, 2000, GIS in Schools, Environmental Systems Research Institute, Inc., Redlands, CA, pp. 109

Levin, D. R., and Montvilo, J.A., 1998, Applied Coastal Oceanography – A Course that Integrates Science and Business, Journal of College Science Teaching, 28:28:3, 329-333

Levin, D. R., and Montvilo, J.A., 1996, Shipwreck Salvage: A Unique Approach to Integrating Science with a Business Curriculum, Journal of College Science Teaching, 26:1, 26-30.

McNutt, M.K., 2001, Testimony on Ocean Exploration, *http://www.agu.org/sci_soc/policy /mcnutt_testimony.html*

McLean, C, 2000, 2002 Ocean Exploration and Research Initiative, NOAA Management Presentation, p.27-29

Rubec, P.J., S.G. Smith, M.S. Coyne. M.White, A. Sullivan, T.C. MacDonald, R.H. McMichael, D.T. Wilder, 2001, Spatial Modeling of Fish Habitat Suitability in Florida Estuaries. Spatial Processes and Management of Marine Populations, Alaska Sea Grant College Program, AK-SG-01-02, 2001

Sullivan, D, J.Zande, S. Butcher, T. Murphree, and B. Ford, 2003, Using Marine Technology to Develop Ocean Literacy and Teach Workplace Competencies. The Journal of Marine Education, V 19:3:20-26

Tunis, E., 1931, An Historical & Literary Map of Maryland, Enoch Draft Free Library.

University of New Hampshire, Joint Hydrographic Center & Center for Coastal and Ocean Mapping, 2000, Sea Technology, Reprinted from Sea Technology.

Walker, S.H., P. Coble, F.L. Larkin, 2000, Ocean Sciences Education for the 21st Century, Oceanography, 13:2, 32-39

THE "GREENPROOFING.ORG" CONSULTANCY – AN EXPERIENCE IN PURPOSE-DRIVEN BUSINESS MODEL DESIGN

Dr. Jonatan Jelen and Dr. Megan Wiley

Departments of Economics and Civil Engineering, The City College of New York

The Motivation

The Environmental Entrepreneurship Partnership (EEP) Program brought together several civil engineering and several economics students and professors in an effort to crossfertilize research and forge a crossfunctional perspective on issues around water resources management in the greater New York area.

Quickly, this particularly diverse combination generated extraordinary levels of genuine inquiry and authentic concerns beyond water resource issues into the economic and administrative contexts as well as the engineering alternatives and choices for an ecologically more sustainable future. The need for broadening the scope of the research, i.e. to general social and particularly environmental concerns with respect to sound choices, sustainable technology, and healthy living spaces became obvious; the work, the discussions, and the projects were rapidly expanding to integrate alternative energy sources, ecologically sustainable architectural models, and environmentally friendly products. In the course of several very productive sessions, the idea began crystallizing to leverage these interests into some form of continuous learning experience and sustained action, action that would transcend the scope, scale, and the timeframe of the grant activities.

The preferred vehicle to channel and tackle those concerns was deemed a not-for-profit model form of a "business". Such an undertaking is beneficial for three reasons: (a) the particular organizational model underlying a not-for-profit disjoints funding sources and resource uses at the level of the service itself, i.e. the paying parties are not the using entities; to reconcile this they have to and can only be related through a solid mission and purpose for the organization; to galvanize the efforts, extreme focus and care needs to be taken with respect to mission and purpose, i.e. the social role that such an organization would occupy and the value it would generate for society to be sustainable; this is a tremendous opportunity to foster purpose and mission-driven ethical business thinking; (b) such a learning laboratory would still, and even in a more precise manner due to its strong ontological focus, allow students to acquire theory and practice of (social) entrepreneurship through 'business plan development' and thus provide valuable skills and enable them particularly well for later activities in the business world; (c) also, this approach would serve as a communication and education platform for community development with respect to ecological problems as well as broader issues of social sustainability.

Purpose and Mission

The organizational model best suited for holding the space in which such a learning organizations can carry out as broad a mission as the present, i.e. 'to integrate resources for sound choices, sustainable technology, and healthy living spaces by facilitating meaningful information exchange', is the not-for-profit entrepreneurial organization. Both these areas, i.e. social entrepreneurship and ecological awareness, have been strongly gaining momentum. They are associated with a general increasing unease about the fundamental choices for our institutions and are paving a way away from managerial self-interest, expensive control structures, and questionable asymmetric wealth appropriation; with a perspective on social value creation they are reshaping our ontology with respect to our environment, our communities, and our institutions. Such a paradigm shift is, however, larger than just the recognition of the issues. It requires new models, new frameworks, new parameters. Some of these will include a new understanding

and practice of leadership, social responsibility, and ethical business behavior.

Action

Via the vehicle of a not-for-profit entrepreneurial organization and based on purpose-centered business plan development we propose to form a consultancy-type of business that would become a platform for a wide array of contributors in the are of healthy living spaces, products, and processes, sound ecological architecture, technology, and construction, and sound choices for future projects, development, research, and innovation. Much like the very successful new network based models of eBay, Google, and Amazon, it would be primarily an Internet-enabled platform for information exchange, though dynamic, creating capacity beyond the individual contributors and actors in the field, incorporating for all the possibility to interact, interconnect, cooperate, and collaborate. It would facilitate new partnerships to be forged, it would integrate diverse products for common projects, it would enable distant producers of partial solutions to find resources and alternatives for further completion and evolution of their ideas. Rather than a mere website, it would create a "webspace" for interaction between a large number of interested parties. Moreover, it would support producers and consumers of ecologically sound choices alike by providing the information collected back to the public. It would dynamically and continually integrate and leverage new partners, ideas, and products, support research, and education in the field. And it would finally be a sounding board to these communities and parties for ecologically motivated controversies and problems. What better combination than a group of highly enthusiastic, motivated, and particularly skilled individuals integrating the skills of engineering and entrepreneurship to support such an ambitious endeavor.

THE USE OF REGRESSION DATA IN WEATHER PREDICTION: AN EXERCISE FOR HIGH SCHOOL INTERNS IN A COLLEGE SUMMER ENVIRONMENTAL WORKSHOP AT A MINORITY-SERVING INSTITUTION (MSI)

Jeremy R. Montague, Ph.D.

SNHS-Biology 305, School of Natural and Health Sciences, Barry University, Miami Shores, FL 33161

305-899-3218 • *jmontague@mail.barry.edu* • *http://snhs-jmontague.barry.edu*

Abstract

Barry University, a Catholic, coeducational, Minority-Serving Institution in South Florida, developed in 2004 a summer environmental workshop course (BIO 295) that enrolled high school students traditionally underrepresented in the NOAA-related sciences. Ten participants were selected from Dade County high schools for this first-time offering. These students earned two credit hours of college lab science by completing a variety of biological, chemical and physical lab exercises over a three week period (14 June – 1 July). These included collection of field data on incident solar radiation and ground temperature. These data were used in regression analyses similar to those developed for simple hurricane models. The students learned theoretical approaches to weather forecasting, and methods in data measurement, website data downloads, spreadsheet calculations, and Microsoft PowerPoint" file designs. The students made formal presentations to the faculty. The post-program assessment data indicated that the students responded positively to the exercise.

"In a very crude sense, [weather] forecasting simply means calling up someone to the west of you and asking them to look out their window." (Junger, 1997, p. 99).

If only things were that simple. Forecasting events such as stock market fluctuations, elections results, sports championships, or (more dreadfully) land-falling hurricanes, has never been any sort of exact science. Yet the costs of a bad prediction can be high. I write these very words today with apprehension, as Hurricane Frances moves just to our north and Hurricane Ivan approaches from the southeast.

Hurricane modeling began in earnest during the 1960's (Saffir, 1973). The techniques have become increasingly powerful and the forecasts increasingly accurate. But surprises do occur, and mistaken forecasts can lead to catastrophic damage and loss of life for those areas left unprepared (Powell and Houston, 1996; Powell, et al., 1996; Rappaport, 1994; Vickery, et al., 2000; Willoughby and Black, 1996).

Hurricane modeling remains in its infancy, particularly in terms of our understanding of causes and effects of broader global influences such as greenhouse warming or El nino weather events (Landsea and Knaff, 2000).

Further complicating matters, some experts believe we may be entering a decadal period of increased tropical storm activity during which hurricanes may become not only more frequent, but more powerful and more unpredictable as well (Goldenberg, et al., 2001).

Can we minimize the errors? That depends partly on the students we train today. How best to prepare the next generation of hurricane forecasters? This is a concern for educators in the NOAA-related sciences, particularly at colleges and universities that enroll large numbers of students traditionally left out of disciplines such as oceanography or meteorology. We need to tap the largest available talent pools.

Here I report on one particular exercise developed for a three-week summer college workshop for high

school students interested in the NOAA-related sciences. The exercise involved measurement of ground surface temperature and incident solar energy (measured in lux units); these data were then incorporated into a simple linear regression using temperature and incident radiation as the dependent and independent variables.

Training New Forecasters

Barry University is a Catholic, coeducational, and Minority-serving institution in South Florida. Of the undergraduate biology majors in the School of Natural and Health Sciences, roughly 75% are female, and roughly 54% are minority (mainly Hispanic, Caribbean and African-American); these are students who have been traditionally underrepresented in the NOAA-related sciences.

To better serve our students we designed our BIO 295 Summer Environmental Sciences Workshop, and we recruited ten talented teenagers from local high schools to fill our inaugural class in 2004. We focused on developing hands-on lab and field projects covering topics in biodiversity, ecosystem restoration, technological applications in sciences, enhancement of computer skills, etc. This design attempts to integrate computer-based exercises (so-called "virtual labs:" Carnevale, 2003) into a traditional lab science curriculum, and it addresses recent concerns about the levels of science and math skills for entering college students (Anonymous, 2004).

Hurricane Models

Atlantic hurricane forecasting is mainly the responsibility for the Tropical Prediction Center of the National Hurricane Center (NHC). NHC today relies on nearly twenty different operational and experimental computer models, each using hundreds of complicated mathematical equations requiring enormous memory storage and very high calculating speeds (DeMaria, 1997; Elsner, 2003; Elsner and Jagger, 2003, Weber, 2003; Zorita and von Storch, 1999). Some of the models, e.g., CLIPER (the CLImatology and PERsistence model), and GFDL (from Princeton University's General Fluid Dynamics Lab) have been refined and upgraded over many years. Others, e.g., UKMET (from U.K.'s Meteorological Office) or FSU (Florida State University's super-ensemble) are much more recent packages.

Each model requires numerical input in the form of oceanographic and meteorological variables, such as sea-surface temperature (SST), wind velocity, degrees latitude/longitude, etc.

There are two basic types of hurricane models used by NHC: (1) statistical (those that predict a current storm's future behavior based upon historical data from previous storms) and (2) dynamical (those that use current global atmospheric and oceanographic conditions to forecast the behavior of the current storm). In practice, forecasters use these in combinations. This paper focuses mainly on the statistical models that rely on regression equations (for example, see Aberson, 1998).

Regression Using Historical Data

Suppose we want to predict the sea-surface temperature (SST) for a particular storm 24 hours ahead of time. We begin by selecting a random sampling of past storm data, say, SST at 11 a.m. on day 5 during ten different storm histories (storm-A, storm-B, etc.). Each SST is then paired with the SST 24 hours later for the same storm (Figure 1).

A simple linear regression equation may be generated in the form of T°C at t0+24 = slope*(T°C at t0) + y-intercept. The scatter of data points creates a predicted range of statistical error.

Such a hurricane model, then, incorporates many thousands of such regression calculations per model run.

In general, a model is initialized with current (state) parameters at the start of a six or twelve-hour run, and its results are compared later with the updated storm condi-

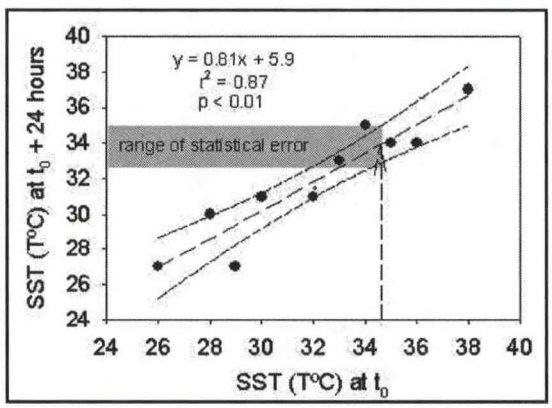

Figure 1. Linear regression (with 95%-CIE boundaries) using hypothetical SST data (n = 10 randomly selected storm days).

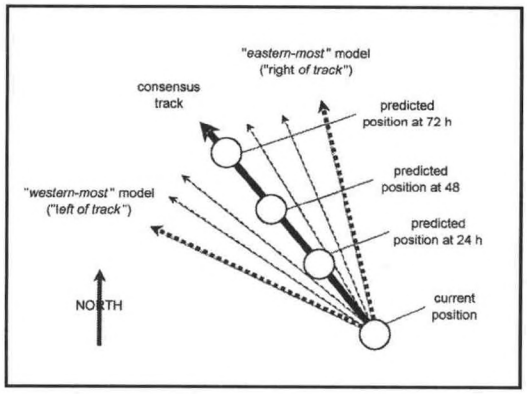

Figure 2. Hypothetical example of a consensus storm track.

tions. The future conditions are then predicted by forecasters who use their experience and intuition to choose among the better-performing models from run to run.

The result is a consensus track based on a compromise solution among all the competing models (Figure 2). Current state-of-the-art modeling produces 24-hour, 48-hour and 72-hour predicted positions with up to hundreds of miles of potential error (in a so-called "increasing cone-width") at the end of the forecast period. NHC seeks to minimize the cone-width of uncertainty.

The hurricane models may also be subdivided into two functional types: (1) track guidance models that forecast direction of movement, and (2) intensity models that forecast strength and wind velocities. In theory, each model predicts both track and intensity, but in practice, the track models tend to be poorer at predicting intensity, and vice versa. No one model has an outstanding performance record; each has its limitations. A model's success varies season to season. In addition, models performing well early in a storm's history have been known to become quirky and unpredictable later in the same storm, behaving erratically over short periods of time (Weber, 2003).

To assess the output of any one model requires an understanding of the statistical nature of data sampling and its use of regression equations. It is this understanding we'd like to pass onto our students.

Workshop Exercise

Rather than focusing on prediction of future values of a single variable (as in our previous SST example), we designed a regression exercise that would explore the statistical relationship between two variables. This approach allowed us to retain the advantages of correlation and regression while giving the students an opportunity to examine the interaction of actual physical and meteorological variables.

To stimulate student curiosity about the relationship between thermal heat absorbed by the ocean surface and subsequent change in SST, we devised an outdoor exercise using a thermometer and a hand-held digital photometer.

We assigned pairs of students to three 20-m linear transects per team stretched across our main campus quadrangle. Each transect included mainly grassy surface with an occasional concrete sidewalk surface; we did not quantify the percent of transect length intersected by concrete. At every 5-m intercept, the students recorded ground temperature to the nearest degree Celsius, and incident solar radiation in relative lux units using a digital photometer (Model DLM2, J.J. Electronics). We made no allowances or adjustments for cloud cover, and so we collected a variety of points in both shade and direct sunlight (Figure 3; n = 90 x,y data points recorded).

The students downloaded the data from the course website and used simple linear regression to calculate a predicted temperature from any given lux value (Figure 4).

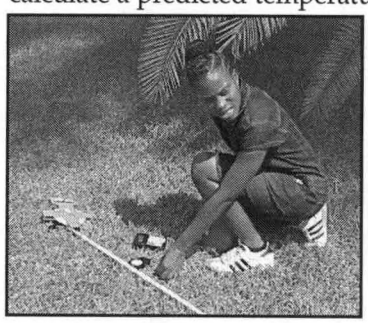

Figure 3. Collecting the field data.

Note that the regression analysis revealed a non-significant relation between the variables ($p = 0.16$), an important lesson for our students. Our data showed that incident solar radiation would not be a reliable predictor for ground temperature. Given the theoretical expectation that increased solar flux would lead to increased ground temperature, our results seem at first glance surprising. But the students soon recognized the problems in not accounting for variability in surface textures (grass vs. concrete) or in cloud cover. Thus, our results focused their attention on re-designing the methods.

The Presentations

Each student was assigned to describe and present the results of an exercise in an oral format to the SNHS faculty on the last day of the program (to be accompanied by Microsoft PowerPoint" slides of their own designs). We spent two weeks on training the students with spreadsheets and PowerPoint, techniques, and they relished an opportunity to get up and perform. Each chose his or her own color schemes, graphic designs, etc. This was a process they seemed to really enjoy.

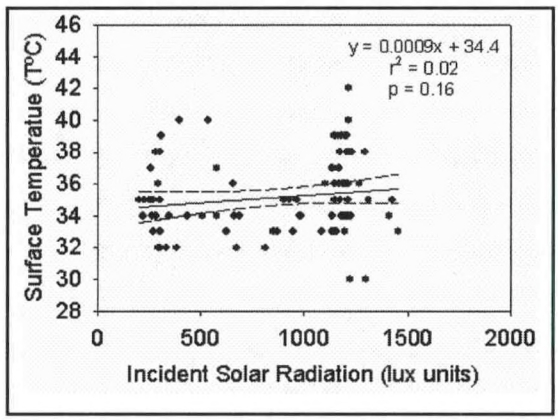

Figure 4. Regression (with 95%-CIE boundaries) collected from 20-m transects (n = 90).

The Post-Workshop Assessment

The students completed an anonymous, post-workshop assessment instrument concerning their likes, dislikes, and expectations for their summer experience; this was included in our Six-Month Period Progress Report to NOAA (July 2004). Our major findings were that the students were very enthusiastic about the introduction to computer software packages such as Microsoft Excel, and PowerPoint,,. Though some of the students had some experience with the packages, all reported learning many new techniques they planned to use in their future studies.

During informal discussions, several students reported being pleasantly surprised with the basics of statistical inference and regression modeling, which I believe will lead them into detailed explorations in this field.

Perhaps 20 years from now, we'll discover that one of the great hurricane modelers of the 21st-Century had actually sat in our classroom this past summer. I certainly hope so.

Conclusions

The NOAA/EPP Award gave us the opportunity to recruit and train a hitherto underrepresented cohort of young high school students. The summer workshop gave the students a taste of the college experience, as well as two hours of college credit. The particular exercise using regression statistics and predictive modeling allowed them to consider the career possibilities and opportunities in the NOAA-related sciences.

ACKNOWLEDGMENTS

Significant assistance on this project came from Sister John Karen Frei, Ph.D., Gerhild Packert, Ph.D., Silvia Macia, Ph.D., David Molnar, Ph.D., and Linda Johnson, B.S. This project was funded by NOAA Award No: NA03OAR4810129 (2003-2006), Barry University EPP/MSI Environmental Entrepreneurship Program.

CITED LITERATURE

Aberson, S.D., 1998: Five-day tropical cyclone track forecasts in the North Atlantic basin. *Wea. Forecast.*, **13**, 1005-1015.

Anonymous, 2004: Average national ACT score rises for first time since 1997, but many students still not ready for college science and math courses. Online National Data Release from: http://www.act.org/news/releases/2004/8-18-04.html (viewed 8-18-2004).

Carnevale, D., 2003: The virtual lab experiment. *Chronicle Higher Ed.*, **49**, 30-32.

DeMaria, M., 1997: Summary of the NHC/TPC tropical cyclone track and intensity guidance models. *http://www.nhc.noaa.gov/aboutmodels.shtml* (viewed 9-1-2004).

Elsner, J.B., 2003: Tracking hurricanes. *Bull. Amer. Meteor. Soc.*, **84**, 353-356.

Elsner, J.B. and T.H. Jagger, 2004. A hierarchical Bayesian approach to seasonal hurricane modeling. *J. Climate*, **14**, 2813-2827.

Goldenberg, S.B., C.W. Landsea, A.M. Mestas-Nuñez, and W.M. Gray, 2001: The recent increase in Atlantic hurricane activity: causes and implications. *Science*, **293**, 474-479.

Junger, S., 1997: *The perfect storm*. HarperPerennial, NY (236 pages).

Landsea, C.W., and J.A. Knaff, 2000: How much skill was there in forecasting the very strong 1997-98 El Niño? *Bull. Amer. Meteor. Soc.*, **81**, 2107-2120.

Powell, M.D., and S.H. Houston, 1996: Hurricane Andrew's landfall in South Florida. Part II: Surface wind fields and potential real-time applications. *Wea. Forecast.*, **11**, 329-349.

Powell, M.D., S.H. Houston, and T.A. Reinhold, 1996: Hurricane Andrew's landfall in South Florida. Part I: Standardizing measurements for documentation of surface wind fields. *Wea. Forecast.*, **11**, 304 - 328.

Rappaport, E.N., 1994: Hurricane Andrew. *Weather*, **49**, 51-61,

Saffir, H.S., 1973: Hurricane wind and storm surge. *The Military Engineer*, **423**, 4-5.

Vickery, P.J., P.F. Skerlj, and L.A. Twisdale, 2000: Simulation of hurricane risk in the U. S. using empirical track model technique. *J. Struct. Engineering*, **126**, 1222-1237.

Weber, H.C., 2003: Hurricane track prediction using a statistical ensemble of numerical models. Month. *Wea. Rev.* **131**, 749-770.

Willoughby, H.E. and P.G. Black, 1996: Hurricane Andrew in Florida: dynamics of a disaster. *Bull. Amer. Meteror. Soc.*, **77**, 543-549.

Zorita, E., H. von Storch, 1999: The analog method as a simple statistical downscaling technique: comparison with more complicated methods. *J. Climate*, **12**, 2474-2489.

ORAL SESSION D1
Atmospheric Sciences

The Thermodynamic Impact of Saharan Dust in the Lower Atmosphere of the Tropical North Atlantic during AEROSE 2004

Everette Joseph and Francis Mensah
Howard University

The 2004 Aerosol and Ocean Science Expedition (AEROSE) was a multidisciplinary oceanographic field campaign conducted onboard the NOAA Ship Ronald H. Brown (NOAAS RHB) in the tropical North Atlantic Ocean from 29 February to 26 March 2004, with funding support granted to the NOAA Center for Atmospheric Sciences (NCAS) at Howard University (HU/NCAS). The following were overall mission objectives. 1) Obtain a set of critical measurements to help characterize the impacts and microphysical evolution of Saharan dust aerosol transport across the Atlantic Ocean. 2) Obtain bio-optics and oceanographic observations to assist in studying the effect of dust on the marine boundary layer, characterizing water masses throughout the transects, and investigating upwelling conditions off the Northwest coast of Africa. 3) Provide complementary visible and infrared (IR) measurements and analysis that can support the validation of radiometric data and derived products from advanced satellite instruments, including the NASA Aqua Atmospheric Infrared Sounder (AIRS), the NOAA Advanced Very High Resolution Radiometer (AVHRR/3),and the NASA Terra/Aqua Moderate Resolution Imaging Spectroradiometer(MODIS).

The present study provides preliminary analysis of aerosol optical depth derived from sun photometers, solar and IR fluxes from radiometers and meteorological measurements from balloon borne soundings during dust events and in pristine conditions. The results show the impact of dust on the thermodynamics of the lower atmosphere, and suggest the possible climatic influences of the dust.

Mapping Asthma Hot Spots: The Geography of Asthma and Air Pollution in the Bronx, New York City

Dr. Juliana Maantay, Juan Carlos Saborio, Dellis Stanberry, Holly Porter-Morgan

Lehman College, City University of New York, Department of Environmental, Geographic, and Geological Sciences

This project examines the spatial correspondence between the incidence of asthma and the locations of environmentally-burdensome land uses and activities. We propose that there is a spatial correspondence between areas having high rates of asthma hospitalization and areas in close proximity to sources of air pollution. To test this hypothesis, we are using Geographic Information Systems (GIS) to map and model the major mobile and stationary sources of air pollutants in the Bronx, New York City.

Recent studies [Ciccone et al., 1998; Edwards et al., 1994; English et al., 1997; Van et al., 1997] have linked high concentrations of known air pollutants to respiratory disease, demonstrating that increased air pollution is a serious public health and environmental concern. Reduced air quality and respiratory health problems, particularly asthma, have been associated with a number of sources, including toxic air emissions from industrial processes, particulate matter and increased levels of NOx and SO2 from truck traffic, and increased pollution from other noxious land uses (e.g. waste-related facilities, medical institutions, power plants). These issues are of particular interest to the Bronx community, because residents of the Bronx, specifically children under the age of 14, suffer from one of the highest rates of asthma hospitalization in the country [New York City Department of Health, 1999]. In addition, the Bronx has a disproportionate number of Stationary Point Sources (SPS) and TRI (Toxic Release Inventory) facilities [Maantay, 2002], and these are mainly concentrated in the South Bronx, where the asthma rate is relatively high. The South Bronx also has the highest volume of vehicular traffic in the nation, which greatly lowers air quality [Jackson, 1995]. There have been no major geographic studies of New York City that have addressed the potential connection between noxious land uses and asthma.

We are addressing the following questions using the methods discussed below: 1) What are the major sources of air pollution in the Bronx? For each source, what are the quantities and characteristics of pollutants emitted? 2) What is the geographic extent of pollutant dispersion (impact zone)? 3) What are the characteristics (age, socio-economic, and racial/ethnic) of populations potentially most affected by these pollution sources? 4) Is there a spatial correspondence between areas having high asthma hospitalization rates and areas in close proximity to major sources of air pollution? 5) Is there a connection between age, income, race/ethnicity, high rates of hospitalization for asthma, and environmental burdens?

We located and mapped major sources of air pollution in the Bronx: facilities that emit, use or store toxic substances (i.e. TRI); facilities that emit criteria pollutants (i.e. SPS); limited access highways (LAH); and major truck traffic routes (MTR). Buffers were created around the above listed major sources of air pollution. Using Census Bureau information at the block level, we mapped the potentially-impacted population by socio-economic and demographic indicators, such as race and ethnicity, and poverty status. We conducted a geoprocessing operation called "Clipping" in order to select the portions of the block groups and asthma hospitalization cases that lie within the buffers. This was done for each separate buffer type and for the combined buffer, using case data for each separate year. Statistical analyses were conducted on the difference of case counts and rates between areas within the buffers and areas outside the buffers.

The odds ratios for children (age 0-15 years) and adults (16 years and older) for asthma hospitalizations for each year from 1995-1999 were calculated, comparing those who lived in buffer areas surrounding Toxic Release Inventory (TRI) facilities, Stationary Point Sources (SPS), along Major Truck

Routes (MTR), and/or Limited Access Highways (LAH), and compared to other Bronx residents living outside these buffer zones. Patterns of increased risk for those living within the buffers were consistent from year to year. For adults living near TRI facilities, the increased risk for asthma hospitalization ranged from 29-60%, for SPS sites from 26-66%, along MTRs from 7-17%, and in all buffer zones from 28-30%. The increased risk for children living near SPS sites ranged from 14-30%, for TRI facilities 16-31%, and for combined buffer zones 11-17%. No increased risk was found along LAHs and none for children living along MTRs. The increased risk for the total population living in all buffer zones was 25-29%.

Hierarchical linear regression analysis was conducted to determine if combined pollution buffer zone area (measured as the percent of total land area) significantly predicts asthma hospitalization (measured as hospitalizations per 1,000) after controlling for the effects of poverty (% of population below poverty level) and minority composition (% of the population who report themselves as a member of a minority group). This analysis was conducted at the Census Block Group (CBG) level.

The resulting analyses indicate that the overall model comprised of the three variables (combined buffer zone, minority, and poverty status) significantly predicts hospitalizations due to asthma. The 3-factor model accounts for 45% of the variance in asthma hospitalizations. The model coefficients indicate that all 3 factors are significant, and indicate positive relationships with hospitalization rates.

REFERENCES

Ciccone, G., et al, 1998: Road traffic and adverse respiratory effects in children. *Occupational and Environmental Medicine* **55**: 771-778.

Edwards, J., Walters, S., and R.C. Griffiths, 1994: Hospital admissions for asthma in pre-school children: relationship to major roads in Birmingham UK. *Archives of Environmental Health* **49**: 223-227.

English, P., Neutra, R., Scalf, R., Sullivan, M., Waller, L., and L. Zhu, 1997: Examining associations between childhood asthma and traffic flow using a geographic information system. *Environmental Health Perspectives* **107**: 761-767.

Jackson, K., ed. 1995: *The Encyclopedia of New York City*, Yale University Press, New Haven, CT.

Maantay, J.A., 2002: Mapping Environmental Injustices: Pitfalls and Potential of Geographic Information Systems in Assessing Environmental Health and Equity. *Environmental Health Perspectives* **110** (Supp. 2):161-171.

New York City Department of Health, 1999: Asthma Facts, New York City Childhood Asthma Initiative, New York, NY.

Van Vliet, P., Knape, M., de Hartog, J., Janssen, N., Harssema, H., and B. Brunekreef, 1997: Motor vehicle exhaust and chronic respiratory symptoms in children living near freeways. *Environmental Research* **74**:122-13

Location of Patients Admitted to the Hospital for Asthma in 1999

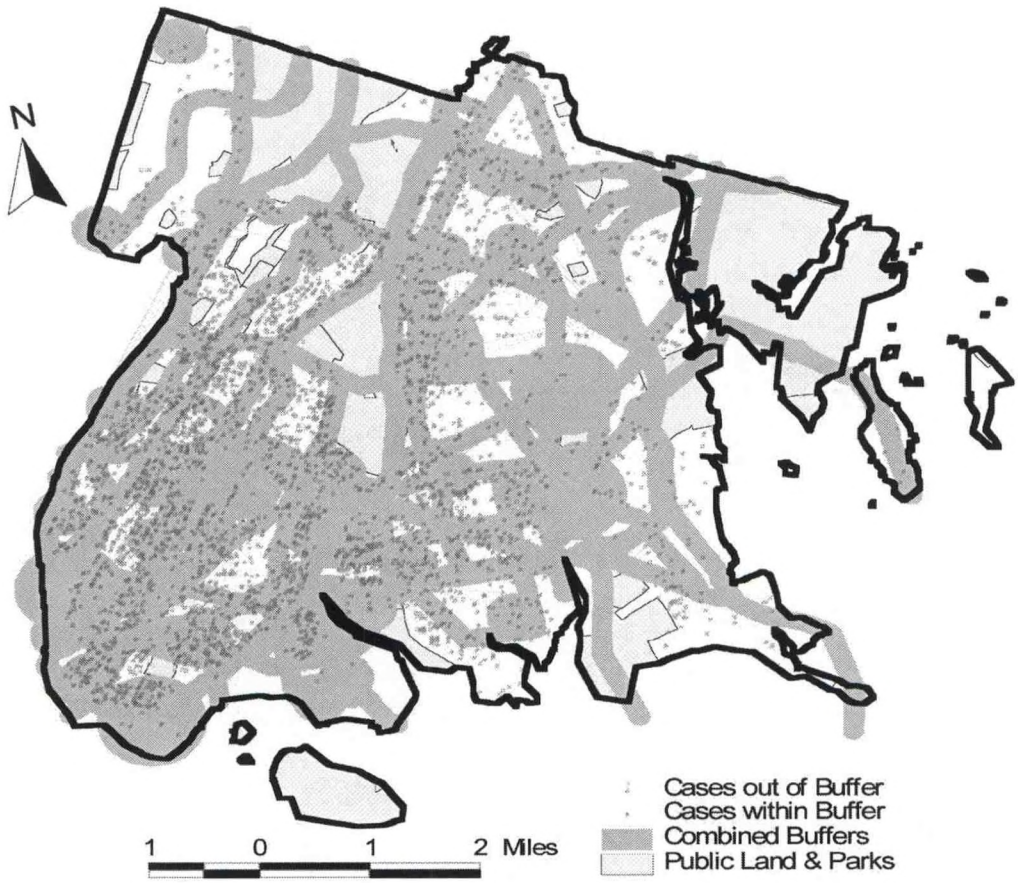

Each dot represents the residence of one Bronx person admitted to the hospital for asthma in 1999. Some dots represent multiple admissions of the same person, or multiple people admitted from the same address. The multiple cases are not shown as individual dots on the map, but have been included in statistical calculations.
There were 8,188 hospital admissions for asthma in 1999: 5,876 of them from within the areas of the combined buffers and 2,312 of them from the areas outside the buffers.
Overall in 1999 a Bronx resident was 27% more likely to be admitted to the hospital for asthma if living within a buffer area than if living outside a buffer area

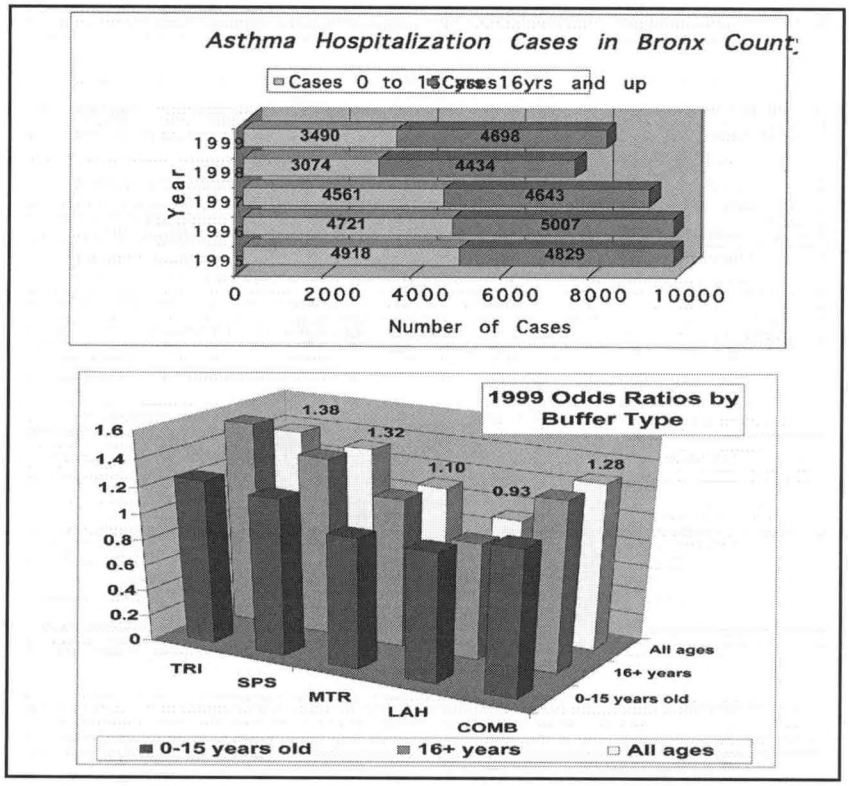
Asthma Hospitalization Cases in Bronx County
Cases 0 to 15yrs
Cases 16yrs and up
Year
1999
1998
1997
1996
1995
3490
4698
3074
4434
4561
4643
4721
5007
4918
4829
0
2000
4000
6000
8000
10000
Number of Cases
1999 Odds Ratios by Buffer Type
1.6
1.4
1.2
1
0.8
0.6
0.4
0.2
0
1.38
1.32
1.10
0.93
1.28
TRI
SPS
MTR
LAH
COMB
All ages
16+ years
0-15 years old
0-15 years old
16+ years
All ages

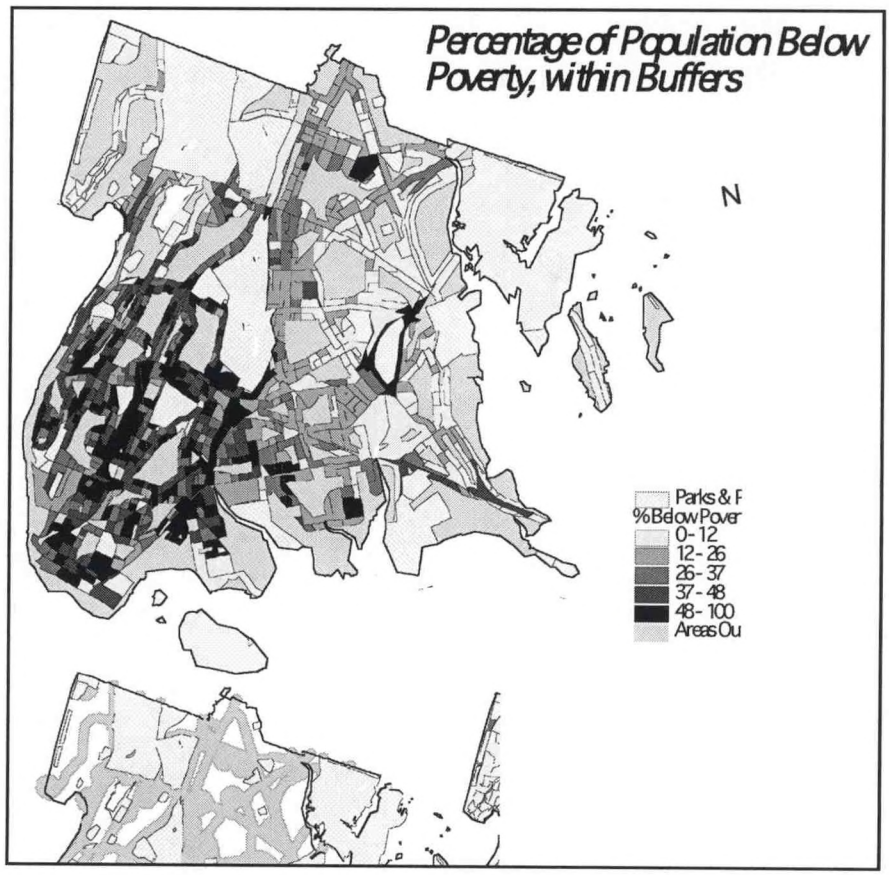
Percentage of Population Below Poverty, within Buffers
N
Parks & F
%Below Pover
0-12
12-26
26-37
37-48
48-100
Areas Ou

Mississippi Mesonet: Moving from Initial Demonstration to Statewide Implementationy

Dr. Loren White and Dr. James Finney
Jackson State University, Jackson, MS

The Mississippi Mesonet (mesoscale network) is a project led by Jackson State University's Meteorology Program that is projected to place at least one research-quality electronic weather station in each of Mississippi's 82 counties. A prototype station has been established in Newton County as a result of collaboration with local and federal agencies. Each Mesonet station will collect one-minute resolution data and present it on the world-wide web within minutes of observation. Variables include wind speed and direction (2m and 10m heights), temperature (1.5m, 2m, 9.5m and 10m), relative humidity (2m and 10m), total and photosynthetically active solar radiation, barometric pressure, precipitation (with a backup), soil temperature under bare soil (5cm, 10cm and 20 cm depths), and soil temperature and moisture under vegetation (5cm, 10cm, 20cm, 50cm and 1m depths). Expansion to the full network is expected to be a cooperative effort among several universities, community colleges, secondary schools and primary schools along with many federal, state and local agencies

Comparison of Aerosol Microphysics and Mycology of Saharan Dust Particles in Canary Islands, Puerto Rico and Dominica

Lizette Roldán[a] , Vernon R. Morrisa[b], and Yasmín Detrés[c]

[a]Atmospheric Sciences,, Howard University,, Washington, DC 20059

[b]Department of Chemistry, Howard University, Washington, DC 20059

[c]Department of Marine Sciences, University of Puerto Rico Mayaguez, Mayaguez, PR 00680

The characteristics of Saharan dust aerosols which had undergone trans-Atlantic transport were studied in three areas in along the trajectory coinciding with the westward transport. One of the areas selected was the Canary Islands due to its proximity to the west coast of Africa. The other two areas were Puerto Rico and Dominica both located in the Caribbean. We report measurements of aerosol mass density and number distributions for the island of Canary Islands and for Puerto Rico. We also have microbiological analysis of filter samples from Canary Islands and the island of Dominica.

We will present a comparison of the aerosol mass and number density distributions for the Canary Islands and Puerto Rico as determined by a six-stage quartz crystal microbalance (QCM) cascade impactor and a six-stage laser particle counter. Results of mycological analyses on filter samples obtained from the Canary Islands and Dominica will also be presented.

CO AND O3 CONCENTRATIONS DURING A SAHARAN DUST STORM

Michelle Strachan*, Vernon R. Morris*,**

*Howard University Program in Atmospheric Sciences,
**Department of Chemistry, Howard University, Washington, DC 20059

Abstract

The NOAA Center for Atmospheric Sciences (NCAS) conducted a combined atmospheric and oceanographic experiment aboard the NOAA Ronald H. Brown ship to characterize the physicochemical evolution of the Saharan Aerosol Layer during its long-range transport into the eastern seaboard of the United States and the Caribbean, and to quantify its effects on the regional environment and climate. The NCAS Trans-Atlantic Aerosol and Oceanographic Science Expedition (AEROSE-04) departed on February 29, 2004 from Bridgetown, Barbados and concluded in San Juan, Puerto Rico on March 26, 2004. During AEROSE-04, CO and O3 concentrations were measured to study the effects of Saharan dust on the chemistry of the atmospheric environment. Tropospheric O3 and CO were measured in-situ and on a continual basis during several dust storms that occurred during the month of March.

Introduction

Ozone is an important greenhouse gas whose presence in the stratosphere serves to protect life, while its presence in the troposphere could lead to life's demise. In addition to being an important greenhouse gas, ozone regulates the oxidizing capacity of the troposphere and can influence background levels of trace chemical species.

Dust plumes off the coast of Africa commonly include continental aerosols and smoke from biomass burning. Biomass burning produces chemically active atmospheric gases, including carbon monoxide, nonmethane hydrocarbons, and nitric oxide. Along with methane, these gases, can lead to the production of tropospheric ozone. The West African biomass burning season generally spans from December through February.

While surface level measurements over the Atlantic are sparse and heavily dependant on research vessel routes and measurement obligations, in-situ measurements are essential for understanding regional environments. In-situ measurements can provide validation of satellite observations, and chemical transport and radiative transfer models. In addition, surface level measurements can provide a more accurate quantification of tropospheric ozone concentrations than satellite observations.

This presentation will highlight the atmospheric measurements of CO and O3 that were taken during the AEROSE-04 mission.

Measurement Strategy

The NOAA R/V Ronald H. Brown departed Bridgetown, Barbados (13N, 59W) on February 29, 2004 and arrived in Las Palmas, Gran Canaria (28N, 15W) on March 15, 2004 (fig. 1). During this 15-day trans-Atlantic journey, CO and O3 concentrations were measured continuously using the TEI model 48C nondispersive infrared gas filter correlation

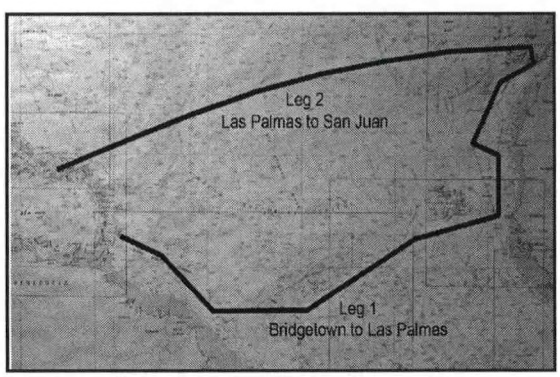

Figure 1. AEROSE-04 cruise tracks.

instrument and the TEI model 49 UV photometer respectively. Both instruments recorded data in one minute intervals and corresponding data was analyzed using 30 minute averages.

The instruments were housed on the 03-deck of the ship and were covered by tarp to protect them

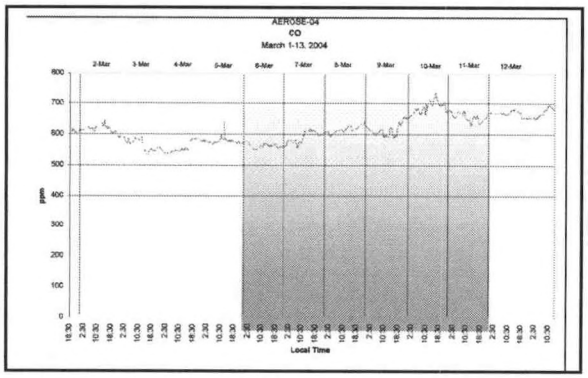

Figure 2. 30-minute average of CO concentrations measured along the complete eastward leg of the cruise.

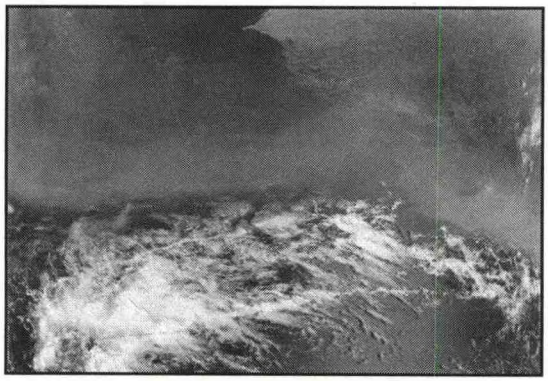

Figure 3. MODIS image on March 6, 2004 showing persistent fires on the west coast of Africa. Red spots on the image indicate active fires.

from sea spray and sea salt. Measurements were taken through Teflon tubing that was connected to the instruments and extended to a shrouded intake about three meters above the deck.

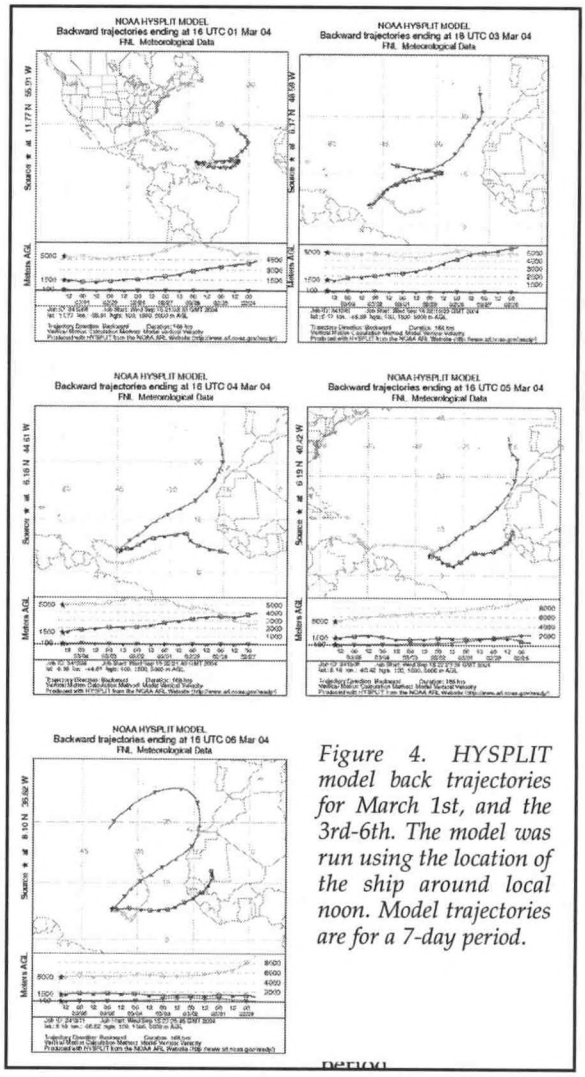

Figure 4. HYSPLIT model back trajectories for March 1st, and the 3rd-6th. The model was run using the location of the ship around local noon. Model trajectories are for a 7-day period.

Observations and Data

Figure 2 illustrates 30-minute averages of the CO concentration along the eastward track of the cruise. The shaded area on this image designates days when the ship was traveling through the heaviest dust storms. In total, AEROSE-04 encountered four distinct dust storms.

Initially, typical CO continental concentrations of about 600-614 ppm were measured near Bridgetown, and a slight decrease of about 13% was observed as we moved further out to sea. However, as we began to encounter the dust on March 5th and as we approached the most intense dust storm around March 9th, CO concentrations began to rise. An increase of about 39% in CO concentrations was observed as we moved out of pristine ocean air and traveled eastward into the Saharan dust storms. This increase indicates the presence of smoke from biomass burning. This is to be expected, as we were approaching the west coast of Africa during the end of the biomass burning season for that region. A March 6th MODIS image (fig. 3) shows active biomass burning taking place

in West Africa.

HYSPLIT model back trajectories were used to determine the origination of air masses that we encountered during the cruise. Figure 4 shows lower-level air masses from West Africa moving westward across the Atlantic.

The O3 concentrations we observed near Barbados also appeared to be typical of continental ozone concentrations. On March 4th we observed a major decrease in the O3 concentration and noted error messages on the output screen of the instrument. Thus, due to equipment malfunctions, the O3 dataset contains gaps during which the instrument was turned off for repair. While there was a significant drop in concentration, one can observe a gradual increasing and then decreasing pattern in the time series.

O3 concentrations for March 8th, 10th, and 11th were selected for analysis because these were the days we encountered the most intense dust storms. Figure 5 illustrates the O3 concentrations for the selected days. Since we were traveling under a thick dust layer, intense solar radiation was inhibited and consequently a diurnal cycle is not clearly observed in the O3 data.

Again, back trajectories using the HYSPLIT model provided an image of the long-range transport of continental aerosols. Figure 6 shows lower level air masses that appear to have originated in Europe and were transported down and across West Africa.

Upper level trajectories showed air masses that originated high in the atmosphere and remained aloft during the model run. These trajectories were removed from the graphs because they do not imply any mixing with lower levels, and thus have a minor impact on the chemistry of lower level constituents.

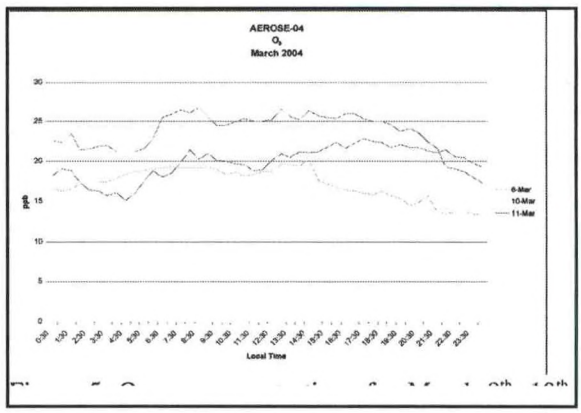

Figure 5. Ozone concentrations for March 8th, 10th, and 11th.

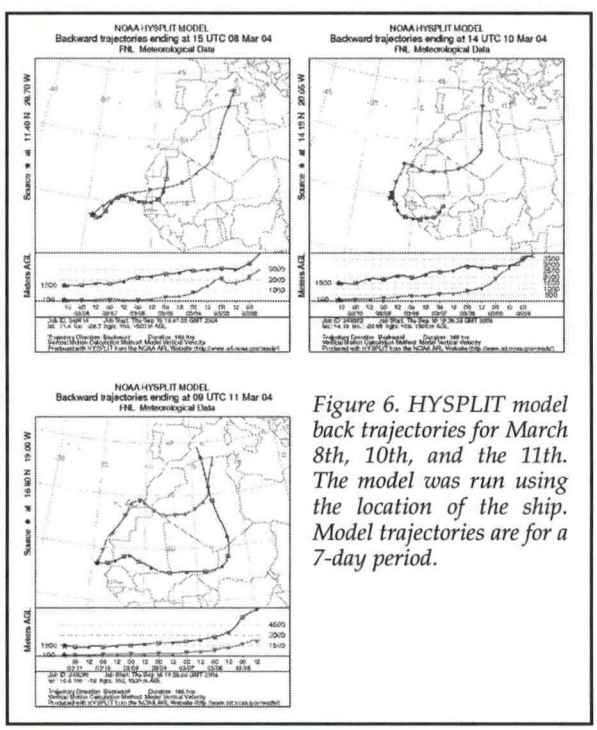

Figure 6. HYSPLIT model back trajectories for March 8th, 10th, and the 11th. The model was run using the location of the ship. Model trajectories are for a 7-day period.

Future Analysis

AEROSE-04 produced a suite of in-situ measurements during its trans-Atlantic voyage. In the near future, the datasets described here will be compared with aerosol optical thickness observations and black carbon concentrations that were measured aboard the ship. We will also compare our datasets with similar CO and O3 measurements from previous research cruises. In addition, an analysis of past ozone climatology over the tropical Atlantic ocean using TOMS data will provide a better understanding of background ozone concentrations in this region. Furthermore, detailed modeling of air mass history will provide an understanding of the long range transport of atmospheric constituents into this region and its effect on regional atmospheric chemistry over the Atlantic Ocean.

REFERENCES

Bates, T.S., P.K. Quinn, D.J. Coffman, J.E. Johnson, T.L. Miller, D.S. Covert, A. Wiedensohler, S. Leinert, A. Nowak, C. Neususs, 2001. Regional physical and chemical properties of the marine boundary layer aerosol across the Atlantic during Aerosols 99: An overview. *J. Geophys. Res.*, **106(D18)**, 20,767-20,782

Draxler, R.R. and Rolph, G.D., 2003. HYSPLIT (HYbrid Single-Particle Lagrangian Integrated Trajectory) Model access via NOAA ARL READY website (http://www.arl.noaa.gov/ready/hysplit4.html). NOAA Air Resources Laboratory, Silver Spring, MD.

Lelieveld, J., J. van Aardenne, H. Fischer, M. de Reus, J. Williams, P. Winkler, 2004: Increasing ozone over the Atlantic Ocean. *Science*, **304**, 1483-1487

Rolph, G.D., 2003. Real-time Environmental Applications and Display System (READY) website (http://www.arl.noaa.gov/ready/hysplit4.html). NOAA Air Resources Laboratory, Silver Spring, MD.

Stehr, J.W., W.P. Ball, R.R. Dickerson, B.G. Doddridge, C.A. Piety, J.E. Johnson, 2002. Latitudinal gradients in O3 and CO during INDOEX 1999. *J. Geophys. Res.*, **107(D19)**, 8015, 10.1029/2001JD000446

Thompson, A.M., B.G. Doddridge, J.C. Witte, R.D. Hudson, W.T. Luke, J.E. Johnson, B.J. Johnson, S.J. Oltmans, R. Weller, 2000: A tropical Atlantic paradox: Shipboard and satellite views of a tropospheric ozone maximum and wave-one in January-February 1999. *Geophys. Res. Lett.*, **27**, 3317-3320

Thompson, A.M., J.C. Witte, R.D. Hudson, H. Guo, J.R. Herman, M. Fujiwara, 2001. Tropical tropospheric ozone and biomass burning. *Science*, **291**, 2128-2132

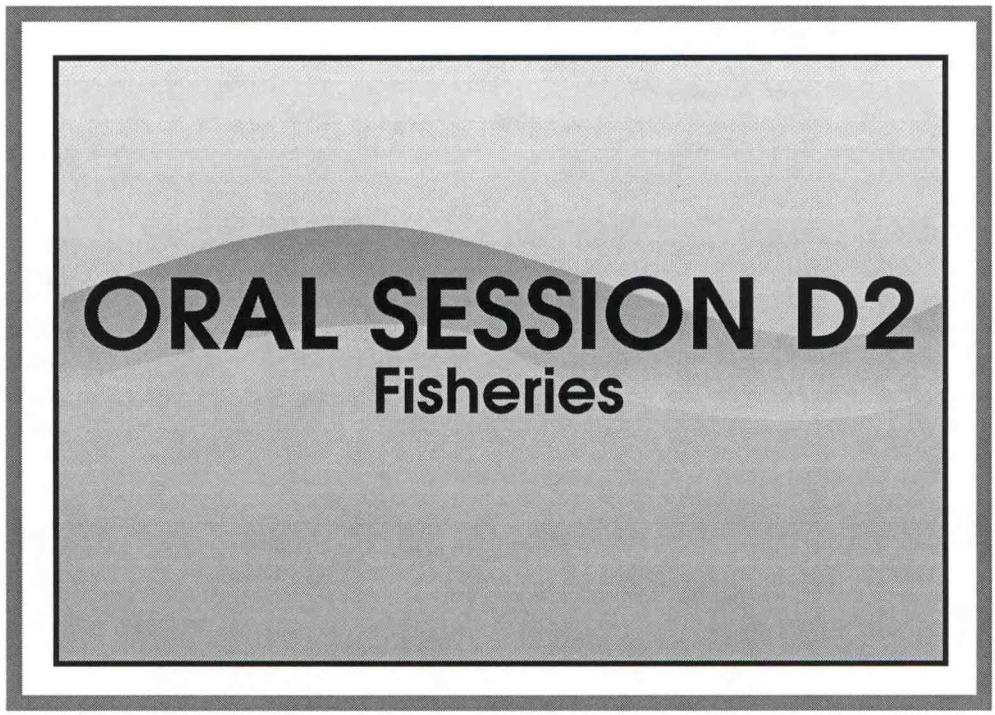
ORAL SESSION D2
Fisheries

A PILOT STUDY ON THE MARK AND RECAPTURE MODEL FOR YELLOWTAIL FLOUNDER *(LIMANDA FERRUGINEA)* OFF NEW ENGLAND

Larry A. Alade[1]*, Steven Cadrin[2] and Eric May[1]

[1]Living Marine Resources Cooperative Science Center, Department of Natural Sciences, University of Maryland Eastern Shore, Princess Anne, MD.
[2]Northeast Fisheries Science Center, NMFS/NOAA, Woods Hole, MA
*Email address: *oaalade77@yahoo.com*

Managing the recovery of yellowtail flounder (Limanda ferruginea) resources and maintaining optimum yield require precise stock assessments and accurate forecasts of the population and fishery. Although yellowtail flounder stock assessments have provided valuable information for fishery management advice, several sources of uncertainty persist. Assessments of all three New England yellowtail flounder stocks tend to overestimate stock size and underestimate fishing mortality, leading to considerable uncertainty in catch forecasts. The source of this apparent bias is not well known, but may result from insufficient data on dispersal, mortality and harvesting. Thus, a study was developed to provide estimates on mortality and migratory patterns on yellowtail flounder that will complement the current programmatic data collection and analytical methods to reduce uncertainty in stock assessment and management advice. A mark and recapture (movement-mortality) model was fitted to data presented by Royce et. al in the 1940's to estimate fishing mortality and proportion of movement in all New England yellowtail flounder stocks (Cape cod, Southern New England and Georges Bank). Preliminary results from the study suggested that fishing mortality is fairly high with a high level of residency and minimal migration between fishing grounds. Results from these data will provide information about the accuracy of the model and how to improve on the model development in the future.

Investigations Into Factors that Influence Larval Transport into a Mid-Atlantic Estuary

Keisha English*, Joseph W. Love, James Wiley, Eric B. May

Living Marine Resources Cooperative Science Center, Department of Natural Sciences, University of Maryland Eastern Shore, Princess Anne, MD.
*Email address: *Kenglish@umes.edu*

The watershed of the Maryland and Virginia coastal bays totals 482 km2 with portions extending into Delaware. Four major tributaries deliver freshwater to the bays. Saltwater from the Atlantic Ocean enters the bays through the Ocean City Inlet in Maryland and the Chincoteague Inlet in Virginia. The significance of the Maryland and Virginia coastal bays as nurseries and source of recruitment for fishes along the Atlantic Coast have yet to be established. Understanding the influence of physical factors in determining the number of juveniles that will inhabit the coastal bays as nurseries will consequently allow greater comprehension of the potential for the bays to serve as a source of recruitment for the Atlantic Coastal stocks. Larval fish originating from spawning stocks off the Atlantic Coast will be sampled to determine the rate of immigration into the Maryland Virginia Coastal Bays. Sampling will be done with cone-shaped plankton nets, equipped with a plastic container on the cod end and a flow meter at the mouth of the net. The nets will be arrayed vertically at different depths and at differing locations in each of the inlets. Variation in the vertical distribution of larvae will be examined. Physical factors such as wind speed, wind direction, current direction, current flow, temperature, and salinity will be sampled at each location. The relationships between species composition and species abundances, and the environmental variables will be made, as well as comparisons between the two inlets.

DETERMINING THE VIABILITY OF MARYLAND AND VIRGINIA COASTAL BAYS AS NURSERIES FOR SUMMER FLOUNDER *(PARALICHTHYS DENTATUS)*

Elden Wayne Hawkes Junior*, Joseph Love and Eric B. May

Living Marine Resources Cooperative Science Center, Department of Natural Sciences, University of Maryland Eastern Shore, Princess Anne, MD
*Email address: *Ewhawkes@umes.edu*

The aim of this project is to determine the distribution and dispersal patterns of summer flounder (Paralichthys dentatus) across the coastal bays of Maryland, Virginia, and Delaware (U.S.A). Specifically, we will assess the viability of these bays as nursery grounds for summer flounder. Coastal bays will be divided into five sectors according to geographic location. Within each sector a series of ten randomly generated sites measuring 10m by 10m will be sampled using an otter trawl. Environmental variables such as salinity, conductivity, dissolved oxygen and pH will be taken at each site using a Hydrolab H2O. Paralichthys dentatus will be measured for total length and tagged. Age will be estimated using length frequency charts. Individuals will be classed as juveniles and sub-adults in order to: (1) determine distribution/habitat associations of summer flounder juveniles and sub-adults; (2) determine temporal changes in the distribution of summer flounder sub-adults; and (3) provide initial information on movement patterns of summer flounder juveniles and sub-adults in the Maryland, Virginia, Delaware coastal bays.

Potential Impacts of Mycobacteriosis in Striped Bass on Chesapeake and Atlantic Coastal Stocks

Eric B. May[1], V. Pernell Lewis[1], Anthony M. Overton[2], John Jacobs[3], and Larry Alade[1]

University of Maryland Eastern Shore[1]
East Carolina University[2]
Cooperative Oxford Laboratory NOAA/NOS[3]

Until recently, natural mortality rates for striped bass in harvest control models have been held constant at 0.15 across all age groups. However, an evaluation of striped bass harvest using tag returns taken from the Atlantic Coastal stocks has suggested that those tagged in the Chesapeake Bay are being reported at a reduced rate, and that this reduction may be related to increased natural mortality.

Since 1997 striped bass that are residents to the Chesapeake Bay have been infected with *Mycobacterium* spp.. There is evidence that the infections may have existed prior to 1994 where it could have been concurrent with the epizootic attributed to *Edwardsiella tarda* in fish taken from the Potomac River. The infection appears to be increasing in its intensity with greater numbers of striped bass affected in main stem of the Bay. Recently evidence has been obtained that suggests the infection has spread to the Atlantic Coastal stocks.

These two independent lines of inquiry create uncertainty about the health of striped bass stocks and the potential impact of Mycobacteriosis on recruitment. Information presented here will provide evidence of progression for the disease suggesting that a significant number of striped bass are at risk of dying as a result, that the disease is spreading to the Atlantic Coastal Stocks, and that there is a need to employ a broad epidemiological approach in evaluating the situation. A conceptual approach for such an approach will be presented.

Recreational Angler Creel Survey on Maryland's Coastal Bays

Brandon Fortt[1]*, Ward Slacum[2], Jon Volstad [2], James W. Wiley[1] and Eric May[3]

[1] Maryland Cooperative Fish and Wildlife, University of Maryland Eastern Shore, Princess Anne, MD.
[2] Versar, Inc. Columbia, MD,
[3] Living Marine Resources Cooperative Science Center, Department of Natural Sciences, University of Maryland Eastern Shore, Princess Anne, MD
Email address: *bcfortt@umes.edu.*

Recreational fishing is enjoyed by millions of anglers around the world and it can impose severe pressures on natural resources if it is not managed properly. In light of this, the Maryland Department of Natural Resources (MDDNR) in collaboration with the University of Maryland Eastern Shore and Versar Inc. is implementing a two-year creel survey within Maryland's coastal bays scheduled to begin in the spring of 2005. A pilot creel survey was initiated in the summer of 2004 and was designed to gather information that could serve to refine the creel survey methodology and uncover crucial aspects of this recreational fishery. The goals of the pilot study are to identify all relevant components in the coastal bay recreational fishery and evaluate initial angler effort at all access point locations. This will be accomplished by: 1) using existing information, and defining all important angler access points in the coastal bays, and 2) conduct instantaneous counts at all known access points at randomly chosen times. The purpose of this pilot creel survey was to gather information to refine creel survey methodology and to improve our understanding of the recreational fishery.

ORAL SESSION D3
Satellite Remote Sensing

AEROSOL RETRIEVAL OVER URBAN AREAS USING SPATIAL REGRESSION BETWEEN V/NIR AND MIR HYPERION CHANNELS

Barry Gross*, Min Min Oo, Oluwatosin Ogunwuyi, Fred Moshary, Samir Ahmed
Optical Remote Sensing Laboratory, City College of New York, NY, NY, USA 10031
Brian Cairns
Department of Applied Physics, Columbia University, NY, NY, USA 10027

Abstract

Determination of aerosol optical depth from satellite remote sensing measurements is extremely complex due to the large variability of aerosol optical properties. Significant simplification occurs when measurements are taken over water since the ocean reflection signal can be taken as negligible in the NIR.. Unfortunately, over land, most of the signal can be attributed to ground reflectance. While conventional approaches look for "dark" pixels in an image to isolate aerosols, these pixels are subjected to increased noise. In this paper, we explore the feasibility of a regression approach utilizing correlations between the VNIR and MIR channels to extract the aerosol reflection signal over urban areas. This approach is applied to hyperspectral high resolution Hyperion data where the aerosol reflectance signal is shown to agree very well with coincident Aeronet derived reflectance spectra..

Introduction

The remote sensing of aerosol over the land stems follows from the relationship between the measured reflectance $R_m(\mu,\mu') = R_a(\mu,\mu') + T_d(\mu)R_g T_u(\mu') \equiv R_a + T_{atm}(\mu,\mu')R_g$

at the top of the atmosphere and the surface reflectance (assumed lambertian). Under the assumptions of small atmosphere – ground coupling, this relationship is given by where μ' is the satellite view direction, μ is the solar zenith angle, R_a is the atmospheric reflectance, R_g is the ground reflectance and T_d, T_u are the downward and upward total diffuse atmospheric transmission. From this formula, it is clear that for sufficiently small ground reflectance, the TOA reflectance would gived a reasonable estimate to the atmospheric signal. Since many land covers (such as vegetation and some soils) are dark in the red (0.60-0.68 μm) and blue (0.4-0.48 μm) wavelengths it is reasonable to use the darkest pixels in the image to probe the aerosol optical properties. However, in order to retrieve aerosol optical thickness, the surface reflectance of these dark pixels have to be estimated within a small uncertainty of $\Delta R_a < \pm .01$. This absolute accuracy makes absolute thresholding very difficult except over very dark surfaces. The first use of dark targets in an aerosol retrieval algorithm (Kaufmann et al 1988) was based on the detection of green forests as dark pixels using the vegetation index (NDVI) and the near IR reflectance. Dark vegetation was determined by a combination of high NDVI and low reflectance in the near IR.

On the other hand, the surface reflectance across the solar spectrum is correlated to some extent. Soils usually have an increasing reflectance as a function of the wavelength with correlation between the reflectances slowly decreasing with an increase of the wavelength span. Parallel physical processes affect the reflectance in the 0.47 and 0.66 μm channels and in the 2.1 and 3.8μm channels. For example, the presence of vegetation decreases the reflectivity in the visible channels due to chlorophyll absorption and in the mid- IR channels due to absorption by liquid water associated with the plant. In particular, wet soil has a lower reflectance in the visible channels due to light trapping, and in the 2.1 and 3.8 μm channels due to the liquid water absorption. Furthermore, surface roughness, shadows and angular orientations

decrease the reflectance uniformly across the whole solar spectrum (Kaufman et al 1994) and is a critical correlation mechanism for urban land cover where large variations in shadowing and surface orientations exist.

To utilize this correlation, it is necessary to observe that in the 2.1 and 3.8 μm channels, the aerosol signature is negligible and the TOA reflectance in the MIR can be taken as the ground reflectance. Using correlations based on a-priori estimates of land cover type, the 0.47 and 0.66 mm ground reflectances can be estimated thereby allowing an improved estimate of atmospheric reflectance (Holben et al),. Finally, as pointed out (Kaufman et al 1997) the 3.8μm channel is often contaminated by significant thermal emission and is therefore not used in the operational MODIS aerosol retrieval over land un less it is expected that large aerosol modes such as Saharan dust and/or smoke are present.

Based on these principles, the basic approach for an operational and unsupervised aerosol remote sensing algorithm for the MODIS sensor is described within the ATBD document (Kaufman et al 1998) as :

1. Determination of the presence of the dark pixels in the blue (0.47 μm) and red (0.66 μm) channels using their remotely sensed reflectance in the mid- IR channels (2.1 μm).

2. Estimation of the surface reflectance of the dark pixels in the red and blue channels using the measurements in the mid-IR and information on surface type when possible.

3. Determination of the aerosol type using information on the global aerosol distribution and the ratio between the aerosol path radiance in the red and blue channels.

4. Inversion of the measured radiance at TOA into the aerosol optical thickness, volume (or mass) concentration and spectral radiative forcing using radiative transfer look-up tables.

Finally, it is necessary to point out that even with accurate atmospheric reflectance values, aerosol retrieval is hardly straightforward. In order to derive the optical thickness from the atmospheric reflection, the aerosol size distribution, single scattering albedo and refractive index have to be assumed Sensitivity studies showed that in a general case these assumptions generate substantial errors in the derived aerosol optical thickness (~30%). To reduce the errors, a good model of the aerosol properties based on measurements is required (Martins et al; Remer et al) In regions where the model is most applicable, we can expect the remote sensing procedure to be more accurate.

While the above approach has been shown to be useful over dark and fairly uniform land cover types, the inherent weaknesses which make the approach less useful for aerosol monitoring over urban areas. In particular, the spatial heterogeneity of the surface reflection makes the identification of dark pixels more difficult and since the dark pixels are by definition low signal pixels, the uncertainty in the dark pixel threshold is greatly increased. To beat down the noise, we propose the use of a regression approach between the VIS and MIR channels and extrapolating the regression line to zero MIR reflectance to better estimate the VIS reflectance. While this regression approach will also have difficulties when a variety of land surfaces are present, shadowing effects

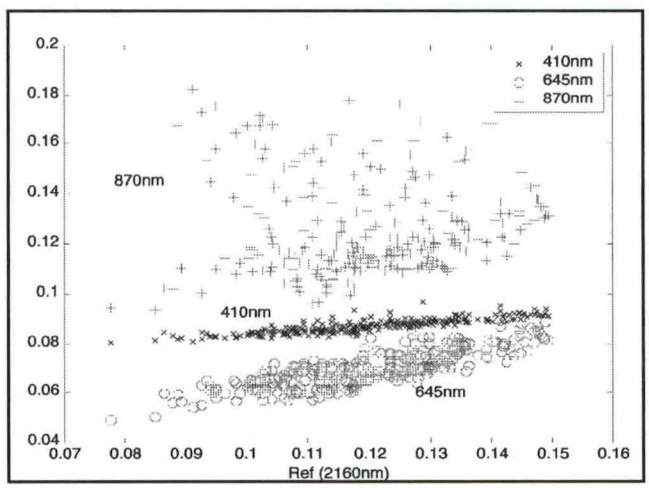

Figure 1 VIS - MIR regression for MODIS from a 25km x 25km box.

that are most strongly present in urban environment significantly increases the dynamic intensity range thereby stabilizing the regression.

Finally, the advent oof hyperspectral sensors can provide complete atmospheric reflectance spectra which can better refine the type of aerosol model assumptions used making this approach more attractive to next generation sensors.

Procedure

Using equation (1) and assuming a linear correlation exists between the VIS and $R_{vis}^{TOA} \approx kR_{MIR}^{TOA} + R_{vis}^{Atm}$ MIR channels, simple algebra relates the TOA reflectances as and in the limit of zero MIR reflectance R_{MIR}^{TOA} Æ 0 fi $R_{vis}^{TOA} = R_{vis}^{Atm}$.

The applicability of these relations is clearly exhibited in figure 1 where the regressions between the VIS and MIR are shown for a MODIS image in a midwestern crop type surface. The regressions are formed by correlating 25 x 25 1km pixels. Note in particular, the excellent regressions of the blue and red channels against the MIR but the poor correlation in the NIR limiting this approach to the VIS. In addition, it is clearly unnecessary to know the particular surface correlation but simply extrapolate the regression line to zero.

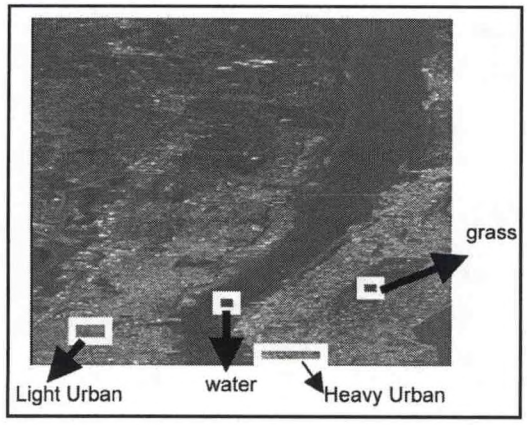

Figure 2. Hyperion image of New York City (600nm)

While the MODIS sensor can apply this regression technique to fairly homogeneous surface types, urban environments require higher spatial resolution. To test the approach over more complex ground terrain useful for urban areas, we make use of Hyperion data that was taken over NYC (Sept 12, 2001) with spectral coverage from 400nm to 2800nm with 10nm resolution and 30meter footprint. The image does not include the WTC and the winds were blowing the smoke and ash in a southerly direction away from the image resulting in a very low aerosol loading.

In figure 2, we focus on several regions of the Hyperion image representing water, vegetation (central park), low urban and high urban scenery and examine the applicability of the correlation approach for these different surface types. In figure 3, inter-comparisons of the regression curves for the different urban zones selected are shown. These curves illustrate that the regression to zero MIR reflectance gives similar values over all surface types as expected. However, it should be pointed out that problems utilizing dark pixel determination appear. In particular, there is a wide spread in the pixels especially at low reflection values making regression absolutely necessary.

To illustrate the spectral limits of the correlation approach, we plot in figure 4 the correlation coefficient between the MIR band reflection and the reflection over 500-1100nm. Over vegetation, a sharp break in the correlation coefficient at 700nm from high correlation to zero correlation is consistent with vegetation behavior while in light urban areas, a similar behavior is seen except there is a slight correlation due to a small but measurable shadowing effect that is wavelength independent. This shadowing effect manifests itself most strongly in the more highly urban region where a near wavelength independent correlation is exhibited.

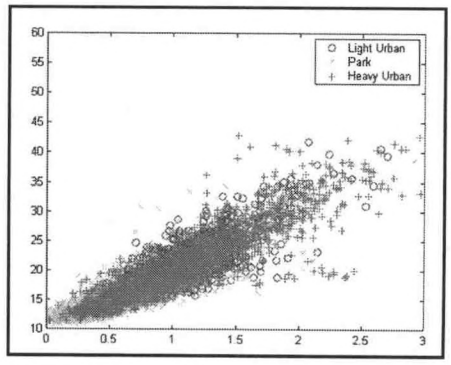

Figure 3: VIS - MIR regression for different urban scenes (arb units)

Validation

Validation of the approach can be seen in Figure 5 where

the aerosol reflection as a function of wavelength obtained by this method is calculated and referenced to the reflection obtained from Aeronet estimates of single scattering albedo, phase function and wavelength dependant optical depth using the single scattering approximation given by (2) which is valid since the aeronet optical depths < 0.05.

Further validations were also performed on AVIRIS Hyperspectral data of an urban area as seen in figure 6.

In this data set, a sharp boundary between water and land was present and used to assess the quality of the atmospheric retrieval by comparing it to the water leaving reflectance for both urban cover types in figure 7. The atmosphere reflection signal was then compared to the water leaving signal which should be approximately the sum of the water leaving radiance and the atmospheric signal. The differential signal should then approximately equal the water leaving radiance. The differential signal is plotted in figure 8 for both surface types and shows significantly improved results when the atmospheric reflection was derived over significant shadow regions.

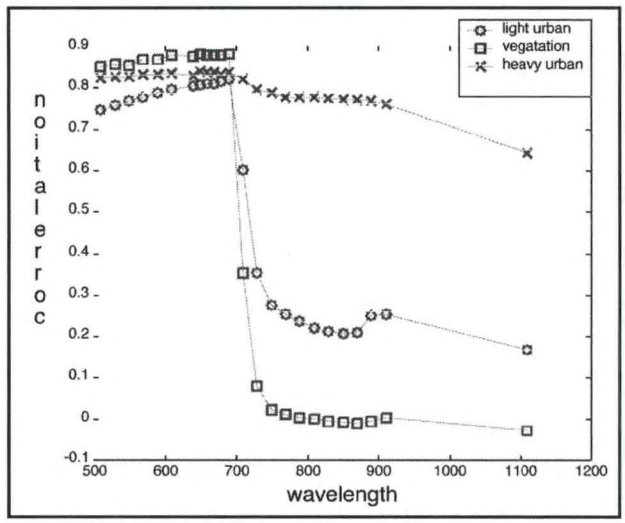

Figure 4. VIS - MIR correlation wavelength dependence

Conclusions

Strong correlations between the VIS and MIR bands have been utilized to improve MODIS aerosol products over land but the approach utilizes detailed data on surface types which are not adapted to urban environments. On the otherhand, a simple modification of the approach which does not require knowledge of the ground surface is used to decouple the atmospheric path radiance (reflectance) signal from the ground signal. The understand the capabilities and limits of the approach, we examined hyperspectral data from the Hyperion sensor over NYC. Data analysis shows that within the spectral range , strong correlations between the VIS and MIR bands exist allowing effective decoupling. For , the correlations over vegetative and low shadow regions decrease sharply preventing any useful decoupling. However, in areas with significant shadowing and large spreads in surface orientation, band correlations are nearly constant which is consistent with theoretical analysis that show how shadowing can be used to enhance the regression dynamic range and overcome ground model diversity.

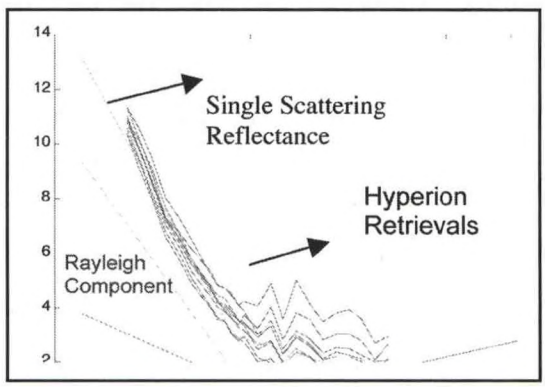

Figure 5. Wavelength Dependant atmospheric reflectances obtained in heavily urban areas.

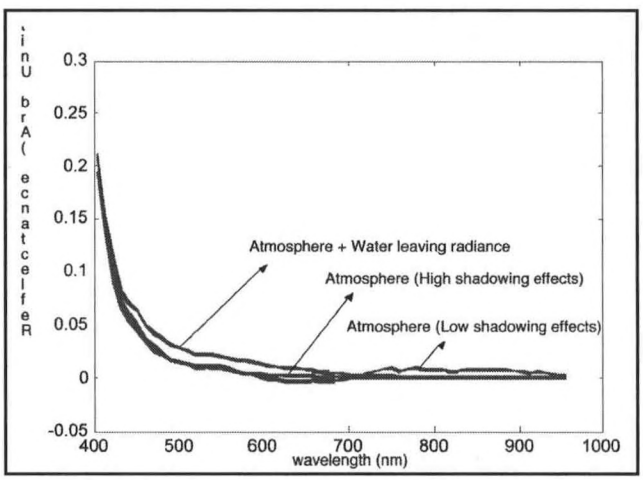

Figure 6. AVIRIS image of an urban / watger interface with both low and high urban shadowing effects.

The results were validated by comparing the retrieved aerosol reflectance with data from coincident aeronet measurements. In particular,

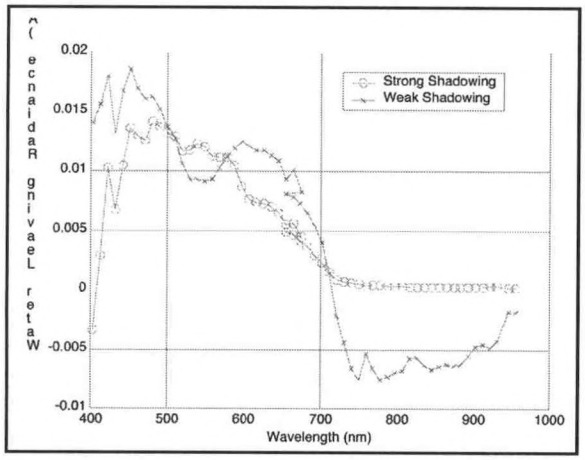

Figure 7. Atmospheric reflectance signal retrieved over land compared to water leaving signal.

using derived values of aerosol optical thickness, single scattering albedo and phase function, very strong agreement between the total reflectance was obtained. For the data available, the single scattering approximation was valid and was used for the validation. Complementary validation using AVIRIS data was also performed. In this case, comparisons between the total reflectance over water were compared to atmospheric reflectance over land. By subtracting the high quality atmospheric reflectance data from the total water leaving signal, reasonable water leaving radiance spectra were obtained.

Further work with hyperspectral data having higher optical depth loading conditions is necessary to further characterize the promise of this approach and numerical simulations using correlated ground models have already shown (Wen et al) that TOA radiances have linear properties but preliminary calculations show that perhaps a quadratic regression will fit the data better and allow better extrapolation.

ACKNOWLEDGEMENTS

This work is supported by grant from NOAA #NA17AE1625. We would also like to thank Raytheon for their support of this project.

REFERENCES

Holben B.N., Vermote E., Kaufman Y.J., Tanré D., Kalb V., Aerosols retrieval over land from AVHRR data-Application for atmospheric correction, *IEEE Transactions on Geoscience and Remote Sensing*, 30, 212-222, (1992).

Kaufman, Y. J. and C. Sendra,: 'Algorithm for atmospheric corrections', Int. *J.Rem. Sens.*, 9 , 1357-1381 (1988)

Kaufman, Y. J. and L. Remer: 'Remote Sensing of Vegetation in the mid-IR: the 3.75μm channels', IEEE *J. Geosc. and Rem. Sens.* 32, 672-683 (1994)

Kaufman, Y.J.; Wald, A.E.; Remer, L.A.; Bo-Cai Gao; Rong-Rong Li; Flynn, L.; 'The MODIS 2.1- mu m channel-correlation with visible reflectance for use in remote sensing of aerosol'; *IEEE Transactions on Geoscience and Remote Sensing* 35 1286-98, (1997)

Kaufman, Y.J.; Tanre, D. "Algorithm for remote sensing of tropospheric aerosol from modis" MODO4 ATBD Document (1998)

Wen, G.; Tsay, S-C,; Calahan, R.F. ; Oreopoulos, L.; 'Path Radiance Technique for retrieving aerosol optical thickness over land', JGR 104 31321-31332 (1999).

Martins, J.V.,Tanre, D., Remer, L., Kaufman, Y., Mattoo, S., Levy, R. , 'MODIS cloud screening for remote sensing of aerosols over oceans using spatial variability '; Geophysical Research Letters .29, no.12 : MOD4-1-4, (2002)

Remer, L.A.; Wald, A.E.; Kaufman, Y.J.; 'Angular and seasonal variation of spectral surface reflectance ratios: implications for the remote sensing of aerosol over land' ; *IEEE Transactions on Geoscience and Remote Sensing* 39, 275-83, (2001)

NEURAL NETWORK APPROACHES IN CLASSIFICATION OF MICROWAVE REMOTE SENSING DATAA

Hosni Ghedira

Assistant Professor, City College of the City University of New York Convent Ave. at 138th street, New York, NY 10031 Telephone: (212) 650 8536, Facsimile: (212) 650 6965, Email: *ghedira@ce.ccny.cuny.edu*

Abstract

Artificial neural networks have been successfully applied to image processing, and have shown a great potential in the classification of a wide range of remote sensing data. The major advantages of neural network algorithm over traditional classifiers are its non-parametric nature and its easy adaptation to different types of data format from multiple sources. However, a successful application of neural networks in remote sensing data classification requires a good comprehension of the effect of some internal parameters related to the neural network structure and training process. In this work we report the application of backpropagation neural network in classifying natural wetlands vegetation using SAR data. The effect of some parameters related to the architecture and the training process on classification performance was investigated and new techniques for ameliorating this performance are discussed. The results showed that the variations of the number of hidden layers and the number of nodes by layer have not a substantial effect on classification accuracy but affect only the training time. However, other parameters related to the neural algorithm computation (such as the threshold value) affect significantly the overall classification. It is concluded that, although the neural network method have a great potential in remote sensing data classification, a rigorous choice of the threshold value still necessary to optimize the ratio of the incorrectly and the correctly classified pixels.

Introduction

Artificial neural networks have been applied to a wide range of problems in several disciplines. They have been increasingly used since 1988 for the classification of remotely sensed images. Multi-layer perceptron trained by the backpropagation algorithm is the most commonly used neural network for image classification. This type of neural network has been successfully applied to image processing and has shown a great potential in the classification of different types of remotely sensed data. A useful review of the application of neural networks in remote sensing may be found in [1] and [2]. In this brief communication, we demonstrate the successful application of the neural network approach in Radarsat-1 image classification.

A Quick Review of Artificail Neural Networks

A multi-layer neural network (or perceptron) consists of a number of interconnected nodes. Each node in the network is interconnected with all nodes in the preceding and following layers. There are no interconnections within nodes of the same layer. The number of layers and the number of nodes by layer represent the network architecture. Each node is a simple processing element (fig. 1). The nodes are organized into layers where each node transforms the inputs received from other nodes. The adjacent layers are fully interconnected. The input (Ij) to a node (j) is the weighted sum of the outputs (Oi) from the nodes of the layer below (i). This sum is then passed through an activation function (f) to produce the node's output (Oj). The activation function is usually a sigmoid or hyperbolic tangent, which are non-linear functions that have an asymptotic behavior. Further details concerning the training algorithm can be found in [3].

Figure 1: The basic element of a neural network: node computation.

The input layer serves as an entry for the vector of data (or feature) presented to the network. In this layer,

each node corresponds to one element of the feature vector. The output layer represents the output data. For an image classification, each node in the output layer corresponds to one class and the number of nodes is equal to the number of classes. All layers between the input and output layers are referred to hidden layers.

Study Area and Data Set

A multi-temporal and multi-angle dataset of Radarsat-1 images were used. A total of six images were acquired between August 3rd, 1998 and June 11th, 1999 in two Standard beam modes: steep mode (S1) with an angle of incidence between 20 and 27 degrees and shallow mode (S7) with an angle of incidence between 45 and 49 degrees. The study area is located in the Lac Saint Jean region, in the province of Quebec, Canada (48°50' N 72°00' W). The sub-image area retained in this project covers 112.2 km2 (40% wetlands and 58% forest). This sub-image was the only area in which inventoried wetlands could be imaged in one scene by both S1 and S7 modes. Each sub-image contains 1056 rows and 680 columns in which four dominant classes of land cover are present: forest, woody wetlands, woody-shrubby wetlands and shrubby wetlands.

Optimization of Neural Netwaor Parameters

A. Architecture Optimization

The best neural network architecture can only be determined experimentally for each particular problem. In order to optimize the architectural parameters, several tests have been realized by varying the number of hidden nodes. Each texture channel was represented by one neuron in the input layer. For the output layer, the number of nodes is determined by the number of categories to be classified. The number of hidden nodes and hidden layers cannot be specified by the problem formulation, and can only be determined experimentally for each particular application. The number of hidden nodes should be large enough to ensure a sufficient number of degrees of freedom for the network function and small enough to minimize the problem of loss in generalization ability of the network. Furthermore, it's important to note that a useless increase of the neural network size will lead to a significant increase in training and classification time.

To optimize the architectural parameters of the neural network, the number of hidden nodes has been varied between 6 and 14. Each architecture configuration was trained ten times with different weight initializations. Then the best network was retained to compute the overall accuracy. For all training tests, four neurons were used in the output layer, with each neuron corresponding to one land cover class. It is important to note that, for the same training set, the number of training cycles required to achieve the same convergence criterion can vary considerably with different initial weight choices. Consequently, we have trained the same network architecture 10 times with different sets of initial weights to select the optimal accuracy for a given architecture

The results shown in Table 1 indicate that the variation of the number of hidden layers and the number of nodes by layer do not have a substantial effect on classification accuracy. Furthermore, the use of more than one hidden layer did not improve the classification performance. Thus, with a three-layer neural network, the classification accuracy was not improved by using more than 12 hidden nodes and the highest overall accuracy computed on the validation set is reached with less iterations.

TABLE 1: THE EFFECT OF THE ARCHITECTURE ON THE CLASSIFICATION ACCURACY

Architecture	Number of weights	Average accuracy (%)	Number of iterations
6-6-4	60	83	415
6-8-4	80	83	395
6-10-4	100	84	300
6-12-4	120	85	268
6-14-4	140	84	241
6-6-6-4	96	84	554
6-8-8-4	144	83	268
6-10-10-4	200	82	237
6-12-12-4	264	83	401
6-14-14-4	336	83	310

The results obtained for different architecture tests indicated that the variation of the number of hidden nodes affects the performance of the network within an interval of 2% for the test group and 1% for the training group. However, to reach the same performance, a neural network with a high number of hidden nodes requires less iterations than the one with fewer nodes (415 iterations for 6 hidden nodes and 241 iterations for 14 hidden nodes). The same observation has also been reported in [4] in comparing two networks trained by successively 24 and 37 hidden neurons.

The architecture optimization results indicated also that, with a three-level neural network, the number of training cycles necessary to meet the convergence criterion decreases when we increase the number of hidden nodes. On the other hand, the relationship between the number of training cycles and the number of hidden nodes becomes random when we use a neural network with two hidden levels. This random variation of the training process is more likely due to the complication of the discriminating curve (or classification space) produced by the four-layer network.

The reduction of the number of training iterations by using a large network size does not result in a reduction in the total training time since the time necessary to execute one iteration is proportional to the number of neurons in the network. Consequently, the time that is necessary to execute 415 training cycles with a network of 60 neurons is practically equivalent to the time necessary for 241 training cycles with a network of 140 neurons (table 1). Indeed, if the same performance was reached with two network configurations with different sizes, it will be more advantageous to use the smaller one in order to keep the classification time reasonable. For this project, we retained the architecture with only one hidden level having twice the number of neurons in the input layer. In reference [5], it has also suggested the use of this architecture configuration. This number represents a compromise providing enough node connections to associate pixel values and thematic classes without increasing the processing time unnecessarily.

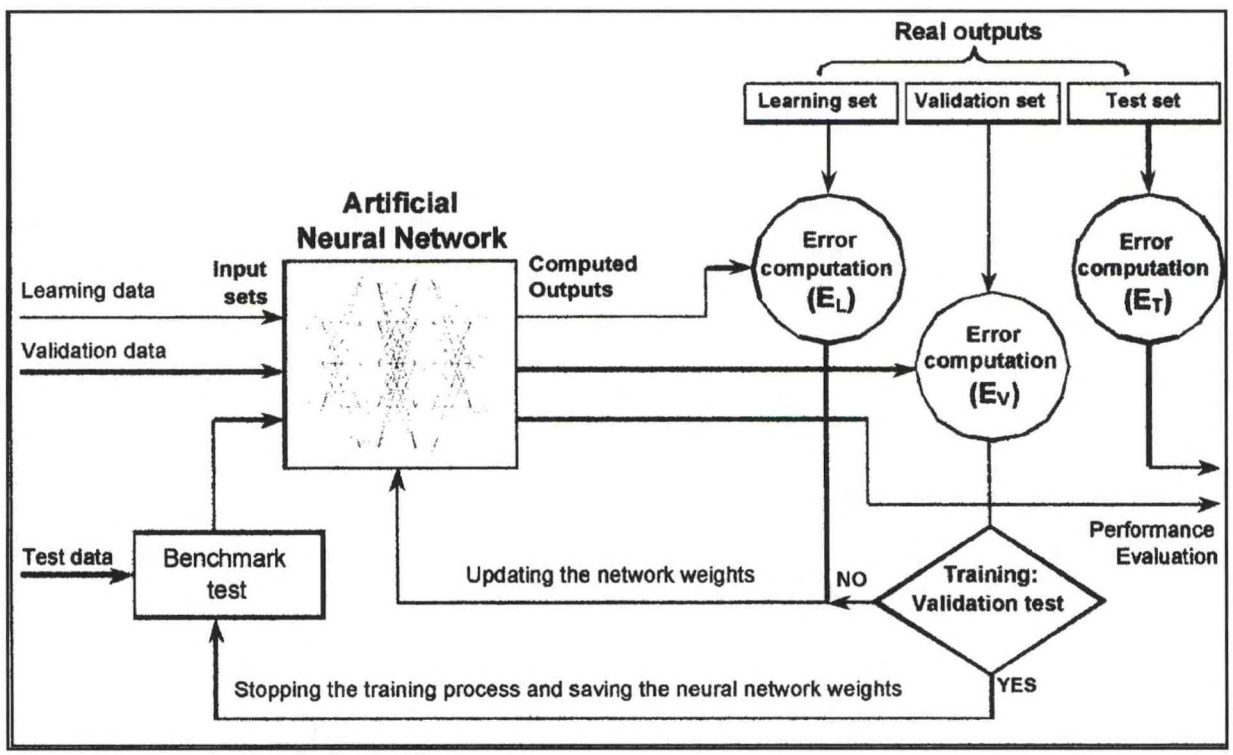

Figure 2: Contribution of each training group to the global training process.

B. Training Process

The training stage consists in adjusting the connection weights (randomly initialized) in order to decrease the difference between the network output and the desired outputs. The training data were presented to the input layer and propagated through the hidden layer to the output layer. The differences between the computed and the desired outputs were computed and fed backwards to adjust the network connections. This iterative process continued until the mean square error reached a preset threshold or when the validation criteria were reached. When one of the two criterions is met, the training is stopped and the weight values saved. The trained network may now be used as a classifier.

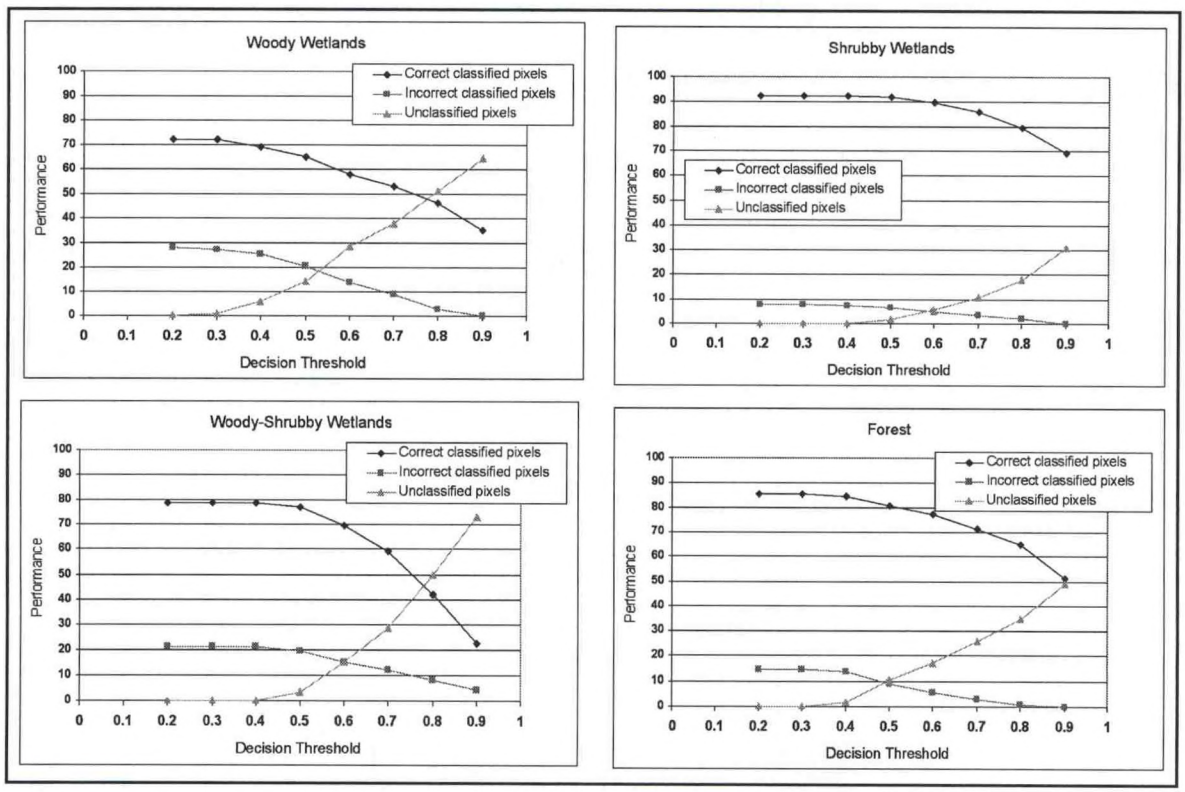

Landsat image of research area in Baja

The proper selection of training data is a crucial step in achieving best results. Training samples should adequately represent all classes. In this project, the training sets consisted of 6000 pixels (1500 pixels for each ground class). The available training data has been divided into three subsets. The first one is the learning set whish is used for computing and updating the network weights. The second subset is the validation set, which is used for stopping the training by monitoring the validation error during the training process. The third subset (test set) is not used during the training process, and is only used to benchmark the neural network and to compare different models. The methodology used in the training process is illustrated in the diagram of Figure 2.

The network retained in this project was configured with one 12-nodes hidden layer and four nodes on the output layer (one node per class). It was trained with an adaptive learning rate which allows for a faster convergence of the training algorithm than with a constant learning rate. One output neuron was assigned for each ground cover class.

One of the major concerns in the process of neural network training is the over-training. The neural network's generalization ability is then compromised and the classification space becomes narrowly

defined around the training pixels. Normally, as it is the case for the learning set error, the error computed on the validation set decreases during the initial phase of training. However, when the network begins to overfit the learning data, the error on the validation set will begin to increase slowly for the next iterations. At this time, the training process must be stopped, and the neural network weights corresponding to the minimum validation error must be identified and maintained for the next steps.

C. Threshold Optimization

One output neuron was assigned for each ground cover class. Therefore, for each pixel presented in the input layer, a high value (near one) will be assigned to the neuron that does correspond to the pixel's assigned class and a low value (near zero) will be assigned to the remainder neurons. However, during the classification, a continuous range from the low value to the high value will be computed for each output neuron. This variability can be explained by the fact that the neural network could not be trained to produce a zero error on the training data. Furthermore, the data being classified can be more diversified than the data used in the training. To overcome this problem, the class of the output neuron having the highest value will be assigned to the corresponding input data. However, to avoid that the network forces the classification of all pixels, we have introduced a threshold (value between 0 and 1) to decide if a class will be assigned to the input pixel or if this pixel will be considered as unclassified. Thus, a pixel is considered unclassified if all output values are lower than this threshold; otherwise the pixel is assigned the class corresponding to the neuron with the highest value.

The optimal threshold value cannot be identified with certainty without measuring its effect on the overall accuracy of the neural network classification. In this project, the threshold value has been varied from 0.2 to 0.9. The effect of the decision threshold on the precision of each class is illustrated in the Figures 3. Those figures show that the increase of the threshold value affects the overall classification significantly. Results indicate that the increase of the threshold decision value above 0.4 results in a simultaneous decrease of the percentage of incorrect and correct classified pixels and an increase in the percentage of unclassified pixels. Thus, while we increase the threshold decision value, a part of incorrectly and correctly classified pixels will be classified as null pixels.

V. CONCLUSION

The purpose of this study was to explore the ability of neural networks to improve Radarsat-1 data classification and to draw the best practice recommendations for this technique. Results indicate that neural networks can be considered as an accurate tool in microwave image classification. The results have shown the ability of neural networks to weight differently the importance of each input data in the discrimination process.

REFERENCES

[1] J. Paola, and R. A. Schowengerdt, "A review and analysis of backpropagation neural networks for classification of remotely-sensed multi-spectral imagery". International Journal of Remote Sensing, vol. 16-16, pp. 3033-3058, 1995.

[2] I. Kanellopoulos, and G. Wilkinson, "Strategies and best practice for neural network image classification," International Journal of Remote Sensing, vol. 18-4, pp. 711-725, 1997.

[3] D. E. Rumelhart, G. E. Hinton, and R. J. Williams, "Learning internal representation by error propagation, Parallel distributed processing : Exploration in the microstructure of cognition," M.I.T. , Cambridge Press (MA), pp. 318-364, 1986.

[4] P. D. Heermann, and N. Khazenie, "Classification of Multispectral Remote Sensing Data Using a Back-Propagation Neural Network". IEEE Transactions on Geoscience and Remote Sensing, vol. 30, no. 1, 81-88, 1992.

[5] M. T. Fardanesh, and O. K. Ersoy, "Classification Accuracy Improvement of Neural Network Classifiers by Using Unlabeled Data". IEEE Transactions on Geoscience and Remote Sensing, vol. 36, no. 3, 1020-1025, 1998.

MICROWAVE REMOTE SENSING OF SOIL MOISTURE UNDER VEGETATION COVER

Mohammad Razani, Ph.D,

Professor , Electrical Engineering Technology Department, New York City College of Technology, CUNY

300 Jay Street, Brooklyn, NY 11201 *mrazani@citytech.cuny.edu*

The presence of vegetation layer on top of a soil surface causes the level of emission intensity to increase, thereby decreasing the radiometric sensitivity to soil moisture variations. This phenomenon is due partly to the screening of soil moisture by the vegetation layer and partly to the inherent emission of radiation from the vegetation layer itself.

Having established the fact that thermal emission of soil in the microwave frequency range is sensitive to soil moisture content makes Microwave Radiometers valuable tools for soil moisture determination. This phenomenon has been studied during the last three decades and although during this period an extensive database has been created and the theoretical concepts have been developed to explain certain behavior of such phenomenon, there is still room for further research in this area.

In this paper, while the effect of the vegetation cover on the radiometric sensitivity to soil moisture is discussed, a brief survey of these studies and developments will be also covered. Finally it is recommended that further studies in this area could be formatted into a proposal in which faculty and students could engage in research work investigating the different aspects of this issue that has not yet been addressed or not sufficiently looked into.

Introduction

Soil moisture plays a crucial role in most land surface processes and therefore large-scale soil moisture mapping would be very valuable. Microwave remote sensing technology has been shown during the last two and half decades to be an effective tool to infer soil moisture on a global basis. Both active and passive microwave remote sensors have been used to show their capabilities of estimating soil moisture content individually and jointly through different experiments worldwide.

Soil moisture radiometric investigations conducted to date have been concerned with the effect of soil surface random roughness [1], row direction [2], and to some extend to the screening effect of vegetation cover by NASA/Goddard Space Flight Center, USDA Beltsville Agricultural Research Center [3], investigation in the USSR [4] and University of Kansas Remote Sensing Laboratory at Space Research Center [5]. Some of these studies were based on experimental observations made from truck- mounted platforms and some were based on airborne observation.

A summary of the passive sensors used for soil moisture determination is given in table 1 [6]. The objective of the truck measurements were basically to determine the effect of :

- Permittivity profile
- Temperature profile
- Surface roughness
- Vegetation cover
- Row directions and soil type, and
- The maximum sensing depth for the determination of soil moisture

The objective of aircraft measurements were to:

- Evaluate and verify the results of truck mounted measurements by acquiring data for a large number of fields and field conditions
- Improve the statistical confidence in the results.

The presence of vegetation layer on top of a soil surface causes the level of emission intensity to increase resulting in reduction of radiometric sensitivity to soil moisture variation.

Emission from a vegetation canopy

Treating a vegetation canopy as a lossy dielectric layer characterized by a volume absorption coefficient κ_a, bounded by a smooth soil surface on the bottom and by a diffuse canopy-air boundary at the top and assuming isotropic scattering pattern from the vegetation in the canopy resulting in a scattering albedo small enough ($\omega < 0.2$) to ignore multiple scattering, then the solution of the radiation transfer equation [7] leads to:

$$T^i_{B,can}(\theta) = \left[\left(1+\frac{\Gamma^i_s(\theta)}{L(\theta)}\right)\left(1-\frac{1}{L(\theta)}\right)(1-\omega)\right]T_V + \left[\frac{1-\Gamma^i_s(\theta)}{L(\theta)}\right]T_s \quad (1)$$

where,

$T^i_{B,can}(\theta)$ = canopy brightness temperature for polarization i, °k

T_V = physical temperature of vegetation, °k

T_s = physical temperature of soil, °k

i = polarization index (i= h or v for horizontal or vertical, respectively)

ω = $\kappa_s/(\kappa_a+\kappa_s)$, single scattering albedo

$L(\omega) = T^{-1}(\theta) = \exp(\kappa_e h \sec\theta)$, Canopy loss factor (2)

$T(\omega)$ = canopy transmission factor

κ_S = volume scattering coefficient of canopy layer, $m^2 m^{-3}$

κ_a = volume absorption coefficient of canopy layer, $N_p m^{-1}$

$\kappa_e = \kappa_S + \kappa_a = \kappa_a/(1-\omega)$, volume Extinction coefficient, $N_p m^{-1}$

h = canopy height, m

_ = angle of incidence, relative to nadir

$\Gamma_s^i(\theta)$ = reflectivity of soil surface for polarization i

The first term in equation (1) is the emission from vegetation layer and the second term is due to soil emission attenuated due to propagation through the vegetation layer. The effect of soil surface roughness is accounted for by using the approximate model [1]:

$$\Gamma_s^i(\theta) = |R^i(\_)|^2 \; e^{-h' \cos^2\theta} \quad (3).$$

Where h′ is an effective roughness parameter and $|R^i(\_)|^2$ is the Fresnel power reflection coefficient.

Measured and Calculated Brightness Temperatures

The data used in the calculation of brightness temperature is the results of airborne observations made at 1.4 and 5 GHz during six flights over a test site in the vicinity of Colby, Kansas in 1982.

The test site consisted of bare soil, wheat stubble, and corn fields. The above radiometric transfer model was used in the analysis of these data. The brightness temperature measured during the airborne observations of corn fields is shown in Fig. 1 for 1.4 GHz at normal incidence. The solid curve was calculated using equation (1) and the parameter given in the figure. The value for _ , L, and h_ were determined by fitting the calculated values of ($T_{B,can}$) to the measured values. The dashed curve is a plot of ($T_{B,soil}$) for value of h_ determined by fitting the measured data to the calculated values. The difference between the two curves represent the influence of the vegetation cover.

Another case is shown in Fig. 2 for 1.4 GHz but at _ =40°. The last two cases are shown in Fig. 3 for the 5 GHz at 0° & Fig.4 for 5 GHz at _ = 40°. Figures 3 & 4 show that the brightness temperature is almost insensitive to soil moisture variations in the presence of green corn plants. From the above figures one can note that the radiometric sensitivity to soil moisture under vegetated conditions decreases with the increase in angle and frequency.

More recent investigation has been carried out to show the effectiveness of active/passive microwave remote sensing in soil moisture measurement. An experiment was conducted near Huntsville, Alabama in 1996 and again in 1998 [8]. The objective was to test and refine algorithms used to estimate surface soil moisture using microwave remote sensing. In this study it was shown that the remote sensing instruments were able to detect both the large surface moisture change due to rainfall and subsequent drying as well as the diurnal fluctuations in moisture.

Learning that both passive and active remote sensing could be utilized in soil moisture determination, the combination of the two would give even more promise in estimating soil moisture. Recent study by P.O'Neill et al [9] through an extensive field experiment showed that the combination of simultaneous radar and radiometer data could enhance soil moisture retrievals especially in the presence of dynamic vegetation. In this study a tower mounted 1.4 GHz radiometer (Lrad) and a truck mounted dual-frequency (1.6 GHz and 4.75 GHz) radar system were used. In this study, the ground measurements were obtained from twenty-one sampling locations on two sides of the microwave footprint. The similarity of the pattern of the curves of radar backscatter data over time in this experiment showed the direct relation-

ship between radar backscatter and surface soil moisture over the course of several wetting and drying cycles. It was also shown that, as expected, the increase in both soil moisture and overlaying vegetation biomass serves to dampen the diurnal microwave response observed by Lrad. This experiment verified the earlier results that the attenuation increases with incidence angle due to greater path length through the canopy and also that attenuation is greater at vertical polarization than horizontal polarization due to the erectophile nature of com when the majority of crop water in contained in the vertical stalk. Overall the results of the recent studies have verified the earlier investigations referred to in this paper i.e. in the presence of vegetation, in order to be able to measure soil moisture accurately, both active and passive remote sensing measurements should be made. In these studies much work have been carried out to determine the three major sensor related parameters. These are the parameters that when chosen accurately, will optimize the soil moisture estimation with a very high degree of accuracy. Polarization, look angle, and frequency are the key elements in such optimization process.

The results show that lower microwave frequencies (around L-band), small incidence-angle (between 0 and 10 degrees), and horizontal polarization are the optimum parameters for a passive microwave sensor in estimating soil moisture under a vegetation canopy.

Although much work has been carried out in this field, but there is still room for further investigation. Some of these areas are as follows:

- Further work is needed to determine the individual roles of leaves, stalks, and fruits of corn plants with regard to their emission, absorption, and scattering properties.
- Additional radiometric measurements are needed for different types of crops at various stages of growth.
- More experimental and theoretical investigations to are needed to determine the dielectric properties of vegetation material at microwave frequencies.

These and many other areas to be studied could be formatted in forms of proposals where faculty and students can participate in such research work.

TABLE 1

PASSIVE SENSORS

Sensor	Organization	Platfonn	Angular Range
L/C (MFMR)	JSC	C-130 '(Nose)	0°-60° (Sel)
K-Bands (MFMR)	JSC	C-130 (Lower Cargo Door)	0°-69° (Sel)
L-Band Radiometer	GSFC	CV-990	
PMIS	JSC	C-130 (Lower Cargo Door)	50° Aft
MSAS	JSC/TAMU	Ground (Truck)	0°-70°
L-, X-, K-Bands	JPL	Ground (Truck)	0°-80°
S-, C-Bands, (IMRS)	KU/RSL	Ground (Truck)	0°-60°

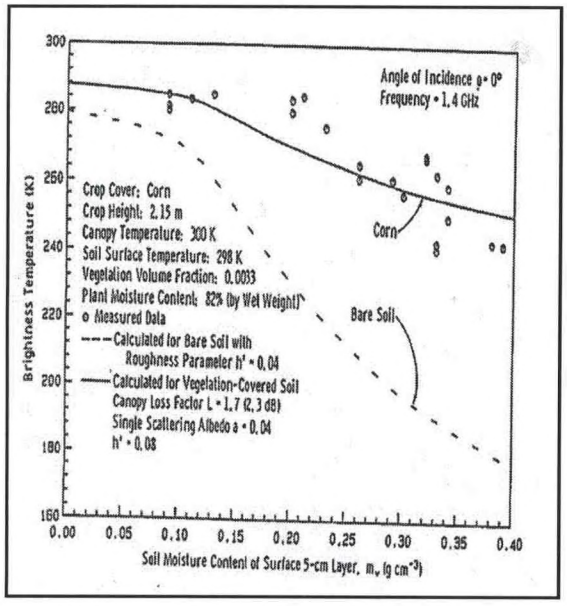

Fig. 1 Measured and calculated brightness temperature of corn fields at 1.4 GHz at normal incidence.

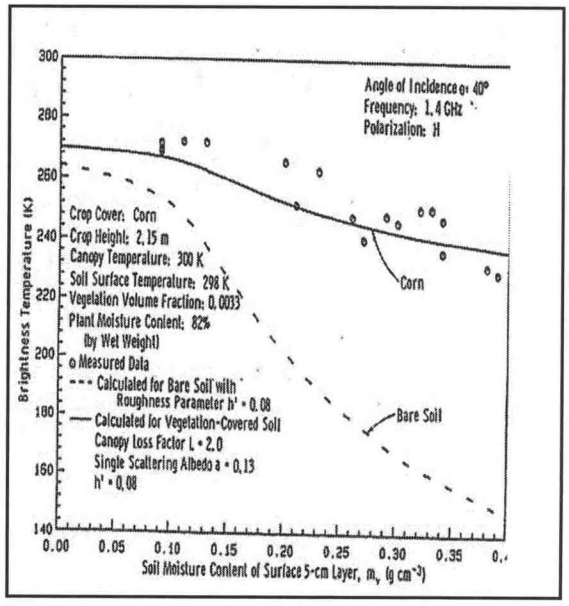

Fig. 2 Measured and calculated brightness temperature of corn fields at 1.4 GHz, H polarization and 0 = 40°.

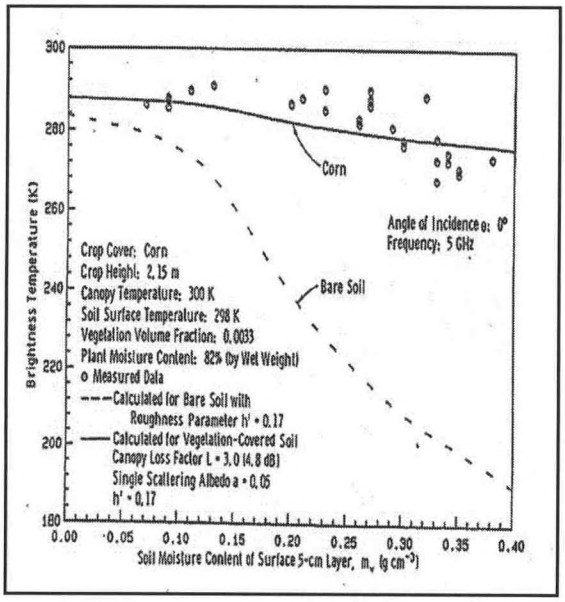

Fig. 3 Measured and calculated brightness temperature of corn fields at 5 GHz at normal incidence.

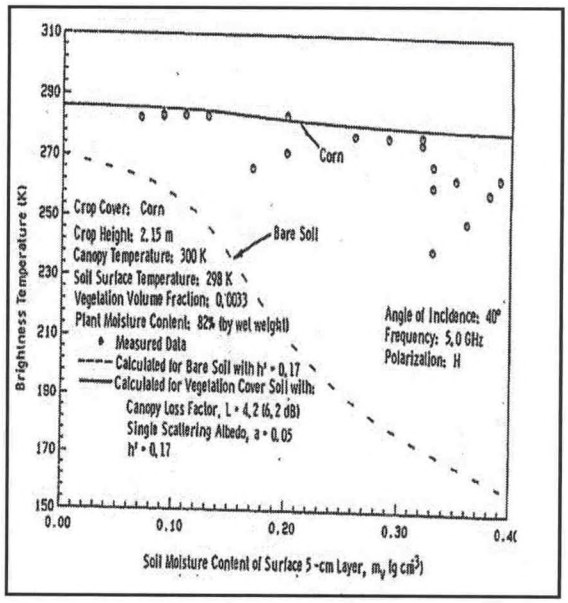

Fig. 4 Measured and calculated brightness temperature of corn fields at 5.0 GHz, H polarization and 0 = 40°.

A Ground-Based Procedure for Estimating Latent Heat Energy Fluxes[1]

Eric Harmsen[2], Richard Díaz[3] and Javier Chaparro[3]

[1]This material is based on research supported by NOAA-CREST and NASA-EPSCoR (NCC5-595).

[2]Associate Professor, Dept. of Agricultural and Biosystems Engineering, University of Puerto Rico-Mayagüez Campus, *eric_harmsen@cca.uprm.edu*

[2]Undergraduate and Graduate Research Assistants, respectively, University of Puerto Rico – Mayagüez Campus.

Abstract

The ability to estimate short-term fluxes of water vapor from the land surface is important for validating latent heat flux estimates from high resolution remote sensing techniques. A new, relatively inexpensive method is presented for estimating the ground-based values of the surface latent heat flux or evapotranspiration.

The method used in this study consists of equating two different evapotranspiration flux equations; one based on the Penman-Monteith energy method and the other on the vapor gradient method. The resulting equation has a single unknown parameter, the bulk surface resistance (rs). Because rs can not be solved for explicitly, in the procedure, the value of rs is adjusted iteratively in the two equations until their ET curves approximately coincided.

In this paper, the methodology was applied to a set of meteorological data collected from a grass-covered field on February 11, 2004, at the University of Puerto Rico's Agricultural Experiment Station, Rio Piedras, PR. The estimated bulk surface resistance was determined to be 90 s m-1, and the total evapotranspiration for the 8-hour study was 3.6 mm and 3.7 mm for the energy-based and vapor gradient-based equations, respectively. The estimated value of the bulk surface resistance is consistent with other studies.

Introduction

Various efforts have been made to estimate the latent heat flux using remote sensing techniques (e.g., Jarvis 1981; Luvall et al., 1990; Holbo and Luvall, 1989; Quattrochi and Luvall, 1990; Turner and Gardner, 1991). These methods typically rely on an equation of the following form (Luvall et al., 1990):

$$LE = \left(\frac{\rho \cdot c_p}{\gamma}\right) \cdot \frac{(VD_a - VD_s)}{R_s} \qquad (1)$$

where LE is latent heat flux (MJ m^{-2} day), _ is density of air (kg m^{-3}), c_p is specific heat of air (MJ kg^{-1} $°C^{-1}$), VD_a is water vapor density of the air (kg m^{-3}), VDs is saturated water vapor density of the air at the vegetation canopy, based on surface temperature obtained by remote sensing (kg m^{-3}), _ is psychrometric constant (kPa $°C^{-1}$), and Rs is stomatal resistance (s m^{-1}).

To validate LE estimates from remote sensing techniques, LE must be determined at the ground surface. In this paper LE will be expressed as a quantity of water evaporated per unit time, otherwise known as the evapotranspiration (ET) and is expressed in units of mm per hour. LE and ET are related by the latent heat of vaporization (2.45 MJ per kg of water). Current ground-based ET measurement techniques include: weighing lysimeter, eddy covariance, and the water balance methods. Each of these methods is expensive and has certain disadvantages. In this study ET was determined using a new ground-based procedure based on the less expensive yet sufficiently accurate energy balance and vapor gradient methods.

Methods

Data Analysis

The methods used in this study consisted of equating the ET flux equations based on the Penman-Monteith (PM) energy method with a vapor gradient method. By equating the two equations, a single unknown parameter, bulk surface resistance (rs), could be solved for. In the procedure, the value of rs was adjusted iteratively in the two equations until their ET time series curves approximately coincided.

The PM energy equation is given as follows (Allen et al., 1998):

$$ET = \frac{\Delta \cdot (R_n - G) + \rho_a \cdot c_p \cdot \dfrac{(e_s - e_a)}{r_a}}{\lambda \cdot \left[\Delta + \gamma \cdot \left(1 + \dfrac{r_s}{r_a}\right)\right]} \qquad (2)$$

where _ _is slope of the vapor pressure curve (kPa°C^{-1}), R_n is net radiation (MJ m^{-2} hr^{-1}), G is soil heat flux density (MJ m^{-2} hr^{-1}), _a is air density (kg m^{-3}), cp is specific heat of air (MJ kg-1 °C-1), $_a$ is psychrometric constant (kPa°C^{-1}), T is air temperature at 2 m height (°C), u_2 is wind speed at 2 m height (m/s), e_s is the saturated vapor pressure and ea is the actual vapor pressure (kPa), r_a is the aerodynamic resistance (s m-1) and rs is bulk surface resistance (s m^{-1}). The two resistance factors in equation 2 are shown schematically in the Figure 1.

In this study the aerodynamic resistance will be estimated from the following equation (Allen et al., 1998):

$$r_a = \frac{\ln\left[\dfrac{(z_m - d)}{z_{om}}\right] \cdot \ln\left[\dfrac{(z_h - d)}{z_{oh}}\right]}{k^2 \cdot u_2} \qquad (3)$$

where z_m is height of wind measurement 2 m), z_h is height of humidity measurement (2 m), d is zero plane displacement height is 0.67 h, z_{om} is roughness length governing momentum transfer is 0.123 h, z_{oh} is roughness length governing transfer of heat and vapor is 0.1 z_{om}, k is von Karman's constant (0.41), and h is crop height (0.12 m). Allen et al. (1998) have reported that equation 3 and the associated estimates of d, z_{om} and z_{oh} are applicable for a wide range of crops. Equation 3 is restricted to neutral stability conditions, i.e., where temperature, atmospheric pressure, and wind velocity distribution follow nearly adiabatic conditions (no heat exchange). A study of surface and aerodynamic resistance performed by Kjelgaard and Stockle (2001) determined that equation 3 will produce reliable estimates of r_a for small crops.

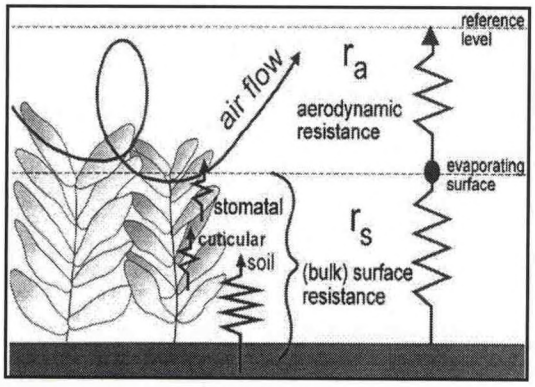

Figure 1. Simplified representation of the (bulk) surface resistance and aerodynamic resistances for water vapor flow (from Allen et al., 1998).

Evapotranspiration can also be estimated by means of a vapor gradient equation as given below:

$$ET = \left(\frac{\rho_a \cdot c_p}{\gamma \cdot \rho_w}\right) \cdot \frac{(VD_L - VD_H)}{(r_a + r_s)} \qquad (4)$$

where $_w$ is density of water, VD_L is absolute vapor density at height L and VD_H is absolute vapor density at height H. In this study L and H were 0.3 m and 2 m, respectively. All other variables were previously defined.

Field Data Collection

Initial test using two temperature/relative humidity (Temp/RH) sensors simultaneously, positioned at the same height in close proximity revealed non-constant differences in RH between the two sensors. Differences in RH ranged from -5% to +8.5% (see Figure 2). Errors of this magnitude are clearly unacceptable for use in estimating the vertical humidity gradient. Therefore, to obtain accurate estimates of the humidity gradient, a single Temp/RH sensor (CS HMP45C) was used, which was manually moved between two vertical positions (0.3 m and 2 m) over short time periods (2 minutes). The vapor densities (VD) were estimated from the temperature and RH data, which were recorded by the data logger every 10 seconds.

Climatological data were saved on a Campbell Scientific (CS) CRX10 data logger every 10 seconds. Net radiation was measured using a CS NR Lite Net Radiometer. Wind speed was measured at 30 cm and 3 m above the ground, respectively. The upper sensor was a MET One 034B wind speed and direction sensor. The lower wind speed was measured using a HOBO wind speed sensor. The wind speed at 3 m was adjusted to the 2 m height using the logarithmic relation presented by Allen et al. (1998). Soil water content was measured using a CS616 Water Content Reflectometer. Soil temperature was measured using two TCAV Averaging Soil Temperature probes, and the soil heat flux at 8 cm below the surface was measured using a HFT3 Soil Heat Flux Plate. Soil heat flux at the soil surface was estimated using the average soil temperature, soil heat flux at 8 cm and water content data.

Results and Discussion

Figure 3 shows an example of some RH data collected from the single Temp/RH sensor located in a field of grass at the University of Puerto Rico (UPR) Experiment Station in Rio Piedras, PR, during February 2004 (Harmsen and Díaz, 2004). Figure 4 shows the estimated ET for the same day based on equations 2 and 4, respectively. Note that the measured vertical air temperature gradient was negligible, confirming the presence of aerodynamically stable conditions during the study (Figure 5).

The ET results from equation 4 indicated much more temporal variation than the ET estimated using equation 2. The probable cause of this variation is that equation 4 is more sensitive to variations in wind speed (via the aerodynamic resistance factor) than equation 2. Figure 6 shows the variation in wind speed at the study site at 0.3 and 2 m heights, respectively, during the eight hour test.

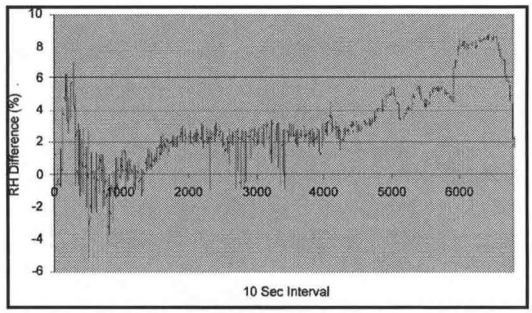

Figure 2. Differences in measured RH between two sensors located in close proximity, 2 meters above the ground.Landsat image of research area in Baja

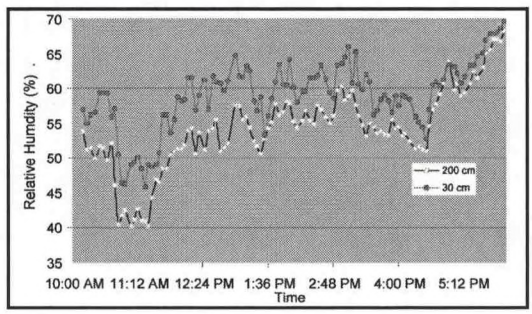

Figure 3. Measured relative humidity at 0.3 m and 2 m above the ground between 10 AM to 6 PM on February 11, 2004.

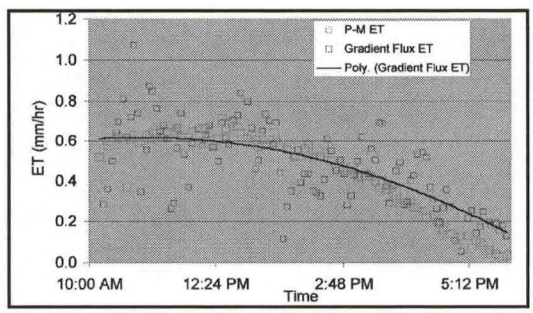

Figure 4. Calculated latent heat flux using equations 2 and 4 from 10 AM to 6 PM on February 11, 2004.

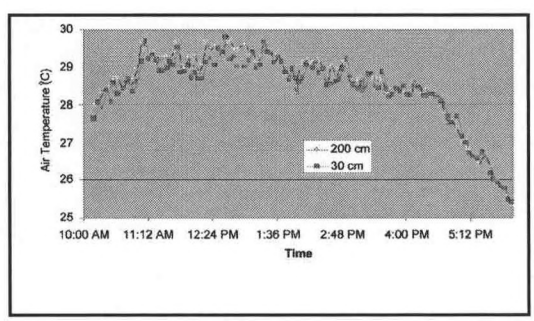

Figure 5. Measured air temperature at 0.3 m and 2 m above the ground between 10 AM to 6 PM on February 11, 2004.

To improve comparison of the two methods, a best-fit 2nd order polynomial equation was developed for the equation 4 data and the polynomial curve was then compared with the P-M curve (Figure 4). The best-fit value of r_s was found to be 90 s m^{-1}. This value of r_s is consistent with the imaginary reference grass defined by the United National Food and Agriculture Organization (FAO), having a value of r_s equal to 70 m/s (Allen et al., 1998). The total estimated vapor flux for the eight-hour study period was 3.6 mm and 3.7 mm from equations 2 and 4, respectively.

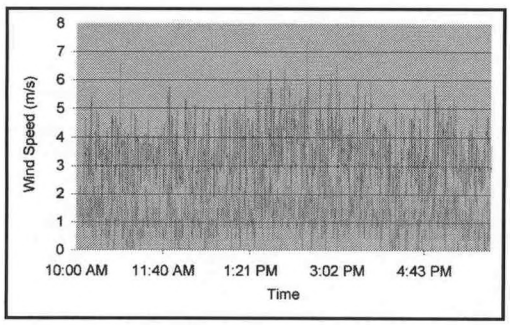

Figure 6. Measured wind speed from 10 AM to 6 PM on February 11, 2004. The lower plot is for wind speed measured at 0.3 m above the ground. The upper plot is for wind speed at 2 m above the ground (adjusted from 3 m data).

Future Work

Manually moving the Temp/RH sensor between the two vertical positions was very labor intensive. Therefore, an apparatus for automatically moving the Temp/RH sensor has been developed at the University of Puerto Rico. The apparatus consists of an aluminum frame with a 12 volt DC motor attached at its base. One end of a chain is connected to a sprocket on the motor and the other end connected to a sprocket at the top of the frame. The 2 m frame height was selected because this is the standard reference height defined by the FAO for estimating evapotranspiration with the Penman-Monteith equation (Allen et al., 1998).

Limit switches are located at the top and bottom of the frame which are contacted when the Temp/RH sensor, attached to the chain, is raised or lowered. A programmable logic controller (PLC) is used to hold the sensor in the "up" position (2 m) for a 2 minute period, during which RH measurements are recorded every 10 seconds. At the end of the 2 minute period, the RH sensors is lowered (travel time approximately 10 seconds) to the "down" position (0.3 m) and held for 2 minutes while Temp/RH data is recorded. This sequence of movements is continued for periods of up to one or two days. The CR10X weather station data logger has been programmed to communicate with the PLC and to record the vertical position of the Temp/RH sensor. This information is important during the post-processing phase when the "up" data is separated from the "down" data in order to calculate the humidity gradient.

Future work also includes validation of the new methodology by comparing ET estimates with estimates from a soon-to-be-installed NASA eddy covariance system located in Lajas, PR (L. Pérez Alegría, personal communication).

During 2005, the measurement system will be used to validate LE estimates from the Moderate Resolution Imaging Spectroradiometer (MODIS) for four different vegetation types. The spatial resolution of MODIS is 250 m, however, with an interpolation technique developed at the University of Puerto Rico, it will be possible to obtain resolutions on the order of 65 m or 1 acre in area.

Summary and Conclusions

A method was presented for estimating ground-based values of evapotranspiration or the latent heat flux. The methodology will be useful for validating latent heat flux estimates based on remote sensing techniques. The methods used in this study consisted of equating the ET flux equations based on the Penman-Monteith (PM) energy method with a vapor gradient method. By equating the two equations, a single unknown parameter, bulk surface resistance (r_s), could be solved for. In the procedure, the value of r_s was adjusted iteratively in the two equations until the ET curves approximately coincided.

The method was applied to ground-based meteorological data measured on February 11, 2004 at the University of Puerto Rico Agricultural Experiment Station located at Rio Piedras, PR. The estimated bulk surface resistance was 90 s m^{-1}, and the total evapotranspiration for the 8-hour study was 3.6 mm and 3.7 mm for the energy-based and vapor gradient-based equations, respectively. To reduce the labor associated with manually moving the Temp/RH sensor between the two vertical positions, an apparatus is currently under development to automate the process.

REFERENCES

Allen, R. G., L. S. Pereira, Dirk Raes and M. Smith, 1998. Crop Evapotranspiration Guidelines for Computing Crop Water Requirements. FAO Irrigation and Drainage Paper 56, United Nations, Rome.

Harmsen, E. W. and R. Díaz, 2004. Ground-based energy flux measurements for calibration of the Advanced Thermal and Land Applications Sensor (ATLAS). NOAA-CREST Research Symposium. Hampton University. April 20-22, 2004.

Holbo, H. R. and J. C. Luvall, 1989. Modeling surface temperature distributions in forest landscapes. Remote Sens. Environ. 27:11-24.

Jarvis, P. G., 1981. Stomatal conductance gaseous exchange and transpiration. Plants and their Atmospheric Environment (J. Grace E. D. Ford and P. G. Jarvis editors) Blackwell, Oxford U.K. pp. 175-204.

Neural Network Application Using Passive and Active Microwave Data for Soil Moisture Estimation

Tarendra Lakhankar (Ph.D. student), Hosni Ghedira (Asst. Professor), and Reza Khanbilvardi (Professor)
Civil Engineering Department, City University of New York

Abstract-

Artificial neural networks have been successfully applied to image processing, and have shown a great potential in the classification of a wide range of remote sensing data. However, a successful application of neural networks in remote sensing data classification requires a good comprehension of the effect of some internal parameters related to the neural network structure and training process.

In this paper we report the application of backpropagation neural network in estimating the soil moisture level from Synthetic Aperture Radar (SAR) data. The potential of SAR images in spatial soil moisture estimation depends on the ability of the neural network algorithm to define the complex relationship that exists between the backscattered energy and the moisture content of the soil. A study area located in Oklahoma (97d35'W, 36d15'N) has been chosen for this project. Two Radarsat-1 images acquired in Scansar Mode during the summer of 1997 were used in combination with soil moisture data measured by ESTAR Instrument (Electronically Scanned Thinned Array Radiometer) during the SGP97 campaign (operated by NASA).

The effect of some parameters related to the architecture and the training process on classification performance was investigated. The preliminary results showed that the variations of the number of hidden layers and the number of nodes by layer have no significant effect on classification accuracy. However, other parameters related to the neural algorithm computation (such as the threshold value) affect significantly the overall classification.

Introduction

Soil moisture is the amount of water in the top layer of the earth surface. With the actual field measurement techniques, it is very difficult to have a spatial measurement of this parameter, as it varies from place to place and its value is generally affected by different soil surface characteristics.

Microwave systems (passive and active) have been used to measure soil moisture on the basis of large contrast in the dielectric constant values between liquid water and dry soil. For the passive microwave systems, the brightness temperature decreases with the increase of the soil moisture. However, in the case of active microwave systems, the stronger radar backscattering values are observed when soil moisture is high (Ulaby et al 1986).

This paper deals with the application of neural network to estimate the spatial distribution of soil moisture by using active microwave data. An attempt has been made to improve overall accuracy of estimation of soil moisture by two ways: first, by optimizing the neural network parameters, second, by using additional vegetation information such as optical depth and NDVI.

Microwave Remote Sensing and Soil Moisture Relationship

The passive sensors measure the natural thermal emission (or brightness temperature) of the land surface at microwave wavelengths. The microwave brightness temperature of the land surface is a function of the thermodynamic temperature of the soil and surface emissivity. For example, in the case of bare soil, the measured brightness temperature is directly related to soil water content and temperature of surface emission. The vegetation cover emits its own microwave energy and may scatter or attenuate the energy emitted by soil surface. Therefore, the measured brightness temperature contains the information

about soil moisture as well as vegetation characteristics (Schmugge 1998, Engman and Chauhan 1995).

Active remote sensing estimation of soil moisture involves the measurement of backscattering from the soil. The backscattering consists of backscatter from vegetation and soil, and attenuation caused by the vegetation canopy. The vegetation canopy affects the backscattered energy in two ways: first, the vegetation layer attenuates the soil backscatter contribution and second, the vegetation canopy contributes to the final backscatter component (Kasischke et al 2003, Ulaby et al 1981). The total amount of attenuation and backscatter depends on some vegetation parameters which include optical depth, vegetation height, leaf area index, and vegetation water content.

Used in this study were

Data Acquisition and Study Area

The study area is located in Oklahoma, USA (97d35'W, 36d15'N). One Radarsat-1 image acquired on July 12th, 1997 by ScanSAR Narrow Mode at an incidence angle range of 20∞-39∞ with a resolution of 25 m was used in this study. The soil moisture and other vegetation data (NDVI, vegetation water content, vegetation b parameter, etc) were collected during this mission have been used in this research. The SGP97 experiment was a large, interdisciplinary experiment carried out in 1997 with the objective to test formerly established soil-moisture retrieval algorithms for the ESTAR Instrument (Electronically Scanned Thinned Array Radiometer) L-band passive microwave radiometer at 800-meter resolution (Jackson et al 1999).

The PCI-Geomatica software was used to co-register soil moisture and other images with SAR using hydrological structure present in the both images. The study area covers 2534.4 km2 (96 km x 26.4 km) in the Southern Grain Plains region. The high resolution SAR data (25m x 25m) has been aggregated to soil moisture resolution using a mean filtering algorithm (800m x 800m). For the first step of this project, the soil moisture data was classified in 3 classes based on soil moisture values: class 1 (dry soil 0-10%), class 2 (slightly wet soil 11-20%), and class 3 (wet soil +21%).

The general relationship between SAR backscattering values in ScanSAR mode and soil moisture for the three classes are illustrated in figure 1. The first statistical analysis of the backscattering data shows that the correlation between SAR backscattering values and soil moisture is better with higher soil moisture content (wet soil).

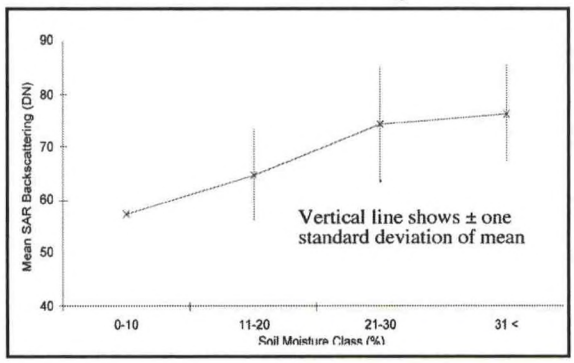

Fig 1: Relationship of backscattering value (DN) with Soil Moisture Classes (July 12, 1997 SAR image of study area)

Neural Networks

Artificial neural networks have been applied to a wide range of problems in many disciplines. They have been increasingly used since 1988 for the classification of remotely sensed images (Benediktsson et al 1990, Paola, and Schowengerdt 1995). The rapid increase of neural network applications in remote sensing is due mainly to their ability to perform more accurately than other classification techniques. Multi-layer perceptron trained by backpropagation algorithm is the most common neural network used for image classification. This type of neural network have been successfully applied to image processing and have shown a great potential in the classification of different remotely sensed data. A useful review of the application of neural networks in remote sensing may be found in (Benediktsson et al 1990) and (Paola and Schowengerdt 1995). The major advantages of the neural network method over traditional classifiers are (Ghedira et al 2000):

- Easy adaptation to different types of data and input configuration. Moreover, neural networks can easily incorporate ancillary data which would be difficult or impossible with conventional techniques.
- The traditional parametric classification methods, such as, the Maximum Likelihood classifier make unreasonable assumptions about the statistics proprieties of the data, specifically

that they are normally (or Gaussian) distributed for each ground cover class. However, this assumption is not always satisfied.

• Neural network use its complex configuration to find the best nonlinear function between the input and the output data without the constraint of linearity or pre-specified non-linearity which is required in regression analysis.

• Neural networks are able to assign more than one label of land cover classes to each pixel in an image. This propriety resolve the mixed pixel problem usually observed in image classification.

Given this list of advantages and the several unique capabilities of neural networks in remote sensing, it will become interesting to test the ability of this tool for estimating soil moisture scales from RADARSAT-1 images.

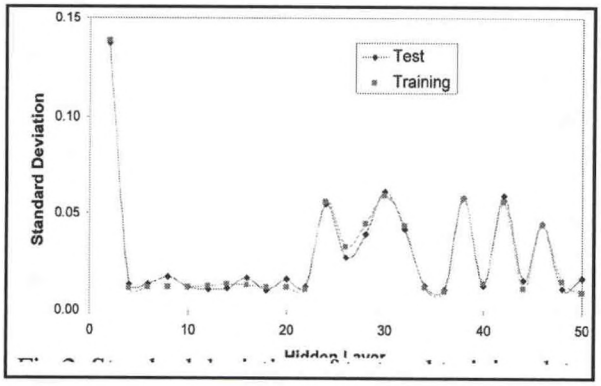

Fig 2. Standard deviation of test and training data with variation in hidden layer

Neural Network Internal Parameter Optimization

A best neural network is described as a combination of better accuracy, reliability and processing time. Those three parameters depend on the desired size and the network complexity, which is function of the number of network layer and number of nodes in each layer.

To optimize the internal configuration of the neural network, the same network was run 25 times for each architectural configuration. The results showed that, using two hidden layers with an equal number of nodes in each layer, the standard deviation of the 25 runs is very low. Further, the increase of the number of nodes in each hidden layer does not improve the overall accuracy. The results indicate also that the classification accuracy increases when the number of hidden nodes is equal in each of the hidden layers.

When using a single layer, the number of nodes should be greater than the number of input data to get reliable results. Further, as shown in figure 2, the variance becomes stable when the number of hidden nodes is less than 22.

Neural Network Training

A multi-layer neural network (or perceptron) consists of a number of interconnected nodes. The nodes are organized into layers where each node transforms the inputs received from other nodes. The adjacent layers are fully interconnected. The input to one node is the weighted sum of the outputs of the previous layer nodes. This sum is then passed through an activation function to produce the final output. The activation function is usually a sigmoid or hyperbolic tangent, which are non-linear functions that have an asymptotic behavior. Further details concerning the training algorithm can be found in (Rumelhart et al 1986).

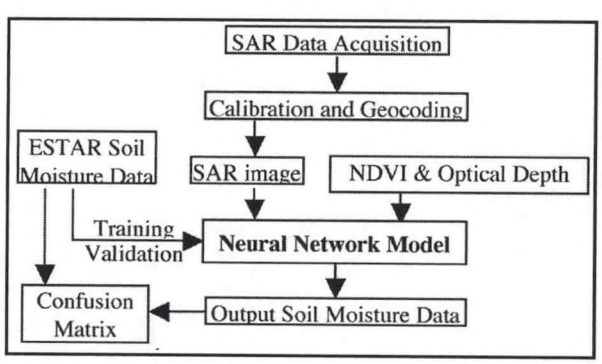

Fig 3. Methodology applied in soil moisture estimation.

The training stage consists in adjusting the connection weights (randomly initialized) in order to decrease the difference between the network output and the desired outputs (truth data). The training data were presented to the input layer and propagated through the hidden layer to the output layer. The differences between the computed and the desired outputs were computed and fed backwards to adjust the network connections. This iterative process continued until the mean square error

reached a preset threshold or when the validation criteria were reached. When one of the two criterions is met, the training is stopped and the weight values saved. The trained network may now be used as a classifier. In this project, one output neuron was assigned for each soil moisture class. The methodology used in the training process is illustrated in the figure 3. The data selected for training (500), validation (200) and testing (200) by random process from total 900 pixels which are randomly selected from image having total of 3960 pixels (120 x 33).

Analysis of Neural Network Output

A. Confusion matrix

The confusion matrix also known as an error matrix is a tool to compare accuracies of different classes or groups in the same region (Smits et al 1999). The confusion matrix is a symmetrical array of the number of classified pixels compared to the ground truth data. The diagonal values (in bold in the two following tables) represented the percentage of correctly classified pixels in each class.

Table 1: Normalized Confusion matrix using SAR

True class	Classify as C1	C2	C3	Total
C1	**0.68**	0.24	0.08	77
C2	0.26	**0.55**	0.19	122
C3	0.06	0.21	**0.73**	101
	Overall accuracy			**0.64**

Table 2: Normalized Confusion matrix using SAR, NDVI and optical depth for 200 test pixel

	Classify as C1	C2	C3	Total
C1	**0.81**	0.14	0.04	77
C2	0.15	**0.64**	0.21	122
C3	0.04	0.21	**0.75**	101
	Overall accuracy			**0.70**

Soil moisture Class: C1 = ≤10 %; C2 = 11-20%; C3 = 21+

The normalized confusion matrix was calculated by iterating (proportionally) the confusion matrix until the sum of each row and each column will be equal to one. A normalized confusion matrix permits to compare directly main-diagonal and the off-diagonal values of confusion matrices obtained by different classification algorithms. In this study the normalized confusion matrix is used to evaluate the accuracy of the three soil moisture classes. The normalized confusion matrix illustrated in Table 1 shows the accuracies obtained with a neural network trained with backscattering values only. The accuracies shown in Table 2 represent the results of a neural network trained with backscattering values, NDVI and optical depth data. These results show that the major confusion is between the immediate classes of soil moisture. The comparison between the Table 1 and 2, show that the addition of optical depth and NDVI information in conjunction with backscattering values have significant effect on overall classification.

B. Effect of vegetation optical depth

The pixel emissivity from ground surface is affected by the vegetation optical depth. In this application the vegetation cover is acting as an attenuating layer with transmissivity (_) and incidence angle. The vegetation optical depth (_) is the function of vegetation dielectric properties, the plant shape or structure, the wavelength, polarization, and the look angle (_) measured from nadir. The transmissivity is defined by (Jackson and schmugge 1991):

$$\gamma^2 = e^{[-2\tau(\sec\theta)]} \qquad (5)$$

The vegetation optical depth ( ) is a microwave parameter directly related to the vegetation water content ( ) and biomass. The vegetation optical depth was defined by (Jackson, and Schmugge, 1991) as follows

$$\tau = bw_{veg} \qquad (6)$$

Where, b is a parameter related to the nature ot the vegetation cover.

A research carried by Quesney et al (2000) shows that strong vegetation attenuation on radar signal reduces the accuracy of estimation of soil moisture. In the present study, the predicted soil moisture data from neural network has been compared to the ESTAR soil moisture data. The results illustrated in figure 3 show that the classification of pixels with high optical depth values was less accurate than pixels with low optical depth values. This indicates that confusion in classifying pixel increases when the optical depth increases.

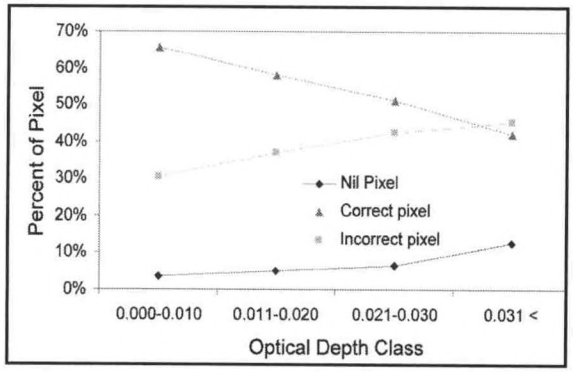

Fig 3. Effect of optical depth class on classification accuracy

C. Effect of NDVI and optical depth on accuracy

Three major input parameters i.e. SAR backscattering, optical depth and NDVI are used in different combinations as inputs to the neural network model. Accuracy assessment was carried out using confusion matrix to evaluate the performance of the final classification. For each input combination, a confusion matrix was generated from the comparison between the real soil moisture values and the neural network predicted values for different soil moisture classes. The overall accuracy for different combinations of inputs is given in Tables 1 and 2. These results clearly show the effect of optical depth and NDVI parameter on accuracy of soil moisture classification. Using only radar backscattering values as input to the neural network gives an overall accuracy of 66%. However, the addition of the optical depth and NDVI parameter improves the accuracy to 70%.

Conclusion

This study demonstrates a promising capability to generate the soil moisture maps from active microwave data. The relationship can be generated with better accuracy although it influences by various surface and sensor properties. The influence of various parameters can be better understood by the classifiers like neural network, where more than one input parameter can be used to improve the final classification.

The additions of optical depth and NDVI information to NN model have significant effect on the final soil moisture accuracy. The higher optical depth and NDVI values lead to confusion to NN model. However, the pixels having lower NDVI and optical depth values have a good chance to be accurately classified.

REFERENCES

Benediktsson, J., Swain, P., and Ersoy, O. K., 1990: Neural network approaches versus statistical methods in classification of multi-source remote sensing data. *IEEE Transactions on Geoscience and Remote Sensing*, **28-4**, 540-552.

Ghedira, H., Bernier, M., and Ouarda, T.B.M.J., 2000: Application of neural networks for wetland classification in RADARSAT SAR imagery. *International Geosciences and Remote Sensing Symposium, IGARSS'2000*, **2**, 675-677, Honolulu Hawaii USA, July 24-28.

Jackson, T., and Schmugge, T., 1991: Vegetation effects on the microwave emission of soils. *Remote Sensing Environment*, **36**, 203-212.

Jackson, T., Le Vine, D., Hsu, A., Oldak, A., Starks, P., Swift, C., Isham, J., and Haken, M., 1999: Soil moisture mapping at regional scales using microwave radiometry: the Southern Great Plains Hydrology Experiment. *IEEE Trans. Geoscience Remote Sensing*, **37**, 2136-2151.

Kanellopoulos, I., and Wilkinson, G., 1997: Strategies and best practice for neural network image classification. *International Journal of Remote Sensing*, **18-4**, 711-725.

Kasischke, E., Smith, K., Bourgeau-Chavez, L., Romanowicz, E., Brunzell, S., and Richardson, C., 2003: Effects of seasonal hydrologic patterns in south Florida wetlands on radar backscatter measured from ERS-2 SAR imagery. *Remote sensing of environment*, **88-(4)**, 423-441.

Paola J., and Schowengerdt, R.A., 1995: A review and analysis of backpropagation neural networks for classification of remotely-sensed multi-spectral imagery. **International Journal of Remote Sensing,** 16-16, 3033-3058.

Quesney A., Hegarat-Mascle, S., Taconet, O., Vidal-Madjar, D., Wigneron, J., Loumagne, C., and Normand, M., 2000: Estimation of watershed soil moisture index from ERS/SAR data. *Remote Sensing Environment,* **72**, 290-303.

Rumelhart D.E., Hinton G. E., and Williams R. J., 1986: Learning internal representation by error propagation, Parallel distributed processing: Exploration in the microstructure of cognition," M.I.T., Cambridge Press (MA), 318-364.

Schmugge T., 1998: Application of passive microwave observation of surface soil moisture. *Journal of Hydrology* **212-213**, 188-197.

Smits P.C., Dellepiane S.G., and Schowengerdt R.A., 1999: Quality assessment of image classification algorithms for land-cover mapping: a review and a proposal for a cost-based approach. *International Journal of Remote Sensing*, **20-8**, 1461-1486.

Ulaby F., Dobson M., and Bradley G., 1981: Radar reflectivity of bare and vegetation covered soil. *Advanced Space Research*, **1**, 91-104.

Ulaby F., Moore R., and Fung A., 1986: Microwave *Remote Sensing, Active and Passive*, vol. 3. From, Theory to Applications, Artech

Inter-Annual Variations and Inter-Hemispheric Differences in PMCs, Temperature, and Water Vapor Observed by HALOE

Jonathan E. Wrotny and James M. Russell III
Center for Atmospheric Sciences, Hampton University, Hampton, VA

Abstract

Data from the Halogen Occultation Experiment (HALOE) are being used to study Polar Mesospheric Clouds (PMCs), their long-term variations with time, northern and southern hemispheric asymmetries, and variations with time and latitude during the summer season. HALOE has been observing the polar summer region since the end of 1991, which has provided 12 northern and 13 southern seasons of data. HALOE typically makes 2-3 sweeps through the high latitudes each summer that provide approximately 600 polar observing opportunities each PMC season. Measurements of temperature and water vapor are also made in the mesosphere simultaneously with the PMC measurements. Analyses of the HALOE data have shown that PMC occurrence frequency and PMC extinction coefficients vary with time and latitude over the course of the summer season, with the largest values nearest the highest latitudes and about 2 _ weeks after solstice. In addition, temperature and water vapor show a very similar temporal and spatial dependence, with PMCs correlated with water vapor and anti-correlated with temperature. PMC occurrences and PMC extinction were found to be generally higher in the northern hemisphere, possibly due to the slightly colder temperatures (~4 K) observed by HALOE in the northern hemisphere polar summer. Northern hemisphere PMC altitudes were also found to be approximately one kilometer lower in altitude, on average. A technique is discussed that is being developed to examine trends in high latitude water vapor and temperature trends, and also trends in PMC occurrence and PMC extinction.

Introduction

Polar Mesospheric Clouds occur in the upper mesosphere of the Earth's atmosphere. They are perhaps the most dramatic cloud to observe visually (see Figure 1), but at the same time, possibly the least understood in terms of their scientific explanation. To ground-based observers, they are known as noctilucent ("night shining") clouds (NLCs) because they reflect sunlight off the clouds back to the Earth. Making them even more unusual is the fact that they can only be seen at certain locations on the Earth, generally in the high latitudes poleward of 50∞ and from ~6 weeks before to ~10 weeks after summer solstice in each hemisphere. It is believed that PMC occurrence at the above locations and times is related to the unique meteorological conditions that occur due to the global circulation of the middle atmosphere. Upward movement of air cools adiabatically and lowers the temperatures to ~140∞K near the mesopause, however, the exact understanding of the dynamics that controls this process is not well understood. This action helps create the conditions favorable for clouds to form (Gadsden and Schröder, 1989).

Due to very cold temperatures of the summertime mesopause, it has long been believed that at least some PMCs are made of water-ice particles, created during a supersaturated atmosphere. This belief has recently been proven with the study of HALOE (Halogen Occultation Experiment) data from the UARS (Upper Atmosphere Research Satellite) (Russell, 1993) confirming that the brightest clouds are indeed made of water-ice (Hervig et. al., 2001). Therefore, it is also necessary for water vapor to be present in the upper mesosphere to make PMCs and understanding the environment in which the clouds form would require extensive knowledge of the water vapor content and temperatures at high latitudes during summer. Unfortunately, there is very little global data on these two parameters, however, HALOE data

may be able to give some insight into this matter since the UARS satellite makes several sweeps through the high latitudes where PMCs form during each summer season.

From the earliest documented observations of PMCs (Backhouse, 1885; Wegener, 1912) to later researchers, scientists likely studied these clouds simply to describe and understood a new phenomenon that they had seen. This continues today, but also because it appears that there are more clouds occurring today than in the past (Fogle, 1965). This increase has sparked a widespread interest in PMCs from many people all over the world. Since the number of clouds has increased, this could mean that long-term changes in the Earth's climate are occurring. Since PMC formation seems to be related to water and temperature, much of the focus has been on finding long-term changes in these parameters. Observational evidence to explain the increase in PMC observations has either been lacking or contradictory, and the question of what is causing the changes remains unresolved. In other words, there is no 'smoking gun' when it comes to explaining PMC formation or changes in the number of PMCs observed over time. Other open questions are PMC particle size, how dynamical and extraterrestrial forcings influences the upper mesosphere and how this translates into PMC formation, and possible PMC nucleation mechanisms.

Figure 1. Photograph of noctilucent cloud. (http://lasp.Colorado.edu/noctilucent_clouds)

Inter-hemispheric differences in PMCs.

One task of the above research has been to analyze the observed inter-hemispheric differences in PMC extinction, PMC altitude, and PMC occurrence frequency observed by HALOE. Using all PMC events seen by HALOE, the northern hemisphere (NH) PMCs were found to have larger extinctions on average (~32%) than the SH PMCs, the NH PMCs were 0.9 km lower in altitude on average, and PMCs occurred about twice as frequently in the NH versus the SH. These differences persist from year to year as well when grouping a given NH PMC 'season' with the previous SH PMC 'season.'

Figure 2 shows the PMC extinction distributions for all NH and SH PMCs seen by HALOE. The distributions are displayed as a percentage of PMCs for a given extinction value, so a value of 15 % means that 15% of the PMCs (for a given hemisphere) have that particular extinction value. From the plot, it can be seen that the NH distribution is shifted towards the right (higher extinction values). This shift illustrates that the NH PMCs make up a larger percentage of the high extinction values compared to the SH PMCs.

The observed differences between the NH and SH PMCs are important because they point to possible differences in the state of the atmosphere between the two hemispheres. Indeed, this is already what has been observed in HALOE data. For example, the temperatures observed by HALOE for the NH and SH polar summer reveal slightly colder temperatures (~ 4K) in the NH versus the SH (see Figure 3). Since PMC nucleation and growth depends very sensitively on the temperature of the mesopause region, we believe that these inter-hemispheric differences in temperature are mostly responsible for the observed inter-hemi-

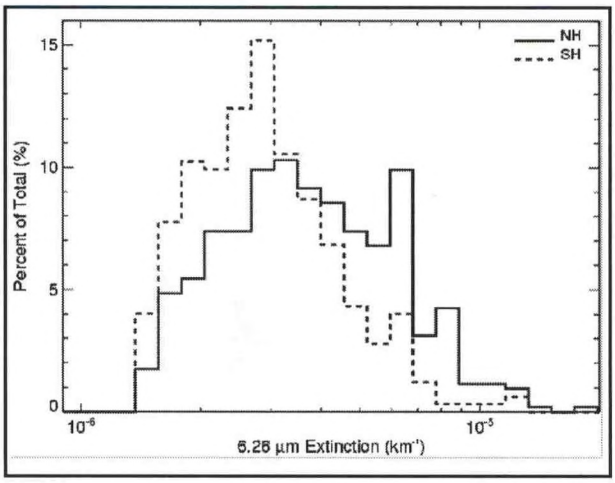

Figure 2. The PMC extinction distributions for all PMCs observed by HALOE between 1991 and 2003 and latitudes from 55° to 75°.

spheric differences in PMC characteristics.

The use of 'time-latitude' bins to study inter-annual variability in the polar summer.

The polar summer mesosphere is a difficult region to study due to its tenuous nature and its drastic variations on small time scales. This region can be studied with the HALOE instrument and, more recently, with SABER on the TIMED satellite. Inter-annual variability is difficult to study for the polar latitudes using HALOE data, in particular because of the poor spatial and temporal coverage of these latitudes and the difficulty in separating inter-annual variations in the data from seasonal and latitudinal variations in the data.

A technique is now being developed that may help with the above problems associated with calculating inter-annual variability using HALOE data. It is based on binning HALOE data in 'time-latitude' bins, as opposed to simply averaging data in time bins (for a given latitude). The benefit of this approach is that it will remove the seasonal cycle in temperature, for example, from the time series so that variations in temperature from year-to-year are due only to true inter-annual variations in temperature. This is necessary because the irregular sampling of the polar summer by HALOE from year to year would otherwise introduce seasonal variations into the time series due to different sampling of the seasonal cycle from year to year.

The HALOE temperature data at the mesopause has been averaged over time and latitude into bins of 1 month and 10° degrees in latitude (all longitudes are included in a given bin also). All HALOE data for every year is binned and a contour plot is made (see Figure 3). It is obvious that temperature has strong seasonal and latitudinal structure during the NH and SH summer. Also, as function of latitude and time, the temperature contours roughly follow elliptical patterns. For HALOE data inside of two adjacent contour lines, the average temperature has nearly the same value. In other words, data inside of this 'time-latitude' bin exhibits no seasonal dependence. So, if this same 'time-latitude' bin is constructed for every year, the seasonal cycle of temperature will be removed for each year, provided that the bin follows the temperature contours for each year. Then, it will be possible to average data within the bins for each year and construct a time series that has no contributions from the seasonal cycle in the temperature (or other parameter being studied).

It is necessary that the same seasonal and latitudinal temperature structure that is evident in Figure 3 occur in a temperature contour plot for every year for this technique to be valid. This is expected to occur, however, it cannot be confirmed with HALOE data due to large gaps in the coverage for a given year. This will be examined by using data from HRDI on UARS to make contour plots of temperature as in Figure 3 for each individual year. This will also be done with WINDII (UARS) and SABER data as well. If confirmed, the time-latitude binning approach will be used to compute seasonally averaged quantities such as temperature, water vapor, and ultimately, PMC extinction, occurrence frequency, and altitude. These time series will be useful in determining if the above parameters vary from year-to-year, and hint at the causes of variation (e.g. the solar cycle). Since PMCs are believed to depend strongly on temperature, temperature bins will be used to define regions in latitude and time over which to average PMC quantities and construct time series.

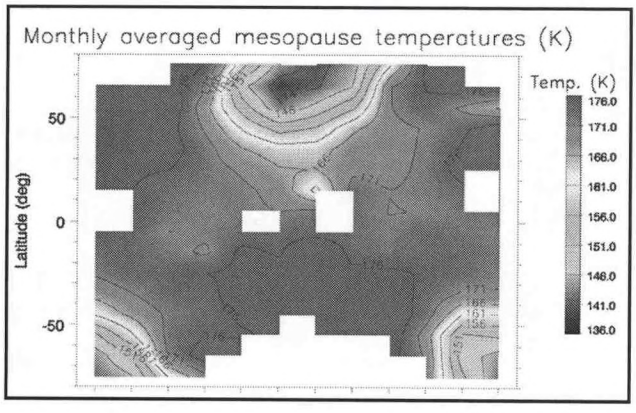

Figure 3. The monthly average mesopause temperatures for all 13 years of HALOE data (1991 to 2003) averaged over time and latitude.

ACKNOWLEDGEMENTS

I would like to thank NASA for supporting this research. I would like to thank NOAA-CREST for allowing me to present my research at the annual conference. I would like to thank my research advisor, Dr. James M. Russell III, for his plentiful help and support without which I would not be

able to take part in this research.

Also, I wish to thank Mr. Martin McHugh, Mr. Robert E. Thompson, and Mr. Mark Hervig of GATS, Inc. for their help in answering many of my questions.

REFERENCES

Backhouse, T.W., 1885: The luminous cirrus cloud of June and July, Meteorol. Mag., 20, 33.

Fogle, 1965: J. Geophys. Res..

Gadsden, M. and W. Schröder, Noctilucent Clouds. In Physics and Chemistry in Space Planetology 18, L.J. Lanzerotti, M. Hill, D. Stiffler, Mnster (eds) Springer-Verlag.

Hervig, M.E., R.E. Thompson, M. McHugh, L.L. Gordley, J.M. Russell III, M.E. Summers, 2001: First confirmation that water ice is the primary component of polar mesospheric clouds, Geophys. Res. Lett., 28, 971-974.

Russell, J.M. III, L.L. Gordley, J.H. Park, S.R. Drayson, W.D. Hesketh, R.J. Cicerone, A.F. Tuck, J.E. Frederick, J.E. Harries, and P.J. Crutzen, 1993: The Halogen Occultation Experiment, J. Geophys. Res., 98, 10,777-10,797.

Wegener, A., 1912: Die Erforschung der obersten Atmospharenschichten", Gerlands Beitr. Geophys., 11, 102.

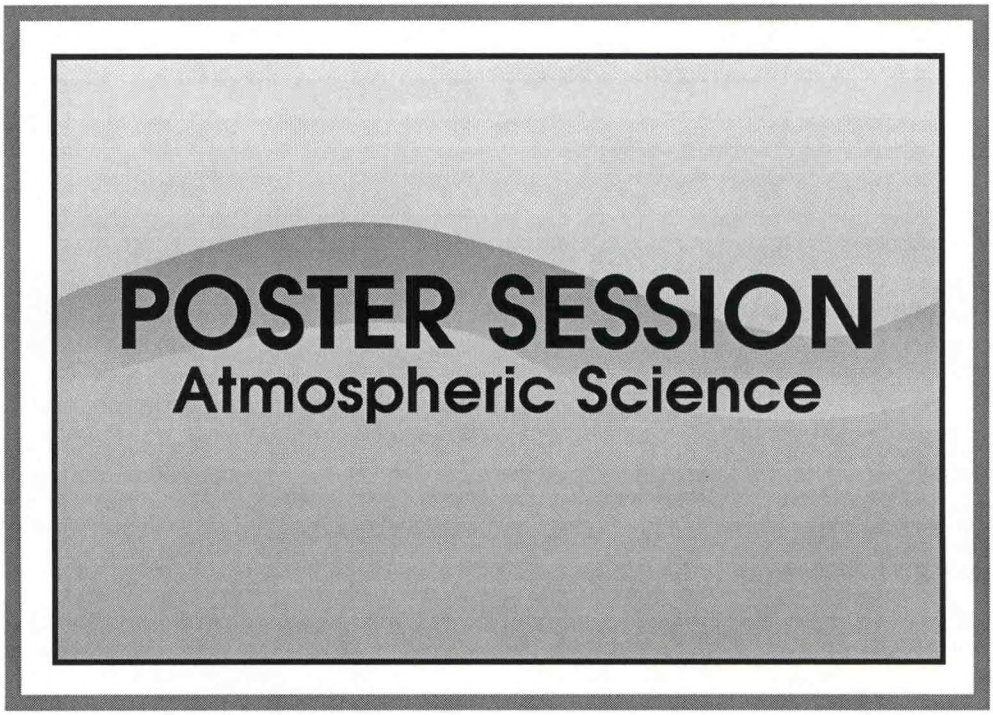
POSTER SESSION
Atmospheric Science

Examination of Heavy Metals and Particulate Matter Exposures and Their Effects in Susceptible Wards Within Washington, DC

Natasha A. Greene*
Program in Atmospheric Sciences, Howard University, Washington, DC
Vernon R. Morris, Ph. D.
Department of Chemistry and Program in Atmospheric Sciences, Howard University, Washington, DC

Abstract

The District of Columbia has one of the greatest health disparities in the nation and ranks seventh highest as one of the unhealthiest places to live due to poor air quality (EPA Report, 1999). The 1999 report from the Centers for Disease Control reports that the District had the highest overall rate of cancer incidence in the nation. Particulate matter is one of the major contributors to pollution in the Washington, DC environment. Quite often ambient airborne toxics are closely associated with particulate matter. Fine aerosols are characterized as particles with diameters smaller than 1 μm and are easily deposited into the alveolar regions of the human lungs, which can impose severe health risks. In this study, high-resolution aerosol measurements of $PM_{2.5}$ and heavy metals like chromium, lead, cadmium and arsenic, in four observed wards of Washington, DC was executed. Spatial distributions of both aerosols and heavy metals have been characterized as a function of size and mass properties.

Introduction

It is well known that the DC area has one of the greatest health disparities throughout the nation (CDC U.S. Cancer Statistics, 1999). Yet, there have been few publications regarding the effects of airborne chromium and other heavy metals in the DC environment and none, particularly discussing its relation to epidemiological data. This research was developed to characterize particulates (PM2.5 and heavy metals) and assess their effects on public health within a metropolitan region.

Through the development of this study, three questions are to be addressed:

- What is the spatial distribution of aerosols in this urban area?
- Is there a meaningful relationship between aerosol-borne toxins or heavy metals (Cr, Pb, As, Cd) and any significant health indicators in the Washington, DC area?
- What is the seasonal (Summer and/or Fall) variability in toxic exposures of heavy metals in the Washington, DC region?

The objective of this study is to enable the development of a climatology of urban aerosols and an improved exposures model for particulate matter and heavy metals (Cr, Pb, As, Cd) for the four chosen wards of Washington, DC. The measurement data sets will be compared to health outcomes obtained from various sources (e.g. the DC Public Health Department). The power of this study lies in its ability to quantify emitted heavy metals and particulate matter to the amount that people are exposed to via air in selected wards of Washington, DC. During the year 1999, EPA reported the following emissions data for the District of Columbia: PM2.5 (200 Tons/yr), PM10 (390 Tons/yr), Chromium Compounds (189 Pounds/yr), Lead Compounds (834 Pounds/yr), Arsenic Compounds (63.6 Pounds/yr), and Cadmium Compounds (70.9 Pounds/yr) (EPA, 2000).

* Corresponding author address: Natasha A. Greene, Howard University, Program in Atmospheric Sciences, Washington, DC 20059; email: tashism26@hotmail.com

Discussion of Selected Wards.

Four Washington, DC wards were selected for this study. Those wards are: Ward 1, Ward 4, Ward 5, and Ward 7 (refer to Figure 1). More than others, Ward 4 is of particular concern due to its persistently high cancer death rate (average of 246) according to the DC Public Health data from 1995 to 1999, as shown in Table 1. Ward 5 is a close second to this data with an average of 214.4 cancer deaths per 100,000 persons. A recent report in The Washington Post stated that Washington, D.C. had the highest overall rate of cancer incidence (667.1) during 1999 in the nation (CDC U.S. Cancer Statistics, 1999). It also reported biases in specific cancers, such as: prostate cancer for whites was 144 cases per 100,000 population, whereas blacks was 275, a 91% increase; lung cancer had a rate of 63.7 cases per 100,000 population, whereas blacks more than doubled that number with 134.6. The primary focus of this study is to provide a dataset that may ultimately be used to clarify both acute and cumulative impacts of heavy metals and particulate matter in Washington, DC. Further, the dataset may enable the determination of an environmental influence, if any, on the observed health disparities in Washington, DC.

Ward 1 is home to Howard University and Adams-Morgan. It is mostly residential, with more than 80% of its land devoted to housing units. It has a population of 73,364 with 45.7% Black, 31.7% White, 24.7% Hispanic, and 3.5% Asian.

Table 1

Cancer Death Rate During 1995-1999 for Wards in Washington, DC

	Ward 1	Ward 4	Ward 5	Ward 7
1995	139	265	238	213
1996	137	250	224	197
1997	112	218	191	155
1998	136	265	209	179
1999	134	232	210	183
Average	131.6	246	214.4	185.4

Ward 4 has 87% of its land devoted to residential use, which is the highest percentage of any ward. A stretch of the city's longest commercial corridor, Georgia Avenue, runs through the middle of Ward 4. There is a population of 74,092 with 70.7% Black, 17.7% White, 12.5% Hispanic, and 1% Asian.

Ward 5 is home to two major commuter arteries, New York Avenue and Rhode Island Avenue, which are gateways to the District. The ward has more industrial acreage than any other in the city, including welding and cement facilities. The population is 72,527 with 86.7% Black, 9.4% White, 2.6% Hispanic, and 0.8% Asian.

Ward 7 uses much of its land as parkland and sits on the right bank of the Anacostia River. However, this ward is home to the Pepco- Benning power plant, a primary source of heavy metal emissions. The population in Ward 7 is 70,540 with 96.8% Black, 1.4% White, 0.9% Hispanic, and >>1% for all other.

Operational Strategy and Instrumentation.

The project is implemented in three distinct phases. During the first phase, a study to determine all possible heavy metal exposure pathways in the Washington, DC environment and an emissions inventory focused on heavy metal particulate matter was developed. This provided the baseline for identifying measurement needs for the following phases. The second phase executed a three-part series of focused field measurements in DC to quantify heavy metal exposures near known sources and in neighborhoods having high cancer incidences. Phase three will incorporate the emission inventory and measurement data from phases one and two to refine the particulate matter exposure for each chosen ward in the D.C. area by determining tracer metals from collected samples. The PM data, as will the heavy metal dataset, was integrated into a GIS database to perform a spatial analysis of the exposure pathways in each of the four chosen wards.

Measurements were obtained using a laser particle counter (LPC) and quartz crystal microbalance (QCM) cascade impactor, to measure in situ aerosol data in the DC area. The CLiMET LPC provides number densities for six size distributions of measurements (> .3, > .5, > 1.0, > 3.0, > 5.0, and > 10 _m). A quartz crystal microbalance (QCM) cascade impactor was used to obtain size and mass properties of particulate matter. The QCM is also a six-stage instrument providing aerodynamic size-cuts at 0.15, 0.3, 0.6, 1.2, 2.5, and 5.0 _m. The aerosol samples collected in this study focused on diameter ranges of 2.5 microns or less.

The plan for the intensive observational period (IOP), or the portion of the study dedicated to the field measurements, was to complete the data collection for all four wards once each week for a consecutive six-week period. This resulted in a total of 32 measurement locations throughout DC, sampling about 7-9 sites per day (Ward 1 - 7 sites, Ward 4 – 9 sites, Ward 5 – 9 sites, Ward 7 – 7 sites), as shown by the points noted in Figure 1. There were three consecutive ten minute measurements performed at each location to gain an average of aerosol measurements. The number of source points, sites that are noted as sources of heavy metals, such as welding services, recycling sites, and gas stations, also varied within each ward. Wards 1 and 7 had a total of two source points per ward, Ward 4 had three source points, and Ward 5 had four source points. The average distances between these source locations and the other measuring sites within the wards were: Ward 1 - 1.16 miles, Ward 4 – 1.45 miles, Ward 5 – 1.78 miles, and Ward 7 – 2.38 miles. This IOP was carried out for both the summer and fall period so that a comparative analysis of the two seasons could be completed.

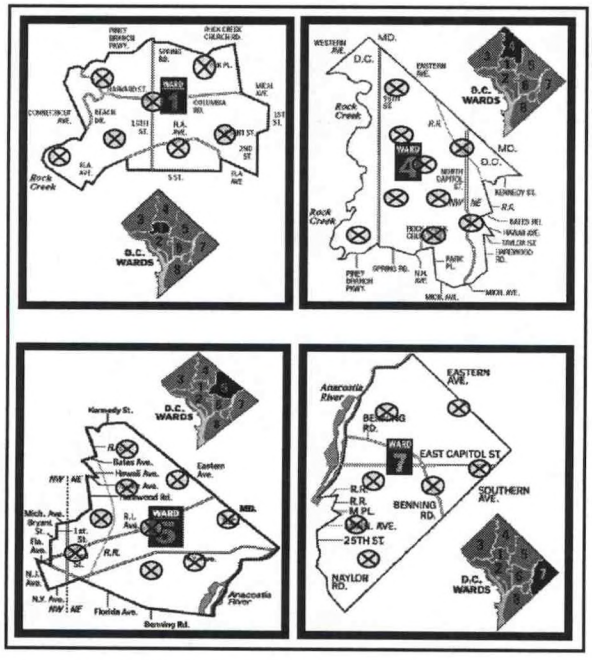

Figure 1. Sampling Wards and Site Locations

Preliminary Analyses.

The summer and fall IOP weekly charts of averaged concentrations for each selected ward showed that there are peak concentrations on *different* days of the week for each ward. For instance, Ward 1 has its peak concentration on Tuesday and Ward 4 has its peak on Thursday. This shows a progressive trajectory of particles throughout the wards. It also brings focus to rain influence. The meteorological data collected (not shown here) has reflected that the day with a higher relative humidity in a particular ward, neglecting days that had rain influences, yields higher concentration of the 0.3 or 0.15μm particles, and thus the peak concentration for the week. These particular influences now present the biggest challenge to analyzing the data because a *typical* summer in the Washington, D.C. area is not as inclined to rain. Hence, the data collected in the 2003 summer IOP tends to differ from trends, in which higher values of $PM_{2.5}$ emissions are in the peak of the summer season, and lower values in the fall, spring, and winter months due to *precipitation*, lower temperatures, and snow.

Analyses of the weekly average concentrations for each selected ward showed that each peak day, the day with the highest concentration value, focused on the 0.3 μm mode size during the summer IOP and primarily on the 0.15 μm mode during the fall IOP (refer to Figures 2-3). This is consistent with the fact that the diameter size of toxic airborne particles is commonly 1μm or less, thus plays an extremely significant role in the study. Ward 4 consistently ranked highest in concentration values for $PM_{2.5}$ during the summer IOP (refer to Figure 2). The 0.30 μm particle concentration in Ward 5 exceeds the distribution for Ward 4 and vice-versa for the 0.15 μm size distribution during the fall IOP (refer to Figure 3).

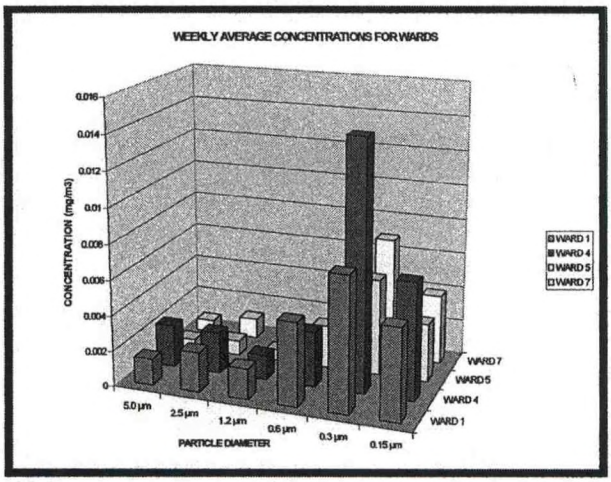

Figure 2. Summer Weekly Avg. of PM Conc.

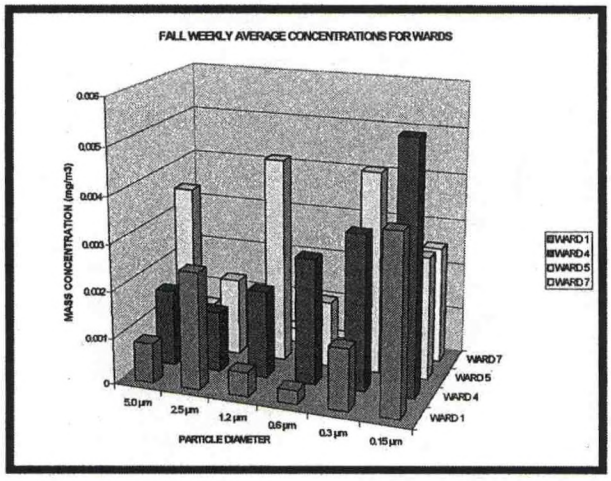

Figure 3. Fall Weekly Avg. of PM Conc.

The summer IOP charts of mass distribution reveal that the 0.3 μm particle distribution for all wards coincides with the ranking of average cancer incidence rate in the D.C. area (Figures 4 and 6) (Ward 4 – 47%, Ward 5 – 42%, Ward 7 – 38%, and Ward 1 – 32%), which may yield pertinent information in the development of this project. The mass distribution during the fall IOP (Figures 5 and 7) differs slightly with the focus predominantly on the 0.15 μm size led by Ward 7 (home to Pepco-Benning power plant). Additionally, the ranking of the 0.30 μm mode differs from the summer IOP with

Ward 7 at 30%, Ward 5 at 24%, Ward 4 at 21%, and Ward 1 at 14%.

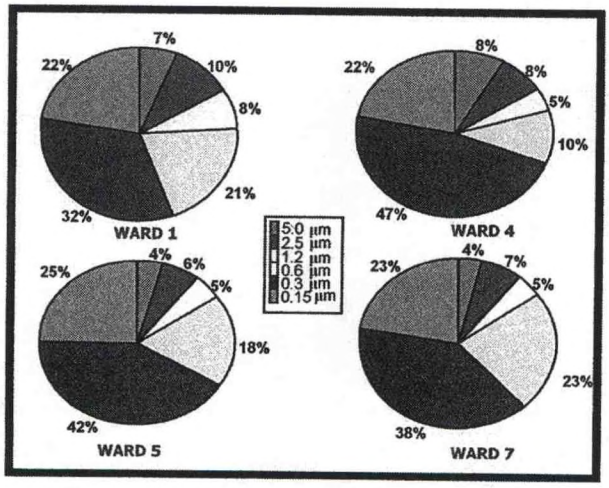

Figure 4. Summer Ward Mass Distribution

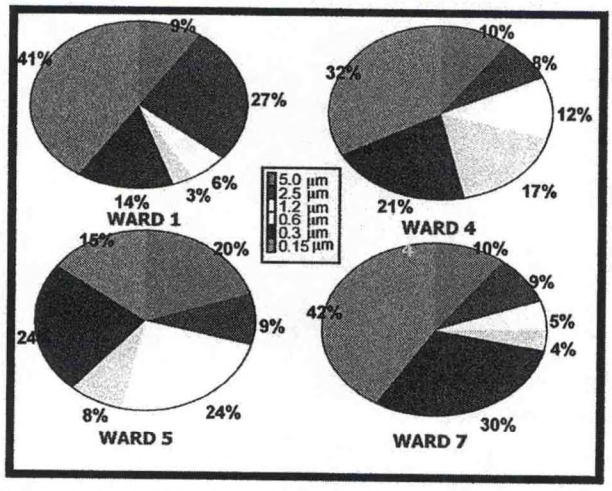

Figure 5. Fall Mass Distribution for Wards

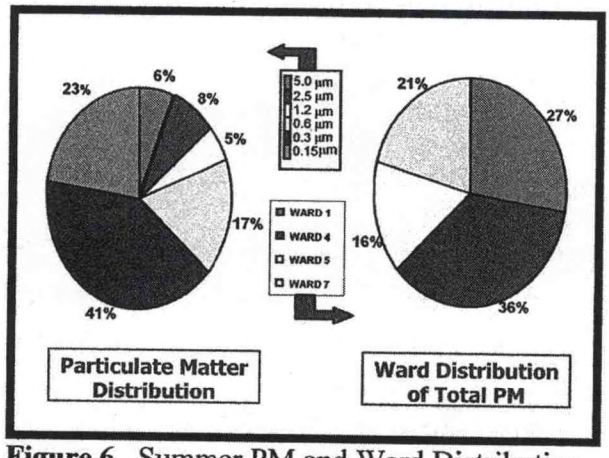

Figure 6. Summer PM and Ward Distribution

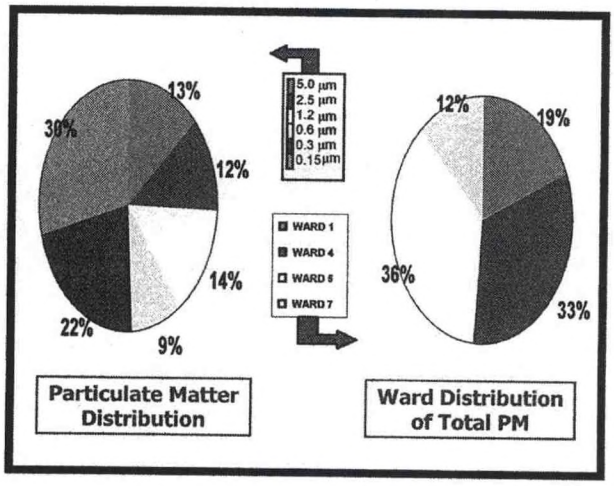

Figure 7. Fall PM and Ward Distribution

Figures 8 through 10 show the GIS mapping of the particulate matter data collected for the summer and fall IOPs. Due to the fact that we are most concerned with particles that are easily deposited into the alveolar regions of the lungs, which are less than 1.0 µm in diameter, mappings of 1.20 µm particles (obtained from QCM measurements) and 1.00 µm particles (from the CLiMET 550) are displayed. Although the output of the summer PM mapping shows differently from the mass distribution of total particles, Ward 4 still ranks amongst the top two wards in PM distribution. On the other hand, both the fall QCM and CLiMET mappings show a correlation with the total particle distribution as shown in Figure 7.

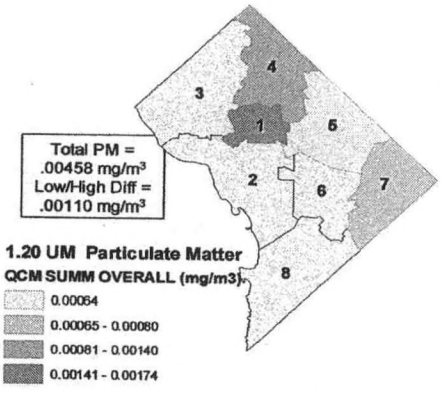

Figure 8. Summ QCM GIS Map for Wards

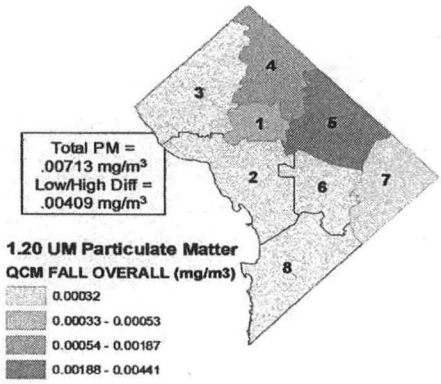

Figure 9. Fall QCM GIS Map for Wards

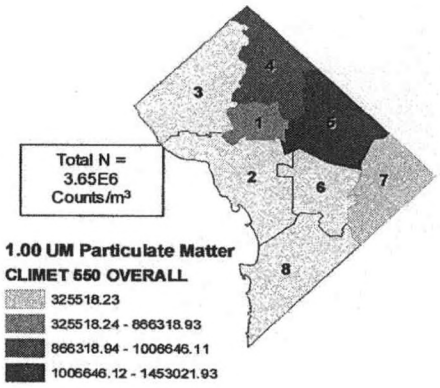

Figure 10. Fall CLiMET GIS Map for Wards

Data Summary.

In summary, the study has shown:

- Overall, there was a higher concentration of particles during the summer (83.7 $\mu g/m^3$) than in the fall (49.8 $\mu g/m^3$). There is a factor of ~1.7 times more in total particulate matter.
- The Fall IOP generated a higher percentage of 0.15 μm (30%) particles, whereas the summer revealed a greater concentration of 0.30 μm (41%) particles. This is generally consistent with colder temps and lower RH in the late fall season than in the heated summer period.
- Ward 4 consistently ranks among the highest wards in total PM concentration (1st – Summer IOP, 2nd – Fall IOP), which is also the highest ranking ward in cancer incidence rates from 1995-1999.
- During the Summer IOP, the rank in mass distribution of 0.30 μm particles for all wards coincides with the ranking of cancer incidence rate in the D.C. area.
- During the Summer IOP, there was not much variation of particle distribution in Wards 1 and 4 and not much variation in Wards 4 and 5 during the Fall IOP, resulting in a higher concentration of particles in these wards respectively.

References.

CDC, 1999: CDC U.S. Cancer Statistics. Center for Disease Control, Washington, DC.

DC Department of Public Health, 1995: Vital Statistics Data Sheet, Washington, DC.

DC Department of Public Health, 1996: Vital Statistics Data Sheet, Washington, DC.

DC Department of Public Health, 1997: Vital Statistics Data Sheet, Washington, DC.

DC Department of Public Health, 1998: Vital Statistics Data Sheet, Washington, DC.

DC Department of Public Health, 1999: Vital Statistics Data Sheet, Washington, DC.

EPA. 2000 Toxics Release Inventory (TRI) Public Data Release Report. Office of Environmental Information, Washington, DC. EPA-260-R-02-003.

Analysis of the Transport of Volcanic Ash from the July, 2003 Eruption of the Soufriere Hills Volcano on Montserrat to Puerto Rico

Jason White[a], Lizette Roldán[a], Dr. Vernon Morrisa[b]

[a]Howard University Program in Atmospheric Sciences (HUPAS)

[b]Department of Chemistry Howard University, Washington DC 20059

Abstract

The Soufriere Hills Volcano is located on the southern half of the Caribbean island of Montserrat. Montserrat is situated in the northern part of the Lesser Antilles, and is one of the volcanic islands formed along the junction of the Atlantic tectonic plate and the Caribbean plate. On July 12, 2003, a lava-dome of the volcano collapsed and led to several days of explosions that rocked the island and injected ash into the atmosphere. This work presents an analysis of trajectory modeling and in-situ observations in Puerto Rico in order to examine the impact of regional transport of the volcanic ash on regional ambient aerosol distributions.

Introduction

The island of Montserrat is located in the West Indies at 16.72° N, 62.18° W.

Montserrat is only 16 km long and 10 km wide, and is built almost exclusively of volcanic rocks. The island is comprised of three volcanic centers. These are, from oldest to youngest: the Silver Hills in the north; the Centre Hills in the center; and the active volcano of the Soufriere Hills in the south. During the last 100 years, there have been several failed eruptions associated with the Soufriere Hills volcano. These occurred in the 1890's, the 1930's and the 1960's [4] With the exception of a 17th-century eruption, no historical eruptions were recorded on Montserrat until 1995. Long-term small-to-moderate ash eruptions beginning in that year were later accompanied by lava dome growth and explosions [3]. On July 12, 2003, a lava-dome of the volcano collapsed and led to several days of explosions that rocked the island and injected ash into the atmosphere.

At the time of the July 12, 2003 eruption, the Howard University NOAA Center for Atmospheric Sciences (NCAS), was conducting in-situ measurements in La Parguera on the southwestern coast of Puerto Rico. The measurements were a part of an aerosol monitoring project set up to help characterize the microphysical evolution of the Saharan Aerosol Layer (SAL) during its long range transport into the eastern seaboard of the United States and the Caribbean, and to quantify the effects of the SAL on the regional environment and climate [8]. Aerosol size distributions and number data collected during this period were used in conjunction with trajectory modeling for this study.

Experimental Methodology

The HYSPLIT (HYbrid Single-Particle Lagrangian Integrated Trajectory) model is the newest version of a complete system for computing simple air parcel trajectories to complex dispersion and deposition simulations. HYSPLIT computes the advection of a single pollutant particle, or simply its trajectory [2]. The model was used to characterize the air mass history and movement of the ash.

The NCEP/NCAR Reanalysis is a project that uses a state-of-the-art analysis/forecast system to perform data assimilation using past data from 1948 to the present [7]. Reanalysis-2 data is based on this widely used NCEP/NCAR Reanalysis data. The goal of the Reanalysis-2 is to improve upon the NCEP/NCAR Reanalysis by fixing the errors and by updating the parameterizations of the physical processes [1]. Reanalysis-2 data was used to obtain wind patterns at specific heights in the atmosphere

during the specific times of the volcanic eruption and transport of the ash [5]. This wind data was plotted for an area that includes both the starting point and the endpoint of the transport path being analyzed. Wind data taken from atmospheric soundings launched from Guadeloupe, a neighboring island of Montserrat, and from San Juan Puerto Rico, are consistent with the wind patterns obtained from the R-2 data.

In-situ measurements of size-resolved aerosol number and mass distributions were taken at La Parguera, on the southwest coast of Puerto Rico in the days before, during, and after the lava-dome collapse. The instruments used were the California Measurements Quartz Crystal Microbalance (QCM) cascade impactor Model PC6-(S2) and the control Climet Instruments Laser Particle Counter (LPC) Model : CI- 550. The QCM is an air particle analyzer which provides aerosol size and concentration data. It is made up of a multistage quartz crystal microbalance cascade impactor and a control unit. The Climet is a laser diode based aerosol particle counter that monitors particles in six size ranges: 0.3, 0.5, 1.0, 3.0, 5.0 and 10 μm.

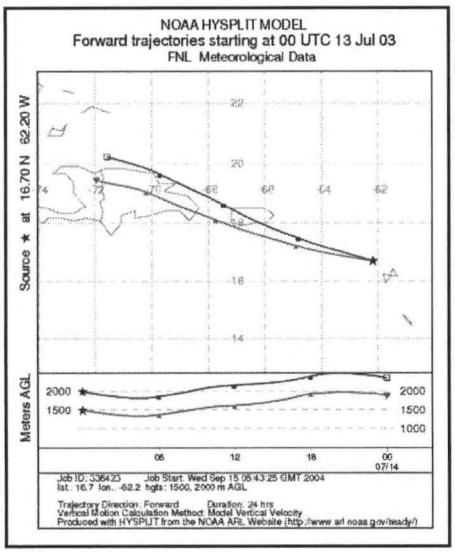

Figure 1

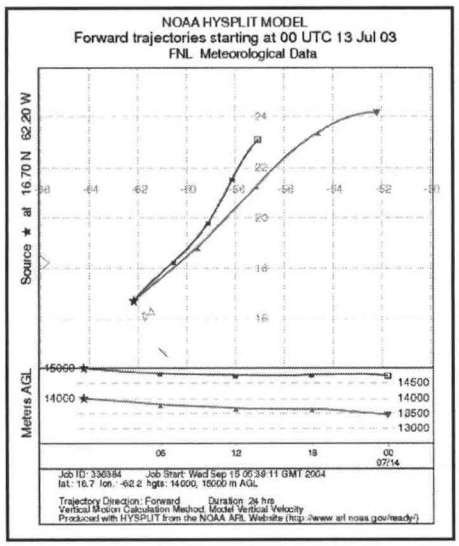

Figure 2

Data Analysis

Meteorological Analysis

On July 12, 2003 when the lava dome of the volcano collapsed, a number of explosive events took place with the largest occurring between 2300 and 2400 [3]. The ash clouds from the eruptions rose to a maximum height of 15 km. At 0910 on July, 13 an eruption occurred with clouds rising to 12 km [6]. Since the elevation of Soufriere Hills is 915 m, and the maximum height of the ash cloud was 15km, ash entered the atmosphere at different levels. The HYSPLIT model was used to obtain the trajectory of the transport path of the volcanic ash that was injected into the atmosphere at different levels.Figure 1 shows the model trajectory for the ash at 1500m (850mb) and 2000m (800mb) starting at 0 hr on July 13 right after the largest eruption took place.

The model predicts a trajectory for the ash that leads it directly to the southwest coast of Puerto Rico. However, for the ash at higher levels in the atmosphere at the same time period, such as those above 5000m (500mb), the model shows the ash being transported along a northeastern trajectory. Figure 2, shows the trajectories for 14000m (150mb) and 15000m (125mb). Reanalysis-2 data was used to obtain the wind data that corresponded to the model runs for various times and heights in the atmosphere. Figure 3 shows the wind streamlines for July 13, at 0h at the 850mb height (1500m). The pattern of the winds is consistent with the trajectory to the southwest coast of Puerto Rico predicted by HYSPLIT for 1500m.

Figure 4 shows the wind streamlines for the same time period, but at a height of 150mb (14000m).

The pattern of the winds is consistent with the northeastern trajectory predicted by HYSPLIT for 14000m. Wind data taken from atmospheric soundings launched from Guadeloupe, a neighboring island of Montserrat, and from San Juan Puerto Rico, are also consistent with the wind patterns obtained from the R-2 data.

Figure 5 is a TOMS image that shows the SO2 cloud that was produced by the large explosion when the lava dome collapsed on July 12. [9]

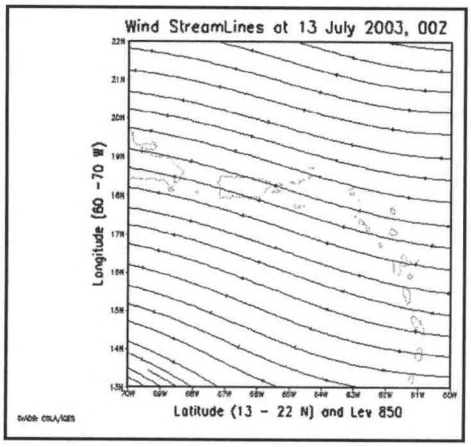

Figure 3

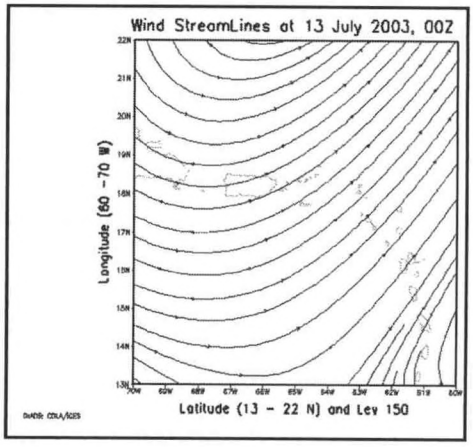

Figure 4

The satellite probe captures the formation of the cloud from above, and its path corresponds with the wind streamlines for the same time period at the upper level height of 14000m (150mb) shown in Figure 4. It also matches the northeastern trajectory predicted by HYSPLIT for 14000m shown in Figure 2.

In-situ aerosol measurements

The largest eruption of the volcano occurred between 2300h and 2400h on July 12, followed by the next largest at 0910h on July 13, 2003. Volcanic ash is usually 2mm in diameter or smaller, and the smallest particles can be around the size of 1 micron. The size of the ash particles generally decrease exponentially with increasing distance from the volcano [10]. The data collected from in-situ measurements taken at La Parguera on the southwestern coast of Puerto Rico, shows an increase in the number density of aerosols for all size ranges measured (.3 microns - >25 microns). An example of the increases is shown in Figure 6, which shows the number density of aerosols for the 1.0 – 5.0 micron range.

For this range, there is a 200% increase in the number density of the aerosol particles at that location beginning at midday on July 13. The increases for all ranges begin around midday, July 13 which is consistent with the twelve hour travel time predicted by HYSPILT for the ash to reach the southwestern coast of Puerto Rico after the largest eruption.

Next Step

The next step in this project will be to incorporate satellite imagery into the study of the volcanic ash's transport pathways, and to use satellite data products in

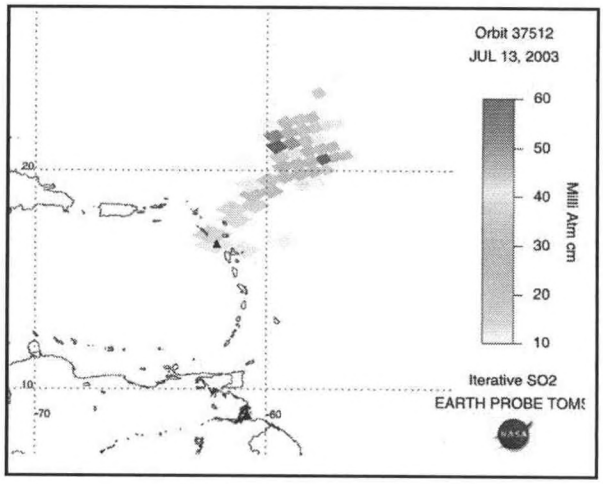

Figure 5

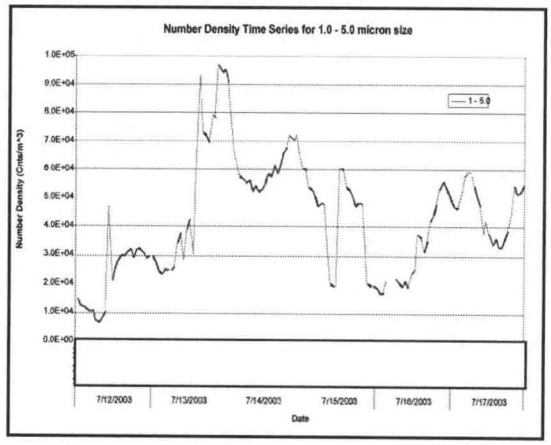

Figure 6

studying the effects that the ash has on the regional environment and climate. Also, data obtained through in-situ measurements at La Parguera will be used to determine the effects of the ash on the local aerosol mass distributions. Scanning electron microscopy will be then be used to learn the chemical composition and identify samples taken at La Parguera during the time period of the eruptions.

REFERENCES

1. Data Support Section of the Scientific Computing Division at the National Center for Atmospheric Research, Cited 2004: NCEP/DOE AMIP-II Reanalysis [Available online at http://www.dss.ucar.edu/pub/reanalysis2/]

2. Draxler, R.R. and Rolph, G.D., Cited 2004: HYSPLIT (HYbrid Single-Particle Lagrangian Integrated Trajectory) Model access via NOAA ARL READY [Available online at http://www.arl.noaa.gov/ready/hysplit4.html.] NOAA Air Resources Laboratory, Silver Spring, MD.

3. Global Volcanism Program, Cited 2004: SI/USGS Weekly Volcanic Activity Report [Available online at http://www.volcano.si.edu/gvp/reports/usgs/index.cfm]

4. The Montserrat Volcano Observatory, Cited 2004: Chronology of the 1995 to 2004 Eruption of Soufrière Hills Volcano [Available online at http://www.mvo.ms/]

5. NOAA Operational Model Archive Distribution System, Cited 2004:

[Available online at http://www.nomad2.ncep.noaa.gov/ncep_data/

6. NOAA Satellites and Information, Cited 2004: Washington VAAC - Volcanic Ash Advisories [Available online at http://www.ssd.noaa.gov/VAAC/messages.html]

7. NOAA-CIRES Climate Diagnostics Center, Cited 2004: NCEP/NCAR Reanalysis 1

[Available online at http://www.cdc.noaa.gov/cdc/data.ncep.reanalysis.html]

8. NOAA/NESDIS/ORA, Cited 2004: NCAS Trans-Atlantic Saharan Dust AERosol and Ocean Science Expedition (AEROSE), [Available online at http://orbit-net.nesdis.noaa.gov/orad/sar/oceansar/AEROSE2004//]

9. TOMS Volcanic Emissions Group, Cited 2004: TOMS Volcanic Image Archive [Available online at http://toms.umbc.edu/]

10. U.S. Department of the Interior, U.S. Geological Survey, Cited 2004: Volcanic Ash...What it Can do and How to Prevent Damage

[Available online at http://volcanoes.usgs.gov/ash/index.html]

Altitude-Dependent Aerosol Optical Depths and Number Densities at El Teide, Canary Islands

Lizette Roldán and Vernon R. Morris

Howard University Program in Atmospheric Sciences (HUPAS), Graduate School

The Canary Islands are an archipelago of volcanic origins just off the coast of some of the most active dust storm regions in Northwest Africa. The islands are the first landfall of the airborne Saharan dust and often blanketed by these aerosol during the spring and summer months.

We report on sunphotometer measurements of aerosol column optical depth and aerosol number distributions taken in March 2003 and March 2004 during the ascent and descent of El Teide in the Canary Islands.

These measurements allowed for characterization of the vertical structure of the aerosol layer throughout the depth of the troposphere. The primary objective was to explore the relationship between optical depth, vertical distribution of aerosols, air mass source region, and vertically-resolved size distribution for the two cases in spring during March 2003 and 2004.

Our results confirm that the aerosol layer is largely confined within the first 2 km of the atmosphere.

Analysis of Monsoon Precipitation in the El Paso Del Norte

Karina Apodaca[a] and Vernon R. Morrisa[b]

[a]Graduate Program in Atmospheric Sciences, [b]Department of Chemistry, Howard University, Washington, DC 20059

The El Paso Del Norte (EPDN) region has been suffering from one of the most devastating droughts in recent decades. The EPDN gets between 60 and 70 percent of the total yearly precipitation during the months of July through September; this time coincides with the North American (Mexican Monsoon). Though bi-national efforts have been initiated to assess water conservation strategies, several key factors that may influence this drought still require further study. Sea surface temperature (SST) anomalies in the tropical Pacific Ocean and in the Gulf of California may be responsible for dry weather conditions. We present an analysis of satellite and buoy derived SST data along with in-situ rain gauge and National Weather Service observations to characterize physical and statistical relationships between precipitation occurrence, precipitation amounts, SSTs in the tropical Pacific Ocean and in the Gulf of California, and dust activity in the EPDN region during monsoon season.

Size-Resolved Aerosol Mass and Aerosol Number Distributions During the NOAA Center for Atmospheric Sciences (NCAS) Trans-Atlantic Saharan Dust Aerosol and Oceanographic Science Expedition (AEROSE)

Vernon Morris and Lizette Roldan
Atmospheric Sciences, Howard University
Roy Armstrong and Yasmin Detres
Department of Marine Sciences, University of Puerto Rico Mayaguez

Abstract

The NOAA Center for Atmospheric Sciences (NCAS) conducted a combined atmospheric and oceanographic experiment aboard the NOAA Ronald H. Brown ship to characterize the physico-chemical evolution of the Saharan Aerosol Layer during its long-range transport into the eastern seaboard of the United States and the Caribbean, and to quantify its effects on the regional environment and climate. The NCAS Trans-Atlantic Aerosol and Oceanographic Science Expedition (AEROSE-04) departed on February 29, 2004 from Bridgetown, Barbados and concluded in San Juan, Puerto Rico on March 26, 2004. This paper discusses size-resolved aerosol measurements during the first leg of the research cruise.

The NOAA Center for Atmospheric Sciences (NCAS) at Howard University successfully led a 27-day Trans-Atlantic Saharan Dust AERosols and Oceanographic Science Expedition (AEROSE) in 2004, designated as RB-04-02. The mission began on February 29, 2004 in Bridgetown, Barbados and ended in San Juan, PR on March 26 with a stopover at Las Palmas, Gran Canaria. The Chief Scientist of the mission was Dr. Pablo Clemente-Colón of NOAA National Environmental Satellite Data and Information Service (NESDIS). The Principal Investigator and co-Chief Scientist was Howard University Associate Professor, Dr. Vernon R. Morris. NESDIS scientists and graduate students from Howard University and Senagal provided shore-side support for AEROSE through meteorological forecasting and satellite data analysis. The AEROSE ship tracks are shown in Figure 1.

In addition to HU, AEROSE included the participation of the University of Puerto Rico at Mayagüez (UPRM), the Canary Institute of Marine Sciences (ICCM), the Spanish Institute of Oceanography (IEO), the Laboratory of Atmospheric Physics Siméon Fongang (LPASF) in Dakar, Senegal, the University of Miami Rosenstiel School of Marine and Atmospheric Science (RSMAS), the University of Washington Applied Physics Laboratory (UW/APL), the City University of New York (CUNY) and the NOAA CREST center at CUNY, the NASA Goddard Space Flight Center (GSFC), NASA Jet Propoulsion Laboratory (JPL) and NOAA/NESDIS/ORA.

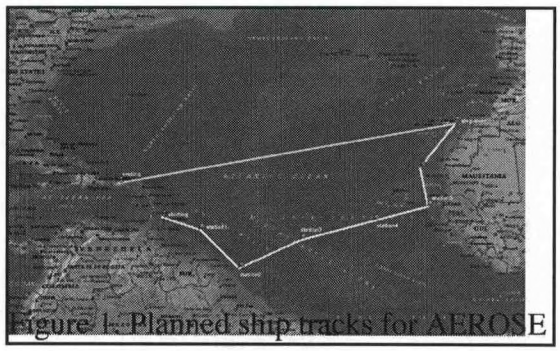

Figure 1. Planned ship tracks for AEROSE

In addition to the first-rate science, this mission was also distinguished by being the first to be led by an HBCU, the first to be led by an African-American, and the first to have a majority of scientists from underrepresented backgrounds in the sciences (African-American, Puerto Rican, and female). The cruise was be followed by middle school students at St. Thomas More in

Washington, DC and an elementary school in Mayaguez, Puerto Rico.

An interactive website maintained at NESDIS featured a daily log from the ship, location-tracking, satellite imagery, question-and-answer communications between scientists and students, and photos of the research activities. AEROSE scientists fielded questions from the schoolchildren as well as from the general public throughout the cruise. The web address is: http://orbit-net.nesdis.noaa.gov/orad/sar/oceansar/AEROSE2004/.

AEROSE received an overwhelming amount of national and international press coverage. Press conferences were held in both Las Palmas, Gran Canaria and in San Juan Puerto Rico. AEROSE scientists were interviewed for both newspaper articles and TV news broadcasts in both cities. Samples of the news item listing of AEROSE from a recent web search are provided in Appendix 2. Other news articles from Gran Canaria and Puerto Rico will be placed on the AEROSE website.

AEROSE04 is the first of three planned cruises. The follow-on experiments have been proposed for summer and winter 2006 (in collaboration with Chile and Spain). Howard University is planning to lead the atmospheric sciences components of each of these missions.

AEROSE Science

The primary mission of the AEROSE 2004 cruise was to provide a set of critical measurements to characterize the impacts and microphysical evolution of Saharan dust aerosol transport across the Atlantic Ocean. The cruise supported a full complement of atmospheric and aerosol measurements, bio-optics and oceanographic observations including water sampling, spectroradiometry, and in-water optical measurements. These observations are being used to study the effect of the dust on the marine boundary layer, to characterize water masses along the cruise path, and to investigate upwelling conditions off the Northwest coast of Africa.

The key areas of focus during AEROSE were climate impacts of aerosols, heterogeneous chemistry, aerosol microphysics, atmospheric deposition and impact. The three central questions guiding the science in AEROSE were: (1) How does Saharan dust affect atmospheric and oceanographic properties during trans-Atlantic transport? (2) How do the Saharan dust aerosol distributions evolve physically and chemically during transport? and (3) How well are the above processes resolved from satellite measurements? A brief summary of the scientific results follows.

The AEROSE mission obtained high-resolution sounding measurements of both the atmosphere (through the entire troposphere – upwards of 25,000 ft) and ocean (down to 2000 ft below the surface) along the cruise track from Barbados to the Canary Islands and back to Puerto Rico.

A sample of the radiosonde data obtained during the cruise is shown below. This figure depicts the boundary-layer evolution during March 3- 9, 2004. The intrusion and affects of the continental air mass on the marine boundary-layer virtual potential temperature and water vapor mixing ratio are quite marked. The drying corresponds well to other physical observations during the dust storm.

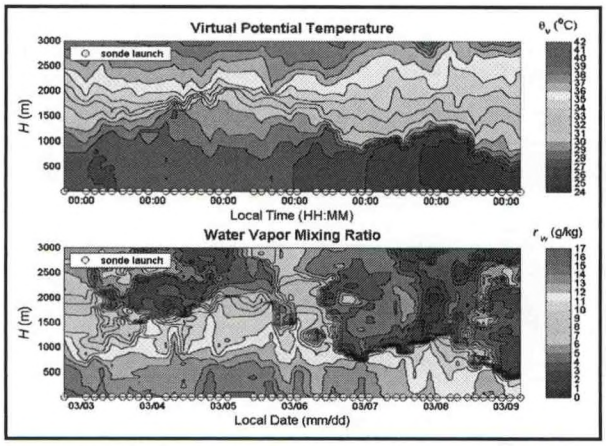

Figure 2. Radiosonde Data for Eastward Leg of AEROSE

The focus of this paper is an overview of the extensive suite of aerosol measurements and size-segregated sampling performed to characterize aerosol mass distributions, number densities, black carbon content, $PM_{2.5}$, aerodynamic size, and chemical composition throughout the cruise. Ambient samples were collected using $PM_{2.5}$ and PM10 RAAS high-volume air samplers (Figure 3) and a quartz crystal microbalance (QCM) cascade impactor.

The QCM instrument obtains much smaller samples (a few nanograms maximum) but allows for a much more finely resolved sample. Two

QCMs were deployed during AEROSE. The size fractions were 0.15, 0.3, 0. and 5.0 mm. Figure 4 shows the evolution of the mass distribution as determined by the six-stage QCM during March 3-9, 2004. The 1.2 μm size fraction was determined to be the most sensitive to mineral dust. Changes in the 2.5 μm size fraction were the most indicative of new dust intrusions.

The aerosol samples were obtained in various portions of the plume to characterize the chemical aging of the dust as it crossed the Atlantic Ocean. These measurements and subsequent analyses were performed by Howard University and UPRM scientists and students. An agreement has been reached with CREST scientists to collaborate on the elemental analysis of the filters.

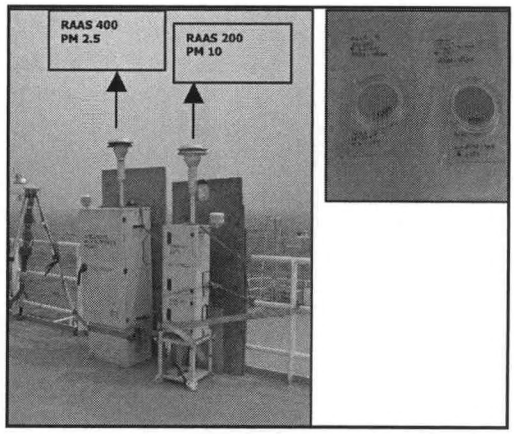

Figure 3. High-volume air samplers and filter samples from AEROSE.

The bar charts shown above illustrate the daily averaged PM_{10} and $PM_{2.5}$ values as determined by the HU QCM during the forward leg of AEROSE. There is a clear mismatch between the two integrated size fractions indicating a mixed air mass with preferential loading of larger particulate, especially during the March 9-13 time period. This corresponds to increased levels of dust loading nearer to the source region as well as differing amounts of smoke from the biomass fires in West Africa.

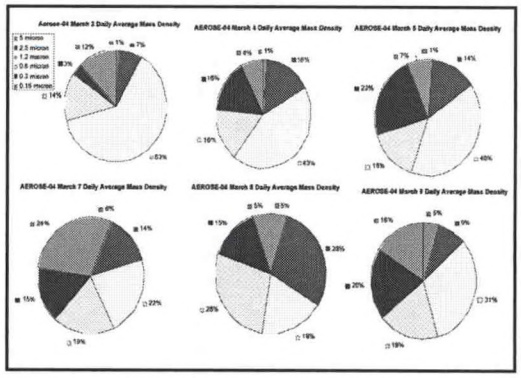

Figure 4. Evolution of the QCM Daily Averaged Mass Distributions for March 3-9, 2004.

A limited set of chemical measurements were performed during the forward leg of AEROSE – ozone and carbon monoxide. The objectives for the ozone measurements were to investigate the impact of the dust layer on ambient ozone levels and gain insight on changes in oxidizing capacity during dust episodes. The measurements of carbon monoxide were used as a tracer of biomass burning or continental air masses. These data were useful in interpreting the aerosol distribution information.

Finally, AEROSE provided satellite validation experiments for three satellite instruments: NOAA's advanced very high resolution radiometer (AVHRR) (measuring sea-surface temperature, skin temperature, and column water), NASA's Moderate Resolution Imaging Spectrometer (MODIS) (measuring column water, temperature profile, and aerosol optical thickness) aboard the AQUA and TERRA satellites, and the Atmospheric Infrared Sounder (AIRS) (measuring air temperature, surface temperature, and column water) also aboard the AQUA satellite. Plans to provide validation for a fourth satellite instrument, the NASA Geoscience Laser Altimeter System (GLAS), aboard the ICESat satellite were cancelled due to instrument problems aboard this platform. NCAS scientists continue to collaborate with GLAS scientists to analyze data obtained during AEROSE. Another NASA collaboration within AEROSE was an agreement with the international space station (ISS) team to take photos of events along the AEROSE cruise tracks.

The validation experiments consisted of hourly sun photometer measurements, 3-hourly radiosonde launches, and sea-surface temperature (SST), skin temperature, and surface temperature measurements taken every minute throughout the cruise. This work was performed in collaboration with the University of Wisconsin, the University of Miami (RSMS), between Howard University, and NESDIS.

Outcomes and Outlooks

By using a combination of satellite observations and meteorological forecasts, NCAS was able to steer the vessel directly into one of the largest (with respect to spatial extent) dust storms observed dur-

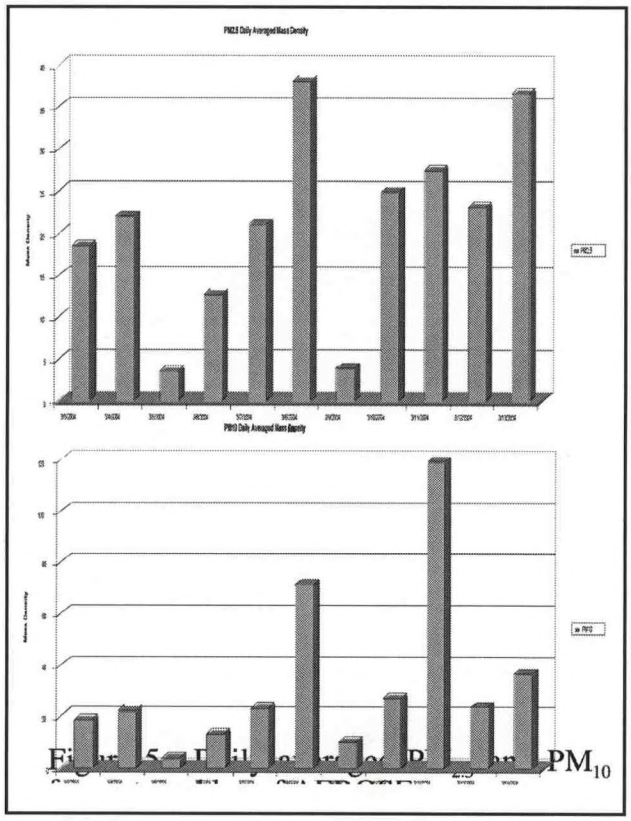

Figure 5. Daily averaged PM2.5 and PM10 for eastward leg of AEROSE

ing March ever recorded. The AEROSE team encountered several separable dust events, completed the intensive column measurements to secure a unique and valuable open ocean data set, successfully obtained the validation data for three US satellite instruments, and obtained a rich data set of aerosol properties before, during, and after a major dust event.

One of the interesting "experiments of opportunity" was the observation of smoke-influenced dust storms. The figure below shows data from the HU Multi-Angle Aerosol Photometer (MAAP) which measures black carbon aerosol.

Figure 7 immediately above shows the profile of black carbon during the large dust storm encounter during March 8-11. The black carbon content of the plume rose steadily during March 8 to a sharp peak value on March 9, and decreased throughout the remainder of the time in the storm.

This point was recognized by the NOAA administrator, Vice-Admiral Conrad C. Lautenbacher, Jr., US Navy (Ret.) in a NOAA press release issued during the second leg of the AEROSE mission as "... one example of the continuing efforts by NOAA and its partners to advance understanding of natural activities and how they interrelate on this planet we share."

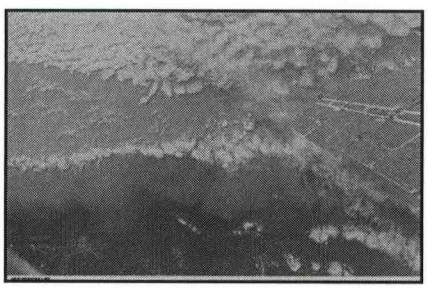

Figure 6. Space station photo on March 8, 2004 encountered by AEROSE during March 8-11, 2004

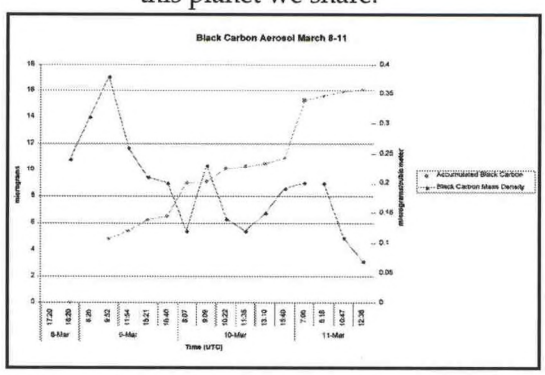

Figure 7. Black carbon measurements during AEROSE.

ACKNOWLEDGEMENTS

The authors would like to express thanks to the following elements of NOAA for sponsorship and support of the AEROSE mission: OMAO, the NWS, EPP/MSI, and NESDIS ORAD. We also acknowledge the AEROSE science team members, the outstanding crew of the Ronald H. Brown during RHB-04-01, and the MODIS, GLAS, and SeaWiFS support from NASA.

TECHNICAL DESIGN CONSIDERATIONS FOR A WATER VAPOR/AEROSOL RAMAN LIDAR SYSTEM

R. Connell*, D. D. Venable*, E. Joseph*

NOAA Center of Atmospheric Science, Howard University, Washington, DC 20059
* Department of Physics and Astronomy

We are developing a Raman lidar system that is designed to measure both water vapor and aerosols. The system is designed for both daytime and nighttime measurements. The lidar is a three-channel system and the laser operates at the third harmonic of Nd:YAG. The lidar uses narrow band-pass filters to measure the three wavelengths of interest that correspond to the elastic backscattered and pure rotational Raman signals, the Raman scattered photons from nitrogen molecules, and the Raman scattered photons from water vapor molecules. The lidar will be used to characterize the temporal and vertical distribution of water vapor and dynamics processes in the boundary layer for evaluation of mesoscale models and to measure cirrus cloud optical depths. It is only one of an extensive set of atmospheric measurement instruments housed at the Howard University Beltsville Laboratory – a comprehensive atmospheric properties measurement facility in Beltsville, MD. We also propose to use the lidar as a part of a regional network of lidar systems. In this paper we present the technical specifications of the lidar system and the results of preliminary measurements made with the system.

The Accuracy of SAGE III: Comparing Limb Scattering measurements

Kristie V. Lee and Robert Loughman

Center for Atmospheric Sciences, Hampton University, Hampton, Virginia

Abstract

Our intent is to compare the SAGE III limb scattering (LS) data to other instruments measuring similar ozone profiles. Comparisons made show an agreement in the mean ozone profile between SAGE III and OSIRIS LS measurements. Similar comparisons show an agreement between SAGE III and SOLSE/LORE data. Both comparisons show an accuracy and precision of relatively ten percent. The quality and accuracy of the SAGE III LS measurements will be assessed after additional data becomes available.

Introduction

The Stratospheric Aerosol and Gas Experiment (SAGE III) instrument was designed to retrieve the vertical distribution of several atmospheric gases during solar and lunar occultation. It was launched in December 2001 in a sun-synchronous orbit with ascending node at 9:00. The SAGE III instrument is a grating spectrometer, measuring the ultraviolet and visible radiances from 280 to 1040 nm at a spectral resolution of 1.0 to 4 nm. Between occultation events, it has been deployed to make LS measurements, by directing its line of sight to measure profiles of the scattered radiance along a tangent path through the atmosphere. The advantage to this method is that the line of sight is not restricted to the solar direction. The limb is scanned at one scan per minute and spectral data is recorded from the ultraviolet, visible, and infrared on a total of 340 channels with a vertical resolution of 0.5 km.

The observer looks at the edge (or "limb") of the atmosphere (just above the horizon), and measures the scattered solar radiance as a function of tangent height, wavelength, illumination, geometry, and viewing direction.

Nadir Looking Backscatter Ultraviolet Measurements

Another method, used by the Solar Backscatter Ultraviolet (SBUV) instrument for retrieval of ozone profiles, is to take nadir looking backscatter ultraviolet measurements over the entire globe. It analyzes the amount of ultraviolet energy reflected back up to the spacecraft, producing profiles of how thick the ozone is in different altitudes and locations. It is sensitive to radiant energy in the ultraviolet region of the spectrum. Taken advantage of is the fact that molecules and aerosol particles reflect certain wavelengths of ultraviolet rays versus ozone that absorbs other wavelengths at different levels in the atmosphere. While nadir looking backscatter ultraviolet measurements effectively depict the total ozone column, LS measurements provide enhanced information, taking accurate measurements of each layer within the profile. Other methods of ozone profile retrieval include visible and infrared limb occultation and infrared limb emission.

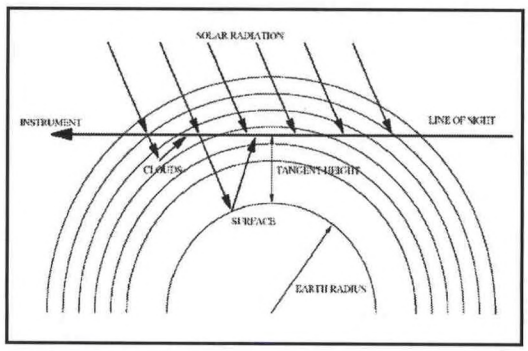

Fig. 1. Illustration of Limb Scattering Geometry.

Shuttle Ozone Limb Scattering Experiment – Limb Ozone Retrieval Experiment

SOLSE images the limb of the earth onto a CCD array through a spectrometer, forming a multi-wavelength image –530nm to 850nm, at a 0.7 nm resolution. Shorter wavelengths (near 300nm), that are highly sensitive to ozone, are used to measure the ozone profile up to 50 km, while longer, less sensitive wavelengths (near 600nm) measure ozone in the lower stratosphere, possibly down to 10 km. SOLSE is a Czerny-Turner imaging spectrometer designed to produce a high quality image of the limb of the earth while minimizing internal scattered light. The resolution of the vertical image is better than 1 km. Internal scattering can be a problem because there is more than two orders of magnitude dynamic range in the image from the short wavelength high altitude part to the long wavelength low altitude part (*http://code916.gfsc.nasa.gov/Public/Space_based/solse/solse.html*).

LORE is a small camera system that accompanies SOLSE in its demonstration flight. LORE is a filter radiometer with a linear diode array detector that is flown in the SOLSE canister to measure the limb-scattered radiance at ultraviolet and visible wavelengths. Wavelengths near 600nm are used to measure ozone in the 15-30 km region using Chappuis band absorption. A channel near 760nm is used to measure oxygen absorption, while a channel near 760nm is used to measure oxygen absorption, while a channel at 322nm measures zone above 30km, and a third channel at 350nm provides pointing information (*http://code916.gfsc.nasa.gov/Public/Space_based/solse/lore.html*).

OSIRIS Instrumentation

OSIRIS (the Optical and Infrared Imager System) was launched in February of 2001 in a sun-synchronous orbit with ascending node at 18:00. It measures profiles LS radiance spectra from 280-800 nm at 1 nm resolution, and retrieves ozone using the retrieval algorithm proposed by Flittner et al. (2000). For further information, consult von Savigny et al. (2003) and Petelina et al. (2004).

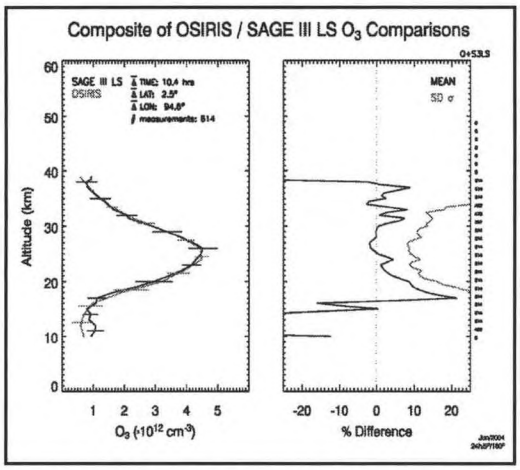

Fig. 2. OSIRIS / SAGE III LS O3 Profile Southern Hemisphere Comparison.

Composite SAGE III LS vs. OSIRIS LS Comparisons

Figure 2 compares the mean ozone profile retrieved from SAGE III LS measurements on February 22, 2004 with the ozone profile from the OSIRIS LS measurements. In this case, Φ ranged from –46° to –30°, or 30°-46° S. A coincidence is defined as two measurements made within 24 hours of each other, in which the latitudes of the tangent points differ by less than 5 deg. The average difference in latitude, longitude and time for the population of coincidences is given at the top of the left panel, as well as the number of coincidences. The horizontal bars on the left panel indicate the standard deviation of the ozone concentration for each instrument as a function of altitude. (Not every altitude is labeled, to make the labels on the two ozone profiles distinguishable).

The right panel shows the mean of the difference between the ozone profiles obtained from the two sets of measurements, as well as the standard deviation of the mean, as a function of altitude. The small digits on the right of the right panel indicate the number of coincidences that contributed to the mean at each altitude (which varies because the vertical extent of the retrieved profile varies from one event to the next).

Another group of coincidences occurred in the 0 deg – 10 deg N latitude range (see Figure 3). Unfortunately, many of the SAGE observations occurred during a gap in the Earth Probe TOMS (total ozone mapping spectrometer) data coverage, making comparison of the TOMS total ozone column impossible. The agreement in the northern hemisphere comparison is poorer than in the southern hemisphere comparison, with SAGE III LS profile roughly 10% larger than the OSIRIS LS profile altitudes between 20 and 40 km. At altitudes greater than 15 km, the SAGE III LS profile consistently exceeds the OSIRIS LS profile.

SOLSE /LORE O3 vs. SAGE III Comparisons

On Jan 27, 2003, an excellent coincidence was arranged: The SAGE III and SOLSE/ LORE-2 lines of sight are aligned to within 7° in azimuth, the tangent points coincide to better than 2° in both latitude and longitude, and the observation times are separated by < 20 min (see Figure 4).

For SOLSE/LORE and SAGE III, height registration of the measured radiance profile is done by the "RSAS" method (Janz et al., 1996), which uses the shape of the UV radiance profile at ozone–insensitive wavelength of 350 nm. Its demonstrated accuracy is ~1 km. SOLSE/LORE-2 has the added complication that the LORE 350 nm filter measurement needed for the RSAS method and the SOLSE measurement used for ozone retrieval often are not simultaneous (and are frequently separated by > 30 s). Synchronization between the LORE 350 nm image and the SOLSE image is excellent in the case illustrated in Figure 4 (Dt = 1s), so the time interpolation error in the tangent height registration for SOLSE is minimized. No obvious tangent height mismatch existed here between the SAGE III and SOLSE/LORE-2 data. Two neutral density filters were inserted in order to minimize stray light in the SOLSE data. Known artifacts are introduced into the radiance profile at 36 and 10 km (in the vicinity of the filter boundaries), and the radiance profile is not always continuous across these boundaries. Therefore only data from the 12-30 km tangent range is used at present.

SAGE III uses the RSAS method to reduce the tangent height error. The SAGE III 1017 nm channel observation shows a sharp feature at 12 km, while the SOLSE/LORE-2 data shows a similar feature at 5 km. Despite their close proximity in space and time, this suggests that each instrument detected different cloud scenes.

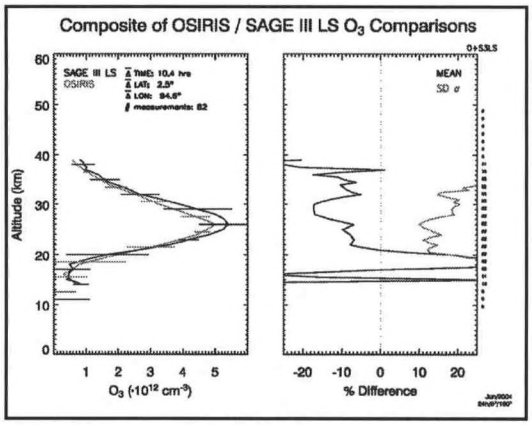

Fig. 3. SAGE III LS/ OSIRIS LS Comparison for the Tropics (-4° < Φ< 12°)

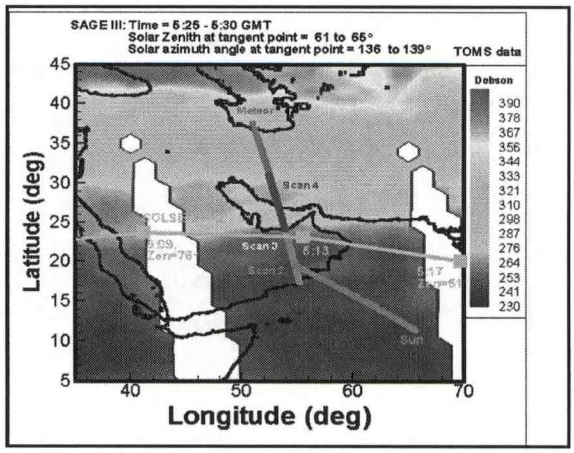

Fig. 4. SOLSE/LORE O3 Retrieval for Jan. 27, 2003.

Conclusions

There is very little indication of a tangent height registration bias in the SAGE III / OSIRIS LS comparisons so far. The standard deviation and accuracy of the measurement are relatively ten percent. Agreement in the mean profile is better than 10% at altitudes > 15 km, with larger errors below that altitude. In the southern hemisphere, the OSIRIS mean ozone profile exceeds the SAGE III LS profile for altitudes between 15 and 25 km, with the opposite true for altitude < 15 km. The OSIRIS retrieved ozone is smaller than the SAGE III LS retrieved ozone at altitudes < 15 km even for the comparisons that were similar in latitude and total ozone.

In most SAGE III/SOLSE LORE comparisons, time interpolation introduces a difficult-to-quantify error in the SOLSE tangent height registration. Transferring

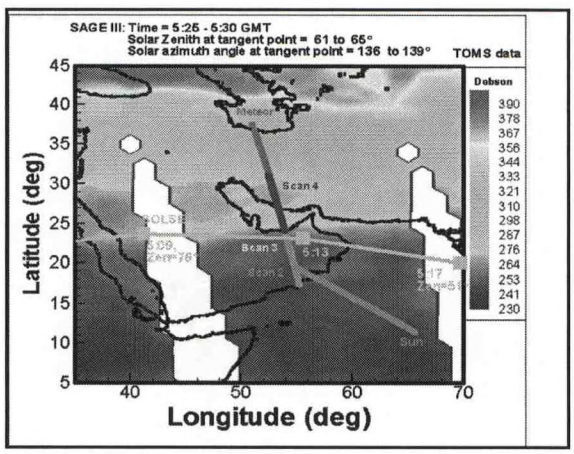

Fig. 5. SOLSE/LORE O3 retrieval Comparison to SAGE III ozone retrieval for Jan. 27th, 2003.

tangent height registration from LORE to SOLSE (by assuming that the instrument bore sights are aligned), introduces additional error. Agreement between the SAGE II and SOLSE/LORE-2 retrieval presented (see Figure 5) would be improved by a 1 km relative shift in the tangent height registration, but the comparison of the radiance does not indicate such a shift is warranted. Measurements for SOLSE/LORE and SAGE III generally agree within their error bars for altitude > 15km.

On other days, SAGE observations were tailored to provide coincidences with POAM, SAGE II, and HALOE data, with results pending. The more difficult lower stratosphere and upper troposphere comparisons will prove to be less problematic once more ozone sonde data becomes available.

ACKNOWLEDGEMENTS

We gratefully acknowledge the efforts of the entire SAGE III mission operations team to make these limb scattering measurements possible. The opportunity to look at "quick look" SAGE III occultation data for the preliminary analysis was also greatly appreciated. The SOLSE/LORE-2 team also deserves thanks for their efforts to prepare that dataset for use. We received support from Ted Llewelyn in our OSIRIS data comparisons, and appreciate the OSIRIS team's efforts to make their data available.

REFERENCES

Flittner, D.E., P.K. Bhartia, and B.M. Herman, 2000: Ozone profiles retrieved from limb scatter measurements: Theory. Geophys. Res. Lett., 27, 2601-2604.

Von Savigny, C., et al., 2003: Stratospheric ozone profiles retrieved from limb scattered sunlight radiance spectra measured by the OSIRIS instrument on the ODIN satellite: Methods and first results, Geophys. Res. Lett., 30, 1755-1758.

Petelina, S., et al., 2004: Comparison of the Odin/OSIRIS stratospheric ozone profiles with coincident POAM III and ozonesonde measurements. Geophys. Res. Lett. 31, doi:10.1029/2003GL019299.

Janz, S. J., E. Hilsenrath, D. Flittner, and D. Heath, 1996: Rayleigh scattering attitude sensor. Proc. SPIE Int. Soc. Opt. Eng., 2831, 146-153.

SHIPBOARD MEASUREMENTS OF SAHARAN DUST NEAR PUERTO RICO DURING SUMMER 2002 AND 2003

Lizette Roldán
Program in Atmospheric Sciences, Howard University, Washington, DC
Vernon R. Morris
Department of Chemistry and Program in Atmospheric Sciences, Howard University, Washington, DC

Introduction

Saharan dust storm events are responsible for injecting huge amounts of mineral dusts into the atmosphere - by some estimates as much as two billion metric tons annually [Griffin, 2002]. Improvements in satellite technology and retrieval methods has enabled the observation of Saharan dust transport into Europe, western Asia, the eastern seaboard of the US, the Caribbean, and to South America [Prospero, et al., 1970]. The quantity of dust has the potential to induce regional health impacts - such as asthma outbreaks, particularly in sensitive subpopulations like the elderly, infants, and adolescents, and ecosystem responses, such as red tides or degradation of coral reefs due to infestation of foreign fungal or microbial populations [Shinn et al, 2001; Shinn, 2001; Walsh et al, 2001]. Saharan dust transport is also responsible for critical heavy metal and mineral deposition to the tropical Atlantic and may have impacts on regional atmospheric chemistry - via dust-induced smog and heterogeneous reactions [Goudie, et al., 2001]. Saharan or mineral dust has recently been implicated as a significant force factor in regional climate changes, specifically in influencing local precipitation patterns [Rosenfeld, et al., 2001].

The effects of Saharan dust in the Caribbean have been monitored for several years, particularly in terms of total mass deposition and potential relationships to respiratory ailments in the region [Griffin, et al., 2001]. Regional hazes associated with Saharan dust storms have also been reported more frequently over the last decade, reducing visibility and causing poor air quality.

A complete understanding of the impacts of Saharan dust in the Caribbean and eastern Atlantic seaboard requires that a complete set of direct measurements be obtained. This complete set of measurements must include basic number densities, size distributions, mass distributions, chemical composition, optical properties, and basic microphysical properties.

An understanding of the microphysical and chemical evolution of the mineral dust will benefit the scientific community by enabling:

- More accurate modeling of cross-Atlantic transport of the Saharan dust
- More accurate initialization of chemical modeling of Saharan dust impacts on the atmospheric chemistry of the Caribbean
- Improved understanding of mineral deposition from Saharan dust to land surfaces and into the Caribbean Sea
- Improved understanding of regional cloud processing of aerosols and their affects on local cloud properties
- Improved retrievals of ocean properties from satellite measurements
- More accurate initialization of dust optical properties for regional climate modeling.

Measurement strategy

Our measurements were performed aboard the former NOAA research vessel (R/V) Chapman during cruises to an oceanographic serial station (30 miles due south of La Parguera). The Chapman is 127 ft; it was decommissioned on June 2, 1998 and since then was given to the University of Puerto Rico – Mayaguez campus. Surface measurements were performed at the Isla Magueyes Field station in La Parguera, Puerto Rico. Figure 2 shows a picture of the tower where the Quartz Crystal Microbalance Cascade Impactor (QCM) and the Laser Particle Counter (LPC) were located during the land-based measurements. The land and shipboard instruments are identical and consist of optical characterization (laser particle counter), gravimetric and size-fractionation characterization (QCM cascade impactor). Our primary instruments and their measurement capabilities are more fully described in Table 1

	Climet	*QCM*
Description	• Laser particle counter (0.3, 0.5, 1.0, 5.0, 10, 25) • 6 size cuts • Accuracy size resolution – 0.03 μm • Sensitivity – 0 as per ASTM F-50	• Quartz crystal microbalance cascade impactor • Six-stage (5 μm – 0.15 μm) and ten-stage units (25 μm – 0.05 μm) • Mass and aerodynamic size fractional samples • Continuous sampling • Sensitivity ~0.1 μg, ~0.1 ng
Capabilities	• Continuous/variable average • Number densities • Size distribution • Integrated and differential measurements	• Mass fractionated sampling • Total suspended particulate mass • Size-fractionated samples • Post analysis with SEM, EDX • Calibrated and traceable

Table 1. Instruments and Measurement Capabilities

The specific objectives of the study are:

1. To obtain comprehensive in-situ measurements of Saharan dust aerosols in the Caribbean and more specifically in Puerto Rico,

2. To quantify the microphysical (with focus on morphology, aerodynamic, and optical properties) and chemical evolution of the Saharan dust during transport through the Caribbean and across the island of Puerto Rico,

3. To determine the changes in total suspended mass of aerosols, $PM_{2.5}$, PM_{10}, and respirable aerosol in the Caribbean as a result of Saharan dust events, and

Summer Intensives

In this paper we discuss the impacts of Saharan dust on ambient total suspended mass and size distributions for sizes ranging from 25 μm to 0.15 μm. We conducted two measurement intensives in Puerto Rico during summer 2002 and 2003. The first intensive was designed to be a proof of concept experiment to test the instrument sensitivity, configurations, and sampling strategy.

The second intensive was planned to measure pre dust event, dust event, and post dust event aerosol properties in the marine boundary layer in the tropical Atlantic and Caribbean Sea. The dates for this series of measurements were

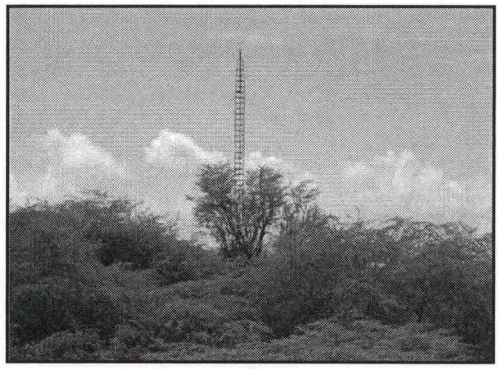

Figure 2. Photo of the tower where the instruments were mounted

planned based on a combination of NAAPS model predictions and satellite observations (TOMS and SeaWIFS). The NAAPS is the Navy Aerosol Analysis and Prediction System. This is a global multi-component aerosol analysis and modeling capability developed by the Navy Research Lab (NRL) to enable global forecasts of aerosol distributions.

On June 20th the 6-stage Quartz crystal Microbalance (QCM) cascade impactor was set up to collect measurements in Isla Magueyes. The aerosol-sampling platform was located about 40 m above sea level. The QCM measured size-resolved aerosol mass fractions for aerodynamic diameters between 5 - 0.15 m. On June 25th we collected ocean-based measurements aboard the RV Chapman. The RV Chapman traveled 30 km South (17° 36′ N, 067° 00′ W) of Puerto Rico. Samples were collected for a period of 9 hours beginning at approximately 4:45 am. The QCM measured semi-continuous and the LPC measured continuously.

A clearly defined haze layer was observed shortly after sunrise that persisted throughout the day of June 25, 2002. No observable evidence of dust was noted during the ten days of the August cruise. The figure below shows a satellite image of the June 2002 event. The dust layer was still present in the region on the following day (June 26, 2002)

Results

We observed that the number density for the 0.5 to 5 mm size range increased by a factor of 2 to 3 (Figure 3). The larger increase was found in the 0.3 – 1.0 micron ranges. The greatest number density was observed for the smallest size fraction in both cases. A back trajectory analysis was performed to determine the origin of the air parcels that were encountered during the June 25 measurements. Figure 4 shows the results for three characteristic 10 - day back trajectories beginning on June 25, 2002. Air masses below 750 meters above ground level (AGL) originated from the northern subtropical marine environment. Air masses between 750 – 3500 meters AGL originated from the Sahara desert, above 3500 meters AGL the originated in tropical marine environment. The model results provide further evidence that an air mass of Saharan origin was encountered on June 25, 2002.

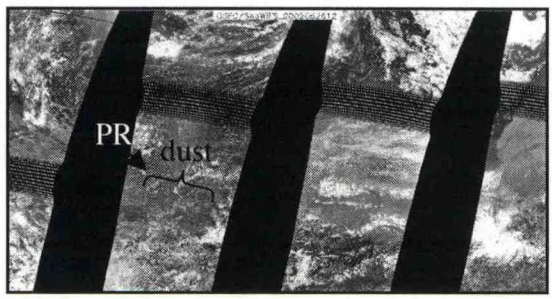

Figure 3. June 26, 2002 SeaWIFS image

Figure 5 shows the PM2.5 observations of the aerosol mass density distribution for nine days during the summer of 2003. All measurements were land-based measurements during June 27, 29 and July 11 – 17, 2003. The first peak corresponds to a dust storm entering the area on June 27. The following two peaks represent the air mass that was influenced by both dust and volcanic ash from the Soufriere volcano. The average aerosol mass density was 164 mg/m^3 for this period. This average mass density excludes the measurements for when the air mass was influenced by the Soufriere volcano eruption and dust event. This measurement exceeds the EPA 24-hour National Ambient Air Quality Standards (NAAQS) of 65mg/m^3. On the 13 and 14th of July there was a mixture of dust and ash from the Montserrat

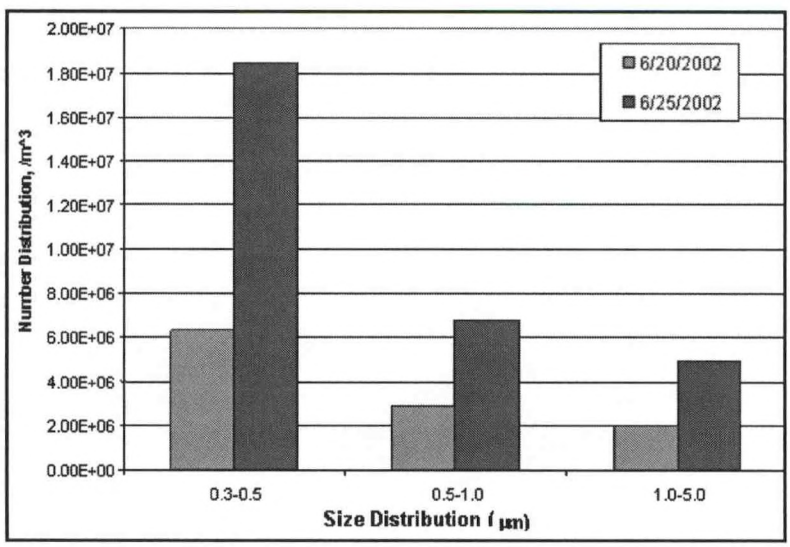

Figure 3. Daily averaged number density for non-dust storm vs. dust storm cases

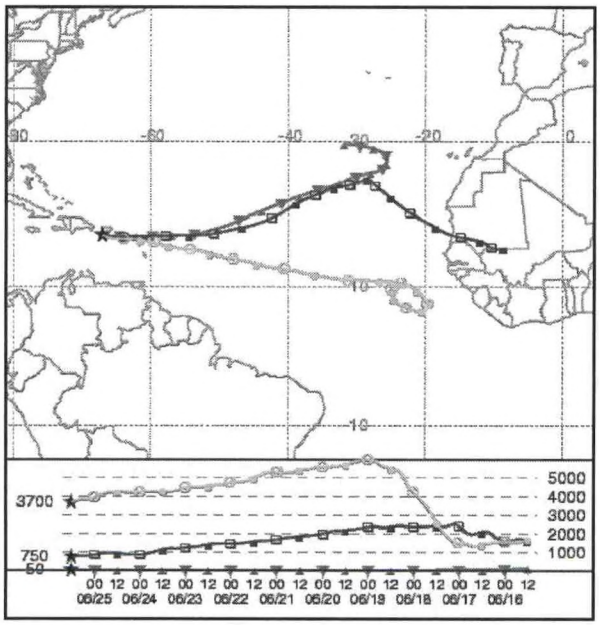

Figure 4. NOAA HYSPLIT back trajectories for June 25, 2002

Volcano eruption. A detailed analysis of this event is provided in this same volume in the paper by White et al.

ACKNOWLEDGEMENTS

This research was performed under the sponsorship of the Department of Commerce and NOAA under award number NA17AE1623. We also would like to acknowledge our collaborators at the University of Puerto Rico at Mayagüez, Department of Marine Sciences, Drs. Roy Armstrong and Yasmin Detrés. We thank the Caratlan cruise research team for granting space aboard the RV Chapman.

The authors gratefully acknowledge the NOAA Air Resources Laboratory (ARL) for the provision of the HYSPLIT transport and dispersion model and/or READY website (http://www.arl.noaa.gov/ready.html) used in this publication.

REFERENCES

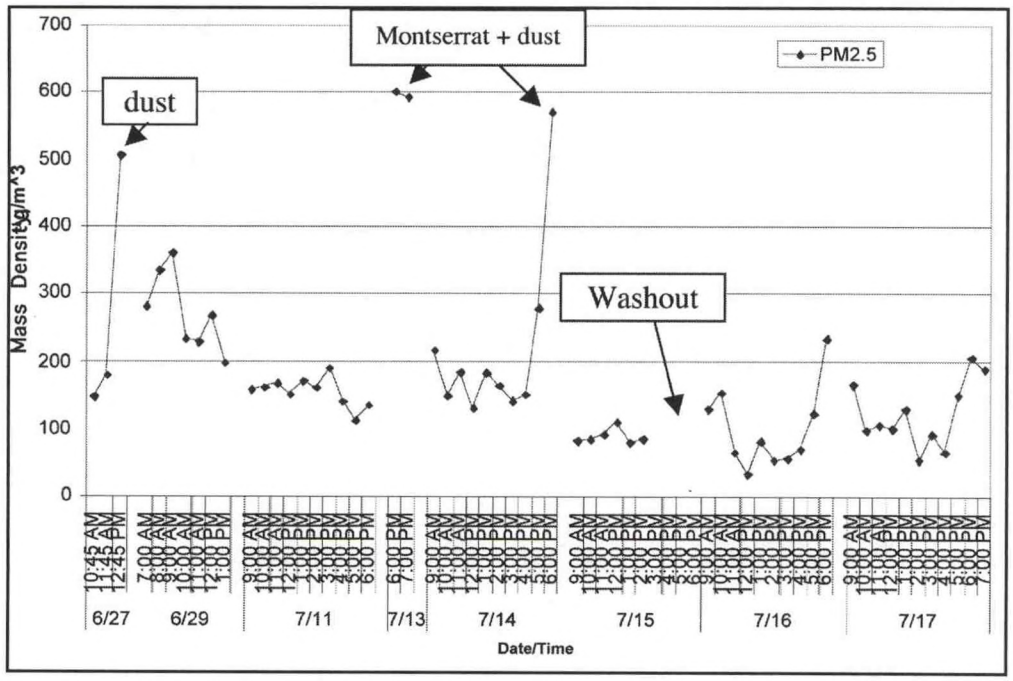

Figure 5. Daytime PM2.5 mass density June 27th and 29th and July 11 – 18, 2003

Draxler, R.R. and Rolph, G.D., 2003. HYSPLIT (HYbrid Single-Particle Lagrangian Integrated Trajectory) Model access via NOAA ARL READY Website (http://www.arl.noaa.gov/ready/hysplit4.html). NOAA Air Resources Laboratory, Silver Spring, MD.

Goudie, AS and Middleton, N.J., 2001: Saharan dust storms: nature and consequences. Earth Science Reviews, 56, 179-204.

Griffin, D., Garrison, V.H., Herman, J.R. and Shinn, E.E., 2001: Desert dust in the Caribbean atmosphere: Microbiology and public health. Aerobiologia, 203-213.

Griffin, D., Kellogg, C.A., Garrison, V.A. and Shinn, E.A., 2002: The global transport of dust. American Scientist 2002, 90, 228-235.

Prospero, J.M., Bonatti, E., Schubert, C and Carlson, T.N., 1970: Dust in the Caribbean atmosphere traced to an African dust storm. Earth and Planetary Science Letters, 9, 287-293.

Rolph, G.D., 2003. Real-time Environmental Applications and Display sYstem (READY) Website (http://www.arl.noaa.gov/ready/hysplit4.html). NOAA Air Resources Laboratory, Silver Spring, MD.

Rosenfeld, D., Rudich, Y. and Lahav, R., 2001: Desert dust suppressing precipitation: A possible desertification feedback loop. PNAS, 98, 5975-5980.

Shinn, E.A., Smith, G.W., Prospero, J.M., Betzer, P., Hayes, M.L., Garrison, V., Barber, R.T., 2000: African Dust and the demise of Caribbean coral reefs. Geophysical Research Letters, 27, 3029-3032.

Shinn, E., 2001: African dust causes widespread environmental distress. USGS.

Walsh, J. and Steidinger, K.A., 2001: Saharan dust and Florida red tides: The cyanophyte connection. Journal Geophysical Research, 106, 597-11612.

A Pilot Study of Ozonesonde in the Baltimore/Washington Region

Vincent Davis[1], Omar Hylton[1], Mahkada Taylor[1], Lauren Zamora[2], Jeff Liesch[2], Anne Thompson[3], and Everette Joseph[1]

Howard University[1]
University Maryland College Park[2]
NASA Goddard Space Flight Center[3]

Over the past 9 years the Washington metropolitan region has experienced an average of 10 code red ozone days per year. Better understanding of the chemical and meteorological processes that contribute to high ozone events is needed to help develop cost-effective control strategies and accurate forecasting capabilities. A particular area that is in need of further investigation and focus for air quality monitoring is the contribution of intrastate pollution to high ozone episodes. The predominant westerly wind flow and the low level nocturnal jet are the key mechanisms for transport of intrastate pollution.

A pilot study was conducted by a team of students and scientists from Howard University Department of Physics and Program in Atmospheric Sciences, University of Maryland, Maryland Department of the Environmental, NASA Goddard Space Flight Center (GSFC), to characterize ozone during the summer 2004 pollution season. These measurements were taken at the Howard University atmospheric measurement site in Beltsville, Maryland and also contributed to the NOAA and NASA INTEX-NA/ION experiments. Students performed ozonesonde measurements weekly and for code orange and red episodes June – September. Surface observation we also taken. The following analyses are conducted:

- Ozone profile interpretation w/ trajectory
- Comparison/calibration of sondes with surface ozone measurements, Microtops and TOMS
- Analysis of historical surface ozone data at Beltsville for seasonal and diurnal cycles
- Comparison of aircraft (from UMCP flights) and ozonesonde profiles

Investigation of Biomass Aerosol on Cloud Particle Properties and Precipitation Patterns

Vernon R. Morris

Department of Chemistry and Program in Atmospheric Sciences, Howard University, Washington, DC 20059

Abstract

The term "chemical meteorology" has been used to describe the observable manifestations of the causal connections between atmospheric chemistry and weather phenomena. Recently, it has been shown that the inclusion of biomass aerosols into warm clouds can also inhibit precipitation (Rosenfeld, 1999). However, several reported case studies in the literature report precipitation enhancements due to aerosol entrainment as well. (Ramanathan et al, 2001) While inferences of the of these indirect effects of aerosols can be made from recent developments in satellite technology, current global and regional climate models continue to exhibit large uncertainties in predictions of the global influences of aerosols on cloud properties. Furthermore, quantitative relationships between the indirect forcing from clouds and anthropogenic aerosol inclusions have not been developed to a point where the even the prediction of cloud optical properties is reliable. The problem is the lack of understanding of the basic microphysical processes governing cloud droplet nucleation and evolution. This level of understanding requires that the physical chemistry of the systems be well understood. Because such a large fraction of anthropogenic aerosol and specifically biomass aerosol are organic in nature, we have developed a study to perform laboratory simulations of the nucleation of aerosols with organic inclusions.

Introduction

Biomass burning is a long-term historical practice for slash and burn agriculturalists in the tropics, it results from brushfires, land clearing, and cloud-to-ground lightning strikes. Several investigators have estimated the global amount of aerosols generated from these types of processes and their significance has been discussed at length. One of the unique features about the biomass burning aerosols is that its sources are overwhelmingly confined to the tropics despite evidence that their effects may be global in extent (Crutzen and Andreae 1990, Gregoire et al 1999, Eck et al 2001, Liousse 2004).

The pattern of biomass burning in Africa exhibits a strong seasonal signature above and below the equator, oscillating with wet and dry season and is bounded to the north by the Sahel. Satellite estimates of biomass burning activity in Africa can be obtained from the Advanced Very High Resolution Radiometer (AVHRR) (Figure 1).

Biomass aerosol can have two primary physical affects in the atmosphere: direct climate forcing via scattering and absorption of atmospheric radiation or indirect climate forcing via modification of cloud radiative properties. Changes in cloud albedo due to variations in size droplet distributions and composition can be marked (Twomey, 1974 Fiengold and Penner 2000).

Long-range transport of biomass pollutants has been observed in the tropics and attributed to several global and mesoscale chemical phenomena including the southern Atlantic tropospheric ozone maximum (Jenkins et al 1997). The focus of most of these studies was the gaseous components, rather than the carbonaceous aerosols.

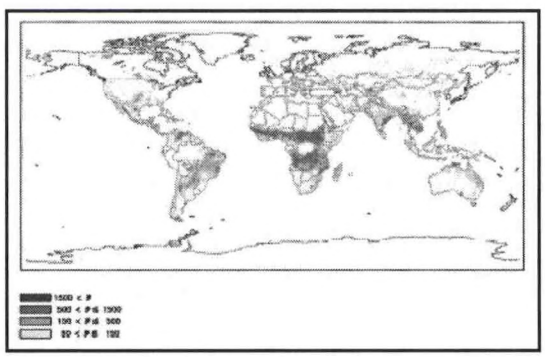

Figure 1. AVHRR-derived global distribution of vegetation fires for 1993.

The heterogeneous chemical effects of the biomass (carbonaceous) aerosols are poorly understood and even more crudely implemented in atmospheric models (if at all). The problems are two-fold: the number of degrees of freedom is large in comparison to homogeneous chemical systems. Further, the sensitivity to changes in the atmospheric state is both nonlinear and strongly coupled to the microphysics of the chemical system. Note that a 10% change in RH produces a dramatically different atmospheric state versus a 10% change in the concentration of a reactant most often produces a negligible effect on a reaction branching ratio.

Another atmospheric affect of biomass aerosol is the influence that they may have on cloud properties and seasonal precipitation patterns (Rosenfeld 1999, Ramanathan 2001, Menon 2002). Rosenfeld published the first satellite evidence for this affect. In this study, TRMM data was used to show that biomass aerosols might inhibit precipitation in clouds by directly influencing cloud droplet distributions and temperature profiles. A far-reaching implication would be that biomass aerosols may cause drought in regions where significant amounts of biomass aerosol emitted into the atmosphere can inhibit large-scale precipitation. This effect has been reported in China (Menon 2002). Definitive proof for this phenomenon has not been established, but it provides sufficient motivation for study.

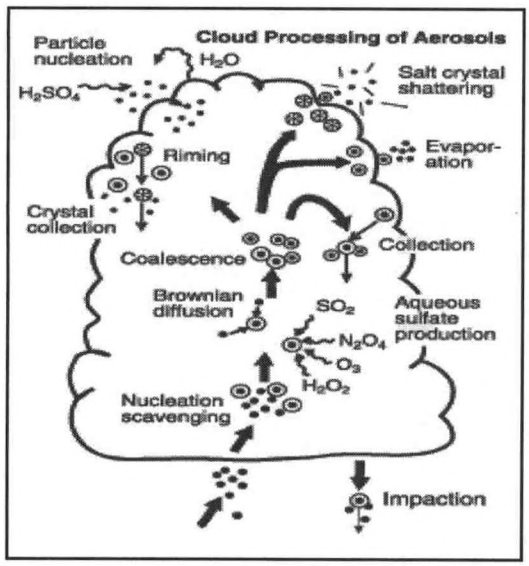

Figure 2. Adapted from Hegg 2001

Further, clouds are both a source of new aerosols as well as a medium for chemical evolution of "old" aerosols. Figure 1 illustrates several of the processes observed in mixed-phase clouds.

In order to quantify the affect of biomass aerosols on cloud properties, the microphysical properties of the aerosols must be understood. The basic microphysical properties of interest are size distribution, nucleation potential, and optical extinction characteristics (scattering phase function and absorption).

Another important aspect is whether an atmospheric signature is deducible from satellite observations of biomass aerosol and fire emissions, cloud patterns, and precipitation. The development of a quantitative predictive model remains a challenge given the difficulties in resolving the seasonal nature of precipitation and biomass burning in the tropics.

Our group has undertaken a study to investigate the effects of biomass aerosols on cloud properties and precipitation patterns by performing laboratory-based simulations of the nucleation of organic aerosols together with an analysis of the climatology of biomass burning emissions, clouds, and rainfall patterns in tropical Africa.

The goal of this project is to understand the influence of the microphysics of organic aerosols on cloud properties and precipitation patterns. We will achieve this goal by targeting the following strategic objectives:

- Characterize the size and number distributions of organic aerosol under tropospheric conditions (temperature, pressure, relative humidity)
- Characterize the homogeneous nucleation properties of organic aerosols as a function of select chemical properties (electron delocalization, reactivity, pH, etc.)
- Characterize the homogeneous and heterogeneous nucleation properties of organic aerosol as a function of such microphysical properties as vapor pressure, solubility, and presence of a nucleating agent.
- Develop a predictive model for nucleating efficiency and cloud properties based on these properties

Carbonaceous aerosols are chosen for study because they are known to be primary constituents of biomass fire emissions, their nucleating properties are least studied, and their potential

for being adsorbed into aqueous droplets or forming aerosols is very high. Our laboratory set-up consists of various aerosol generation techniques (including a vibrating orifice generator (VOAG), a constant output atomizer, and several small furnaces) coupled to a differential mobility analyzer, a condensation nuclei counter, and a laser particle counter system. This system will enable us to characterize the preferential size and number distributions of selected organic aerosols and their nucleating potential under various tropospheric conditions. The system also enables a study of the condensation growth properties of the different organic aerosols as a function of chemical nature, vapor pressure, generation technique, presence of a nucleating surface, and relative humidity.

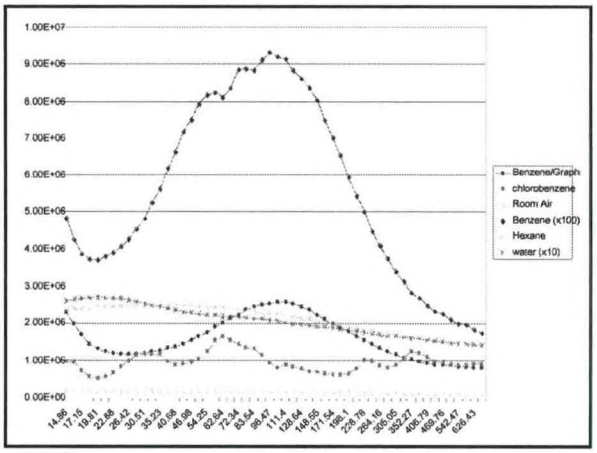

Figure 3. Comparison of condensation nuclei size distributions.

Experimental Considerations

Studies of soot generated from organic charring and combustion have reported soot structure is predominantly aromatic with surface coverage by oxygen-containing functional groups ~50% and large fractions of surface aromatic groups (Smith and Chughtai 1995, Sergides 1987). Further studies have provided strong evidence for the potential for soot and biomass burning products to produce secondary organics within cloud droplets (Decasari 2002). The first compounds chosen for study were the family of C6 organics including cyclohexane, benzene, aniline, toluene, nitrobenzene, and chlorobenzene. This series of compounds exhibits a systematic progression of physical and chemical properties that can be correlated with the microphysical properties of their aerosols.

The aerosols investigated in the experiments reported in this paper were generated with a constant output atomizer. Typical concentrations were on the order of 1.0 x 10-3 M for the homogeneous mixtures with an added 1 mg/m3 of STM graphite for the heterogeneous mixtures.

Figure 3 shows data from baseline experiments using water and room air in comparison to benzene, chlorobenzene, and hexane aerosols. These data clearly show an enhancement in the absolute numbers of condensation nuclei as a direct result of organic inclusion. Additionally, the size distributions of condensation nuclei obtained for the organic aerosols are distinct from that of water and dry (15% RH) room aerosols.

Size distribution and number density data for condensation nuclei generated from the benzene, chlorobenzene, and chlorobenzene/graphite experiments are shown in Figures 4-6, respectively. The overall results show a strong enhancement in number density with increasing aromaticity and a suppression of the condensation nuclei formation in the presence of graphite with a tendency towards larger CN.

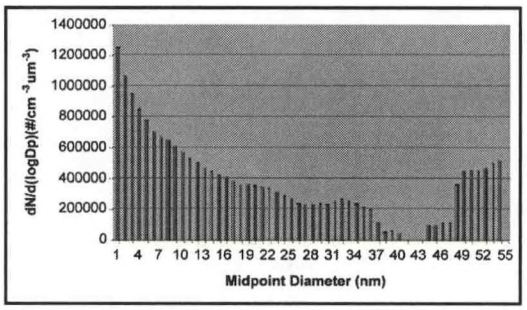

Figure 4. Condensation nuclei size distribution data for homogeneous benzene experiments.

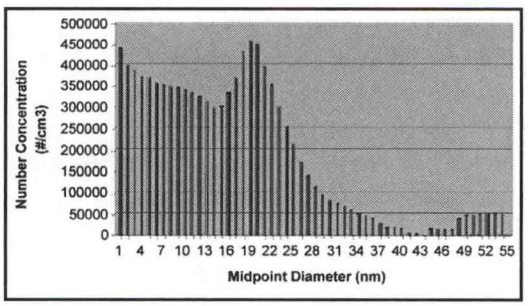

Figure 5. Condensation nuclei size distribution data for homogeneous chlorobenzene experiments.

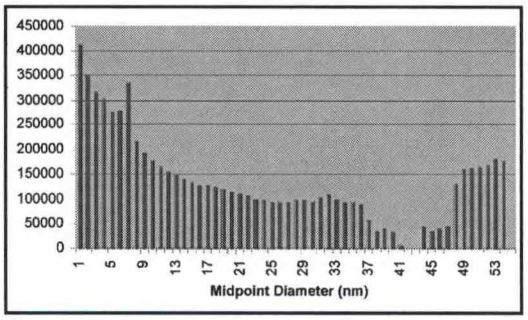

Figure 6. Condensation nuclei size distribution data for benzene/graphite experiments.

Summary and Future Directions

Several C6 organics: hexane, cyclohexane, benzene, chlorobenzene, nitrobenzene, and toluene were investigated for nucleation properties. Preliminary analyses of data for hexane, benzene, and chlorobenzene indicate that there are consistent variations in the observed condensation microphysics under homogeneous conditions which re amplified in the presence of graphite as a nucleating surface.

We plan on undertaking a complementary climatological study of biomass fires, clouds, and precipitation patterns will use a combination of satellite data products including; AVHRR(NOAA), SSMI(DoD), TRMM(NASA), SeaWiFS(NASA), TOMS(NASA), and MODIS(NASA). Our region of study is located in tropical Africa and is bounded by the +10o latitudes about the equator and the longitudinal lines on the east and west, respectively.

REFERENCES

Crutzen, P. and Andreae, M. Biomass Burning in the Tropics: Impact on Atmospheric Chemistry and Biogeochemical Cycles Science 250, 1669 (1990)

Decesari, S., Facchini, M. C., E. Matta, Mircea, S, Fuzzi, A. Water Soluble Organic Compounds Formed by Oxidation of Soot Atmos. Environ. 36, 1827 (2002)

Eck, T. F. , Holben, B. N. , Ward, D. E., Dubovik, O., Reid, J. S., Mukelabai, M. M., Hsu, N. C., O'Neill, N. T., Slutsker, I. Characterization of the Optical Properties of Biomass Burning Aerosols in Zambia During the 1997 ZIBBEE Field Campaign J. Geophys. Res. 106, 3425 (2001)

Fiengold, G. and Kreidenweis, S. Does Cloud Processing of Aerosol Enhance Droplet Concentrations J. Geophys. Res. 105, 24351 (2000)

Gregoire, J.-M., Pinnock, S. Dwyer, E. and Janodet, E. Satellite monitoring of vegetation fires for EXPRESSO: Outline of activity and relative importance of the study area in the global picture of biomass burning J. Geophys. Res. 104 (D23), 30691 (1999)

Hegg, D. IGAC tivities Newslette Issue 23, April 2001, page 3-6

Jenkins, G. S., Mohr, K., Morris, V. R., Arino, O. The Role of Convective Processes Over the Zaire-Congo Bason to the Southern Hemispheric Ozone Maximum J. Geophys. Res. 102, 18963 (1997)

Liousse, C., Andreae, M. O., Artaxo, P., Barbosa, P., Cachier, H., Gregoire, J-M., Hobbs, P., Lavoue, D., Mouillot, F. Penner, J., Scholes, M. "Deriving Global Quantitative Estimates for Spatial and Temporal Distributions of Biomass Burning Emissions" IGAC Book on Emissions (In Press, 2004)

Menon, S., Hansen, J. E., Nazarenko, L., Luo, Y. Climate Effects of Black Carbon Aerosols in China and India Science 297, 2250 (2002)

Ramanathan, V. P., Crutzen, P., Kiehl, J. T., Rosenfeld, D. Aerosols, Climate, and the hydrological Cycle Science 294, 2119 (2001)

Rosenfeld , D. TRMM Observed First Evidence of Smoke from Forst Fires Inhibiting Rainfall Geophys. Res. Lett. 26, 3105 (1999)

Sergides, C. A., Jassim, J. A., Chughtai, A. R., Smith, D. M. The Structure of Hexane Soot 3. Ozonation Studies Applied Spectrocopy 41, 482 (1987)

Smith, D. M., Chugthai, A. R. The Surface Structure and Reactivity of Black Carbon Colloids and Surfaces A: Physicochemicaal and Engineering Aspects, 105 47 (1995)

Twomey, S. Pollution and the Planetary Albedo Atmos. Environ. 8, 1251 (1974)

ACKNOWLEDGEMENTS

I would like to acknowledge the following students responsible for generating and analyzing data described in this paper: Evans Dure, Angelina Amadou, and Betty-Ann Garriques.

The Impact of Soil Moisture Initialization on Seasonal Precipitation in the West African Sahel Using the Regional Spectral Model

Andrea M. Sealy, E. Joseph, C.-H. Lu, and H.-M. H. Juang
Howard University, Washington, DC

This study investigates the extent to which prior knowledge of soil moisture states can influence seasonal precipitation predictability in the West African Sahel. This region has been characterized as a semi-arid region which is the transition zone that model studies have suggested that the impact of land state initialization on precipitation predictability may be most significant. Results will be presented from (1) a preliminary sensitivity analysis that consists of a one-month integration to assess the atmospheric response to extreme dry and wet soil conditions, (2) an EOF analysis of 22 years of May/June monthly Reanalysis-2 soil moisture data to identify the leading modes of soil moisture variability in the region and (3) a sensitivity analysis that consists of a seasonal integration (May-October) initialized with soil moisture patterns that are characteristic of the first two leading modes of soil moisture variability.

PRELIMINARY COMPARISON OF RADIOSONDE AND LIDAR MEASUREMENTS FROM HOWARD UNIVERSITY BELTSVILLE SITE

Segayle Walford, Belay Demoz, Demetrius Venable, Everette Joseph, Rasheen Connell
Howard University, Washington, DC 20059

On June 21- 30, 2004 an instrumentation workshop was conducted at the Howard University research site located in Beltsville, MD. This workshop was designed to examine the dynamics and thermodynamics of the boundary layer, aerosol and cloud radiative and microphysical processes, precipitation processes, and the regional geo-chemical processes using a suite of instruments. In this presentation, we particularly focus on the radiosondes and Raman lidar observations used to derive the temporal and vertical evolution of the boundary layer. The lidar was operational for a 24 hour period and during that time radiosonde launches were conducted approximately every 3 hours. A second intensive period of lidar and radiosonde observations were conducted in late August and will also be used in the comparison. The boundary layer height was calculated from the lidar and the radiosonde based measurements and compared. In addition, we are able to detect the evolution of the boundary layer using the Raman lidar and the radiosonde based observation. A generally good agreement of the boundary layer height was found between the lidar and radiosonde data. Preliminary results also show that the lidar was able to distinguish atmospheric structures in the day and at night. Further analysis, including statistical comparisons of the instruments will be conducted and presented.

THE OFFLINE COMPARISON AN ALTERNATIVE INFRARED RADIATION SCHEME FOR USE IN NCEP'S GLOBAL SPECTRAL MODEL AND REGIONAL SPECTRAL MODEL

Johnny Seymore, III
Howard University, Atmospheric Science

In a preliminary assessment of the National Centers for Environmental Prediction (NCEP) Global Spectral Model (GSM), a bias in the zonal mean temperature structure reveals a warming in the northern and cooling in the southern hemispheres for the month of December 1989 (Seymore, 2002). Comparing the GSM model output of top-of-the-atmosphere (TOA) clear-sky longwave radiation to NASA Earth Radiation Budget Experiment observed data, a discrepancy in the results arise. Improvements in these biases were achieved after NASA's Chou and Suarez (1994) infrared radiation (IR) scheme was implemented into the GSM. Specifically, the tropics showed considerable improvements in the free troposphere where the water vapor continuum is a dominant factor (Seymore, 2002).

The Chou and Suarez IR scheme differs from the default IR code in the GSM (Fels and Schwarzkopf, 1975) as follows: the calculation of cooling rates, treatment of temperature profile, and the gas treatment of major and minor constituents in the atmosphere. In the present study detailed calculations are conducted to further evaluate the Chou scheme, and to examine the differences in atmospheric heating and surface energy budget as calculated by the two schemes. An update version of the Chou scheme is also evaluated: Chou et al. (2002). This scheme includes multiple scattering and cloud overlap features not present in the earlier version. Also a stand-alone version of the Fels and Schwarzkopf IR scheme was developed for this study. The following calculations are conducted: heating profiles, TOA and surface fluxes based on standard atmosphere (McClatchey, 1971) for tropical, mid-latitude summer, and sub-artic winter conditions; and TOA and surface fluxes based on observed data from the Atmospheric Radiation Measurement (ARM) and Howard University Beltsville, MD sites. In the latter case flux measured by surface radiometers and satellites are used to evaluate the surface and TOA fluxes, respectively. Both clear and cloudy sky conditions are considered.

NOAA 11 SBUV: Ozone Analysis at 15 Pressure Levels

Kristofer B. Macklin, Kris Ford, and John Anderson

Center for Atmospheric Sciences, Hampton University, Hampton, VA

Abstract

Remote analysis of the Earth's atmosphere provides valuable information regarding past, current, and even future implications of life on our planet. Our atmosphere's balanced composition has supported life and life-supporting environments for ages, yet there are many concerns as to its current and future stability. Our objective was to gather measurements of the atmospheric ozone at 15 different pressure levels beginning in 1988 using the NOAA-11 SBUV/2 satellite launched on September 24, 1988. Passive remote sensing is the method behind Solar Backscatter Ultraviolet detection. It is essentially an analysis of the atmosphere without a direct interaction with particles and other constituents of the atmosphere. It employs measurements of the solar ultraviolet light entering the atmosphere at a particular wavelength, as well as the solar ultraviolet light that is scattered back from the surface of the atmosphere at the same wavelength. The 15 pressure levels used in this study are at 50 millibars (mb), 40 mb, 30 mb, 20 mb, 15 mb, 10 mb, 7 mb, 5 mb, 4mb, 3 mb, 2 mb, 1 mb, 0.7mb, and 0.5 mb. Comparisons at varying latitude regions starting at (-75 and ending at 75), divided into 15 bins (each ranging 10 degrees), as well as time were made using the data NOAA-11 ozone data. Measurements of ozone at particular times, locations, and pressure levels is the result of such measurements, which will lead to many more valuable discoveries about the characteristics of our changing atmosphere. Interesting fluctuations were noticed in the ozone levels with regard to yearly comparisons, however, monthly averages shall prove to be more specific with regard to ozone levels within the specified latitudinal bins.

Introduction

The National Oceanic and Atmospheric Administration's (NOAA) NOAA-11 SBUV satellite was launched on an Atlas E Star 37S-ISS rocket on September 24, 1988 to remotely gather data on ozone prevalence in the years between 1988 and 1994, as well as between 1998 and the present. NOAA-11 was placed in a near circular polar orbit. The spacecraft was rectangular in shape (166" long by 74" high) and powered by a solar array that is 191" by 94". It was Earth-oriented and three-axis stabilized. The satellite also weighed approximately 2000 pounds. The primary objectives of the NOAA-11 satellite included cooperation with the NOAA 10 satellite and the replacement of NOAA 9. The achievement of these objectives will provision continuous coverage of Earth and will also provide high resolution global meteorological data. On September 14, 1994 the primary sensor of the mission, the Advanced Very High Resolution Radiometer, failed and the satellite was placed on standby mode in March 1955. However, NOAA-11's services were soon needed again to provide sounding data due to the failure of NOAA-12's sounder in May of 1997. The NOAA 11 SBUV/2 also serves as the primary source for the National Weather Service (NWS) and Environmental Protection Agency (EPA) ultraviolet index, which is used to advise U.S. citizens on their daily exposure to the sun. NOAA-11 was the fourth operational satellite in the Advanced TIROS-N series. These satellites are part of the ongoing US series of polar-orbiting weather satellites. They are employed in the measurement of atmospheric temperature and humidity, cloud cover, surface temperature, water-ice moisture boundaries, and space proton and electron fluxes. They are capable of receiving, processing, and retransmitting data from free-floating balloons, buoys, and remote automatic stations around the globe. The satellites are managed by NOAA and NASA is responsible for designing and launching the instruments.

Instrumentation that was included on the NOAA-11 satellite included but was not limited to: the Advanced Very High Resolution Radiometer (AVHRR), Tiros Operational Vertical Sounder (TOVS), solar

proton monitor, and the Search and Rescue Satellite-aided Tracking (SARSAT) system. Also included was the Earth Radiation Budget Experiment (ERBE) instruments which consisted of short and long wave radiometers. These instruments were incorporated in the analysis of Earth's albedo in an attempt to recognize and interpret seasonal and annual climate fluctuations. Lastly, but most importantly in the context of this study, is the SBUV radiometer that is on-board the NOAA-11 satellite. This device was included in the payload of NOAA-11 due to the intention of NASA and NOAA to replace the NOAA 9 satellite which had previously carried the SBUV radiometer.

Theoretical Background

Passive remote sensing methods allow for analysis of the atmosphere without a direct interaction with particles and other constituents of the atmosphere. The solar backscatter ultraviolet technique is one such method that employs measuring the solar ultraviolet light entering the atmosphere at a particular wavelength, as well as the solar ultraviolet light that is scattered back from the surface of the atmosphere at the same wavelength. One primary utility of this method is the measurement of ozone within the Earth's atmosphere. The detection of significant trends pertaining to the levels of ozone is one benefit of such measurements, which will lead to many more valuable discoveries about the characteristics of the changing atmosphere.

The data collected over approximately 12 years is the subject of this particular study. The primary focus is to both examine which parameters hold the most apparent influence on the prevalence of ozone at 15 constant pressure levels as well as identify any trends regarding the presence or absence of ozone that may exist at these same pressure levels. Seasonal as well as geophysical variances are suspected to hold a significant impact upon the trends that exist in this data analysis. However, it is observed that human activity is the most influential factor in the fluctuating trends of atmospheric ozone. Further application of such findings include, but are not limited to: comparisons with other instruments that were operational within the same time period, as well as the inclusion of findings into an analysis that includes trends of volcanic as well as human activity taking place during the same time period.

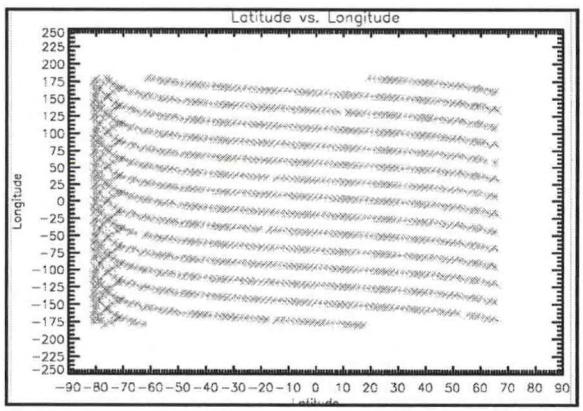

Fig. 1. Corresponding latitudinal and longitudinal positions.

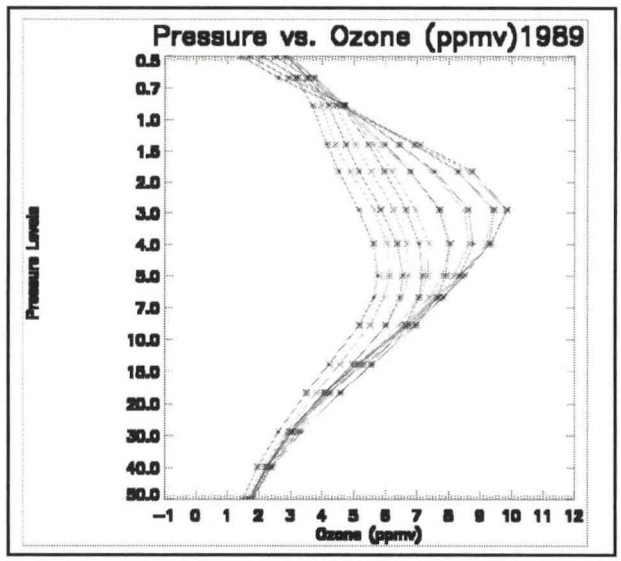

Fig. 2. Ozone zonal profilel averages for 1989 at 15 pressure

The Data & Results

Figure 1 shows the latitude and longitude locations for the SBUV instrument. Figures 2, 3, and 4 show yearly zonal profile averages for 1989, 1990, and 1991 respectively for southern hemisphere (green profiles) and northern hemisphere (red profiles) latitude bands. These profiles were averaged in 10o latitude bins. These ozone profiles at the 15 pressure levels show some fluctuation from year to year. For instance, the averages for the corresponding latitude bin of -75 (+/-5) show periodic fluctuations over the four consecutive years. This aspect will be better defined in using monthly averages to consider seasonal or other influences.

Summary and Conclusions

Further investigation into the average monthly trends of NOAA-11 data will prove useful in a more specific analysis of ozone variability. With yearly averages there is insufficient information in regards to the specific periods of fluctuation. The ozone variations that NOAA-11 data will show, is a key factor into a number of topics that have a direct impact on how we as humans will perceive our activities and interaction with Earth.

REFERENCES

Grenfell, T. G. and S. G. Warren, 1999: Representation of a nonspherical ice particle by a collection of independent spheres for scattering and absorption of radiation

Key,J.,and J. INtrieri, 2000: Cloud particle phase determination with the AVHRR, J. Appl

Sample, S. 2004. National Oceanic and Atmospheric Satellite-11 (NOAA-11). http://www.earth.nasa.gov/history/noaa/noaa11.html

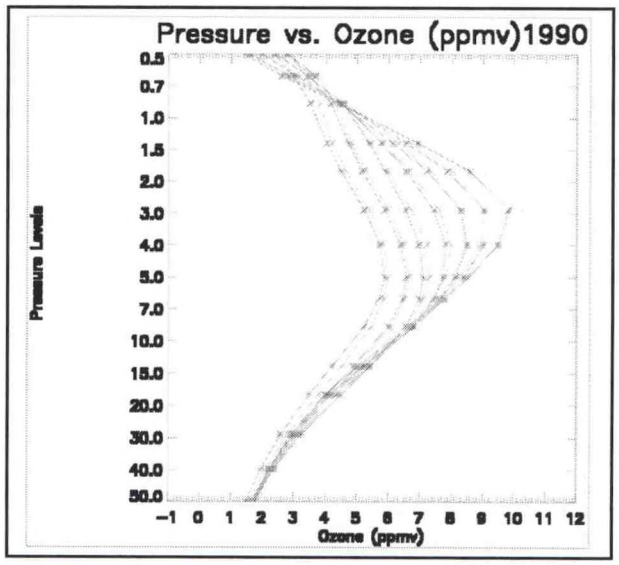

Fig. 3. Ozone zonal profile averages for 1990 at 15 pressure levels.

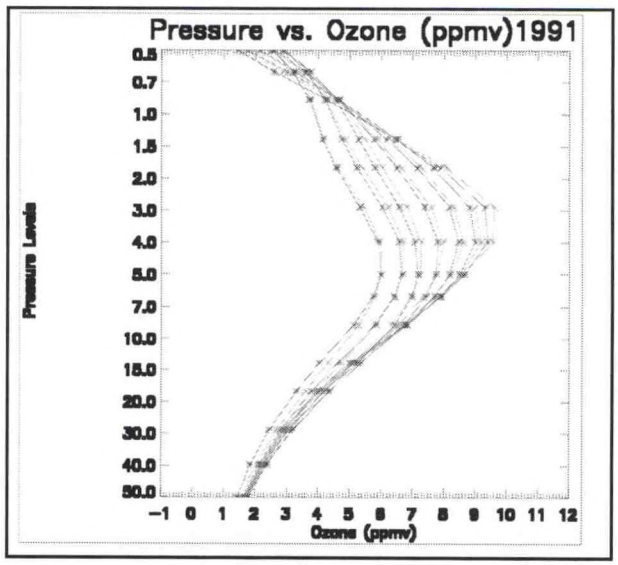

Fig. 4. Ozone zonal profile averages for 1991 at 15 pressure levels.

Comparison of AVHRR_NDVI and Modeled Leaf Area Index

Landon K. Haywood and Ayman Suleiman

Center of Atmospheric Sciences, Hampton University, Hampton, VA

Abstract

Vegetation is very important in today's time. We research vegetation so we can know the best way to grow crops in the future. Without vegetation there would be no food for us to eat and live off of. Our objective was to compare the Advanced Very High Resolution Radiometer Normalized Difference Vegetation Index (AVHRR_NDVI) to a molded Leaf Area Index (LAI) of four different cropland locations for more ten years. These four locations are Richmond, VA; Baltimore, MD; Springfield, IL and Albany, NY. The NDVI is obtained from two satellite channels namely the visible band (VIS) and near infrared (NIR). The NDVI is calculated as (NIR – VIS)/(NIR + VIS). The NDVI is related to vegetation because healthy vegetation reflects well near infrared part of the spectrum. Normalized Difference Vegetation Index provides an estimate of vegetation health and can observe the changes in vegetation over time. Leaf Area Index (LAI) is the one-sided green leaf area per unit ground area of crops such as wheat, corn and soybeans. The LAI was simulated for the four locations by running the Decision Support System for Agrotechnology Transfer (DSSAT 3.5). In order to run the DSSAT 3.5 the weather, the farm management, soil and the plant characteristic data were needed for each site. After some of the information was gathered, The DSSAT 3.5 was run for wheat, corn, and soybean for each year after making many assumptions on many of the plant, management, and soil inputs since they were hard to get. For instance the exact planting dates for the different crops in the different years at the different sites was not readily known. In any case, to compare the DSSAT_LAI with AVHRR_NDVI, one should know what crops AVHRR_NDVI represents. From Mid October (planting of wheat) to the end of April (before corn or soybeans planting), the AVHRR_NDVI represents the growth of wheat only. After the planting of corn, the AVHRR_NDVI represents wheat and corn growth at the same time until the harvest of wheat when AVHRR_NDVI start to represent only corn. Later when soybean is planted, the AVHRR_NDVI represent corn and soybean until mid October when both are harvest wheat is planted. Based on this understanding, a weekly weighted average of DSSAT_LAI of the three crops were compared with the weakly AVHRR_NDVI to look at their behavior. An average DSSAT_LAI was used because each crop (wheat, corn, soybean) covers part of the land (cell) that is seen by satellite. Although LAI and NDVI are different vegetation indices, overall the AVHRR_NDVI and DSSAT_LAI had to some extent similar trends. In the coming months, MODIS_LAI will be used to validate the DSSAT_LAI at the different sites.

Introduction

Vegetation is very important in today's time. Without vegetation we would not have any food for us to eat or live off of. We research vegetation so we know the best way to grow crops in the future. Vegetation is not just important to us for food but it is important to us as a way of income in our economy. We researched vegetation such as wheat, corn and soybean.

The objective of our research was to compare the Advanced Very High Resolution Radiometer Normalized Difference Vegetation Index AVHRR_NDVI) to a molded Leaf Area Index (LAI) of four different farmlands locations for more then ten years. The four locations were Richmond, VA; Baltimore, MD; Springfield, IL and Albany, NY. These four farmlands were selected because there are in different regions in the United States that has different weather climates.

Theoretical Background

Vegetation Greenness Maps are derived weekly from Normalized Difference Vegetation Index (NDVI) data obtained from two satellite channels. The two satellite channels namely the visible band (VIS) and near infared (NIR). The Normalized Difference Vegetation Index is calculated as (NIR-VIS)/(NIR+VIS). The NDVI is related to vegetation because healthy vegetation reflects well near infrared part of the spectrum. The data and information obtained from the Normalized Difference Vegetation Index provides an estimate of the vegetation growth and health. NDVI can also observe the changes in vegetation over a period of time.

Leaf Area Index (LAI) defines an important structural property of a plant canopy, which is the one-sided leaf area per unit ground area of crops such as wheat, corn and soybeans. Leaf Area Index are biophysical variables which describes canopy structure and are related to functional process rates of energy and mass exchange. The LAI has been used extensively

as satellite derived parameters for calculation of surface photosynthesis and evapotranspiration.

The data obtained from photosynthesis and evapotranspiration are important in calculating terrestrial energy, carbon, water cycle process and biogeochemistry of vegetation.

The Leaf Area Index was simulated for the four locations by running Decision Support System for Agrotechnology Transfer (DSSAT3.5). Farm management, weather, soil and plant characteristics were needed for each site to be able to run DSSAT3.5. Decision Support System for Agrotechnology Transfer (DSSAT3.5) was run for wheat, corn and soybean for each year after making many assumptions on many of the plant, management and soil inputs since they were hard to get.

To compare the Decision Support System for Agrotechnology Transfer Leaf Area Index (DSSAT_LAI) with Advanced Very High AVHRR_NDVI. Resolution Radiometer Normalized Difference Vegetation Index (AVHRR_NDVI) we needed to know what crops AVHRR_NDVI represents. Wheat was planted in mid-October to the end of April before corn or soybeans were planted, during this time period AVHRR_NDVI represents the growth of wheat only. After corn is planted the AVHRR_NDVI represents the growth of wheat and corn respectively at the same time until wheat is harvested and then AVHRR_NDVI represents only corn. Later in the year when soybean is planted, the AVHRR_NDVI represents corn and soybean at the same time respectively until mid-October when both are harvested and wheat is planted again.

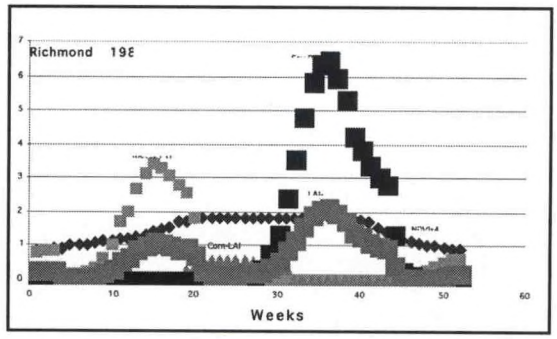

Fig. 1. Molded wheat, corn, soybean, LAI average and

A weekly weighted average of DSSAT_LAI of three crops were compared with the weekly AVHRR_NDVI to look at there behavior respectively. An average DSSAT_LAI was used because each crop wheat, corn and soybeans covers part of the land (cell) that is seen by satellite.

The Data & Results

The LAI and NDVI are vegetation indices but with different values so there values cannot be compared but rather their trends. The AVHRR_NDVI and DSSAT_LAI had to some extent similar trends from week 1 to 15 and from week 30 through 54 (Figure 2). However, from week 15 to 30 their trends were somewhat different. That suggested that the planting date used for soybean was 3-4 weeks later than it should have been. Finding this is encouraging since it means that the use of AVHRR_NDVI can help crop modelers identify the plating date for the different crops. That can also be applied to the harvest date because

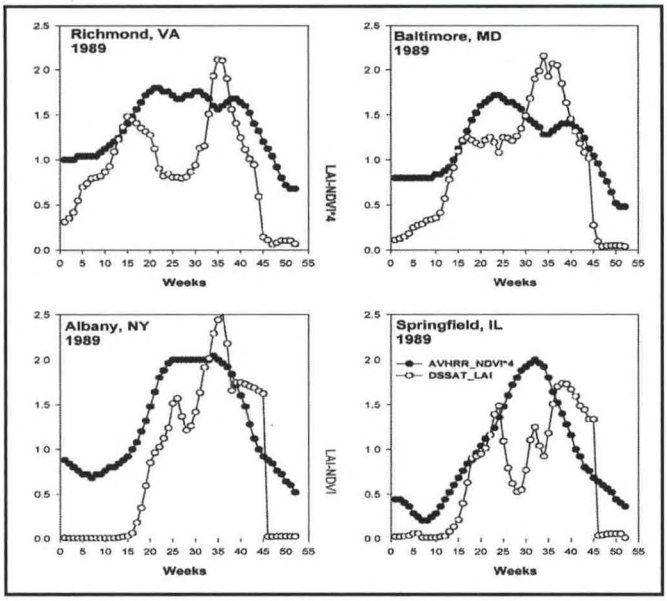

Fig. 2. Molded leaf area index (DSSAT_LAI) and AVHRR normalized difference vegetation index (AVHRR_NDVI).

that affects the trend as well. Knowing the planting date helps the crop modelers start the crop simulation at the right date while knowing the harvest date helps the crop modelers verify the model estimate of the development stages.

Summary and Conclusions

DSSAT 3.5 will be run for the other years (1991-2002). Available LAI and NDVI from MODIS instrument (2000-2002) will be used to validate the DSSAT_LAI and AVHRR_NDVI. Also, MODIS_LAI provides finer scale than AVHRR allowing farmers and agronomists to manage farms using precision farming techniques. It may give them a chance to predict yield maps before harvest. That may help in expanding the scale of crop models from point to regional and in helping hydrological modelers convert remotely sensed NDVI into leaf area index (LAI) for the years before MODIS_LAI was available.

REFERENCES

Al-Bakri, J., and A.A. Suleiman. 2004. NDVI response to rainfall in the different ecological zones in Jordan. International J. for Remote Sensing. (In press).

Crago, R., and A.A. Suleiman. 2004. Heat flux parameterization for sparse and dense grasslands with the Analytical Land-Atmosphere Radiometer Model (ALARM). Boundary Layer Meteorology (In review).

Ritchie, J.T., U. Singh, D.C. Godwin, and W.T. Bowen. 1998. Cereal growth, development and yield. p.79-98. In G. Y. Tsuji et al. (ed.) Understanding options for agricultural production. Kluwer Academic Publisher, Dordrecht.

Suleiman, A.A., and R. Crago. 2002. Analytical Land Atmosphere Radiometer Model applied to a Dense Canopy. Agricultural and Forest Meteorology 112:151-159.

Suleiman, A.A., and J.T. Ritchie. 2003. Modeling soil water redistribution under second stage evaporation. Soil Sci. Soc. Am. J. 67(2): 377-386.

MODELING OF SBUV AND SBUV/2 OZONE TIME SERIES

Kris Ford and John Anderson

Center for Atmospheric Sciences, Hampton University, Hampton, VA

Abstract

This proposal presents work to model ozone using data retrieved from both the SBUV and SBUV/2 satellite instruments. Both satellites are used conjointly so that the longest possible time period of ozone retrievals from SBUV can be incorporated into the model. These data will be used to produce time series of ozone density delineated by atmospheric pressure level and latitude band. The time series will be then used to fit a model that will accurately represent the variations in ozone density over time. Programs using the IDL programming language are produced to perform a least squares fit of the data using singular-value decomposition. The model is intended to capture annual and semi-annual cycles, effects of the quasi-biennial oscillation (QBO), as well the eleven-year ozone cycle. An overall trend for the entire time series will be modeled also. The model will take into account the effects of observed solar flux on ozone density in the stratosphere. This work will be used in future trend analysis studies of atmospheric ozone.

Introduction

The SBUV (Solar Backscatter Ultraviolet) instrument was launched on October 1978 aboard the Nimbus 7 satellite by the National Oceanic and Atmospheric Administration. The purpose of this satellite is to supply researchers with high-resolution meteorological data on a global scale. To achieve this global coverage, the satellite is flown in polar orbits. The satellite is able to make approximately 14 orbits per day. The actual SBUV instrumentation is a nadir- viewing double grating monochromator, of Ebert-Fastie design (Hoffman, et. al 2003). As the name of the instrument implies, this device measures the ultraviolet light that is backscattered by the earth's atmosphere. Ozone measurements are retrieved at wavelengths of 256, 273, 283, 288, 292, 298, 302, 306, 312, 318, 331,340nm. When calculating the backscattered ultraviolet light, the equation used takes into account Rayleigh scattering and ozone absorption only. The equation used is:

$$I_{SS}(\lambda) = F_\lambda \beta_\lambda P(\theta)/4\pi \exp[-S(p)\{\alpha\lambda X(p) - \beta_\lambda p\}]dp \quad (1.1)$$

where Fl is the solar flux at wavelength l, bl is the effective Rayleigh scattering coefficient per unit pressure, and $P(\theta$ is the Rayleigh scattering phase function for scattering angle θ (Hoffman, et. al 2003). The $\alpha\lambda$ term is the effective ozone absorption coefficient per unit ozone amount, S(p) is the slant path, and finally X(p) is the column ozone above pressure p. The instrument measures ozone in Dobson Units for thirteen different layers, which are delineated by pressure. Measurements are also made of the mixing ratio in ppmv and are done for 15 levels. It is this latter set of measurements that will be used for inter-comparison purposes.

The SBUV aboard the Nimbus 7 satellite ceased operation in June 21, 1990. An SBUV/2 instrument was launched September 9, 1988 aboard the NOAA-11 satellite. Like the Nimbus 7, NOAA-11 is a polar-orbiting satellite and was, until its deactivation in June 2004, the country's longest serving satellite of this type. NOAA-11 was placed in standby mode in 1995 but was later reactivated. Subsequently there is a break in the continuity of data from this period that is reflected in the time series. The wavelengths measured by SBUV/2 are similar to that of the Nimbus 7, with the exception that channel one was moved to 252.0 nm. This was done to avoid emission in the nitric oxide gamma band that was a source of corrupted data in the SBUV channel one measurement (Hoffman et. al 2003). Data from the NOAA-11 SBUV/2 is available through 2001.

Research Motivation

Ozone is a naturally occurring gas in the Earth's atmosphere. About 90% of the Earth's ozone is located

in the stratosphere (Fahey 2002), a region that begins roughly at 10km and extends upwards to 50km in altitude. The remainder of the Earth's ozone is situated in the tropopause, the region of the atmosphere that extends from the Earth's surface to about 10km. The stratosphere is the region that, because of its high percentage of atmospheric ozone, contains what is referred to as the ozone layer. The ozone found near the earth in the troposphere occurs primarily from the chemical reaction of oxygen with both naturally and artificially produced gases. This ozone does not significantly contribute to stratospheric ozone levels due to comparatively little mixing between the troposphere and stratosphere.

This layer of stratospheric ozone is important to the earth because it absorbs ultraviolet UV-B radiation from the sun. UV-B is high frequency light with a wavelength between 270-320nm. Exposure to UV-B radiation has been linked to cellular damage in both human and non-human species. Damage can be caused through the absorption of UV-B be DNA which results in the breaking of the bonds that hold the DNA together. Melanomas, cataracts, and damage to marine life are among the issues when discussing the impact of UV-B exposure. It is for these reasons and others that it is important to have an understanding of the coverage of ozone throughout the Earth. Monitoring the extent to which ozone levels are influenced by man-made and naturally occurring output is of particular concern in maintaining the protection that is enjoyed by stratospheric ozone.

Modeling ozone enables us to make a determination as to trends in ozone over some set period of time. Due to the periodic oscillations in ozone density, examinations of ozone in the short term most likely will not provide an accurate picture of the true behavior. However, over a span of a decade or more, a model can reveal significant information about the overall trend in ozone concentration and help make projections as to expected behavior. When policies are enacted with the intent of increasing atmospheric ozone, a model can be used to determine when, if any, increase has been experienced and to what extent. Accurate models can also be used in the validation of other ozone measuring instrumentation to verify new data. This validation is crucial to perform before further statistical analyses can proceed.

SBUV Time Series and Models

Programs were written using the Interactive Data Language (IDL) version 6.0 to read in the data from the SBUV and SBUV/2 text files. The data were sorted into bins that arranged the ozone mixing ratios by pressure level and latitude band. The latitude bands were centered at the multiples of 10 between 90S and 90N with a range of +/-5 degrees (ex. 0° +/-5 , 10° +/-5°, etc.). This process was done to find the average mixing ratio for the respective bins for individual months, covering the entire SBUV and SBUV/2 ozone record from 1978 through 2001. These bins were used to produce time series showing monthly averages of ozone for a particular latitude band and pressure level. Figures 1-4 depict four such examples of time series all centered at 0 or -10 degrees latitude and four different pressure levels. The time series indicate the variations in ozone mixing ratio for the time period from 1978 through 2001. The plots exhibit the ozone annual cycle as well as the semi-annual oscillation that ozone undergoes. Ozone also experiences an eleven-year cycle that is evidenced in these time series that span over two decades. These time series were then modeled with a least-squares regression using a singular value decomposition fit. The function used to fit the data is expressed in equation 3.1:

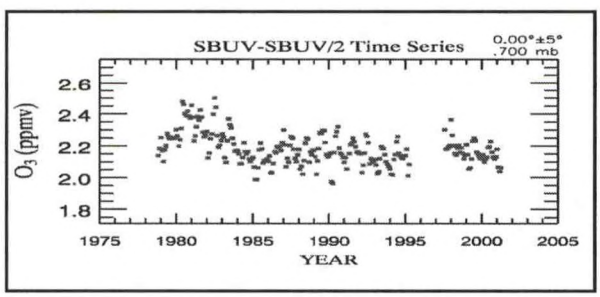

FIG. 1. Ozone (ppmv) time series for 0 degree latitude band and 0.7 mb pressure level.

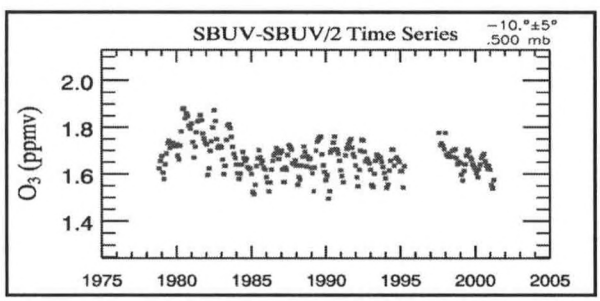

FIG. 2. Ozone (ppmv) time series for 0 degree .

The A_0 term is the ozone mean term of the model and the A1t (time independent) is the linear trend term. This trend term is intended to reveal the over-

all increase or decrease in ozone over the time series. The cos(2πt) and sin(2πt) terms model the annual cycle of ozone while the cos(4πt) and sin(4πt) handle

$$O_3(t) = A_0 + A_1 t + A_2\cos(2\pi t) + A_3\sin(2\pi t) + A_4\cos(4\pi t) + A_5\sin(4\pi t) + A_6 F10.7 \quad (3.1)$$

the semi-annual oscillation component of ozone. The last term is aterm that is meant to model the contribution of observed solar flux. Molecular oxygen is dissociated by ultraviolet light into atomic oxygen, which in turn reacts with other molecular oxygen to form ozone. Ozone is then dissociated and the cycle is repeated (Fahey 2002). Because of this influence it is vital to include effects of solar flux in a model of ozone levels.

IDL 6.0 was used to perform a least squares singular value decomposition fit to the individual time series. Using this fit residues are calculated and plotted separately. Figures 5 and 6 present two cases of the modeling of the time series and the resulting residues. The models produced mean percent differences of 3.2 and 3.7 respectively. Although more terms will be added to the model, further examination of the details of the regression calculations is to be performed to determine if the seven-term model is providing the most accurate fit of these data for all latitude bands. Following this step the next addition to the model will be a term to accurately model the effect of the quasi-biennial oscillation (QBO) (Hobbs et. al 1977) on ozone concentrations. The model will use data from the Singapore winds to characterize the QBO and be represented as the eighth term in the model. Principle component analysis will be used to approximate the dynamic effect of the QBO and its effect on ozone trends.

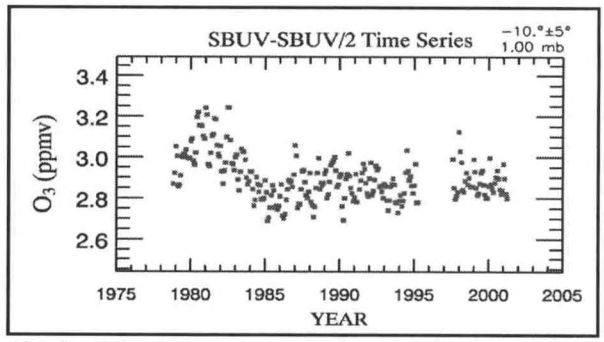

FIG. 3. Ozone (ppmv) time series for -10 degree latitude band and 0.5 mb pressure level.

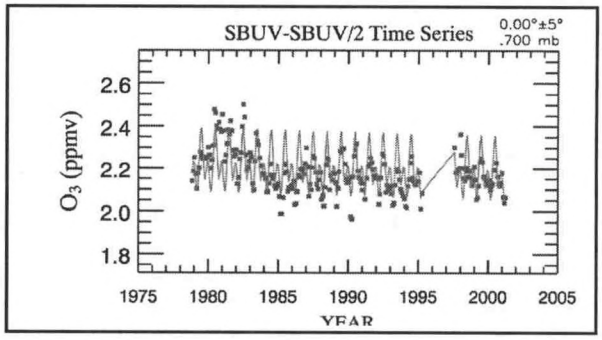

FIG. 4. Ozone (ppmv) time series for 0 degree latitude band and 1.0 mb pressure level.

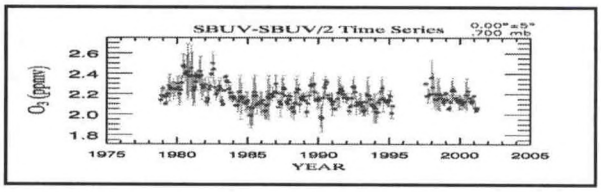

Fig. 5. (a) Singular value decomposition (red) plotted over 0 degree 0.7 mb time series (blue) and (b), residue plot for 5(a). Mean % difference = 3.2%.

ACKNOWLEDGEMENTS

Acknowledgement and thanks are given to NOAA-Crest, NASA, the Hampton University Center for Atmospheric Science, Dr. M. Pat McCormick, Mr. Michael Hill, and Mr. Charles Hill for the invaluable assistance they have provided.

REFERENCES

Fahey D.W., 2003, Scientific Assessment of Ozone Depletion: 2002: Report No. 47, Q.3-Q.6.

Gumley L., 2001: Practical IDL Programming, 1st ed.

Hobbs P.V., J.M. Wallace, 1997: Atmospheric Science: An Introductory Survey, 30.

Hoffman D., C. Rodgers, J.M. Russell III, H.G. Smit, R. Stolarski, W. Randel, 1998: Assessment of Trends in the Vertical Distribution of Ozone, 39-51.

http://www-rab.larc.nasa.gov/

Official NASA Langley Website.

AIR DISPERSION MODEL SELECTION AND ADAPTATION FOR THE BRONX ASTHMA AND AIR POLLUTION PROJECT

Dellis Stanberry and Dr Juliana Maantay

Dellis Stanberry and Dr Juliana Maantay , Lehman College, City University of New York, Department of Environmental, Geographic, and Geological Sciences, September 2004

The objective of this research is to examine appropriate existing air dispersion models, and select the model best suited for the Bronx air pollution and asthma project, adapting the model as required for local conditions (Tsai M.Y., Chen K.S., 2004). Prior research undertaken by NOAA-CREST researchers on the Bronx air pollution and asthma project has focused on emissions from stationary point sources, such as Toxic Release Inventory (TRI) Facilities. Emissions of criteria pollutants from stationary point sources in the Bronx includes Nitrogen Oxide (NOx), Particulate Matter (PM10), Sulfur Dioxide (SO2), Volatile Organic Compounds (VOC), Carbon Monoxide (CO), Particulate Matter (PM25), and Ammonia (NH3), as well as toxic substances such as Xylene, Zinc Compounds, Trichloroethylene, and Glycol Ethers (from Bronx TRI facilities).

Circular buffers were used to determine the likely extent of the areas in proximity to these facilities that would potentially be impacted by their emissions. The use of circular buffers, however, assumes that the pollutants are dispersed equally in all directions from the source and with the same (constant) concentration levels throughout the impact area. Use of dispersion models is a more realistic way of determining the extent of impact resulting from these facilities' emissions (O'Malley M., 2004).

Several types of air dispersion models suitable for estimating pollutant dispersion extents and concentration levels from stationary sources will be evaluated. Existing models were developed primarily by the National Oceanographic and Atmospheric Administration (NOAA) and the United States Environmental Protection Agency (US EPA), although dense urban conditions in the Bronx may require modification in model parameters and inputs (Kumar A., Bellam N.K., Sud A. 1999).

Various factors are typically considered when executing an air dispersion model. These include wind speed, wind direction, stack height, type of chemical being emitted, and chemical temperature. Models that are available include Industrial Source Complex Model (ISC), Assessment systems for Population Exposure Nationwide (ASPEN), American Meteorological Society/Environmental Protection Agency (AMS/EPA) Regulatory Model (AERMOD), Regulatory Modeling System for Aerosols and Deposition (REMSAD), and Areal Locations of Hazardous Atmospheres model (ALOHA).

Some models which do not consider wind speed and turbulence in the vertical direction are known as Gaussian Plume models. These are usually used for large geographic areas as the impact is greater in the horizontal direction than the vertical (Jin-Sheng L., Hildermann, L., 1997). ISC and ASPEN are Gaussian Plume models.

The models' output will be shown in one of two ways: either as plumes, ellipsoidal in shape, depicting the actual shape and direction of the pollutant, or will be plotted as contours of the concentration levels for the particular chemical emitted. The results from the air dispersion models will be imported into ArcGIS (computer mapping and spatial analysis software) and analyzed with demographic and asthma hospitalization data for the Bronx to determine the environmental health and justice implications of air pollution from stationary sources.

Several factors will be considered when choosing a dispersion model for the Bronx air pollution and asthma project. Each TRI facility can have a number of stacks or point sources emitting several different types of chemicals. The chemical from each stack or point source has to be analyzed, and plumes

or concentration level contours generated for each one. The model selected should be able to take input for multiple point sources and chemicals so a composite of emissions from all stack and/or point source for each TRI facility can be generated. It would also be beneficial if there is a model that can handle more than one TRI facility and generate results for the entire Bronx.

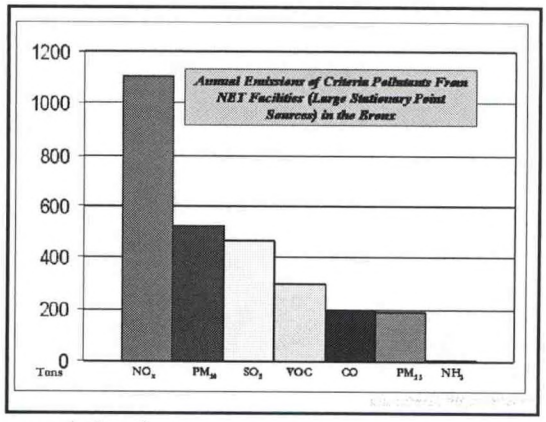

ALOHA is one model that will be evaluated. It predicts the location and extent to which gases may disperse in the atmosphere after an accidental release. Climatic data, location information, and chemical type are inputted. The model has an extensive chemical library so the physical properties of the chemical do not need to be entered. Footprints of the plume are displayed within a user defined area where it is anticipated that the concentration of chemical will not be exceeded. Concentration levels and release rate over a given time period can also be plotted using ALOHA. Data from a portable meteorological station can be configured to download to ALOHA automatically while the model is being run. This allows real time modeling of emissions. The footprints produced by ALOHA can be displayed along with maps of the area of interest. MARPLOT is one type of software that can be used with ALOHA to display maps showing buildings and other areas of interest in proximity to the area of impact.

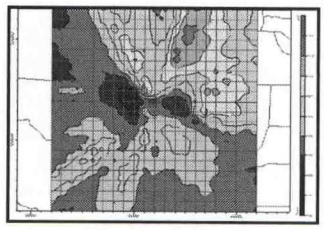

Example of concentration contours from AERMOD

AERMOD model is another model that will be evaluated for use on the Bronx air pollution and asthma project. It is used to calculate concentration of chemicals emitted from TRI Facilities. This model requires two types of meteorological data files, one containing surface scalar parameters and another containing vertical profile. These files can be obtained from the National Climatic Data website for most major cities in the US. These meteorological data files need to be processed before they can be used in the AERMOD model. Rammet and Aermet are the two programs used to process the meteorological data files. The results from these two programs are used as input in the AERMOD model. Other inputs for the model include the coordinates for the stack, stack height, stack diameter, emission rate of the gas, stack gas exit temperature and stack gas exit velocity. AERMOD can also import building footprints so the effects of building downwash can be incorporated.

Most of these models are based on typical settings, where the terrain is level or undulating and there are few buildings to affect the plume rise. In dense urban areas however the topography is usually flat, with many buildings close to each other, creating an "urban canyon" effect. This layout causes emissions from stacks or point sources to behave differently than in open areas. For this reason the model chosen has to incorporate the effects of urban conditions (Walcher S., Altschuh J., Schramm K.). The chosen models will be used to obtain outputs for a TRI facility and the results compared. The results will be critically evaluated, and the model that yields the best results will be used in the Bronx air pollution and asthma project.

REFERENCES

How are the Toxics Release Inventory Data Used? May 2003. US Environmental Protection Agency. 15 Mar. 2004 <http://www.epa.gov/tri/guide_docs/2003_datausepaper.pdf>.

Jin-Sheng L., Hildermann, L. "Modeling Vertical Spread of Airborne Pollutants from Sources Near Ground Level – Comparison with Field Measurements." Journal of Environmental Engineering Volume 123, Issue 12 (December 1997). pp. 1194-1202.

Kumar A., Bellam N.K., Sud A. "Performance of an industrial source complex model: Predicting long-term concentrations in an urban area." Environmental Progress Volume 18, Issue 2 (Summer 1999). pp. 93-100.

O'Malley M., Barry T., Verder-Carlos M., Rubin A. "Modeling of methyl isothiocyanate air concentrations associated with community illnesses following a metam-sodium sprinkler application." American Journal of Industrial Medicine Volume 46, Issue 1 (July 2004). pp. 1-15.

Perlin, S.A, Wong, D & Sexton, K. "Residential Proximity to Industrial Sources of Air Pollution: Interrelationships among Race, Poverty, and Age." Mar. 2001. Journal of the Air & Waste Management Association. 16 Mar. 2004 <http://www.awma.org/journal/pdfs/2001/3/406-421p.pdf>.

Raza S., Avila R., Cervantes J. "A 3D Lagrangian particle model for the atmospheric dispersion of toxic pollutants." International Journal of Energy Research Volume 26, Issue 2 (February 2002). pp. 93-104.

"School Haze: Air Pollution Near California Schools." @risk. 1998. Environmental Working Group. 17 Mar. 2004 <http://www.ewg.org/reports/schoolhaze/execsum.html>.

Tsai M.Y., Chen K.S. "Measurements and three-dimensional modeling of air pollutant dispersion in an Urban Street Canyon." Atmospheric Environment (September 2004).

Walcher S., Altschuh J., Schramm K., Mayer S. "Estimates in deterministic fate modelling of environmental chemicals." Environmental Modelling & Software Volume 18, Issue 10 (December 2003). pp. 929-936.

Characterization and Comparison Between Aerosols of the Chihuahua Desert and the Sahara Desert

Roderick Pearson, Oscar Calvo and Rosa Fitzgerald

Physics Department, University of Texas at El Paso El Paso, TX 79968-0515

Aerosol optical depth measurements, in conjunction with novel inversion techniques, are used to determine the size distribution of airborne particulates in the El Paso-Juarez Airshed. In particular, we will focus on the Chihuahua desert. Our inversion method was developed using Twomey's regularization method as a base. In our methodology novel algorithms are used to determine the constraint coefficient and the regularization matrices. The extinction coefficient of the airborne particulates is calculated utilizing the T-matrix code. Subsequently, we will apply our inversion techniques to analyze the Saharan dust aerosols using optical depth data gathered in the NCAS ship expedition. Patterns and correlations with the Chihuahua desert will be sought.

Characterization and Transport of Aerosols in Southwest Cities

Roderick Pearson
Physics Department, University of Texas at El Paso El Paso, TX 79968-0515
Rosa Fitzgerald
Physics Department, University of Texas at El Paso El Paso, TX 79968-0515

Abstract

Aerosol optical depth measurements, in conjunction with novel inversion techniques, are used to determine the size distribution of airborne particulates for the El Paso-Juarez Airshed and neighboring cities. The inversion method was developed using Twomey's regularization method as a base. In our methodology novel algorithms are developed to determine the constraint coefficient and the regularization matrices. The extinction coefficient of the airborne particulates is calculated utilizing the T-matrix code. SEM images of regional airborne particulates are analyzed to validate the inverse reconstruction methodology used. In addition, the curvature of log-log plots of aerosol optical depth versus wavelength is analyzed to determine the applicability of the technique of using wavelength dependence of optical depth data to differentiate between urban aerosols and desert dust. The NOAA HYSPLIT model is further utilized to perform trajectory modeling to give insight into the regional influences on the aerosol concentrations.

Introduction

The El Paso del Norte Airshed is in non-compliance with U.S. Standards for particulate matter, with frequent days of severe air pollution. Studies have been undertaken to understand the causes and sources of the contamination. Research is currently being conducted to characterize and inverse reconstruct the size distribution of the aerosols for the El Paso-Juarez Airshed and neighboring cities.

The current methods in use by state agencies for monitoring airborne particulates include passing air through a series of air filters with successively smaller pores. One of our goals will be to implement and validate a light scattering technique for monitoring aerosols in conjunction with robust inverse reconstruction techniques.

Methodology

The inversion reconstruction code was created to solve the equation

$$\tau_t(\lambda) = \int_0^\infty \pi r^2 Q_{ext}(r,\lambda) n_c(r) dr$$

Where r is the effective radius, Q_{ext} is the extinction coefficient as a function of r and wavelength and nc is the size distribution.

This problem is ill-posed and requires a constrained, regularized solution as given by Twomey(1977). After the inversion algorithm was written in FORTRAN, validation of the code, was first performed using simulated experimental optical depth data. In order to achieve this, SEM images of captured aerosols were analyzed for particle effec-

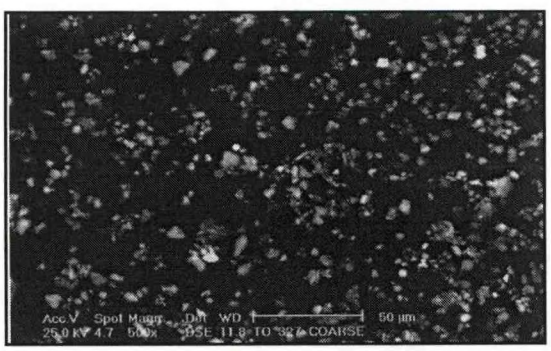

Figure 1 SEM images of the aerosols captured during routine local air quality monitoring efforts (with scale added for reference).

tive radius and size distribution, see figure 1.

The aerosols were captured on multiple filters during routine air quality monitoring in the local airshed. Inspection of the resulting images was guided by the criterion that the particles in the image not be overlapped to the degree that individual particles were not discernible. All particles that overlapped or were on the edges of the image were excluded from analysis. For all remaining particles, the effective radius and variance were calculated by the method given by West, et.al.

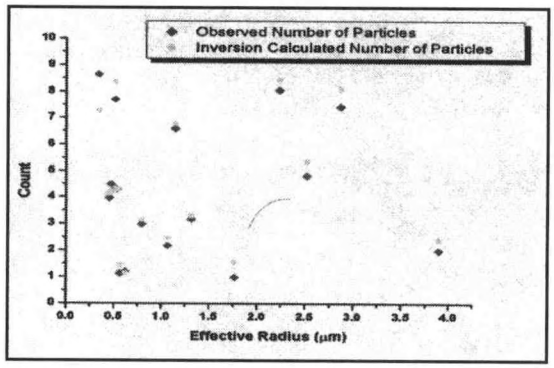

Figure 2 Results of the inversion process compared against simulated experimental data. The effective radius is given in microns on the horizontal axis.

Using the T-matrix algorithm (Mischenko and Travis 1998), the extinction coefficient was calculated for the effective radii at wavelengths of 415, 500, 610, 665, 862 and 940 nm. The optical depth and matrix of $\pi r^2 Q_{ext}$ were put into the inversion code to solve for the size distribution. The inversion code gives results in the form of the number of particles for each effective radius across all the wavelengths. Results of a sample case where the simulated data is compared against the results of our inversion code are shown in figure 2.

In figure 2 it is observed that the number of particles calculated from the inversion process is higher for every effective radii except for the smallest radii. Several cases were analyzed; overall the agreement was good in all of them, thus validating the inversion code.

Subsequently, experimental optical depth data was obtained from the USDA radiation monitoring site located at the Jornada Experimental Range, just north of Las Cruces, NM. The data was total horizontal, direct normal and diffuse radiation, per wavelength. Using this data the aerosol optical depth was calculated using a Langley regression technique (Alexandrov 2002) to find the total optical depth.

$$\ln F = \ln F_0 - \tau m + \ln(C)m$$

where F is the radiation at the radiometer, F_0 is the radiation at the top of the atmosphere, C is a calibration coefficient, m is the air mass and _ is the total optical depth.

The aerosol optical depth was then calculated with the following equation,

$$\tau_a = \tau_t - \tau_R - \tau_o - \tau_{wm}$$

where ozone, _o, water/molecular, _wm, and Rayleigh, _R optical depths are subtracted from total optical depth.

These optical depths along with the extinction coefficients calculated previously were input in the inversion code to determine aerosol size distributions. To help understand these distributions, log-log plots of optical depth versus wavelength were produced. Eck (2000) showed that this technique allows for the determination of particle types influencing the optical depth. Additionally NOAA's HYSPLIT model is used to perform 24hr duration backward trajectory calculations ending at the MFRSR location. Analysis of these trajectories shows the influence of various land uses on the aerosol composition. For this research work, October 2000 was chosen for analysis.

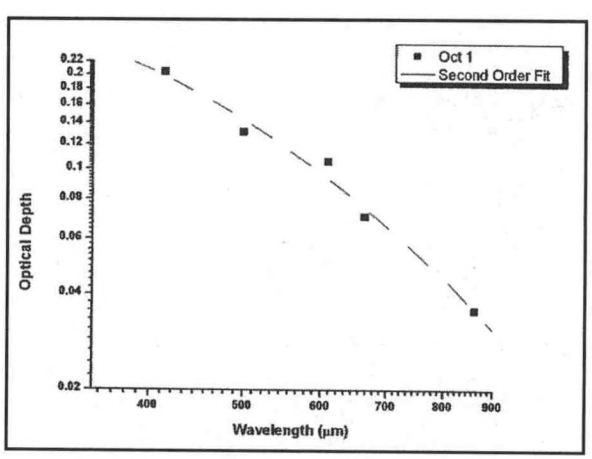

Figure 3 October 1, 2000 (a) Log-log plot of Optical Depth vs. Wavelength.

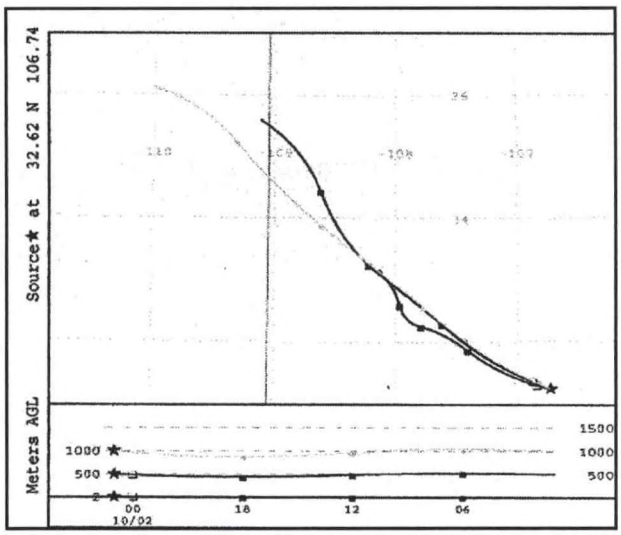

Figure 3 (b) Trajectory plot for October 1, 2000

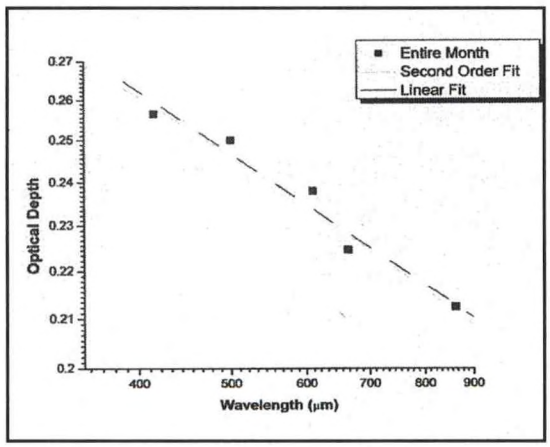

Figure 4 Log-log plot for the month of October, 2000.

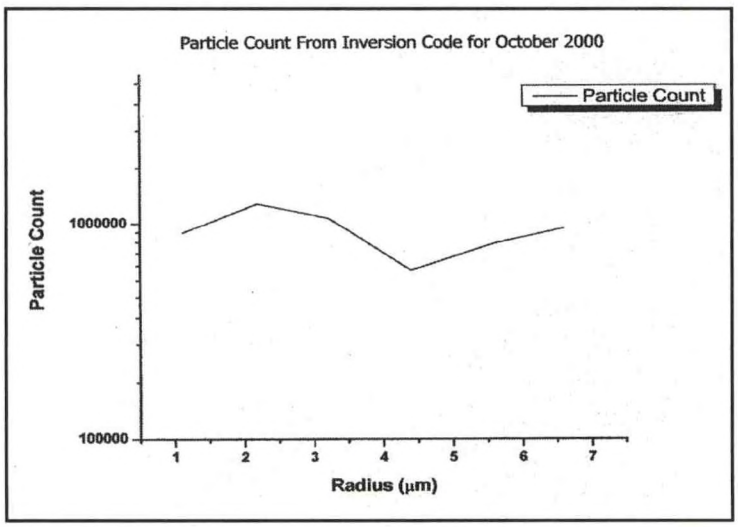

Figure 5 Particle count from inversion of optical depth for October, 2000.

Figure 3, a and b, show an example of the log-log plot of the optical depth for the given day with a trajectory plot for the corresponding day.

The log-log plot in figure 3 (a) shows little curvature with respect to the 2nd order fit indicating a mixed mode of aerosols. The slight downward nature of the curve implies the predominance of fine mode particles (biological in origin). The trajectory plot, figure 3 (b), shows a lifting of aerosols from the forested mountainous areas of New Mexico and also from Northern Arizona. The trajectory allows for the transport of fine mode aerosols into a region dominated by coarse particles.

Figure 4 shows the aerosol size distribution for the entire month. The lack of curvature of the plot implies that there was a mixed mode of fine and coarse particles. Checks were performed on the quality of the data. No data for the month was flagged as being out of compliance with the quality control measures.

Figure 5 is performed for a representative case sample, showing the particle size distribution inverted from the optical depths for the entire month. The inverted size distribution shows no dominance by either fine or coarse particles. This is in agreement with the log-log plot for the corresponding month.

Conclusions

Our inverse reconstruction methodology was successfully validated. The algorithm is capable of accurately calculating the size distribution of aerosols. Successful analysis of particulate matter was performed for southwestern cities using the current methodology. Its advantage over other existing techniques is that it can analyze the aerosols as they exist in the troposphere. These techniques may be used in any area of the country, but are especially relevant to southwestern U.S cities, like El Paso, which experiences severe air pollution, such as fugitive dust source contaminants, etc. This will allow a better understanding of their environmental impact and permit proper evaluation of the effectiveness of alternative air pollution control measures for regulatory compliance purposes.

BIBLIOGRAPHY

Alexandrov, M. D., A. A. Lacis, et al. (2002). "Remote Sensing of Atmospheric aerosols and trace gases by means of Multifilter Rotating Shadowband Radiometer, Part I: Retrieval Algorithm." Journal of the Atmospheric Sciences 59: 524-543.

Eck, T. F., B. N. Holben, et al. (1999). "Wavelength dependence of the optical depth of biomass burning, urban, and desert dust aerosols." Journal of Geophysical Research 104(D24): 31,333-31,349

Mischenko, M. I. and L. D. Travis (1998). "Capabilities and Limitations of a Current FORTRAN Implementation of the T-Matrix Method for Randomly Oriented Rotationally Symmetric Scatters." Journal of Quantitative Spectroscopy & Radiative Transfer 60(3): 309-324.

Twomey, S. (1977). Introduction to the Mathematics of Inversion in Remote Sensing and Indirect Measurements. Amsterdam, Dover Publications.

West, R., L. Doose, et al. (1997). "Laboratory measurements of mineral dust scattering phase function and linear polarization." Journal of Geophysical Research 102(D14): 16,871-16,881.

Observing Aerosol Direct and Indirect Effects from Spectral Radiometric and In Situ Measurements

Fonya Nzeffe*, Everette Joseph*, and Qilong Min**

* Howard University, ** State University of New York at Albany

Aerosols influence the Earth radiation balance and thus the climate through direct interaction with solar radiation, and by indirect effect on cloud life cycle and radiative properties. The latter effect is believed to be the most dominant effect of aerosols on climate, and estimated in the 3rd IPCC assessment to produce a global mean radiative forcing of as much as -2 W m-2. This estimate, however, is highly uncertain; thus, considerable research effort continues to be directed towards better understanding of aerosol indirect effect.

A recently developed method is applied for observing cloud and aerosol optical and microphysical properties from spectral irradiance measurements at the surface to extended observations at 2 sites with different aerosol concentration and composition to assess the influence of natural and anthropogenic CCN on cloud radiative properties. In particular, cloud optical depth and effective radius for both warm and ice clouds are simultaneously retrieved at all sites, and combined with information on aerosol composition and microphysical properties from in situ measurements and laboratory analyses. Observations are use from the Atmospheric Radiation Measurement site in Oklahoma, and the Howard University atmospheric measurement site in Beltsville Maryland. The latter site is currently being established through a cooperative agreement between NOAA/NWS and Howard University (NOAA/Howard University Center for Atmospheric Sciences; NCAS). A comprehensive set of surface-based instruments (spectral radiometers, microwave radiometer, and LIDAR) is being deployed there to observe cloud and aerosol properties, fluxes, surface energy budget, soil properties, boundary layer (tower and upper air sounding, and water vapor LIDAR), and atmospheric chemistry (gas phase and aerosols).

SENSITIVITY OF THE RETRIEVAL OF CLOUD TOP HEIGHTS TO SPECTRAL RESPONSE FUNCTION UNCERTAINTY

Min Min Oo, Barry Gross

Optical Remote Sensing Lab, EE Dept, NOAA-CREST, CCNY, Changyang Cao NOAA-NESDIS

Abstract

The height and location of the cloud can be retrieved using High Resolution Infrared Radiation (HIRS) data from National Oceanic and Atmospheric Administration (NOAA) polar orbiting satellites. LBLRTM (line by line radiative transfer model) may be applied to find the radiation emerging from the top of the cloud, which will depend strongly on the cloud top temperature. Knowing the cloud top temperature and the profiles from a clear sky, cloud heights may be inferred. Given the uniformity of the CO2 mixing ratio, signal ratios at TOA in the CO2 absorption line will depend primarily on the cloud top pressure. However, when applying this method to both the NOAA14 and NOAA15 satellites, a significant bias between satellite retrievals were found for clouds at height above 6 km (approximately 100 ~ 200 mbar). This result is seen in the long cloud frequency records where the high cloud frequency for NOAA 15 is lower in the upgraded HIRS-3 sensor. In this paper, we explore both internal errors such as incorrect cloud and / or temperature profiles and external errors such as mischaracterization of the spectral response functions (SRF). In particular, we show that internal errors cannot account for the observed net biases but center wavelength (CWN) shifts of the SRF functions can account for the observed biases. More directly, we show the domain of all spectral shifts that account for the observed biases.

Introduction

Cloud top pressure (CTP) is generally determined by CO2 slicing method (Menzel, 2001) and the accuracy of the CTP depends on the atmospheric models using in the calculation ratio. However, it has recently been observed that different cloud height retrievals between the NOAA 14 HIR2 sensor and NOAA 15 HIRS3 sensor are obtained (Wylie, 2004) as seen in figure 1. In this paper, imprecise characterization within the original instrument specifications of the satellite's filter spectral response function (SRF) is shown to be able to account both qualitatively and quantitatively for the cloud top pressure. Recent measurements done on the filters at National Institute of Standards and Technology (NIST) confirm that significant CWN calibration errors exist.

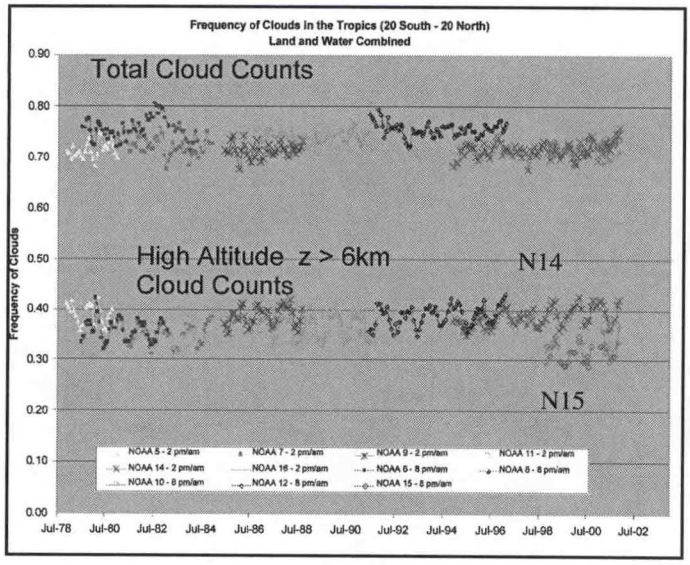

Figure 1: Frequency of cloud in tropical region

These results encourage finding the affect of filter's SRF ambiguity on the cloud top pressure retrieval biases and to compensate properly for them.

Theoretical Background

The CO2 slicing method calculates the CTP by using the ratio of the cloud signal in channels 4/5, 5/6, 5/7 and 6/7. (Channel 4, 5, 6, 7 have CWN at 696nm ,711nm, 733nm and 748 respectively) These channels see different CO2 absorption loadings depending on their height and for opaque clouds, the

cloud top is the IR source which depends on the temperature so the ratios are very sensitive to the cloud top height\ as seen in figure 2. In addition, close lying bands have similar emmisivities so ratios are quite insensitive to the highly variable emissivities of clouds.

This ratio between TOA radiances is described in equation (1) where the left hand side is the measured ratio and right hand side is the calculated ratio. Here, the channel index i is lower than the channel index j. Note that all ratios are referenced to clear sky pixel to help with the calibration.

$$\frac{I(v)^{Ch\_i} - I(v)^{Ch\_i}{}_{clear}}{I(v)^{Ch\_j} - I(v)^{Ch\_j}{}_{clear}} = \frac{I(v)^{Ch\_i}{}_{cld\_mdl} - I(v)^{Ch\_i}{}_{clear}}{I(v)^{Ch\_j}{}_{cld\_mdl} - I(v)^{Ch\_j}{}_{clear}} \quad (1)$$

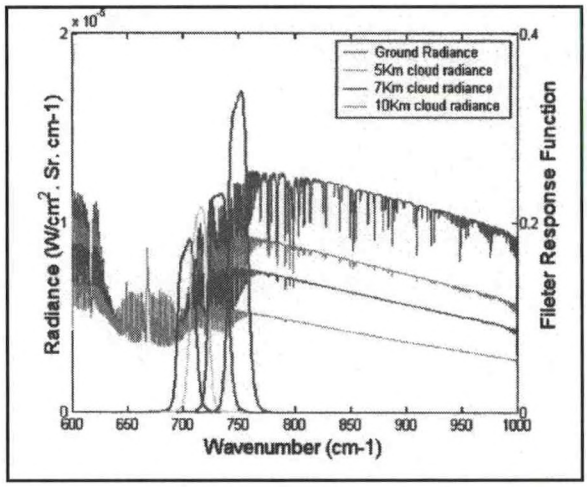

Figure 2: TOA Radiances calculated with line by line code LBLRTM to resolve very sharp Filter perturbations (for illustration, a convolution of 1cm^-1 was applied)

To calculate equation (1), a line by line radiative transfer model (LBLRTM) is used to get the infrared radiance from the ground (clear sky model), and the cloud top IR radiance from different cloud models This approach ios necessary since we a prbing pertunbations in the SRF of less than 0.1 cm-1. Neglecting aerosol scattering processes, the infrared clear sky radiance from the ground for specific spectral channel with assumption perfect emissivity of ground (=1) and 100% clear FOV to the ground is

$$I(v)_{cloud} = (1-\varepsilon_v)B_v(T_s)\tau_v(p_s) + (1-\varepsilon_v)\int_{p_{surface}}^{p_{cloud}} B_v(T(p))d\tau_v + \varepsilon_v B_v(T(P_{cloud}))\tau_v(P_c) + \int_{p_{cloud}}^{0} B_v(T(p))d\tau_v \quad (2)$$

On the other hand, the radiance from the top of the cloud is

$$I(v)_{clear} = B_v(Tp_s)\tau_v(p_s) + \int_{p_{sur}}^{0} B_v(Tp)d\tau_v \quad (3)$$

where ε_v represents the emittance of the cloud. The first two terms are contribution from below the cloud, the third term is the cloud contribution, and the forth term is the contribution from above the cloud. After subtraction of equation (2) to equation (3), the right hand side of the equation (1) becomes

$$T1 = [\beta_{v1}(T_{p_s}) - \beta_{v1}(T_{p_c})][\tau_{v1}(p_s) - \tau_{v1}(p_c)]$$

$$T2 = \int_{p_s}^{p_{cld}} B_{v1}(T_p)\frac{d\tau_{v1}}{dp}dp$$

$$T3 = [\beta_{v2}(T_{p_s}) - \beta_{v2}(T_{p_c})][\tau_{v2}(p_s) - \tau_{v2}(p_c)]$$

$$T4 = \int_{p_s}^{p_{cld}} B_{v2}(T_p)\frac{d\tau_{v2}}{dp}dp$$

$$RHS = \frac{\eta\varepsilon_{v1}(T1+T2)}{\eta\varepsilon_{v2}(T3+T4)} \quad (4)$$

In equation (4), fractional cloud cover within FOV is . If two channels have the same FOV and the channels' wave number are close enough to assume

$$\frac{\varepsilon_1}{\varepsilon_2} \cong \frac{(1-e^{-\kappa_1 \tau})}{(1-e^{-k_2 \tau})} \approx \frac{k_1}{k_2} \approx 1, \quad \text{equation (4)}$$

The right side is calculated from known (or assumed) temperature profile and the atmospheric profile of CO2 as function of pressure. Therefore, the CTP could be determined from the measured HIRS data.

This is illustrated in figure 3 where the "calibration function" is plotted as a function of cloud pressure. If a measurement is given, the intersection of this measurement with the calibration curve would give the cloud pressure. Therefore, the CTP could be determined from the measured HIRS data.

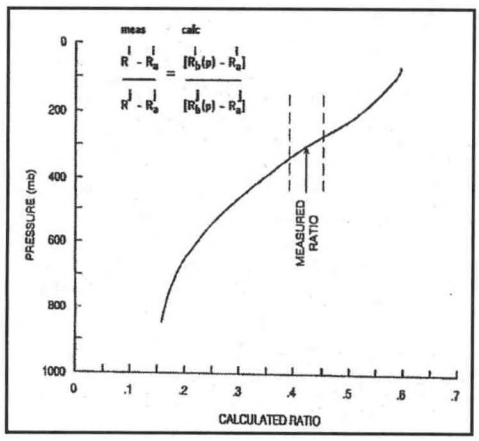

Figure 3: Ratio of measured cloud signal compare to theoretical calculated ratio curve to determined cloud pressure

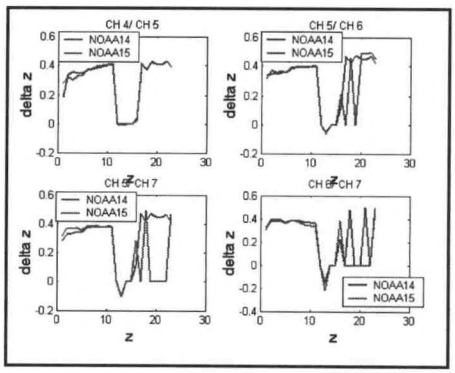

Figure 4: The biases of different cloud model using in CO2 slicing method in NOAA14and NOAA15

Results

It is clear that if accurate knowledge of the underlying clear sky profiles and filter responses were known and sufficient data existed for calibration, then no bias should result. However, if the underlying model is wrong, either the cloud model or the temperature model etc, it might be possible that net biases between the different sensors may occur. To see if this is the case, we examiuned one type of model uncertainty and examined the effects of two different cloud models where one cloud model is a 1km thick OD=1 cirrus cloud which is compared to the ideal OD=INF, width=0km idealized case. While it is clear that for each sensor, using different models changes the calibration curve and therefore each sensor would have a bias, we see clearly in figure 4 that while each sensor has a bias, the net bias between the satellites is zero. Therefore, internal model uncertainties cannot explain the observed biases. On the other hand, if the SRF of one of the sensors was incorrect, net biases can be expected to occur. As seen from figure 1, HIRS-2 sensor on board NOAA-14 over counts the number of high altitude clouds meaning that NOAA 14 must be assigning pressures which are too low. Calculations show that a pressure bias of 50-100 mbars is sufficient to explain this effect. Furthermore, these biases on the order 50-100 mbar has been documented for all cloud top sounding channels. To see if the SRF uncertainty can explain these results, we will perform a sensitivity study where all channel CWN's can shift on the order of the uncertainties seen in the NIST measurements.

Before examining the full "shift" space, we focus on the effects due to miscallibration of a single CWN by shifting channel 4 or 5 in the 4/5 ratio over the range (-2.0 ~ +2.0 cm -1) and recalculating the calibration curve for these 4 cases. The results are shown in figure 5. The cloud top pressure retrieval bias can be calculated to be the difference in retrieved pressures between the original and shifted curves. For example, if channel 5 has a positive CWN shift or channel 4 has a negative CWN shift, the resultant pressure bias is about -50 mbar which would account for the measurements. Of course, if the shifts are reversed, an increase in cloud pressure estimates would occur.

From the previous discussion, it was evident that only some shifts in CWN can account for the positive biases. Therefore it is important to see exactly which CWN shifts can account for the observed biases. The results over all possible shifts are plotted in figure 6. In particular, all possible shifts for all channel ratios are considered.

To agree with the biases, we need to determine the subset of CWN shifts which can account for $\Delta p_c \leq -50\,mbars$. The regions satisfying this constraint simultaneously are shown surrounded by white boundary lines. Most important is the existence of a significant region in the CWN shift space that can account for these biases.

From these results, it was observed that CWN shifts on the order of 1cm-1 can account for the biases which lies within the specifications of the vendor. However, recent measurments performed on similar filters which comprise the HIRS-2 sensor have been made by NIST. According to NIST (Kaplan, 2002), ITT Industries provided 23 filter samples and all of them were samples of the actual flight filters for the HIRS/H304 (ITT, 2003) instrument. The analysis result of these filters showed that the NIST measured SRF of NOAA 14 HIRS sensor will have a spectral response error due to filter temperature changes.

Table 1 provides the center wave number, and the equivalent width of the filter spectral response functions and shows how much error could be expected in the HIRS-2 sensors on NOAA14

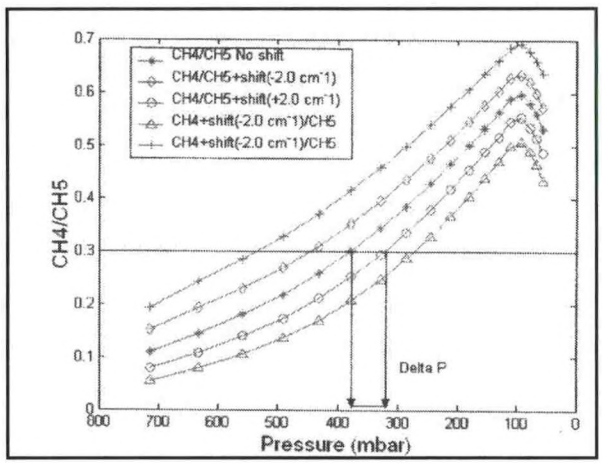

Figure 5: Cloud Top Pressure Retrieval Bias (Delta P) due to inaccurate spectral response on channel 5 with CWN shift +2 wave number (cm-1)

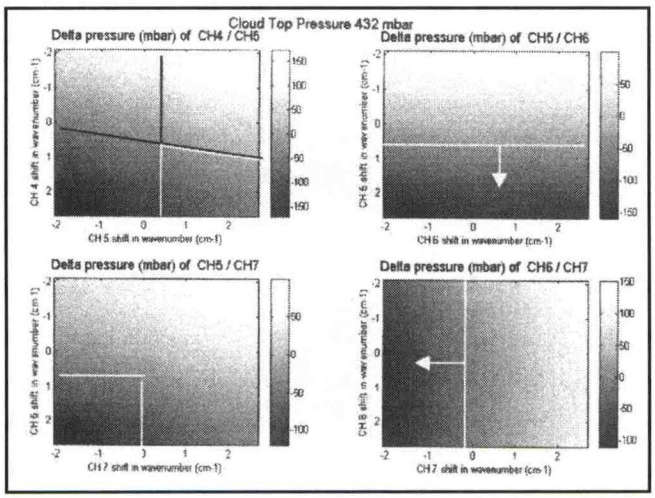

Figure 6: Cloud Top Pressure Retrieval Bias (Delta P) due to CWN shifts for all sounding channels

Conclusions

Internal model approximations (cloud thickness model initial temperature profile etc.) cannot account for observed cloud height biases between NOAA14 and NOAA15. However, spectral mischaracterizations of both the center wavelength and filter widths within possible errors can account for the magnitude of cloud height biases observed. These uncertainties have recently been documented with extended post launch measurements of the HIRS-2 NOAA 14 sensor and shows that the SRF function for cloud height determination must be rigorously calibrated pre-launch. Further work will focus on determining how best to compensate for these biases.

	NIST@20C		ITT		Differences		Specification
Channel	CWN	EQW	CWN	EQW	CWN	EQW	CWN
4	704.9	15.8	703.9	16.2	1.0	-0.4	703.0 +/-1.8
5	717.9	16.8	716.4	16.6	1.5	0.0	716.0 +/- 1.8
6	733.8	17.2	731.2	16.9	2.6	0.3	733.0 +/- 1.8
7	750.2	16.4	749.4	16.7	0.8	-0.3	749.0 +/- 1.8

Table 1. Center Wavenumber(CWN) and Equivalent Band Width(EQW) Comparison (NIST vs. ITT) of Channel 4,5,6,7

ACKNOWLEDGEMENTS

This work is supported by grant from NOAA #NA17AE1625.

REFERENCES

Kaplan, Simon, 2002, Transmittance Measurements of 19 Witness Infrared Bandpass Filters from the HIRS/4 Instrument, project report, Optical

SIGNAL-TO-NOISE CONSIDERATIONS IN DESIGN AND PERFORMANCE ANALYSIS OF A LIDAR SYSTEM

Yasser Hassebo , Badr El-Manuoii, Yu Zhao, Barry Gross, Fred Moshary, Sam Ahmed
Optical Remote Sensing Lab- City College of New York NOAA-CREST

Abstract

The Raman lidar approach is a powerful method which can decouple the aerosol extinction and backscatter coefficients by using a the Raman-shifted nitrogen backscatter signal. In particular, the backscatter coefficient is determined solely from the ratio of the two return signals (as well as a model specific correction parameter which compensates for the mismatch between the raman and elastic wavelengths) which leads to independence of the requirement of a full overlap between laser beam and telescope field-of-view. Due to the low intensity of the Raman scattering, this technique is usually restricted to night-time, when the background from the sky is low enough. Due the weakness of the Raman Lidar return signal, the background noise elimination is very important. Numerical results show that significant improvements in background rejection can occur if the telescope aperature is designed properly and this design is range dependant.

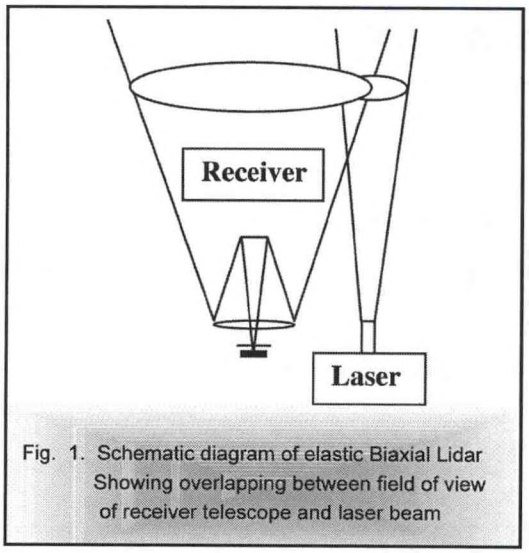

Fig. 1. Schematic diagram of elastic Biaxial Lidar Showing overlapping between field of view of receiver telescope and laser beam

Introduction

The Geometric Factor (GF) or overlap function has a great effect on reducing the background radiation in a LIDAR system GF .depends on the range you need to take measurements. The laser radar observations of aerosols for short distances have been discarded because of the unknown factor of insufficient overlapping between the transmitting laser beam and the field of view of the receiving optics. On the other hand, it is commonly assumed that once the FOV of the Lidar Transmitter and receiver are overlapping, the efficiency of collection is unity (Measures). However, this analysis does not properly take into account the position of the collected beam on the image plane of the detector and therefore, the true efficiency factor can be thought of as a product of the GF and the collection efficiency at the image plane. To understand these effects more accurately, we first look at the GF for a Bi-axial arrangement. which is consistent with the arrangement for Raman Lidar systems.

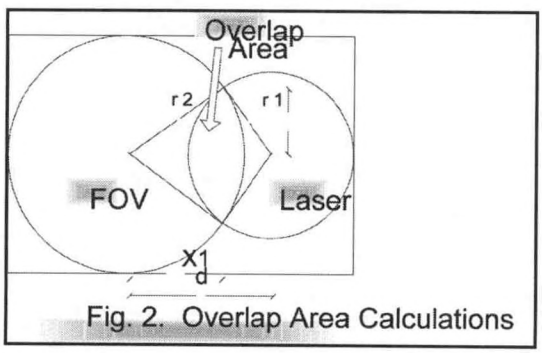

Fig. 2. Overlap Area Calculations

As the range increases, there will be a point of partial overlap and then complete overlap. They intersect at some distant point so that the ratio of the overlapping area to the laser beam cross section is small at short distances, i.e. small geometric factor as shown in figure 1.

It is clear that simple geometric arguments can estimate the GF efficiency as a function of range and the receiver and the transmitter parameters and that this term could theoretically be compensated for as illustrated in figure 2.

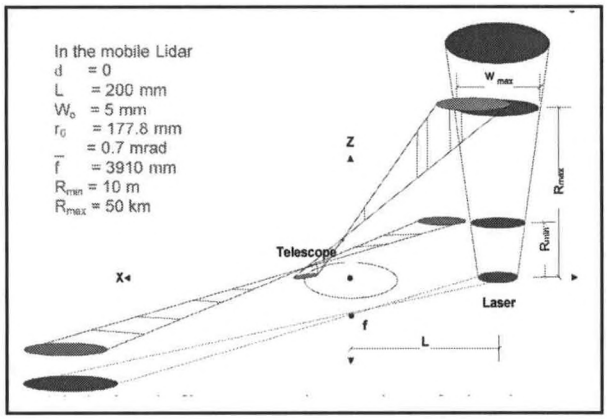

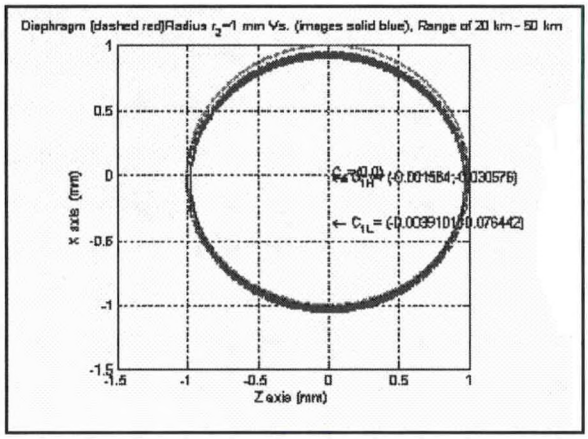

Figure 3. Modification of image spot on image plane at different ranges.

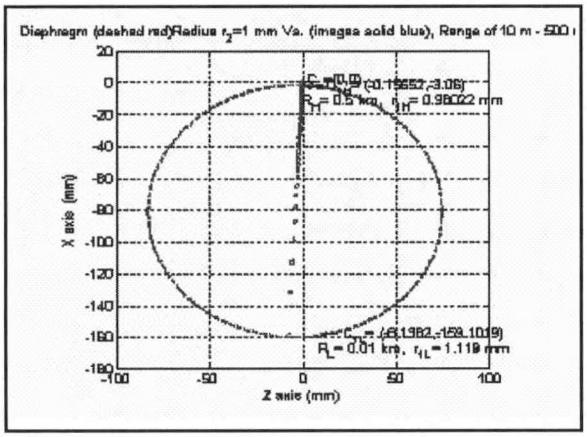

Figure 4a. Variation of the Image Spot on the image plane for far field

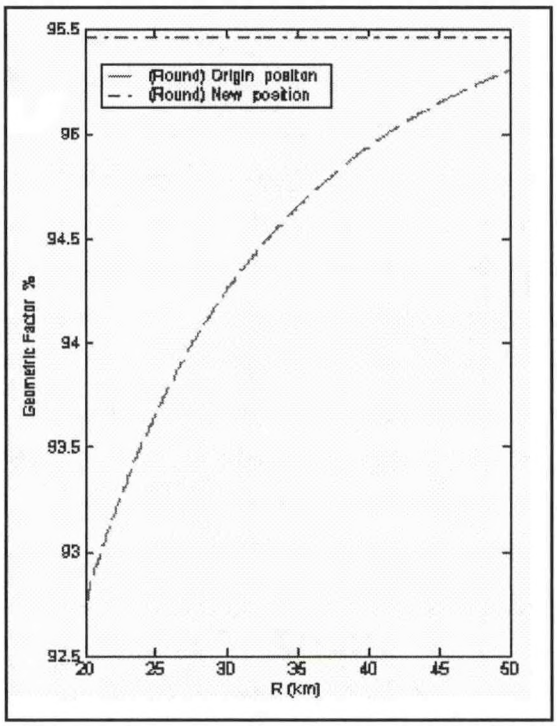

Figure 4b. Efficiency parameter of original and redesigned aperture for far field

It should also be pointed out that these effects are very sensitive to misalignment in the optical system making near field observations impossible. On the other hand for sufficiently large ranges, the misallignement and sensitivity issues become less problematic so that reasonable optical designs are simplified and the design of a unique aperature to cover certain desired ranges become feasible (Sasano et al).

However, if this is the only compensation performed, the analysis will be incomplete. The imaging properties of the telescope are such that only if a light source is at infinity will the telescope image the object directly onto an aperture located on the optical axis. As the range gets closer, the object no longer is illuminated on the optic axis so that when going through the lens collection, will focus the light both off the optic axis as well as deform the image from a symmetrical circular pattern. This behavior which is relevant to biaxial arrangements is illustrated in figure 3. In particular, we see that as object gets closer, the center of the image moves significantly off of the geometric center and that this rapid movement of the image on the detector plane makes it almost impossible to detect unless the aperature is so big that it is swamped with background noise. While it is clear that this is effect does not affect the conclusions of the GF which states that no useful collection can occur in the near field, this mechanism can have significant impact even at far distances where the GF would be unity.

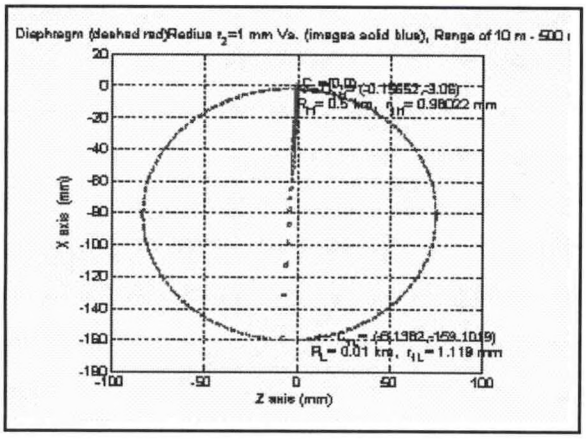

Figure 5a. Variation of the Image Spot on the image plane for near field

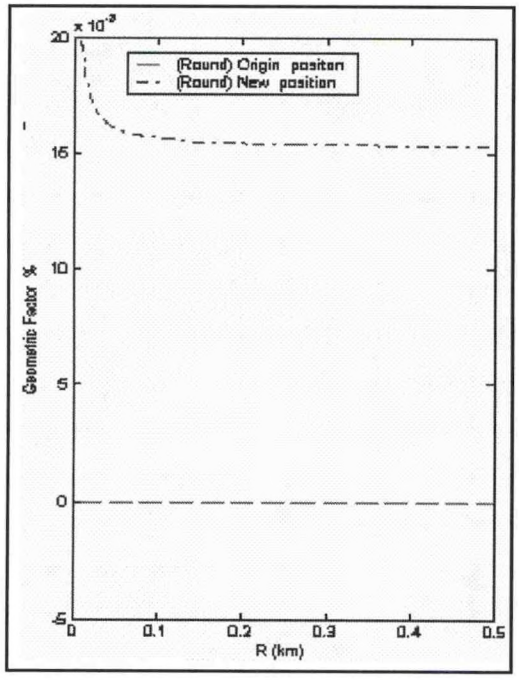

Figure 5b. Efficiency parameter of original and redesigned aperture for near field

It is this region which is of the most importance since it can is the most relevent for Lidar sensing.

Results

The basic theory to analyze the image spot for a biaxial lidar and the relative efficiency which is defined as the ratio of the image spot on the focal plane to the aperature can be calculated (Agishev et al 2002). In particular, it was illustrated within this theory that circular aperatures may not have the best efficiency since the tracks of the image spots can vary but that certain wedge shape apertures may be more efficient. In this paper, we reexamine this idea with a particular emphasis on developing a design criterion for a set of operating regions. To see the problems in the most glaring way, we first examine the cases in the far field which we define as R > 20km.

For this case, we observe in figure 4a that the image spot as we vary the range from 20km to 50km is quite stable and does not vary much over the field aperature. If we use the original aperature, the movement of the image spot will cause a range dependant efficiency factor (gain) to occur. While it is not very problematical in this region where only 2% variation is observed, it can be alleviated by redesigning the aperature to be the smallest circular aperature which captures the entire image spot over the entire range. It is clear that this will result in less efficiency as more background light is collected so there will be a tradeoff between range independent gain and increased noise. This result is seen in figure 4b.

In Figure 5, we illustrate the near field behavior corresponding to the object at range of 500 meters to 2 km verses for the two different aperature designs.

In this case, the image moves completely off the optic axis thereby resulting in an efficiency or GF of zero. On the other hand, it is conceivable that a sufficiently large aperature could capture the signal but tat the expense of significantly increased noise as illustrated in Fig. 5b.

In the most important region between 2 and 20km, the tradeoffs become more acute. In Figure 6a, we see the significant variation in the signal efficiency when using the original aperture. If we use the gain flattening aperture, we see that significant background radiation will occur.

Conclusions

For Raman lidar applications where the aperature size needs to be as small as possible, we show that such a choice results in strong range dependant gain effects. This trade off of undesirable effects makes it necessary that more complex field apertures be constructed which can maximize the efficiency. Calculations which will examine the improvement of wedge type apertures over circular apertures still needs to be investigated.

ACKNOWLEDGEMENTS

This work is supported by grant from NOAA #NA17AE1625.

REFERENCES

Agishev, Ravil R. and Adolfo Comeron, "Spatial filtering efficiency of monostatic biaxial lidar: analysis and applications", Applied Optics 41, 7516-7521, 2002

Sasano, Y. H. Shimizu, N. Takeuchi, and M. Okuda, Geometrical form factor in the laser radar equation: an experimental determination, Appl. Opt 18, 3908-3910 (1979)

Measures R.M , Laser Remote Sensing: Fundamentals and Applications, Wiley New York, (1984).

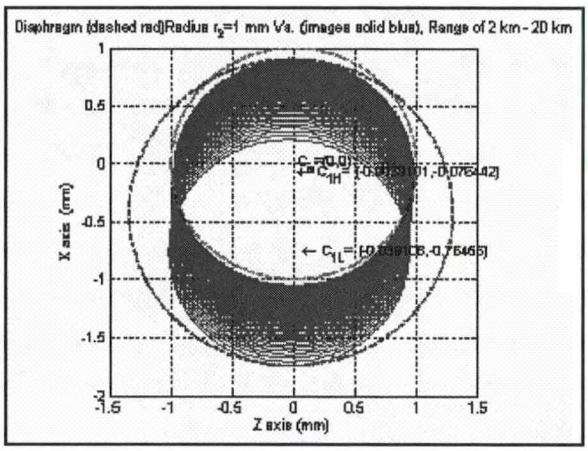

Figure 6a. Variation of the Image Spot on the image plane for far field

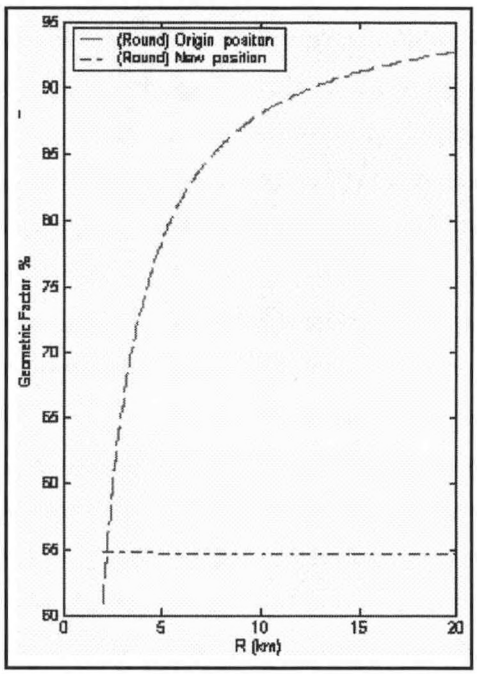

Figure 6b. Efficiency parameter of original and redesigned aperture for near field

Mapping Nevada Biomass using Optical Scattering Spectrometry and a Modified Vegetation Index Procedure

Nick Steiner, Marco Vargas, Sasha Alimova, Glenn Minko, Al Katz and Jeffrey Steiner
EAS Dept, CCNY, NY 10031

Optical scattering spectra for sagebrush and other plants collected over an area of more than 10,000 square kilometers of north eastern Nevada show a broad maximum in the visible to near infrared range centered at approximately 680 nm. Big Mountain Sage spectra exhibit a single, well-defined maxima with an intensity dependent in part on soil chemistry; other sage show a split maxima with bands on either side of the 690 chlorophyll absorption band: a stronger peak at 750 nm and a weaker, broad maxima at 600 nm. A synthetic soil-vegetation profile yields several discriminations of vegetation type in an ASTER Satellite image using ENVI computer 'decision' algorithms. In combination with established spectra for commercially grown and wild grass varieties, this permits the construction of a time series evaluation of the encroachment behavior and environmental interactions between these several types of sage plants. Preliminary Fourier Transform Infrared measurements of combustion products are of potential use for detecting brush fires.

Time Series Characterization of New York City Aerosols: Geochemistry and Optical Spectrometry Data

Aparna Lakhankar, Marc Cesaire, William Dennis, John Sangobowale, Elizabeth Rudolph and Jeffrey Steiner

The heavy metal content of the total suspended aerosol masses collected using a MetOne E-Bam beta attenuation impactor and a polycarbonate filtration system for the summer of 2004 variations in heavy metals correlate to a first approximation with the optical density data measurements produced by the Aeronet sensors. A preliminary assessment indicates that the net iron and titanium content of the total suspended aerosol mass create more than seventy five percent of the optical absorption signal. Analyses by x-ray fluorescence, and plasma emission show that the net barium content can exceed 45,000 ppm in a 4 hour collection interval on polycarbonate filter papers; similarly, lead concentrations can reach 35 ppm over the same interval. Scanning electron microscope and energy dispersive micro-analyses show that lead is present both as individual lead particles and as lead sulfate.

Water Vapor Turbulent Flux Over a Heterogeneous Landscape

Miliaritiana L. Robjhon, Everette Joseph, Jose D. Fuentes
NOAA Program on Atmospheric Sciences, Howard University

In this presentation, the water vapor exchanges between the surface and the atmospheric boundary layer over a complex heterogeneous landscape are examined. The water vapor turbulent flux is observed at the Howard University Beltsville site (39.054° latitude; -76.877° longitude) in an open area covered by grass and surrounded by trees. The site is in close proximity to urban and industrial zones which make it suitable for flux computations over a rural-urban landscape. The Howard University Beltsville site includes a 30-meter flux tower, fully instrumented with meteorological sensors including three-dimensional sonic anemometers and trace gas analyzers. The purpose of this study is to establish continuous and high quality water vapor flux datasets at the site, and to investigate the processes governing water vapor transfer within the lower layers of the atmospheric boundary layer during the forest defoliation period. The water vapor fluxes are all so employed to assess the fidelity of the water vapor exchanges treatment in the Weather Research and Forecasting mesoscale model.

AEROSE 2004: Bioaerosols and PM 2.5 Mass Determination

Yasmín Detrés and Roy Armstrong

NOAA Center for Atmospheric Sciences (NCAS), University of Puerto Rico at Mayagüez

The transport of Saharan dust across the Atlantic Ocean has a significant impact in the dispersal of microorganisms such as fungi, bacteria, and virus into the Caribbean. The smaller fraction of these bioaerosols, measured as PM 2.5, has the potential to induce regional health impacts, such as asthma and allergic reactions in sensitive individuals. High volume air sampling of PM 2.5 was one of the measurements integrated in the atmospheric component of the Aerosol and Ocean Science Expedition (AEROSE). This sampling, coordinated by NCAS researchers from the University of Puerto Rico at Mayagüez, took place from 1 to 15 March 2004 during the forward eastward trans-Atlantic leg of the cruise, from Barbados to the Canary Islands. The air sampling station consisted of a Thermo Andersen RAAS 2.5-400 cascade air sampler and a RAAS 200 reference sampler installed to collect PM 2.5 and PM 10 dust fractions, respectively, across the Atlantic. Both air samplers operated continuously at intervals of 48 hours. Samples were collected in Teflon and quartz filters (47 mm in diameter, 0.2µm pore size). Filtered samples were collected for gravimetric measurements (µgm-3), trace metal, minerals and microbiological analyses by molecular techniques. Concentration of PM 2.5 particles ranged from 0 to 120 µgm-3. Peak values were observed on filters from March 5 - 9 when the ship encountered a massive plume of Saharan dust. Details about the employed molecular techniques and the identified species will be presented.

SABER Temperature Validation Using Ground-Based Instruments

Moogega Cooper and James Russell III

Center for Atmospheric Sciences, Department of Physics, Hampton University, Hampton, VA 23668

moogega.cooper@pipeline.hamptonu.edu

The MLTI (Mesosphere Lithosphere Thermosphere Ionosphere) region of the earth's atmosphere is explored through the Sounding of the Atmosphere using Broadband Emission Radiometry (SABER) instrument. SABER is one of the four instruments housed on the Thermosphere Ionosphere Mesosphere Energetics and Dynamics (TIMED) satellite. SABER uses infrared limb emission to sound the atmosphere and measures accurate values of temperature, ozone, water vapor, carbon dioxide, and key parameters describing the energetics of the high atmosphere. SABER results are being used to study the chemistry and dynamics of the mesosphere and the effects on the atmosphere due to major solar storm events. The temperature data from SABER measurements is plotted against temperature measurements collected from several ground based instruments for the purpose of verifying the SABER data. These ground based instruments are located all over the world, including e.g. Boulder, Colorado; Mauna Loa, Hawaii; and parts of Russia. The ground based instruments used for validation of SABER temperatures have already undergone scrutiny and error analyses, and are used as a benchmark to validate data collected from SABER. Furthermore, nitric oxide measurements collected during a period of heightened solar activity is used to create global plots to illustrate the changing atmosphere as the Sun's radiation interacts with the Earth's atmosphere. These solar activity global plots illustrate the effects on the atmosphere as a result of solar

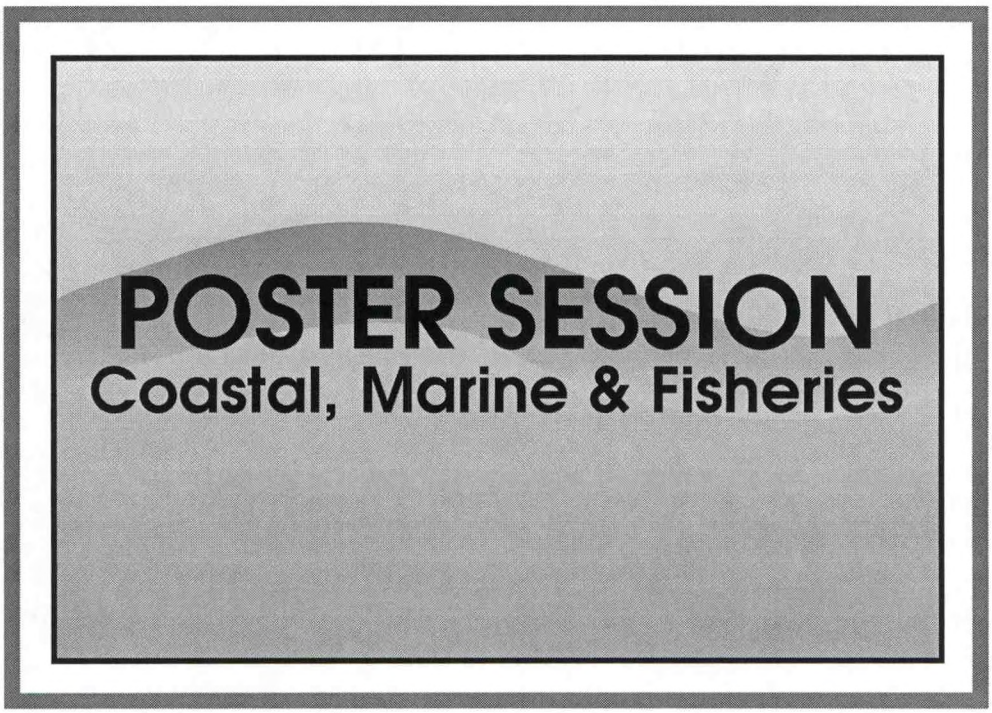
POSTER SESSION
Coastal, Marine & Fisheries

Endocrine and Social Mechanisms Underlying the Regulation of Sexually Dimorphic Behavior in a Protandrous Hermaphrodite, *Sparus Aurata*

José J. Reyes

Center of Marine Biotechnology, University of Maryland Biotechnology Institute;
701 E. Pratt St., Baltimore, MD 21202

Dr. Yonathan Zohar, Advisor

Sequential hermaphrodite fish are very useful models in the study of neuroendocrine factors controlling sexually dimorphic behavior because the same individual can express both male and female characteristics at different periods in its adult stage (Warner, 1975; Cardwell and Liley, 1991). Most of the research on sexually dimorphic behavior has focused on coral reef hermaphrodites. Reef-dwelling species are commonly used as research subjects in these studies because their ecology and ethology are well known. Many non-reef dwelling species are economically important and have the advantage of a protracted sex changing period, however because their behavior is not well known, they are not common research subjects. The gilthead sea bream is a protandrous pelagic hermaphrodite from the Mediterranean that has important economic value as an cultured species. In contrast to coral reef species, every sea bream individual undergoes a round of sex reversal every year (Zohar et al., 1995). Although, this life history strategy is more complex, it also offers the opportunity of a more predictable model. Furthermore, since the sexual inversion process in sea bream is longer than in reef fishes, any changes in the gonads or the brain can be studied at a higher time resolution. Behavioral differences between male and female fishes have been established for reef-dwelling hermaphrodites (Warner, 1975), but little is known about pelagic hermaphroditic species, including sea bream. Ethological studies of sexually dimorphic behavior in these animals are challenging because of the lack of conspicuous phenotypic differences between males and females, even during the spawning season. This lack of obvious differences exacerbates the common problem associated with ethological observations: the inaccuracy added by the subjectivity of the human observer. To establish an objective and accurate method for the study of sexually dimorphic behavior in sea bream and to eliminate the most common problems associated with ethological observations, I have developed a software-based method for analyzing the captive behavior of this fish. Transient whole-body and partial-body color changes in which a fish changes from light grey to dark grey (a melanic color morph) have been observed in sea bream during the spawning season. These color changes are often associated with characteristic chases which seem to be part of territorial aggression in sea bream. Preliminary observations have suggested that these melanic colored animals are the most aggressive individuals in the tank. As I expected females to be the most aggressive individuals in a sea bream spawning aggregate, I hypothesized that these melanic (dark) individuals are females. The software was designed to track only these melanic individuals by segmenting images based on color intensity. This computer program was written entirely in Microsoft Visual Basic 6.0 (VB 6), with specialized subroutines that can access the Windows API to load the individual frames that make up the AVI (movie) file. By transferring each of these frames from the AVI file into a VB 6 array, the entire image can be easily manipulated from within VB 6. Although, the program can handle full color images at resolutions up to 640 x 480 pixels, the image was segmented using only information from the green channel. Before analyzing each file, the user can enhance the dark regions in the images to compensate for the lack of uniform lighting inside the aquaculture raceways. This enhancement is very simple and involves setting up a reference "masking" image, based on a "no-animal" background-only image. The masking image overlaps the darker regions based on information from the red channel. This is done using a threshold value for the red channel which segments the image into dark and not-dark areas. A brightness filter is then applied on these dark areas only,

increasing the intensity of all channels. This is in essence analogous to shining a light selectively only in the dark regions. Although this could cause further lighting heterogeneousness, it serves the purpose of slightly homogenizing brightness without the use of complex filters. After this simple enhancement of dark regions, the user can select a threshold and can manually corroborate that the image segmentation only results in identifying the darker fish. Once this threshold is selected, it can be applied to all the videos, thus eliminating the subjectivity that is often associated with ethological quantification of color changes. Each fish in the tank was tagged, according to sex, with a small colored bead surgically attached to the dorsal fin. The computer was able to detect these colored tags accurately, using information from all three channels. The software grouped the data according to the presence of colored tags on fish. To detect these tags, the user selects upper and lower bounds thresholds for each of the three channels representing the range of colors that correspond to the tags. In this manner, each tag color will have a unique set of upper and lower boundary thresholds. The accuracy of this method is in part due to the fact that sea breams are grey or dark-grey, while the tags are usually yellow or red. Since the program only scans the area inside the fish, it can detect the tags a majority of the time without confusing them with other colored objects in the arena. From the positional information gathered by image analysis, the software calculated such parameters as the amount of time that the fish spent as a melanic color morph, the average speed of the animal, and the apparent size of the animal. Fish were held indoors in a six foot circular raceway with a video camera placed above the center of the tank. The camera was connected to a personal computer equipped with a video capture card and the system was set to record at 6 frames / second for 30 minutes at predetermined intervals. On two occasions, once early in the spawning season and then later in the spawning season, a group of four fish from one of our broodstock tanks was anesthetized with 2-phenoxyethanol, then sexed and tagged, and finally transferred to the filming tank. The first group consisted of three females and one male, while the second group had two females and two males. A third group with three females and one male was taken out of the brood-stock tank before the spawning season ended in order to tag the fish according to sex. These fish were placed in another tank and segregated according to sex using two concentric divisors inside an identical 6-foot raceway. This group of fish was held together with other sea bream from a similar year-class which were used in earlier experiments. This third group of animals was considered a non-spawning control group, because they would be filmed only after the spawning season had ended, which I had hypothesized should be a time of lessened aggression since in sea bream gonad regression occurs around this time. At the end of each experimental run, the animals were euthanized. Total length, total weight, and gonad weight were measured. Because I am interested in the control of behavior by specific neuroendocrine factors from the brain, the brains of the animals were collected under dry ice to measure mRNA levels of the peptides of interest (discussed below). Results from two different experimental groups showed that the female fish spent significantly more time as a melanic color morph than males (paired t-test). Average speed of the males in the tanks was significantly slower when compared to females. Furthermore, the presence of melanic color morphs was observed even after the spawning season. In the two experimental groups, the melanic individuals were present for many days after the beginning of the experiment. However, in the control group the melanic individuals were only present for a few days after the beginning of the experiment. This could suggest that the intensity of social aggression diminishes after the spawning season ends. Using this program, I have also ascertained other relevant baseline behavioral data, such as the circadian rhythm of this species in captivity. Indeed, the technology developed in this project for the analysis of behavior in captive pelagic fishes, could be applied to other studies of social structures in federally managed and economically relevant species.

Arginine vasotopressin (AVT), the teleost analogue of arginine vasopressin (AVP), has been identified in other species as a candidate neuroendocrine factor that can influence sexually dimorphic behavior (see for review Insel and Young, 2000). AVT controls calling behavior in birds and fish, and it can induce oviposition in hens, and it could be involved in the spawning behavior of many fishes. Other neuroendocrine factors may be involved in controlling sexually dimorphic behavior in fish, including the different isoforms of GnRH. How these factors interact with one another is not known. To study the role of AVT in the sexually dimorphic behavior of sea bream, I first localized the neurons that produce AVT in the brain of sea bream. As expected, these cells were found mostly in the pre-optic area of the hypothalamus. I have also cloned the full length AVT cRNA, using a sea bream brain RACE library. Using the sequence

obtained from the cloning experiments, I have developed a real-time fluorescence-based PCR assay to quantify the levels of mRNA in the brain of the fish observed in the behavioral experiments described above. Preliminary data suggests that males have lower levels of AVT mRNA when compared to females. I am currently working on cloning the AVT receptor, in order to investigate putative interactions between the AVT and the GnRH system.

Social control of sex reversal have been suggested in many species, including species in which the sex ratio of the population is maintained or changed according to the social structure of the population, such as occurs in sea bream. Because my observations suggest that the sexually dimorphic aggressive behavior is expressed year-round in sea bream, and because it is known that in other hermaphrodite species these aggressive interactions can affect the sex ratio of the population, understanding the factors controlling this behavior could lead to methods of controlling the sex ratio of spawning populations, both in the wild and in captivity. Also, because mating behavior in pelagic spawners, such as sea bream, consists of highly coordinated and stereotyped behavioral events, the ability to analyze and quantify this behavior is also a major contribution of this research. To my knowledge, this is the first time that a software-based method has been applied to the quantification of behavior associated with color changes in schooling fish.

ACKNOWLEDGEMENTS

I thank Steve Rodgers, Eric Evans and Dr. Brent Whitaker of the Center of Marine Biotechnology's Aquaculture Research Center, as well as Dr. Ten Tsao Wong of the Zohar Lab and Dr. Frank Hanson from University of Maryland Baltimore County, for their assistance in this research. This work was funded, in part, by the Living Marine Resources Cooperative Science Center (LMRCSC) of NOAA's Educational Partnership Program.

REFERENCES

Cardwell, J. R., and Liley, N. R. (1991). Hormonal control of sex and color change in the stoplight parrotfish, Sparisoma viride. Gen Comp Endocrinol 81, 7-20.

Insel, T. R. and Young, L. J. (2000). Neuropeptides and the evolution of social behavior. Current Opinion in Neurobiology 10:784-789.

Warner, R. R. (1975). The adaptive significance of sequential hermaphroditism in animals. The American Naturalist 109 (No. 965): 61-83.

Zohar, Y., Harel, M., Hassin, S. and Tandler, A. (1995). Broodstock management and manipulation of spawning in the gilthead seabream, Sparus aurata. In: "Broodstock Management and Egg and Larval Quality" (N. R. Bromage and R.J. Roberts, eds.) pp. 94-114. Blackwell Press (London, UK).

GRANULAR STARCH AS A CARBON SOURCE FOR ENHANCING DENITRIFICATION IN BIOFILTERS CONNECTED TO MARINE RECIRCULATING AQUACULTURE SYSTEMS

Megan M. Morrison[1,2], Yossi Tal[1] and Harold J. Schreier[1,2]

[1]Center of Marine Biotechnology, University of Maryland Biotechnology Institute, 701 E. Pratt St., Baltimore, MD 21202
Phone: 410-234-8874,FAX: 410-234-8896 e-mail: *Schreier@umbi.umd.edu*

[2]Department of Biological Sciences, University of Maryland Baltimore County, 1000 Hilltop Circle Baltimore, MD 21250

Introduction

Recirculating aquaculture systems (RASs) have become a preferred mariculture operation for farming fish due to their advantage in providing high yields of fish stock. Because the success of commercial aquaculture depends on creating an environment optimized for rapid growth, one of the potential benefits of using a semi-closed culture unit is the manageability of water parameters that influence fish health and growth rates densities (Timmons et al., 2001; Cytryn et al., 2003). At the same time, a major drawback of RASs stems from significant loading of organic matter derived from uneaten food and fecal excretion, which leads to oxygen depletion and the accumulation of toxic nitrogen compounds such as ammonia and nitrite (Prinsloo et al., 1999; Cytryn et al., 2003). As part of the remedy for these problems, solid wastes are usually removed by mechanical filtration or sedimentation. Also, RASs incorporate biological filtration that includes nitrification to remove toxic inorganic nitrogen. This microbially-driven process oxidizes ammonia to nitrite and, subsequently, nitrate, under aerobic conditions (van Rijn and Barak, 1998; Chen and Fornshell, 2000; Prinsloo et al., 1999). To alleviate the threat of low oxygen levels, oxygen is pumped directly into the culture chamber and heavy aeration is employed to ensure nitrifying bacteria receive ample oxygen for their oxidizing activity (Timons et al., 2001; Rusten et al., 1998).

Given the adequate treatments for such limiting factors, one of the biggest challenges is attending to oxygen or ammonia levels, but how to treat the accumulation of nitrate in recirculating systems that occurs as water exchange rates are reduced (Owsley, 2000). Up until now, few studies have focused on nitrate removal because high concentrations had not been considered to directly impact most cultured organisms (van Rijn and Barak, 1998). Yet, control of nitrate levels is justified as at least one fish species has been shown to suffer from nitrate stress (Hrubec et al., 1996) and waste management and disposal has become increasingly important in aquaculture operations as environmental regulations have become stringent (Arbiv & van Rijn, 1995; Owsley, 2000; Stuven & Bock, 2000).

The successful removal of nitrate from wastewater has been accomplished by the inclusion of biological denitrification, an anaerobic process that reduces nitrate to nitrogen gas. This process requires a suitable electron donor as a carbon and energy source to fuel the heterotrophic activity (Lee & Welander, 1996; van Rijn, 1996; Phillips and Love, 1998; Gomez et al., 2000). Denitrification of industrial wastewater containing high nitrate (>1000 mg-N/L influent) has been accomplished using an activated sludge process (Glass and Silverstein, 1999). van Rijn and Rivera (1990) attempted a similar nitrate reduction treatment by leading organic matter derived from uneaten feed and fish waste collection of an intensive tank through a denitrifying fluidized bed reactor. However, performance was unstable and highly unpredictable. A follow-up study that incorporated soluble carbon products readily improved denitrification (by Arbiv and van Rijn, 1995) suggesting that carbon limitation was the likely underlying cause for such poor initial activity (van Rijn and Rivera, 1990).

Because the concentration of available carbon substance in RASs may be insufficient for self-sus-

taining nitrate removal, an external source must be added (Isaacs et al., 1994; Phillips and Love, 1998). Chemostat experiments demonstrated the ability of activated sludge to yield comparatively high denitrification rates (from 26-76 mg NO_3-N/g TSS*h) when fed with carbohydrate carbon sources including hydrolyzed starch, methanol, acetic acid and crude syrup (Lee and Welander, 1996). Alternatively, Chen et al (1991) combined a nitrification loop and denitrifying submerged bioreactor, with excess methanol, in long-term continuous cultivations to show that 200-1000 mg NO_2-N/L could be completely reduced. In a more recent study on groundwater nitrate contamination, sucrose, ethanol and methanol were evaluated for their influence on denitrification potential of a submerged filter (Gomez et al., 2000). It was determined that a carbon source dosage is required to treat groundwater containing 100 mg/L NO_3-N nitrate, and, furthermore, alcohols were particularly effective.

In the present study, we sought to examine the influence of granular starch on stimulating denitrification activity of heterotrophic bacteria associated with a marine recirculating fish system biofilter. The low solubility of granular starch (compared to soluble starch or other soluble carbon sources such as glucose and acetate) suggests that it would be able to provide a long lasting source of carbon that could sustain nitrate reduction over time. Furthermore, its low cost, ease of usability, and non-toxic nature makes it an ideal exogenous carbon source to incorporate into RAS denitrification bioreactors. Our preliminary findings indicated that granular starch was effective in reducing nitrate and nitrite, as well as minimizing sulfide accumulation.

Materials and Methods

Batch experiments. Batch experiments were performed using polystyrene beads removed from high and low organic load recirculating saltwater biofilter systems. High biofilm load biofilters were obtained from a 2 m^3 nitrifying moving bed bioreactor (MBB) filled with a bead volume of 1 m^3. The aerobic MBB linked two 4.2 m^3 tanks containing 5-10 kg/m^3 of gilthead seabream, Sparus aurata, and a 150 L anaerobic cylindrical denitrification tank densely packed with 1-2 m^3 of polyethylene beads having a specific surface area of 500 m^2/m^3. The system was maintained with a salinity of 17 ppt was operated as described previously (Tal et al., 2003). Low organic load biofilter beads were collected from a separate nitrification unit that was connected to a large 6.3 m^3 culture tank consisting of full-strength seawater holding a variety of marine fish at stock density of approx. XX kg/m^3

Under anaerobic conditions and in the presence of nitrate, beads were incubated at room temperature until all endogenous organic sources were consumed. Once nitrate utilization could no longer be supported, corn starch, wheat starch, rice starch, soluble starch, glucose and (potassium) acetate was added to evaluate their ability to independently stimulate denitrification. Biofilter beads from the low organic load biofilter system were partitioned into 200 mL glass tubes containing 31 ppt synthetic saltwater media (Tal et al., 2003) at pH 7-7.5 and supplemented with 130 mg NO_3-N/L and carbon at a final concentration 2.7 mg/mL. The high organic load bead samples were treated in the same manner except that the salinity was maintained at 15 ppt. All sample solutions were flushed with nitrogen gas and tubes were immediately incubated at room temperature and rotated continuously at 10 rev/min in an Amersham Hybridization Oven/Shaker.

Sampling procedure. During the course of incubation, 1 ml samples were removed from each tube, centrifuged at 12,000 x g for 5 minutes and concentrations of nitrite, nitrate, total carbon (TC), and total available carbon (TAC) were determined using the supernatant fractions. Periodically, pH was adjusted to within the 7-7.5 range. All measurements were done in duplicate within 24 hours of collection and, when not analyzed immediately, were stored at 4°C.

Analytical determination. Nitrite and nitrate concentrations were determined as described by Tal et al. (2002). Biomass estimation of low and high load biofilters was achieved by drying beads at 90°C for 24 hours, followed by at least 15 hours of dessication and weighing. Beads were then completely stripped of organic matter by soaking in 10N sulfuric acid at 37°C for 24 hours, followed by vigorous vortexing in a warm 1% SDS solution for 5 minutes. After several rinses with deionized water, beads were incubated at 90°C for 24 hours, then dessicated for several hours before weighing. Biomass was estimated by subtraction. All analytical measurements were ±20%. TAC and TC of starch solutions were determined using the anthrone reagent as described previously (Tal et al., 1999).

Results

Effect of carbon source on denitrification potential of low organic load beads. To examine the ability of individual carbon sources to stimulate denitrification, low organic load beads from an active nitrifying biofiltration unit (see Materials and Methods) were incubated under anoxic conditions in the presence of nitrate (130 mg/L) in order to promote complete utilization of endogenous carbon sources. Our previous study showed that nitrate removal by denitrifying heterotrophs established within the nitrifying community could be stimulated after several days of incubation under anaerobic conditions (Tal. et al. 2003). Once nitrate utilization could no longer be detected, beads were then distributed equally in individual test tubes and nitrate removal was measured in the presence of acetate, soluble starch, and granu-

Figure 1. Nitrate removal for low load beads.

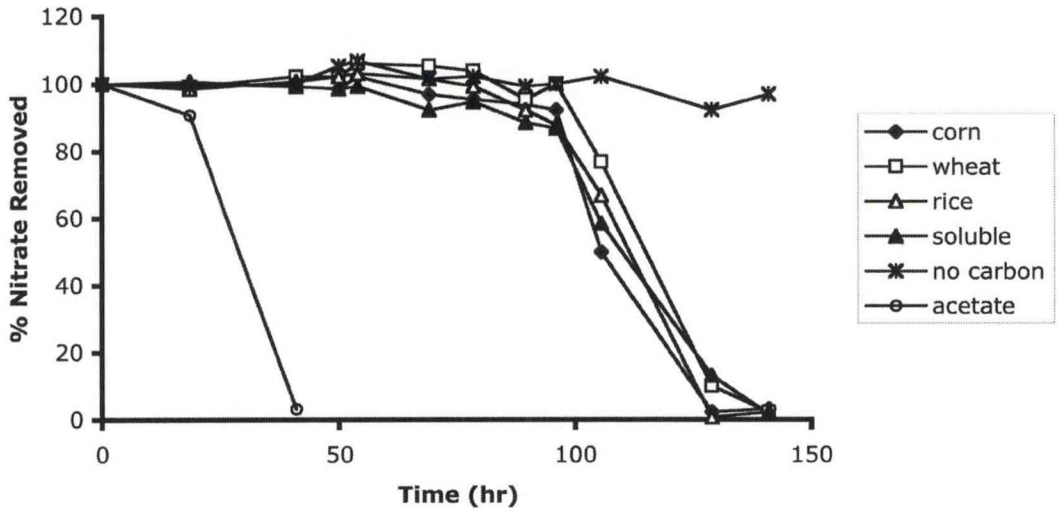

with soluble starch. These results suggest that the granular starches

Figure 2. Nitrate removal after treatment with additional nitrate (see text for details).

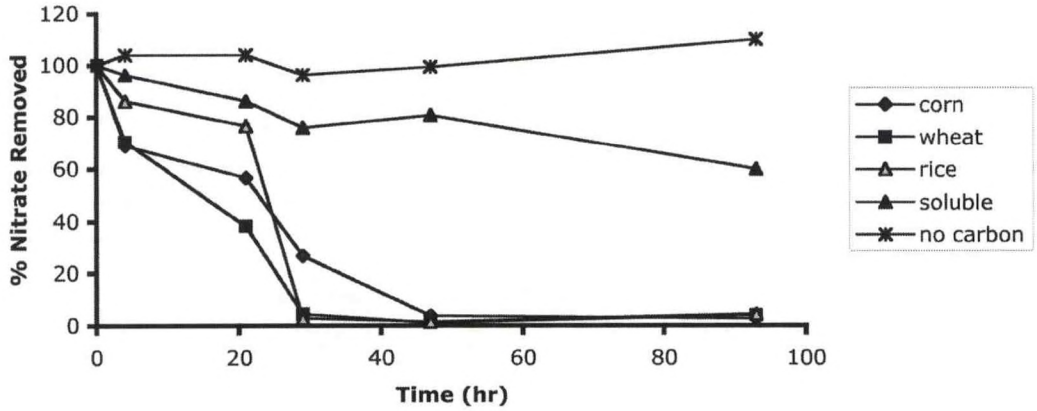

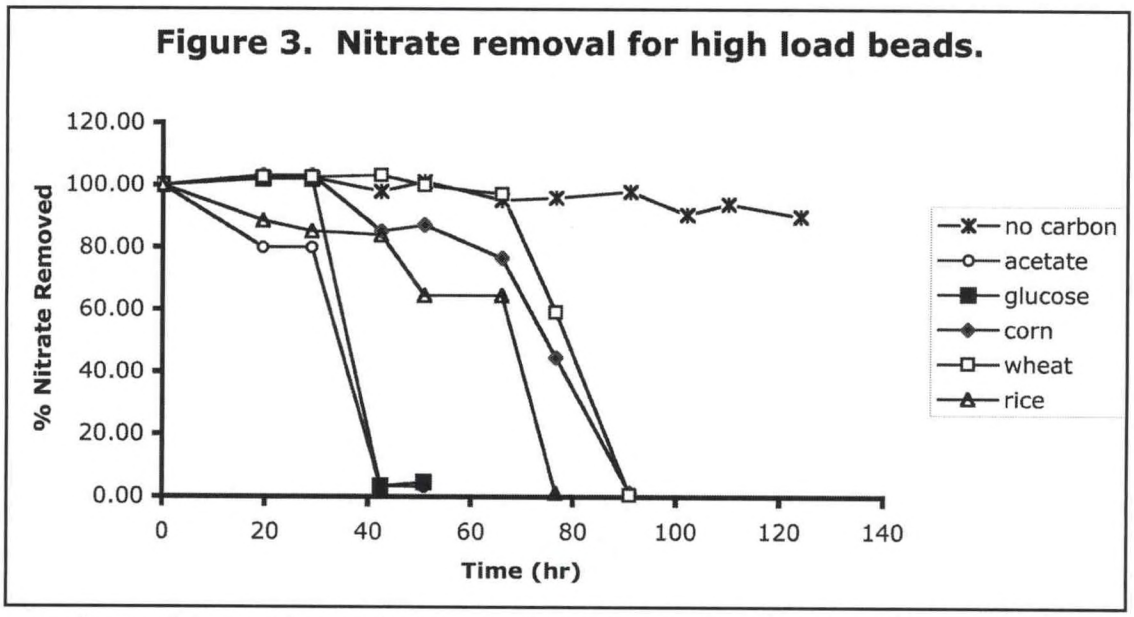

lar corn, wheat and rice starches, as described in Materials and Methods. As can be seen in Figure 1, compared to control (no carbon source addition), all carbon sources were capable of providing the reducing power necessary for nitrate utilization. While nitrate removal rates were similar for all sources, activity with acetate occurred almost 75 hours before the more complex sugars. Furthermore, we did not detect any difference between soluble starch and any of the granular starches in nitrate removal rates.

In all cases, nitrite was found to accumulate and then disappear within a ten-hour period prior to the onset of nitrate removal (not shown). At 21 hours following addition of acetate, nitrite was at its highest level (20 mg/L) and completely disappeared after nitrate was utilized. Similarly, at 96 hours, nitrite levels peaked between 35 and 50 mg/L for corn, wheat and rice starches and 21 mg/L for soluble starch. At 106 hours, or at the time just prior to the onset of nitrate removal, nitrite levels decreased to approx. half the maximum levels, and completely disappeared after all nitrate was utilized.

Upon cessation of nitrate utilization we could not detect the presence of any soluble carbohydrates in filters supplemented with soluble and granular starches. To assess any denitrification potential remaining within these filters, we treated them with a second dose of nitrate (130-180 mg/L) at 160 hours after carbon source addition. The results, shown in Figure 2, revealed that filters that had been supplemented with granular starch were capable of eliminating this additional nitrate within 20-30 hours at rates comparable to the rates obtained from the first nitrate treatment, with wheat and corn starch responding faster than rice. The filter supplemented with soluble starch, on the other hand, was very slow in removing nitrate, with 60% remaining after 90 hours (Figure 2). Similar results were obtained for the granular starches when we treated the filters with a third dose of nitrate, with nitrate removal not observed for the filter supplemented with soluble starch. These results suggest that the granular starches provide a carbon source reservoir....

Denitrification potential of high organic load beads with added carbon source. The characteristics of beads from a high organic load biofiltration system were examined in the same manner as the low organic load beads (Figure 3). After determining that the beads were not capable of utilizing nitrate in the absence of carbon source we added acetate, corn, wheat and rice starches as well as glucose as carbon sources. As was observed for the low organic load beads, all carbon sources were capable of stimulating nitrate removal, with both acetate and glucose yielding 100% removal approx. 40 hours after addition. For the granular starches, however, reduction of nitrate appeared earlier for the high load system and at a faster rate than the low-load system, with some differences obsesrved between corn, wheat and rice starches.

Discussion

In systems relying on activated sludge or submerged filters to reduce nitrate, ethanol and methanol, as well as acetate, have been supplied as suitable carbon sources (Lee and Welander, 1996; Stief,

2000; Yoon and Park, 2001). However, these substances are expensive and require a high degree of maintenance due to the need for frequent application. The fact that simple carbon sources are readily available to denitrifying bacteria means it is favored for nitrogen removal over more complex ones (Gomez et al., 2000) and will be used up at a fast rate. Our results are consistent with this observation since the low and high organic load biofilters derived from partially closed recirculating aquaculture systems strongly reduced nitrate when presented with acetate. On the other hand, when soluble starch was used for denitrification, this carbon source was very effective in reducing nitrate in the low organic system.

The fact that the nitrifying biofilters originating from the RAS involving a denitrification loop means it is likely that these biofilters are already primed with denitrifiers. This would obviously lead to faster denitrification, which would account for the initial nitrate removal rates for acetate and glucose trials.

Experimental conditions employing granular starch led to more stable denitrification For both biofilter sets, a similar pattern was seen in that corn, wheat and rice starch-filled tubes showed comparable denitrification rates during the first stage of the experiment. The sample with soluble starch acted in the same manner as the granular forms when present with low organic level beads, but differential activity was observed immediately following the first nitrate spike that occurred at 160 hours. As granular starch trials proceeded to take nitrate, soluble did not. TAC and TC readings did not reveal any detectable carbohydrate (starch) levels in the tube solutions. Since the control did not take nitrate, we deduce carbon must have been supplied by starch, which was visibly tied up in filters. All three granular starches that were tested in this study are composed of varying particle size, which may influence its metabolism by heterotrophs. Corn, rice, and wheat starch have a reported diameter of 3-5 microns, 2-6 microns, and a mixture of 5-10 micron and 20-50 micron size, respectively (International Starch Institute). On the other hand, soluble starch samples displayed undetectable levels for carbon substrate at 160 hours and at just 19.5 hours in the high load biofilter treatments, accordingly. To summarize, soluble starch ran out much faster than the granular starches.

Conclusion

According to the present study, it appears that granular starches, in the form of small particles, can act as a slow-release carbon source to sufficiently fuel biological denitrification. Up to now, the majority of studies on this wastewater treatment process have focused on mixed liquors. Recently, the granular polymer polyhydroxybutyrate, a constituent of sludge, was successfully implemented as an external carbon source to stimulate denitrification. However, these alternatives are costly and there is both an economical and practical advantage to using granular starch. Furthermore, the characteristically low solubility of starch seems to contribute to a more predictable and stable denitrifying environment. This information will prove to be helpful in selecting the most appropriate form of starch for a RAS. In order to strategically design the best denitrification bioreactor for a given operation, it is necessary to characterize the relationship between starch characteristics and anaerobic nitrate reductive pathways that are driven by heterotrophs. We have applied granular starch as an electron donor to a large-scale intensive recirculating aquaculture system and have effectively maintaind safe levels of nitrate with minimal nitrite accumulation within the culture tank.

ACKNOWLEDGEMENTS

We thank Steve Rodgers, Eric Evans and the staff of the Center of Marine Biotechnology's Aquaculture Research Center for their assistance in this research. This work was funded, in part, by the Living Marine Resources Cooperative Sciences Center (LMRCSC) of NOAA's Educational Partnership Program. Megan Morrison is a LMRCSC graduate fellow.

REFERENCES

Arbiv R and van Rijn J. "Performance of a treatment system for inorganic nitrogen removal in intensive aquaculture systems." Aqua. Eng. 14 (1995): 189-203.

Chen S.-K., Juaw C.-K., and Cheng S.-S. "Nitrification and denitrification of high-strength ammonium and nitrite wastewater with biofilm reactors." Water Sci. Tech. 23 (1991): 1417-1425.

Cytryn E, Gelfand I, Barak Y, van Rijn J, and Minz D. "Diversity of microbial communities correlated to physiochemical parameters in a digestion basin of a zero-discharge mariculture system." Env. Micro. 5 (2003): 55-63.

Hrubec T.C., Smith S.A., and Robertson J.L. Nitrate toxicity: a potential problem of recirculating systems. in Libey GS and Timmons MB (eds). Proceedings from the Successes and Failures in Commercial Recirculating Aquaculture Conference. Northeast Regional Agricultural Engineering Service, Ithaca, NY. 1996. pp. 41-48.

Isaacs S., Henze M., Soeberg H., and Kummel M. "External carbon source addition as a means to control an activated sludge nutrient removal process." Water. Res. 28 (1994): 511-520.

Glass C. and Silverstein J. "Dentirificaiton kinetics of high nitrate concentration water: pH effect on inhibition and nitrite accumulation." Water Res. 32 (1998): 81-839.

Gomez M.A, Gonzalez-Lopez J., and Hontoria-Garcia E. "Influence of carbon source on nitrate removal of contaminated groundwater in a denitrifying submerged filter." J. Haz. Mat B 80 (2000): 69-80.

Kelso B.H., Smith R.V., and Laughlin R.J. "Effects of carbon substrates on nitrate accumulation in freshwater sediments." Appl. Env. Micro. 65 (1999): 61-66.

Lee, N.M. and Welander, T. "The effect of different carbon sources on respiratory denitrification in biological wastewater treatment." J. Ferm. Bioeng. 82 (1996): 277-285.

Oh J, Yoon S.M., and Park J.M. "Denitrification in submerged biofilters of concentrated nitrate wastewater." Water Sci. Tech. 43 (2001): 217-223.

Owsley, David E. Water management: hatchery water and wastewater treatment systems. (2000) pp986-994.

Prinsloo J.F., Roets W., Theron J, Hoffman L.C., and Schoonbee H.J. "Changes in some water quality conditions in recycling water using three types of biofiltration systems during the production of the sharptooth catfish Clarias gariepinus (Burchell)." Water SA 25 (1991): 239-252.

Phillips, J. B. and Love, N.G. "Biological denitrification using upflow biofiltration in recirculating aquaculture systems: pilot-scale experience and implications for full-scale." Proceedings from International Conference on Recirculating Aquaculture, Roanoke, VA, (1998) pp.171-178.

Stuven, R. and Bock, E. "Nitrification and denitrification as a source for NO and NO2 production in high-strength wastewater." Water Res. 35 (2001): 1905-1914.

Tal Y., Watts J.E., Schreier S.B, Sowers K.R., and Schreier H.J. "Characterization of the microbial community and nitrogen transformation processes associated with moving bed bioreactors in a closed recirculated mariculture system." Aquaculture 215 (2003): 187-202.

Tal Y, van Rijn J, and Nussinovitch A. "Improvement of mechanical and biological properties of freeze-dried denitrifying alginate beads by using starch as a filler and carbon source." Appl. Microbiol. Biotechnol. 51 (1991): 773-779.

Timmons M.B., Ebeling J.M., Wheaton F.W., Summerfelt S.T., and Vinci B.J. Recirculating Aquaculture Systems. Cayuga Aqua Ventures (2001) pp.650 Ithaca, NY.

van Rijn, J. and Rivera, G. "Aerobic and anaerobic biofiltration in an aquaculture unit- nitrite accumulation as a result of nitrification and denitrification." Aquacult. Eng. 9 (1990): 217-234.

van Rijn, J. "The potential for integrated biological treatment systems in recirculating fish culture- A review." Aquaculture 139 (1996): 181-201.

van Rijn, J. and Barak, Y. "Denitrification in recirculating aquaculture systems: from biochemistry to biofilters." Proceedings from Third International Conference on Recirculating Aquaculture, Roanoke, VA, (1998) pp.179-187.

EFFECT OF TOXIN ISOLATED FROM THE CHESAPEAKE BAY DINOFLAGELLATE, *KARLODINIUM MICRUM* ON SUCCESS OF THE PARASITIC DINOFLAGELLATE, *AMOEBOPHYRA* SP.

Samala Lewis[1] and Allen R. Place[2]

Morgan State University[1] and Center of Marine Biotechnology, University of Maryland Biotechnology Institute[2], LMRCSC graduate student

Marine biotoxins and harmful algae represent a significant and expanding threat to coastal and freshwater fisheries throughout the United States. We have recently shown that *Karlodinium micrum* produces a unique suite of marine biotoxins with hemolytic, cytotoxic, and ichthyotoxic properties. Moreover, these toxins have been isolated from natural waters at the sites of fish kills. Parasitic dinoflagellates of the genus *Amoebophrya* infect and kill bloom-forming dinoflagellates, including the toxic species *Karlodinium micrum*. Unlike non-toxic hosts, *K. micrum* is partially resistant to infection, a trait that may be related to toxin production. Here we tested the hypothesis that parasitism of *K. micrum* is inversely related to toxin concentration in the culture medium. Time-course studies were conducted to determine the influence of extracted toxin and toxin carrier (methanol) on host growth, parasite load, and parasite prevalence. Methanol concentrations below 0.1 % had no effect on these variables. When methanol concentration was maintained below 0.1 %, extracted toxin equivalent to 102 - 105 *K. micrum* ml-1 had no effect on host abundance or parasite prevalence. Parasite load, however, differed across treatments, with the mean number of infections host-1 occurring at intermediate toxin concentrations. We also considered the effect of intracellular host toxin on success of *Amoebophrya* dinospores when inoculated to *K. micrum* cultures of differing toxicity (strain SERC>B1>C6>GE2). Parasite prevalence and load was consistent across strains. Results indicate that *K. micrum* toxin is not an effective defense against parasitism by *Amoebophrya* sp. Thus, it seems unlikely that the partial resistance to infection observed in *K. micrum* is related to toxin production.

Changes In Expression of eIF4E-3 During Muscle Development In Zebrafish

Kibwe Lee*, Bhavesh Joshi and Rosemary Jagus

Center of Marine Biotechnology, University of Maryland Biotechnology Institute
*LMRCSC undergraduate intern

Muscle growth depends on sustained muscle protein synthesis, which in turn is regulated by the translational initiation factor eIF4E. eIF4E (recently renamed eIF4E-1) recruits mRNAs to the ribosome through its ability to recognize and bind to the 5' cap structure. In addition, eIF4E-1 interacts with another translational initiation factor, eIF4G and a group of competitive inhibitors of eIF4G binding, the 4E-BPs. Recently, the Jagus laboratory has identified additional eIF4E-like proteins, 4E-LP and eIF4E-3, that exhibit differing characteristics to eIF4E-1 and appear to play a role in the regulation of protein synthesis. It is hypothesized that each member of the eIF4E-family fills a specialized niche in the recruitment of mRNAs by the ribosome through differences in their abilities to bind cap and/or in their relative abilities to interact with eIF4G and the 4E-BPs, adding complexity to the regulation of mRNA recruitment. Although eIF4E-1 and 4ELP are ubiquitously expressed, the expression of eIF4E-3 has only been found in muscle. Like eIF4E-1, eIF4E-3 interacts with the 5' cap structure, and eIF4G, but not with the 4E-BPs. In this study, the expression of eIF4E-3 has been monitored during development in zebrafish embryos by whole mount in situ hybridization and compared with the expression of eIF4E-1 and 4E-LP, as well as the muscle-specific mRNA, MyoD. Sequences from the nucleotide databank at NCBI (GenBank) were probed with the amino acid sequence of zebrafish eIF4E-1 using the NCBI BLAST search software. cDNAs corresponding to 4E-LP and eIF3 were identified and used to generate constructs transcribing antisense RNA to 4E-LP and eIF4E-3. The dig-labeled antisense RNA has been used to probe whole mount embryos of zebrafish over the first 24 h of development to include somitogenesis.

CHANGES IN GENE EXPRESSION OF THE MIH ENDOCRINE SYSTEM IN THE BLUE CRAB (*CALLINECTES SAPIDUS*) DURING A MOLT CYCLE

Richard Hodges[1]* and John M. Trant[2]

Savannah State University[1] and Center of Marine Biotechnology, University of Maryland Biotechnology Institute[2], *LMRCSC summer intern

The changes in endocrine hormones associated with molting in crustaceans has been well described but the use of molecular tools permits an examination of the mechanism by which these changes are driven. In this study, immature blue crabs were isolated and monitored for molting activity in captivity. Eye stalks (site of MIH production in the X-organ/sinus gland), Y-organs (site of production of the steroidal hormone, ecdysone), mandibular organs (site of MF production) and blood (for the determination of hormonal titers in plasma) were taken from crabs at discrete times throughout the molt cycle. Using the sensitive method of real-time, quantitative RT-PCR, transcript abundances (a measure of gene regulation) were determined for MIH (molt inhibiting hormone), CYP4 (the regulatory enzyme for ecdysone production), and OMT (the regulatory enzyme of the MF pathway). Radioimmunoassays (RIA) were utilized for the determination of ecdysone titers in hemolymph. This preliminary study will form the basis for more intensive studies of the mechanisms by which reproduction and molting processes are regulated. An understanding and potential manipulation of these processes represents a critical component in our ability to efficiently culture these organisms for both commercial (e.g., aquaculture) and fisheries (e.g., stock replenishment) interests.

Analysis of the Microbial Community of the Chesapeake Red Beard Sponge, *Microciona prolifera*

L. T. Isaacs, J. Kan[2], S. Sidiqqi[3], D. Horn[1], F. Chen[2], T. Wright[4*], J. Enticknap[2] and R. Hill[2]

[1]Goucher College, Towson, MD; [2]Center for Marine Biotechnology, University of Maryland Biotechnology Institute, Baltimore, MD; [3]Becton Dickinson Microbiological Systems, Sparks, MD, [4]University of Maryland, Baltimore, MD., *LMRCSC undergraduate intern

Prokaryotes form a major proportion of sponge wet mass and are thought to have co-evolved with sponges over a period of 500,000 years. This symbiosis is interesting from the aspects of host-microbe interactions, microbe to microbe interactions, microbial diversity, and as a potential pharmacopeia. Total counts of microbes from nine sponge samples of *Microciona prolifera*, from three collection sites, were determined by counting DAPI-fluorescent cells from homogenized sponge tissues. Many cells exhibited autofluorescence, one of which was characteristic of chlorophyll. Plate counts of serial dilutions indicate that about 1% of microbes from the sponge was cultivable on marine agar medium. Five colonial morphotypes were collected from each plated sponge sample. Sponge-associated actinomycetes were isolated from ISP2 and starch casein agar media. DNA was extracted from lyophilized sponge tissue, PCR amplified for 16S rDNA, and analyzed by DGGE. Three different DGGE analyses indicated the presence of five major bands of 16S rDNA and several minor bands, a pattern very different from the 16S rDNA fingerprints of Chesapeake Bay water samples, suggesting that sponge microbial community differ from that of the Chesapeake Bay water in which they are found. Residue homogenate of sponge tissue from DNA extraction inhibited the growth of *Mycobacterium tuberculosis*. Since sponge growth is in millimeters per year, any pharmacological potential of sponges can only be realized through sponge culture or through isolation of any microbe(s) producing the bioactive metabolites. Eight samples of *Microciona prolifera* were maintained in captivity, initially in a flow through aquaculture system, and subsequently in recirculation tanks. Feeding frequency to maintain viability was determined. Wild and captive sponge yielded bacterial isolates with distinct morphotypes indicating changes in cultivable bacteria during captivity.

Optimization of Aquaculture Rearing Systems for Blue Crabs (*Callinectes Sapidus*)

Patrick Enekwe[1]*, Odi Zmora[2], Yonathan Zohar[2]

University of Maryland Eastern Shore[1] and Center of Marine Biotechnology, University of Maryland Biotechnology Institute[2], *LMRCSC summer intern

A rearing experiment to determine the possibility of blue crab growth constraints dependent upon the size of habitat was carried out to determine the feasibility of optimization aquaculture rearing systems. During June to August 2004, one hundred and twenty C-3 blue crabs were obtained from photoperiod manipulated brood stock. A feeding protocol based on adult *Artemia*, sliced squid and Ziegler® 1/8" pellets. Forty replicates of three types of compartmental cell were used to determine if there is any significant difference in growth, molt length and molt percent size increase. The result of the experiment determined, using the chi-squared data analysis with a P-values <0.05 accepted as significant, that juvenile blue crabs (*Callinectes Sapidus*) in varied sized individual cell compartments exhibit no significant difference in growth, molt length and molt percent size increase.

COLOR ADAPTATION OF THE BLUE CRAB, *CALLINECTES SAPIDUS*

Jelani Clement[1]*, J. Sook Chung[2], Odi Zmora[2], Jana Davis[2]

Hampton University[1] and Center of Marine Biotechnology, University of Maryland Biotechnology Institute[2]

*LMRCSC summer intern

Juveniles of the blue crab *Callinectes sapidus* can change their body color, to adapt to the color of environment. They responded to dark background condition by expansion of a high level of dark pigment in chromatophores. On lighter color conditions, they adjusted the their body to pale light color by reducing dark but dispersing red pigment. Pigment dispersing hormone (PDH)-I , when injected into the blue crab, caused a black color expansion, whilst the injection of red pigment concentrating hormone (RPCH) resulted in the dispersion of red color. Our results indicated that these hormones might be responsible for color adaptation, when the crabs were placed to different backgrounds. The RT-PCR was used to determine the expression levels of RPCH, PDH-I and PDH-II.

USE OF CLAY MINERAL (MONTMORILLONITE) FOR REDUCING POULTRY LITTER LEACHATE TOXICITY (EC50)*

Gian Gupta and William Gardner
University of Maryland Eastern Shore

Poultry litter (PL) has useful nutrients and is therefore used as manure. In addition to N, P and K, PL also contains some heavy metals (As, Cd, Cu, Mn, Pb and Zn), antibiotics, antioxidants, mold inhibitors and other organic compounds. Poultry litter aqueous leachate (PLL) has been shown to be toxic to many organisms; PLL is more toxic than the aqueous leachate of other animal manures used on agricultural soils. Clayey soils are known to retain toxic heavy metals. The objective of this study was to measure the change in toxicity (EC50) of PLL on the addition of clay mineral – montmorillonite. A significant reduction (124%) in toxicity of the clay-poultry litter leachate (CLL) after 7 d was observed compared to the toxicity of the PLL alone after 1 d. This indicates that some of the toxic components of the litter were adsorbed by the clay.

*This article has been accepted for publication (J. Haz. Mat.)

ENDOCRINE DISRUPTER –ESTRADIOL- IN CHESAPEAKE BAY TRIBUTARIES*

Gian Gupta and Nelum Dorabawila
University of Maryland Eastern Shore

Exogenous chemicals that interfere with natural hormonal functions are considered endocrine disrupting chemicals (EDCs). Anthropogenic EDCs released to the environment cause hormone imbalance in natural systems and thus mimic or modulate endogenous hormones. Estradiol (17b-estradiol or E2) is the most potent of all xenoestrogens. E2 is bioactive at remarkably low environmental concentrations. Induction of vitellogenin (VTG) production in male fish occurs at E2 concentrations as low as 1 ng l-1.

E2 reaches aquatic systems mainly through sewage and animal waste disposal. Surface water samples from ponds, rivers (Wicomico, Manokin and Pocomoke), sewage treatment plants (STPs), and coastal bays (Assawoman, Monie, Chincoteague, and Tangier Sound – Chesapeake Bay) on the Eastern Shore of MD were analyzed for E2 concentrations using ELISA (enzyme linked immuno-sorbent assay). E2 concentrations in river waters varied between 1.9 – 6.0 ng l-1. Highest E2 concentrations in river waters were observed immediately after the STPs. The effluent released from Salisbury, MD STP into the Wicomico River, which is considered to be one of the most polluted rivers, showed a high E2 concentration of 53 ng l-1. Two of the ponds showed E2 levels < 2.3 ng l-1; the relatively higher E2 concentration (7.6 ng l-1) observed in the Princess Anne, MD pond can be attributed to the presence of over 100 Canada geese. E2 concentrations in all the coastal bays tested were about 2.3 ng l-1 each.

*This article has been submitted for publication (ENV. POLLUT.)

Nonylphenol Toxicity and its Occurrence in Delmarva's Rivers and Coastal Waters

Tedra Booker and Gian Gupta
University of Maryland Eastern Shore

There have been many concerns raised recently regarding the environmental impacts of alkylphenol ethoxylates, as they have been shown to be endocrine disruptors. Alkylphenol ethoxylate are nonionic surfactants, which are used in laundry detergents, the textile industry, and in the manufacture of paper. The main metabolites of alkylphenol ethoxylates are nonylphenol and octylphenol. This research focuses on nonylphenol. Nonylphenol has been shown to have a higher acute toxicity than its parent compound to freshwater fish and is estrogenic at low concentrations. The estrogenic effects have been demonstrated in rainbow trout and chicken embryos. Nonylphenol (1.8 _g/L) has been found to produce egg yolk protein (vitellogenin) in male rainbow trout; vitellogenin is absent in male fish growing in clean water. In this research, we will measure the amount of nonylphenol in Delmarva's rivers and coastal waters using gas chromatography/mass spectrometry. We have measured the toxicity of nonylphenol using the Microtox_ (Photobacterium phospherum) toxicity testing system. We will also study its toxicity to *Daphnia magna*.

The Application of Production Agriculture Technology to Large-Scale SAV Restoration in the Chesapeake Bay

Tony Mazzaccaro, Scott Jones, Michael Bonsteel

Department of Agriculture, University of Maryland Eastern Shore, Princess Anne MD 21853

In the past half century, research on submerged aquatic vegetation (SAV) in the Chesapeake Bay and elsewhere has increased at a dramatic pace. There are many reasons for the emphasis in this area of science but the most important is concern for the health of the estuaries, inland bays, and coastal areas where these plants exist. SAV beds are habitat and nursery areas for small fish and crustaceans, buffer wave action, and actively improve water quality by acting as sediment and nutrient traps and releasing oxygen into the aquatic environment. The absence of SAV, particularly eelgrass (*Zostera marina*), in the Chesapeake Bay is one of the major contributing factors to its decline as a healthy, productive ecosystem.

In the 1930s, a "wasting disease" decimated the eelgrass beds along the eastern United States seaboard. Since then, there has been slow repopulation of historic grass bed areas. This loss prompted the initial research on eelgrass restoration procedures. The most common restoration approach used in the past forty years is to manually harvest plants from "donor beds" and transplant them in areas deemed suitable for eelgrass growth. This procedure is very costly and time ineffective. A maximum effort transplant project yields one acre of plants in one week at the cost of approximately $100,000. This manual transplanting procedure is analogous to the agricultural techniques of humankind millennia ago.

We at University of Maryland Eastern Shore feel that these results are not acceptable considering the goals set by the Chesapeake Bay Program and the technology available to improve restoration efforts. The CBP set a goal of 114,000 acres of restored eelgrass beds to be achieved by 2008, which would represent almost 20% of historical acreage (compared to the current level of 10%). To reach this goal restoration procedures must be updated. Production agriculture offers a simple solution to the slow and costly current techniques for eelgrass restoration: greenhouse produced seedlings and mechanized planting of these seedlings.

Currently, there is one SAV planting machine in use on the eastern seaboard. This was conceived of and constructed by Jim Anderson of Florida, and has been used with success in Florida, the Rappahannock River of Virginia, and other sites. This vehicle is currently used in transplanting eelgrass harvested from one site to a nearby restoration area. Unfortunately, plants must be taken from donor beds, thereby weakening these existing beds, to create new beds. The use of a mechanized planter is a valuable practice when combined with a sustainable supply of cultured plants.

We at UMES are currently in the first year of a three-year greenhouse SAV seedling production project funded by NOAA. This project will produce Eelgrass seedlings in multi-celled horticultural trays or flats, to be used by a mechanical transplanting vessel. We are experimenting with cell size and shape, planting mediums, and biodegradable containers such as, but not limited to, peat pots. The greenhouse allows for environmental control to maximize growth as conditioned water is circulated over the plants. While we are now working with eelgrass, a marine species, future plans include dedicating part of the greenhouse to accommodate fresh water species, such as wild celery (*Vallisneria americana*).

While this greenhouse system should have great success, producing large numbers of SAV seedlings without the means to have them planted efficiently has marginal merit. If large scale SAV restoration is to be achieved, both large numbers of cost effective seedlings must be produced and a means of mechanically planting them developed. The goals for our proposed mechanical planting vessel are to plant _ hectare per workday with plants on _-meter centers in one meter of water. Our hope expectation is that this highly efficient method of planting, when combined with a production agriculture approach to grow large numbers of SAV seedlings, will become one of the new standards of large-scale SAV restoration projects.

ESSENTIAL FISH HABITAT AS DETERMINED THROUGH FRESHWATER HABITAT UTILIZATION PATTERNS OF AMERICAN EELS (*ANGUILLA ROSTRATA*) IN THE ST. JONES RIVER, DELAWARE

Jessie C. Thomas, Dewayne A. Fox, and Michael A. Reiter

Department of Agriculture and Natural Resources, Delaware State University, Dover, DE 19901-2277

According to recent surveys, American eel (Anguilla rostrata) stocks along the Atlantic coast are thought to be in decline. To this end, the ASMFC Fishery Management Plan cites a need for studies focused on identification of habitat and movement patterns for American eels. We plan to document yellow-phase American eel habitat utilization using telemetry in the Delaware National Estuarine Research Reserve, St. Jones River, Delaware. Like many areas surrounding Delaware Bay, the St. Jones River watershed is currently experiencing changes due to increased urbanization. Through the use of telemetry, we will document long term (>9 months) spatial and temporal patterns of American eel behavior and habitat utilization. Ultimately, we hope to develop a habitat suitability model for American eels in the St. Jones River watershed. Our proposed research will provide needed information to assist in refining American eel management strategies and habitat restoration efforts in the mid-Atlantic region.

Species Diversity and Composition of Coastal Bay Estuaries of Maryland

Joseph W. Love and Eric B. May

Living Marine Resources Cooperative Science Center, University of Maryland, Eastern Shore, Princess Anne, MD 21853

Managing essential fisheries habitat along the eastern coast of the United States must include an understanding of how estuarine fish assemblages are influenced by water quality and the surrounding landscape. Northern coastal bays of Maryland are highly urbanized, and are often subjected to algal blooms and hypoxia. Although these bays are likely nursery grounds for several species of fish, the relationships among land use, water quality, and fish assemblage structure are not well-understood. Water quality variables were measured and fish assemblages were sampled monthly (April 1996 – November 1999) for 1,161 sites. From 1996 – 1997, a total of 93,812 ray-finned fishes were collected using otter trawls. The most abundant species was the bay anchovy (Anchoa mitchilli), which usually occupied greater than 50% of the catch for both years. Atlantic herring (Clupea harengus), Atlantic silverside (Menidia beryllina), and spot (Leiostomus xanthurus) were also abundant depending on the sampling location and month of collection. We initially divided sampling locations by the level of human impact: low impact, moderate impact, and high impact. Species number ranged from 38 to 62 across levels and years, and was highest during mid-summer when abundance, salinity, and water temperatures peaked. Ordination methods and multi-response permutation procedures will be used to explore how assemblage structure differs across space and time, and how species are associated with environmental gradients. Preliminary data suggest that monthly variation in diversity is highest in high-impacted sites, and that diversity differed little among levels and between years for each level. We will develop regression models that predict diversity from water quality and land-use variables using data from 1996 – 1997 for all species, resident species of the coastal bays, and species that utilize sea grass beds. The accuracy of the model will be assessed using two independent data sets from 1998 and 1999.

Sedimentary Organic Content and Grain Size Distributions of Bare and Vegetated Salt Marsh in Savannah, GA

J. Pearson and C. Pride

Savannah State University, Savannah, GA

This study was conducted to better understand the impact of Spartina alterniflora dieback on sediment properties and detrital food availability through comparison of bare and adjacent vegetated salt marsh areas. This project is part of an ongoing study of the sedimentary organic matter content and grain size distributions of Georgia coastal salt marshes. The study was conducted in Savannah, Georgia at Talahi Island, Skidaway Island, and Lazaretto Creek in spring 2004. Each site was selected due to the presence of bare patches within otherwise vegetated marsh and to ensure inclusion of both high and low marsh regions. Push cores were used to take 3 replicate samples from each bare patch and adjacent vegetated marsh near low tide. All samples were dried to determine the water content and combusted to analyze the organic content of the sediment. Grain size analyses were conducted on the Talahi Island samples through wet sieving techniques using 63, 125, 250, 500, and 4000 μm sieves. Organic content was determined for each size fraction.

The Skidaway Island low marsh sediments had greater mean water content than the Skidaway high marsh site due to greater submergence time and less drainage time as the tide receded. There was a significant difference between the mean water content of Lazaretto vegetated (53.86%) and bare high marsh (41.65%) with greatest water retention in the vegetated zone. However, there was no significant difference between vegetated and bare patch water content at the remainder of the sites.

Samples collected on Skidaway Island high marsh locations had lower mean combustible matter content than in the low marsh, yet there was no significant difference between bare and vegetated sedimentary organic content in either the low marsh or high marsh sites at Skidaway. In contrast, vegetated zones of both the Lazaretto (high marsh) and Talahi (low marsh) had greater organic content (~20%) than adjacent bare spots (~14%). At the Talahi site, ~60 to 87% of the organic matter was in the smallest (<63 μm) size fraction, with the highest values found in the site that had likely been bare the longest. Second in abundance in all Talahi sites was the >4000 μm fraction size (~3-33%). Variations in the size distribution of organic particle size could have implications for food availability for marsh detritivores.

Introduction

Salt marsh die back has a affected a little over a thousand acres was first noticed in Georgia around the spring of 2002 when local residents noticed that there were bare patches in the salt marsh.. Salt marshes rank among the most productive ecosystems on the earth and are the habitat for many animals and plants. Bare mud had been observed sloughing into the water at some dieback sites in Georgia indicating the potential for habitat loss (Alber and Flory, year???). The marsh has since shown sign of recovery but the full impact of this drought-related event is unknown. Detritus from dead marsh plants is a source of nourishment for many species. This study will give more insight into the impacts of dead marsh syndrome and bare patches of other origins on the sediments and detritus in the marsh. The sedimentary organic content and grain size distributions of vegetated and bare salt marsh patches will be compared.

Materials/Methods

Samples used in this study were taken from three different marshes in the Savannah, GA region: Lazaretto, Talahi, and Skidaway marshes. Lazaretto marsh is located near a tidal creek and an access road to a fish-

ing pier on the Lazaretto Creek near Tybee Island, . The bare patch and adjacent vegetated marsh samples taken at Lazaretto were in a narrow high marsh region not far from the road. The Talahi site is located on a large residential hammock (Talahi Island) inland from Tybee and is situated very close to homes. There is little high marsh at this site. Talahi samples were taken along a transect monitored as part of an ongoing study at Savannah State University and at two additional locations ("extremely bare" and "extremely vegetated" sites beyond the transect). The Skidaway Island samples were taken from a research boardwalk in the marsh. Both high marsh and low marsh samples were taken here.

Samples were collected in March 2004. Push cores were used to collect 3 replicate samples from both healthy and bare sites at Talahi Island, Skidaway Island, and Lazeretto Creek. Crucibles were cleaned, dried in a 60°C drying oven, and weighed. Each sample was homogenized and then an aliquot was taken for combustion. The subsamples were dried at 60°C overnight, stored in the dessicator for 1 hour, weighed and placed into the muffle furnace at 550 °C for 2 hours. After they had cooled, the samples were placed in the dessicator for 1 hour and then weighed.

Grain size analyses were completed on the Talahi Island samples. Each sample was homogenized and a subsample was weighed. Samples were wet sieved with sieve sizes: 4000µm, 500µm, 250µm, 125µm, and 63µm. Each size fraction was rinsed onto filter paper, dried overnight at 60°C and weighed. The samples were then transferred to crucibles and placed in a 550°C combustion oven for 2 hours so that the organic content of each grain size could be determined.

Results

Trip 1 Skidaway Island 8 March 2004

The mean percentage of water content was 70.36% in the Skidaway bare low marsh. In Skidaway healthy low marsh, the mean percentage of water content was 70.47%. Skidaway healthy low marsh had a higher percentage of mean water content than Skidaway bare low marsh. Mean percentage of combustible matter was 19.11% in Skidaway bare low marsh. In Skidaway healthy high marsh, the mean percentage of combustible matter was 15.74%. Skidaway bare low marsh had a higher mean percentage of combustible matter than Skidaway high low marsh.

The mean percentage of water content was 42.99% in Skidaway bare high marsh. Skidaway healthy high marsh has a mean percentage of water content of 44.90%. Skidaway healthy high marsh has a higher percentage of mean water content than Skidaway bare high marsh. The mean percentage of combustible matter is 6.98% in Skidaway bare high marsh. The mean percentage of combustible matter is 7.26% in Skidaway healthy high marsh. Skidaway healthy high marsh has a higher mean percentage of combustible matter than Skidaway bare high marsh.

Mean water content percentage was higher in Skidaway low marsh than Skidaway high marsh sites (Refer to Table 1).

Trip 2 Lazeretto Creek 8 March 2004

Lazeretto bare has a mean water content percentage of 41.65%. Lazeretto healthy has a mean water content percentage of 53.86%. Lazeretto healthy has a higher mean water content percentage than Lazeretto bare. The mean combustible matter percentage was 14.24% in Lazeretto bare. The mean combustible matter percentage was 19.78% in Lazeretto healthy. Lazeretto healthy has a higher mean combustible matter percentage than Lazeretto bare (Refer to Table 1).

Comparsion Trip 1 to Trip 2

Skidaway low marsh has a higher mean percentage of water content than Lazeretto and Skidaway high marsh. Lazeretto bare had the lowest mean percentage of water content than Skidaway and Lazeretto bare. Bare sites had a lower percentage mean of water content than healthy sites.

Lazeretto and Skidaway bare high marsh have a lower percentage of mean combustible matter than Skidaway and Lazeretto Healthy. Skidaway bare low marsh had a higher mean percentage of combustible matter than Skidaway healthy high marsh. The lowest mean percentage of combustible matter was 6.98% in Skidway bare high marsh. The highest percentage of mean combustible matter was 19.78%

in Lazeretto healthy high marsh. Lazeretto had a higher percentage of combustible matter than Skidaway high marsh. Skidaway high marsh has a lower in percentage of combustible matter than Lazeretto and Skidaway low marsh.

Trip 3 Talahi Island 9 March 2004

(Data still in progress)

Discussion

Skidaway high marsh has a lower in percentage of combustible matter than Lazeretto and Skidaway low marsh. This could be due to larger impacts of energy such as higher tides and more wave action. This study has several trends for instance Skidaway low marsh has a higher mean water percentage of water content than Lazeretto and Skidaway high marsh.

This study should be replicated to see if the same trends occur. There were several errors such as two crucibles dropped and the sample was spilled. One Talahi sample was not weighed before being sieved as a result weights could not be compared. This study should be conducted for a longer period of time to see if there were any changes in the data due to water content. Some samples were not placed in the dessicator after being dried and weighed. Several mussels, crabs, and shells were observed in the bare patch samples however, a more extensive study should be conducted. It would be interesting to test for CaCO3 content. I did observe lots of shells in several sieved samples. Some paper was scraped into the samples.

REFERENCES

Department of Environmental Protection, Florida Marine Research Institute. "Marshes". http://www.dep.state.fl.us/coastal/habitats/saltmarshes.htm.

2. Flory, J. Alber, M. "Dead Marsh Information. Georgia Coastal Research Council. 2002.

3. Leeder, M.R. "Sedimentology Process and Product. 1982.

4. Wenner, Elizabeth. Dr. "Salt Marshes." Sea Science.
http://www.dnr.state.sc.us/marine/pub/seascience/dynamic.html

Evolution of Defenses Against Biotoxins by Daphnia pulexa

Victoria G. Taibe[1] and James F. Haney[2]

[1]V.G.Taibe-MEES-University of Maryland at Eastern Shore

[2]J.F. Haney-Department of Zoology, University of New Hampshire

Clonal populations of Daphnia exposed to toxic cyanobacteria undergo evolution in a relatively short amount of time, less than 30 years. We examined changes in adaptations of clones of Daphnia pulex to toxic Microcystis aeruginosa strain 2385, to determine whether these represent short-term or long-term genetic/evolutionary adaptations.. The Daphnia population was fed toxic M. aeruginosa and studied for four generations, roughly the equivalent to one growing season, to track changes in their response to the biotoxin microcystin. We were testing the hypothesis that evolution can occur in a single growing season.

Clearance rate and feeding rate did not vary significantly between any of the four generations, whereas body weight and total mortality decreased significantly ($p<0.05$ for each successive generation exposed to the toxic cyanobacteria. MC accumulation trends show increased resistance to the toxin, with decreased MC accumulation across the successive generations. The feeding response (thoracic beats, post-abdominal rejections) trends show increased fitness for each successive generation. The trends shown by measured parameters indicate that evolutionary changes have occurred in one growing season.

THE INTESTINAL MICROFLORA OF FARM RAISED STRIPED BASS (*MORONE SAXATILIS*) AT DIFFERENT STAGES OF FISH DEVELOPMENT

Khalia A. Boyd[1]*, Clytrice Austin-Watson[2], Carolyn B. Brooks[1,2] and Salina Parveen[2]

[1]Department of Natural Sciences,
[2]Food Science and Technology Program, University of Maryland Eastern Shore, Princess Anne, MD

*Email address: *KhaliaBoyd@hotmail.com*

Striped bass is a popular species for recreational fishing and a major aquaculture product. Knowledge of the intestinal microflora of striped bass in aquaculture is important in the overall fish nutrition and prevention of disease in both the fish and the consumer. Therefore, the intestinal bacterial flora during the early stages of ontology was determined using the plate count method under aerobic condition. The total counts at 30, 60, 90, 150, and 180 days post-hatch ranged from 104 to 106 per gram of gut material. Predominant bacteria at 30 days post-hatch were Pseudomonas (52%) and Bacillus (26%). At 60 and 90 days post-hatch, the dominating bacteria were Aeromonas (39%), Bacillus (33%), and Aeromonas (58%) and Pseudomonas (32%), respectively. At 150 and 180 days post-hatch, Aeromonas was dominant (63% and 99%, respectively) bacterium. These results suggest that the intestinal flora of the fish primarily consisted of Aeromonas, Pseudomonas and Bacillus.

DETECTION OF HEMATODINIUM PEREZI IN BLUE CRABS (*CALLINECTES SAPIDUS*)

Lara Nagle*, Andrea Johnson, Joseph Pitula and Eric May

Living Marine Resources Cooperative Science Center, Department of Natural Sciences, University of Maryland Eastern Shore, Princess Anne, MD

*Email address: *lnagle@mail.umes.edu*

Hematodinium perezi is a parasitic dinoflagellate infecting blue crabs (*Callinectes sapidus*) and other crustaceans, including the Tanner crab and Norway lobster. In blue crabs the parasite has been found along the eastern coast of the United States from Delaware to Florida, and in the southern portion of the Chesapeake Bay. First reported in the Maryland Coastal Bays in the 1980s, *H. perezi* has become a significant cause of mortalities in the coastal bays resulting in loss of resource and diminished blue crab harvests. The current histological method used to diagnose infections in blue crabs is considered to be relatively insensitive and inefficient. To overcome the issues of sensitivity and inefficiency, an enzyme-linked immunoabsorbant assay (ELISA) is being proposed as a means of diagnosing *H. perezi* infections in blue crabs. This method has been used successfully to detect other pathogens and has been applied with limited success to H. perezi infections in the Norway lobster. If a more sensitive and efficient technique can be developed, filed assessments using the method could provide more detailed information on the distribution of the pathogen during its earliest stages of infection, relationship of infection rates to host density, and infection level required to cause mortalities.

A Pilot Study on Tag-Induced Mortality of Yellowtail Flounder (*Limanda Ferruginea*)

Larry A. Alade[1]*, Azure Westwood[2], Andrea Johnson[1], Steve Cadrin[2], Paul Rago[2] and Eric May[1]

[1]Living Marine Resources Cooperative Science Center, Department of Natural Sciences, University of Maryland Eastern Shore, Princess Anne, MD.
[2]Northeast Fisheries Science Center, NMFS/NOAA, Woods Hole, MA

*Email address: *oaalade77@yahoo.com*

A Mark and Recapture model is being developed by the Northeast Fisheries Science Center (NEFSC) that will provide accurate forecasts of yellowtail flounder (Limanada ferruginea) populations in the Northeast. However, the model carries uncertainties about the survival following the tag and release of fish. To determine the significance of mortalities and their effect on forecast models, a short-term holding experiment was conducted to consider the effects of capture and tagging procedures on the survival of yellowtail flounder. Fish were collected with an otter trawl and transported to the Northeast Fisheries Science Center (NEFSC) Woods Hole laboratory where they were acclimated for a period of 10 days. Fish were then randomly sub-sampled and tagged with Petersen disc tags. Histological assessment on acute (48 hrs) and short-term chronic (168 hrs) tissue response to the Petersen tags were done to evaluate the differences in tissue morphology between tagged and control groups. Additionally, a separate study was carried out on a set of pre-tagged fish to evaluate the patterns of daily mortality in both groups. Daily mortality rate (Z_) for tagged fish was modeled by adding a post-tag traumatic stress parameter (Z_) as a source of tag-induced mortality. Preliminary results from the model indicated an earlier and continuous decline in survival rate in tagged fish (50% in 15 days) compared to the controls (50% in 23 days). Model results suggest a daily mortality rate (Z_) of 0.12 (tagged and control) and an additional post-tag traumatic stress mortality rate (Z_) of 0.03 in tagged fish. In contrast, histology suggests no differences between both groups. Although the outcome of this study was inconclusive, information from the study should provide the basis for a future cage study to improve our mortality estimates for the yellowtail flounder cooperative tagging project.

PRELIMINARY EVALUATIONS OF BIOENERGETICS MODEL APPLIED TO STRIPED BASS (*MORONE SAXATILIS*)

S. E. Wood* and E. B. May

Living Marine Resources Cooperative Science Center, Department of Natural Sciences, University of Maryland Eastern Shore, Princess Anne, MD

*Email address: *swood@umes.edu*

Bioenergetics equations are typically used to estimate either growth or consumption rates in an individual or population, but as interest grows they are being readily adapted to investigate many other relationships such as predator-prey interactions, forage efficiency, etc. To better understand the relationships between consumption and the energy demands from growth and metabolic waste production used in bioenergetics models, experimental feeding trials will be conducted using striped bass (Morone saxatilis). Fish will be fed for twelve weeks. Daily consumption (g), weekly weight (g) and length (cm) will be measured. Blood samples will be collected every 4 weeks for analyses of blood parameters reflective of diet. At the end each trial fish will be euthanized, sexed, and analyzed for proximate body composition. Data will be compared across age classes to explore how ontogenetic shifts in diet influence the variables within the bioenergetics model. Results of this experiment will also be compared to subsequent studies in striped bass fed a more natural diet.

Toxicity of Nonylphenol in Delmarva's Rivers and Coastal Waters

Tedra Booker* and Gian Gupta

Living Marine Resources Cooperative Science Center, Department of Natural Sciences, University of Maryland Eastern Shore, Princess Anne, MD

*Email address: *TBooker@umes.edu*

There have been many concerns raised recently regarding the environmental impacts of alkylphenol ethoxylates, particularly their potential role as endocrine disruptors. Alkylphenol ethoxylate are nonionic surfactants, which are used in laundry detergents, the textile industry, and in the manufacture of paper. The main metabolites of alkylphenol ethoxylates are nonylphenol and octylphenol. This research focuses on nonylphenol. Nonylphenol has been shown to have a higher acute toxicity than its parent compound to freshwater fish and is estrogenic at low concentrations. The estrogenic effects have been measured in rainbow trout and chicken embryos. Nonylphenol (1.8 _g/L) has been found to produce egg yolk protein (vitellogenin) in male rainbow trout. In this research we will measure the amount of nonylphenol in Delmarva's rivers and coastal waters, using gas chromatography/mass spectrometry.

THE EFFECT OF CHEMICAL CONTAMINANTS ON DEVELOPMENTAL STAGES OF (*MORONE SAXATILIS*) EGGS AND LARVAE

William Gardner* and Eric May

Living Marine Resources Cooperative Science Center, Department of Natural Sciences, University of Maryland Eastern Shore, Princess Anne, MD

*E-mail address: wdgardner@mail.umes.edu

Striped bass (*Morone saxatilis*) is an anadromous species of fish with a long history of scientific investigation. The striped bass fishery in the Chesapeake Bay is tightly guarded due to drastic population declines during the 1970's and 1980's. These declines were attributed to over fishing which resulted in an increase susceptibility to pollution and natural stresses. Understanding striped bass larval mortality rates is essential in predicting population dynamics. Previous research indicates organic and inorganic contaminants inhibit survival of striped bass larvae during early life stages. Striped bass produce small eggs which contain egg yolks for several days of consumption. Larvae feed on their yolk supply for about 5 days after hatching. Toxic contaminants in striped bass egg yolk can potentially have a negative impact on larval development. The objective of this research will be to investigate the relationship between toxic contaminants in striped bass egg yolk and larval survival.

Role of Trace Element Contaminants and Nutrient Deficiency in Idiopathic Cardiomyopathy Affecting pygmy Sperm Whales, Kogia Breviceps

Ai'sha P. Washington* and Shawn White

Living Marine Resources Cooperative Science Center, Department of Natural Sciences, University of Maryland Eastern Shore, Princess Anne, MD

*Email address: *apwashington@umes.edu*

After many well-documented stranding events and corresponding pathobiological examinations, it was found that pygmy sperm whales exhibit signs of ventricular dysfunction and enlarged/weakened heart muscle, a condition known as cardiomyopathy. This condition occurs in approximately 50% of the stranding cases. Numerous factors may contribute to the development of cardiomyopathy in pygmy sperm whales, such as parasites, genetics, viruses, trace element contaminants and nutrient deficiencies. The role of trace element interactions in pygmy sperm whales was examined in order to study their potential contribution to cardiomyopathy in the species. The levels of arsenic, cadmium, and selenium in liver samples were determined using inductively coupled plasma mass spectrometer (ICP-MS) and correlated to the health of the animal in an attempt to unravel the cause of death of these marine mammals.

SUCCESS OF *SPARTINA ALTERNIFLORA* TRANSPLANTS AT A GEORGIA DIEBACK AREA: A PRELIMINARY STUDY

Hoskins D. L.
DOC/NOAA/NMFS and Marine Science Program, Savannah State University, Savannah, Georgia, USA, *Dionne.hoskins@noaa.gov*

Woolford, E.
Savannah State University, Savannah, Georgia, USA, *woolfor@savstate.edu*

Tenholder, P.
Savannah State University, Savannah, Georgia, USA, *tenholdp@savstate.edu*

Jenkins, J.
Savannah State University, Savannah, Georgia, USA, *jenkj@savstate.edu*

Nimrod, M.
Savannah State University, Savannah, Georgia, USA

This pilot project was part of a larger study to monitor *Spartina alterniflora* dieback sites in coastal Georgia and to determine the role of environmental and biotic factors that cause marsh dieoff. In June 2003, thirty-six shoots of *Spartina alterniflora* were taken from a healthy marsh and transplanted in a subsection of a large dieback site on Talahi Island, GA (USA). Thirty six shoots were also planted at healthy site on Country Club Creek, GA, (USA). Plants were monitored short and long term for plant health and colonization by macrofauna. Within 30 days, plants at the dieback site had noticeably declined and *Littorina* snails were also abundant. Plants in the healthy marsh were taller and had produced multiple shoots. After six months, plants at the dieback site were alive but significantly smaller than those at the healthy site. However, after twelve months no statistically significant differences in shoot production or growth were observed between plants grown at both sites. Date effects on growth were statistically significant and consistent with the natural senscence of *S. alterniflora*. Data from this project and another monitoring study at this site suggest that the Talahi dieback site appears to be in recovery.

HYPOXIA-INDUCED IMMUNE RESPONSE IN ATLANTIC MENHADEN, *BREVOORTIA TYRANNUS*

A.K. Johnson[1], J.F. Levine[2], C.A. Harms[2], James A. Rice[3] and J. McHugh Law[2]

[1] Living Marine Resources Cooperative Science Center, Department of Natural Sciences, University of Maryland Eastern Shore, Princess Anne, MD 21853, USA

[2]College of Veterinary Medicine, 3Department of Zoology, North Carolina State University, 4700 Hillsborough St., Raleigh, NC 27606, U.S.A.

Mass mortalities of Atlantic menhaden (*Brevoortia tyrannus*) attributed to low dissolved oxygen (DO) are relatively common in estuaries along the eastern United States. However, little is known about the sublethal health effects of these low DO events. The effects of acute and subacute exposures to low DO were evaluated in Atlantic menhaden under controlled laboratory conditions. Atlantic menhaden were acclimated for 2 weeks in 2000-L circular tanks (closed-aquaria) prior to initiation of the study. Hematology, plasma chemistry, and spleno-somatic indices were measured at five different oxygen saturations (5, 10, 15, 20, and 84%) in the acute study. Splenic transforming growth factor-b (TGF-b) mRNA, lymphocyte mitogenesis, and blood parameters were measured at 20% and 84% oxygen saturation in the subacute exposure study. In both experiments, glucose and electrolytes were the blood parameters most affected by hypoxic conditions. Blood glucose concentrations were elevated in both studies. Fish exposed to 5% oxygen saturation in the acute study displayed "relative" blood acidosis while those exposed to 20% oxygen saturation in the subacute exposure study displayed "relative" blood alkalosis. These effects may have consequences in estuarine systems where fish are exposed to multiple stressors, which may cumulatively affect their ability to endure adverse environmental conditions and resist disease.

EFFECTS OF THE GULF PERWINKLE *LITTORINA IRRORATA* DENSITY ON SMOOTH CORD GRASS *SPARTINA ALTERNIFLORA*

Crystal Jackson

Biology Program, Savannah State University, Savannah, Georgia 31404

Spartina marshes in coastal Georgia and southern Louisiana have been impacted by a phenomenon called "deadmarsh" (in Georgia) or "brownmarsh" (in Louisiana). The deadmarsh phenomenon is the dieback of over 100,000 acres of smooth cord grass. It is believed to be caused by one of four factors: microbes, drought, pollution, predation, or a combination of the above. While snails have been widely discounted as a singular casual factor, *Littorina irrorata* was in high densities at an impacted are currently under study. The feeding activity of the snails has the potential to damage plant leaves and make them more susceptible to microbial or fungal infection we choose to investigate their effect on plants grown in sediment from the dieback site and a healthy site. The objective of this research was to observe the health and growth of *Spartina alterniflora* plants grown in sediment from a healthy (SSU) or dying marsh (Talahi Island). Additionally, plants were exposed to different densities of *Littorina irrorata* to determine if their feeding produced any secondary effects on plant health.

SEASONAL VARIATION IN THE ABUNDANCE OF MEIOFAUNA IN AREAS DISTURBED BY RAY FEEDING PITS

Dwight A. Ebanks and Mary Carla Curran
Marine Sciences Program, , Savannah State University

Abstract

Bioturbation such as ray feeding pits disrupts meiofaunal communities, which are a food source for marine larval and juvenile fish including some of commercial value. These pits are seasonal and tend to be prevalent in warmer months. The objectives of this study were to determine whether there was seasonal variation in the abundance of meiofauna in undisturbed areas and whether there was seasonal variation in meiofaunal abundance in ray feeding pits relative to outside feeding pits. Core samples (1.1 cm wide x 3.0 cm deep) were collected monthly from August 2003 – July 2004 and enumerated for nematodes, copepods, ostracods, oligochaetes, polychaetes, and nauplii. Pits were only present from August – October 2003 and April – July 2004. Total meiofauna were always more abundant outside feeding pits than inside and the peak value was 4515.0 + 555.73 S.E. individuals•10 cm-2 in May 2004. The lowest value of total meiofauna in undisturbed areas occurred in October 2003 and was 1462.7 + 120.48 S.E. individuals•10 cm-2. Total meiofauna remaining after pit formation ranged from 73.8% of the undisturbed value in May (early in the season of ray activity) to only 28.5% of the undisturbed value in September (late in the season). The reduction in meiofaunal abundance may be due to a cumulative effect of ray bioturbation as the season progressed. Nematodes were consistently the most abundant meiofaunal taxon inside and outside of pits and were at least 89% of the total number. Because some meiofauna prey upon bacteria, fluctuations in meiofaunal abundance may influence the microbial loop and ultimately higher trophic levels of the food web.

The Abundance and Distribution of Zooplankton in and About Hudson Canyon

Erik Davenport, Livingston Marshall Jr., Christian Reiss, and John Govoni

The Hudson canyon, an east coast submarine canyon, is perceived as a "hot spot" for recreational and commercial fishing. The presence of high fish concentrations in canyons has been attributed to upwelling events that are associated with enhanced nutrients and higher zooplankton biomass than the adjacent shelf. Hudson canyon, in contrast, is characterized as a downwelling canyon. Downwelling is usually not associated with high fish or zooplankton concentrations. Therefore a fundamental question about secondary production in Hudson canyon remains: "Is Hudson canyon more productive than the adjacent shelf?"

Hudson Canyon was studied during a cruise (from May 10 to 15, 2001) aboard NOAA's RV, Albatross IV. Hydrographic data and zooplankton samples were collected from the Hudson Canyon area using a Multiple Opening Closing Net Environmental Sampling System (MOCNESS). Temperature, salinity, and density were used to define water types and measure horizontal and vertical changes in the canyon, adjacent shelf, and adjacent slope. Hydrographic data indicated shelf-slope mixing at locations in the canyon only. Zooplankton biomass at the canyon head and adjacent shelf were similar to each other, but were different from other locations within and seaward of the canyon. Zooplankton biomass was positively correlated with copepod concentration and negatively correlated with temperature, salinity, and density. Although the Hudson canyon was not more productive than the adjacent shelf; variations in copepod concentrations in association with hydrographic changes suggest a relationship between zooplankton biomass and shelf-slope exchanges within the canyon.

DEVELOPMENT OF A GIS FOR MAYAGÜEZ BAY

Ruben D. Raimundí and Fernando Gilbes

Geological and Environmental Remote Sensing Laboratory, UPRM-Department of Geology

Abstract

Mayagüez Bay, a semi-closed bay in western Puerto Rico, presents a complex dynamics due to river discharge and anthropogenic effects. River discharges show seasonal changes due to rainy patterns and anthropogenic activities include dumping of a Tuna Factory and Sewage of Treated Water. The main purpose of this project was to develop new ways of visualization and analyses for land-sea interactions in Mayagüez Bay. The field data were processed and organized in tables. Measurements of salinity, temperature, sediments, fluorescence and bio-optical properties were collected during the dry season (January to April) and rainy season (August to November). Graphical analyses were initially developed to evaluate the temporal and spatial variability of these parameters along the bay. However, this type of visualization presented major difficulties. In this work we created better and easier ways to understand how the different parameters interact and change in time and space. GIS maps were created using ArcGIS 8.3 using DOQ's and 3D Analyst procedures. These new visualization techniques are helping to better understand the oceanographic processes and bio-optical dynamics of Mayagüez Bay.

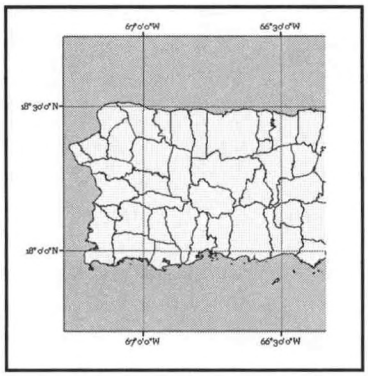

Figure 1 West Puerto Rico map, rectangle indicates the Mayagüez Bay area

Introduction

Mayaguez Bay (Figure 1) is a semi-enclosed bay in the west coast of Puerto Rico that suffers spatial and temporal variations in water quality parameters, due to seasonal discharge of local rivers and anthropogenic activities. The Añasco River is the largest river of the west coast, and although its basin was used for agriculture in the past, nowadays is much more developed. The Yagüez basin is highly developed and highly influenced by anthropogenic activities. The Guanajibo basin was traditionally dedicated to agriculture, especially to the sugar cane industry, but it is not being cultivated actively in the present. Beside these rivers, a number of smaller streams discharge to the bay. (Figure 2)

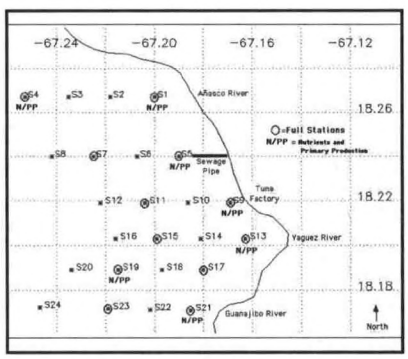

Figure 2 Map of the Mayagüez Bay, the location of the 24 survey station and the three main rivers, Añasco River, Yagüez River and Guanajibo River

The location of tuna processing facilities close to the Yagüez River mouth is another source of nutrients and particulate matter to the bay. These industries dump wastewaters into the bay (18°13.171'N 67°10.237'W) on a regular basis. Mayagüez Bay is also subjected to sewage waters input. The Puerto Rico Waters Authority also discharges primary treated water from the city sewer systems through a diffuser tube located between the Añasco River mouth and the tuna factories (18°14.022'N 67°11.467'W). Both the riverine and the anthropogenic inputs to the bay supply nutrients and suspended particles to the system. (Gilbes, 2002)

The large spatial and temporal variability of bay's optical properties makes very difficult to apply conventional remote sensing techniques for the estimation of these parameters. However, field data were collected with a custom-made rosette with several optical instruments helped to provide detailed analyses of the bio-optical properties. All data collected in the field was in tabulated form

(Figure 3). Visualization and interpretation of data was difficult due to their spatial and temporal distribution.

It was decided to use another approach, a program that generates thematic maps. But a new problem arises. The distribution of the data looks fine but they have a lot of distortion with the actual shape of the bay in aerial photographs and the topographic quad maps. (Figure 4). Therefore, we decided to do a new approach using a Geographical Information System. (GIS).

Methodology

Geographical Information Systems (GIS) are created by computer software that links the data in tables with

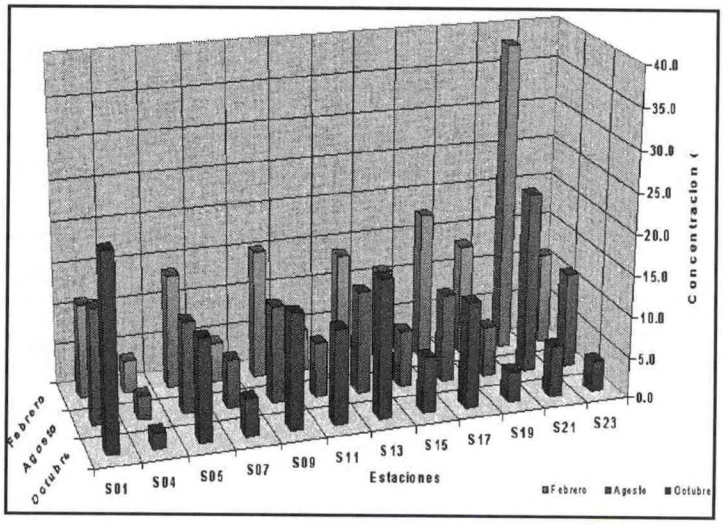

Figure 3 Example of the tabulated data. It is very difficult to visualize the dynamics of the different parameters studied in the bay.

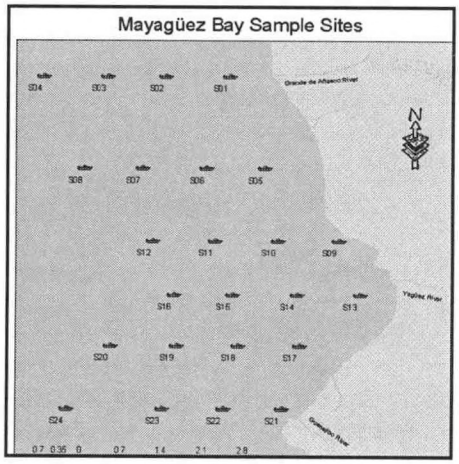

Figure 5 Map created in GIS using GPS position of each stations.

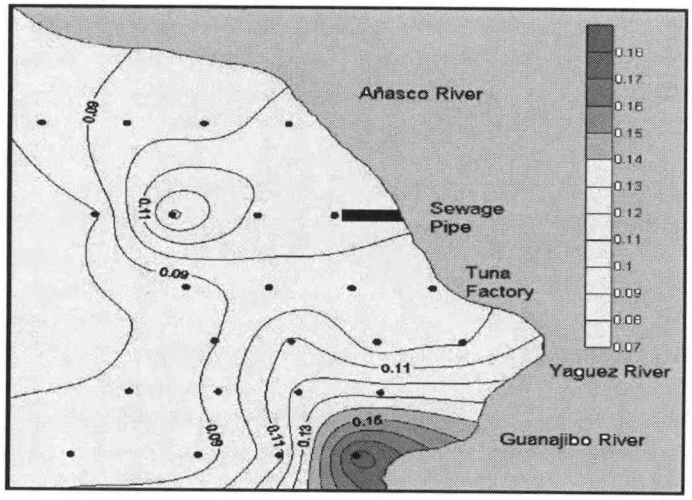

Figure 4 Example of thematic map with distortion, the bay looks compress from north to south.

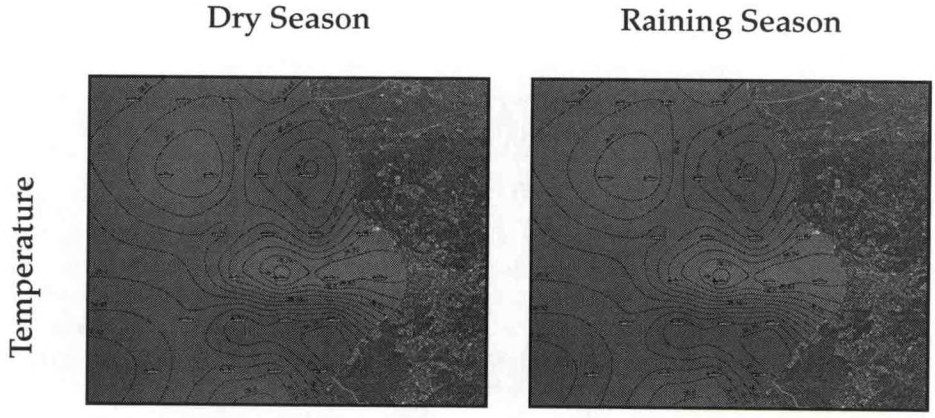

Figure 6 Map of temperature of the Mayagüez bay, dry season vs. raining season.

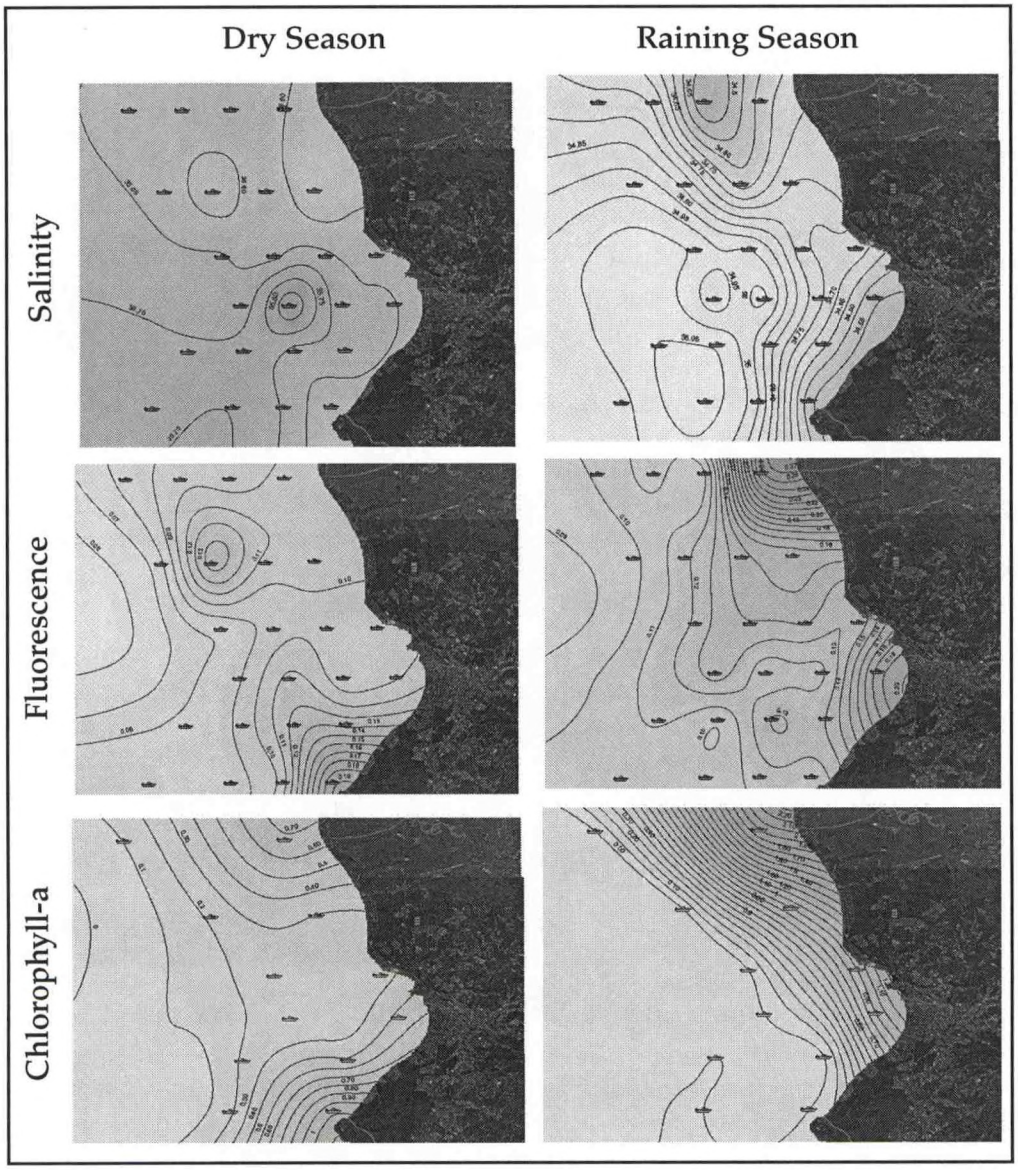

Figure 7 Map from Mayagüez bay, thematic map of salinity, fluorescence and Chlorophyll-a. These maps are par of the first generation maps. Salinity parameters are from a minimum of 34 psu and a maximum of 36 psu. Fluorescence measurement: low is 0.05 RU and the high is 0.30 RU. For Chlorophyll-a the lowest concentration is 0.0 ug/L and the highest is 3.0 ug/L.

geographical information like aerial photograph, satellite images, and survey stations. During field surveys many parameter were measured and samples were taken for laboratory analysis. For example, Salinity, temperature, backscattering, sediments were tabulated.

All the information required to create the GIS was gathered. The aerial photograph or satellite images that work as background were processed to create a mosaic to have a more real visualization from Rincon through Cabo Rojo.

Coordinates of the survey stations were gathered with the help of Global Positioning System (GPS). All data were converted to the same coordinate system of aerial photographs or satellite images. The tabulated data were processed with MS Excel and later converted to Dbase4.

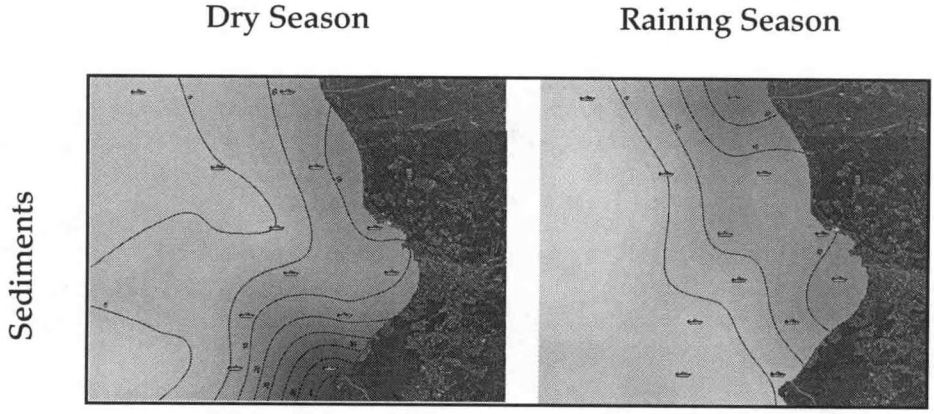

Figure 8 Mayagüez bay maps with sediment concentration. The lowest concentration is 0.0 mg/L and the highest is 45.0 mg/L.

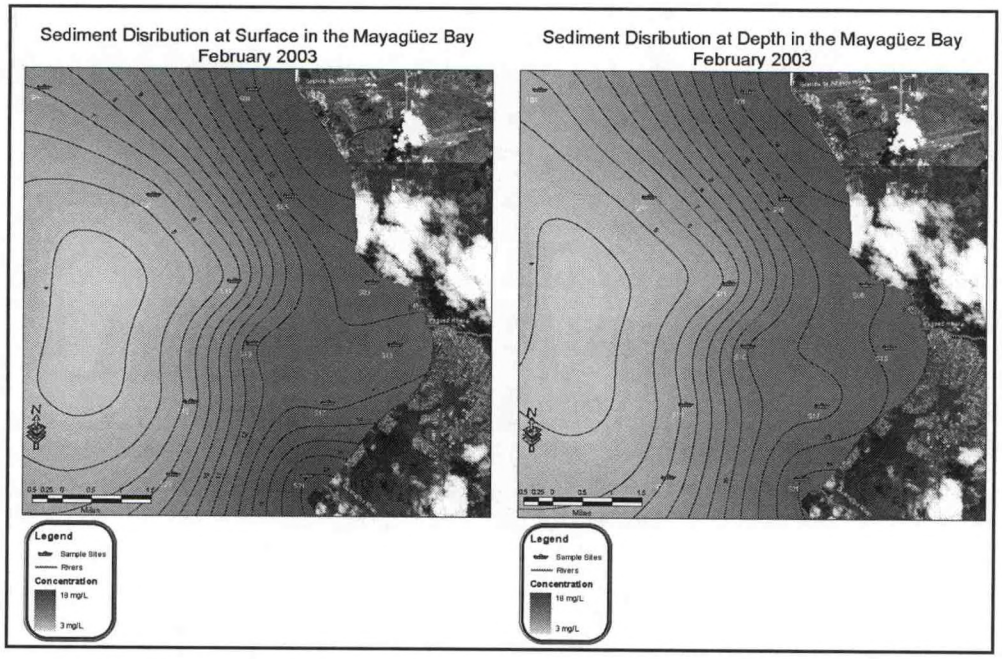

Figure 9 Second-generation sediment maps created with the IKONOS satellite images. The maps are presented in the final layout. In this case instead of comparing dry season vs. raining season, both maps are from the dry season one represents concentration from the surface and the other represents the concentration of sediment at depth. The depth of the measurement depends by the bathymetry of the survey station.

All this information was put together using ESRI ARC GIS 8.3. A polygon shape files was created to delineate the study area digitalizing over the image or photograph. Also a line shape file was created to delineate the different rivers using the same method as for the study area. Using the command (create point by coordinate) the survey stations were created and later the tables were related. (Figure 5). Then using ESRI 3-D Analyst extension, and the raster interpolation command, the new thematic maps were created.

Results

We have created the first generation of GIS thematic maps using DOQ for our database of Mayagüez Bay. Maps of temperature, salinity, fluorescence, chlorophyll-a and suspended sediments for the dry and rainy seasons were made (Figures 6-8).

The second generation of those maps includes color satellite images taken by the IKONOS sensor. Processed to created mosaic with 1- meter resolutions for the entire bay. They had clouds in most part of the Bay, but they are the only dataset available (Figure 9).

Conclusion

The development of a GIS for the Mayagüez bay is helping us in the analyses of the different measured parameters. The GIS gives a better and more accurate way to visualize the spatial and temporal variability of each parameter.

The use of the DOQ and IKONO images helps in the understanding of the interaction of land-water, one example is in Figure 8 when the concentration of the sediment are directly related to the river discharge. When comparing the data in graphical form as presented in Figure 3 is harder to understand this dynamics.

Other case is the salinity, which is affected by the river discharge (Figure 7) during the raining season and compared to the dry season where the evaporation rates are higher and the salinity values became higher.

When the different parameters change from tabulate form to a map view the information obtained is much easier to interpreted, analyze and compare with other parameter, having a completed picture of the interaction in the complex dynamic of this bay.

The GIS also allows us to study the effect of the bathymetry with the studied parameters. The correlation between parameters is now easier to do and we can incorporate different databases or data sources of any parameter to this research.

The development of a GIS to this research represents an important tool in the understating of the dynamics in the Mayagüez Bay; any scientist can contribute to the study because of the easy visualization that this represents and simple enough that any person can understand.

ACKNOWLEDGEMENT

Thanks to Dr. Fernando Gilbes for giving me this opportunity and his advice.

This work was sponsored by NOAA-CREST grant number NA17AE1625. Thanks to Mr. Roy Ruiz and the PASCOR program for providing the aerial photograph and the IKONOS images.

REFERENCES

ESRI 2002. Arc GIS 8.2 User Guide 3D Analyst, 77-183.California, ESRI Press

Gilbes, F. 2002. Development and Validation of Bio-optical algorithms in coastal water. NASA Partnership Final Report. 23-24

PRELIMINARY STUDIES OF TOXIC EFFECTS OF LEAD AS LEAD NITRATE ON RED SWAMP CRAYFISH, *PROCAMBARUS CLARKII*

Ana Balarezo[1], Paul B. Tchounwou[1], and Paulinus Chigbu[1]

[a]Environemental Toxicology Research Laboratory and Marine Science Program, NIH-Center for Environmental Health, College of Science, Engineering, and Technology, Jackson State University, 1400 Lynch Street, P.O. Box 18540, Jackson, Mississippi 39217, U. S. A.

A study was conducted with adult red swamp crayfish, *Procambarus clarkii. P. clarkii* is widely farmed in the southern states of Louisiana and Texas, and the most valuable of commercial crayfish species in the United States, where they are considered a delicacy. During recent years, the resources of red crayfish have increased and pollution of water bodies decreased. Heavy metals are among the most persistent environmental contaminants since they cannot be degraded or destroyed; thus, they tend to bio-accumulate in the aquatic food chain with potential risk to humans through fish consumption. Behavioral and morphological reactions are the most sensitive reactions of an organism to toxic materials. The data of a 24, 48, 72, and 96-hours lethal toxicity test, conducted by us at laboratory conditions, have shown that the mean lethal concentrations of one of the most toxic metals, Pb2+, to adult red swamp crayfish are: ≥ 16,000; 4,800±1,680; 2,900±510; and £ 100 mg/l of Pb(NO3)2, respectively.

Keywords: red swamp crayfish, lead, lethal toxicity, acute toxicity tests.

ACKNOWLEDGEMENTS

This research was financially supported in part by a grant from the National Oceanic and Atmospheric Administration – NOAA Grant No. NA17AE1626, Subcontract No. 27-0629-017 to Jackson State University.

ASSESSMENT OF THE MICROBIOOLOGICAL QUALITY OF WATER IN THE PEARL RIVER AND THE ROSS BARNETT RESERVOIR

Melvin Amos, Stephen S. Kishinhi, Marcus Sims, Ibrahim O. Farah, Paulinus Chigbu, and Paul B. Tchounwou

Department of Biology, College of Science, Engineering and Technology, Jackson State University, Jackson, MS 39217, USA

The Pearl River and Ross Barnett reservoir represent a major source of water supply for the city of Jackson, the capital of the State of Mississippi. Of about 32 million gallons operated by the city, 90% is diverted from the Pearl River basin and Ross Barnett reservoir. These water resources also constitute the primary sites for recreational activities for residents of several counties including the Hinds, Madison and Rankin counties in the central region of the State. In recent years, there have been concerns over the microbiological quality of the Pearl River and associated streams due to the development of several anthropogenic activities along its shore, including agriculture, poultry and livestock operations, and wastewater discharges. There has therefore been an increasing awareness from government agencies and the general public for the need to implement a monitoring program with regard to the assessment of water quality in these water resources. In response to this call for action, we recently initiated a research project to investigate the microbiological characteristics of water in the Pearl River and Ross Barnett reservoir. From April 2004, water samples were collected aseptically twice a month, and the numbers of heterotrophic bacteria, total coliforms, fecal coliforms (Escherichia coli), and fecal streptococci were determined following the Membrane Filtration Technique as described in Standard Methods for the Examination of Water and Wastewater. The preliminary results indicate significant variations in the numbers of bacteria with regard to the type of organisms (the heterotrophic bacteria were more abundant that the total coliforms that also seemed to be larger that the fecal streptococci and fecal coliforms), sampling site, and sampling time. For example, on April 16, 2004, the mean levels of bacteria were 5.8 x104 + 2.0x104, 1.8 x103 + 1.3 x103, 67.4 + 71.8, and 34.4 + 33.1 cfu/100mL for heterotrophic bacteria, total coliforms, fecal streptococci, and fecal coliforms (Escherichia coli), respectively, while fecal coliform counts were 34.4 + 33.1, and 79.4 + 75.7 in April 16, 2004, and July 09, 2004, respectively. Further data analysis is underwater to examine the relationships between bacterial levels and environmental characteristics at specific sampling sites, and to compare the study data to regulatory standards and guidelines.

Key words: Pearl River, Ross Barnett reservoir, water quality, bacteria, public health

ACKNOWLEDGMENTS

This research is financially supported by a grant from the National Oceanic and Atmospheric Administration through the Environmental Cooperative Science Center, NOAA-ECSC Grant # NA17AE1626, Subcontract No. 27-0629-017 to Jackson State University.

ASSESSMENT OF MACROBENTHI INVERTEBRATE ABUNDANCE AND DISTRIBUTION IN THREE MISSISSIPPI GULF COAST BAYOUS

Jonathan Watkins[1], Paulinus Chigbu[1], Paul Tchounwou[1], Ibrahim Farah[1], Marcus Sims[1], David Ruple[2], and Mark Woodrey[2]

[1]Department of Biology, Marine Science Program and Environmental Science Ph.D. Program, Jackson State University, Jackson, MS, USA

[2]Grand Bay National Estuarine Research Reserve, Moss Point, MS, USA

Macrobenthic invertebrates are useful as indicators of environmental change. They are also important components of the estuarine food web. From October 2003 to August 2004, benthic macroinvertebrate samples were collected approximately bimonthly to compare densities, species composition and diversities among Bayou Heron and Bayou Cumbest, located within the GBNERR, and Bayou Cassotte located in a more industrialized area. Replicate samples were collected at four sites in each Bayou, as well as in offshore areas within Mississippi Sound, using a Ponar Grab. In addition, water characteristics were measured including, temperature, salinity, dissolved oxygen, depth, pH and turbidity. Preliminary analysis indicates that mean density of benthic macroinvertebrates in October 2003 was 592.7 m^{-2} ranging from 172.4 m^{-2} to 1,163.8 m^{-2}. Macrobenthos densities were higher in the more offshore areas in Mississippi Sound (811.8 m^{-2}) than in Bayou Cumbest (581.9 m^{-2}), Bayou Heron (287.4 m^{-2}) and Bayou Cassotte (215.5 m^{-2}), and were dominated by annelids, particularly polychaetes (492.2 m^{-2}). Average densities of other major invertebrate groups; echinoderms (46.7 m^{-2}), molluscs (28.7 m^{-2}), arthropods (23.3 m^{-2}) and flatworms (1.8 m^{-2}) were relatively low. Data analysis is continuing to evaluate benthic macroinvertebrate species composition, distribution and abundance in relation to environmental factors.

ACKNOWLEDGEMENTS

This research was financially supported by NOAA-ECSC Grant No. NA17AE1626, Subcontract No. 27-0629-017 to Jackson State University.

BACTIRIOLOGICAL ASSESSMENT OF WATER QUALITY IN THE GRAND BAY NERR, MISSISSIPPI

Stephen S. Kishinhi[1], Marcus Sims[1], Ibrahim O. Farah[1], Paulinus Chigbu[1], Mark Woodrey[2], Dave Ruple[2] and Paul B. Tchounwou[1]

[a]Department of Biology, and Environmental Science Ph.D. Program, College of Science, Engineering and Technology, Jackson State University, Jackson, MS 39217, USA

[2]Grand Bay National Estuarine Research Reserve, Moss Point, MS, USA

The Grand Bay National Estuarine Research Reserve (NERR) is an important ecosystem in the Mississippi Gulf coast. Located within the reserve are bayous, brackish lakes and bays that served as important nursery areas for juveniles of many species of fish. The water bodies are also used for fishing, oyster tonging and recreation. However, the area is often closed to shellfish harvest because of high fecal coliform levels. The purpose of this study was to assess the bacteriological quality of water for better water quality management in the Grand Bay NERR. From December 2003 to July 2004, water samples were collected approximately monthly from 15 stations in Bayous Heron and Cumbest, and also from Bayou Cassotte located near a highly industrialized area. Samples were processed by membrane filtration and incubation on selective media, within 8 hours of collection, to determine the concentrations of total heterotrophic (HPC), total coliform (ENDO), fecal coliform (FC/E.coli), and fecal streptococcal bacteria (ENTERO). Mean bacteria levels expressed as colony forming units per 100ml, ranged from 4.1x103+4.3x103 to 5.9x104+4.3x104 (HPC), 20.7+14.7 to 1117.1+678.4 (ENDO), 14.3+22.3 to 396.5+254.3 (FC/E.coli), and 15.6+20.9 to 246.1+105.3 (ENTERO). These results suggest that a considerable level of pollution is occurring in the area. Further studies are needed to identify the sources of the bacterial pollution as well as evaluate the influence of environmental factors on bacteria levels.

Key words: Grand Bay NERR, microbial water quality, public health.

ACKNOWLEDGMENTS

This research is financially supported by a grant from the National Oceanic and Atmospheric Administration through the Environmental Cooperative Science Center, NOAA-ECSC Grant # NA17AE1626, Subcontract # 27-0629-017 to Jackson State University.

A Comparative Study of Contamination in Three MMississippi Gulf Coast Bayous

Joyce Williams[1], Paulinus Chigbu[1], Paul B. Tchounwou[1], Ibrahim Farah[1], David Ruple[2], and Mark Woodrey[2]

[a]Environmental Toxicology Research Laboratory and Marine Science Program, College of Science, Engineering and Technology, Jackson State University, Jackson, MS, USA

[2]Grand Bay National Estuarine Research Reserve, Moss Point, MS, USA

Abstract

The concentrations of selected metals in water and sediments in Bayou Heron and Bayou Cumbest located within the Grand Bay National Estuarine Research Reserve (GBNERR), a relatively pristine area, and Bayou Cassotte located outside the GBNERR in a more industrialized area were examined. Samples were collected in October and December 2003 from 4 sites along each bayou, and were analyzed for lead, cadmium, chromium, nickel, manganese, molybdenum and copper using a graphite furnace atomic absorption spectrophotometer. Lead (average: 149 – 278 mg/kg) and nickel (average: 148 – 250 mg/kg) had the highest concentrations in the sediment whereas cadmium (average: 3 – 6 mg/kg) and molybdenum (average: 8 – 14 mg/kg) had the lowest concentrations. Similarly, lead (0.07 – 0.16 mg/l) and nickel (0.02 – 0.05 mg/l) concentrations in water were higher than the concentrations of other metals (< 0.01 mg/l) examined. Lead (277.8 mg/kg) and cadmium (6.4 mg/kg) levels were higher in sediments from Bayou Cassotte than in sediments from Bayou Cumbest (172.3 mg/kg Pb; 4.4 mg/kg Cd) and Bayou Heron (148.6 mg/kg Pb; 2.6 mg/kg Cd). This may be due to the proximity of Bayou Cassotte to industries in the Mississippi Gulf Coast. Studies are on-going to characterize seasonal variations in metal levels in the bayous.

Keywords: toxic metals, water, sediments, Mississippi Gulf Coast

ACKNOWLEDGEMENTS

This research was financially supported in part by a grant from the National Oceanic and Atmospheric Administration – NOAA/ECSC Grant No. NA17AE1626, Subcontract No. 27-0629-017 to Jackson State University.

ESSENTIAL FISH HABITAT AS DETERMINED THROUGH FRESHWATER HABITAT UTILIZATION PATTERNS OF AMERICAN EELS (*ANGUILLA ROSTRATA*) IN THE ST. JONES RIVER, DELAWARE

Jessie C. Thomas, Dewayne A. Fox, and Michael A. Reiter

Department of Agriculture and Natural Resources, Delaware State University, Dover, DE 19901-2277

According to recent surveys, American eel (*Anguilla rostrata*) stocks along the Atlantic coast are thought to be in decline. To this end, the ASMFC Fishery Management Plan cites a need for studies focused on identification of habitat and movement patterns for American eels. We plan to document yellow-phase American eel habitat utilization using telemetry in the Delaware National Estuarine Research Reserve, St. Jones River, Delaware. Like many areas surrounding Delaware Bay, the St. Jones River watershed is currently experiencing changes due to increased urbanization. Through the use of telemetry, we will document long term (>9 months) spatial and temporal patterns of American eel behavior and habitat utilization. Ultimately, we hope to develop a habitat suitability model for American eels in the St. Jones River watershed. Our proposed research will provide needed information to assist in refining American eel management strategies and habitat restoration efforts in the mid-Atlantic region.

Contemporary Population Status and Identification of Spawning Locations of Delaware River Atlantic Sturgeon

Dewayne A. Fox and Lori M. Brown

Department of Agriculture and Natural Resources, Delaware State University, Dover, DE 19901

The worldwide distribution of Atlantic sturgeon (*Acipenser oxyrinchus oxyrinchus*) at one time was centered in the Delaware River. In fact, in the late 1800s the Delaware River supported the largest recorded fishery for Atlantic sturgeon. Unfortunately, this harvest was not sustainable and quickly led to the collapse of the Atlantic sturgeon population. Present day status of this historically important fish is unknown in the Delaware River. We plan to utilize a combination of gillnetting and telemetry to assess the contemporary status of Atlantic sturgeon in the Delaware River from approximately the Delaware-Pennsylvania border up to and above the area surrounding Philadelphia. Histological analysis of gonadal biopsies will be used to determine the sex and reproductive status of individuals. Telemetry results and egg sampling will be used to identify Atlantic sturgeon spawning sites and to examine the roles that sex and reproductive status play in migratory behavior. Through the implementation of this project we will provide information on the status of the Delaware River Atlantic sturgeon including insights into present day status of the adult stock and both the temporal and spatial distribution of spawning locations and river residence which will form the basis of critical habitat designations.

DECREASED HABITAT AVAILABILITY, ALTERED POPULATION STRUCTURE, AND RISK OF EXTIRPATION: IMPACTS OF INVASION BY *PHRAGMITES AUSTRALIS* IN MID-ATLANTIC ESTUARIES ON RESIDENT MARSH FISHES

Karen L. Hunter[1], Dewayne A. Fox[2], Lori M. Brown[2], Kenneth W. Able[1]

[1]Institute of Marine and Coastal Sciences, Marine Field Station, Rutgers University, 800 Great Bay Blvd, Tuckerton, NJ, 08087

[2]Department of Agriculture and Natural Resources, Delaware State University, Dover, DE 19901

We are studying the distribution and abundance of marsh fishes along a gradient of invasion by common reed, *Phragmites australis*, in three study areas across the mid-Atlantic region of the US. Based on our preliminary sampling periods (n=7), results indicate that abundance of Fundulus spp. decline, or are not present in more advanced stages of the invasion. Because *Phragmites* is rapidly invading a large geographical area, there are important implications for the conservation of essential fish habitat along the east coast of North America.

A PRELIMINARY EXAMINATION OF EXTERNAL TAG RETENTION AND POST TAGGING SURVIVAL IN DELAWARE BAY WEAKFISH (*CYNOSCION REGALIS*)

Gary Kennedy[1], Grant S. Blank[1], John Clark[2], Lori M. Brown[1], Dennis McIntosh1 & Dewayne A. Fox[1]

[1]Department of Agriculture and Natural Resources, Delaware State University, Dover, DE 19901

[2]Delaware Division of Fish and Wildlife, Little Creek, DE 19961

In recent years, trawl survey data from the mid-Atlantic has indicated both a decline in abundance and a truncation of age structure for weakfish (Cynoscion regalis). Delaware Bay is located in the center of weakfish distribution and is considered a major spawning area. Both fisheries dependent and independent data from Delaware Bay support the overall decline in weakfish abundance and spawning. To this end, the Delaware Department of Fish and Wildlife has proposed a large scale tagging program to elucidate patterns of migration and fishing mortality rates. Due to previously documented low rates of return for large scale weakfish tagging programs a refinement of tagging protocols is required to increase tag retention and survival. Initial results from a tag retention study currently being conducted at Delaware State University indicate both tagging protocols and tag type influence tag retention and survival in age-1 weakfish held in a recirculating seawater system. This information on tag retention and survival is vital for the success of any proposed large scale weakfish tagging program.

Flow Cytometry and Sample Preservation in Marine Phytoplankton Analyses: A Brief Protocol

Gulnihal Ozbay[a], Monica Jackson[a], Lori M. Brown[a] and Gary H. Wikfors[b]

[a]Delaware State University, Department of Agriculture & Natural Resources
1200 North Dupont Highway, Dover, DE 19901

[b]NOAA, National Marine Fisheries Service, Northeast Fisheries Science Center, Milford, CT 06460

Introduction

Flow cytometry (FCM) is a technology that simultaneously measures and analyzes multiple optical characteristics of single particles as they flow in a fluid stream through a beam of laser light. The technique was initially applied to eukaryotic cells. The properties measured include a cell's relative size, relative granularity or internal complexity, and relative fluorescence intensity at several wavelengths. Any cell from 0.2 to 150µm in size is suitable for analysis. Techniques have also been developed for the analysis of cell viability, metabolic state, and antigenic markers.

FCM is becoming increasingly popular among limnologists and marine biologists for laboratory and field studies of microorganisms. Since phytoplankton is typically in suspension, flow cytometry is an ideal way of identifying, enumerating, and estimating cell densities and relative proportions of phytoplankton and picoplankton cells as small as 0.2µm in diameter (Marie et al. 1999, BD Biosciences 2003). Major advantages include rapid and accurate measurements of individual particles as well as the discrimination between cells, detritus, and suspended sediments. Although there are a number of publications relating to the use of FCM in phytoplankton studies, protocols have been omitted and the techniques not readily adaptable to other samples and equipment.

Only a limited number of studies have mentioned the effects of preservatives on quantitative and qualitative accuracy of FCM (Vaulot et al. 1989). The accessory pigments in phytoplankton that may be utilized in FCM are particularly sensitive to preservation methods. According to Vaulot et al. (1989), a method to preserve picoplankton samples for FCM analyses must meet several criteria including the preservation of the individual scattering and pigment fluorescence properties of the picoplankton populations. Classical phytoplankton preservation methods such as formalin or Lugol's fixation do not generally meet these criteria, as the former modifies cell shape and latter drastically affects fluorescence. We wish to share some of our findings in relation to the preservation and cell quantification.

Chlorophyll and phycoerythrin are easily distinguished by fluorescence methods and commonly utilized in phytoplankton FCM. Therefore, in this study we examined fresh and preserved phytoplankton samples based on their fluorescence intensities against known concentration of micro-beads (2µm microspheres). The protocols presented here are part of preliminary studies conducted to accurately quantify phytoplankton samples including several cultured species. The methods may need to be modified for other applications.

Materials and Methods

The analysis of algal samples allows us to obtain information on the abundance, cell size and pigment content of the major photosynthetic phytoplankton groups. This type of analysis can be performed either on fresh or preserved samples (Vaulot et al. 1989, Campbell 2003; Alix and Wikfors, 2004). Samples in this study were analyzed immediately. However, if immediate analysis is not possible, samples may be preserved to minimize degradation of the phytoplankton cells (typically with a 2 or 4% formalin solution).

a) Algae Collection and Preparation

Live samples of *Tetraselmis chui* (strain PLY-429) were collected from our algae culture laboratory for use in this study. A portion of the samples were preserved using 2 or 4% formalin solution and the rest were analyzed live. Fresh phytoplankton samples were analyzed with as little delay as possible. Cell counts were done using a hemocytometer (Fisher Scientific) prior to any analysis to determine cell densities under the microscope (SWIFT compound microscope). In order to examine the effects of both beads and formalin on algae, samples were prepared A) fresh, B) 2% formalin-preserved, C) 4% formalin-preserved, D) with microspheres, E) 2% formalin-preserved with microspheres, and F) 4% formalin-preserved with microspheres. The concentrations and sizes of phytoplankton cells are determined by comparison to the included internal standard consisting of fluorescent 2.0μm diameter microspheres (Polysciences, Inc.) of known concentration and size. Samples were analyzed on the day they were collected and every day following for a total of four to six days in order to track any shifts in the algae population. After sampling, algae were stored dark at 4°C to retard cell division in the live samples.

Tube preparation:

A) 461,666 cells/ml algae

B) 452,400 cells/ml algae with 60 μl of 2 % formalin solution

C) 443,200 cells/ml algae with 120 μl of 4% formalin solution

D) 446,300cells/ml algae with 4,415,000beads/mlmicrospheres

E) 437,000cells/ml algae with 4,415,000beads/ml microspheres with 2 % formalin

F) 426,200cells/ml algae with 4,415,000beads/ml microspheres with 4% formalin.

Samples were diluted 50% and similar preparation was followed for diluted samples.

Note that five-fold lower microspheres counts were observed than manufacturer's counting methods (6,622,561 000 beads/ml vs. 1,324,512,000 beads/ml).

b) Instrument and Instrument Settings

A four color BD FACSCalibur automated benchtop flow cytometer was used to analyze algae samples. Cells in suspension were analyzed for size, complexity, and fluorescent intensity by the flow cytometer/sorter with a 488 nm argon laser and 635 nm diode-laser for multi-color flow cytometry. An argon laser is used for detecting FSC (cell size and shape), SSC (internal complexity), FL1 (greenfluorescence), FL2 (orange fluorescence) and FL3 (dark red fluorescence), whereas a diode-laser is used for detecting FL4 (red fluorescence) only. Fluorescence derived from each particle is split by a 595 nm dichromic mirror and is received by photomultiplier tubes located at 90° to the intersection of the laser beam and sample stream. Further specifications about FACSCalibur flow cytometry can be found at the BD Biosciences web-site (http://www.bdbiosciences.com/immunocytometry_systems/) and manual.

In order to reduce the effects of osmotic stresses and to limit possible contaminants, 0.22 μm filtered seawater was used rather than standard sheath fluid. CellQuest was used to acquire and analyze data collected from samples.

In our analysis, we chose to focus on fluorescent intensity of algal cells to determine populations.

It is possible to use cell size and granularity (Forward Scatter and Side Scatter respectively), but due to the relative small size of our algae and have to use the logarithmic scale, we felt the fluorescent intensity better represented the algae population.

In this study, the parameters of interests were examined on FL1at X axis and FL3 at Y axis. Using the right settings that are good for all of the particles that are in the sample will provide better perspective and accurate results of our samples (species, beads, bacteria). The FL1 channel, which is a green fluorescence and the FL3 channel, which is a red fluorescence have been shown to be optimal for *Tetraselmis chui* in previous studies and were therefore utilized in this study. The fluorescent range of the species of interest will determine which channels should be used for optimal visibility. A threshold was set in order to

reduce the amount of noise and background interference present. For the purposes of this study, three thresholds where used in order to determine an optimal setting for *Tetraselmis chui*. Threshold settings were optimized to minimize background noise while still showing the maximum amount of algae and microspheres.

Setting 1 - Side Scatter threshold of 52 was found to be optimal for microspheres, but not algae

Setting 2 - Side Scatter threshold of 421 was found to be optimal for algae, but not microspheres

Setting 3 – FL3 threshold of 52 showed the highest amounts of algae with microspheres

Sample tubes having only microspheres were analyzed by flow cytometry to locate and gate the microspheres on the plots. This allows the separation of microspheres from the actual algal cells on the plots. By gating each cell population on the plot, algal cell numbers were estimated proportional to number of microspheres observed on the plots. After settings were optimized, regions were created for the algae population and also for the microspheres in order to calculate amounts after acquisition. Each instrument varies slightly and settings vary a good deal with different algae species and combined samples.

c) Data Acquisition

There are three instrument settings that can be used for algal analysis: 1) Low: delivers 12ml/min 2) Medium: delivers 35ml/min, and 3) High: delivers 60ml/min of sample through the sample flow cell. Data was acquired with the instruments sampling mode set on "low" (12 µl/min). This reduced the probability of doublet or triplet cells being miscounted and also conserved the amount of sample for a six day experiment time. In order to reduce cross-contamination, 0.22 µm seawater was run in between samples. This process flushed out any remaining particles from the previous sample and also removed any particles that may have adhered to the SIP (potentially contaminating later samples). While seawater was still flushing, we examined the acquisition dot plot for any unexpected events to verify the system flush. This process is very important when you are running samples with multiple species or varying cell concentrations.

Each sample was vortexed for ten to twenty seconds before being placed on the SIP in order to assure that clumps are broken up and cells and microspheres are suspended. Data was acquired for one minute. Three datasets were acquired for each sample at each of the threshold settings. This was done so an average of event rates could be taken for each of the samples in order to account for any anomalies like cells or microspheres clumping.

Results and Discussion

Understanding the functions and applications of FCM for marine phytoplankton analyses can be a challenge for scientists and educators, despite training in clinical protocols provided by the manufacturers. Limited information is currently available concerning marine phytoplankton samplings. Sampling marine phytoplankton with flow cytometry can be fairly easy if the protocol developed can be applied to your samples. There are a number of studies published on marine phytoplankton analysis, however further details on the instrument settings and operation, and sample preservation will be necessary to perform FCM analysis without a long and frustrating training period. Generally, instrument and threshold settings play a major role for an accurate quantification of algae cells. Simple methods of preserving phytoplankton samples may have some effects on quantification, but these effects may not be as significant as others caused by analytical differences (instrument settings, threshold, plot determination...etc.). We used formalin preservation in this study because of their common use in flow cytometry.

We examined algae concentrations in a feeding chamber with 60 small oysters over a 3-hour period in the preliminary experiments. We measured samples right after sampling was finished and kept one group with and without formalin at 16% at 4°C in the first experiment while applied formalin at 1.6% and 16% in the second and third experiments. In these trials, fresh algae samples were compared with samples maintained in the dark at 4°C and with formalin-preserved samples after 3 days in experiments one and two, and 6 days in experiment three. Lower cell counts were observed in 16% formalin-preserved samples, but this level was not statistically different ($P>0.05$) from the other samples during 3 days.

Samples preserved with 1.6% formalin showed some higher cell numbers from fresh samples and 16% formalin-preserved samples in the second experiment. The only significant difference ($P<0.05$) was observed between fresh and the 6-day stored samples while readings from formalin-preserved samples were not significantly ($P>0.05$) different from fresh samples. In all these trials, counting beads were used for algae quantification, and differences were not significant in bead counts in the samples. All these trials were run at FL3 threshold setting of 52 on FL1 vs. FL3 plot. In previous studies, we examined a number of samples for optimum threshold setting and plot determination (FL1 vs. FL3 plot). We used SSC threshold settings, but SSC 421 gave the maximum algae count while showing minimum bead count and SSC52 gave the minimum algae count while showing maximum bead count. Observations of algal sample shifts from three previous experiments were the impetus for this study. We conducted the present study to go beyond direct observation to include monitoring for significance. We compared samples which are a) fresh, b) preserved with 2% formalin, c) preserved with 4% formalin, d) with beads, and e) 2 % formalin-preserved with bead, and f) 4 % formalin-preserved with bead added to the samples initially and tested over a one-week period.

Threshold settings had significant impacts on the sample count. SSC52 threshold settings showed lower algal concentrations than SSC 421 and FL3 52 in most cases. Results of comparison between fresh, old and preserved samples showed differences in cell counts on the FL1 vs. FL3 graphs. We observed that the gate established for an algal cell of interests was shifted in samples preserved with formalin solution. Fluorescence intensities of samples with the beads and preserved were significantly shifted to the right and down from the defined gate for fresh samples (Figure 1). We also noted a slight shift in samples with beads, and with formalin and beads together. We monitored some differences in the sample counts among the samples analyzed over a 4-day period. Data analysis is still in progress to find any significance. If the gate is shifted as the sample shifts, the algae cell counts are similar in fresh and formalin-preserved samples. Differences between 2 and 4% formalin-preserved samples were not noticed in the present study. Differences in cell counts were visible in samples preserved with 2% formalin with microspheres (Figure 1). Threshold settings and plot templates were changed to observe these differences. Shifts from the initial gate determined for *Tetraselmis chui* can be seen in the analysis dot plots (Figure 1). One would expect to find slight differences in the fluorescence properties of cells in formalin-preserved samples; however this shift in algae samples with beads was unexpected. A possible reason for this shift may be a higher number of counting beads possibly interfering with the fluorescence properties of the cells. Microscopic examination of fresh and preserved samples showed some reduction in fluorescence intensities of the cells in formalin-preserved samples. For instance, *Tetraselmis chui* samples were extensively examined on FCM, and were then examined under the microscope (Nikon TE200 Inverted Microscope) for comparisons of their cell properties. Microscopic examination showed fading of bright yellow fluorescence of preserved phytoplankton cells as observed in fresh samples.

This protocol may not be helpful for species smaller than 2µm or for fragile algal forms. Vaulot et al. (1989) preserved picoplankton and fragile algal cells by fixing with 1% glutaraldehyde followed by storage in liquid nitrogen. This method resulted in very little cell loss in their study.

The FL3 threshold setting of 52 appeared to show the greatest amount of algae and microspheres (Table 1). A possible explanation for this is that SSC could not accurately represent Tetraselmis chui cells in a logarithmic scale for Tetraselmis chui cells in this study. The fluorescent intensity of a cell is not altered by the use of the logarithmic scale and is a more accurate representation of the cell. This is why we chose to use it for our acquisition plots as well as our threshold settings. Because, the very low FL3 threshold is not eliminating anything but electronic noise, essentially all particles are being included as we expected. The beads show up above the threshold because the green fluorescence is so strong it is being detected in FL3.

Important things to consider during FCM analysis are the uses of the proper settings and thresholds for the algae/beads that are being analyzed, settings change based on not only sample ages and how it is preserved, but also various algal species you may use, and if using more than one species, or if using algae and counting beads on the same plot, sometimes one may compromise on the settings to obtain both populations of interest. There may be an ideal setting for each of the components separately, but in order

to get the total picture you may lose some of the quality. Because the more complex the sample and the more detectors in use, the more one needs to compromise individual components (Wikfors 2004 – personal communication).

The intention of this study has been to create some guidelines and protocol development methods for flow cytometry as it relates to phytoplankton analyses. Further studies need to be done in order to examine these interactions with other individual cultured algae species, instrument settings as well as with samples collected from natural ecosystems.

References

Alix J.H., & Wikfors, G.H. 2004. A flow-cytometric method for counting microalgal and bacterial cells in the same sample. J. Shellf. Res. (in press).

Becton & Dickinson Biosciences. 2003. FACS Training Manual. BD Immunocytometry Systems. 2350 Qume Drive, San Jose, CA 95131-1807.

Campbell L. 2003. Methods in Microbiology: Chapter 12. Flow Cytometry. Department of Oceanography, Texas A&M University, College Station, TX 77843-3146.

Marie, D., F. Partensky, and D. Vaulot. 1999. In "Current Protocols in Cytometry", (ed J.R. Robinson), Enumeration of phytoplankton, bacteria, and viruses in marine samples. pp. 11.11.1-11.11.1.5, John Wiley & Sons, Inc. New York.

Vaulot D., C. Courties, and F. Partensky. 1989. Heterogeneity in Fragility and Other Biochemical and Biophysical Properties. A Simple Method to Preserve Oceanic Phytoplankton for Flow Cytometric Analyses. Cytometry 10:629-635.

Economic Impact Study of Summer Tourism to St. George Island State Park, Florida: An Extended Abstract

La Marr Joseph
Environmental Cooperative Sciences Center, Florida A&M University, Tallahassee, Florida 32307
David Harding, Ph.D.
Florida Fish and Wildlife Conservation Commission, Tallahassee, Florida
Michael H. Thomas, Ph.D.
Environmental Cooperative Sciences Center, Florida A&M University, Tallahassee, Florida 32307
Carol A. Forthman, J.D.
Environmental Cooperative Sciences Center, Florida A&M University, Tallahassee, Florida 32307

Introduction

Florida's beaches and environs have long been a destination for people throughout North America and the world. During the course of one year it is estimated that over 18 million visitors make trips to the 157 state parks located in Florida (Florida Department of Environmental Protection, 2003).

Located in northwest Florida, the barrier island of St. George is home to the Dr. Julian G. Bruce St. George Island State Park (SGISP), administered by the Florida Department of Environmental Protection, Division of Recreation and Parks (DRP). During the fiscal year 2002-2003 over 220,000 people visited SGISP (Florida Department of Environmental Protection, 2003).

Many people visit the island annually and it is listed as one of the Florida's top beach destinations. Park visitation has important implications for the state, regional and local economies because expenditures help create economic activity, generating jobs and providing a source of tax income for governments.

During the summer of 2004, this study produced a survey that was administered to over 400 park visitors. Participants were asked detailed questions about their trip, including types and amounts of trip related expenditures, reason(s) for their visit, their choice of activities, their opinion of park features, group characteristics and choice of substitute sites.

Sampling was interrupted on two of the three principle summer holidays; a personnel shortage during the Memorial Day weekend greatly restricted survey distribution and Hurricane Frances closed the park during the Labor Day weekend. Otherwise, surveys were distributed randomly during the operational hours and days of the week.

This study has several objectives:

1. Document the level of economic impact resulting from the use of SGISP and determine the level of money transferred to the local economy.
2. Characterize and compare the demographics of visitors to SGISP to local residents.
3. Determine the rank-order importance of activities and park characteristics.
4. Estimate total attendance (visitor and resident) to the park over the summer season (May 2004 – September 2004).
5. Estimate the economic impact of visitor spending to the local economy

Input/Output Analysis and Tourism Economics

With the seminal work of Leontief (1951), input/output analysis (I/O) has been demonstrated to be an effective method of measuring the impact of expenditures on an economy, with others, including Isard et al. (1960), Miernyk (1965), Tiebout (1969) and Miller and Blair (1985), providing additional mathematical foundation. When applied to tourism related expenditures, I/O analysis permits the estimation of income, employment and production required to satisfy tourism demand. Additionally, the model generates estimates of multipliers that include secondary impacts in an evaluation (Kottke, 1988). Multipliers capture the secondary effects of visitor spending to various industries located in the local economy and those located outside the region. Secondary effects include indirect effects which are changes in income, sales and employment in a region. For example, visitor spending will increase sales for businesses, which can then hire extra help. Another secondary effect is induced effects which are changes in spending for households. For example, a person employed in a tourism related industry will spend their income within the region which will generate income and employment throughout the region.

A primary advantage of the I/O approach to economic impact analysis is the broad, economy-wide perspective it takes. This approach provides a general equilibrium framework instead of single – market analysis, or partial equilibrium analysis and examines not only the primary transactions, but also includes all related markets and sectors of the economy. For instance, within the typical I/O model the general economy can be disaggregated into sectors that are important to the study, enabling policy makers to consider the repercussions of public policies and events (Fletcher, 1989).

Surveying and Input/Output Models

There are various approaches to estimating tourist economic impacts depending on varying degrees of detail, accuracy and expense. According to Stynes (1997) there are four levels in which these analyses can be done.

The first level consists of subjective estimates that rely mainly on expert opinion or use of an engineering approach. In an engineering approach, estimates of the costs of a trip are done by itemizing typical cost for each input. For example, a typical overnight trip for a party of two, staying one night, will cost $40 per night for the motel room, $25 per person per day for meals, $15 on gas and $50 for souvenirs. This amounts to $155 per party per trip. Level two uses existing tourism counts for the area or total estimates from a similar area or facility, therefore using multipliers from similar studies or published sources. Level three estimates tourism by activity or revised estimates of that segment from another area, therefore using published sector-specific multipliers. Finally, at level four one can survey visitors to estimate the number of tourists or use a demand model. One can randomly survey visitors to estimate the average spending by segment category and use an I/O model to estimate the impact on the region's economy. As stated above, tourist impact studies are typically analyzed with I/O models and survey instruments.

Tourism Economics and IMPLAN

In the mid 1970s, the U.S. Forest Service called for economic analyses of proposed national forest management plans to investigate the role of forest activities on regional economies. As a result, the computer modeling system "IMpact Analysis for PLANning": IMPLAN, was created under the National Forest Management Act of 1976 (P.L. 94-588) and its associated regulations (36 C.F.R. 219, Subpart A, September 1979) to assist with the agency's forest management planning requirements involving regional economic impact assessments. IMPLAN was developed using a series of secondary databases from the Survey of Current Business and the U.S. Department of Commerce's Bureau of Economic Analysis assessments (Alward and Palmer, 1983) because a series of studies and literature published in the 60s and 80s indicated that a "nonsurvey approach" to conducting input/output models was less expensive than traditional methods (Bourques and Hansen, 1967; Schaffer and Chu, 1969; Strang, 1970; Jensen, 1980; Round, 1983; Stevens et al., 1893).

Since its implementation, IMPLAN has had several revisions including the addition of the social account matrices (SAM) (Engineering-Economics Associates, 1985, Alward, 1985), other refinements (Stynes and Propst, 1992, 1994) and software development (Minnesota IMPLAN Group, 1996) completing its structure as a nonsurvey I/O system traditionally used for measuring timber industry economic

impacts (Alward and Lofting, 1985). In 1993, the U.S. Forest Service has operated under a multiplier use mandate (Cubbage et al., 1993), making IMPLAN effective for use for tourism and recreational economic impact studies.

Basics of Economic Impact Assessments

One can formulate an economic impact by following basis steps:

1. Estimate number of visits associated with the action being evaluated. The number of visits is equates to the amount of spending by the visitors in the local area.

2. Spending is then applied to a region's economy to estimate the effects in terms of sales, employment, income and tax revenues. Collectively, these effects are considered direct effects.

3. Multipliers embedded within a model will estimate the secondary effects of visitor spending. Secondary effects include those associated with changes in sales, income quality, quantity of goods, property and other taxes, social and environmental change, and household spending.

Economic impacts can be narrowed down to include spending on different levels:

1. Dividing visitors into different spending patterns, i.e. classification as day users, campers, or overnight stays in lodging facilities.

2. Selection of spending categories, i.e. travel expenses due to fuel and oil, vehicle rentals, food & groceries, restaurants, bars, lodging, and fees.

Finally, economic impact can be determined as:

$$\text{Impact} = N * AS * M$$

Where: N = number of visitors,

AS = average spending per visitor, and

M = multiplier.

Methods

To assess certain aspects of visitor behavior a survey booklet was developed and distributed to visitors as they entered SGISP between May 12, 2004 and September 6, 2004. Visitors were directed to complete the survey during their park visit and return the completed booklet as they exited the park to a collection box located by the park gate. Questions were designed to determine the primary purpose for a trip to SGISP, activities that visitors might engage in, importance and quality of the activities presently at the park and the importance of additional features they wish to see. Other questions included in the survey assess expenditure patterns, i.e. how much money was spent to make a trip to SGISP.

Presently, these data are being coded and keyed into a computer data set for analysis.

REFERENCES

Alward, G. and C. Palmer. 1983: IMPLAN: An input-output analysis system for Forest Service planning. Proceedings of the First North American Conference on Forest Sector Modeling. Oxford, UK: AB Academic.

Alward, G. and E. Lofting, 1985: Opportunities for analyzing the economic impacts of recreation and tourism expenditures sing IMPLAN. Paper presented at the 30th Annual Regional Science Association Meeting, Philadelphia, PA.

Alward, G., 1985: Extending the IMPLAN I/O system: The social accounting matrix. Paper presented at the Midwest Forest Economists' Meeting, Ames Iowa.

Bourque, P.J. and G. Hansen, 1967: An inventory of regional input-output studies in the United States (Occasional Paper No. 17). Seattle: University of Washington, Graduate School of Business Administration.

Cubbage, F., J. O'Laughlin and C. Bullock, 1993: Forest resource policy. New York: Wiley.

Engineering Economics Associates, 1985: Economic impact analysis: From input/output to social accounting matrices (Report EEA-85-TN-02). Berkeley, CA: Engineering Economics Associates, Inc.

Fletcher, J.,1989: Input/output analysis and tourism impacts studies. Annals of Tourism Research, 16, 514-529.

Florida Department of Environmental Protection, 2003. Florida State Park System Economic Impact Assessment for Fiscal Year 2002-2003. 9-pp.

Isard, W., D. Bramhall, G. Carrothers, J. Cumberland, L. Moses, D. Price, and E. Schooler, 1960: Methods of Regional Analysis: An Introduction to Regional Science. New York: The Technology Press.

Kottke, M., 1988: Estimating economic impacts of tourism. Annals of Tourism Research, 15, 122-133.

Jensen, R., 1980: The concept of accuracy in regional input-output models. International Regional Science Review, 5, 139-154.

Leontief, W., 1951: The Structure of American Economy, 1919-1939. New York: Oxford University Press.

Miernyk, W., 1965: The Elements of Input/output Analysis. New York: Random House.

Miller, R. and P. Blair, 1965: Input/output Analysis: Foundations and Extensions. Englewood Cliffs NJ: Prentice-Hall.

Minnesota IMPLAN Group, 1996: IMPLAN Professional: User's Guide, analysis guide, data guide. Stillwater, MN: Minnesota IMPLAN Group, Inc. (www. IMPLAN.com)

Propst, D., 1994: Documenting for trips and durable bridge tables. In D.J. Stynes and D.B. Propst, MI-REC: Micro-Implan Recreation Economic Impact Estimation System Users' Manual, Version 3.0 (Appendix D). Michigan State University: Agricultural Exp. Stn. and Dept. of Park and Recreation & Tourism Resources.

Propst, D; D. Stynes, and R. Jackson, 1992: A summary of spending profiles for recreation visitors to Corps of Engineers projects. (Technical Report R-92-1, pp. 16) Vicksburg, MS: U.S. Army Engineer, Waterways Experiment Station.

Round, J., 1983: Non-survey techniques: A critical review of the theory and the evidence. International Regional Science Review, 8, 189-212.

Strang, W., 1970: Recreation and the local economy: An input-output model of a recreation-oriented economy (Sea Grant Technical Report 4, WIS-SG-71-204). Madison, WI: University of Wisconsin

Schaffer, W. and K. Chu, 1969: Non-survey techniques for constructing regional inter-industry models. Papers of the Regional Science Association, 23, 83-101.

Stevens, B., G. Treyz, D. Erlich, and J. Bower, 1983: A new technique for the construction of nonsurvey regional input-output models and comparisons with two survey-based models. International Regional Science Review, 8, 271-286.

Stynes, D., 1997: Economic Impacts of Tourism: A Handbook for Tourism Professionals. Illinois Bureau of Tourism: pp.5-29.

Tiebout, C., 1969: An Empirical Regional Input/output Projection Model: The State of Washington 1980. Review of Economic and Statistics, 51, 334-340.

The Effects of Floating Dock Structures on Benthic Communities

Khalia A. Boyd
University of Maryland Eastern Shore, Princess Anne, MD 21853 *khaliaboyd@hotmail.com*
Hoskins D. L.
DOC/NOAA/NMFS and Marine Science Program, Savannah State University, Savannah, Georgia, USA, *Dionne.hoskins@noaa.gov*

Many studies have examined trawling effects on benthic communities. However, few have focused on the effects of floating docks. In areas where tidal fluctuations may cause floating docks to come into contact with the sediments at each low tide, the presence of floating docks may disturb the substratum (Sanger and Holland, 2002). This cyclic disturbance may therefore cause changes in the sediment and faunal composition of benthic environments, therefore affecting the ability of benthic communities to recolonize the area (Zajac and Whitlatch, 2003). Increased development along the coast potentiates a magnified impact of private docks on benthic communities associated with tidal creeks. In this study, two floating docks and adjacent control sites were selected to examine the effects of repeated dock impact on the macrofauna that live directly below the dock floats. Privately owned docks on two tidal creeks located on the Herb River (Savannah, Georgia USA) were chosen because of their accessibility, exposure to moderate traffic, and tendency to empty completely at low tide. Cores (5cm diameter, 10cm depth) were taken directly under each dock and at a control site 20 meters from the dock (n=15). Each sample was sieved on a 500 um sieve, fixed in 10% buffered formalin, sorted and identified to the family level. Preliminary comparison of the sites indicates that syllids form the dominate macrofaunal group and that the biomass is very low under the dock floats and at the control locations.

A Bathymetric Study of Agricultural Surface Impoundments along the Abrams Creek watershed within the Flint River Basin

Warren V. Carmichael Jr., Carol Forthman
Florida A&M University, Environmental Sciences Institute, Tallahassee, FL USA
Gary Mahon, Richard Marella
USGS-FISC Florida Integrated Science Center, Tallahassee, FL USA

Surface water impoundments used for agricultural irrigation have affected the available water in the Apalachicola, Chattahoochee, and Flint River basin. Thousands of relatively small impoundments have retained water that would otherwise flow directly into creeks and tributaries of the Flint and Chattahoochee Rivers in southwest Georgia. In addition, many impoundments are augmented with ground water. Geographic Information System coverages of these impoundments have been developed, but the volumes of water retained have not been established. Through analyzing topographic maps, aerial photos, and ground truthing, the surface impoundments will be located and verified. Land elevations will be compared to the water table, and depth measurements will be taken in accordance with land owners. This research within the Abrams Creek watershed will help quantify volumes retained in a small watershed and help define a methodology to use for future studies.

FIBER-OPTIC TECHNIQUE FOR IN-SITU FINE PARTICLE SIZING IN WATER

Jing Zhou, Alex Gillerson, Barry Gross, Fred Moshary, and Sam Ahmed
Optical Remote Sensing Lab, EE Dept, NOAA-CREST, CCNY

Abstract

Field instrumentation design and analysis techniques are introduced for determination of fine particle size distribution, concentration in water using extinction measurments in the visible spectrum. The focus of this work is to build field portable, inexpensive instrumentation for a water particle size monitor. The optimization technique based on both a single mode and a two mode Particle Size Distribution (PSD) gaussian model is developed. Experimental measurements have been performed and excellent inversion results have been demonstrated on single mode PSD with narrow width. Inversions of bi-modal bi-modal distributions are ongoing

Introduction

In-situ particle size monitoring in water is fundamentally important for it provides insight into the ecological dynamics of marine water (Boss et al). Compared to other methods for obtaining the particle size distribution (PSD) in water such as coulter counter analysis of a discrete sample which requires long flow through times, optical methods can measure the scattering properties of the medium in bulk. Due to the geometrical layout of any fiber optic type measurement, the inherent properties of the sample (i.e. the extinction and volume backscatter coefficients) are often difficult to extract and experimental and data processing techniques must be applied. While optical measurements are useful, the most common approach are laser based methods using Quasi-Elastic Scattering (QELS) but can be quite expensive and optically difficult and uses the forward scattering angle dependence on particle size (Nefedov et al). In this mode, many approximations

are needed and the analysis can be quite complex. On the other side, white light sources fiber optic sources offer a cheap and efficient approach and can yield spectral information (as opposed to angular information) on the extinction and backscatter . In addition, this sensing technique based on white light and incorporating compact fiber optic design makes it practical in the development of a portable, inexpensive field instrument suitable for the real time water suspended particle size analysis (Kitagawa et al, Canpolat et al). Spectral extinction is one of the standard optical properties, which has been applied to the characterization of aerosols and hydrosols. This is because it is very simple in terms of measurement principal optical arrangement (Ferri et al). However there are two difficulties in terms of experimental set-up and data retrieval process. One is overestimation of spectral extinction data due to the effect of the low angle scattering, the other is the highly ill-posed kernel results in unstable and unphysical inversion from the data containing measurement noise (Swanson et al). In this research, a

measurement system with a variable aperture before the collecting system has been applied to see the influence of forward scattering on the extinction spectrum for water samples with mono-dispersion particles. Due to the ill-posed nature of the extinction measurements, we have decided to constrain the PSD to a superposition of fine and coarse modes. This choice is based on the limited size resolution of the extinction spectra which would not be able to extract more complex modes. A least square fitting procedure of the measured extinction data is developed and applied to the retrieved obtain the PSD basedon the two-mode Gaussian model.

Background

When light I_0 passes through a random media, its intensity I decays exponentially by scattering and attenuation according to beer's law:

$$I = I_0 \exp(-\sigma L) \qquad (1)$$

where L is the path length, σ is the extinction coefficient due to both scattering (σ_s) and attenuation (σ_a). Strictly speaking, the above equation is applicable only when the scattering back into the optical path is negligible, which means an effort has to be made to limit the aperture of the detector to avoid the low angle scattering. Failure to do so will result in underestimate of the extinction coefficient since not only the transmitted signal but also some of the forward scattering signal are collected by the system, especially for particles very large compared to the wavelength, for which scattering is more pronouncedly peaked in the forward direction.

If no attenuation is present (σ_a =0) and the optical depth is small enough to validate the single scattering assumption, then $\sigma = \sigma_s$ which depends on the PSD and can be described by a Fredholm integral equation of the first-kind using Mie scattering theory assuming a spherical shape of the particles:

$$\sigma_s(\lambda) = \int_0^\infty Q(x, n_1) \cdot \pi r^2 f(r) dr \qquad (2)$$

$$\text{with size parameter } x = \frac{2\pi n_2}{\lambda} r = kr$$

Here, k is the wave vector in medium, n_1 and n_2 are the refractive index of the particles and the medium respectively. The scattering extinction factor Q is a function of both size parameter x and the particle refractive index and f(r) is the PSD as a function of particle radius r.

Unfortunately this kind of equation belongs to the class of ill-posed problems, where, in the presence of noise on the data, the solutions might be highly unstable and truly unphysical as well. In order to obtain the stable and meaningful solution, either constraints based on the specific PSD have to be imposed or constraints about the smoothness and positivity of the solution is required. This is true no matter which class of inversion algorithm is applied, ie. linear or nonlinear iterative algorithm. Since proper assumptions for a particular physical circumstance are necessary to make better result, we have decided that it is more important to resolve the modes of the distributions. It is well-known that the particles in the ocean body can be well represented by two kinds of particles: small and large particles so we use a two-mode Gaussian model to describe the PSD in water for the most general case:

$$f(r) = N_f G(r, \bar{r}_f, \delta_f) + N_c G(r, \bar{r}_c, \delta_c) \qquad (3)$$

where f stands for fine mode and c is for coarse mode. G is the normalized

Gaussian function with mean radius r and variance δ and N is the total particle concentration. Of course, we can also use log-normal modes but for a preliminary test, since we know a-priori that the particles have narrow distributions, gaussian modes are sufficient. The average radius ranges from 0.1μm to 1μm for the fine mode, from 1μm to 10μm for the coarse mode. The variance changes from 0.01μm to 0.4μm for the fine modes and from 0.3μm to 3μm for the coarse mode. In order to avoid the time consuming mie calculation, a lookup table is generated before the fitting by dividing r and δ for both modes into 10 grid points equally spaced in log scale for r and in linear scale for δ. Once this LUT for both modes is constructed using as reference $N_f = 1, N_c = 1$, the optical data can be very efficienty calculated for an arbitrary choice (guess) of the bimodal parameters, $(N_f, \bar{r}_f, \delta_f, N_c, \bar{r}_c, \delta_c)$ by first interpolating using on the LUT to obtain the optical data for $(N_f = 1, \bar{r}_f, \delta_f, N_c = 1, \bar{r}_c, \delta_c)$ and then multiplying each particle mode optical data by the desired densities N_f, N_c. Therefore the retrieval of PSD is equivalent to finding the six parameters within the boundary of the r-δ space on the basis of the two-mode Gaussian model to optimize the following goal function:

$$\min \sum_{i=1}^{41} (\sigma_m(\lambda_i) - \sigma_c(\lambda_i))^2 \qquad (4)$$

with σ_m is the measured extinction and σ_c is the calculated extinction using eq. (2) and (3).

In our experiments, the extinction spectrum has 1.5nm resolution between 0.4μm and 0.8μm. but since this data is over resolved, we undersample to 41 (10nm separation) wavelengths.

Experiment

The measurement of the extinction coefficient $\sigma_s(\lambda)$ were carried out on aqueous suspensions of standard polystyrene particles with known radius and refractive index of 1.589. The particle samples were from Duke Sci. Corp.; their radius varies from 0.1μm to 1μm which is the typical size ranges of mariner particles. The size distribution of each sample was nearly mono-dispersed with a standard deviation of less than 5% as provided by the company. As seen in Fig1, two multimode fibers with NA=0.22 and 200μm core size in diameter are used, one for delivery the light from tungsten lamp and the other for collecting the transmitted signal into the computer controlled spectrometer SQ2000 from Ocean Optics. A calibrated iris diaphragm was placed before the collecting system to prevent low angle scattering from entering the collection optics. The diameter of the iris can be varied from 1mm to 12mm and the path length of the sample cell is 5cm.

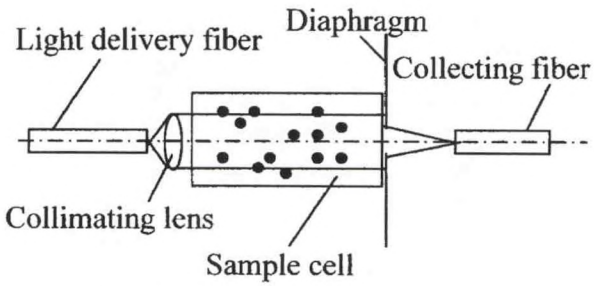

Fig1. Experimental Set-up

Fig2 a) shows that there is little influence of different iris sizes on the

extinction spectrum data for the particles with r=1.01μm.

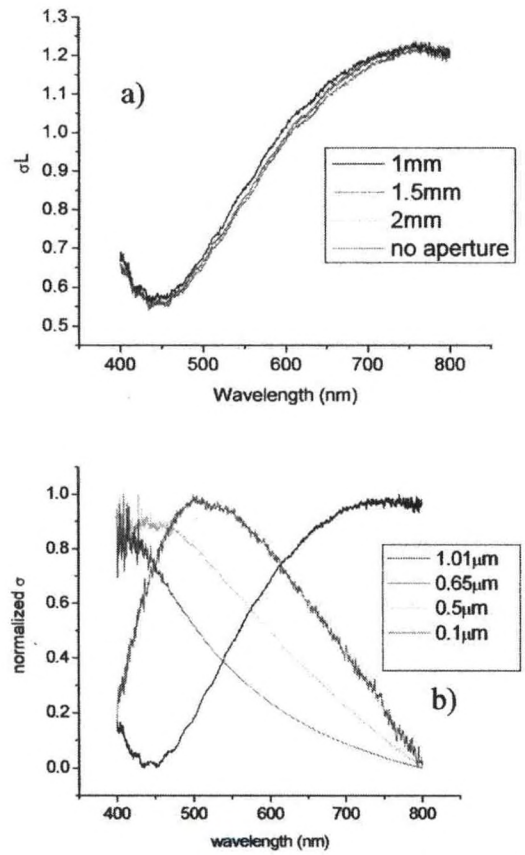

Fig2.a) Optical depth for particles with r=1.01μm with different iris diameter

b) Normalized extinction spectrum for four different particle sizes

This is probably the result of the small collecting area of the fiber which already eliminates most of the small angle scattering in the forward direction. Therefore, we remove the iris to simplify the system without sacrificing much of the data quality. The normalized extinction data obtained without the iris is showed in Fig2(b).

Inversion

We first use the single fine mode the by making N_c=0 to test the validity of the Gaussian model. The results have been displayed in the table1 and the corresponding calculated extinction coefficients are compared with the measured ones in fig3.

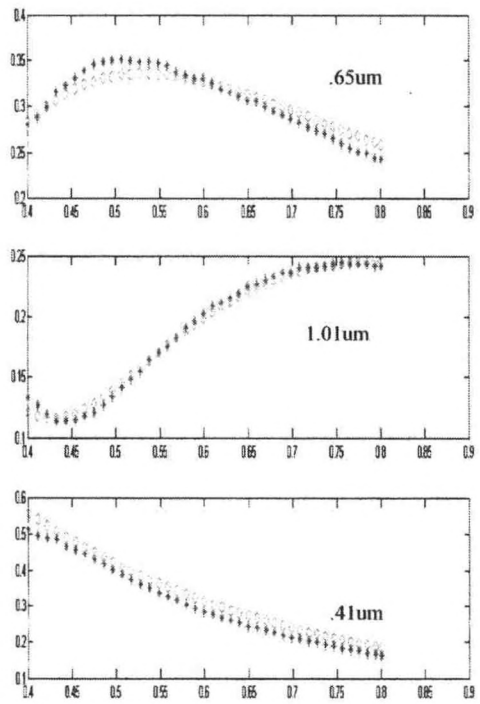

Fig3. Comparison between the measured and calculated extinction data for the three size distributions

The biggest discrepancy between the actual and retrieved sizes happens for particles with r=0.41μm. We believe this is mainly due to the measurement errors of the system. Actually comparing the two spectral extinction calculated by input the nominated and retrieved r and δ, the latter is even closer to the measurement data than the former. Even though considering this error, this fitting method is still able to retrieve r, δ and N

in a reasonable good accuracy. Another issue about this optimization is that how the convergence to the final answer depends on the choice of initial guess. Of course, its behavior is determined by r and δ. In mono-dispersed water samples here, the retrieved results are not sensitive to the initial guess for particles larger than 0.5μm in radius but for particles with radius smaller than 0.5μm the result sometimes converge to a local minimum which is different for different initial guess and more care in defining a minimum must be made. The test of the two modes Gaussian model is our next step which is under development.

Table 1 Retrieval results

Standard particle			final result		
r(μm)	δ(μm)	N	r(μm)	δ(μm)	N
0.65	0.03	0.083	0.64	0.03	0.073
1.01	0.03	0.022	1	0.04	0.021
0.41	0.01	0.33	0.34	0.03	0.53

Conclusion

A fiber optical instrument is built for in-situ particle sizing in water by spectral extinction of white light scattering. Although a lens-pinhole design is usually used to prevent the low angle scattering from entering the detector, it has been shown experimentally that the small core area of the collecting fiber and its limited NA are already enough to remove the small angle scattering effectively without iris. An empirical Gaussian model with fine and coarse modes was suggested to characterize the general PSD in water. By imposing these features which is unique for hydrosols, an optimization searching process is applied for the size retrieval from the measured extinction spectrum. The single mode model has first been tested on the standard polystyrene particles with radius smaller than 1μm and the retrieval results are satisfactory considering the measurement error.

Future work

This empirical model will be tested on water samples with broader distribution to simulate the more general circumstances. On the other hand, we are considering developing a system which is capable of measuring the spectral forward extinction and the backward scattering at the same time. The spectral extinction is not as sensitive to particle refractive index as that of backscattering coefficient and the variety of the refractive index is limited. Taking advantage of this, for a set of possible refractive index values corresponding PSD parameters can be obtained from the spectral extinction data. From this data, the direct calculation of the backscattering from these candidates is compared with the backscattering measurement. By this way, not only the PSD but alos refractive index of the particles in water can be retrieved from the combined extinction and backscattering data.

Acknowledgements

This work is supported by grant from NOAA #NA17AE1625.

Reference

Swanson N. L. , B. D. Billard; "Limits of optical transmission measurements with application to particle sizing techniques". Appl. Opt. 38, 5887-5893. (1999)

Ferri F., A. Bassini; "Commercial spectrophotometer for particle sizing. Appl. Opt. 36, 885-891. (1997)

Kitagawa Y., A. Hayashi; "Fiber-optic particle size monitor based on white-light scattering" Appl. Opt. 31, 859-865 (1992)

Boss, E. , M. S. Twardowski; "Shape of the particulate beam attenuation spectrum and its inversion to obtain the shape of the particulate size distribution." Appl. Opt, 40, 4885-4893 (2001)

Nefedov A. P., O. F. Petrov "Analysis of particle sizes, concentration, and refractive index in measurement of light transmittance in the forward-scattering-angle range", Appl. Opt. 36, 1357-1366 (1997)

Canpolat, M., J. R. Mourant; "Particle size analysis of turbid media with a single optical fiber in contact with the medium to deliver and detect white light" Appl. Opt. 40, 3792-3799 (2001)

BIO–OPTICAL OCEANOGRAPHY MEASUREMENTS DURING AEROSE 2004

Roy A. Armstrong, Yasmín Detrés, Jorge Corredor, Julio Morell, José López, Aurora Justiniano, Graciela Garcia-Moliner, Ramón López, and Miguel Canals

NOAA Center for Atmospheric Sciences (NCAS), University of Puerto Rico, Mayaguez, PR 00681

Abstract

The Aerosol and Ocean Science Expedition (AEROSE) 2004 combined atmospheric and oceanographic measurements acquired with a large number of in-situ and spaceborne sensors. The cruise departed from Bridgetown, Barbados on February 29 and returned to San Juan, Puerto Rico on March 26. Continuous surface measurements were made throughout AEROSE in addition to five oceanographic stations that where occupied during the eastward Trans-Atlantic leg of the cruise. Bio-optical oceanographic measurements were obtained to characterize water masses along a gradient traversing the subtropical North Atlantic Ocean across the area of influence of Saharan dust plumes. Apparent and inherent optical properties were measured at each station. Even though the Tropical North Atlantic Ocean has been described as an oligotrophic region with low primary productivity, spatial variation was observed along the AEROSE transect. Enhanced values of productivity were recorded near coastal waters and in the upwelling regions off Mauritania. Lowest values were found in the more oligotrophic regions of the North Atlantic Ocean.

Introduction

Deposition of iron and inorganic nutrients from atmospheric aerosols is thought to modulate biogeochemical processes in the ocean by fertilizing surface waters enhancing primary production. In conjunction with efforts to characterize the dust plumes emanating from the African continent during the AEROSE expedition, we seek to assess these processes in near-surface waters of the tropical Atlantic by quantifying the photosynthetic efficiency of phytoplankton and their rates of C fixation. One of the goals of AEROSE was the quantification of these processes along a gradient traversing the oligotrophic subtropical North Atlantic Ocean across the area of influence of Saharan dust plumes during this time of the year.

Bio-optical oceanographic measurements were obtained to address the effects of dust aerosols on the marine boundary layer. Apparent and inherent water optical properties such as upwelling radiance, downwelling irradiance, remote sensing reflectance, backscattering, and diffuse attenuation coefficients were measured at each station.

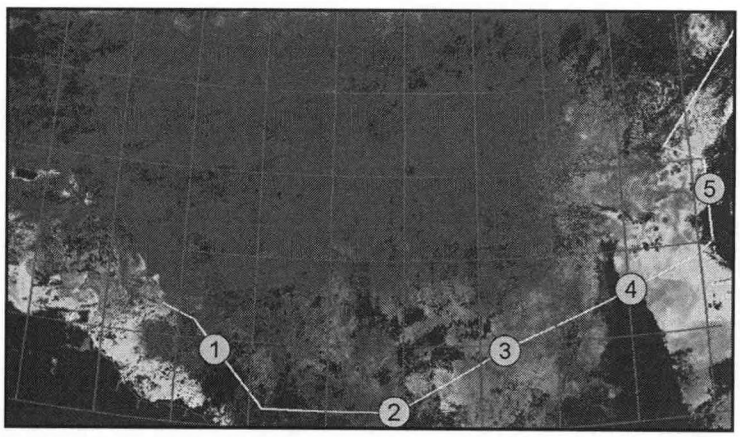

Figure 1. MODIS Chlorophyll-a composite (March 2- 12, 2004) with the eastbound AEROSE cruise tract and station numbers.

Methods

The NOAA Ship Ronald H. Brown departed from Bridgetown, Barbados on February 29 and returned to San Juan, Puerto Rico on March 26. Continuous surface measurements were collected from the flow-through system

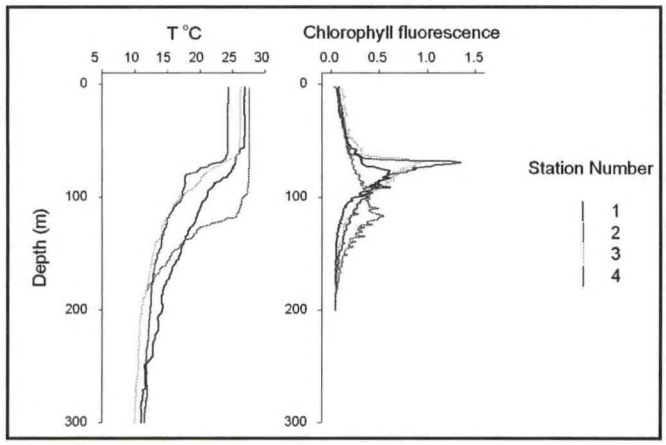

Figure 2. Profiles of temperature and chlorophyll fluorescence at AEROSE stations 1-4.

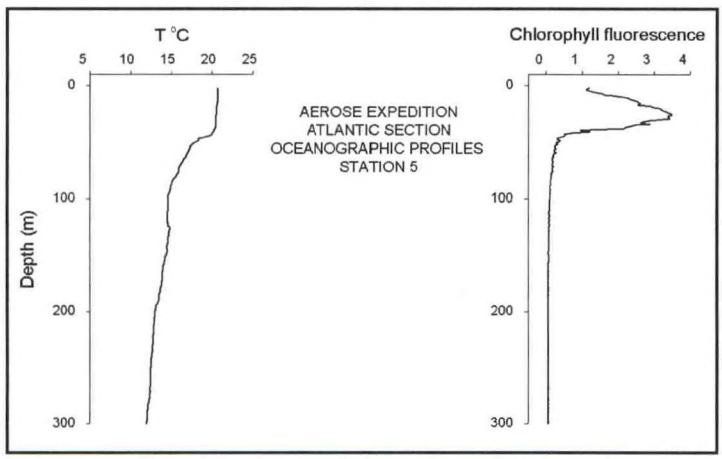

Figure 3. Profiles of temperature and chlorophyll fluorescence at station 5.

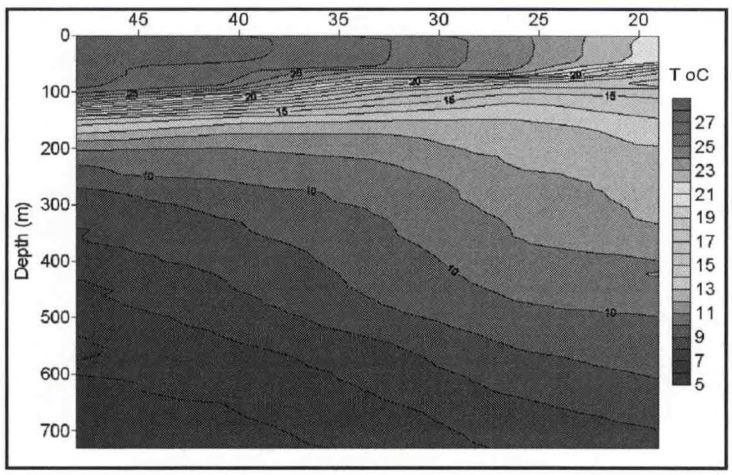

Figure 4. Zonal XBT temperature section along the AEROSE transect.

of the Ronald Brown Ship and in five oceanographic stations that where occupied during the eastward Trans-Atlantic leg of the cruise (Figure 1).

Profiles of apparent water optical properties such as upwelling radiance (Lu), downwelling irradiance (Ed), and the diffuse attenuation coefficient (Kd) were measured at each station. Hyperspectral Lu and Ed profiles were obtained with a Satlantic Hyperpro free-fall spectroradiometer. A Biospherical Instruments PRR-600 provided profiles of Lu, Ed, and Kd at six spectral bands. A GER 1500 spectroradiometer was used from the ship to measure Lu, sky radiance (Ls), and Ed, which are used for calculating remote sensing reflectance (Rrs).

The backscattering coefficient was measured to 200 m using a HOBI Labs Hydroscat-6 at wavelengths of 442, 470, 510, 589, 620 and 671 nm. Photosynthetic efficiency was determined by Fast Repetition Rate Fluorometry (FRRF). C-fixation was measured using a 14C tracer through "photosynthetron" incubation for the derivation of Photosynthesis vs. Irradiance curves. Water samples for the FRRF measurements, Carbon 14 productivity analysis, and for photosynthesis-irradiance experiments were obtained at 10 m and at the deep chlorophyll maximum while on station, and at 5 m from the ship's flow-through system while underway. Expendable bathythermographs (XBT's) were launched at intervals of ca 120 miles along the transect.

Results

Vertical profiles for temperature and chlorophyll fluorescence at stations 1-4 are shown in Figure 2. Mixed-layer depth was greatest (ca. 120 m) at Station 2 in the western tropical Atlantic and stabilized at 60-70 m in the central Atlantic (Sta. 2-4).

Except for temperature at Sta. 1, which was slightly cooler, a consistent West-East gradient was observed in temperature as well as other mixed-layer properties. Thermocline waters showed weak temperature gradients in the West and became increasingly sharper

towards the East. The deep chlorophyll maximum shoaled across the transect, from a maximum depth of 117 m at Sta. 1 to a minimum of ca. 60 m at Sta. 3 and 4. At station 5 in the area of influence of the Cap Blanc upwelling off the coast of Africa, the mixed layer shoaled to 28 m and chlorophyll fluorescence in this thin layer increased dramatically (Figure 3).

Water mass structure is more clearly depicted in the finer-grid XBT series (Figure 4) where shoaling and cooling of the mixed layer accompanied by sharpening of the thermocline from west to east is apparent. Intrusion of southern Atlantic Central Water occurs from the east to ca. 35 oW. The water mass occupies a broad range between 100 and 350 m at its easternmost extreme.

The AEROSE 2004 expedition presented the opportunity to examine the spatial variation in water optics and primary productivity along the Tropical North Atlantic Ocean, from open water oligotrophic waters to areas of coastal upwelling.

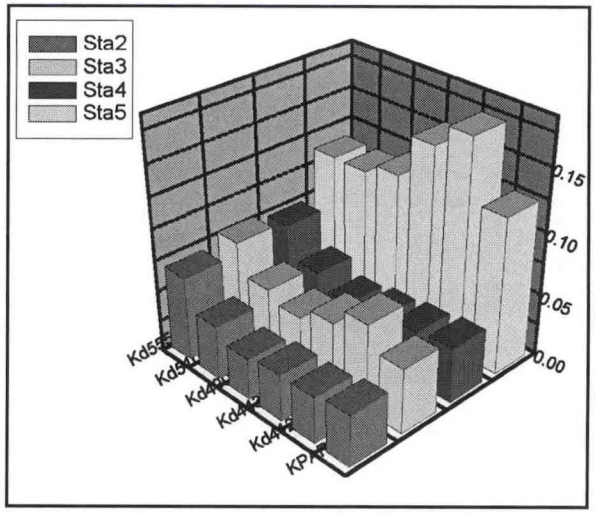

Figure 5. Mean Kd or diffuse attenuation coefficients for oceanographic stations 2-5.

The diffuse attenuation coefficient (Kd), as computed from light extinction profiles obtained with the PRR600 at stations 2-5, are shown with maximum values, at all wavelengths, at station 5 (Figure 5). KPAR values ranged from a low of 0.041 at Sta 2 to a high of 0.125 at Sta. 5 in the upwelling zone. High attenuation in the 555nm band may be explained by high Trichodesmium populations as these organisms contain the accessory pigment phycoerythrin which absorbs in this band.

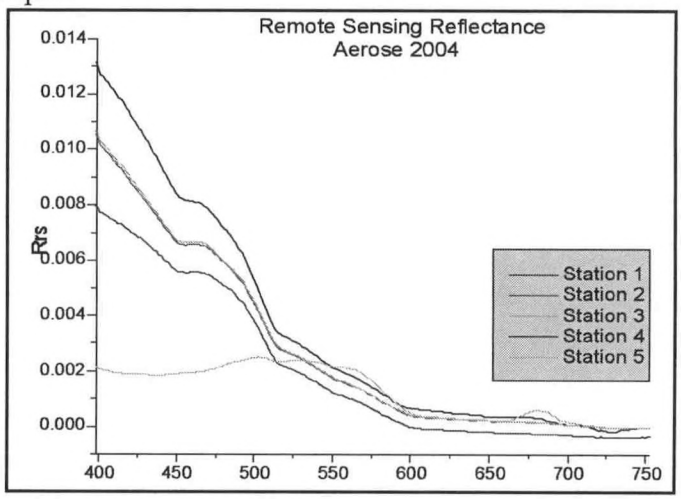

Figure 6. Remote Sensing reflectance of surface waters at the five AEROSE stations.

Remote sensing reflectance measurements of near surface waters show a West-East gradient as decreasing values in the blue wavelength region between 400-500 nm (Figure 6). This is due to absorption of blue wavelengths by chlorophyll-a, which dominated optical variability in these waters. At station 5 in the upwelling region off Africa, the highest chlorophyll values are responsible for the lowest Rrs values <500 nm. Station 5 also shows a small Rrs peak at 683 nm which is due to natural fluorescence of chlorophyll in this spectral region.

Photosynthetic efficiency has been related with nutrient stress. Variations in fluorescence quantum yield are observed as a result of nutrient availability. When this stress is alleviated as a result of an episodic nutrient pulse such as coastal upwelling, river water inputs, or Aeolian nutrient (e.g. iron) deposition, an increase in photosynthetic quantum yield can be observed. Several portions of the cruise track were sampled by Fast Repetition Rate Fluorometry in order to characterize photosynthetic efficiency along the eastward transect of AEROSE.

Higher potential for productivity was found near coastal waters off South America and Northwestern Africa and lower values in the central gyre of the Tropical North Atlantic (Figure 7).

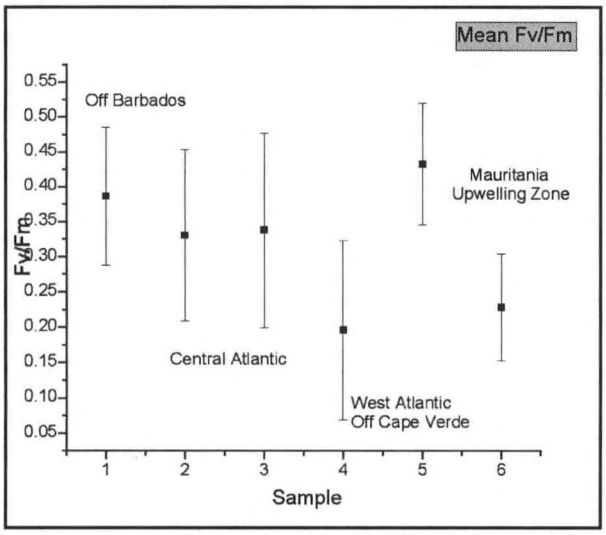

Figure 7. Photosynthetic efficiency measured in surface waters during AEROSE.

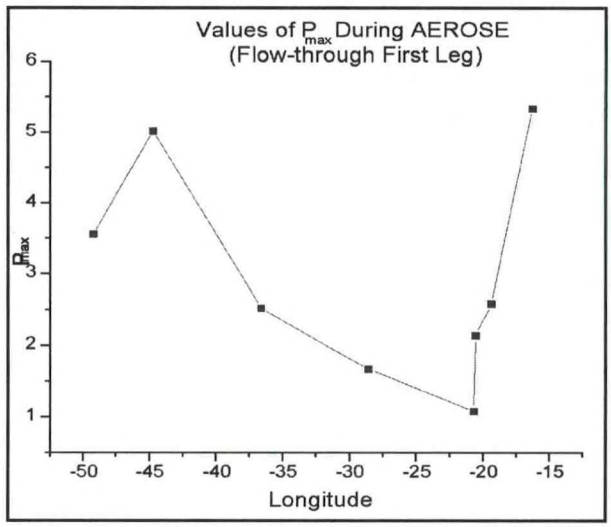

Figure 8. Pmax values during the eastbound transect of AEROSE.

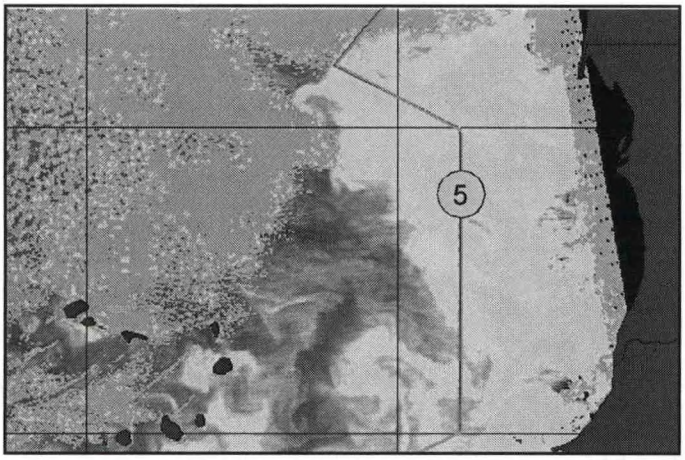

Figure 9. MODIS chlorophyll-a image of the upwelling region off Mauritania during AEROSE with the location of Station 5.

Near-surface Pmax values for samples taken from the flow-through system of the ship at 5 m depth ranged from 1.08 to 5.33 mg C mg Chl-1 hr-1 near the Canary Islands (Figure 8).

Of the AEROSE eastward bound stations, the highest value was recorded on Station 5 at both 10 m and DCM depths. This station was located near the coast of Africa and was influenced by the upwelling of Mauritania (Figure 9).

Results show relatively high values of Kd, photosynthetic efficiency, and primary productivity off South America due to the influence of the Amazon River plume. Highest values for all these parameters were found near the upwelling region of northwestern Africa. Lowest values were recorded in the more oligotrophic regions of the center Tropical North Atlantic Ocean with some small variability between stations 2-4. This variability could be due to the effects of variable Saharan dust deposition along the cruise tract. Lowest values of Rrs were obtained at station 5 due to high absorption by chlorophyll-a in these highly productive waters.

ACKNOWLEDGEMENTS

This research was funded by NOAA's Center for Atmospheric Sciences (NCAS) under the Educational Partnership Program and by NASA's Tropical Center for Earth and Space Studies (TCESS) at UPRM.

Analyzing Nesting Periods and Cyclical Return Patterns of Leatherback Sea Turtles (Dermochelys coriacea) on Sandy Point Beach, St. Croix, United States Virgin Islands

Kemit-Amon Lewis,

Marine Sciences Program, , Savannah State University

Abstract

The resilience of the leatherback sea turtles (Dermochelys coriacea), an endangered species, is evident in an increase in nesting activities on St. Croix, United States Virgin Islands. Females nest during the months of February through August along Sandy Point Beach, located on the southwestern coast of St. Croix. To better understand variations in nesting periods and cyclical patterns, I analyzed data collected by the Earthwatch organization in collaboration with the Department of Planning and Natural Resources Division of Fish and Wildlife of the US Virgin Islands. Between 1982 and 2002 sum of the annual total nesting females observed on Sandy Point Beach was 1205. For the same period (1982-2002) there were 9482 activities recorded. The mean number of activities per turtle was approximately 7.9. Return nesters were as much as 57% of the total number of nesting females for a given year. The most frequent return patterns were two- (33.1%) and three-year (39.7%) cycles, which supports the current theory on leatherback nesting behavior.

Introduction

According to Lutz and Musick (1997) the leatherback sea turtle, (Dermochelys coriacea), is considered the most pelagic sea turtle. It may reach sizes between 1.8 to 2.4 m and weigh between 544 to 680 kg. Female leatherbacks reach sexual maturity at 10 to 15 years of age. This species of sea turtle migrates from foraging to mating areas. From there, males return back to foraging areas while females travel to nesting areas. Female leatherbacks can store semen that is used throughout the nesting period. Leatherbacks prefer open access beaches, although such beaches with little shoreline are susceptible to beach erosions. In a nesting season leatherbacks lay approximately 6.17 clutches, approximately 81.5 eggs per clutch and renest about every 9.5 days.

Leatherbacks are listed as a worldwide protected endangered species by the Federal Government of the United States. The decline in leatherback populations is due mainly to loss of nesting habitat, destruction of nests by poachers, ingestion of marine debris, propeller wounds and interaction with commercial fishing operations. They have historically been poached for their meat as well as for their eggs.

The largest nesting assemblages found in the Atlantic and Caribbean are found in the US Virgin Islands, Puerto Rico, and Florida. The increase in nesting leatherbacks has been largely attributed to the assistance of government agencies and non-profit organizations. On St. Croix, information is gathered each year by the Division of Fish and Wildlife through the Earthwatch organization. The purpose of my study was to analyze nesting periods and cyclical return patterns of nesting leatherback sea turtles on Sandy Point Beach, St. Croix.

Materials and Methods

From 1982, during February and August of each year, the Earthwatch organization has worked towards the continued increase in leatherback activity on Sandy Point Beach National Wildlife Refuge, St. Croix, United States Virgin Islands. Earthwatch volunteers observed activity on the beach from approximately 8:00 pm each night to 5:00 am the following morning or until the last female leaves the beach. Sandy Point Beach is 3.0 km long. Stakes have been planted along the beach, near the vegetation line, each

separated by 20 m. A triangulation method (measure from the two stakes the nest is between) is used to record the location of nests.

As adult leatherback females move onto shore, Earthwatch volunteers used tag scanners to identify the turtle. Leatherbacks without tags were tagged before they returned to the ocean. While on shore, the activity of the turtle was observed and recorded. Activities include arriving, body-pitting, digging, laying, and leaving. In the event that a female turtle nested in an area thought unsafe, volunteers collected the eggs and relocated the nest.

For the years 1994 to 2000, I calculated occurrence percentages of return patterns. To determine the activity of nesting females, I compared the nesting female to nesting activity ratio.

Results

The total number of female turtles that nested at Sandy Point generally increased over time (Figure 1). 1997 and 2001 had the highest activity recorded (1,144 and 1,267, respectively). Those years also had the most female turtles: 118 in 1997 and 186 in 2001. The lowest activity was recorded in the years 1982 (158) and 1986 (139).

Between 1982 and 2002 the sum of total nesting female turtles observed on the island of St. Croix was 1205 exhibiting 9482 nesting activities. The relationships between the number of females and the number of activities were generally directly proportional. The average amount of activity per female turtle ranged between 6.7 (1984) and 9.7 (1997), with an overall mean of 7.9. The nesting activities were normally greatest between mid April and mid June.

The return pattern of 94 nesting females on Sandy Point Beach was analyzed between 1994-2000. The most common return patterns were a two-year (33.1%) and a three-year (39.7%) cycle (Table 1). A four-year pattern was observed 17.4% of the time, a five-year pattern 8.3% of the time, and a one-year pattern 1.7% of the time. Return nesters were as much as 57% of the total number of nesting females for a given year.

Discussion

The number of nesting activities on Sandy Point Beach was directly related to the number of nesting females (Figure 1). Also, my results support the theory that female leatherbacks generally nest on two- or three-year cycles (Table 1). The one-, four-, and five-year patterns may be caused by the following reasons. One hypothesis for the one-year return pattern is that the female was sexually active and nesting in consecutive years. Another hypothesis is that the female may have returned to Sandy Point beach in consecutive years but without fertilized eggs and unable to nest. Also, there may be some social behavior attributable to the return. Four- or five-year return patterns may be a result of females being sexually inactive between the years they were observed on Sandy Point. There is also the chance that those females may have been undetected in other years. However, the likelihood of this is slim as nesting females are observed more than once throughout the nesting period and may beach six or seven times. Moreover, we are still not aware of whether or not females that nest on Sandy Point Beach do so exclusively, so they could be nesting on other beaches during this time. Again, all of the data that I analyzed supports the theory that nesting female leatherback sea turtles return to the same site, normally on a two- or three-year cycle.

REFERENCE

Lutz, P. and Musick, J. 1997. The Biology of Sea Turtles. CRC Press.

ACKNOWLEDGEMENTS

I thank the employees of the United States Virgin Islands Department of Planning and Natural Resources Division of Fish and Wildlife and the Earthwatch staff: Jeanne Alexander, Sean Deishley, Kendra Garrett, Peter Dutton, Donna Dutton, Rafe Boulon, Scott Forbes, Janet Cowden, James Rebholz, Janine Ferguson, Barry Krueger, Ana Barragan, John Shih, Liz Taylor, Philippe Mayor and Violet Mayor for the

work they have done on Sandy Point Beach. I would like to give special thanks to Dr. William Coles at the USVI Division of Fish and Wildlife for introducing me to leatherback turtles, Dr. Mary Carla Curran as well as Dr. Dionne L. Hoskins, Megan Bradley, Dr. Matthew Gilligan, Dr. Joseph Richardson and Dr. Carol Pride at Savannah State University for all of their assistance and support.

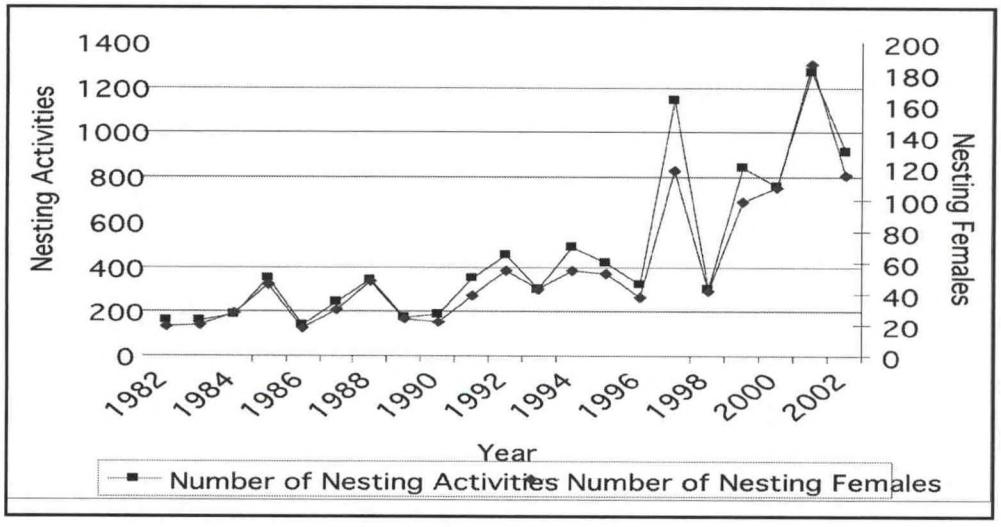

Figure 1: Frequency of nesting Leatherback Sea turtles versus their activities on Sandy Point Beach, St. Croix, USVI.

Return Pattern (Cycle)	Incidence of Occurrence	
One Year	2	1.7%
Two Year	40	33.1%
Three Year	48	39.7%
Four Year	21	17.4%
Five Year	10	8.3%

Table 1: 1994 to 2000 return patterns on Sandy Point Beach, St. Croix (n=121).

GC/MS Characterization of Terrestrial Lipid Biomarkers in Recent Sediments of a Fresh Water River (Pocomoke River, MD)

Nianhong Chen[2],Gerald Kananen[1], and Eric May[1]

[a]University of Maryland Eastern Shore; Princess Anne, Maryland

[2] Old Dominion University; Norfolk, Virginia

Surface sediments were collected from three locations at the lower Pocomoke River characterized by wetland deciduous forest (Site 1), wetland marsh (Site 3), and a transition zone between the two types (Site 2). Acceleration solvent extractor (ASE) was used to extract free lipids from the sediments, followed by GC/MS screening of solvent-extractable lipids compounds. Results show distinctly different lipid composition between Site 1 and the other sites. Teracosane (n–C24) is the most abundant n-alkane at Site 1 and there was no minimal odd/even preference (OEP). In contrast, n-alkanes at Sites 2 and 3 show strong odd over even predominance with peak at nonacosane (n-C29). Long chain n-alkenes, n-alkan-2-ones and n-aldehydes were detected at Sites 2 and 3 but not detected or very low at Site 1. n-Alkan-2-ones follow the same OEP as n-alkanes, while the alkene and n-aldehyde show even over odd predominance. These results suggest that the long chain n-alkanes at Site 1 without OED are predominantly derived from fossil sources. Similarity in distributions between aliphatic lipids (n-alkene, n-alkan-2-one and n-aldehydes) in sediment samples and the aliphatic lipids recovered form sulfur bound organic matter in deep sediments of the Mud Lake (Florida) supports the view that reactive aliphatic lipids are precursors of aliphatic sulfuric bound organic compounds.

THE CASE FOR USING REVOCABLE ACTIONS IN PROTOCOLS GOVERNING THE RELEASE OF POTENTIALLY INVASIVE AQUATIC SPECIES [1]

Michael Thomas, Ph.D.
Environmental Cooperative Science Center, Florida A&M University

Introduction

Problems related to the intentional introductions of potentially invasive aquatic species (PIAS) are well documented and have a long history in North America (Courtenay and Stauffer, 1984; Benson, 2000; Dextrase and Coscarelli, 2000) and have been the interest of United States policy makers via legislation for the past 100 plus years; Lacey Act of 1900, National Environmental Policy Act of 1969, the Endangered Species Act of 1973 the Aquatic Nuisance Prevention and Control Act of 1990 (ANPCA) and its material amendment the National Invasive Species Act of 1996 (NISA).

Because historic introductions of invasive aquatics have caused several noteworthy environmental problems in the past, policy makers and life scientists have developed an ever evolving series of decision protocols to guide their actions and reduce the likelihood of harmful releases. Unfortunately, the results of these efforts have been mostly ambiguous, in part because of their motivating paradigm: ecology. While carefully designed to reduce harmful environmental consequences, the ecological paradigm fails to adequately address the fundamental cause of all intentional introductions; human actions, based on preferences and incentives.

A review of historic protocols reveals several common traits (see Thomas, 1996). Most protocols have a proprietary clause that strongly discourages action outside the protocol. Each protocol is designed to force introspection, deliberation and care into the decision making process. Furthermore, as vehicles of deliberation, protocols depend on making knowledgeable decisions necessitating the collection of information. Protocols differ primarily in the type of information collected and its means of compilation. They can also differ in their primary motivation, e.g., protect-the-environment, vs. protect-social-interests.

Generally, the features to most protocols can be summarized as follows:

1. Protocol Propriety: Each protocol stresses the importance that all decisions work within its framework exclusively. Exceptions to the protocol are discouraged and would likely reduce the effectiveness of the protocol.
2. *Ex ante* Information: Using expert opinion, field experimentation, literature review and simulation, *all protocols stress the importance of determining the expected outcome of a release before its approval.* These efforts involve resolving environmental interactions and species life histories.
3. *Ex post* Information: Using trials with varying degrees of revocability, all protocols stress gathering information on the *actual* affects of releases. This information does not require a detailed understanding of the host or contributing ecosystem, only the ability to observe outcomes and know if harm has occurred to either the host environment or society.
4. Decision Criteria: Basically environmentally centered, these criteria stress the avoidance of actions with potential deleterious effects on the environment. They can range from avoid any action with even the potential of environmental harm, to an environmental benefit/cost test. Such decisions are typically made by panels of biologists empowered to make decisions based on their weighing of environmental gains and losses.

[1]This is based on an earlier draft of a paper pending publication in the Journal of Aquaculture Economics and Management.

5. Truth in Release: All protocols stress the importance to release only the under consideration and avoid the accidental release of associate species such as parasites or disease. Quarantines are the rule of order.

All protocols share these components, but differ in their emphasis and ordering. Established protocols were written by biologists and reflect their environmentally centered view of the decision process rather than those that are more socially motivated. For those approaches that consider economics, the initial decision criterion is environmentally based, with economics not entering the decision process until the end, and then only in the case of ambiguous results.

Even with present day approaches initiated by the NISA, most protocols are typically most concerned with gathering *ex ante* information. This emphasis likely reflects a natural inclination by biologists to attempt a full understanding of the species and its potential interactions both within its native environment and the potential host environment. Environmental and systems biologists are trained to solve the inter-workings of the environment and so naturally avail themselves to opportunities to unravel the complexity of the ecosystem. While knowledge is a good thing, protocols that foremost stress the collection of information are not necessarily the most efficient or effective in preventing harmful releases.

Collecting *ex ante* information under uncertainty reveals two burdens: it can be costly to gather, and is often indeterminate. While *ex ante* information may help identify the possibility of a harmful outcome or even a catastrophe, it cannot be counted upon to totally relieve the risk of uncertainty. Its indeterminate nature allow for the possibility of information gathering becoming more and more costly as research continues to delve further and further into ecosystem complexities. Often in search of a thorough nderstanding, researchers discover only increasing degrees of complexity and uncertainty, eventually concluding that they will never know enough to fully understand the effects of a release. It is this inability to fully understand all possible outcomes prior to a release that leads many agencies to restrict adherence to protocols by a finite budget. The failure or success of a release is then determined by the penchant of agency budgets.

The second approach to decision making is to only take revocable actions, permitting an *ex post* reversal of a harmful release. This may avoid the twin burdens of *ex ante* information; the need for costly information and, if one can reverse a harmful action with certainty, then the outcome is determinant.

Thomas and Randall (2000) combined these two approaches to develop a protocol that uses both imperfect *ex ante* information and imperfect revocability to demonstrate an incentive structure with moral hazard. This paper will develop the theoretical basis for the advantage of revocable actions over *ex ante* information, providing the motivation for the Thomas and Randall protocol's dependence on revocable actions.

Methodology:

Consider that the action of deciding whether or not to release a PIAS into a new host environment is akin to a decision maker in pursuit of a global optimum. The decision maker desires to take actions that they believe will improve the human condition, but there are risks associated with their actions. Much like a climber in search of a hill top in uncharted terrain, the decision maker is searching for the high ground while trying to avoid harmful outcomes.

Reconsider the two approaches to avoiding harmful outcomes from PIAS; *ex*

ante information and *ex post* revocability. Thomas (1996) showed that these approaches can be used in search of optimal outcomes while avoiding harm.

The obvious first approach is to *ex ante* incrementally learn all there is about the alternative actions and when all *ex post* outcomes are known with certainty then move toward the desired outcome with due deliberation, avoiding all harm. If the goal is to improve utility while avoiding a catastrophe, then an acceptable result might be any outcome that avoids the catastrophe. With fully informed decisions, however, the decision-maker could choose the global optimum and thereby do better than simply avoiding the catastrophe.

The second, subtler, approach is that of taking only actions that have revocable outcomes. If a decision maker can look at the outcomes after the fact and reverse those actions that lead to harmful outcomes before they reach fruition, the harm is avoided. While the process of revoking a decision is *ex post*, it singularly depends upon the *ex ante* selection of only those actions that can be reversed and outcomes revoked.

The key difference between these two approaches then becomes revocability of outcomes. Within the revocability framework, the process of *ex post* evaluation entails a sequential movement through a series of actions, with the assurances of good record keeping and revocation to allow backtracking when needed. The pathway of actions can always be reversed with a return to either a more desirable previous outcome or the avoidance of a pending catastrophe resulting from the most recent action.

To more formally compare these two approaches to decision-making, define $U_d(X)$ as a desired or baseline level of a decision-maker's utility based upon X, an *ex post* outcome or vector of events resulting from an action and from which utility is derived. Let $U_i(X_i)$ represent the decision-Maker's utility from the *ex post* outcome resulting from the action of selecting alternative i. Alternatively, if action j was selected, its *ex post* outcome would generate utility $U_j(X_j)$. If one assumes well behaved preferences, i.e., completeness, reflexivity, continuity, strong monotonicity, local nonsatiation, and strict convexity, then the *ex post* outcomes from different actions can be compared and ranked ordered by preference. Assume that a utility improving decision-maker has some lower level of utility below which life becomes completely intolerable, $U_{min}(X)$. Then define any outcome resulting from action i that results in $U_i(X_i) < U_{min}(X_{min})$ as a catastrophe.

Looking at only the results of this complex system, the *ex ante* outcomes may be described using the rules of probability. To the outside observer of this complex system, the *ex ante* outcome set that could result from selecting action i would be the n array of possible outcomes $\hat{X}_{i,j}$, j = 1, n, and their associated probabilities $\hat{p}_{i,j}$ where $\Sigma \hat{p}_{i..} = 1$. After the action is taken, an outcome results from the *ex ante* outcome set. The *ex post* outcome is a single vector of events with probability of $p_{i,k} = 1$, if outcome k occurs *ex post*, with the other n-1 outcomes not occurring.

Assume a decision-maker decides among alternative actions based upon his evaluation of the *ex ante* outcome set. Further, assume that a utility improving decision-maker may choose from either the full *ex ante* information or revocability strategies in his quest for a utility improving outcome. The *ex ante* full information approach involves knowing not the *ex ante* outcome set, but the *ex post* outcome associated with each possible action, rank ordering the *ex post* outcomes and selecting the action that leads to the outcome with the largest utility gain.

The second method of taking utility improving actions would depend upon the ability of a decision-maker to revoke an action that produced an undesirable *ex post* outcome, and return to the *status quo*. A complete search with revocability would reveal all outcomes *ex post*, with backtracking to the one providing the largest utility gain. Considering the choice between these two searching procedures consider the following results reported by Thomas (1995):

1. If *ex ante* full information is costless, a decision-maker would choose an action that yields a utility maximizing *ex post* outcome.
2. Using *ex ante* full information, if at least one *ex ante* outcome set is unbounded (unknown number of possible *ex ante* outcomes within a set), it is not certain that the decision-maker can achieve the utility maximizing outcome.
3. If outcomes within the *ex ante* outcome set are not known with certainty, i.e., only $\hat{X}_{i,j}$ and $\hat{p}_{i,j}$ are known, there is no certainty that the decision-maker will avoid a utility loss or catastrophe, U_{min}, from the *status-quo* position of U_s, so long as $P(U_i < U_s) > 0$, or $P(U_i < U_{min}) > 0$, for every possible action.

From these three points, one can draw the following conclusions: (a) If *ex ante* full information is unbounded, the decision-maker can at best maximize not U, but its expected value, E(U). (b) Assume every possible action has at least one *ex ante* outcome $\hat{X}_{i,j}$, and $\hat{p}_{i,j} > 0$ that it is harmful. Then the decision-maker, while choosing an E(U) maximizing action, cannot avoid harm with certainty. (c) Assume every possible action has at least one *ex ante* outcome $\hat{X}_{i,j}$, and $\hat{p}_{i,j} > 0$ that is catastrophic. Then the decision-maker, while choosing an E(U) maximizing action, cannot avoid the catastrophe with certainty. (d) Retaining the assumptions of conclusions 1b, and 1c, the decision-maker cannot, by investing in better *ex ante* information, avoid harm or catastrophe with certainty. (e) Assume some (but not all) possible actions have *ex ante* $\hat{p}_{i,j} = 0$ of harmful or catastrophic outcomes. Then the decision-maker can avoid harm or catastrophe with certainty by choosing from this subset of actions that have $\hat{p}_{i,j}=0$, perhaps at the cost of foregoing maximizing E(U). (f) Retaining the assumptions of conclusions 1d and 1e, the decision-maker, by investing in better *ex ante* information, enjoys the possibility of avoiding harm or catastrophe with less sacrifice to E(U), by better characterizing $\hat{X}_{i,j}$ and $\hat{p}_{i,j}$.

Additionally Thomas (1996) showed that:

4. If revocability of outcomes is costless, the decision-maker will choose an action that yields a utility maximizing *ex post* outcome.

From this point, consider the following: (a) Let revocability be costly. The decision-maker cannot assure an U_{max} *ex post* outcome (because he might exhaust his resources during revocation before reaching the U_{max} *ex post* outcome.) (b) Let revocability be costly. The decision-maker cannot avoid harm or catastrophe for certain (because he might exhaust his resources just when he encounters a harmful *ex post* outcome.) (c) Let revocability be costly. If the resource budget permits at least one revocation of an *ex post* harmful or catastrophic outcome, the chances of avoiding harm are improved. The following improve chances of avoiding harm; i.) $p_{i,j}$ decreasing, where $X_{i,j}$ is the harmful outcome, ii.) c(r) decreasing, where c(r) represents the cost of revoking an outcome, and iii.) resource budget increasing. (d) If some but not all possible actions are revocable, there is no guarantee of obtaining

the global optimum by following pure startegies of ex post revocability. It may be possible thet the global optimum is obtainable only by a sequence including one or more irrevocable actions.

5. Lastly, Thomas (1995) stated that with at least one outcome stochastic and catastrophic in the *ex ante* outcome set for each and every alternative action, the utility improving decision maker cannot avoid catastrophe with certainty except with costless revocability of outcomes.

Assume that the real world is characterized by complex systems replete with unbounded *ex ante* full information, costly better *ex ante* information and costly and uncertain revocability of outcomes. From the conclusions above, if the possibility of harmful or catastrophic outcomes exists for each and every possible action, pursuing *ex ante* information to maximize the expected utility E(U) will not avoid these bad outcomes with certainty. Corollaries 1f and 1g would suggest a safe approach to seeking maximized E(U) would be to limit actions to only those that have *ex ante* $\hat{p}_{i,j} = 0$, of harm or catastrophe. However, this action may cause the decision-maker to forego maximizing E(U). Furthermore, in a real world the set of actions with $\hat{p}_{i,j} = 0$ for harmful or catastrophic outcomes may be empty. Then better *ex ante* information will be of little help in avoiding the harmful or catastrophic outcome while searching for the maximized E(U).

For a moment, return to the two search strategies for consideration by the decision-maker. One could invest more resources on *ex ante* better information which will reduce the sacrifice of E(U). The second strategy would be that of revocability which reduces the chance of harmful or catastrophic outcomes. Now consider revocability with positive cost. If the utility maximizing objective is unknown *ex ante*, it is possible that the quest for the optimal outcome could exhaust a finite budget before ex post identification and backtracking to U_{max}. Now assume some, but not all possible actions are revocable; confining the search to the revocable subset could sacrifice some expected utility E(U). By investing in the technology of revocation, it may be possible to reduce the sacrifice of E(U). The following strategies have considerable appeal: 1.) Using estimates of $\hat{X}_{i,j}$ and $\hat{p}_{i,j}$ for as many decisions as there are reasonable *ex ante* estimates, choose the action that maximizes the expected utility E(U). This will not require *ex ante* full information, only reasonably available information. If the action results in a reduction of utility, then revoke it. Unfortunately, this process will not guarantee harmless *ex post* outcomes because revocability of utility decreasing outcomes could be costly. With bad luck, a series of utility decreasing outcomes could exhaust a finite budget. However, the process is still likely to lead to utility increasing outcomes while avoiding harm. 2.) Now assume that the utility increasing decision-maker can insure against non-catastrophic harm. Then a second strategy would be to choose an action that maximizes the expected utility net of insurance costs, or E(U - insurance costs). As with the previous strategy, the decision-maker could revoke any action that results in a catastrophe, and while the possibility of costly revocation prevents guarantees that this will always avoid a harmful outcome, the chances are good that utility-increasing outcomes will result while avoiding the catastrophe. Insurance of non-catastrophic harm improves chances of avoiding bad *ex post* outcomes because the probability of harmful and catastrophic outcomes is larger than the probability of catastrophe alone.

Conclusion:

Ecologists have long warned society to take species introductions, be they direct or indirect, seriously and have developed protocols to help guide decisions concerning intentional releases. They typically argue against introductions until the full spectrum of implications are understood. Their protocols stress collecting better, but costly *ex ante* information in the quest for *ex ante* full information. This has proved burdensome for releasing agents; consequently these protocols are often not followed.

When decisions have the possibility of uncertain and potentially catastrophic outcomes, the importance of revocability in decision-making is clear. The current process of pursuing *ex ante* full information before taking action can provide no promise to avoid catastrophes when the decision is shrouded by uncertainty and/or complete ignorance. The tradeoff becomes better but costly *ex ante* information versus incomplete but costly revocability of actions.

Presently, ecologically grounded decision protocols regarding the intentional introduction of PIAS are based on two clear premises; first, do no harm to the host ecosystem, and second, provide an obvious benefit to society or the host ecosystem. However, the process of seeking *ex ante* fully informed decisions concerning highly complex systems have created protocols that leave most introductions doomed to rejection. Even after costly efforts to remove uncertainty, the final outcome of much research is ambivalent at best, resulting in the all-too-common mantra, "further research is needed for clear conclusions." As a result of these restrictive and potentially expensive procedures, decision-makers may ignore present day protocols and make their decision based upon private preferences and not the possibly of large social losses.

Mixing *ex ante* information and fully revocable actions, provides a robust approach for more effective protocols in the future to govern the release of PIES.

Literature Cited:

Benson, A.J, 2000. Documenting Over a Century of Aquatic Introductions in the United States. Chapter 1 in Claudi, R and Leach, H eds, *Nonindigenous Freshwater Organisms: Vectors, Biology and Impacts*. Lewis Publishers.

Courtenay, W.R. and J.F. Stauffer, 1984. *Distribution, Biology and Management of Exotic Fishes*. Johns Hopkins University Press, Baltimore, Maryland.

Dextrase, A.J. and M.A. Coscarelli, 2000. Intentional Introductions of Nonindigenous Freshwater Organisms in North America. Chapter 4 in Claudi, R and Leach, H eds, *Nonindigenous Freshwater Organisms: Vectors, Biology and Impacts*. Lewis Publishers.

Thomas, M.H., 1996. Revocability in Decision-Making: A Protocol for the Release of Nonindigenous Aquatic Species. Ph.D. dissertation, School of Agricultural Economics and Rural Sociology, The Ohio State University, Columbus, OH., 84 pp.

Thomas, M.H. and A. Randall, 2000. Intentional introductions of nonindigenous species: A principal-agent model and protocol for revocable decisions, *Ecological Economics* 34(3), 333-345.

IMMUNE RESPONSES OF THE EASTERN OYSTER, *CRASSOSTREA VIRGINICA*, EXPOSED TO POLYCYCLIC AROMATIC HYDROCARBONS VIA MICROPHYTOBENTHIC DIATOMS

April N. Croxton[1,2], Gary H. Wikfors[1], Richard D. Gragg III[2]

[1]NOAA Fisheries, Northeast Fisheries Science Center, Milford CT, 06460

[2]Environmental Sciences Institute, Florida A&M University, Tallahassee, FL 32307

For decades, commercial oyster landings have yielded millions in revenue. Initially reported in the 1940's, oyster diseases have resulted in the decline of oyster populations throughout the United States. Concurrent with worsening oyster mortality, persistent organic pollutants have become a concern of the oyster fishery. Introduced into the environment through point and non-point sources, persistent organic pollutants have the ability to further intensify the decline in oyster populations by altering oyster immune status and, thus, disease susceptibility. Hydrophobic persistent organic pollutants become associated with sediments in aquatic environments. Microphytobenthic communities are microscopic, photosynthetic, eukaryotic algae and cyanobacteria that inhabit sediment surfaces in some environments; they play a major role in primary production in areas where phytoplankton are not abundant. Microphytobenthic production serves as a food source for the eastern oyster and is a possible vector for introduction of polycyclic aromatic hydrocarbons (PAH) into oysters. In this research, the effects of PAHs on the immune functions of the eastern oyster, *Crassostrea virginica*, will be examined through a microphytobenthic, trophic pathway. In preliminary experiments, cultures of the benthic diatom Nitzschia brevirostris, were contaminated with experimentally-varied concentrations of several PAH compounds, and then fed to oysters in the laboratory. Results of this preliminary experiment show an alteration of immune status, as measured by flow-cytometric hemocyte analyses, in oysters that were exposed to the contaminated diatom. Data obtained from this research will aid in efforts to understand the effects of chemical pollutant stress on the eastern oyster and it's susceptibility to pathogens.

The Impact of Environmental Regulation on Small Business in the Chesapeake Bay Watershed: A Study of Northwest Baltimore Automotive Association

Micah Crump

Doctoral Student, Department of Business Administration, Morgan State University, Baltimore, MD 21251
micah.crump@verizon.net

Abstract

Using organizational theory, particularly from an open systems perspective, key events and circumstances concerning automotive repair shops operating in a Northwest Baltimore City region known as the Park Heights community, are explained. The events relate to community and government regulatory perceptions of detrimental impacts caused by the industry members on various facets of the environment. Actions following regulation commencement by the Maryland Department of Environment, and the Environmental Protection Agency to minimize land, air, and water degradation, are discussed. The key actions of the automotive repair shops include the forming of an alliance association, cooptation, environmental enactment, and sharing of organizational resources. The actions are explained as responses to an unfriendly and uncertain environment.

This paper illustrates economic intricacies that relate to the automotive repair industry and its interconnectivities with environmental justice concerns and entities. The paper contributes to the literature as knowledge of how economic entities comprising the small business facet of industry might respond once faced with the prospect of increased environmental regulation.

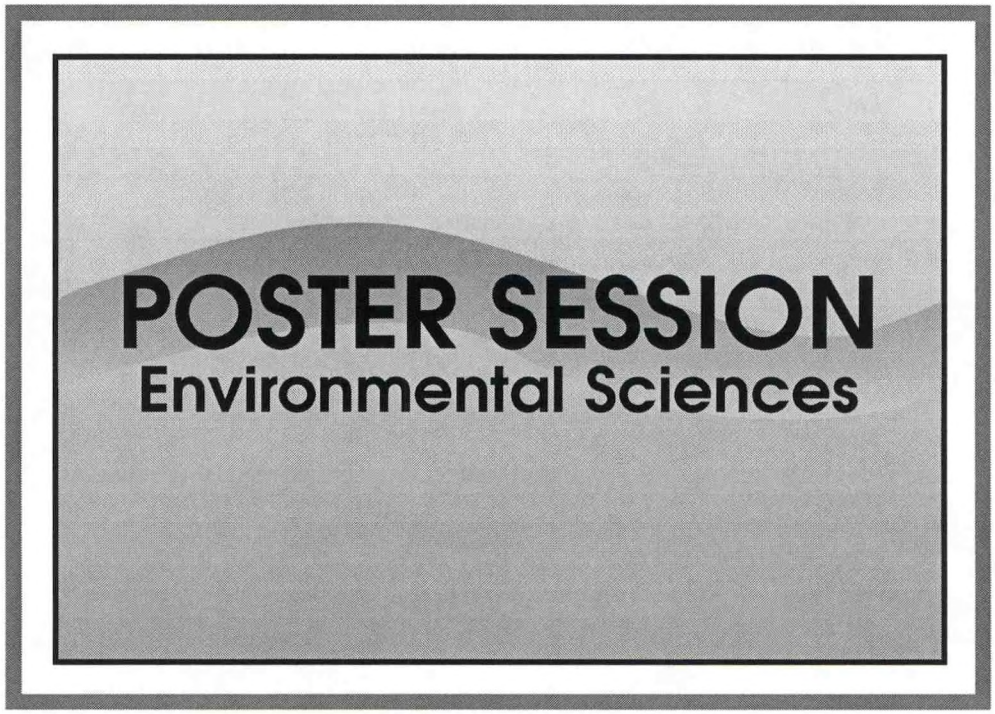
POSTER SESSION
Environmental Sciences

SETTING UP A DATABASE WITH WEB ACCESSA

Jide Aniyikaiye (NOAA CREST Fellow), Manohar Mareboyana (NOAA CREST Faculty), Computer Sciences Department, Bowie State University.

In order to better share information resources among students, faculty and staff working on NOAA CREST-related research projects, we are developing a web-accessible data base to provide access to research "metadata". Metadata is data about data. In the case of our NOAA CREST Metadatabase, the information stores include pointers to data holdings [satellite images], publications, contacts, important web sites and other resources. The basic idea is to share everyones' knowledge and retain information once a participant is no longer working with NOAA CREST. To carry out this project, My SQL database software has been installed with Web access. The server PC runs Apache web server with PHP (Hypertext Preprocessor). The students and faculty participants are given permissions to access and enter information about their research. PHP allows the students to write web applications for querying and updating the database. The students, faculty and others involved use this database for posting their research, references to published articles and any other information deemed of use to NOAA CREST.

THE ST. JONES RIVER WATERSHED MONITORING NETWORKA

Nicholas Munyei, Alicia Revis, Samantha Hollingsworth, and Michael Reiter

Department of Agriculture and Natural Resources, Delaware State University, Dover, DE 19901-2277

The St. Jones River Watershed (SJRW) monitoring network is composed of 21 watershed sites used both to monitor landscape-scale water quality in the St. Jones River DE and to provide input for a future adaptive management program in the watershed. The SJRW drains a portion of the coastal plain in central Kent County, including the capital city of Dover and the surrounding suburbs, industrial, agricultural, and undeveloped areas. The upper St. Jones River is impounded by a dam 10.5 miles upstream from the bay to form Silver Lake, a municipal recreation area. Land use in the St. Jones River watershed is changing rapidly through natural and anthropogenic disturbances. A growing population and the associated nutrient loading from development and agriculture pose a threat of eutrophication to this watershed, particularly in the upstream reaches but potentially throughout the entire watershed. The network will be monitored to obtain nutrient (nitrate, phosphate, ammonia,) and water quality (dissolved oxygen, particulates, reflectance, and chlorophyll) measurements for cross-comparison within the watershed, for future adaptive management programs and comparative research under the ECSC umbrella, and to correlate to land use changes in the SJRW. Reflectance data will be used to create a reflectance-based water quality screening method for the watershed based on algal pigment signatures and/or a modification to Trophic State Index (TSI) equations. Initial data collected in July 2004 indicates that there may be high nutrient loading throughout the watershed, and that there may be sub-watersheds where certain nutrients are particularly high suggesting a possible land use relationship. This monitoring effort is brand new, and more data will be required in order to develop the water quality index and to statistically identify any relationships between nutrients and sub-watersheds, or sub-watersheds and land uses, in those areas.

Preserving Biodiversity through State Land Acquisition Programs in Kent County, Delaware

Barbara E. Murray and Michael A. Reiter

Agriculture and Natural Resources, Delaware State University, Dover, DE 19901-2277

Governments and private land trusts play an increasingly important role in establishing an enduring landscape mosaic by setting aside land for recreational facilities, creating nature preserves to maintain open space and biodiversity, and by purchasing development rights on farms to preserve the agricultural economic base and manage growth. These land use decisions may have a synergistic effect on protecting biodiversity, or they may have a detrimental effect. Delaware preserves land through bond bills set aside by the General Assembly that are dedicated to farmland preservation, outdoor recreation, and state land acquisition through the Open Space Program and the purchase of development rights (PDR) on agricultural land. Between fiscal years 1996 and 2001, $60 million was allocated to farmland preservation and $66 million was allocated to open space acquisition (Delaware Office of Planning Coordination, 2003).

In Delaware, 307 properties encompassing approximately 64,830 acres have been permanently protected through the purchase of agricultural preservation easements; 52% of this total has occurred in Kent County (Delaware Department of Agriculture, 2003). Agricultural land use has been shown to have adverse effects on plant communities through the loss of forests and wetlands, the use of fertilizers and pesticides and the introduction of non-native species. In Canada, agriculture is responsible for 23% of the threats to endangered species, 15% to threatened species, and 16% to vulnerable species (Freemark et al, 2002). On the other hand, agricultural lands can also provide habitat for species requiring non-forested landscapes. In Colorado, ranches had higher plant species richness and fewer non-native species than on either exurban developments or reserves (Maestas, Knight and Gilbert, 2003). Additionally, noncrop habitats on farms may serve to preserve remnant patches of native plant species which once dominated the landscape.

In Kent County, 38,586 acres of land are dedicated to agricultural preservation through the purchase of development rights (PDR) and 47,905 acres of land are located in state and federal parks (Delaware Department of Agriculture, 2004; Delaware State Office of Planning Coordination, 2004). Lands preserved for agriculture offer potential benefits for protecting the biodiversity of an area. Farming may leave land with marginal value for crops, such as wetlands and woodlots, relatively undisturbed so that the land may have value for maintaining biodiversity. Without agricultural land preservation, this marginal land may be converted to other uses. This research will examine the network of preserved lands of Kent County, Delaware to attempt to answer the question: Does the existing network of land dedicated to agricultural preservation protect rare, threatened or declining plant species and thereby contribute to the preservation of biodiversity? And, does this land maintain the same species richness as preserves?

The Mid-Atlantic (Maryland, Delaware, and New Jersey) Gap Analysis Project has completed land cover maps (2 hectare units at a scale of 1:100,000) with vegetation mapped to the alliance or aggregated alliance level. A target thematic accuracy of 80% was set for land cover (Rasberry et al 2003). Data from the Mid-Atlantic Gap Analysis Project for Maryland, Delaware and New Jersey and GIS analysis indicates that the two largest upland vegetative alliances found in the network of preserved lands of the county are coastal plain pine/mixed hardwood forests and coastal plain pine beech-oak forests. These alliances are well represented in both the network of agricultural land in the PDR program and in state and federal parks. Gap analysis mapping and GIS technology will be applied to establish vegetative "polygons" for a stratified sampling effort and to place Kent County within the context of the coastal plain physiographic area of the Delmarva Peninsula.

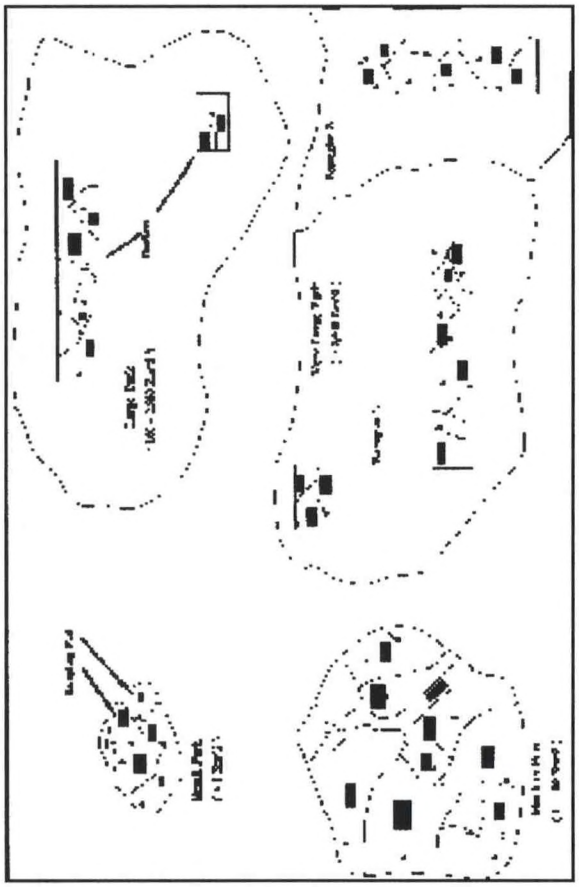

Fig. 1 Sampling Strategy. Source: Reproduced from Field Methods for Vegetation Mapping Final Draft, NBS/ NPS Vegetation Mapping Program, 1994.

The derived polygons representing the pine/mixed hardwood and beech-oak will be used as the basis for a stratified sampling design modified from the methodology utilized by the NBS/NPS Vegetation Mapping Program (Fig. 1) (Nature Conservancy and Environmental Systems Research Institute, Inc, 1994).

Using stratified vegetative sampling, vegetative species and composition on the lands devoted to natural areas will be compared to the lands dedicated to agricultural preservation to determine if the existing network of agricultural preservation land contributes to the preservation of biodiversity by protecting rare, threatened, or declining plant species or vegetative alliances. Statistical tests will determine if there are significant differences in species richness between agricultural land and land preserved for parks, and will compare the similarity in species composition among sites and site types by calculating the Jacard similarity coefficient and determining the significance of the indices.

Differences in species richness between agricultural land and land preserved for parks will be identified, and species clustering by site type and distance to other preserved lands or intact tracts of land will be examined. Species richness and composition can provide an assessment of the conservation value of this existing landscape mosaic with respect to species representation and complementarity. Finally, because local species richness tends to coincide with regional species richness, a departure from this pattern may reveal the need for further conservation efforts or targeted restoration in the network of conserved lands.

REFERENCES

Delaware Department of Agriculture http://www.smartmap.com/dda/dda/htm.

Delaware Office of State Planning Coordination. http://www.state.de.us/planning/dh072498.htm

Delaware Governor's Office http://state.de.us/governor/speeches/state of the state

Freemark, K. E., C. Boutin, and C. J. Keddy. 2002. Importance of Farmland Habitats for Conservation of Plant Species. Conserv. Biol. 16(2):399-412.

Maestas, Jeremy D, R. L. Knight, and W. C. Gilbert, 2003. Biodiversity across a Rural Land-Use Gradient. Conserv. Biol. 17(5):1425-1434.

The Nature Conservancy and Environmental Systems Research Institute, Inc, 1994, Final Draft: Field Methods for Vegetation Mapping. NBS/NPS Vegetation Mapping Program.

Rasberry, D.A., R.A. Eanes, P.G. Becker, R.C. McCorkle, T.A. Palmer, D.L. Limpert, and T.J. Earl. 2003. A Gap Analysis of the land cover of Maryland, Delaware, and New Jersey. Final Report. USGS Biological Resources Division, Gap Analysis Program and the University of Maryland Eastern Shore, Office of Information Technology, EAGLE Lab, UMES Scientific Report Series, EL2003.2. 301 pp.

BIOACCUMULATION OF PCBS IN STRIPED BASS IN JAMAICA BAYA

Mohammed A. Nasher, Student and Megan Wiley, Assistant Professor, Department of Civil Engineering, City College of NY

Bioaccumulation is a process by which the concentration of a chemical increases over time in a biological organism compared to the chemical's concentration in the environment. Compounds accumulate in living things any time they are taken up and stored faster than they are broken down (metabolized) or excreted. PCBs (Polychlorinated Biphenyl) for example, a category or family of chemical compound formed by the addition of chlorine to biphenyl, bioaccumulate in fishes, which can then be eaten by humans. PCBs have been shown to cause cancer, brain damage, and liver defects. Even though the use of PCBs has been prohibited since 1977, existing PCBs continue to pose a problem, finding various pathways to travel through the ecosystem to humans.

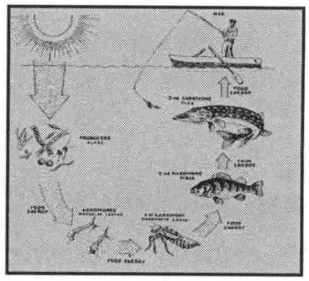

Figure 1: Potential pathway through the food chain of PCBs from algae to humans. [2]

The PCB food chain begins when PCBs bind to sediment particles suspended in water and eventually settle to the rivers, streams, estuaries, or lake-bottom where they accumulate. These contaminated sediments eventually mix into the bottom mud during turbulence created by storms, river currents, and passing boats. Benthic or bottom-dwelling organisms are tiny animals, such as mayfly and dragonfly larvae, that live in sediments (1). As they burrow, benthic organisms absorb PCBs. This begins the process of biomagnification.

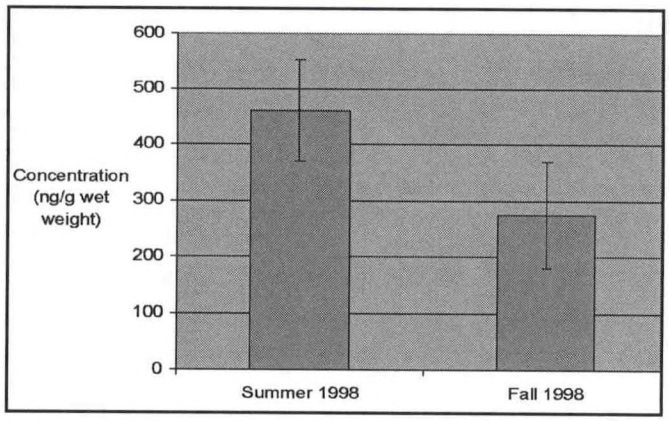

Figure 2: PCBs concentration in Striped Bass in different seasons.

Fishes that are low on the food chain eat these benthic organisms, along with the PCBs they absorbed. Consumption and digestion are the primary means of exposure to and bioaccumulation of PCBs (1). For example, walleye have higher levels of PCBs than perch because they eat perch and absorb PCBs with every contaminated fish they eat. Therefore, even sediment barely contaminated with PCBs can result in high concentrations in both water and land-based life, including humans, which is shown in Figure 1. Moreover, PCBs have a high affinity for organic substances, such as fat molecules. In other words, PCBs accumulate in fat, making women, who on average have a higher body-fat content than men, and the children they bear more vulnerable to these toxic substances (1).

In this study, we are focusing on historical records of PCB concentration in Striped Bass in Jamaica Bay. The reason this species has been chosen is that Striped Bass had been prohibited to eat for 7 years (April 1985 through April 1992) in New York Harbor. The Department of Conservation in the Division of Fish, Wildlife and Marine Resources has been collecting fish samples from Jamaica Bay since 1987. Some important data and graphs are shown below based on those the collected PCBs contaminated fishes.

Based on Figure 2, the concentration of PCBs in summer is higher than that of fall. This may be caused by higher temperature at upper surface of water. Therefore, the fishes go to bottom layer and depend on sediment's food where we have higher concentration of other species, toxic mud and other

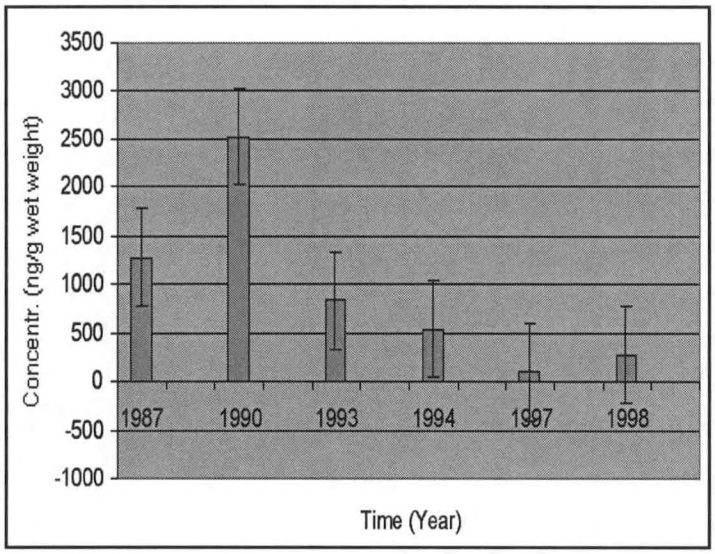

Figure 3: PCBs in Striped Bass in different years in fall.

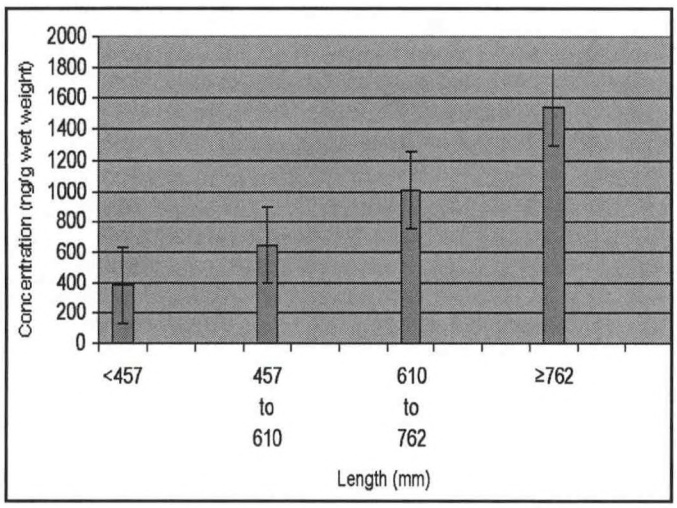

Figure 4: PCBs in different sizes of Striped Bass in fall 1993.

microorganisms compare to suspended contaminated particles at upper surface.

Based on Figure 3, as the time goes on, the concentration of PCBs get smaller. The reason behind is the usages of PCBs have been prohibited since 1976. Therefore, we can predict that if we don't discharge the PCBs in the estuary anymore, most likely we will be able to reduce the PCBs in fishes in time.

Based on the Figure 4, bigger fishes are more contaminated by PCBs. The reason is bigger fishes have more lipid and fat compare to small fishes. The contaminated chemicals such as PCBs accumulate more in the fat or lipid part than other part of a fish body. Also the bigger fishes are at the upper level of food chain (shown in Figure 1) which accumulate higher concentration of PCBs.

While we have qualitative explanations explaining the trends, the next step in the study is to quantify these relationships by correlating trends in PCB levels with environmental parameters such as dissolved and partitioned PCB concentrations and temperature. We plan to test the sensitivity of these environmental factors along with fish parameters including gill uptake rate, back diffusion rate, excretion rate, food ingestion rate, food assimilation efficiency, growth rate, lipid amounts and migration patterns to determine which processes govern PCB accumulation in this case. This understanding will aid policy decisions aimed at reducing PCB levels in Striped Bass.

REFERENCE

(1)www.lakemichigan.org/elimination/sheboygan05.asp

(2)www3.gov.ab.ca/srd/ fw/watch/invert_chains.html

Skinner Lawrence, Jackling Samuel, Kimber George, Waldman John, Shastay Joseph, Newell Arthur 1996: New York State Department of Conservation. Chemical In Fish, Shellfish And Crustaceans From The New York-New Jersey harbor Estuary. PCB, Organochlorine Pesticides and Mercury. Division of Fish, Wildlife & Marine Resources.

Skinner Lawrence, 2001: New York State Department of Conservation. Organic Chemical and Mercury In Selected Fish Species Taken From The New York Harbor. Division of Fish, Wildlife & Marine Resources.

CONTINGENT VALUATION

Chad Noel,

Graduate Student, JD and Marine Affairs & Policy, University of Miami, 2918 Whitehead Street, Miami, Florida 33133.

I will be discussing the contingent valuation method. During the presentation I will broadly describe what the method seeks to measure and how economists employ it to accomplish those objectives. Furthermore, I will discuss the role of contingent valuation in the Oil Pollution Act and how it facilitates a comprehensive assessment of damages. Time providing, I will segue into a brief discussion of the requirements of admissibility of scientific testimony into evidence under the Federal Rules of Evidence.

EFFECTS OF COMMON RATE COEFFICIENTS FOR STATE VARIABLES IN THREE EUTROPHICATION MODELS

Enomen John Okogun, City College of New York
James Fitzpatrick, HydroQual, Inc.
Megan Wiley, City College of New York

Cultural eutrophication is when a body of water such as lakes and estuaries becomes rich in mineral and organic nutrients that promote the proliferation of plant life, especially algae, which then lead to the extinction of marine organisms and in general a reduction in the water quality. Human activity, such as the discharge from wastewater treatment facilities, combined sewer overflows (CSO), atmospheric deposition, as well as agricultural and urban runoff, is primarily the cause of the increased rate of input of these nutrients. These plant nutrients like nitrogen, phosphorous and carbon lead to the excessive growth of algae also called algal blooms, which then cause the depletion of oxygen in the water and result in the disappearance of fish and other aquatic creatures. The death and decomposition of algae cause oxygen to be used up. Also, the algal bloom prevent the penetration of sunlight through the water and this leads to the death of habitats and organisms that are at the bottom of the water body, which are known as benthic organisms. Waterfronts, shorelines and beaches are also fouled up by decaying algae. The Federal and state agencies are working together to monitor and address cultural eutrophication. Mathematical modeling has proved to be an effective tool in this regard.

Mathematical models transform the natural environment into a mathematical environment. For this case, the mathematical model used in this eutrophication study is the "Row-Column Aesop" (RCA). RCA is a general purpose code developed by HydroQual, inc. of New Jersey used to evaluate water quality problem settings. It directly interfaces with the HydroQual's general circulation model, ECOMSED which provides the hydrodynamic, temperature and salinity data. RCA formulates for each model segment differential mass balance equations of biological, chemical, and physical processes taking place within the natural environment. The mass balance equations account for all material entering or leaving the water body, include all horizontal, lateral, and vertical components of advective flow and dispersive mixing between model segments. For each water quality segment or grid cell, it is assumed that the concentrations of each water quality variable are completely uniform within, that is completely mixed. Rate coefficients for the physical, chemical and biological processes or kinetic processes are determined or assigned based on either laboratory or field data or via model calibration. The kinetic equations that model the kinetic processes utilize 26 state variables, listed below:

1. Salinity
2. phytoplankton carbon – winter assemblage (P_{c1})
3. phytoplankton carbon -summer assemblage (P_{c2})

4. phytoplankton carbon – fall assemblage (P_{c3})
5. refractory particulate organic phosphorous (RPOP
6. labile particulate organic phosphorous (LPOP)
7. refractory dissolved organic phosphorous (RDOP)
8. labile dissolved organic carbon (LDOP)
9. algal phosphorous + dissolved inorganic phosphorous (PO_4T / DIP)
10. refractory particulate organic nitrogen (RPON)
11. labile particulate organic nitrogen (LPON)
12. refractory dissolved organic nitrogen (RDON)
13. labile dissolved organic nitrogen (LDON)
14. algal nitrogen + ammonia nitrogen (NH_4T)
15. nitrite + nitrate nitrogen (NO_2 + NO_3)
16. biogenic silica + unavailable (SiU)
17. algal silica + available silica (SiT)
18. refractory dissolved organic carbon (RDOC)
19. labile dissolved organic carbon (LDOC)
20. refractory dissolved organic carbon (RDOC)
21. labile dissolved organic carbon (LDOC)
22. algal exudates dissolved organic carbon (ExDOC)
23. reactive particulate organic carbon (RePOC)
24. reactive dissolved organic carbon (ReDOC)
25. dissolved oxygen equivalent (O_2)
26. dissolved oxygen (DO)

The kinetic equations simulate the annual cycle of phytoplankton production, its relation to the supply of nutrients and its effect on dissolved oxygen. Phytoplankton is a unicellular alga.

For organic carbon, seven state variables are considered: RePOC, ReDOC, LDOC, RDOC, LPOC, RPOC and ExDOC. Reactive, labile and refractory are based on a time scale of decomposition or oxidation. Reactive organic carbon decomposes on a timescale of days to a week to a week or two and it is appropriated for CSO carbon and a portion of the organic carbon from discharge from wastewater treatment plants. The timescales for the decomposition of labile organic carbon is several weeks to two months, while that of refractory organic carbon is on the order of a month to a year. Decomposition of reactive and labile organic carbon occurs primarily in the water column otherwise rapidly in the sediments. While the decomposition of refractory organic carbon which decomposes much slower, occurs almost entirely in the sediments. The principal sources of organic carbon are anthropogenic inputs and detrital algal carbon, which is produced as a result of predation. Zooplanktons take up and redistribute algal carbon to the organic carbon pools via grazing, assimilation, respiration and excretion. An example of a kinetic equation is that for RDOC which is shown below:

$$S_{20} = f_{RDOC} * k_{grz}(T) * P_C - k_{18,20}\theta_{18,20}^{T-20} * RPOC * \frac{P_C}{K_{MP_C} + P_C}$$

$$-k_{20.0}\theta_{20.0}^{T-20} * RDOC * \frac{P_C}{K_{MP_C} + P_C} * \frac{DO}{K_{DO} + DO}$$

Where the reaction rate terms are,

Pc is phytoplankton biomass
f_{RDOC} is the fraction of grazed organic carbon recycled to the RDOC pool
K_{mPc} is the half saturation constant for phytoplankton limitation
K_{grz} (T) is the temperature corrected grazing rate
DO is dissolved oxygen
RDOC is RDOC concentration
$\theta_{18,20}$ is a temperature coefficient
$k_{18,20}$ is hydrolysis rate for RPOC
$\theta_{20,0}$ is a temperature coefficient
$k_{20,0}$ is oxidation rate for RDOC

The eutrophication model includes five principal phosphorous forms, LPOP, RPOP, LDOP, RDOP, and DIP. Phytoplankton growth utilizes inorganic phosphorous, and through respiration and predation phosphorous is returned to the various organic and inorganic forms. An example of the reaction /kinetic equation, which is for RPOP, is presented below:

$$S_5 = a_{PC} * f_{RPOP} * (k_{PR}(T) + k_{grz}(T)) * P_C - k_{5,7}\theta_{5.7}^{T-20} * RPOP * \frac{P_C}{K_{mP_C} + P_C} - \frac{v_{S5}}{H} * RPOP$$

Where the reaction rate terms are,
a_c is phosphorous to carbon ratio
f_{RPOP} is the fraction of respired and grazed algal phosphorous recycled to the RPOP pool
k_{PR}(T) is the temperature corrected algal respiration rate
$\theta_{5,7}$ is a temperature coefficient
$k_{5,7}$ is hydrolysis rate for RPOP
v_{s5} is the settling rate

The kinetic structure for Nitrogen is similar to that for the phosphorous system. A fraction of the cellular nitrogen is returned to the inorganic pool in the form of NH_3, during algal respiration and death. The rest of the cellular nitrogen is recycled to the dissolved and particulate inorganic nitrogen pools. NH_4 is the end-product of the bacterial decomposition of organic nitrogen. Nitrification or the conversion of ammonia nitrogen to nitrite nitrogen and then to nitrate nitrogen occurs in the presence of nitrifying bacteria and oxygen. The reduction of NO_3 to N_2 and other gaseous products such as N_2O and NO is known as denitrification. This process occurs both in the water column and sediment column under different conditions, and is included in the modeling frame work as a sink of nitrate. The reaction /kinetic equation for RPON is shown below:

$$S_{10} = a_{NC} * f_{RPON} * (k_{PR}(T) + k_{grz}(T)) * P_C - k_{10,12}\theta_{10.12}^{T-20} * RPON * \frac{P_C}{K_{mP_C} + P_C} - \frac{v_{S10}}{H} * RPON$$

The two state variables of Silica considered are available SiT and SiU. Diatoms utilize and dissolve SiT during growth for their cell walls. Diatoms are unicellular or colonial alga. Diatom respiration and diatom grazing by zooplankton produce SiU. The state variable or kinetic equation for SiT is shown below:

$$S_{17} = k_{16,17}\theta_{16,17}^{T-20} * BSI * \frac{P_C}{K_{MP_C} + P_C} - (1-f_{ExPP}) * a_{SC} * G_P * P_C$$

Where,
G_P ii the specific phytoplankton growth

rate
$k_{16,17}$ is the mineralization rate of biogenic silica
BSI is biogenic silica concentration
f_{ExPP} is the fraction of primary productivity going to the algal exudate pool

The production of dissolved oxygen is a by-product of photosynthetic carbon fixation. The rate of oxygen production and nutrient uptake is proportional to the growth rate of the phytoplankton, as a result of its fixed stoichiometry. When the available ammonia nutrient source is exhausted the phytoplankton begin to utilize the available nitrate, and this gives rise to an additional source of oxygen. Algal respiration which is the reverse process of photosynthesis and occurs as a result of nitrification reduces the dissolved oxygen in the water column. One of the reaction equations for the dissolved oxygen is shown below:

$$S_{24} = k_{O_2}\theta_{O_2}^{T-20} * O_2 * \frac{P_C}{K_{MP_C} + P_C} * \frac{DO}{K_{DO} + DO}$$

Where,
k_{O2} is the oxidation rate

The kinetics, some of which have been presented above, controls the kinetics and rates of interaction among the water quality constituents and variables. Ideally within a modeling framework they should be independent of location per se. However, they may be functions of variables outside the water body such as temperature and light which may vary with location. This is the basis of this research effort. RCA was transformed into three water quality sub models through a subroutine that includes complex eutrophication kinetics and sediment interactions. Three sub models were developed separately for different reasons and for different locations, as well as calibrated and validated over different time periods. The three sub models are:

System Wide Eutrophication Model, SWEM was developed in order to provide a refined evaluation of proposed water pollution control plant upgrades and other engineering alternatives as well as to ultimately select the best management plan for the east river. The natural environment modeled by SWEM includes all of New York Harbor, Long Island Sound, and the New York Bight. SWEM was calibrated against observed water quality and sediment data for a twelve month period from Octoberl, 1994 through September 1995. It was validated with observed water quality data for a twelve month period from October 1, 1988 through September 1989. Although there are some discrepancies between observed data and model computations, the overall model calibration and validation to the observed data show that SWEM is adequate to the task of evaluating water quality responses to nutrient reduction schemes and other management alternatives.

Jamaica Bay Eutrophication Model, JEM was developed in order to determine to evaluate and determine the effectiveness of various remediation scenarios for reducing the level of eutrophication in the bay, as well as improving the bay's dissolved oxygen levels. The eutrophic condition of the bay is supported primarily by large nitrogen and phosphorous loadings from the discharge of four major treatment plants. Jamaica Bay is located on the

south shore of western Long Island, New York. It is bordered by Brooklyn to the west, Queens to the north, and Nassau County to the east, and Rockaway to the south. Rockaway Inlet provides the path for interchange of water with the Atlantic Ocean. JEM was calibrated against observed data from January through December of 1988 and July 1995 through June 1996.

Massachusetts Bays Eutrophication Model, BEM was developed in order to obtain a more rigorous understanding of outfall relocation from within Boston Harbor into the Massachusetts Bay. The construction of the ocean outfall by the Massachusetts Water Resources Authority (MWRA) will divert treated effluent from the Deer Island Wastewater Treatment Plant to a location fifteen kilometers east of Deer Island into the Massachusetts Bay. This relocation along with improved sewage treatment is expected to significantly improve the water and sediment quality within the Boston Harbor area. However, it is important to determine the effect on other locations within the Massachusetts Bay area, such as Cape Cod. This water quality model made use of a three dimensional time-variable hydrodynamic model developed for MWRA by the United Stated Geological Survey. The calibration of BEM was done against data collected from October 1989 through April 1991, and January 1992 through December 1992. The Model was also re-calibrated against data observed from 1992 through 1994.

This study will examine the behavior of the three different eutrophication water quality models, as an attempt is made to equalize and unify the values of the rate coefficients that determine the kinetics within each eutrophication model's natural environment.

Rate Coeff.	SWEM	BEM
f_{LPOP}	0.250	0.300
f_{RDOP}	0.100	0.100
f_{RPOP}	0.100	0.150
f_{RDOC}	0.100	0.100
f_{LPOC}	0.400	0.350
f_{LPON}	0.300	0.325
f_{RDON}	0.125	0.150

Table 1: Examples of rate coefficient values of SWEM and BEM.

While most of the model coefficients used in these models are the same, some of the coefficients related to the nutrient uptake and nutrient recycle differ across these model applications. Table 1 illustrates this. The behavior of each model is recorded, analyzed and compared to its initial calibration when the rate coefficient values of one model are applied to the other models.

References:

1. HydroQual, Inc, June 2004: User's Guide For RCA (Release 3.0)
2. HydroQual, Inc., June 2002: A Water Quality Model for Jamaica Bay Eutrophication Model (JEM) – Final Report.
3. New York City Department of Environmental Protection, HydroQual, Inc., April 2001: Newtown Creek Water Pollution Control Project East River Water Quality Plan – Task 10.0 System Wide Eutrophication Model (SWEM) – Subtask 10.4: Calibrate SWEM Water Quality and Subtask 10.6: Validate SWEM Water Quality.
4. Massachusetts Water Resource Authority, March 2000: Bays Eutrophication Modeling Analysis for the Period of 1992 – 1994.

PROMOTING GREEN SPACES THROUGH EXCHANGING INFORMATION AND CONNECTING INDIVIDUALS

Tahmeed Ahmed, Ebone Brown, Charles Hammond, Jonatan Jelen, and Camisha Pierre
City College of New York

New York City is witnessing a swell in sustainable development initiatives from environmentally-sound building design to green roof organizations. However, individual people and businesses are not easily able to efficiently tap into these resources. To address this need, members of the Environmental Entrepreneurship Partnership (EEP)Program at City College, eight students and three faculty members from Civil Engineering and Economics, are collaborating to create a business. The mission is to integrate resources for sound choices, sustainable technology, and healthy living spaces by facilitating meaningful information exchange. In developing our business plan, we have positioned ourselves relative to existing companies, determined the way in which we will function as a business, and identified our launching point into the marketplace: a sustainability symposium.

By mapping existing companies and organizations onto a set of axes describing the extent to which they provide products versus services and use a "less bad" versus truly sustainable approach, we identified a need in the marketplace: an interactive information center focused on bringing sustainable businesses to consumers and increasing both the demand for their services and their capacity to provide them. We also differ from existing businesses by a clear educational component to the mission by both informing the public about local environmental issues both on and off-line and teaching the faculty and students of City College about environmental entrepreneurship through the EEP Program.

As an organizational strategy, we will continue to function as equal partners rather than developing a hierarchy. Our focus for the fall semester will be developing our website and organizing a symposium, which will be used primarily as an educational tool for both companies and the general public. It will also allow us to further position ourselves among sustainability consultants by identifying a need (in the businesses that attend) that has not been adequately met.

Determination of Material Type or Soil Moisture Using ENVI Application Software and Radar Signatures

Undergraduate students:

Mairim G. Ramos, Computer Engineering, Alex J. Rivera, Computer Science,
C. Allen Lizárraga, Electrical Engineering

Advisor: Dr. Hamed Parsiani, *parsiani@ece.uprm.edu*

University of Puerto Rico, Mayagüez Campus, Department of Electrical and Computer Engineering

Images obtained by Ground Penetrating Radar (GPR) have information of the media where the signal travels. The reflection retrieved can be processed in order to convert the data into useful parameters, such as material type or soil moisture. During these past months, GPR images have been processed using algorithms developed on MATLAB to determine the Material Type in Fourier Domain (MCFD). Later on this information is input into ENVI (ENvironment for Visualizing Images) application software to build a library as a data base to help identify a material type or soil moisture content.

Field measurements of soil moisture contents have been done, using a GPR. of 1.5GHz (transmitter/receiver) antenna, and a Theta Probe for validation of results. The MCFD algorithms written in MATLAB are currently being tested to determine material type or soil moisture content. The MCFD information is exported to the ENVI software in ASCII format to build the libraries.

Using ENVI's Spectral Library Builder we are currently developing our own soil moisture content plots database. ENVI's Spectral Analyst allows us to compare our data with any unknown information and find the best matches. Past tests showed good results with sand moisture. Presently, tests are being performed for loam and clay, with the goal of widening the database using ENVI for material determination.

High Resolution Vegetation Health Index and its Validation with a Spectrometer

Maritza Torres (Graduate student), Alex J. Rivera

Advisor: Dr. Hamed Parsiani, *parsiani@ece.uprm.edu,*

University of Puerto Rico, Mayagüez, Puerto Rico 00681-5000

The pixel accuracy of some Synthetic Aperture Radar (SAR) satellites is now at near one meter resolution. A new formulation of vegetation index using such sensors will greatly improve the Vegetation health accuracy. It is the goal of this research to define a new vegetation index, using active sensors.

In this research, a correlation is determined between the active and passive measurements of the vegetation index, at very high resolution. The measurements, took place at the near ground level over vegetations from dry to green conditions, using a Ground Penetrating Radar (GPR), and a handheld Spectrometer. Both measurements took place one right after the other, to allow an accurate comparison.

The GPR and the handheld Spectrometer have the same field of view, so it is possible to compare data for the whole range of NDVI. The NDVI is calculated from the reflectance of the leaf taken by the spectrometer, specifically using the red band centered at 682nm with a bandwidth of 4nm and the Near InfraRed centered at 920nm and with a bandwidth of 20nm[P.S. Thenkabail, et al. 2000].

The GPR operating at 1.5 GHz produces images that contain backscatter signals obtained from vegetation. These images are processed by a filter to eliminate clutter and noise. A material characteristics in frequency domain (MCFD) has been defined which characterizes the vegetation health. The average power of the MCFD is calculated for vegetation for two different backgrounds and correlated with the NDVI obtained from the spectrometer. Our results show a linear correlation of 0.9336. As a continuity of this work, the ground data will be correlated with the active/passive satellite sensors for the measurement of vegetation health.

An Analysis and Survey of Maryland Critical Bay Area Manufacturers in Compliance with ISO 14001

Deirdra L. Williams

Department of Industrial, Manufacturing and Information Engineering, Morgan State University, Baltimore, MD 21251, *deirdraw2003@yahoo.com*

Abstract

ISO 14000 is the world's first series of internationally recognized standards for environmental management. The environmental management system standards were created by the International Organization for Standardization (ISO) – a worldwide federation based in Geneva, Switzerland, comprised of more than 110 member countries. The International Organization for Standardization has been working diligently for a number of years to establish environmental quality standards for manufacturers. ISO 14001, established in 1996, requires a facility to develop an environmental policy, set objectives, delineate organizational responsibilities, provide training and documentation, and monitor and correct deficiencies. In order to establish an environmental management system (EMS), an organization must identify the nature of its activities, products, processes, and services, as well as the environmental aspects and impact of its activities. Prior studies have demonstrated that when an effective EMS is in place, an organization can greatly reduce the negative environmental impacts of its activities, products, and services and help maintain the quality of the ecosystem.

Highly industrialized areas of the Chesapeake Bay such as the port of Baltimore have suffered from years of toxic heavy metals and dangerous chemical compounds dumped by neighboring industries. Contaminants include not only heavy metals, PCBs and PAHs, but also substances not usually considered pollutants such as nutrients and sediments. The ultimate goals of coastal management must be to ensure the sustainability and health of the coastal ecosystem and to ensure that the economy of the coastal area prospers. To accomplish the objective outlined above, a GIS model will be created. The model will include economic, social, and environmental components of manufacturing facilities in the Baltimore Critical Area. Development of a GIS model will help manufacturing companies establish priorities for action. The overall objectives are to integrate environmental management considerations into existing operational and product standards in a systematic manner using the ISO 14001 standard.

Keywords: ISO 14001, GIS

Johnson, Perry L. ISO 14000 Road Map to Registration. McGraw-Hill: New York, 1997.

Puri, Subash C. Stepping up to ISO 14000: Integrating Environmental Quality with ISO 9000 and TQM. Productivity Press: Oregon, 1996.

INTEGRATING GEOSPATIAL AND TEMPORAL DATA FOR WATER QUALITY MONITORING IN SOUTHWEST MISSISSIPPI

Deidra Young*, Samuel Adu-Prah, Alton B. Johnson and Rolanda Mayfield
Mississippi River Research Center, Alcorn State University

Abstract

Water quality and conservation are essential in every region of the United States. Monitoring water quality and identifying the location and magnitude of existing and potential pollution sources and impacts are important activities to ensure that there is clean and adequate supply of this natural resource. We used remotely sensed data and geographic information systems (GIS) to assess land use/land cover influence on water quality of streams in the Coles Creek watershed. Eleven monitoring stations were established in the watershed to quantify water quality. At each station, dissolved oxygen, turbidity, pH, specific conductance, total coliform and E. coli were measured. The data was incorporated into the GIS database for the watershed. Preliminary results showed spatial and temporal variability in the parameters measured. Results also showed that irrespective of land use/land cover, rainfall events significantly influenced all water quality parameters measured ($p<0.05$).

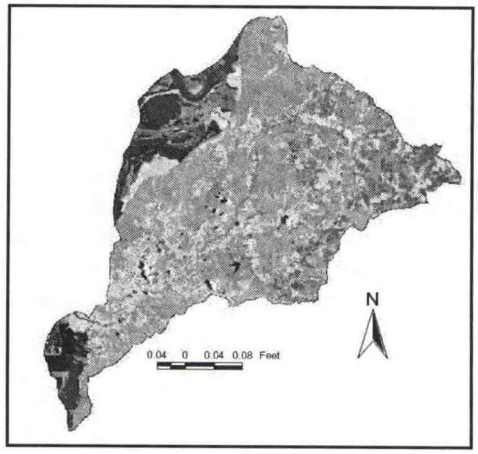

Fig. 1. Lansat 7 Enhanced Thematic Mapper imagery (05/28/2003) of the Coles Creek Watershed

Introduction

The contamination of streams through non-point source water pollution has been well documented (Mallin et al., 1997; Mawdsley et al., 1995) and become a critical concern in many areas of watershed units of which South West Mississippi is no exception. These concerns has prompted the Environmental Protection Agency of the United States to entrust support to help exhibit improved stream water quality through realization of best management practices (BMPs). Currently, in Mississippi silvicultural best management practices (BMPs) have been widely accepted as an effective management tools to minimize non-point source (NPS) pollution associated with forest management activities. In this study, remotely sensed data was used to identify and assess the impact of land use and land cover as well as land use management practices on water quality. To help quantify the impact of land use and land cover on water quality, eleven locations were appropriately established using global positioning system. The main objective of this study was to assess the quality of major streams in the Coles Creek watershed. Increase in concentrations of nutrients and bio-contaminants in water can alter the function and stability of many riparian and aquatic ecosystems. In the past,

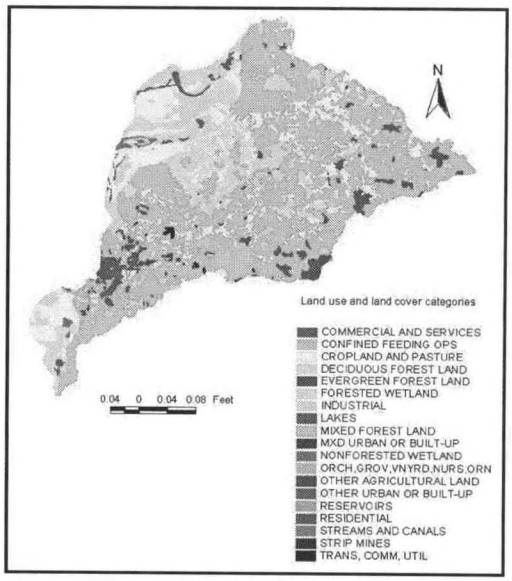

Fig. 2. Land use and land cover categories of the study watershed.

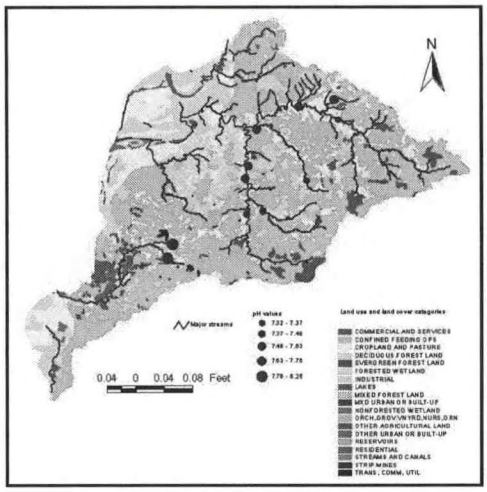

Fig.3. Variability of stream pH in the study watershed.

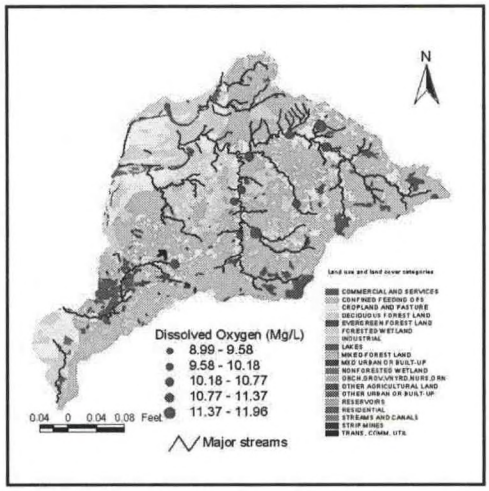

Fig. 4. Dissolved oxygen in stream segments in the study watershed.

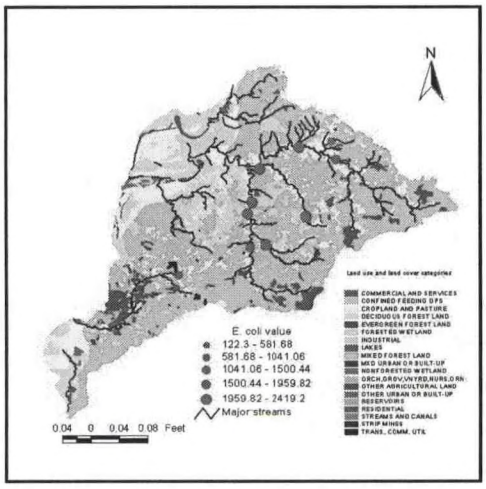

Fig. 5. Distribution of E. coli in streams in the study watershed.

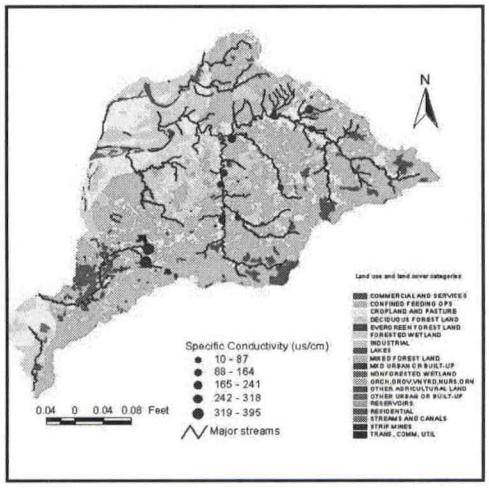

Fig. 6. Spatial distribution of Specific Conductance in the study watershed.

intensive fertilization has contributed to
the accumulation of nutrients in many wetland and aquatic environments (Koch and Reddy, 1992; Lebo and Sharp, 1993; David and Gentry, 2000; Edwards et al., 2000; Sharpley et al., 2000).

Materials and Methods

Satellite Imagery Classification

The Coles Creek watershed (1300 km2) is located in the Southern Mississippi Valley Silty Uplands, major land resource area 134. The watershed lies between latitude 31.380 and 31.920 north and longitude 90.870 and 91.470 west. Our investigation utilized Landsat 7 Enhanced Thematic Mapper (LANDSAT 7 ETM+) (Fig. 1) data covering the study watershed. The satellite data was examined using the standard image processing software ERDAS Imagine 8.7 version. The unsupervised image classification technique using ISODATA (Iterative Self-Organizing Data Analysis Technique) algorithm (Schowengerdt, 1997) was used to cluster imagery into spectrally similar categories. This classification was used over another method, supervised classification using the maximum likelihood parametric method (Jensen, 2003) to derived a highly accurate Land use and Land cover categories (Fig. 2). Groundtruthing data were used for

final classification. The result of the raster data were converted to vector data and used in the Geographic Information system.

Sample Collection

Locations of water quality monitoring stations were identified using the interpreted imagery and global positioning system. A total of eleven monitoring stations were identified and marked. Water samples were collected prior to and after rainfall events (only two sampling times will be presented in this paper). The YSI Sonde model 6600-M coupled with the YSI model 650-MDS was used to measure dissolved oxygen, turbidity, pH, specific conductance, and temperature. Water samples were collected in pre-sterilized bottles and analyzed for total coliform and Escherichia coli (E. coli) using colilert® substrates. Samples were enumerated by the presence or absence in Quanti-Tray® cells and the data expressed as most probable number (MPN) per 100 mL. All data collected were incorporated into the GIS database for the watershed.

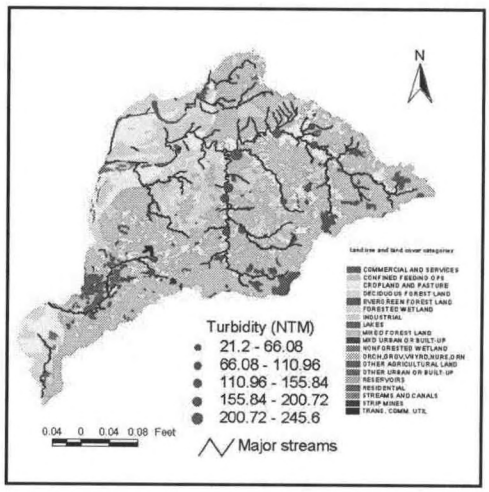

Fig. 7. Turbidity of stream segments in the study watershed.

STA_N	LONG_X	LAT_Y	Time	Temp (°C)	Specific Cond. (us/cm)	DO (mg/L)	Depth (ft)	pH	Turb+ (NTM)	Baro. pressure (mmHg)	E. coli (MPN/100 mL)
1	-91.29329	31.58114	11:56	29.29	395	8.99	0.656	8.09	44.5	762.6	114
2	-91.27951	31.59985	12:14	24.45	395	11.29	0.681	8.26	40	763.7	85
3	-91.18261	31.64242	12:40	27.31	121	10	0.473	7.48	93.8	763.3	457
4	-91.15909	31.64660	1:13	25.44	74	11.64	1.625	7.43	108.9	767.9	457
5	-91.09743	31.69026	1:26	25.34	79	10.68	0.376	7.37	21.2	765.9	830
6	-91.05257	31.77561	1:43	26.03	53	11.27	1.447	7.32	103.1	765.3	870
7	-91.06089	31.80723	1:55	24.78	188	11.96	0.715	7.76	60.8	763.6	1011
8	-91.10805	31.79331	10:17	22.39	62	10.55	1.146	7.63	156.8	762.2	1011
9	-91.16786	31.76082	10:42	22.54	105	10.48	2.045	7.57	245.6	766.1	960
10	-91.17928	31.71054	11:13	24.06	99	10.29	2.142	7.55	180	768.3	914
11	-91.19121	31.69338	11:31	24.78	10	10.14	1.062	7.63	146.1	764.6	870

Table 2. Values of water quality parameters 21 days after a 15-cm rainfall.

STA_N	LONG_X	LAT_Y	Time	Temp (°C)	Specific Cond. (us/cm)	DO (mg/L)	Depth (ft)	pH	Turb. (NTM)	Baro. pressure (mmHg)	E. coli (MPN/100 mL
1	-91.29329	31.58114	12:52	31.77	487	10.93	0.386	8.35	28.2	761.2	196.8
2	-91.27951	31.59985	12:41	27.47	592	11.99	1.12	8.41	7.2	760.4	191.8
3	-91.18261	31.64242	1:16	31.24	419	11.02	0.665	7.78	8.4	763.7	1203.3
4	-91.15909	31.64660	1:27	30.15	288	12.66	2.258	7.67	10.3	763.5	1299.7
5	-91.09743	31.69026	1:41	29.24	188	11.32	0.79	8.07	16.5	761.1	183.5
6	-91.05257	31.77561	2:37	33.48	151	11.47	0.365	8.44	9.9	765.7	249.5
7	-91.06089	31.80723	2:48	27.84	363	11.71	1.125	8.09	10.1	763.3	58.1
8	-91.10805	31.79331	11:29	27.36	218	10.48	0.687	7.97	16.1	760.9	84.2
9	-91.16786	31.76082	11:45	26.94	465	10.35	2.833	8.19	9	762	88.6
10	-91.17928	31.71054	12:02	28.34	374	10.62	0.51	7.93	7.1	761.9	56.1
11	-91.19121	31.69338	12:16	29.05	398	11.23	0.351	8.04	7.4	761.7	125.4

Table 1. Values of water quality parameters measured two days after a 15-cm rainfall.

GIS and Water Quality Parameters Analysis

Geographic Information System (GIS) was used to organize both spatially and temporally data and presented graphically the water quality parameters data for the watershed. The spatial relationship between the water quality parameters (DO, turbidity, pH, specific conductance, total coliform and E. coli.) and the land use and land cover was correlated and the overlay technique (Arnold et al., 1987) used to display spatial patterns.

Results

Preliminary analysis and results showed spatial and temporal variability in the parameters measured (Figs. 3, 4, 5, 6 and 7). Results also showed that irrespective of land use/land cover, rainfall events significantly influenced all water quality parameters measured ($p<0.05$). The parameters measured were overlayed on the land use and land cover categories to establish relationships. Tables 1 and 2 depict water quality parameters taken at the eleven monitoring locations.

Conclusions

Preliminary analysis revealed that rainfall played key role in contaminants found at some sample locations. Subsequent analysis will be done to identify the source(s) of these contaminants and to establish a relationship if any with any category of land use/land cover. Further laboratory analysis will be conducted to quantify phosphate, nitrate, total coliform and E. coli. This will enable researchers address and inform decision makers within the study watershed on issues concerning water quality.

REFERENCES

Arnold, J. G., M. D. Birchet, J. R. Williams, W. F. Smith, and H. N. McGill. 1987. Modeling the effects of urbanization on basin water yield and reservoir sedimentation. Water Res. Bull. 23(6):1101-1107.

David, M.B. and L.E. Gentry. 2000. Anthropogenic inputs of nitrogen and phosphorus and riverine export for Illinois, USA. J. Environ. Qual. 29:494-508.

Edwards, A.C., H. Twist, and G.A. Codd. 2000. Assessing the impact of terrestrially derived phosphorus on flowing water system. J. Environ. Qual. 29:117-124.

Jensen, J.R. 2003. Introductory Digital Image Processing: A Remote Sensing Perspective. Prentice Hall Series: Upper Saddle River, NJ 07458.

Koch, M.S., and K.R. Reddy. 1992. Distribution of soil and plant nutrients along a trophic gradient in the Florida Everglades. Soil. Sci. Soc. Am. J. 56:1492-1499.

Lebo, M.E., and J.H. Sharp. 1993. Distribution of phosphorus along the Delaware, an urbanized coastal plain estuary. Estuaries 16: 290-301

Mallin, M.A., J.M. Burkholder, M.R. McIver, G.C. Shank, H.B. Glascow, Jr., B.W. Touchette, and J. Springer. 1997. Comparative effects of poultry and swine waste lagoon spills on the quality of receiving waters. J. Environ. Qual. 26:1622-1631

Mawdsley, J.L., R.D. Merry, B.F. Pain, and M.K. Theodorou. 1995. Pathogens in livestock waste, their potential for movement through soil and environmental pollution. Appl. Soil Ecol. 2:1-15

Nathon, R. J. and T. A. McMahon. 1990. Evaluation of automated techniques for base flow and recession analyses. Water Res. Research 26(7):1465-1473

Schowengerdt, R.A. 1997. Remote Sensing: Models and Methods for image processing. Academic Press, New York, New York.

Sharpley, A., B. Foy, and P. Withers. 2000. Practical and Innovative measures for the control of agricultural phosphorus losses to water: An overview. J. Environ. Qual. 29:1-9.

An Ecotoxicology Study Using Least Terns Nesting Along the Mississippi Gulf Coast

Angel Wynn and Mark Harwell

Environmental Cooperative Science Center, Environmental Sciences Institute, Florida A&M University

Science Research Center 305, 1520 South Bronough Street, Tallahassee, Florida 32307-6600

Phone 8504127797, Fax 8505612248, *Kano6280@hotmail.com*

Using seabirds as an indicator of environmental conditions is an effective way to monitor coastal and freshwater systems. Because seabirds are close to the top of the food chain, lipid soluble pollutants amplify in concentrations in their tissues, and various levels of heavy metals and organochlorines can be detected. In addition, seabirds are effective biomonitors of climate change and fish stocks and fisheries.

Least terns, the smallest of the North American terns, were used in this study to monitor the potential effects of storm water runoff and non-point source pollution in Harrison County. Feather samples were taken from twelve random tern chicks in each of the three breeding colonies along the Harrison County beaches. Sediment samples and prey items collected with seine hauls were also gathered from the three sites

The samples were then taken to the Savannah River Ecology lab to perform several preliminary analyses to characterize sites and contaminant levels. The samples were tested for heavy metals such as arsenic, lead, mercury, cadmium, zinc, and nickel. The feathers will also be used to characterize stable isotope signatures of carbon and nitrogen to provide a sense of the trophic level that the birds are feeding on. The data from this study will be used to compare and contrast the sites, the contaminant levels, and dietary habits of the terns that nest there.

Analysis of Wildland Fires for the United States 1960-2004

Monique Calhoun and L. Mtetwa
Hampton University

The year 2000 was one of the worst fire year ever recorded in the United States. Fire incidences can be significant in many ways; some are significant because of their size and others because of the value of the resources lost. As of November 14, 2000, a total of 90,674 wildfires burned 7.26 million acres across the United States. Total fire suppression cost in 2000 was about $1.6 billion. Its clear that Fire monitoring is an important social, health, economic, and national security concern. In this study, we present a statistical analysis of fires from 1960 to present. Our data has been derived form different satellite platforms and historical wildland fire statistics from various government agencies that monitor fire activities in the United States. We will also compare different detection methods and their effectiveness for fire detection and monitoring.

Predictive Modeling of Species Distribution Patterns and their Associated Environmental Requirements Using GIS and Remote Sensing

Holly Porter-Morgan, M.S., Ph.D. Candidate & Dr. Juliana Maantay
The Graduate Center & Lehman College The City University of New York
The Department of Environmental, Geographic, and Geological Sciences

Introduction

In the past few decades there have been great advances in both computing capabilities and statistical techniques, enabling scientists to model the potential distribution of various organisms through correlation with environmental variables (Guisan & Zimmerman, 2000; Skov & Borchsenius, 1997). These methods have been especially useful in the realm of species and ecosystem management where the ability to identify and protect areas of high biological diversity is crucial, yet broad-ranging data sets tend to be lacking (Reutter et al., 2003; Vargas et al., 2004). One of the primary methods that has proven highly effective for use in distribution modeling utilizes genetic algorithms for rule set production, The Genetic Algorithm for Rule-set Prediction (GARP) (Stockwell & Peters, 1999). The GARP package has been found to have a particularly strong performance when using data sets that represent species presence, but not species absence, as is typical in a flora inventory (Raxworthy et al., 2003; Zaniewski et al., 2002).

Current administrative and economic pressures on populations of the widespread understory palm Chamaedorea (Arecaceae), locally known as xate, make it expedient to determine the distribution requirements for threatened Chamaedorea species in Central America. Hundreds of millions of Chamaedorea leaves are collected annually from the wild and exported to Europe and the United States for use as greenery within the floral industry. Harvesting pressure has drastically reduced the standing populations of several Chamaedorea species, and therefore the industry threatens to disrupt normal ecosystem processes as these palms represent a dominant element of the understory in the tropical forests where they occur (Garwood et al., 2004). Management plans are currently being discussed in Belize due to the rapid depletion and over-harvesting of Chamaedorea palms. This study investigates the distribution of the four most valuable Belizean species of Chamaedorea: C. elegans, C. ernesti-augustii, C. oblongata, and C. seifrizii. The study is especially significant as it is crucial at this point it time that forest management officials be supplied with more accurate data with greater spatial resolution baseline data on the distributions and habitat restrictions of threatened species (Angermeier & Winston, 1999).

Figure 1: Chamaedorea ernesti-augustii (Arecaceae). Four of the eleven Chamaedorea species that occur in the country of Belize, Central America are considered of economic importance. Of these species, C. ernesti-augustii currently is the most valuable.

Project Statement

The project described here employs statistical modeling (GARP) with GIS and

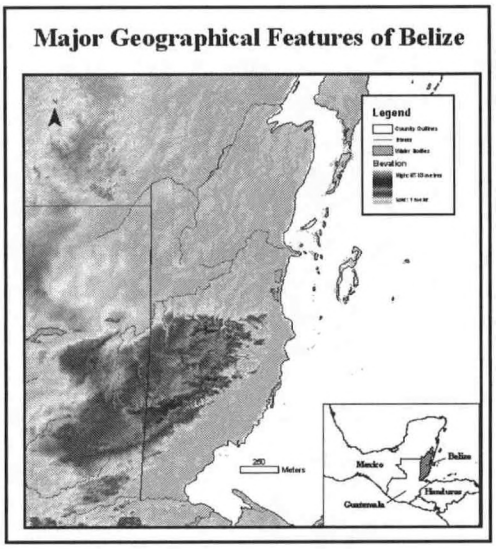

remotely-sensed data in order to determine the distribution of several species of heavily-harvested palms in the genus Chamaedorea that occur in Belize. The following methods and materials are being employed in this research.

Species Occurrences

Species occurrence information to be used in analyses include: (1) data obtained from 1999-2004 surveys by the author (Porter-Morgan et al., 2004) (2) recent locational data from flora inventories conducted by colleagues in Belize (3) localities complied by a through review of herbarium specimens.

Environmental Coverage Data: Numerous GIS coverages are being examined for incorporation in this project. These layers include land cover, precipitation, cloud cover, annual temperature values, elevation, slope, aspect, and hydrology (Fleishman et al., 1999; Vanderpoorten & Engels, 2002). A number of NOAA products will be used in the analysis. For example, a land cover layer will be derived from MODIS 1-km resolution, 16 day 3 level composite, albedo-adjusted reflectance images (MOD 43). Higher resolution imagery will serve as a reference for grouping and editing potential classes to create the final set of land cover classes. In addition, precipitation coverages including annual maximum, minimum, and mean precipitation estimates will be derived from data provided by the NOAA Climate Prediction Center Famine Early Warning System (FEWS). Data coverages will be resampled to approximately 1 kilometer resolution and reduced to an optimal number of ecological variables by variety of statistical methods including jack-knifing and omission statistics (Raxworthy et al., 2003).

Predictive Modelling

The Genetic Algorithm for Rule-set Prediction (GARP) will be employed to determine the ecological niches of study species and provide prediction of their geographic distribution (Stockwell & Peters, 1999). The user inputs sets of point localities where particular species are known to occur and geographic layers representing the environmental parameters that might limit species' ability to survive. The package then uses multiple algorithms to select different decision rules for use in different portions of a species' distribution as needed. Several different methods for building species prediction models are implemented to determine the most accurate rule set. Specifically, a genetic algorithm is used by the model to select those rules, or if-then relationships, that best describe a particular species' ecological niche. These rules are then tested on independently resampled sets of data. Therefore, the resulting rules, which represent a range of possible relationships between the study species and the input environmental variables, have been chosen in a manner that maximizes the predictive accuracy of the model. As the GARP package employs a number of algorithms to create the ultimate rules used in an analysis, including environmental envelopes, logistic regression (Skidmore et al., 1996), and ecological niche factor analysis (Hirzel et al., 2002), it therefore is able to predict species distributions with greater power than any single approach (Anderson et al., 2002).

Expected Results

After the model has been run on each of the species under study, the resulting rule sets will be projected onto the study area along with the environmental coverages to produce maps of geographic distributions for each of the study species. It is important to note that GARP identifies a large number of significant patterns within a particular biological data set such that the associated rules define 'local' rather than 'global' patterns (Stockwell & Peters, 1999). These methods lend the resultant patterns greater significance, greater overall predictive accuracy, and generate more detailed information about the relationships between the study species and their environment (Anderson et al., 2003).

REFERENCES

Anderson, R.P., Gómez-Laverde, M., and A. Townsend Peterson. 2002: Geographical distributions of spiny pocket mice in South America: insights from predictive models. Global Ecology & Biogeography, 11, 131-141.

Anderson, R.P., Lew, D., and A.T. Peterson. 2003. Evaluating predictive models of species' distributions: criteria for selecting optimal models. Ecological Modelling, 162, 211-232.

Angermeier, P.L., and M.R. Winston. 1999. Characterizing fish community diversity across Virginia landscapes: prerequisite for conservation. Ecological Applications, 9, 335-349.

Fleishman, E., MacNally, R., Fay, J.P., and Murphy, D.D. 2001. Modeling and predicting species occurrence using broad-scale environmental variables: an example with butterflies of the Great Basin. Conservation Biology, 15, 6, 1674-1685.

Garwood, N., Penn, M., Porter-Morgan, H., Bridgewater, S., Bol, N., and V. Quiroz. 2004. Preliminary abundance and harvesting data for Chamaedorea (xate) species in the Chiquibul Forest Reserve. Darwin Initiative Report to Government of Belize, The Natural History Museum, London.

Guisan, A. and N.E. Zimmerman. 2000. Predictive habitat distribution models in ecology. Ecological Modelling, 135, 147-186.

Hirzel, A.H., Hausser, J. Chessel, D., and N Perrin. 2002. Ecological-Niche Factor analysis: how to compute habitat-suitability maps without absence data? Ecology, 83, 2027-2036.

Porter Morgan, H., Bridgewater, S., and Bol, N. 2004. Sustainable Harvesting of Fishtail Palms (Chamaedorea ernesti-augustii) in Belize: Fact or Fiction? Darwin Initiative Report to Government of Belize, The Natural History Museum London.

Raxworthy, C.J., Martinez-Meyer, E., Horning, N., Nussbaum, R.A., Schneider G.E., Ortega-Huerta, M.A., and A.T. Peterson. 2003. Predicting distributions of known and unknown reptile species in Madagascar. Nature, 426, 837-841.

Reutter, B.A., Helfer, V., Hirzel, A.H., and P. Vogel. 2003. Modelling habitat-suitability using museum collections: an example with three sympatric Apodemus species from the Alps. Journal of Biogeography, 30, 581-590.

Skidmore, A.K., Gauld, A., and P. Walker 1996. Classification of kangaroo habitat distribution using three GIS models. International Journal of Geographical Information Systems, 10, 441-454

Skov, F., and F. Borchsenius. 1997. Predicting plant species distribution patterns using simple climatic parameters: a case study of Ecuadorian palms Ecography, 20, 347-355.

Stockwell, D., and D. Peters. 1999. The GARP modeling system: problems and solutions to automated spatial prediction. International Journal of Geographica Information Systems, 13, 143-158.

Vanderpoorten, A., and P. Engels. 2002. The effects of environmental variation on bryophytes at a regional scale. Ecography, 25, 513-522.

Vargas, J.H., Consiglio, T., Jørgensen, P.M., and T.B. Croat. 2004. Modelling distribution patterns in a species-rich plant genus, Anthurium (Araceae), in Ecuador. Diversity and Distributions, 10. 211-216.

Zaniewski, A.E., Lehmann, A., and J. McC. Overton. 2002. Predicting species spatial distributions using presence-only data: a case study of native New Zealand ferns. Ecological Mode

Does Environmental Mercury Exposure Affect Hiding and Feeding Behavior in Fiddler Crabs ?

Angel Washington[1,2], Charles Jagoe[1]* and Ambrose Anoruo[2]

[1]University of Georgia, Savannah River Ecology Laboratory, Aiken, SC 29802
[1]Department of Biological Sciences, South Carolina State University, Orangeburg SC 29117

* author to contact – *jagoe@srel.edu*

Mercury is a metal with toxic properties to humans and other organisms at very low concentrations. Mercury affects growth, viability, and reproductive or developmental success. Mercury is also neurotoxic, and so may affect behavior. Fiddler crabs were collected from two locations, the Turtle River marsh near Brunswick, Georgia and the ACE Basin estuary (Seabrook Island, South Carolina). The Brunswick location is near the LCP Superfund site, which is heavily contaminated with mercury, while the ACE basin has no local mercury sources. Although crabs from Brunswick were smaller than those from the ACE basin, they had much higher mercury concentrations (mean + standard error was 39 + 2 ng / g dry weight for the ACE Basin and 344 + 25 ng /g dry weight for Brunswick). We tested for differences in hiding (time to find shelter) and feeding (percentage of time spent foraging) between the populations. Crabs from Brunswick spent less time on food-enriched than those from ACE Basin, indicating less efficient foraging. Fewer crabs from Brunswick were able to find shelter in five minutes or less than crabs from ACE basin. This suggests increased risks of predation in the environment. These behavioral differences may be associated with elevated mercury concentrations at the Brunswick site, and could negatively impact fiddler crab populations in the wild.

MERCURY IN FIDDLER CRABS ALONG SALINITY GRADIENTS IN THE ACE BASIN ESTUARY, SOUTH CAROLINA

Tanjenique I. Paulin[1], Charles Jagoe[1]* and Ambrose Anoruo[2]

[1]University of Georgia, Savannah River Ecology Laboratory, Aiken, SC 29802
[1]Department of Biological Sciences, South Carolina State University, Orangeburg SC 29117

* author to contact – *jagoe@srel.edu*

Abstract

Mercury is a toxic element present in the environment in both organic and inorganic forms, and transformations among inorganic and organic species are mediated by bacteria and physical-chemical processes. Methyl mercury production is stimulated by sulfate, and methylation, transport and bioavailability increase with increased dissolved organic matter. In contrast, high sulfide concentrations, as present in salt marsh sediments, are associated with the formation of insoluble sulfide salts and sequestration of mercury in sediments. This suggests that mercury bioavailability may vary across salinity gradients in estuaries. We collected fiddler crabs (Uca sp.) along salinity gradients in the Ashepoo and Edisto River estuaries, and measured whole-body total mercury concentrations. There were seven sites and a total of 141 specimens; most were *Uca pugnax*. Average Hg concentrations varied among sites (from about 20 to 50 ng/g dry weight), but there were no apparent relationships between mercury concentration and salinity at collection sites. These results suggest that variations in salinity across these estuaries do not significantly influence accumulation of mercury in benthic crustaceans.

Introduction

Mercury is present in the environment in organic and inorganic forms. While both inorganic and organic species are toxic, methyl mercury is generally recognized as the species of major concern to organisms, including humans. There are many human activities that contribute to mercury releases into the environment. Mercury is found in consumer products including batteries, thermometers, thermostats, mercury arc lamps, fluorescent lamps, mercury vapor lamps and mirrors. The most significant mercury sources include waste incineration, coal combustion and chloralkali production.

While mercury can be directly released into waters, much is released into the atmosphere from the combustion and industrial sources listed above. This mercury, in inorganic forms, has a long atmospheric residence time, but eventually returns to earth in precipitation and dry deposition, often in remote areas (Fitzgerald et al. 1999). This inorganic mercury is then methylated in watersheds, wetlands and in the water column, and methyl mercury readily bioaccumulates and biomagnifies through food webs

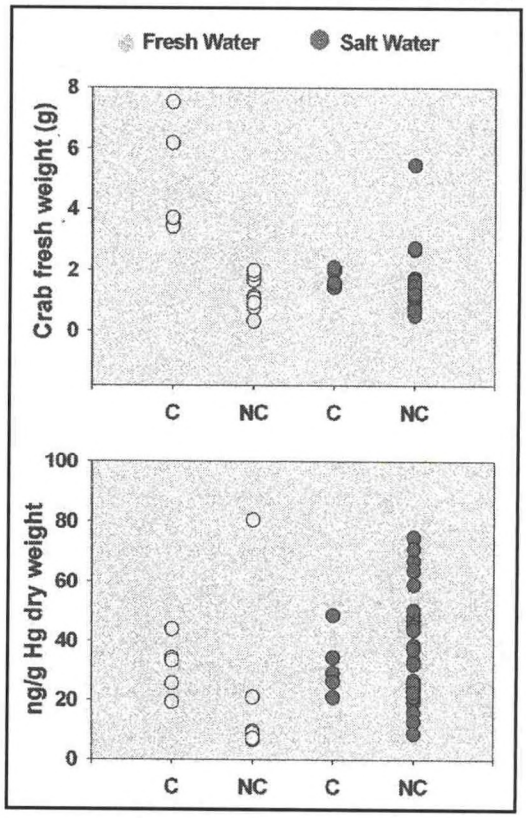

Figure 1. Effects of gut clearance on Hg concentrations in fiddler crabs. C = gut cleared, NC = gut not cleared. Top panel shows live weight of individual

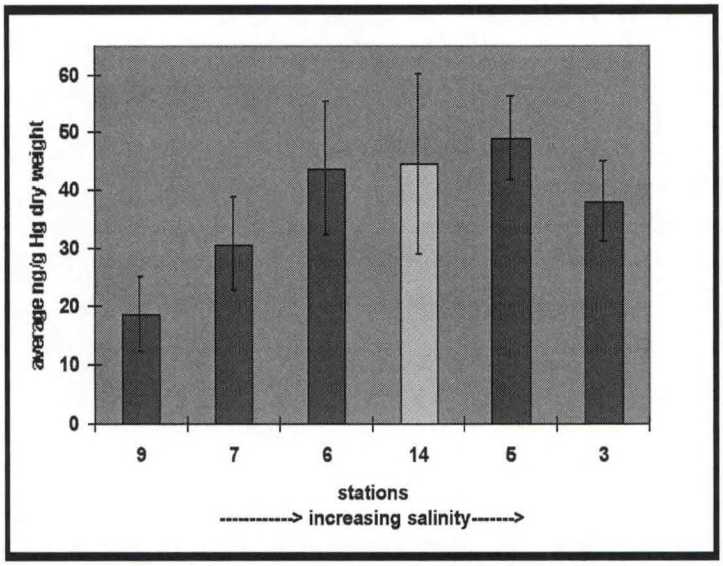

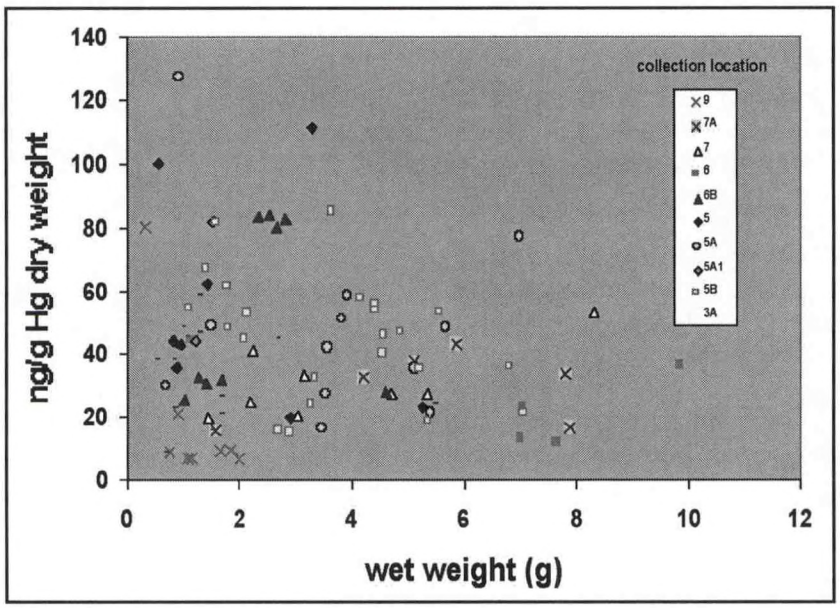

(Wolfe et al. 1998)

Biological and chemical factors that control methylation therefore have major influences on mercury speciation, bioavailability, uptake and toxicity in waters and wetlands. Because mercury methylation is largely performed by sulfate reducing bacteria (Gilmour et al. 1992), sulfur dynamics, redox conditions, and cycling of organic carbon are critical parameters affecting methylation (King et al 1999).

These conditions typically vary with salinity. For example, sulfide concentrations are usually higher in salt marshes than in freshwater wetlands. Because seawater is well buffered, low pH conditions are more likely in freshwater wetlands. These considerations suggest that mercury methylation and bioavailability might vary across salinity gradients. Specifically, mercury methylation and bioavailability should decrease with increasing salinity.

Fiddler crabs are an ideal animal to test this idea. They are common in coastal systems, and live across wide variations in salinity. They are near the base of many food webs, and feed on algae and other organic materials attached to sediment particles. They are also important food items for many species of fish and wildlife, and so may represent an important dietary source of this toxic agent to wildlife, and ultimately, human consumers.

Methods and Materials

The ACE Basin is located in southeastern coastal South Carolina, USA. The acronym ACE refers to the three rivers (Ashepoo, Combahee and Edisto) that discharge into the estuary. The area is recognized as one of the largest undeveloped estuaries on the east coast, and includes a National Estuarine Research Reserve of approximately 54,000 hectares. The collection area had no obvious local pollution sources, and was largely rural with no nearby villages, dwellings or industry.

Fiddler crabs were collected at five stations in the Edisto River and two stations in the Ashepoo River. Salinity at each station was estimated from water conductivity, and salinities ranged

from < 0.1 to 27 parts per thousand. Animals were collected by hand or with dip nets, placed in coolers and returned to the laboratory.

In an initial experiment, some crabs were placed in an aerated aquarium containing artificial seawater and allowed to clear their guts for 7 days before freezing. The remaining crabs were frozen on arrival at the laboratory. All were stored frozen in polyethylene bags until analysis.

Frozen crabs were thawed, identified to species, and individually cleaned of mud and external debris in high-purity deionized water. Crabs were patted dry with Kimwipes, placed in individual vials, weighed, and freeze-dried for 96 hours. After lyophilization, crabs were reweighed to determine body moisture content.

Individual dried crabs were ground using a mortar and pestle, and 75 mg aliquots of the powder were analyzed for total mercury by EPA method 7473 using a Milestone DMA-80 analyzer. Briefly, this automated method involves thermal decomposition of the sample in pure oxygen, trapping and preconcentration of mercury by gold amalgamation, followed by thermal desorption and measurement of mercury in the vapor phase using a dual-path spectrophotometer. For QA/QC purposes, samples were run in batches that included blanks, replicates, and standard reference materials of similar matrix with known, certified mercury concentrations (TORT-2, defatted lobster hepatopancreas, purchased from the National Research Council of Canada). All fiddler crabs contained detectable concentrations of mercury; results are expressed in ng Hg / g dry weight.

Data were analyzed using SAS 9.0 software. Locations and effects of the gut clearance treatment were compared using non-parametric Kruskal-Wallis tests. Spearman's rank correlation was used to test for relationships between crab size and mercury concentration.

Results and Discussion

Fiddler crabs collected in the field included three species: *Uca pugnax, Uca pugilator,* and *Uca minax*. Almost all the crabs we collected were *Uca pugnax*. There were no significant differences in mercury concentration among species (data not presented). Because sample sizes were small for *U. pugilator* and *U. minax*, there were omitted from all statistical comparisons. The results presented here are for *U. pugnax* only.

Some crabs from both fresh and saltwater locations were allowed to clear their guts before analysis. Figure 1 a shows that the crabs from the two environments were not significantly different in live weight. After 7 days of clearance, whole body mercury concentrations in crabs that cleared their guts were not different that in those that did not, regardless of salinity at the collection location (Figure 1b).

In theory, guts could contain sediments that would yield elevated mercury concentrations in whole crabs if the sediments were not cleared before analysis. Alternatively, if sediments were low in mercury, their weight could yield artificially low mercury concentrations (expressed on a mercury per unit weight basis) if they were not cleared before analysis. Our observations suggest that neither of these scenarios is a concern in these animals. Gut clearance had no detectable effect on average whole body mercury concentrations. Therefore, allowing fiddler crabs to clear their guts before analysis is probably unnecessary in future studies. In nature, fiddler crabs are consumed by a variety of wildlife species, and these predators do not allow the crabs to empty their guts before they are eaten. This consideration supports the idea that allowing gut clearance is unrealistic when evaluating potential risks to wildlife from mercury in fiddler crabs.

We tested for differences in mean mercury concentrations among locations. Some differences among locations were found, but these were not directly related to salinity gradients (Figure 2). Mercury concentrations in fiddler crabs appeared to increase with salinity to the middle of the estuary, and then level off with increasing salinity.

Previous studies have suggested that mercury concentrations tend to be higher in prey items of wading birds foraging in freshwater compared to those foraging in estuarine systems (Gariboldi et al.1999), and that mercury methylation and bioavailability influenced by high sulfide concentrations in salt marshes (Benoit et al. 1999a, 1999b). Thus, we hypothesized that mercury concentrations in fiddler

crabs would decrease with increasing salinity. However, our data do not

support this conclusion Additional work in other estuaries is needed to determine whether our observations can be generalized across other salinity gradients.

We tested for relationships between crab size and mercury concentration by location, and with all locations pooled (Figure 3). There were no significant relationships between crab size and whole body mercury concentration.

Relationships between size and mercury concentrations have been well documented in fish and many invertebrates. Although such a relationship was not detected in this study, this may simply be due to the relatively small range in size of the fiddler crabs we collected; we did not collect juveniles, or larger, older crabs.

Future studies that examine fiddler crab mercury concentrations across salinity gradients in other estuaries will be needed to clarify the roles of salinity, sulfur dynamics, and other factors in methylation and bioavailability. It is worth noting that detectable mercury concentrations were found in all the fiddler crabs we sampled, even in this apparently pristine estuary. This illustrates the importance of atmospheric processes in delivering mercury to remote locations (Fitzgerald et al. 1999). The effects of such mercury concentrations on the crabs, as well as their predators, are also fruitful areas for additional studies.

ACKNOWLEDGEMENTS

We thank Heather Brant, Lindy Steadman, William Drayton, and Bill Jagoe for assistance with this study.

This work was supported by N.O.A.A. (through South Carolina State University and the Environmental Cooperative Science Center, Florida A&M University) and the Savannah River Ecology Laboratory under Financial Assistance Award DE-FC09-96SR18-546 between the University of Georgia and the U.S. Department of Energy, Environmental Remediation Sciences Division.

REFERENCES

Benoit, J. M., C. G. Gilmour, R. P. Mason, and A. Heyes. 1999a. Sulfide controls on mercury speciation and bioavailability to methylating bacteria in sediment pore waters. Environ. Sci. Technol. 33:951-957

Benoit, J. M., R. P. Mason, and C. G. Gilmour. 1999. Estimation of mercury-sulfide speciation in sediment pore waters using octanol-water partitioning and implication for the availability to methylating bacteria. Environ. Toxicol. Chem. 18:2138-2141.

Fitzgerald, W.F., D.R. Engstrom, R.P. Mason and E.A. Nater 1998. The case for atmospheric mercury contamination in remote areas. Environ. Sci. Technol. 32: 1-7

Gariboldi, J.C., C.H. Jagoe, and A.L. Bryan Jr. 1998. Dietary exposure to mercury in nestling wood storks (Mycteria americana) in Georgia

Arch. Environ Contam. Toxicol. 34: 398-405

Gilmour, C.C., Henry, E.A., and R. Mitchell, 1992. Sulfate stimulation of mercury methylation in freshwater sediments. Environ. Sci. Technol. 26: 2281-2287

King, J. K., F. M. Saunders, R. F. Lee, and R. A. Jahnke. 1999. Coupling mercury methylation rates to sulfate reduction rates in marine sediments. Environ. Toxicol. Chem. 18:1362-1369.

Wolfe, M.F., S. Schwarzbach, and R.A. Sulaiman. 1998. Mercury effects on wildlife: a comprehensive review. Environ. Toxicol. Chem. 17: 146-160.

Evaluation of Microbial Mats as Biological Filters for Black Sea Bass (*Centripristis striata*) Shoreline Aquaculture Ammonia Management

Carmen Robinson[1], Ifedapo Adeneyi[2], Selassi Blavo[2], Kami Tang-Pack[1,2], Yaw Yeboah[2] and Conrad Ingram[1]

Department of Chemistry[1] and Engineering[2] Clark Atlanta University, 223 James P. Brawley Drive, Atlanta, GA 303140

Kerri Brinkley[3] and Richard Lee[3]

[3]Skidaway Institute of Oceanography, 10 Ocean Science Circle, Savannah GA 31411

Introduction

Large scale operations to produce Black Sea Bass fish (*Centripristis striata*) with aquaculture techniques is of great and growing commercial interest. This is a highly valued and highly priced product in the restaurant industry, especially in the sushi market, where live two- to two and one-half pound fish are sold at $3.50 per pound. Establishing shoreline aquaculture systems for the large scale culturing of Black Sea Bass, using brackish seawater, has tremendous economic advantages. Operations of this kind are, however, hampered by the high levels of ammonia (NH3) and other wastes to be generated and the potentially deleterious impact on surrounding bodies of water, such as estuaries. Developing ammonia filtering and sequestration systems is of critical importance to alleviate this problem.

Previous pilot scale studies conducted at Clark Atlanta University and Skidaway Institute of Oceanography established that ammonia levels could be reduced in Black Sea Bass aquaculture system with microbial mats (Bender et al., 2003). The work demonstrated the ability of the mats to fix nitrogen, transform nitrogenous wastes into cellular protein, and metabolize organic sludge material. The microbial mats accomplished this owing to presence of phototrophic cyanobacteria, which support nitrifying bacteria by producing oxygen through the process of photosynthesis. Thus, ammonia containing fish wastewater could be treated, recycled or discharged to surrounding estuaries without significant deleterious environmental impact.

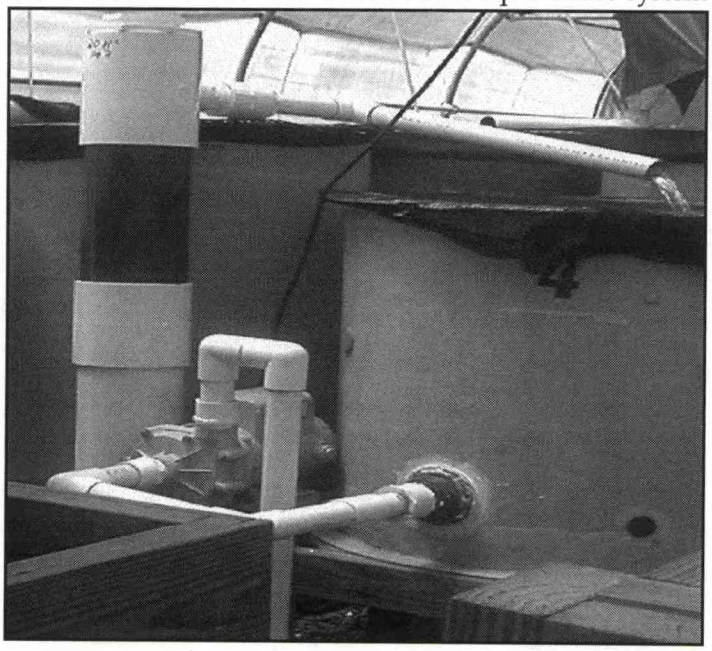

Figure 1. Blue green algae microbial mat in treatment tray used in System #1.

The pilot scale operation involved a system of recycled aquaculture water where wastewater coming from a fish tank flowed under gravity to a delivery tray containing the cultured mats immobilized on a synthetic mesh. The water eluting from the mat is then pumped through a fluidized sand bed which is installed downstream of the tray and which con-

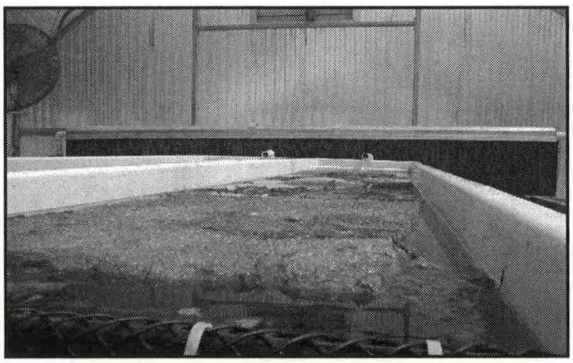

Figure 2. Green filamentous algae used in treatment tray in System #2.

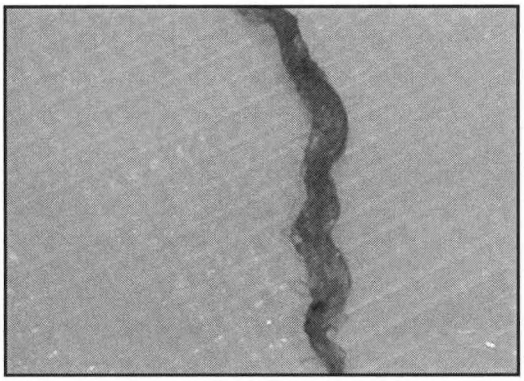

Figure 3. Fluidized sand bed column (left) and fish tank (right) used in System #3.

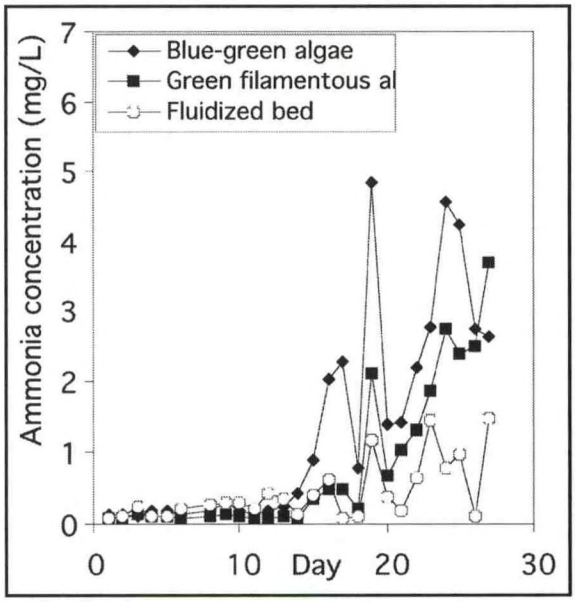

Figure 4. Ammonia concentration with time after the addition of fish to tanks with different treatment systems.

tained nitrifying bacteria. The fluidized sand bed is perceived to further reduce the ammonia levels, but its effectiveness has not being evaluated. During the wastewater residence time in treatment tray the microbial mats would act on the nitrogenous waste and fecal matter in the water, metabolizing them to cellular protein for their own uptake and producing oxygen for nitrifiers present in the tray to do the same. The end result is water is devoid of the majority of its waste, rich in oxygen, of suitable quality for fish survival and growth.

The microbial mats are composed of blue-green algae with photoautotrophic cyanobacteria, (*Oscillatoria sp*) and (*Rhodopseudomonas sp*) predominating as the main microbes (Mehrabi et al., 2001). Heterotrophic bacteria are also present in the bottom layer (the anoxic or anoxygenic layer). In the delivery tray, the heterotrophic bacteria, (both aerobes and anaerobes), and the nitrifiers, fed with oxygen by the oxic layer of the mat, is responsible for removing ammonia from the contaminated water. It was observed during pilot scale operation that a green filamentous algae species (identified as *Rhizoclonium Riparium* and *Entermorph*a) developed and demonstrated preliminary waste removal properties. More interestingly, in the presence of the filamentous algae, the blue green algae became resistant to predatory attacks from snails and insects (Bender et al., 2004). It was therefore of interest to investigate the performance of the green filamentous algae as an independent biofilter for ammonia removal.

For the fludized bed, sand particles are used as the substrate for bacteria to adhere to and grow on. For this aquaculture system, the species of nitrifying bacteria which are reported to adhere to the sand particles include *Nitrosomonas*, *Nitrosospira* and *Nitrospira*. *Nitrosomonas* and *Nitrosospira* convert ammonia to nitrite and the Nitrospira converts this nitrite to nitrate. However, this system was has never been evaluated independently for its ammonia removal properties.

It now became necessary to determine the relative effectiveness of each treatment system (the blue-green algae, the green filamentous algae, or nitrifiers-containing fluidized sand bed) at removing ammonia from the Black Sea Bass aquaculture system. The object of this is project was to evaluate the three systems independently.

Experimental

The three biological filters evaluated included; a) two microbial mats of blue-green algae (System 1) and green filamentous algae (System 2), both immobilized on synthetic mats and b) a nitrifying-bacteria-contain-

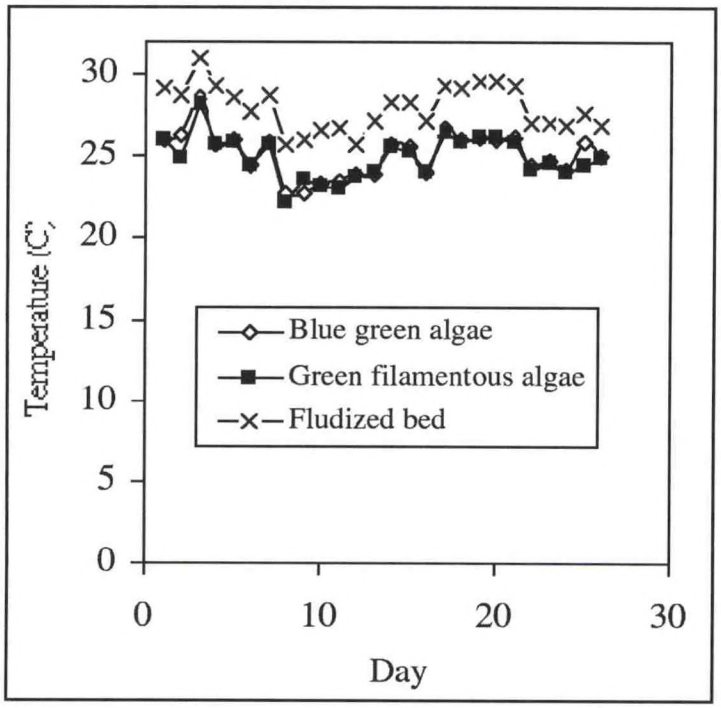

Figure 5. Temperature variation over time after the addition of fish to tanks with different treatment systems.

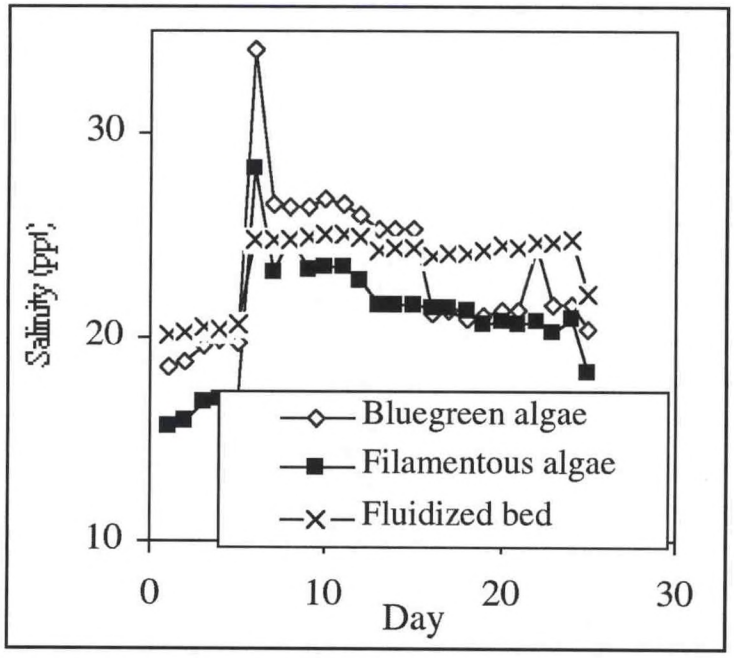

Figure 6. Salinity variation over time after addition of fish to tanks with different treatment systems.

ing fluidized sand bed (System 3). Each system consisted of a 500L inverted silo-shaped fish tank that was three-quarters filled with brackish water. Each tank was also connected to a 60L cylindrical reservoir containing air stones through which air was pumped to increase the concentration of dissolved oxygen. Tanks from Systems 1 and 2 were each connected through flow pipes to trays containing immobilized microbial mats of dimensions 15" long x 10" wide x 2" thickness. The mats were constructed from salts-containing silage; each with a different consortium of microbes. Tank #1 was fitted with a tray containing mats of blue-green algae with the microbes *Oscillatoria sp.* and *Rhodopseudomonas sp.* predominating (Figure 1). Tank #2 was fitted with a tray containing green filamentous algae (*Rhizoclonian riparium* and *Entermorpha flexuosa*) (Figure 2). Problems of algal blooms developing in the trays were overcome by partially shading them from sunlight. Mummi chogs (a small insect-eating fish) were added to the blue-green algae tray to keep predatory insects from attacking the mat system. A third tank, Tank #3, was fitted with a fluidized sand bed containing sand particles colonized by nitrifying bacteria (Figure 3). To promote growth of the nitrifiers on the sand particles, approximately 12 liters of wastewater (taken from already established black sea bass tank) was added. In this system, the fine sand particles are transformed into a fluid like state through the upwelling of high velocity water with the aid of an electric pump (Sweetwater® High Efficiency Pump, 170 Watts, Aquatic Eco-systems, Inc., Apopka, FL)). As the water velocity increased, the particles swirled higher up the column and become more fluidized.

Each tank was loaded with brackish water and four Black Sea Bass. Water was circulated by gravity flow at a low rate through the sides of each tank into the slightly sloped treatment trays and back to the tank. In the case of the fluidized bed, the water was mechanical pumped through the bed in an up-flow mode at

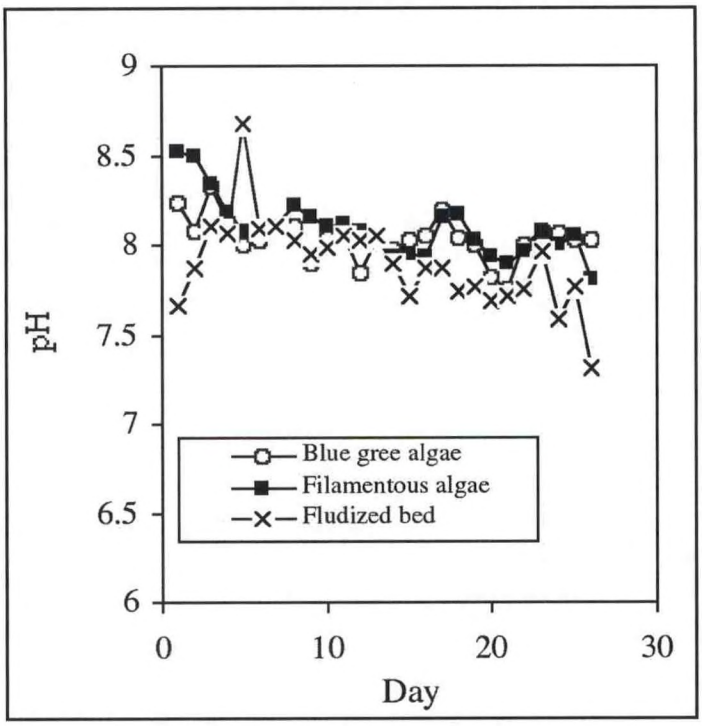

Figure 7. pH variation with over time after the addition of fish to tanks with different treatment systems.

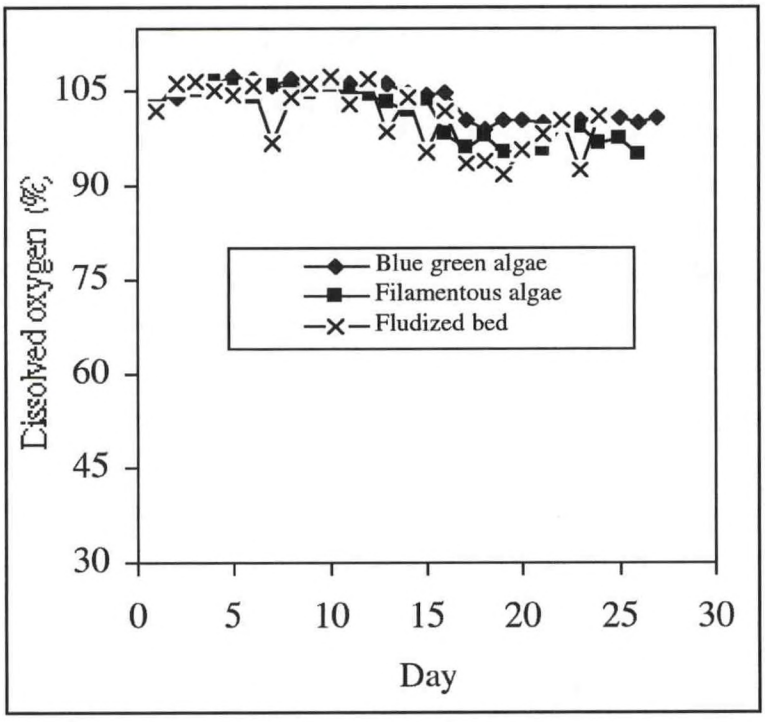

Figure 8. Dissolved oxygen variation over time after addition of fish to tanks with different treatment systems.

flow rate similar to the gravity fed system. In all cases, water flowed through the treatment systems where its fish waste contents were absorbed by the microbes for nutrition, hence purifying the water that returned to the fish tanks in a repetitive cycle.

The fish were fed daily with baby tilapia (*oreochronis aureus*). Daily testing of the dissolved oxygen, pH, water temperature, and salinity were made using a YSI 600 computer-integrated probe system (YSI Co., Yellow Springs, OH). The ammonia concentration measurement was performed by developing a colored complex with ammonia and measuring concentrations colorimetrically (LaMotte Instruments, Charleston, MD).

Results and Discussion

The concentration of NH3 produced by the fish in Tank #1 (with blue green algae filter) increased slowly to approximately 0.3 mg/L after 13 days, then increased sharply to 4.5-5 mg/L as early as day nineteen. The rapid increase in NH3 is attributed to a reduction in NH3 sequestration efficiency resulting from the bleaching of the mat by sunlight and attack by predatory bugs.

Bleaching depreciated the quality and quantity of material available to remediate ammonia and other fish wastes in the systems. NH3 concentration in Tank #2 increased, but at a much slower rate than Tank #1. NH3 concentration in this system was < 0.5 mg/L after 18 days, and increased gradually to 3.5 mg/L after 27 days. The "nitrifying-bacteria-containing" fluidized sand bed (Tank #3) proved to be most effective in removing NH3. In this case, NH3 concentration increased at the slowest rate, gradually reaching a concentration of 1.6 mg/L after 28 days.

On average, the temperature of the tanks was maintained at about 25°C for the 25-30 day duration of the project (Figure 5). System # 3 ran slightly higher temperatures on average than the other because it was

located furthest from the swamp generators used to cool the other systems. It also operated on an enclosed system and did not have delivery trays that were exposed to the atmosphere as the other two did, hence dissipating less heat, especially heat generated by the electric pump within the system.

For the optimal performance of the microbial mats as well as nitrifying bacteria found in the three systems, a pH range between 8-8.5 was maintained over the 25-30 day period (Figure 7). This pH range is reported to provide favorable conditions for optimal performance (multiplication and material transformation) application of nitrifying bacteria, heterotrophic aerobes and anaerobes and phototrophic cyanobacteria all functioning in the aquaculture systems (Bender et al., 2004).

The percentage dissolved oxygen were monitored and maintained maintained dissolved oxygen levels in all tanks ranged between 6.8 to 8.0 mg/L to ensure adequate concentration for fish survival. These percentages were represented approximately 100% dissolved oxygen (Figure 8). It was anticipated that the fluidized sand bed would have had less oxygen than the other two systems, in the due to the absence of photosynthetic bacteria and its only oxygen sources were the air stones placed in the tank. Irrespective of this fact, the dissolved oxygen percentages of Tank #3 never fell below 95 % for the duration of the project.

The aim of the project was to determine the most effective of three different biological filtration systems. The parameters used to make this determination included ammonia concentration and solid waste removal in each of the aquaculture system set-ups. From the data compiled over the duration of the project, the fluidized sand bed was determined to be the most effective at remediating ammonia.

This was possibly due to the constant contact maintained between the nitrifying bacteria and the ammonia-rich water coming into the column. The increased surface area provided by the sand particles and the fluid-like motion of the sand particles, propelled by water pumped at a high velocity, ensured that a continuous reaction between the nitrifying bacteria and contaminated water coming into the column was taking place.

While the fluidized bed was most effective at ammonia removal, System #2 with Green filamentous algae proved to be the most effective at remediating solid waste produced by the fish in that system. Unlike the fluidized sand bed, which is not designed to remediate solid waste (as such waste could clog up the sand column and cause the fluidized sand to collapse and suffocate its nitrifying bacteria), the Green filamentous algae is able to metabolize organic matter with the help of its nitrifiers, while producing carbohydrates for its sustenance and oxygen as a by-product using the process of photosynthesis. Its success can be attributed to its texture and nature, which makes it resistant to bug predation unlike its Blue-green counterpart.

For a future project, a combination of these two set-ups could be considered. If well implemented, a design incorporating both set-ups could serve as an ideal system capable of optimal remediation of ammonia from such an aquaculture system. Such a system could first have its contaminated water run through a delivery tray containing Green filamentous algal mats to remove ammonia and solid waste. The pre-treated water would then be subjected to continuous chemical reaction with nitrifying bacteria in a fluidized bed column.

Conclusion

Ammonia biofilter treatment systems composed of mats of bacteria-colonized Blue green algae, bacteria-colonized green filamentous algae or "nitrifying-bacteria- colonized" fluidized sand bed, independently showed effectiveness in removing ammonia from the recycled water in a Black Sea Bass aquaculture system. The relative effectiveness under the experimental conditions studies was as follows: Fluidized sand bed > Filamentous algae > Blue green algae. This is related to a number of variables for example, the susceptibility of the latter to predatory attacks from snails and insects. In all cases ammonia levels rose slowly, with the fluidized bed doing so at the slowest rate. Other water quality parameters such as temperature, dissolved oxygen, salinity, and pH could be maintained under optimum conditions required for the survival and growth of the fish. Further investigation will be necessary to elucidate reasons for the observed ammonia breakthrough and it gradually rise in concentration in all systems.

REFERENCES

Bender, J., Lee, R. F., Sheppard, M., Bulski, K., Phillips, P., Yeboah, Y., and R. Chee-Wah, 2004: A waste effluent treatment system based on microbial mats for black sea bass Centropristis striata recycled-water mariculture. Aquacultural Eng. 31 (1-2) 73-82.

Mehrabi, S., Ekanemesang, U. M., Aikhionbare, F. O., Kimbro, K. S., J. Bender, 2001: Identification and characterization of Rhodopdeudomonas sp., a purple, no-sulfur bacterium from microbial mats. Biomolecular Eng. 18, 49-56.

This research was funded by NOAA EPP/MSI Award No. NA16AE1706.

NANOPOROUS ALUMINOSILICATE CLINOPTILOLITE FOR AMMONIA REMOVAL IN A SHORELINE AQUACULTURE SYSTEM

Kisha Scarlet[1], Tolulope Akinduro[2], Chloe Poston[2], Amy Tate[2], Feola Odeyemi[2], Yaw Yeboah[2] and Conrad Ingram[1]

Departments of Chemistry[1] and Engineering [2], Clark Atlanta University, 223 James P. Brawley Drive, Atlanta, GA 30314

Kerri Brinkley[3] and Richard Lee[3]

Skidaway Institute of Oceanography[3], 10 Ocean Science Circle, Savannah GA 31411

Introduction

The objective of this research was to evaluate the performance of naturally occurring, inexpensive, nanoporous aluminosilicate zeolite, clinoptilolite, as an adsorbent for ammonia (NH3) reduction in a pilot scale demonstration of a low-cost biosolar Black Sea Bass (*Centripristis striata*) shoreline aquaculture system. Black Sea Bass is a commodity of high commercial value, and is a popular item in several sushi restaurants. An expanded industry surrounding the culturing of this fish in a shoreline aquaculture system is of increasing commercial interest. However, to prevent pollution of the coastal estuaries, a waste removal system will be needed to control the high levels of ammonia that would be generated. Previous pilot scale studies conducted at Clark Atlanta University and Skidaway Institute of Oceanography established that ammonia levels could be significantly reduced in this aquaculture system using biofilters of algae-based microbial mats (containing a consortium of bacteria) in series with a "nitrifying-bacteria colonized" fluidized sand bed (Bender et al., 2004). However, in initial stages of the system operations during which the microbes are establishing themselves, ammonia concentration can spike to levels that are fatal to fish. In addition, the rate of ammonia production in a continuous large scale operation may overwhelm biofilters. An improvement in the design of the filtration system can be envisaged with clinoptilolite replacing the inactive sand particles as the substrate on which to fix nitrifying bacteria in the fluidized bed operation. It is anticipated that significant improvement in the ammonia removal capacity will occur using the composite filter of "nitrifying-bacteria-colonized clinoptilolite" where, through a process of "uptake and release", ammonium ions will be capture from solution into the zeolite matrix for possible subsequent slow release for consumption by the microbial mats. This will serve to prevent ammonia peaks in the early phases of operation of a biofilter system when microbes are establishing themselves, and to sustain low ammonia levels during extended periods operation.

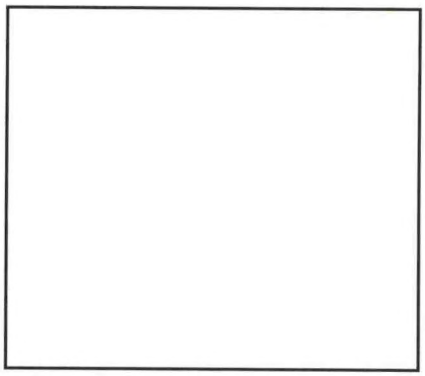

Figure 1. Fish Tank – Fluidized zeolite bed recirulating Black Sea Bass system (Na-clinoptilolite fluidized bed left system -left) and natural zeolite fluidized bed system-right).

Clinoptilolite is a naturally occurring high surface area, nanoporous porous (pore diameter 0.75 x 0.31 nm) low cost mineral, abundantly available in the United States and worldwide and existing mainly in volcanic rocks (Armbruster, T.; 2001). In 1997, 3.6 million tons were produced worldwide, with a typical company mines 20,000-50,000 tons/yr and it is sold at an average cost of $50- $300 /ton. Clinoptilolite ((Na3K3)(Al6Si40)O96.24H2O) is a member of group of natural and synthetic nanoporous alumniosilicates called zeolites. Its inorganic lattice is formed from alternating SiO2 and AlO-2 tetrahedra with a

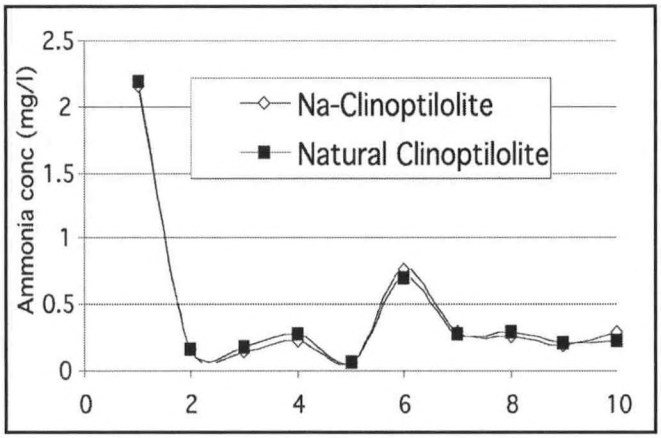

Figure 2. Variation in aqueous ammonium concentration vs time using different forms of clinoptilolite adsorbent as fluidized bed in Black Sea Bass aquaculture systems.

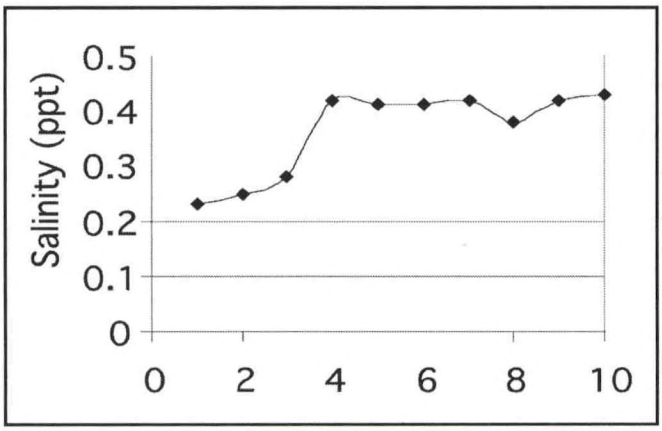

Figure 3. Variation in salinity vs time using Na-clinoptilolite adsorbent as fluidized bed in Black Sea Bass aquaculture system.

resulting negatively charged framework of cation exchange sites, which are accessible through its spores. For this mineral, these sites are generally occupied (balanced) by Ca2+, K+ and Na+ with an average exchange capacity around 2.25 meq/g depending on the source. It will readily release these ions in exchange for more environmental unfriendly cations (e.g. Pb2+ and Cd2+), and is therefore used for the removal of the latter from aqueous waste streams. As a cation exchanger, it has been found to be highly selective for ammonium and is used in a few countries for the removal of this cation from aquaculture wastewater (Armbruster, T; 2001). In this project, the performance of fluidized bed clinoptilolite (in its natural and Na-exchanged form) to remove ammonia, in the absence of nitrifying bacteria, from a Black Sea Bass aquaculture system was investigated.

Experimental

The clinoptilolite (Tradename Zeobest, Northern Filter Media, Inc.) used in this project is a naturally occurring nanoporous mineral with surface area of 43.8 m2/g, cation exchange capacity of 1.2-1.8+ meq/g, bulk density of 88 lbs/ft3, and pore size of 4.0Å . A portion of the natural clinoptilolite was selected and all exchangeable cations were exchanged for sodium by stirring nine kg of zeolite in 30 L of concentrated sodium chloride solution for 24 h. The solid was washed several times with water to remove excess sodium chloride. For the ammonia removal experiments, each of two 600 gallon tanks was connected through flow pipes to a water column (PVC pipe) which later served as the container for a fluidized zeolite bed. Water was continuously re-circulated through each tank- fluidized bed column with the aid of a mechanical pump (Sweetwater® High Efficiency Pump, 170 Watts, Aquatic Eco-systems, Inc., Apopka, FL)). Each fresh water filled tank was loaded with 18 Black Sea Bass of average size of 0.5 inches and average weight of 250 g. Fish feed was water hyacinths, blue-green algae and green filamentous algae. The "fish-containing, zeolite-free, re-circulating systems" were run for several days to allow NH3 build up to approximately 2 mg/l, after which 4.5 kg of clinoptilolite and 2 kg of gravel were added to each fluidized bed column (natural clinoptilolite in one column and Na-clinoptilolite in the other) and systems run continued. Daily testing of the dissolved oxygen, pH, water temperature, and salinity were made using a YSI 600 computer-integrated probe system (YSI Co., Yellow Springs, OH). The ammonia concentration measurement was performed by developing a colored complex with ammonia and measuring concentrations colorimetrically (LaMotte Instruments, Charleston, MD). In preliminary bench tests, the relative capacities of clinoptilolite (natural vs Na-clinoptilolite) for ammonia uptake was compared. Different weights (0.0 to 1.0 g) of each zeolite, was added to 20 ml of ammonia solution in several Erlenmeyer flasks, and the latter agitated for 24 h.. The ammonia concentration in the filtrates was analyzed by colorimetry.

Results and Discussion

Figure 2 shows that for both systems, within 48 hrs of introducing the zeolite beds, NH3 concentration was reduced from 2.5 mg/L to approximately 0.3 mg/l representing 85% removal, and was maintained within this range (except day 6) for the remaining 10 days duration of the project. Both forms of the zeolite (natural and Na-exchanged) appeared to be equally effective in NH3 reduction. However, 100 % removal of ammonia was not attained with either system, probably due to the fact that other cations such as sodium and calcium are present in the fresh water and are competing with ammonium for the cation exchange sites in the zeolite. Since the flow rate through both tanks was really high, the impact of low residence times on the effectiveness of the zeolite cannot be totally ignored. Whether Na-clinotilolite vs natural zeolite had a higher capacity for ammonia was determined from the short time period over which the experiment was conducted. Their relatively effectiveness, needs to be evaluated further based on exposure to increasing amounts of NH3 and the resulting breakthrough capacities.

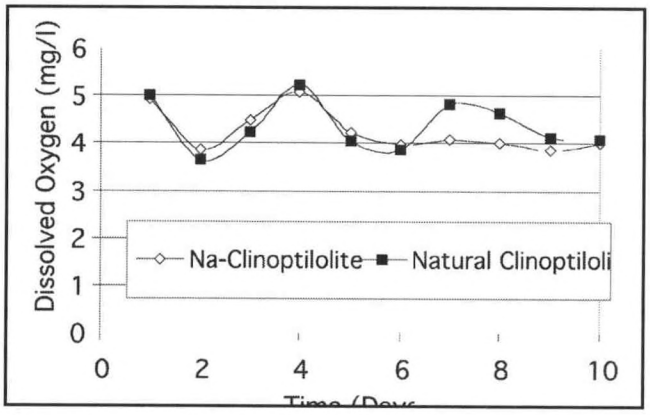

Figure 4. Dissolved oxygen levels vs time using different forms of clinoptilolite adsorbent as fluidized bed in Black Sea Bass aquaculture systems.

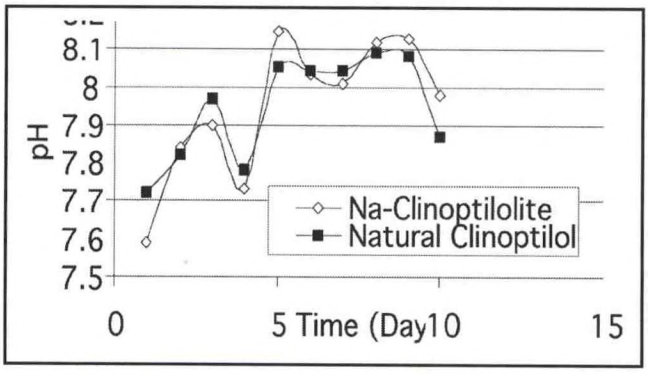

Figure 5. Variation in pH vs time using different forms of clinoptilolite adsorbent as fluidized bed in Black Sea Bass aquaculture systems.

Dissolved oxygen levels fluctuated between 3.8 - 5 mg/L in both systems (Figure 4). Previous research using biofilters reported oxygen levels in the range of 5-10 mg/L (Bender et al., 2004). The relatively low dissolved oxygen concentration in this project was probably due to its reduced solubility at the fairly high water temperature (31-35°C) from the heat generated by the pump.

pH remained generally acceptable within the range of 7.6 to 8.2, though a gradual increase was observed over the range of the 10 days of operation, for unclear reasons (Figure 5).

Conclusion

Both natural and Na-clinoptilolite demonstrated significant potential in removing ammonia from a Black Sea Bass aquaculture system. Under the conditions evaluated, 85 % reduction in ammonia concentration could be achieved as early as 24 h after commencement of operations. The zeolite is therefore potentially useful as a replacement for sand to design a "nitrifying bacteria colonized- clinoptilolite" fluidized bed and should be investigated. Differences in the performance of the two forms of the zeolite were not evident, due to the short period of operation of the systems. Other water quality parameters such as pH, dissolved, oxygen, temperature and salinity remained in the acceptable ranges for fish growth for both systems during throughout the period of operation.

REFERENCES

Armbruster, T., 2001: Clinoptilolite-heulandite: applications and basic research. Zeolites and Mesoporous Materials at The Dawn of the 21st Century; eds. Galarmeau, Di- Renzo, F. Fajula, F., Vedrine, J.; Stud. in Surf. Sci. and Catal. 135 13-27.

Bender, J., Lee, R. F., Sheppard, M., Bulski, K., Phillips, P., Yeboah, Y., and R. Chee-Wah, 2004: A waste effluent treatment system based on microbial mats for black sea bass Centropristis striata recycled-water mariculture. Aquacultural Eng. 31 (1-2) 73-82.

Mehrabi, S., Ekanemesang, U. M., Aikhionbare, F. O., Kimbro, K. S., J. Bender, 2001: Identification and characterization of Rhodopdeudomonas sp., a purple, no-sulfur bacterium from microbial mats. Biomolecular Eng. 18, 49-56.

ACKNOWLEDGEMENT

Funding for this research from NOAA EPP/MSI Award No. NA16AE1706 and NSF Award No. 0120978 (through Water CAMPWS) is gratefully acknowledged.

Near-Real-Time Acquisition of MODIS Satellite Data for Research Within the NOAA CREST 'Swath'

William Lawrence (NOAA CREST Faculty), Manohar Mareboyana (NOAA CREST Faculty), Reginald Lawrence (NOAA NESDIS), Bruce Ramsay (NOAA NESDIS), Jide Aniyikaiye (NOAA CREST Fellow), and Jonathan Bradford (NOAA CREST Fellow)

Access to recently acquired satellite data sets is usually difficult. In the case of MODIS data, most is utilized by MODIS science teams for the production of 'digest' data where data is either turned into a science product, composited through time, or aggregated to lower spatial resolution. These processes often and understandably delay the public availability of data. In the case of time delays, it is difficult to provide timely information to potential users. In the case of spatially aggregated or temporally composited data, information needed by a subset of users may be lost. Through a collaborative effort with NOAA NESDIS, Bowie State University has begun to capture near-real-time MODIS data for NOAA CREST use. Our first users will be NOAA CREST projects at UMBC, where students will convert the raw MODIS data to the MODIS MOD04 optical depth product for posting to the UMBC Air Quality BLOG. The data will be stored in a spatial database and made available through the web. Other products will be created using the new Bowie State University Super Computer Facility [a 400 node Apple parallel processing installation].

Using Side-Scanning Sonar to Map River Contours in the Chesapeake Bay

Jonathan Bradford (NOAA CREST Fellow), Lowell Bahner, Kurt Zegowitz and Steve Giordano (NOAA Chesapeake Bay Office)

Poster/Environmental Sciences

The depth, structure and contours of rivers emptying into the Chesapeake Bay are key indicators useful to environmental monitoring, navigation and fisheries management. As part of the work of the NOAA Chesapeake Bay Office, river bottoms, reefs, ledges and other surface features are routinely mapped using side-scanning sonar, a high resolution oceanographic tool. This project focused on a single river along the Virginia shoreline and once data is fully analyzed, will provide valuable information for management and change detection applications. The primary application of this data will be aimed towards monitoring, evaluation, and enhancement of native oyster populations in the Bay.

MODELING HARMFUL ALGAL BLOOMS IN LONG ISLAND SOUND

Mr. Bernard Mhando (Graduate Student), Dr. Megan Wiley (Assistant Professor), and Dr. Reza Khanbilvardi (Professor), Department of Civil Engineering, City College of New York

Introduction

Long Island Sound (LIS) is a combination of two systems, a sound and estuary. A sound is defined as a relatively narrow passage of water between an island (Long Island - LI) and the mainland (Connecticut) Figure 1, (Random House, 1991) An estuary is defined as a coastal area where fresh water from rivers and streams mixes with salt water from oceans. Examples include bays, sounds and lagoons near the coast. Estuaries also include portions of rivers and streams connected to the. (EPA, 1993)

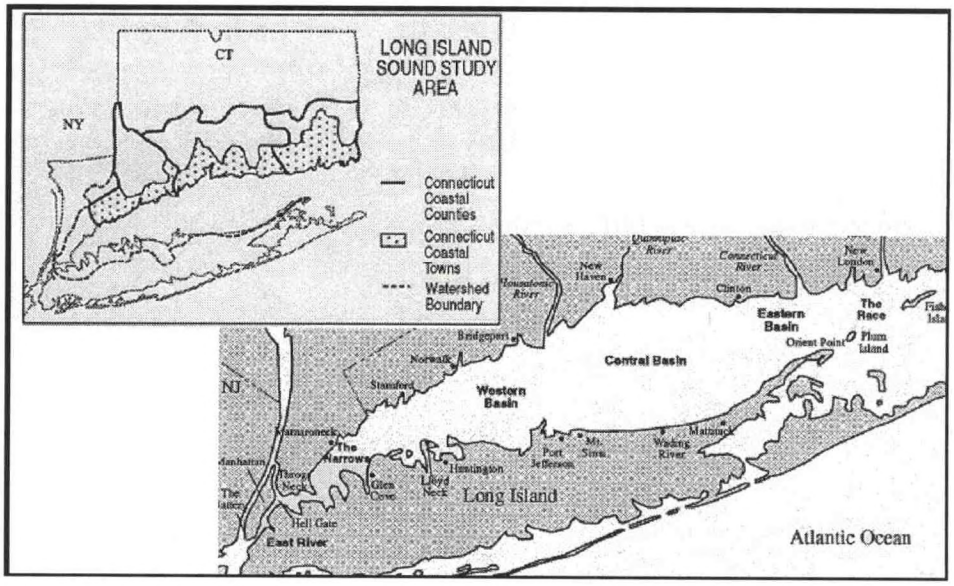

Figure 1: Long Island Sound – Study Area, Source:www.longislandsoundstudy.net/facts.htm

Harmful algae are microscopic, single-celled plants that grow very fast ("bloom"), Figure 2, and accumulate into dense, visible patches near the surface of the water. These algae occur under specific environmental conditions, such as certain levels of temperature and dissolved oxygen (DO) concentration, and from both the influence of human pollutants and as a natural phenomenon

It is on this blooming phenomenon of the algae that the name HAB (Harmful Algal Bloom) was derived. "Red Tide" or sometimes "Brown Tide" are common names given to such a phenomenon as, certain phytoplankton species containing reddish pigments "bloom", causing the water to appear to be colored red. The term "red tide" is thus a misnomer, because most of the algae associated with the tides are usually not harmful, and those species that are harmful may never reach the densities required to discolor the water.

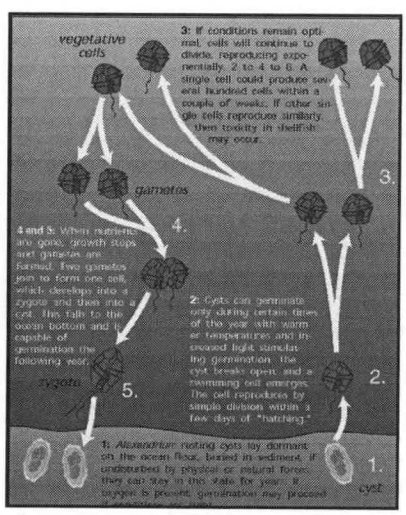

Figure 2: How HABs Occurs – The life cycle of one cell; Source: http// www.whoi.edu

A small number among all species of algae produce potent neurotoxins that can be transferred through the food web, Figure 3, where they affect and even kill the higher forms of life such as zooplankton, shellfish, fish, birds, marine mammals, and even humans that feed either directly or indirectly on them. Evidence suggests that HABs are increasing around the globe, (Boesch et al, 1997) enhancing the need for mech-

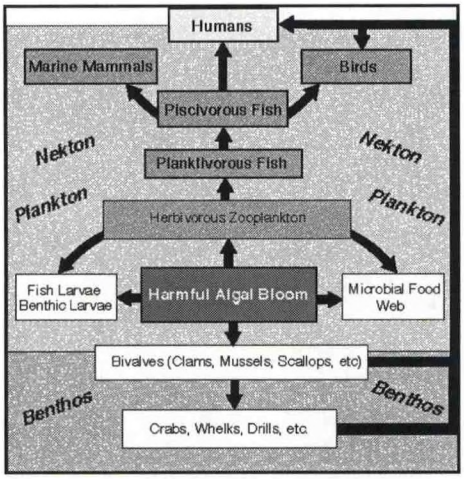

Figure 3: Trophic Linkages between HABs and Their Ecosystems; Source: http//www.whoi.edu

anism to predict their behavior.

Among the coastal issues facing the nation today, harmful algal blooms stand out as one of the most scientifically and nationally relevant problems. In the past, only a few regions of the U.S. were affected by HABs, but now virtually every coastal state has reported major blooms. (Boesch, 1997.)

Management of HABs problems have been entirely dependent on monitoring efforts carried out by the various federal, state and numerous marine agencies. Regular monitoring of plankton and seafood toxins has been carried out to safeguard public health.

Moreover, with the extent of coastline, the unpredictable nature of HABs events, and shortage of skilled manpower and facilities make regular and large scale monitoring very difficult. Thus, monitoring efforts currently carried out by these agencies have concentrated mainly in areas where HAB problems exist.

These monitoring procedures require trained personnel and extensive effort and are not very reliable in prediction of HABs occurrences.

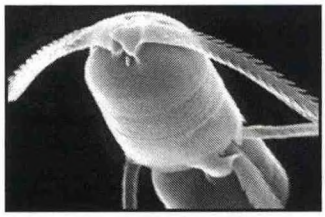

Figure 4. Chaetoceros convolutes;
Source: http//www.whoi.edu

Harmful Algal Blooms Status in LIS

In LIS, brown tides have had a severe impact on commercially valuable shellfish, affecting more than 80% of New York's bay scallop harvest. A massive bloom of Aureococcus anophagefferens was first reported in the bays of eastern LI, New York, in June of 1985. The problem is compounded by wide adoption of the HACCP (Hazard Analysis and Critical Control Point) protocols under FDA (Food and Drug Agency) which require that seafood is certified as safe and wholesome for consumption. Man is exposed principally to the naturally-occurring toxins produced by HABs through the consumption of contaminated seafood products. The most significant public health problems caused by HABs are discussed below.

Paralytic Shellfish Poisoning (PSP) syndrome is life-threatening and can result in respiratory arrest within 24 hours of consuming shellfish laced with toxins from feeding on algae in the genus Alexandrium. (National Center for Costal Ocean Science – NCCOS 2003) There is no antidote. Currently, the entire New England coastline experiences periodic PSP outbreaks with extensive shellfish bed closures and economic losses. PSP impacts more U.S. coastline than any other HAB.

Diarrhetic Shellfish Poisoning (DSP) is considered to be the second important seafood toxicity due to HABs. DSP producing species of phytoplankton such as Dinophysis acuminata and Prorocentrum lima occur throughout all temperate coastal waters of the U.S.

Amnesiac Shellfish Poisoning (ASP) causes the permanent loss of short-term memory and even death. The ASP toxin, domoic acid, is produced by the diatoms, Pseudo-nitzschia multiseries and P. australis. Besides shellfish, it is now known that domoic acid also accumulates in fish and in crab viscera.

Excessive growths of Anabaena, Aphanizomenon, and Microcystis, can lead to Harmful Cyanobacterial Blooms (HCBs) that exhibit severe neuro-, cyto- and hepatotoxicity in a variety of mammals (e.g., humans and farm animals), birds, fish and invertebrates (e.g., zooplankton). HCBs are national economic and environmental threats, occurring in large estuarine systems.

However, this effect may not only occur from the toxic algal species alone, but also from others that do not cause illnesses in humans. (NCCOS 2003) For example, blooms of the diatom, Chaetoceros convolutus, Figure 4, do not produce any toxin but have caused massive fish kills.

Harmful Algal Bloom Monitoring

Monitoring of HABs plankton and seafood toxins has been carried out, regularly to safeguard the pub-

lic health and meet the FDA requirements. However, because of the magnitude of the problem and the resources required under the current monitoring methods, most of these monitoring organizations have concentrated only in areas where HABs problems exist.

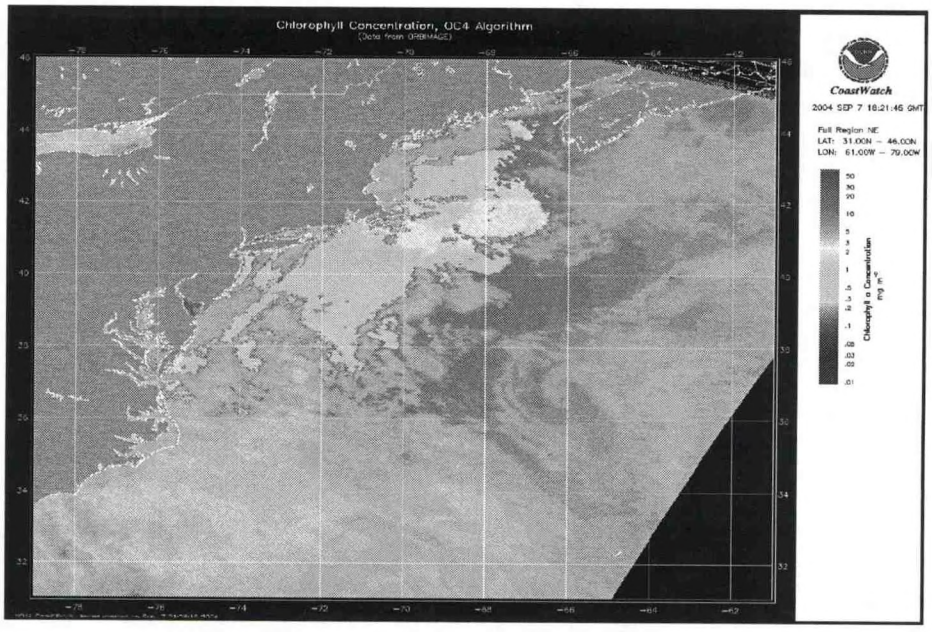

Figure 5. NOAA Satelite Image for Chlorophyll Concentration - North East Coast, US., September 7, 2004 18:21:45GMT, Source: NOAA Coast Watch

Remote Sensing

The uses of satellite imagery in establishing among other things the frequency of occurrence and magnitude of spread of the HABs is our main objective. Satellite imageries are expected to provide interesting prospects in the detection of HAB events and possibly as a monitoring tool. However, verification of satellite data with other ground data is important.

Many researchers and other experts recognize the value of remote sensing in acquisition of planktonic information; Figure 5, however, most of them are still limited in their capacity to go beyond their current uses. (Stumpf, 2001) Advancement on satellite technology has promoted the utilization of satellite imagery for various observatory purposes. This remote sensing technology has provided exciting approaches in management of HABs problems.

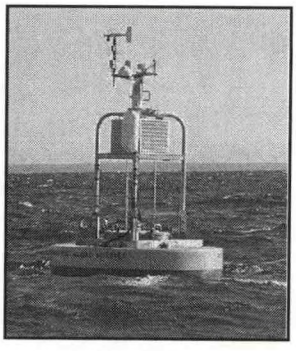

Figure 5. Buoy at Center of LIS
Source: http://www.mysound.uconn.edu/

Satellite imagery can provide records of environmental changes before, during, and after the algal bloom incidences. (Tang, 1998) They may provide means of identifying and quantifying HAB populations at time and space scales that cannot be assessed by marine vessels. (Subramaniam et al, 2000) Study carried out by Tester et al (1998) on Karenia brevis (Gymnodinium breve) showed that the detection limit for the species is 105 cell/L. This is true with the assumption K. brevis bloomed uniformly and the entire signal was derived from K.brevis. Remote sensing provided a significant advancement in early detection of K.brevis blooms and also allowed sufficient time to the related agency to react with the events. However, the detection limit might not be acceptable for other HAB species, since the 105cells/L has far exceeded the safety limit for Pyrodinium bahemense and Alexandrium sp. to cause shellfish toxicity.

In 2001, National Centers for Costal Ocean Science (NCCOS), successfully predicted 20 Karenia brevis landfall events in the Gulf of Mexico. These predictions aid resource managers, industry, and the public by giving them advance warning to prepare for and mitigate the HABs harmful impacts.

Major drawbacks of this application are that the cell number and chlorophyll pigment is not always proportional. (Lim, 2002) Pigment varies with life stage, physiological status and also species dependent. In addition, plankton patchiness, variable optical properties (dissolved organic matter (DOM), light scattering) of the water and certain background pigment level also influence the observed pigment values.

The use of satellite imagery approach is currently incapable of classifying various plankton taxonomic

groups. (Subramaniam et al, 2000) There is also lack of possible mechanism to differentiate between toxic and non toxic groups when it happened to bloom at the same site. However, with recent and planned launches of satellites with improved spectral and spatial resolution sensors, greater application of remote sensing techniques to assess and monitor HABs and water quality parameters in general will be possible.

Meanwhile, the insitu data (plankton analysis) are crucial in verifying information from satellite imagery in order to accurately predict occurrence of HABs events. Development of a model that will link the satellite information to the in situ chemical, physical and other factors seems to be the best way to move to, in order to make it possible to accurately predict HABs events using the satellite information.

In Situ Sampling

Despite of the application of innovative satellite imagery products in the successful prediction of HAB landfall, through assessment of surface chlorophyll concentrations, currently, verification of the information has to be compared with the data from ships, buoy or land sampling.

A network of buoys, Fig 5, equipped with sensors capable of measuring many parameters; such as water temperature, salinity, dissolved oxygen and the speed; currently exists in the LIS and are monitored by the University of Connecticut through the Environmental Monitoring for Public Access and Community Tracking (EMPACT) system.

Sensors to measure nutrients, Chlorophyll-A and surface hydrocarbons can also be added to these buoys to allow for the all-time measurement of these parameters. The information obtained on the Chlorophyll-A, will be useful in confirming the results obtained from the satellite imagery, and together with other available chemical, physical and environmental data collected, will be used in modeling prediction of existence and behavior of HABs.

In addition to buoy data, we also have detailed readings of different HAB population from cruises carried out over the last 6 years in LIS.

Conclusion

Remote sensing has been implemented in early detection of HAB events with some successful cases. While we feel that current remote sensing technologies have some usefulness in detecting chlorophyll-A, limitations in spectral and spatial resolution of current sensors on satellites currently restrict the specific use of satellite data for monitoring HABs.

New satellites and sensors already launched or planned to be launched, will provide the improved spectral and spatial resolutions needed to specifically differentiate HABs species in surface waters from space platforms. Focus will be put on linking hydrodynamic model with the satellite imagery information in a system that can be developed to accurately use the satellite information to predict HABs events. Such model should allow us to move away from the current slow, labor and resource intensive monitoring approach, to approaches that will allow us to use the full resolution electromagnetic spectrum to monitor HAB events.

REFERENCES

Boesch, D. F., Anderson, D. M., Horner, R. A., Shumway, S. E., Tester, P. A., and Whitledge, T. E. 1997. Harmful Algal Blooms in Coastal Waters: Options for Prevention, Control and Mitigation

Lim, P. T., Leaw, C. P. and Usup, G. 2002. Status of HAB and potential remote Sensing application in detection of HAB events in Malaysia water

Stumpf, R. P. 2001. Applications of Satellite Ocean color sensors for monitoring and predicting harmful algal blooms

Subramaniam, A., Hood, R. R., Brown, C. W., Carpenter, E. J. and Capone, D. G. 2000. Detecting Trichodesmium Blooms in SeaWiFS Imagery

Tang, D., Kester, D.R., I-Hsun Ni, Qi, Y., Kawamura, H. In situ and satellite observations of a harmful algal bloom and water condition at the Pearl River estuary in late autumn 1998

Tester, A. P., Stumpf, P. R., Steidinger, K. 1998. Ocean color imagery: what is the minimum detection level for Gymnodinium breve blooms

NON-CULTURAL AND DNA BASED METHOD (MOLECULAR ANALYSIS) FOR DETECTION OF SEDIMENT MICROORGANISMS FROM DIFFERENT SITES OF CHESAPEAKE BAY

Kalpana Dulal, Ali Ishaque, Dwayne Boucaud
University of Maryland Eastern Shore, Princess Anne, MD, 21853

Estuaries and coastal bays, because of their small area and vast biodiversity, are a suitable place to study the ecological diversity of aquatic organisms. Certain DNA targets carry detailed taxonomic information that could be used to identify individual microbes within a target community. The small ribosomal-unit RNA gene, generally referred to as 16S rDNA, is a favorite target for prokaryotic identification. Sequence analysis of 16S rDNA provides information on species composition and individual identity.

Sediment samples, collected from different sites of the coastal bays of Maryland, are being analyzed by molecular (DNA) – based methods for detection, and localization of sediment bacteria. DNA extraction was accomplished by direct lyses of microbial cells in the environmental matrix followed by nucleic acid purification (direct extraction). This was achieved by direct enzymatic lyses of bacterial cells in the sediment and extraction of DNA. Various DNA concentrations were found ranging from 1.39µg/g to 5.39 µg/g of sediment sample. 16S rDNA was amplified by PCR using 2 different sets of primers (27F and 1492R, 338F with GC clamp and 518R) for direct cloning and sequencing and for Denaturant Gradient Gel Electrophoresis (DGGE). For cloning and sequencing, the amplified 16SrDNA was cloned into PCR 4 Blunt-TOPO vector and then sequenced for identification of bacterial species in the sediment. Comparison of 16S rDNA sequences from our samples with the known sequences from the Ribosomal Database Project (RDP) reveals different types of bacteria from different sites. All 50 clones sequenced showed some percent similarity with multiple genuses of bacteria. Far relatives of Bacterial species Shewanella algae were found from most of the clones with maximum similarity of 47.6% but none of the sequences were matching with the known species from RDP.

Total Organic Carbon (TOC) concentration was measured for ecological discussion to be made among the sampling sites. Concentration of TOC in our sediment samples varied from 1.3 mg/g to 31.1 mg/g. Heavy metal concentration will be measured by digesting our sample in microwave digester first and then using ICP-MS to measure the concentration.

Bacterial diversity and abundances will be compared with TOC and heavy metals concentration from all our sampling sites. The results could be use as a bioindicator to monitor bay health condition

The Geography of Aerosol Transport; A Study of Community PM2.5 Mass Concentrations

Heidi Howerton, NOAA-EPP Intern Chicago State University

Maria Bolden, NOAA-EPP Intern Wilbur Wright College

Wilbur Wright College (Wright College) and Chicago State University (Chicago State), with funding from the National Oceanic and Atmospheric Administration Educational Partnership Program (NOAA-EPP) and in cooperation with the Southeast Environmental Task Force (SETF), are investigating concentrations of outdoor ambient particulate matter with aerodynamic diameters less than 2.5 micrometers (PM2.5) in the Lake Calumet Area (Southeast Chicago Area). The Southeast Chicago Area is home to both industries and residential communities. Chicago State, Wright College and SETF began research on appropriate sampling strategies in October 2002 and are now implementing a PM2.5 monitoring program. The PM2.5 monitoring program integrates elements of aerosol and meteorological monitoring, geographic technologies, remote sensing, and dispersion modeling.

Aerosol Transport

Aerosols, or atmospheric particulate matter (PM) is a term used to define particles suspended in air. Research on atmospheric particulate matter has increased as epidemiological studies have begun to link particulate matter with numerous respiratory ailments and premature death. (3) This study focuses on particulate matter with maximum aerodynamic diameter of 2.5 micrometers. PM2.5 is of special concern because of its ability to penetrate into various components of the human respiratory system. (3)

Particulate matter is found in the atmosphere in three different forms; solid, liquid or as a solid core surrounded by liquid. (4) Because of the variation in particle form, source and resultant intrinsic properties, researchers developed the aerodynamic diameter as a method of classifying particle size based on density. (4)

PM2.5 Monitoring

The monitoring of particulate matter mass concentrations is being performed with a Met One Instruments E-BAM 9800. The E-BAM is a portable real time continuous reporting beta attenuation monitor (BAM) and measures mass of particulate matter. (1) The E-BAM is equipped with a PM10 inlet head followed in series by a PM2.5 Sharp Cut Cyclone. (1) Mass measurements of the resulting PM2.5 entrained in the sample air stream are calculated based on the level of beta attenuation across a pre-calibrated section of glass-fiber filter paper. (1) The E-BAM 9800 calculates and stores sample mass, filter and ambient temperature, and internal relative humidity.(1) Additional meteorological monitoring is performed with a Met One Instruments Wind Sensor. This meteorological monitoring unit measures wind speed and wind direction with a three cup anemometer and a balanced anodized aluminum vane. (2) The anemometer and vane are directly attached to the E-BAM 9800 and measurements are recorded simultaneously with PM2.5 mass measurements.

As the E-BAM is a relatively new monitoring technology, work is being done to establish a correlation or side-by-side study with state regulated beta attenuation and filter-based monitors. Data collected from side-by-side studies will be used to create correlation factors between instruments and subsequently allow for comparison of data sets from multiple PM2.5 monitoring devices.

Geographic Analyses

Ambient particulate mass concentration data have quantitative and spatial components. The quanti-

tative component of mass concentrations is being assessed using the E-BAM 9800, as previously described. The spatial components of the PM2.5 monitoring program are being analyzed using multiple geographic technologies. Point monitoring locations are being determined based on analyses of regional atmospheric conditions (e.g. wind speed and wind direction) in relation to geographic conditions, such as location of industrial particulate emissions and community residences. Global Positioning System (GPS) units are used for recording the latitude and longitude of point monitoring locations. GPS data are easily integrated with corresponding mass concentration data in a Geographic Information Systems (GIS) program, ArcMap‰. By combining quantitative particulate data with corresponding spatial components, qualitative particulate matter transport scenarios at the community level are derived.

Regional Remote Sensing Studies

Wright College and Chicago State are researching availability of regional scale PM2.5 remote sensing data, and will use these regional data to compare with the local PM2.5 point monitoring program data. Regional remote sensing data will provide a measure of aerosol concentrations over increased spatial boundaries, including profiles of vertical distribution under measured meteorological conditions. It is estimated that these regional data will provide added insight to PM2.5 background conditions and local transport patterns.

Stationary Source Dispersion Modeling

Additional comparisons of PM2.5 point monitoring data will be made with results from PM2.5 dispersion modeling studies. Dispersion modeling will focus on estimating particulate transport from Southeast Chicago Area industries. A Gaussian plume dispersion modeling program will be used to simulate atmospheric particulate concentrations from these stationary sources. Data collected from point monitoring stations, in conjunction with estimates from the plume dispersion simulations, will be used to refine the point monitoring network and estimate local PM2.5 transport patterns.

Applications of Community Aerosol Study

The goal of this project is to develop an estimated pattern of PM2.5 transport in the Southeast Chicago Area under multiple meteorological conditions. Southeast Environmental Task Force facilitates 'Good Neighbor Dialogues,' a cooperative forum for residents and local industry to discuss mutual concerns. Questions regarding sources and transport characteristics of particulate emissions are currently being discussed from both the industry and residential perspectives. With a better understanding of particulate matter transport characteristics at the local level, industries hope to refine emission practices during critical atmospheric conditions. More specifically, industries will design engineering controls to limit both primary sources of particulate matter and precursors to secondary sources of particulate matter during predetermined sensitive meteorological conditions.

REFERENCES

1. Met One Instruments, Inc., 2003: E-BAM-9800 Operation Manual. Rev., D.

2. Met One Instruments, Inc., Wind Sensor Model 034B Operation Manual. Rev., A

3. U. S. Environmental Protection Agency, 1997: Health and Environmental Effects of Particulate Matter. Technology Transfer Network OAR Policy and Guidance, Fact Sheet.

4. Wilson, Dr. William E., Judith C. Chow, Candis Claiborn, Wei Fusheng, Johann Engelbrecht, and John G. Watson, 2002: Monitoring of Particulate Matter Outdoors. Chemosphere, 49(9): 1009-1043.

STORM WATER MASS BALANCE STUDY OF GREEN ROOFS FOR CSO ABATEMENT

Gary Chan (Undergraduate Student) and Megan Wiley (Assistant Professor)

Department of Civil Engineering, The City College of New York

Green Roofs are emerging as a very effective means of addressing many of the environmental concerns that exist in today's urban centers. In studies, they have shown great promise in reducing the urban heat island effect, improving air and water quality, and increasing the amount of plant life in an urban area. The objectives of this study are to demonstrate how green roofs can play a dramatic role in confronting the problems of storm water runoff. In cities such as New York, where the sewage and storm water systems are combined, Combined Sewage Overflows (CSOs) are a real threat to the surrounding marine and coastal environment any time there is a large rain event.

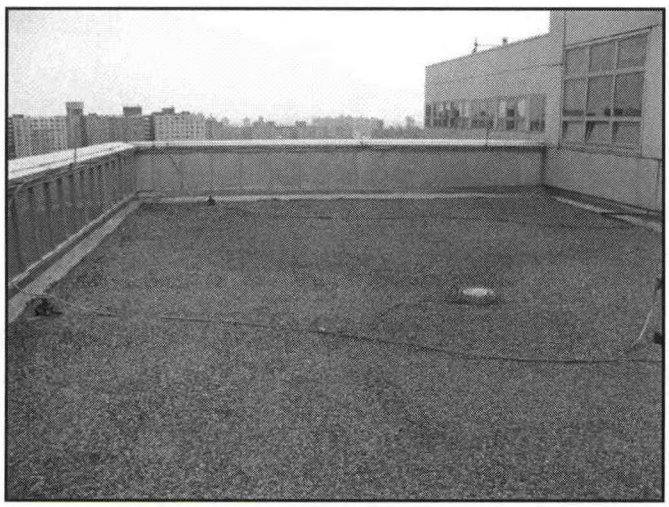

Figure 1 Project location: Roof Section on Steinman Hall, CCNY

In this study, we are constructing an extensive green roof section on Steinman Hall, City College's engineering building (Figure 1). We will test the ability of different green roof designs to hold water during rain events using a mass balance approach. Specifically, we will measure rainfall, soil moisture and drainage from the sections over a calendar year. We will also collect temperature data to quantify the insulating capabilities of the different designs. The last aspect of the research will be a cost/benefit analysis for green roofs versus more traditional CSO abatement measures. The results of this study may yield further evidence that in cities, green roofs can be one of the most prudent solutions to CSOs environmentally and economically.

The decision to use an extensive green roof system as opposed to an intensive green roof is based upon the existing surface available on Steinman Hall. Although intensive green roof systems allow for larger plants that can retain more water, they are by far more expensive and in many cases, they need to be designed into the roof of a building because they are considerable heavier and require additional roof support. Extensive green roofs, like the section we are building, are far more cost effective at least initially and no additional structural support is required in the installation of the green roof. Figure 2 shows the layers in a typical extensive green roof.

In the green roof systems that we are building, we will use several varieties of hearty sedums. These plants are succulents, able to retain a relatively large amount of water considering their small sizes. Because of the ability to retain so much water, succulent plants in green roof systems lowers the amount of maintenance necessary compared with other types of plants. In many cases, sedums are even frost resistant in the winter months. More than one species was chosen to insure that even if a specific species is not able to adapt to the roof environment, there will still be several others that will still be there. Also, several species allows for a more aesthetic looking roof that does not generally increase the cost of the roof system. Each species of sedums used in this study have very fibrous root systems that do not reach deep

into the soil layer. The soil layer in our green roof system will only be from four to six inches. Having plants with short but fibrous roots allows for more water to be retained and the soil to be held in place.

To determine the amount of water held within the roof, we will compare rainfall measurements to the amount of water drained from the green roof section. We will further partition the held water between the soil and plants using soil moisture probes. Two different green roof designs will be assessed in this manner.

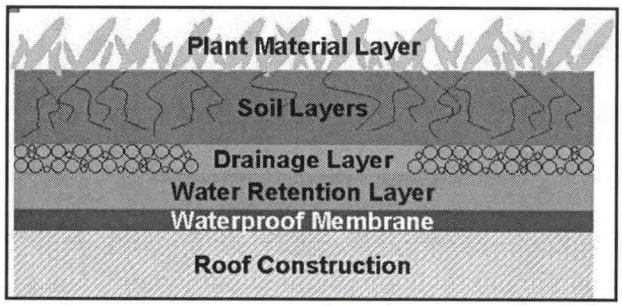

Figure 2 Section of Green Roof Layers (from www.greenroof-plants.com)

Finally, in the cost benefit analysis section of our research, we will evaluate the projected costs that the city and state use and are planning to use in CSO abatement and the added amount of storm water that could be processed following these projects. We will compare these figures to cost of installing green roofs throughout the city, comparing them also with the amount of storm water retention that can be attained from all of these green roofs combined based on the study of our individual green roof system. These findings will demonstrate whether green roofs provide a definite solution or partial solution to CSO abatement in the City.

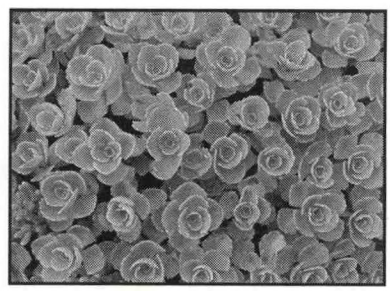

Figure 3 Example of a Sedum Variety (from http://www.virginia.edu/blandy/sedum.jpg)

Predicting West Nile Virus Risk in New York State by Characterizing Optimal Breeding Habitats of Four Mosquito Vectors

Juliana Maantay, Andrew Maroko and Holly Porter Morgan
Lehman College, City University of New York
NOAA-NESDIS Collaborator
Dr. Bruce Ramsay

New York City first witnessed an outbreak of West Nile virus (WNV) during the summer and fall of 1999. The outbreak was particularly significant because it represented the first indication of WNV in the Western Hemisphere, resulting in 62 human cases, 7 of which were fatal [Petersen and Roehrig, 2001]. In 2003, viral activity had been reported in 45 states with a total of 9,389 human cases, 246 of which resulted in death [CDC, 2004].

West Nile virus is a vector-borne disease that can infect humans, birds, horses, and other animals. The general symptoms of West Nile Fever, resulting from infection with West Nile virus, can include fever, rash, and headache, but more importantly meningitis, encephalitis, coma, and death. Approximately one in ten people diagnosed with West Nile fever has died, although this statistic may be a bit misleading since it is likely that the majority of cases of WNV are not reported or clinically apparent due to mild symptoms [Petersen and Marfin, 2003]. The virus is generally found to operate in a bird-mosquito-bird cycle. Human cases have been reported throughout Europe, Asia, Africa, and can now be found in North America as well - possibly as a result of being transported in a person returning from an infected region or by an imported bird or mosquito.

Recent studies have shown the dangers of WNV and the usefulness of mapping mosquito habitat using environmental data [Beck, 2000; Hay, 1998; Hightower, 1998; Kleinschmidt, 2000; Nasci, 2000]. This study seeks to create predictive maps of WNV risk by showing areas of optimal suitability for oviposition and larval growth of known mosquito vectors in New York, thereby assessing regions likely to have a high density of adult mosquitoes and heightened human risk of contraction of the virus. A novel aspect of this study will be the use of near real-time (NRT) and/or frequently updated data for many of the variables. This will allow for dynamic maps able to predict areas with a high probability of presence of vector eggs and larvae.

Using Geographic Information Systems (GIS), optimal oviposition and larval habitat of the primary species of mosquito vectors in New York, *Aedes vexans, Culex restuans, Culex pipiens* and *Culex salinarius* [Bernard, 2001] will be determined by analyzing, modeling, and mapping the relevant variables – vegetation (vegetative index), land use/land cover, temperature, rainfall, humidity, flood plains, soil type, elevation, and water bodies. The majority of remotely sensed data will be obtained from the National Oceanographic and Atmospheric Administration's (NOAA) satellite resources including, but not limited to, a vegetative index - either Normalized Difference Vegetative Index (NDVI) or Enhanced Vegetative Index (EVI) - from the "Moderate Resolution Imaging Spectroradiometer" (MODIS), and "National Land Cover Data" (NLCD - USGS, Multi-resolution Land Characterization Consortium - USEPA, US Forest Service, NOAA). Other data and sources will include Q3 Digital Flood Data from the Federal Emergency Management Agency (FEMA), soil data from the United States Department of Agriculture's State Soil Geographic Database (STATSGO), WNV case data from the Center for Disease Control and Prevention and the New York Department of Health, climate data from National Climatic Data Center (NOAA-NESDIS), digital elevation models (DEMs) from the United States Geological Survey, and census and demo-

graphic data form the United States Census Bureau.

Using the overlay and geo-processing operations of GIS, each layer will be studied individually to determine optimal data ranges, then modeled to form master suitability maps for both oviposition and larval habitat. Since some of the data will be NRT, the map results will be not only predictive, but also dynamic. Although this study will neither include modeling for adult habitats or ranges nor dispersal of newly matured mosquitoes, by identifying current optimal breeding habitats one can simply add the time it takes a mosquito to grow from egg to adult in order to create a generalized prediction of where there is likely to be an abundance of mature, flying insects. These results will also be normalized by both general and elderly human population densities, since it is the elderly and immuno-compromised that may be at highest risk of infection [Weiss, 2001].

For the first phases of this study historical data will be used. A 16-day period, ranging from April 23, 2001 to May 8, 2001, will be the temporal resolution in order to match the NDVI and EVI from MODIS. This will also enable us to compare the results to actual occurrences of WNV (human, equine, and avian cases) which will act as a validation of the model by comparing optimal vector habitat with documented human and animal outbreaks.

Ultimately, if the first phases of this study prove to be a success, the established methodologies could be used to predict WNV vector breeding habitat and WNV risk in a multitude of geographies using NRT data. The study has been specifically designed for large areas, resulting in no ground truthing or fieldwork. This would make it easy and fast to translate into other study areas. Additionally, if the results show high risk areas, fieldwork and ground truthing could be localized to the identified regions.

REFERENCES

Beck, L.R., Bradley M., Lobitz, and B. Wood, 2000: Remote Sensing and Human Health. *Emerging Infectious Diseases* 6(3): 217-226.

Bernard K.A., Maffei J.G., Jones S.A., Kauffman E.B., Ebel G., Dupuis A.P., and the New York State West Nile Virus Surveillance Team, 2001: West Nile virus infection in birds and mosquitoes, New York State, 2000. *Emerging Infectious Diseases*, 7:679-685.

Center for Disease Control and Prevention (CDC) - Division of Vector-Borne Infectious Disease, 2004: *West Nile Virus Website*. http://www.cdc.gov/ncidod/dvbid/westnile/ (3/1/04)

Hay S.I., Snow R.W., and D.J. Rogers, 1998: From predicting mosquito habitat to malaria seasons using remotely sensed data: Practice, problems, and perspectives. *Parasitology Today* 14(8): 306-313.

Hightower A.W., Ombok M., Otieno R., Odhiambo R., Oloo A.J., Lal A., Nahlen B.L. and W.A. Hawley, 1998: A geographic information system applied to a malaria field study in western Kenya. *Am. J. Trop. Med. Hyg*. 58(3): 266-272.

Kleinschmidt I., Bagayoko M., Clark G.P.Y., Craig M. and D.L. Sueur, 2000: A spatial statistical approach to malaria mapping. *International Journal of Epidemiological* 29: 355-361.

Nasci R.S., Moore C.G., Biggerstaff B.J., Panella N.A., Liu H.Q., Karabatsos N., Davis B.S., and E.S. Brannon, 2000: La Crosse encephalitis virus habitat associations in Nicholas County, West Virginia. *Journal of Medical Entomology*, 37(4):559-70.

Petersen L.R., Marfin A.A., and D.J. Gubler, 2003: West Nile Virus, *JAMA* 290(4): 511-515

Petersen L.R., and J.T. Roehrig, 2001: West Nile virus: a reemerging global pathogen. *Emerging Infectious Diseases*. 7(4): 611-614.

Weiss D., Carr D., Kellachan J., Tan C., Phillips M., Bresnitz E., and M. Layton for the West Nile Virus Outbreak Response Working Group, 2001: Clinical Findings of West Nile Virus Infection in Hospitalized Patients, New York and New Jersey, 2000. *Emerging Infectious Diseases*, 7(4): 654-658.

Maps:

Normalized Difference Vegetative Index

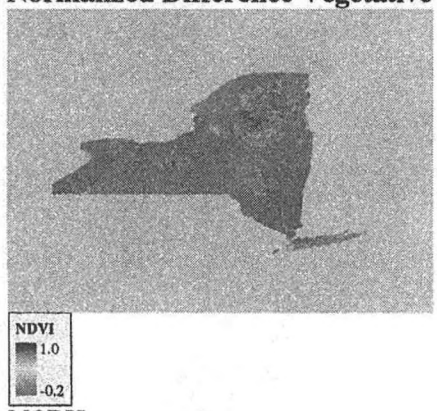

MODIS

Digital Elevation Model

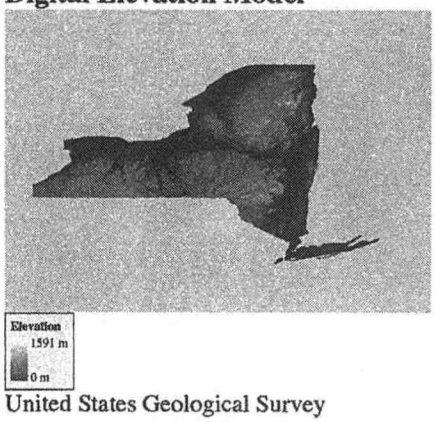

United States Geological Survey

National Land Cover Data (NLCD)

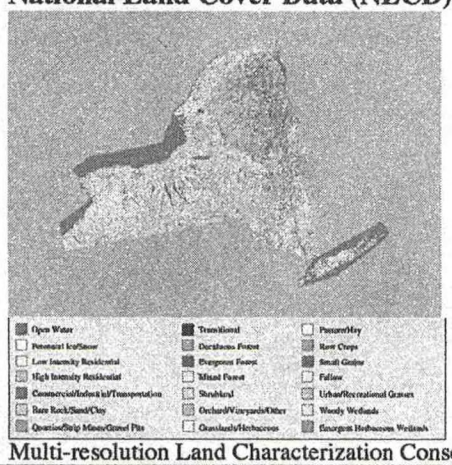

Multi-resolution Land Characterization Consortium

NLCD - Water and Wetlands

Multi-resolution Land Characterization Consortium

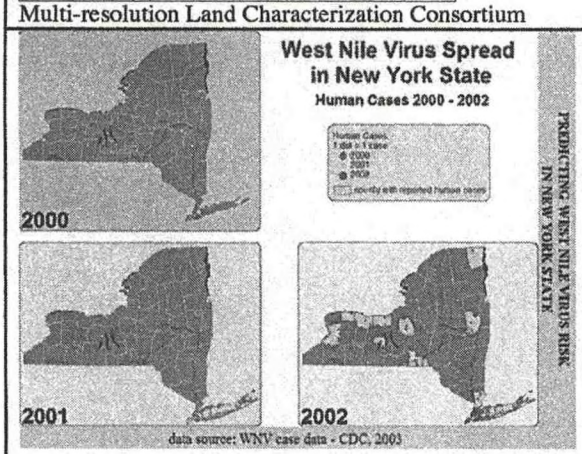

Precipitation, 16-Day Average

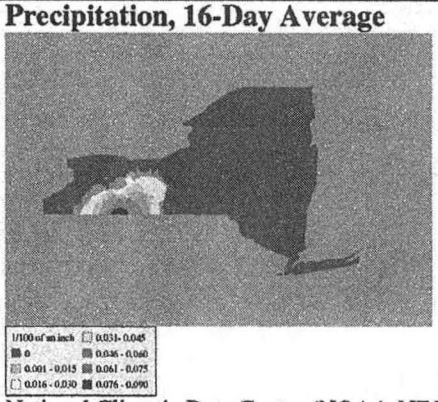

National Climatic Data Center (NOAA-NESDIS)
(interpolations [kriging] done at Lehman GIS lab, 2004)

Maximum Temperature, 16-Day average

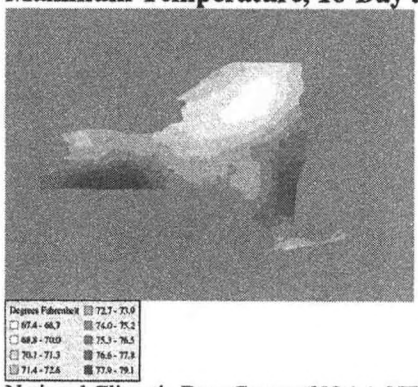

National Climatic Data Center (NOAA-NESDIS)
(interpolations [kriging] done at Lehman GIS lab, 2004)

Minimum Temperature, 16-Day Average

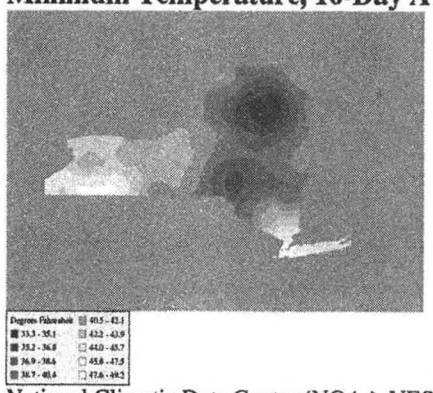

National Climatic Data Center (NOAA-NESDIS)
(interpolations [kriging] done at Lehman GIS lab, 2004)

Q3 Digital Flood Data

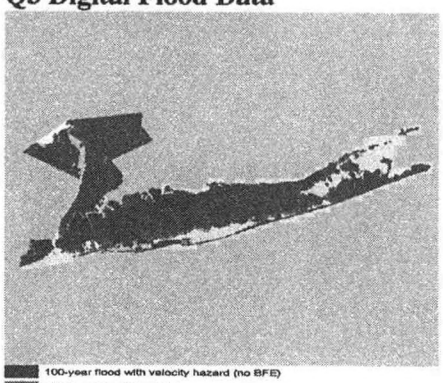

The Federal Emergency Management Agency (FEMA)

Drainage in New York State

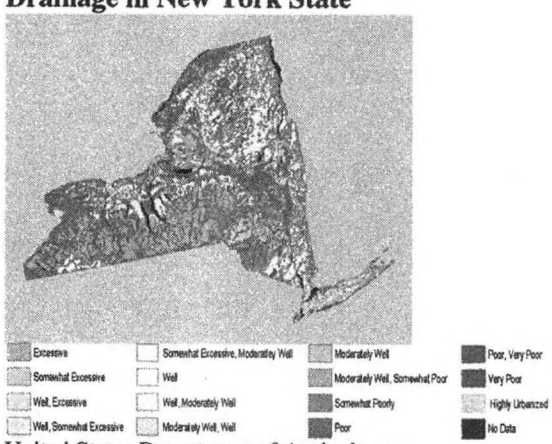

United States Department of Agriculture
State Soil Geographic Database (STATSGO)


POSTER SESSION
Satellite Remote Sensing

USING HYPERSPECTRAL REMOTE SENSING TO DETECT THE EXPANSION OF *PHRAGMITES AUSTRALIS* IN THE ST. JONES RIVER WATERSHED, DELAWARE

Dr. Chunlei Fan and Dr. Michael A. Reiter

Department of Agriculture and Natural Resources, Delaware State University, Dover, DE 19901-2277

The expansion of the invasive *Phragmites australis* in the tidal wetlands of Delaware's estuaries has resulted in a significant loss of more desirable marsh communities. In this project, hyperspectral remote sensing and geographic information systems (GIS) will be used to detect and map the expansion of invasive *Phragmites australis* in the marsh areas located at the Delaware National Estuary Research Reserve (DNERR) site in the St. Jones River watershed. This project will partner with the Environmental Cooperative Science Center (ECSC) and DNERR personnel to collect data, conduct research and analysis, and perform outreach to help students and the general public gain knowledge of GIS/remote sensing. Results from this research will provide new, improved data collection allowing for comparison to 1992 distribution data for *Phragmites australis* in the St. Jones River Watershed. The project will both update past data in order to determine changes in distribution and provide scientific information for future Phragmites control programs at the local and state level.

DEVELOPMENT OF AN AUTOMATED GROUND- BASED VERTICAL HUMIDITY GRADIENT ACQUISITION SYSTEM

Javier Chaparro[1] , Richard Díaz[2] and Eric W. Harmsen[3]

Dept. of Agricultural and Biosystems Engineering, University of Puerto Rico

eric_harmsen@cca.uprm.edu

Evapotranspiration from vegetated land can be estimated using remote sensing techniques. These techniques, however, are still being developed and require validation. In this study, an automated ground-based vertical humidity gradient acquisition system was developed. The measured humidity at two heights above the ground can be used in a vapor gradient flux-type equation for estimating evapotranspiration. The automated device consists of a single temperature/relative humidity (RH) sensor which is moved between the two heights (0.2 m and 2 m) above the ground. The control of the 12 volt DC motor, which raises and lowers the sensor, is performed using a standard programmable logic controller (PLC). RH and temperature measurements are obtained every 10 seconds. The elevator device maintains the RH sensor at the 2 m height for 120 seconds while twelve readings are taken, after which the sensor is lowered (travel time is approximately 10 seconds) to the 0.2 m position where it is maintained for 120 seconds while more twelve readings are taken. The sequence of lowering and raising the sensor continues repeatedly over the period of several hours to several days. As a part of the data collection process, the RH data for the two positions is stored separately in the data logger. The data are subsequently converted into absolute vapor densities for use in the flux equation. Time series of RH and temperature data collected with the automated system are presented.

[1]Graduate Student in the Dept. of Electrical and Computer Engineering, Univ. of Puerto Rico – Mayaguez Campus.

[2]Graduate Student in the Dept. of Civil Engineering, Univ. of Puerto Rico – Mayaguez Campus.

[3]Associate Professor of the Dept. of Agricultural and Biosystems Engineering, Univ. of Puerto Rico – Mayaguez Campus.

USE OF REMOTE SENSING TO TRACK AND PREDICT VECTOR-BORNE DISEASES

Rodolfo Fortich and Leonid Roytman

City University of New York, Convent Avenue at 138th Street, New York, NY 10031, USA

Abstract

Current studies demonstrate that extreme weather conditions in tropical areas have a direct effect in the expansion of malaria, and dengue diseases. The analysis of drought, heavy rain, and infectious syndromes are the primary topics of this research, which may allow us to determine a more precede correlation between weather conditions, infectious deceases, and index of vegetations. In this study, correlation and regression methods are being utilized to analyze factors that contribute to diseases transmission. Since weather events contribute to vegetation conditions and epidemics, remotely sensed data derived from radiances measured by the Advanced Very High Resolution Radiometer (AVHRR) flown on NOAA afternoon polar orbiting satellites, such as, Vegetation Condition Index (VCI), Temperature Condition Index (TCI), and Vegetation and Temperature Condition Index (VTI) has being used as proxies to identify areas in Colombia with high level of outbreaks. In addition, the study of the unusual warming of the sea surface temperatures in the eastern and central tropical Pacific, known as El Niño Southern Oscillation (ENSO), indicates that this phenomenon intensifies the annual cycle of malaria cases for Plasmodium vivax and Plasmodium falciparum in different environmental setting of Colombia, as a consequence of the increase in mean temperature, and decreases the precipitation cycles.

Introduction

Remote sensing techniques have greatly contributed to improve our capacity to observe our environment and its processes. The use of satellite data for epidemiological purposes has been largely promoted for more than 15 years to determine diseases distributions and their variations through time. In some circumstances, when diseases are strongly related to environmental data, such as climate, vegetation, or land-use, remote-sensing techniques can be used to determine and monitor factors involved in the propagation of diseases, which may differ according to the different ecotypes and ecosystems. This paper illustrates how the applications of Vegetation Condition Index (VCI), Temperature Condition Index (TCI), and Vegetation and Temperature Condition Index (VTI) could be used as proxies to identify areas under malaria risk and/or outbreak, and these index data are derived form AVHRR. In addition, it discusses the characteristic of El Niño Southern Oscillation (ENSO) phenomenon and its influence on the Colombia's climatology and malaria outbreak. El Niño refers to the unusual warming of SSTs in the eastern and central tropical Pacific and can occur every 2 to 10 years, with an average of occurrence of 4 years. El Niño events comprise two calendar years and have three anomalies variations of SST that are studied with respect to the Northern hemisphere calendar time. First, SSTs positive anomalies increase during the spring and fall seasons of the first year of El Niño cycle. Second, the maximum SSTs anomalies occur during the winter of the following year. And thirdly, SSTs anomalies recede during the spring and summer of the year after. Furthermore, El Niño Southern Oscillation disrupts the normal patterns of the global atmosphere-oceanic circulation, and the land surface hydrology affecting weather events and climate (Trenberth et al). The associated extreme weather events, including floods, droughts, and heat waves, produce severe socioeconomic and environmental impacts (including crop and fishery failures and food shortages), disrupt infrastructure, cause forest fires, reduce hydropower generation (electricity shortages), harm algal blooms, and spread out diseases. Previous malaria research conducted by Bouma, van der Kaay, Dye, Poveda and Rojas in Pakistan, Venezuela, and Colombia had demonstrated the direct correlation of malaria disease and ENSO phenomena. Addition studies had also demonstrated that malaria disease

involving mosquitoes and rodents may cluster after extreme events (especially flooding) in association with the ENSO phenomenon (Epstein et al. 1995). ENSO is the main forcing mechanism of Colombia's hydro-climatology at inter-annual timescales. During these times, Colombia experiences droughts; has a diminishing rainfall, soil moisture, river discharges and evaporation; and has an increment of air temperature. The impact of ENSO occurs earlier and stronger in western and central Colombia than in the east side. Previous records of El Niño events (inter-annual time scale) demonstrated that there is an increase in the incidence of malaria in Colombia, as reported by Poveda and Rojas (1995), and Poveda et al. (2000). Two-thirds of Colombia's population lives in area where the malaria can be propagated as a consequence of climatic and topographic features (Rojas et al. 1992). There are three types of mosquitoes (vectors) in Colombia that can propagate the malaria: Anopheles albimanus, A. darlingi, and A. nuñeztovari (Quinones 1987). All of them are capable to transmit Plasmodium falciparum (46.5%) and Plasmodium vivax (53.5%) (Molineaux 1988), and in rare cases the Plasmodium malariae (Haworth 1988). The geographical distribution of malaria disease in Colombia is associated with climatic conditions. As malaria is propagated by mosquitoes and mosquitoes are sensitive to change in weather, it is important to determine the common factors that allow malaria disease to spread out in specific locations. In order to obtain these factors, it is necessary to analyze and correlate vegetation health indices with malaria reported cases. Therefore, the goal of this research study is to explore the AVHRR-based indices as a tool for diagnosis of mosquito-borne epidemics.

Data and Methodology

The selected area for this study was the department of Cordoba located in the northwestern of Colombia, see Figure 1. This location was selected due to its high level of malaria reported cases and its record (1985-2003) was provided by the Colombia Ministry of Health. VCI, TCI, and VTI were collected from the Global Vegetation Index (GVI) data set (1985 through 2003) which was provided by NOAA/NESDIS. The GVI has spatial resolution of 4 km (sampled to 16 km) and daily temporal resolution sampled to 7-day composite (Kidwell 1997).

The VCI, TCI and VTI are indices that change from 0 to 100, which represent the reflecting changes in vegetation conditions from extremely unfavorable (vegetation stress) to optimal favorable conditions, and these indices estimate moisture (VCI), thermal (TCI) and combination of both conditions (VTI). The indices values around 50 estimates near normal conditions. If these indices approach to 0 then condition deteriorate indicating vegetation stress. On the other hand, when the indices values approach to 100, the conditions are estimated as favorable.

The indices values of Normalized Difference Vegetation Index (NDVI) and Brightness Temperature (BT) are used to determine the unit-less values of VCI and TCI respectively. The VCI approach to 0 (vegetation stress) when vegetation becomes less green (NDVI decreases). In opposite side, VCI approaches to 100 (favorable condition) when vegetation becomes greener (NDVI increase). The TCI decreases approaching to 0, when weather becomes hotter (BT increases); In contrast, TCI increases approaching to 100, when weather becomes cooler (BT decreases).

To calculate the deviation of malaria for Plasmodium falciparum and Plasmodium vivax, their trends were approximated by utilizing a linear regression model, see Figure 2. The deviation of each annual malaria reported cases from each trend were correlated with the weekly VCI and TCI indices to investigate the most sensitive periods

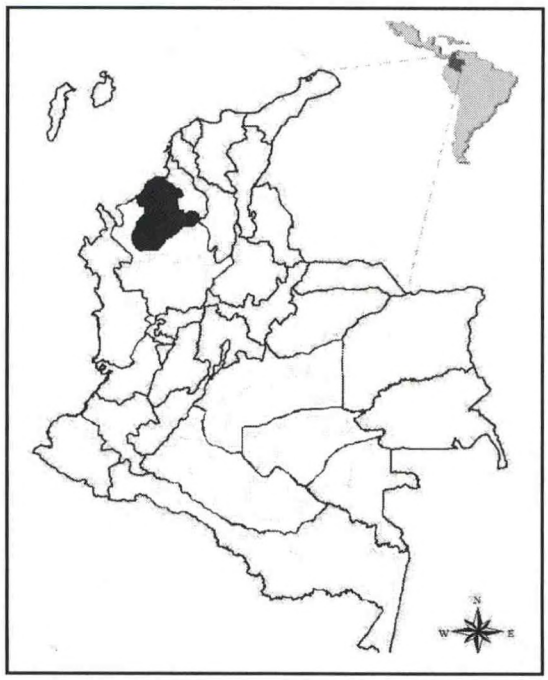

Figure 1: Colombia divisions, including Cordoba

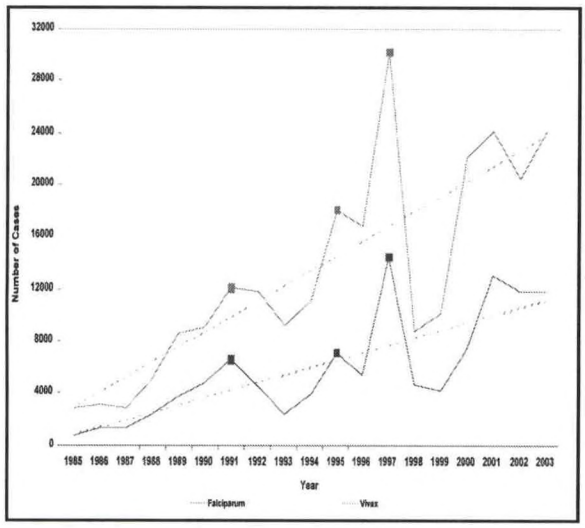

Figure 2: Annual malaria cases for Plasmodium vivax and Plasmodium falciparum with their trends lines in Cordoba division.

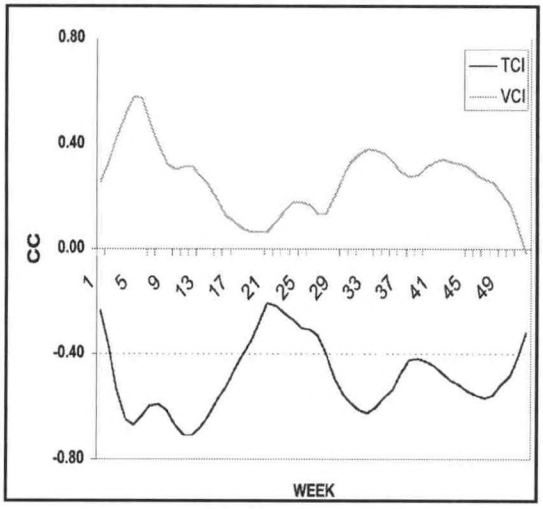

Figure 3: Correlation coefficient dynamics between malaria for plasmodium falciparum deviation versus TCI and VCI.

Results and Discussion

The development of malaria cases in Cordoba for plasmodium vivax and plasmodium palciparum had three important deviation results that occur during El Niño cycles: 1991, 1995, and 1997.

According to NOAA records (NOAA 1997a, 1997b, 1997c, 1998, and 1999), El Niño phenomena of 1997-1998 had a devastated effect in the global weather and ecosystem conditions. Analyzing the annual malaria records, it had found that the highest deviation from the vivax and palciparum trends occur during El Niño cycle 1997-1998. The deviation result for vivax is 1.9 and for palciparum is 1.8.

The differences, in VCI and TCI dynamics were investigated during these years with the extreme differences in malaria deviation (below and above trend), for both correlation figures, 3 and 5, the TCI has a negative correlation with respect to the deviation from trend of malaria for plasmodium falciparum, and malaria for plasmodium vivax deviation, and the VCI has a positive correlation with respect to the both deviation. It had been noticed that the strongest positive correlation for both malaria types deviation exist between the 5th week, with a correlation value of 0.58, and 0.60, for falciparum malaria, and vivax malaria respectively (see figure 4), weaker correlation occurs during the weeks 19th to 21, 51, and 52, with values of 0.06, 0.08, and -0.02, for falciparum malaria, and 0, -0.01, 0.01, and -0.04 for vivax malaria, all them relative to VCI.

The strongest negative correlation occurs during the weeks 12, 13, 31, 32, and 33, for vivax malaria, with values between -0.58 to -0.62 and during the weeks 11, 12, 32, 33, and 34, for falciparum malaria, with values between -0.61 to -0.71 respectively (Fig 6)

and the weakest negative correlation occurs during the week 21 for falciparum malaria, and during the weeks 21 to 23 for vivax malaria, with values between -0.21, and -0.09, respectively, all them respect to TCI. The weekly TCI values for the highest correlation weeks mentioned above, oscillates between 12, and 32, for the years with high malaria deviation (1991, 1995, and 1997), indicating thermal stress during these periods, this preliminary analysis indicated that in the environment of the Cordoba division, thermal conditions are slightly stronger factor for predicting malaria epidemics.

Conclusions

Although malaria is a highly complex multifactorial disease, exist a strong detailed correlation between AVHRR-based indices, malaria for plasmodium vivax, and malaria for plasmodium falciparum in the Colombia's administrative division of Cordoba, especially during the last three Niño years (1991, 1995, and 1997), consistently the augmenting malaria cases, during the occurrence of this phenomena; this suggests that coupling mechanisms between AVHRR-based indices, and malaria should be done in many areas throughout Colombia in order to complement this study, this analysis will be done for each individual department, and by group of them, the use of VTI data is part of the future work, due that it requires a more detailed statistical analysis, sea surface temperature data of the pacific ocean areas that covers El

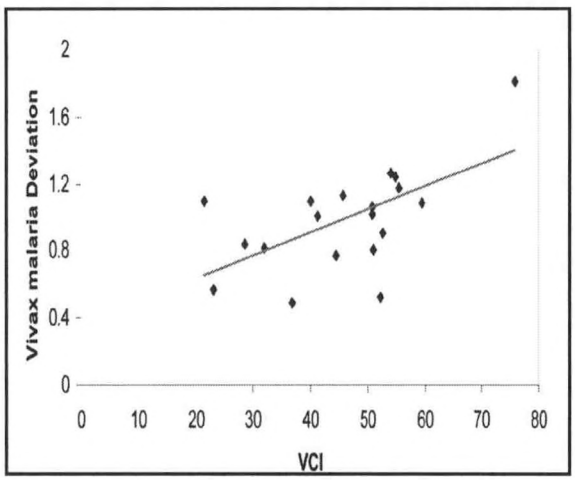

Figure 4: Malaria for plasmodium vivax deviation versus VCI for week number 5.

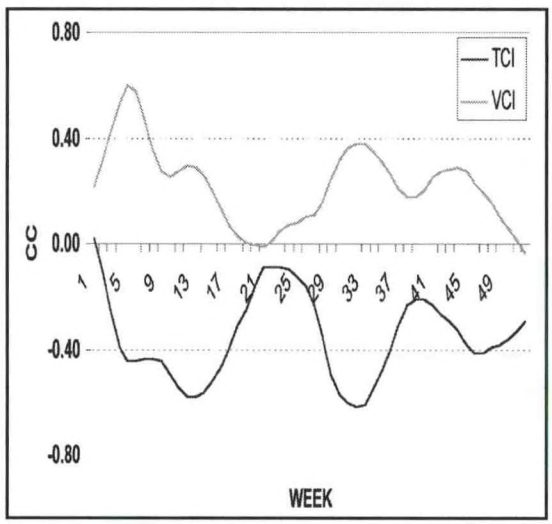

Figure 5: Correlation coefficient dynamics between malaria for plasmodium vivax deviation versus TCI and VCI.

Niño phenomena is under analysis with the object to find more links between this phenomena and malaria in Colombia, environmental factor, such as, humidity, and soil moisture, and non-environmental factors, such as, urbanization, deforestation, irrigation, and agricultural practices will be considered, in order to find additional correlation factors.

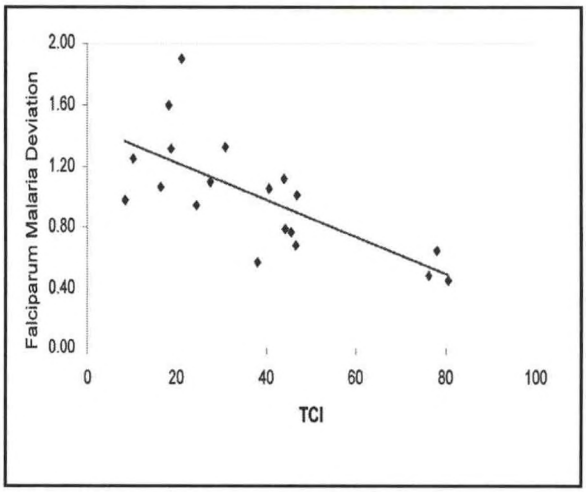

Figure 6: Malaria for plasmodium falciparum deviation versus TCI for week number 12.

REFERENCES

Bouma MJ, Sondorp HE, and van der Kaay HJ. 1994a. Climate change and periodicepidemic malaria. [letter, comment]. The Lancet, 343: 1440

Bouma MJ, Dye C, van der Kaay HJ. 1995. "El Niño Southern Oscillation" as a possible early warning system for falciparum malaria epidemics in Northern Pakistan. In: Epidemiology and Control of Malaria in Northern Pakistan. Dordrecht. pp. 45-57.

Bouma MJ, and van der Kaay HJ. 1996. The El Niño Oscillation and the historic malaria epidemics on the Indian subcontinent and Sri Lanka: an early warning system for future epidemics? Tropical Medicine and International Health, 1:86 – 96 (1996)

Epstein, P.R., 1995: Emerging diseases and ecosystem instability: New threats to public health. American Journal of Public Health, 85, 168–172.

Haworth, J., 1988: The global distribution of malaria and the present control effort. In: Malaria, Wersdorfer, W.H., and McGregor, I. (eds.), Churchill Livingstone, Edinburgh.

Kidwell, K.B., 1997, Global Vegetation Index Users Guide NOAA. Technical Report, NOAA, US Department of Commerce, Suitland, Maryland, 65.

Molineaux L. The epidemiology of human malaria as an explanation of its distribution, including some implications for its control. In: Malaria: Principles and Practice of Malariology Vol 2 (Wersdorfer WH, McGregor I, eds). London: Churchill Livingstone, 1988; 913–998.

NOAA (National Oceanic and Atmospheric Administration) (1997a), El Niño Implications for the 1997 Southwest Drought and Fall / winter Precipitation. Special Climate Summary 97 / 2, July.

NOAA (National Oceanic and Atmospheric Administration) (1997b), Climate diagnostic Bulletin 97 / 9, September.

NOAA (National Oceanic and Atmospheric Administration) (1997c), Climate Conditions Associated with the 1997-1998 El Niño: Impact and Outlook. Special Climate Summary 97 / 3 November.

NOAA (National Oceanic and Atmospheric Administration) (1998), Climate Diagnostic Bulletin, October U.S. Department of Commerce, No. 98 / 10.

NOAA (National Oceanic and Atmospheric Administration) (1999), ENSO advisory, El Niño Southern Oscillation Cold Phase. January, NOAA/National Weather Service, No. 99/1.

Poveda G, Rojas W. Impacto del fenómeno El Niño sobre la intensificación de la malaria en Colombia. In: Proceedings of the XII Colombian Hydrological Meeting, Sociedad Colombiana de Ingenieros, 17–19 July 1996, Bogotá, Colombia. Bogotá, Colombia:Sociedad Colombiana de Ingenieros, 1996; 647– 654.

Poveda G, Rojas W. (1997) Evidencias de la asociación entre brotes epidémicos de malaria en Colombia y el fenómeno El Niño-Oscilación del Sur. Rev Acad Colombia Ciencia 21(81):421–429 Poveda, G, N. E. Gram. P. R. Epstein, W. Rojas, M. L. Quinonez, I. D. Velez, and W. J. Martens, (2000): Climate and ENSO Variability Associated with Vector-Borne Diseases in Colombia. In: Cambridge University Press, pp. 183-204

Quiñones ML, Suárez MF, Fleming, GA. Estado de la susceptibilidad al DDT de los principales vectores de malaria en Colombia y su implicación epidemiológica. Biomedica 7: 81–86 (1987).

Rojas W, Penaranda F & Echavarria M, (1992) Strategies for malaria control in Colombia. Parasitology Today 8, 141- 144.

Trenberth, K., 1991: General characteristics of El Niño–Southern Oscillation. In: Teleconnections Linking Worldwide Climate Anomalies, Glantz, R.M., Katz, R., and Nicholls, N. (eds.), Cambridge University Press, Cambridge, 13–42.

A Comparative Study of Remote Sensing Data and Ground-truth Water Quality Data for Three Coastal Ecosystems

Latrincy Whitehurst and Mark A. Harwell

Environmental Cooperative Science Center, Environmental Sciences Institute, Florida A & M University Science Research Center 305, 1520 S. Bronough Street, Tallahassee, FL 32307-6600

Phone 850-412-7797, Fax 850-561-2248, *Lwhitehurst22@aol.com*

Several water quality parameters can be assessed by using remote sensing techniques, including turbidity, temperature, and suspended sediments, all of which are major factors in determining the total maximum daily loads (TMDL). Spatial and temporal information is provided by thermal and optical sensors on boats, aircraft, and satellites. With this information water quality changes can be better understood in order to develop alternate management practices that improve water quality.

For the proposed research there will be three sampling locations; Apalachicola Bay National Estuarine Research Reserve (ANERR), ACE Basin NERR, and Grand Bay NERR. There will be 25-30 sample sites within each location. At each sample location remote sensing data will be collected using the hyperspectral Airborne Imaging Spectrometer for Applications (AISA) instrument aboard an aircraft managed by the University of Nebraska's CALMIT remote sensing center. AISA is a push-broom imaging spectrometer with a spectral range from 400-900 nm, spectral resolution of 5 nm, and spatial resolution of 3 m in our application. Ground-truth data will be collected by the Environmental Cooperative Science Center (ECSC) water quality research team at Florida A & M University, simultaneous with above and below water surface spectral parameters collected by a spectral team from Creighton University. The data collected by the water quality research team will include salinity, conductivity, dissolved oxygen, and temperature and various water samples will be analyzed for nutrients, dissolved organic carbon and nitrogen, particulate carbon and nitrogen, chlorophyll-a, and phytoplankton.

The Environment for Visualizing Images (ENVI) software will be used to process the remote sensing hyperspectral data collected by the AISA instrument during flyovers conducted at each of the study sites (ANERR, ACE Basin NERR, and GBNERR). A chlorophyll-characterization algorithm developed by Hladik and Schalles at Creighton University will be applied to the AISA data to correlate the ground-truth spectral and water quality data. Adjustments to the algorithm will be made as needed to achieve acceptable relationships between the two datasets. If successful, the use of hyperspectral remote sensing data can provide a very useful tool to characterize coastal and estuarine waters.

Error Correction of NDVI Time Series for NOAA Environmental Satellite

Mohammed Z. Rahman, Prof. Leonid Roytman
NOAA-CREST, CCNY, NY 10031

In this paper we give a new approach on the error correction of NDVI time series for NOAA environmental satellites. Empirical distribution function applied to correct the error of NDVI time series. This paper investigates NDVI stability in the NOAA/NESDIS Global Vegetation Index (GVI) data set during 1982-2003, in the period, which includes five NOAA satellites. Degradation of NDVI over time and NDVI's shifts between the satellites were estimated for china located in different ecosystems. It was found that in grassland and forest ecosystems NDVI time series are relatively stable while in desert and forest targets has considerable time trend. The method of matching empirical distribution function improves the error correction of NDVI time series for all satellites, especially NOAA-9 and NOAA-11.

A Comparison of Spatial Changes in Land Use Between Ponce and Parguera, Puerto Rico

Nathan L. Alexander and L. Mtetwa
Hampton University

Remote sensing is used for sensing the Earth's surface from space by making use of the properties of electromagnetic waves emitted, reflected or diffracted by the sensed objects, for the purpose of improving natural resources management, land use and the protection of the environment. We utilized ENVI (ENviroment for Visualizing Images) software to analyze true color images of Ponce and Parguera, Puerto Rico from the IKONOS satellite (IKONOS stands for satellite-based imagery acquisition systems, 4m multispectral and 1m panchromatic). ENVI is the ideal software for the visualization, analysis, and presentation of all types of digital imagery. ENVI's complete image-processing package includes advanced yet easy-to-use spectral tools, geometric correction, terrain analysis, radar analysis, raster and vector GIS capabilities, extensive support for images from a wide variety of sources, and much more. The Ikonos-2 satellite was launched in September 1999 and has been delivering commercial data since early 2000. Ikonos is the first of the next generation of high spatial resolution satellites. Ikonos data records 4 channels of multispectral data at 4-meter resolution and one panchromatic channel with 1-meter resolution. This means that Ikonos was the first commercial satellite to deliver near photographic high-resolution satellite imagery of anywhere in the world. We studied the vegetation, land cover, and land use characteristics of the two cities.

Analysis of Geological Features in Puerto Rico Using SAR (Synthetic Aperture Radar)

Marion Greene and L. Mtetwa
Hampton University

We analyzed gray scale images of Puerto Rico using SAR (Synthetic Aperture Radar) images. SAR is a method for developing high-resolution images of the earth's surface. Images represent the backscattering of microwave energy. Each pixel is comprised of a radiometric value and a phase value. Radiometry value is a measure of ground reflectivity and phase value is a feature of electromagnetic microwave, expressed as a rotating angle, dependent upon travel time of radar signal. SAR is also dependent on surface characteristics such as moisture, roughness, slope, texture, and dielectric constant. SAR is radar that sends out a pulse of radio waves which bounce off the object to be depicted. Then the scattered pulses return to the radar, where they are captured by the receiving antenna. SAR images resemble photographs and are actually maps in which the brightness shown is a measure of the radar energy reflected back to the antenna. Water droplets in fog and clouds are transparent to radio waves of the proper frequency just as window glass is to light waves of the visible frequency. SAR data is used to study agriculture, ecology, geology, oceanography, and hydrology as well as shipping in ice-covered seas, oil exploration, ocean pollution monitoring, and ocean research. SAR is a valuable remote sensing tool for both military and civilian users. We used SAR to analyze the geological features of Puerto Rico and to locate and find out the progress of hurricanes. We also compared mosaic SAR images from two different SAR platforms, i.e. (i) aerial images using many shots from planes and (ii) three shots from SAR satellite platform.

A STUDY OF REMOTE SENSING IMAGERS

Randy Scott and L. Mtetwa
Hampton University

The two sensing imagers that I will be discussing are the CASI and hyperion. CASI, which stands for compact airborne spectrographic imager, is more efficient when viewing images within an area of no larger than 4-meters. As far as the spectro-resolution, CASI has a wavelength range of 403- 914nm. CASI also consist of 288 bands. Data is also collected at contiguous, narrow band wavelengths for a specific portion of the electromagnetic spectrum through CASI. The Hyperion instrument provides a new class of earth observation data for improved earth surface characterization. The Hyperion instrument is known for its efficiency because it provides resolution of surface properties into hundreds of spectro-bands as apposed to the 10-multi spectro-bands flown on previous imaging missions, such as Landsat. Hyperion allows several hundred bands of data to be collected at a high spatial resolution. Hyperion resolves 220 spectro-bands ranging from .4 to 2.5 micro meters and it has a spatial resolution of 30m. Hyperion can image a 7.5 x 100km land are per image and provides detailed spectro mapping across all of its 220 channels with high radiometric accuracy. In conclusion, the two imagers that are widely used are CASI and Hyperion. Hyperion has its advantages for larger areas due to its larger resolution, and large land area per image range. CASI also has its advantages when viewing images of smaller areas because of its small resolution allows one to focus on particular sections within the images with greater detail.

QUANTIFYING VEGETATION CHANGE USING REMOTE SENSING IN JAMAICA BAY

By Colleen Sheridan
CE Dept. CCNY, NY 10031

Introduction

Wetlands are a vital component to the health of our environment. They improve water quality, provide shoreline stabilization, protect habitats and recharge groundwater. According to the Unites States Global Change Research Program more than 50% of wetlands have been lost in the US since the 1900's. Urbanization, dredging and filling are all major contributors to the loss of wetlands. However, the loss of wetlands due to global climate change has been more difficult to quantify.

In Jamaica Bay dredging and filling are no longer practiced but its wetlands are still disappearing. A study by BioOne indicated that "historical aerial photographs of several islands showed that sampled marshes have diminished in size by 12% since 1959. Overall island low marsh vegetation losses since 1974 averaged 38%, with smaller islands losing up to 78% of their vegetation cover." (Hartig, et al. 2002)[1]. In 1974 dredging and filling became a regulated activity. Photographs obtained by the New York State Department of Conservation in a study required by the Tidal Wetlands Act indicate basic trends in marsh land loss between 1974 and 1999. The conclusion of this initial study indicated that tidal wetland loss was accelerating—from 26 acres a year before 1994 to 44 acres a year [2]. Reasons for these losses include sediment budget disruption, sea level rise, dredging, wave energy, erosion, inlet stabilization, mussel dams on the marshes, and eutrophication. The following aerial infrared photographs demonstrate the loss and change of wetlands in Jamaica Bay after dredging and filling were regulated.

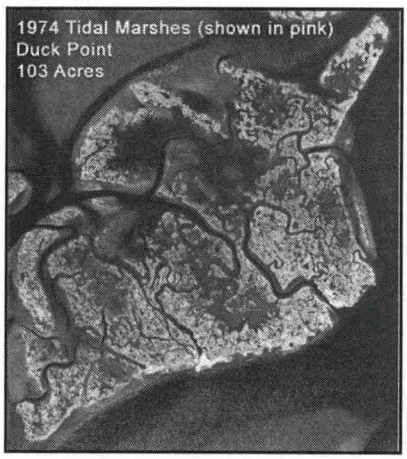

Figure 1. Tidal Marshes on Duck Point, Jamaica Bay, 1974[3].

The purpose of this study is to quantify wetland vegetation change and loss due to sea level rise and temperature change using remote sensing techniques. Because previous studies have indicated that recent land loss in Jamaica Bay may not be attributed to dredging and filling this study will focus on global climate change and its effects in the Jamaica Bay area. Specifically, satellite and aerial photographs will be used to map vegetation type, change, and loss between 1990 and 2004. While the effects of dredging and filling on land loss are relatively immediate the effects of climate change on land loss are gradual. Remote sensing and Geographical Information System (GIS) technology is a useful tool in this The purpose of this study is to quantify wetland vegetation change and loss due to sea level rise and temperature change using remote sensing techniques. Because previous studies have indicated that recent land loss in Jamaica Bay may not be attributed to dredging and filling this study will focus on global climate change and its effects in the Jamaica Bay area.

1) http://www.bioone.org/bioone/?request=get-document&issn=0277-5212&volume=022&issue=01&page=0071
2) http://www.dec.state.ny.us/website/dfwmr/marine/twloss.html
3) http://www.dec.state.ny.us/website/dfwmr/marine/twloss.html
4) http://www.dec.state.ny.us/website/dfwmr/marine/twloss.html
5) http://www.dec.state.ny.us/website/dfwmr/marine/twloss.html
6) http://www.dec.state.ny.us/website/dfwmr/marine/twloss.html

Specifically, satellite and aerial photographs will be used to map vegetation type, change, and loss between 1990 and 2004. While the effects of dredging and filling on land loss are relatively immediate the effects of climate change on land loss are gradual. Remote sensing and Geographical Information System (GIS) technology is a useful tool in this application because it allows a large area to be studied over a long period of time.

Methods

The first step in this research is to collect LANDSAT satellite and aerial photographs from 1994 to 2004. Both visible and infrared pictures will be analyzed. The use of pictures in different wavelengths allows us to conclude with more accuracy what kind of image is being reflected or absorbed in a picture. To analyze the images accurately it is necessary to compare images during the same time of day and same time of year. In addition, cloud cover, humidity, and other weather related occurrences also need to be accounted for. The next step involves collecting field samples. Four major types of vegetation classes will first be collected in Jamaica Bay and then classified for remote sensing purposes. Later these four classes will be broken down into smaller classes. After this stage each image will be divided into a 1000 x 1000 pixilated area. Each pixel will be 5 x 5 meters in area and will be designated as one of the vegetation classes, a combination of the vegetation classes or none of the vegetation classes. Finally, these maps will be analyzed and the vegetation change and loss will be quantified.

Conclusion

The wetlands of Jamaica Bay, influenced by tides, climate change, eutrophication, and urbanization are among the last areas of wetlands in the New York City area. Wetlands assist in keeping water free of nutrients and pollutants, stabilize shorelines, recharge groundwater and provide a habitat for wildlife. According to the NYDEC, at least 326 species of birds have been sighted on the wetland islands in Jamaica Bay, including confirmed breeding by 62 species. It is one of the most important migratory shorebird stopover sites in the New York Bight region. Eighty-one species of fish are known to use Jamaica Bay. Therefore the study of the decline, protection and restoration of Jamaica Bay's wetlands is important to our health and the protection of our natural environment. The conclusion of this study will help determine effects of climate change on wetlands, make predictions of future land loss, and will assist in finding ways to protect and restore wetlands in the future.

Figure 2. Tidal Marshes on Duck Point, Jamaica Bay, 1999 [4].

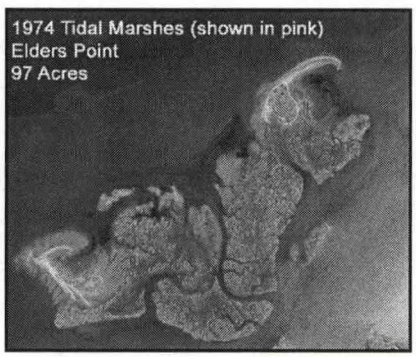

Figure 3. Tidal Marshes on Elders Point, Jamaica Bay, 1974 [5].

Figure 4. Tidal Marshes on Elders Point, Jamaica Bay, 1999 [6].

SCANNING FABRY PEROT IMAGER

Viviana Vladutescu, Mustapha Abdulfattah, Fred Moshary, Barry Gross
Optical Remote Sensing Lab, EE Dept, NOAA-CREST, CCNY
Jeff Puschell; Raytheon

Abstract

It is shown that a Scanning Fabry Perot etalon in combination with a series of appropriately designed broadband filters can be used as a high spectral/spatial resolution imager for satellite platforms. A design procedure is developed for optimization of the number and bandwidth of filter for a given Fabry Perot cavity length and spectral coverage requirements.

Introduction

There is a growing need to obtain simultaneous spectral and spatial resolutions to begin to adequately study full vertical and horizontal gas inventories. In conventional approaches, the spectral selectivity is accomplished by means of interferometry or a sequence of sequential pass-band filters and/or complex optical interferometric gratings selectively positioned to cover the spetral domain of interest [1-2]. However, these systems are quite large (owing to the large path-length differences needed for large resolution) and an alternative technique based on the use of a Planar Fabry-Perot (PFP) filter with a CCD imager has been proposed. However, the systems proposed have been especially designed to work in the MIR region but interest in hyperspectral sensors in the VIS-NIR has led to significant interest in extending the apprach to the VIS-NIR.

The theory of the Fabry Perot Spectrometer for plane waves is standard and can be found in any optical textbook [3]. The most relevent fact in our application is that in order to extend the Free – Spectreal range in the VIS from 400-1000 nm and use Fabry – Perot Etalons of reasonable length requires a large number of synchronized pass-bands to reject multiple resonance orders. To see the conditions imposed on the pass band filters to maintain single resonance operation, we plot in figure 1, the boundaries of the different resonance orders over the etalon.

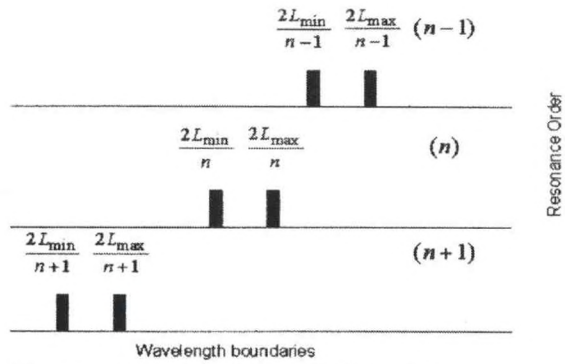

Figure 1: Resonance Boundaries of FP

Simple algebra shows that the single resonance conditions

$$\frac{2L_{\min}}{n-1} > \frac{2L_{\max}}{n}$$

$$\frac{2L_{\min}}{n} > \frac{2L_{\max}}{n+1}$$

lead to $\lambda_{\max} \le \frac{n+1}{n}\lambda_{\min} \le \frac{n}{n-1}\lambda_{\min}$

where $\lambda_{\min} = \frac{2L_{\max}}{n}$ $\lambda_{\max} = \frac{2L_{\max}}{n}$

Results

This observation allows us to define a simple algorithm to determine the passbands for each order that will allow operation of the band of interest

1. Determine as design the smallest FP cavity constructible $L_{cav}^{\min}$
2. For the smallest wavelength in the k[th] filter section, determine the minimum resonance needed
   $n_k = \lfloor 2L_{cav}^{\min} / \lambda_{\min}^{k} \rfloor$
   for the desired cavity length as where for the first section, the smallest wavelength is used.
3. Determine the maximum wavelength in the k[th] section as
   $\lambda_{\max}^{k} = [[n_k + 1]/n_k] - \Delta\lambda_{bound}$
   where a buffer is inserted.
4. This section would then be placed in front/behind a pass band filter covering the section bandwidth making single wavelength operation possible.
5. Once the maximum wavelength of the k[th] section is determined, the k+1 section is considered where
   $\lambda_{k+1}^{\min} = \lambda_{k}^{\max} + \Delta\lambda_{bound}$

In figure 2, we plot both the order of each Fabry Perot stage and the cavity length needed to cover each stage's passband assuming that the minimum cavity length is limited to

$L_{cav}^{\text{Limit}} = 2500nm$

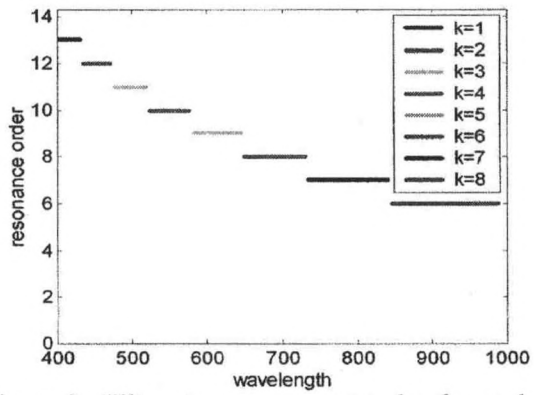

Figure 2a Filter stage resonance order for each passband

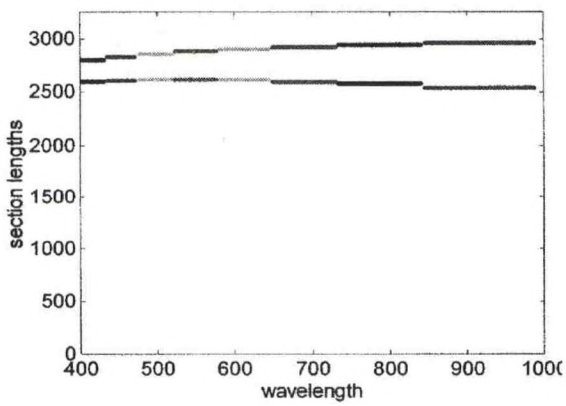

Figure 2b Filter stage length range for each passband

From figure 2, we can see that a minimum of 8 stages are needed to cover the range from 400nm to 1000 nm where each stage uses a subsequently smaller order. In this configuration, it is clear that the same sweeping of the cavity can be used for each pass band so all that is required is a filter wheel mechanism to select each relevent passband.

Once the architecture of the cascade system is determined, the ultimate spatial spectral resolution of the device is needed to acertain the limites of the instrument. The schematic of the instrument can be seen in figure 3

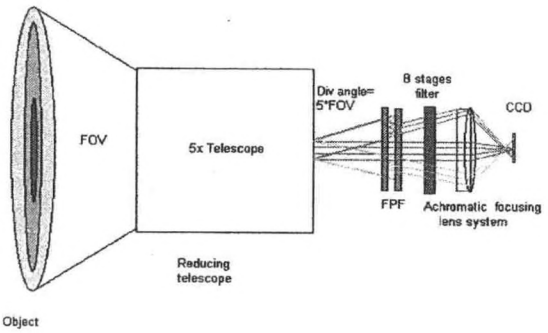

Figure 3. Fabry Perot Schematic

The most important aspect to observe is that the rays going to different CCD pixels pass the Fabry Perot Filter at different angles and that differernt angles will affect resonance of each spatial CCD Pixel. To see how these relationships are connected, we can take an idealized imaging system as given in figure 4 which is relevent to a polar orbiting satellite at 800km orbiting height. The imaging angles are made as small as possible since angle dispersion leads to spectral shifts. For a 1" CCD the spread of angles is ~ 30 mrads.

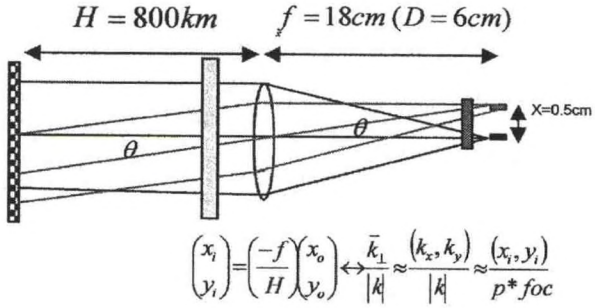

Figure 4. Imaging angles

To understand how the resonances are affected by different angles, a theory of the spectral response due to off-axis rays needs to be given. From the multiple path interaction of the plane wave with the etalon, the mth path accounts for m refleflections, one transmission and the free-space diffraction operator applied to m path lengths [4]. The results is

$$E(x,z) = \sum_{m=0}^{\infty} TR^m E_{diff}(x; z_m) \text{ or in fourier space}$$

$$\hat{E}(k_x, z) = \sum_{m=0}^{\infty} TR^m \hat{E}_{diff}(k_x; z_m) \text{ where}$$

$$\hat{E}_{diff}(k_x; z_m) = \exp(iz_m \sqrt{k^2 - k_x^2})\hat{E}_{in}(k_x;0) \quad z_m = m(2L$$

$$\hat{E}_{out}(k_x, z) = T\left[\frac{1}{1 - \mathrm{Re}\, xp\left(i2L\sqrt{k^2 - k_x^2}\right)}\right]\hat{E}_{in}(k_x;0)$$

From the above expression, the term in the rectangular brackets can function as a spatial-spectral reesponse function. If we re-write the transfer function in terms of spectroscopic variables such as the angle of the ray and the spectral detuning, we obtain the following representation

$$H_{FP}(k_x, k_y, k) = \frac{1-R}{1 - R * \exp\left(i2kL\sqrt{1 - \left(\frac{k_x}{k}\right)^2 - \left(\frac{k_y}{k}\right)^2}\right)}$$

$$\frac{1-R}{1 - R * \exp\left(2\pi i\left[\frac{f}{f_s}\right]\sqrt{1 - \left(\frac{k_x}{k}\right)^2 - \left(\frac{k_y}{k}\right)^2}\right)}$$

$$= \frac{1-R}{1 - R * \exp\left(2\pi i\left[\frac{f}{f_s}\right]\sqrt{1 - \left(\frac{x_i}{p * foc}\right)^2 - \left(\frac{y_i}{p * foc}\right)^2}\right)}$$

where x_i, y_i are the CCD pixel locations, f_S is the free spectral range and f is the optical frequency. To see the effect of

the transverse wave number on the spectral response, we plot the transfer function countour lines in figure 5 below.

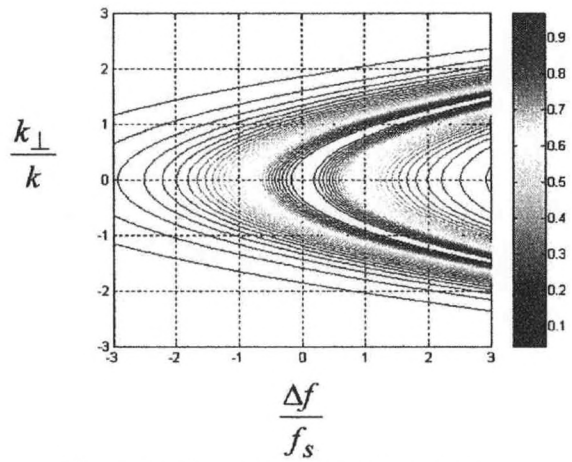

Figure 5. Fabry – Perot Transfer Function contour representation

It is clear that the spectral response shifts in a symmetric way for different angles away from the plane incidence case. Before considering the case relevent to our imager, it is instructive to see the impact of these expressions on tightly focused beams to explore how the plane wave theory breaks down when illuminated by tightly focused beams. By the Fourier Transform theorem, images with high spatial resolution create fields with large transverse spatial wavenumber spectrum which can be mathematically equivallent to a tightly focused beam. Therefore, the traditional FP lorentzian spectral response is no longer valid since it is expected that the resonance condition for of-axis waves will be different. It is clear that the condition for this to occur is that the spatial wave number divergence be sufficiently large so that $\Delta k_T \approx \frac{2\pi\Delta f}{c}$ where Δf is the traditional plane wave of increasing angular divergence changes the spectral and spatial characteristics, we plot the 99% power contours as a function of increasing angular divergence in figure 6. It is clear from this graph that coupling between the spatial and spectral components due to the frequency resonance selection of the filter result in a general broadening and of the spectral and spatial response. The effects of the spatial spectral coupling can be most clearly seen in the spectral broadening and assymetry as the spatial beam size decreases as seen in figure 7.

$$1/2 \geq L/a \geq 1/20$$

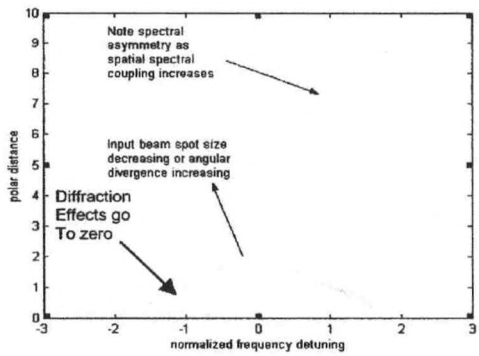

Figure 6. Spatial Spectral 99% power ccontours signifying resaponse of FP filter for different beam radii.

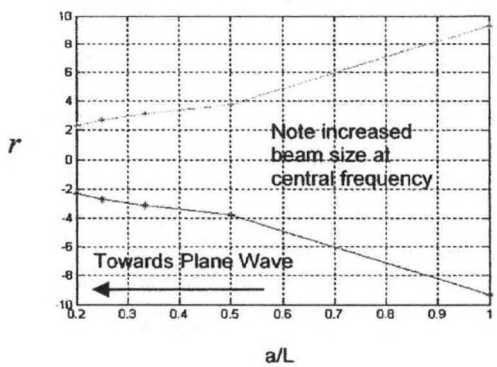

Figure 7a. Spatial extent of transfer function for different beam radii at zero frequency detuning.

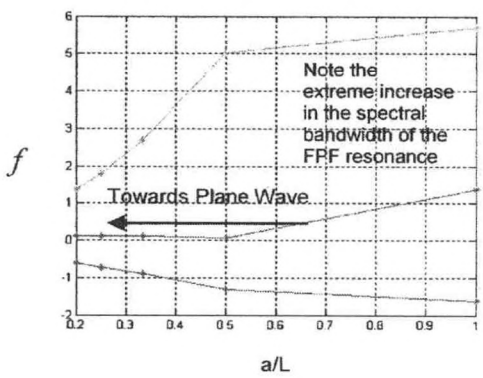

Figure 7b. Spectral extent of transfer function for different beam radii at center of CCD pixel.

We note in the above figure that both spatial and spectral broadening are observed. This is clearly seen from the Fabry Perot response function. On the other hand, the angles encountered in our imager are far smaller than the non-axial beams we are considering here. Therefore, we can derive a linearized expression that quantifies the frequency shift and spread of the transfer function as a function of the input beam angle. In particular, we arrive at the normalized shift as

$$\frac{\Delta\lambda_{shift}}{\lambda_o} = \frac{1}{2}\theta^2 \cong \frac{1}{2}\left(\frac{1}{36}\right)^2 \cong \frac{1}{2000}$$

so for a center wavelength of 1000 nm, we obtain a spectral shift of .5 nm which can be a problem for ocean color applications.

Conclusions

We illustrate that in principle a VIS/NIR Fabry Perot Spectrometer can be developed and develop a design program to calculate the characteristics of the needed pass band filters. It is shown that a set of 8 cascading filters can be used to cover the spectral range from 400nm to 1000nm with the same sweep. It is shown that for sufficiently small imaging systems, the spectral shifts in the response across the CCD are significant but should be easy to compensate for.

Acknowledgements

This work is supported by grant from NOAA #NA17AE1625. We would also like to thank Raytheon for their support of this project.

References

Marinelli, W; C. Gittins, A. Gelb, and B. Green, *"A Tunable Fabry-Perot Etalon-Based Long-Wavelength Infrared Imaging spectroradiometer"*, Applied Optics 38(16), 2594-2604 (2000)

Larar A; and S. Drayson, *"Global tropospheric and total ozone monitoring with a double-etalon Fabry–Perot interferometer. II. Feasibility analysis"*, Applied Optics, 37, 21 (1998)

Hecht E.; "*Optic"s, 3rd Ed.* Addison Wesley (1998)

Lee J.Y; and J. W. Hahn, H-W. Lee, "*Spatiospectral transmission of a plane mirror Fabry- Perot interferometer with nonuniform finite-size diffraction beam illumination*", J.Opt.Soc.Am.A 19 #5, (2002).

The Autoregressive Form of Transfer Function In Soil Moisture Modeling

J. Harold. Cruzado J.[1] (MS), Ramon Vasquez E.[1] (PhD), Nazario Ramirez[2] (PhD), Jorge Gonzalez[3] (PhD)

[1]Department of Electrical and Computer Engineering,
[2]Department of Industrial Engineering
[3]Depart ment of Mechanical Engineering, University of Puerto Rico at Mayagüez

In this work an empirical model to estimate hourly soil moisture is proposed based on transfer function in autoregressive form. The simplex search method of optimization was used to find the best coefficients of the transfer function, using past time series of rainfall and soil moisture as input. It has been shown that transfer function is versatile; the data source for input can be remote sensing observations (NEXRAD) or direct observation by rain gauge (from weather stations), and it is adjusted by using data from particular region at some depth of the soil (2, 4 or 8 in). The model performance can be visualized by temporal and spatial variability. To visualize the spatial variability of the soil moisture for Puerto Rico region, the model can be initialized by constant value everywhere in the region using the data obtained. Under normal atmospheric conditions (without extreme changes), the model shows good results. In case of using radar data (reflectance) the model is less than 50% reliable. However, the map shows very good definitions of wettest and driest regions and reasonable estimations of soil moisture.

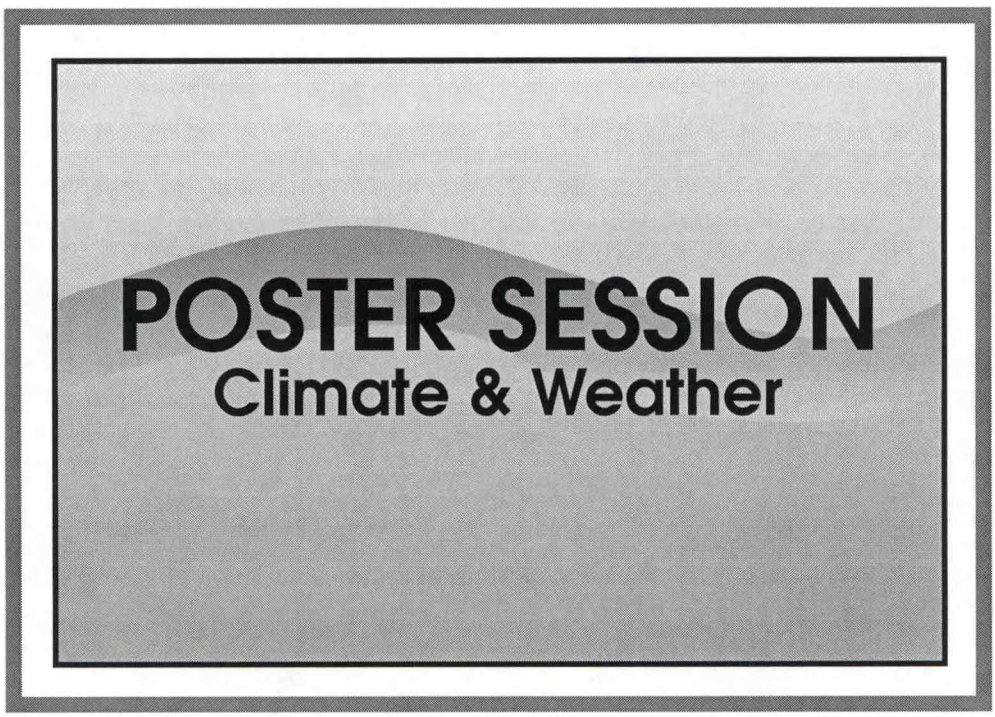
POSTER SESSION
Climate & Weather

Exploring the Relationships Between Snowpack and Modes of Atmospheric Circulation over North America

Stefan Sobolowski[1,2], Shayesteh Mahani[1], Reza Khanbilvardi[1] and Allan Frei[2]

[1]National Oceanic and Atmospheric Administration Cooperative Remote Sensing Science and Technology center, NOAA-CREST Center, Steinman Hall, CM7D, 140th St. at Convent Avenue, New York, NY 10031, United States. (212)650-8099; (212)772-5770; *ssobolow@hunter.cuny.edu*

[1]Hunter College, Dept. of Geography, 695 Park Avenue, New York, NY 10021, United States. (212)772-5322; *afrei@hunter.cuny.edu*

Abstract

Utilizing a gridded SWE dataset developed by Brown and Brasnet, of the Canadian Cryospheric Network, the relationships between snowpack, the Pacific North American pattern (PNA), North Atlantic Oscillation (NAO) and El-Nino Southern Oscillation (ENSO) are examined over the course of North American winters from 1980-1997. This data set is considered to be an improvement over current SWE estimates, especially in observation rich areas south of 55°N. The PNA pattern is the dominant mode of atmospheric circulation over North America for the winter months with the NAO exerting considerable influence over the climatology of the North Eastern part of the continent. ENSO effects on North American climate are well documented but the complex interactions between sea surface temperature (SST) anomalies, preferred modes of atmospheric circulation, and their combined effects on SWE are still poorly understood. The present research examines the statistical significance of the relationships between these three patterns of atmospheric variability and SWE from 35° N to 55° N for the entire meridional extent of the North American continent. Seasonal SWE values are correlated to seasonal mean teleconnection indices of the PNA, NAO and the SST anomalies of the ENSO 3.4 region. Composite analysis is employed to better understand the interactions between the PNA, NAO, ENSO and the winter (January-March) snowpack. SWE has a significant impact on spring snow-melt runoff, water resource availability and may be an indicator for summer temperature variability. Understanding the relationships posited above will aid in water resources planning and research as well as possible benefits to the field of climate prediction. This is research in progress so making any conclusions at this stage would be presumptuous. Preliminary results show negative correlations between the PNA, ENSO and SWE over the Pacific Northwest while the NAO shows some locally strong positive correlations over this region. ENSO is strongly correlated to SWE over the Southwest. PNA and NAO both show negative correlations to SWE over New England and the Ohio River Valley.

Introduction

Atmospheric circulation patterns composed of spatially remote regions of action, with significant correlations of the geopotential height field (i.e. the changes in height of a given atmospheric pressure) between regions, were quantitatively presented to the scientific community by Wallace and Gutzler (1981) among others. At the time, the patterns were observed as standing wave fluctuations in sea surface pressure between two regional centers and analysis was performed via grid point correlation. Atmospheric circulation patterns with two centers of action (or regions, as the singular point implied by use of the term "center" is not quite correct) are often described as oscillations or seesaws, in colloquial terms. Often the amplitude of the system is quantified into an index which is used to describe the characteristics of the oscillation. These patterns and oscillations, which alter moisture fluxes, wind trajectories and temperature gradients and thereby impact climate variability over remote regions, are often termed teleconnections. Teleconnections may be defined by the existence of

strong statistical relationships between climatological variables (i.e. temperature, precipitation or geopotential height) at spatially remote locations. The patterns explored in this study are the Pacific North American pattern (PNA), the NAO and the El-Nino Southern Oscillation (ENSO). Each of these patterns has been shown to influence North American climate to varying degrees depending on season, magnitude of teleconnection index (i.e. highly positive/negative, or warm/cold in the case of ENSO) and other climatological variables (Barnston and Livezey, 1987; Barton and Ramirez, 2004). Of particular interest to this study is the relationship between the aforementioned modes of circulation and Snow Water Equivalent. SWE is literally the mass of water in the snowpack. It provides more detailed information with respect to hydrological issues than snow cover. It is therefore essential for determining spring runoff and hence water resource availability as well as predictive skill for drought/flood conditions. Numerous studies have been conducted in which the impacts of atmospheric circulation on snowfall, precipitation, snowpack and spring runoff predictability have been explored (Barton and Ramirez, 2004).

All of the circulation patterns used in this study are characterized and quantified using indices which are computed with either geopotential height anomalies or SST anomalies. Barnston and Livezey (1987) expanded on Wallace and Guztler's grid-point analysis by applying a Rotated Principle Component Analysis (RPCA) of the geopotential height anomalies. In addition to increasing statistical robustness, RPCA also describes the relative strength of the circulation pattern in question. This method enabled researchers to more accurately describe and locate circulation patterns in space and through time. RPCA is the method currently employed by the National Weather Service, Climate Prediction Center. ENSO refers to a combined atmosphere/ocean phenomenon that includes Sea Surface Temperature (SST) anomalies and an index used to quantify pressure anomalies between Tahiti and Darwin (AU), termed the Southern Oscillation Index. It is the influence of these modes of circulation on North American snowpack that is the concern of this study.

Three central questions, relevant to the present study, seem to arise naturally given the present extent of knowledge about the relationships between atmospheric circulation and winter climate:

1) What are the relationships between PNA, NAO, ENSO and SWE/precipitation?

2) Are these relationships statistically significant?

3) Given statistical significance, do composites of the atmospheric patterns exert influence on the SWE signal, and how strong is that influence?

Data

SWE data for North America was provided by Brown et.al. (2003). This is a 0.25° x 0.25° gridded dataset originally designed for model evaluation, which covers a period of record from 1979-1997 (however due to incomplete records for 1979 this study only uses data from 1980 on). This dataset has not yet been used for a study such as this but has excellent established accuracy over areas with large numbers of observations and is considered to be the best currently available SWE product.

As SWE is the total amount of snow on the ground, not just snowfall, precipitation and temperature data are employed to augment the Brown dataset. This is necessary due to the fact that SWE accumulation and ablation depends on temperature and precipitation. The Wilmott-Matsura dataset, which contains temperature and precipitation data from 1950-1999 at a resolution of 0.5° x 0.5° is used.

The PNA and NAO indices from 1950-present are available for all months through the National Oceanographic and Atmospheric Association. For ENSO, one may use the Southern Oscillation index (SOI), SST anomaly indices for any of the four Nino regions (researchers typically use the Nino 3.4 region as it covers a large swath of both the east and west Pacific) or a combination of the two. A combination of the SOI and Nino 3.4 indices was selected for the analysis in this study.

Methods

The methods employed here are relatively straightforward statistical analyses at a resolution that should allow relationships to emerge. There are four parts to the methodology employed in this study. The first has four components: the period of record, the computation of seasonal values, the removal of grid points with little/no snow and definitions for PNA, NAO and ENSO events. Time series of the seasonal means of the three patterns appear in figure 1. The second and third parts, which have yet to be conducted, consist of correlation

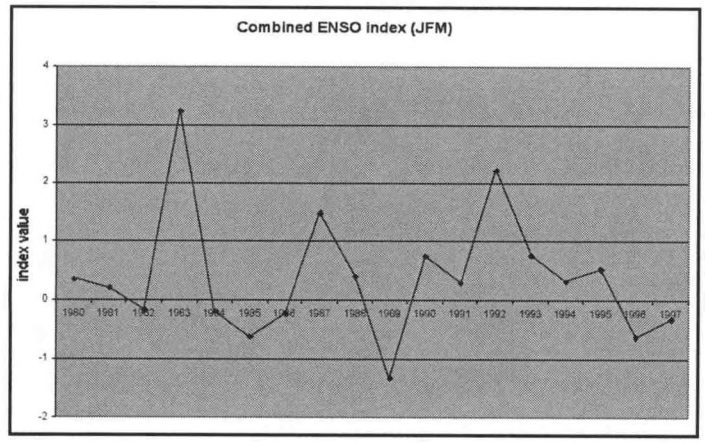

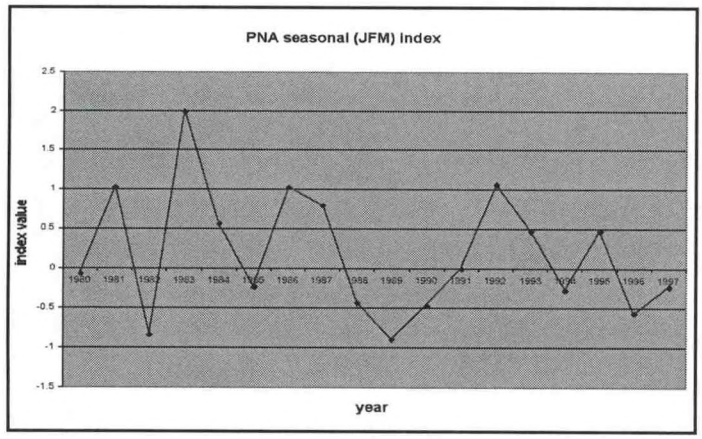

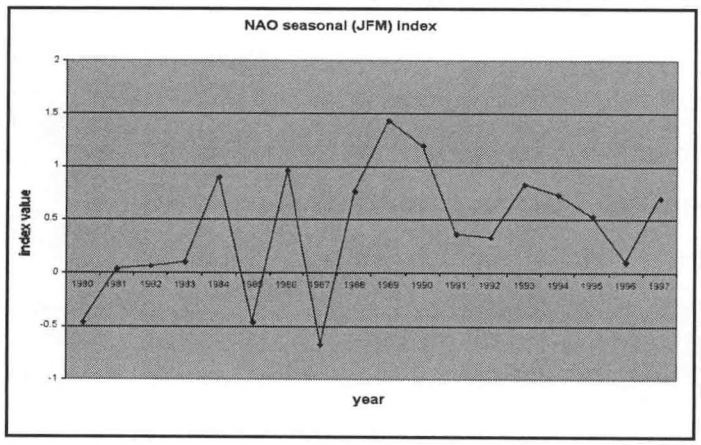

Figure 1. ENSO, PNA and NAO 1980

and rank correlation analysis respectively, while the fourth part is dedicated to the composite analysis.

The period of record is 1980-1997. Although this could negatively affect the composite analysis, a longer study period would force the study to incorporate an additional SWE dataset and nothing comparable to the Brown dataset exists for periods prior to 1980. In order to reduce noise in the SWE dataset nominal and zero SWE grid point values will be eliminated. All remaining values for all variables were temporally averaged to obtain seasonal values for each year in the period of study. The "season" is composed of the winter months of January, February and March. Although some studies use a winter season of DJF it was decided to include March as some more northerly regions experience maximum snowpack during this month and. Also, SWE is a cumulative measurement.

PNA and NAO indices generally range between ±3 with events being described as either positive or negative. As stated previously, CPC generated indices, based on the RPCA of Barnston and Livezey (1987) are used. Cutoff values for high/low PNA and NAO seasons are ±1.0 (based on the seasonal mean, not the individual months) in order to maintain consistency with previous studies (Hurrell, 1995; Straus and Shukla, 2002). As Trenberth (1997) notes, there is no universally agreed upon quantitative definition for ENSO and therefore ENSO events may have different definitions. The NOAA CPC cutoff for all ENSO events is ±0.4°C SST anomaly. ENSO 'extreme' warm/cold events are described as SST anomalies of ±1°C from the long-term mean in the Nino 3.4 region (Straus and Shukla, 2002). As no definitive definitions have been universally accepted both cutoffs are used with the combined SOI/Nino3.4 ENSO index calculated for this study. Seasons with greater than ±0.4 anomalies are referred to as warm(cold) seasons and those seasons exhibiting greater than ±1 anomalies are termed 'extreme' warm(cold) events.

After removal of nominal and zero SWE values, Pearson correlation coefficients (usually called simply "correlation coefficients") were calculated and contour plots generated for SWE/PNA, SWE/ENSO "warm", "cold", SWE/NAO. Pearson correlation coefficients reveal linear relationships quite well however, they are neither robust nor resistant. Strong non-linear relationships may exist that are missed, or poorly characterized, by a calculation of Pearson correlation coefficients. An example of this would be data points that fall along a curve.

It is not resistant because just a few outliers in the data will strongly affect the outcome of the calculations. Therefore a statistical method that is both robust and resistant will also be employed. To this end, the Spearman rank correlation coefficient was calculated for the preceding combinations. With this technique the original time series are ranked prior to calculation of the correlation coefficient. That is the "data" are transformed to ranks ranging from 1 to n thereby eliminating outliers in the data. The strength of the Spearman rank correlation is in its ability to reveal monotonic (i.e. ascending or descending) relationships. Using this technique we may be able to identify relationships between SWE and the circulation patterns that are missed by the ordinary correlation coefficient analysis. It should also be resistant to outliers in the data.

The composite analysis will be comprised of testing the significance of the relationships between SWE and the circulation patterns at various extremes. Results of the correlation and rank correlation analyses assisted our decisions on which composites to calculate. However, extreme SWE seasons may be incorporated into the study at a later date. A number of studies have used a composite analysis approach in their methods (Gershunov, 1998). These previous studies provide useful frameworks, suggestions -and warnings! for carrying out this type of analysis in the present context. As stated previously, strong correlations do necessarily mean strong relationships; a test for significance is needed in order to better characterize the relationships involved in this study.

For this component of the analysis all grid point values in the SWE dataset are used. The full range of composites has yet to be determined, but there are a number that will certainly be explored. These are as follows: PNA high/low, NAO high/low and ENSO warm/cold (using both ±0.4 and ±1.0 event cutoffs as described previously). The analysis itself will be conducted in three parts.

1. Calculation of the composite.
2. Perform t-tests at each gridpoint.
3. Plot the differences.

Significance will be determined via two-tailed t-tests. Many studies make use of GCM simulations to build up large ensembles which effectively increase sample size and lend legitimacy to significance tests (Straus and Shukla, 2002). As the researchers themselves state this reliance on model generated data creates a bias. The alternative is that sample sizes become smaller when specific composites are selected. As the length of record for this study is ~17 years it is likely that some of the composite sample sizes may be prohibitively small and therefore the reliability of significance values may be questionable.

Preliminary Results

The PNA and ENSO show a high degree of variability while the NAO exhibits a strong positive trend (Figure 1, facing page).

Preliminary correlation analysis has revealed regional relationships between the patterns and SWE for the period of record. Negative correlations between SWE and the PNA pattern are in evidence over the Pacific Northwest, the Ohio River Valley and New England (Figure 2). Positive correlations are smaller in magnitude and limited to the central Canadian plains, the mountainous Southwest (NM) and Quebec. The NAO is negatively correlated with SWE along the East coast and the Ohio River Valley while regions of weak positive correlations stretch from the West coast across the Northern plains, Northern half of the Great Lakes region and into Ontario. ENSO is negatively correlated to SWE across the Northern U.S., especially in the Pacific Northwest and the Great Lakes region. Positve ENSO SWE correlations are in evidence in the mountainous regions of the Southwest.

While it is difficult to prematurely claim any results one can, given previous studies and our existing knowledge of climatic processes, suggest some general patterns that might emerge from the analysis. Given that modes of atmospheric circulation examined here exert varying degrees of influence depending on their sign and intensity, it stands to reason that certain patterns will have greater/lesser influence on regional SWE values than others. There is also the strong possibility that positive/negative phases of the atmospheric patterns being examined will augment each other resulting in greater (lesser) SWE anomalies. The reverse may also be true. For example, both PNA and ENSO show negative correlations with SWE in the Pacific Northwest. What happens when ENSO is high (extreme warm) and PNA is high? The completion of this study will seek to address this and other questions that emerge from the preliminary stages of the analysis. We suspect that in this study

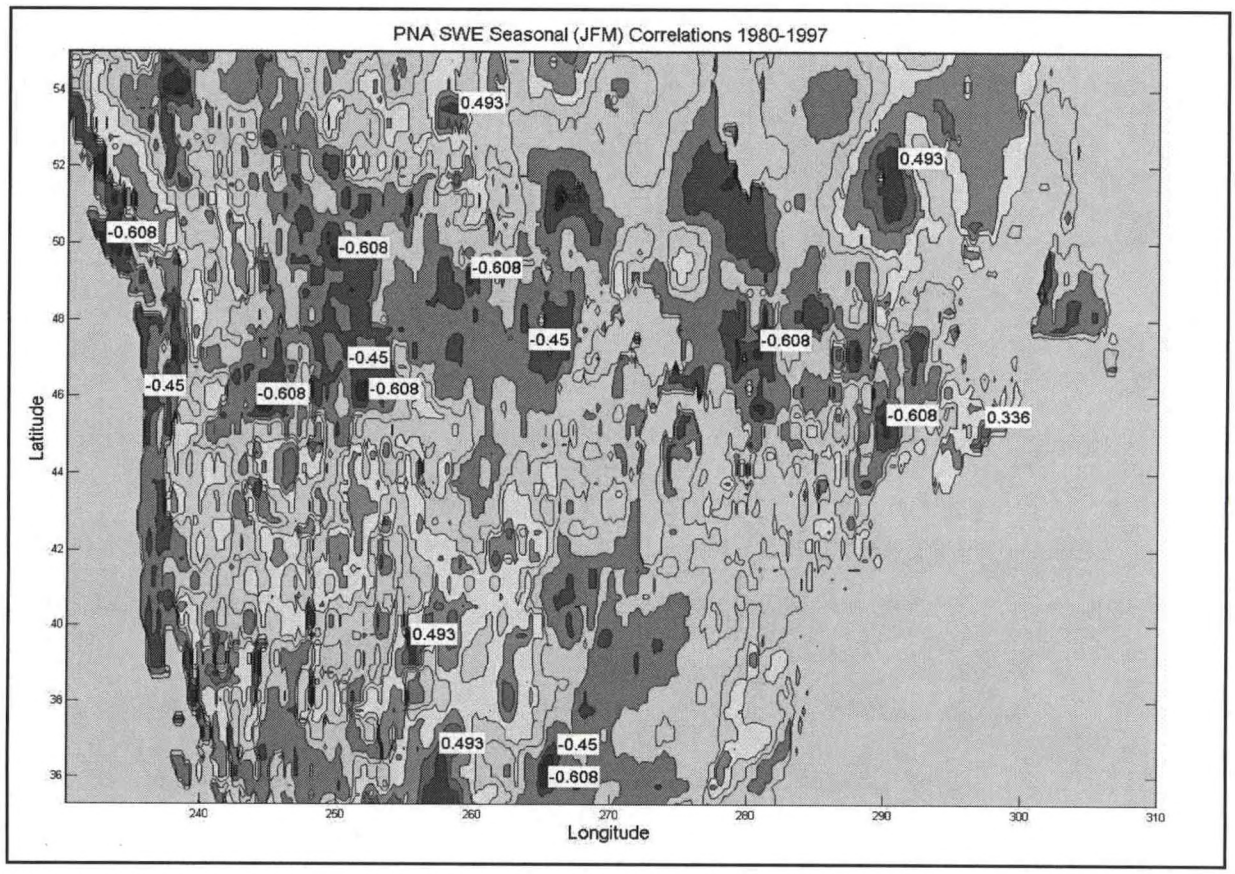

Figure 2. Correlation coefficient map that shows the relationship between PNA and SWE for winter season.

we will see seasonal SWE explained not just by a single mode of atmospheric circulation, but as a product of the influence exerted by a multiple, interacting circulation patterns.

REFERENCES

Barnston, A.G., and R.E. Livezey, 1987:Classification, seasonality and persistenceof low-frequency atmospheric circulation patterns. Mon. Wea. Rev. 115, 1083-1126.

Barton, S.B., and J.A. Ramirez, 2004: Effectsof El-nino southern oscillation and Pacific interdecadal oscillation on water supply inthe Columbia river basin. J. Water Res.Plan. & Man., 130:4, 281-289.

Brown, R.D., Brasnett, B., and D. Robinson,2003: Gridded North American monthly snow depth and snow water equivalent for GCM evaluation. Atmosphere-Ocean,41(1), 1-14.

Gershunov, Alexander,1998: ENSO influenceon intraseasonal extreme rainfall and temperature frequencies in the contiguous United States: implications for long-term predictability. J. Climate, 11, 3192-3203.

Hurrell, J.H., 1995: Decadal trends in the North Atlantic Oscillation: regionalt emperatures and precipitation. Science, 269, 676-679.

Straus, D.M. and J. Shukla, 2002: Does ENSOforce the PNA? J. Climate, 15, 2340-2358.

Trenberth, K.E., 1997: The definition of El- Nino. Bull. Am. Met. Soc., 78(12), 2771-2777.

Wallace, J.M., and Gutzler, D.S., 1981: Teleconnections in the geopotential height field during the Northern Hemisphere winter. Mon. Wea. Rev., 109, 784-812.

VALIDATION OF SATELLITE-BASED NESDIS RAINFALL PRODUCTS

Walid Harrouch, Shayesteh Mahani and Reza Khanbilvardi

National Oceanic and Atmospheric Administration Cooperative Remote Sensing Science and Technology Center, NOAA-CREST Center, Steinman Hall, T-107 140th Street at Convent Avenue, New York, NY 10031, United States. (212-650-8099; *Walid@ce.ccny.cuny.edu*)

Abstract

Evaluating the quality of any satellite-based rainfall product is useful and required for improving its algorithm. The objective of this study is to develop a statistical approach for evaluating the satellite-based NESDIS rainfall products from Hydro-Estimator (HE) algorithm, GOES Multi-Spectral Rainfall Algorithm with Daytime and Nighttime Rain Screen (GMSRA#2), and IR/microwave Blended Algorithm (Blended). Capability of each NESDIS rainfall product is examined with respect to seasonal variability, climate conditions, and storm types over different topographic regions.

paper 203

Ground-based radar and gauge rainfall observations, at high resolution (hourly), are used for validating NESDIS product. In this study, high resolution NESDIS product (hourly 4 Km x 4 Km) is evaluated regionally in details over several small size study sites with high hourly (daily when hourly is not available) rain-gauge density, for instance: specific 1°x 1° degrees. The size of every study site varies from 0.5°x 0.5° to 2°x 2° degrees, depending on the density and distribution of available hourly rain-gauge stations over the study site and storm size. Study time period is from April 2003 to present, when archived NESDIS rainfall products are available.

Three NESDIS rainfall products have been compared with NEXRAD Stage-IV rainfall, rain gauge observations, and GOES infrared (IR) cloud images for four storms during the winter and summer seasons over a 2°x 2° validation study area located in Hernando County, Florida (28°N-30°N and 81°W-83°W). The first test (I) was conducted for a six-hour storm event that took place on 02/24/2004 from 14:00 to 20:00 UTC, the second test (II) was for a six-hour storm that took place on 03/16/2004, from 00:00 to 06:00 UTC, the third test (III) was for a six-hour storm that took place on 08/22/2003, from 18:00 to 24:00 UTC, and the forth test (IV) was for a six-hour storm that took place on 09/03/2003, from 18:00 to 24:00 UTC. The primary results from tests I and II demonstrated that HE estimates rainfall with lower intensity and also over different locations compared to NEXRAD rainfall during the winter but, from tests III and IV, a remarkable improvement has been noticed in the performance of the algorithm which was also confirmed when compared to the rain gauge observations and the GOES infrared cloud images. Those preliminary results confirmed the fact that Hydro-Estimator (HE) has shown a substantially improved ability to estimate precipitation compared to GMSRA#2 and Blend algorithms.

Introduction

Precipitation is a critical component of the hydrologic cycle. An accurate estimate of rainfall over a certain area and for a specific period of time is important to hydrologic modeling, as well as the correct distribution of surface water into runoff, infiltration, evaporation and thus the total water budget over a given watershed. The large variability in the dynamics of precipitation also makes it one of the most difficult atmospheric variables to measure with accuracy acceptable for hydrometeorological applications [Raghavan and Goodman, 1993]. The scales over which precipitation occurs are so large that methods of measurement are wide ranging, and usually complementary: a measurement from a rain gauge is spatially precise but may be imprecise in time and quantity, on the other hand radar and satellite measurements are usually precise in time, less so in space, and much more imprecise in quantity [Schultz and Engman, 2000].

Since April 2003, the personnel at the Office of Research and Applications (ORA) of the National Environmental Satellite, Data, and Information Service (NESDIS) have been archiving quantitative satel-

lite derived precipitation estimates from six different algorithms using data from the Geostationary Operational Environmental Satellites (GOES) Infrared (IR) imagery. In this study, the validation is limited to the evaluation of only three rainfall algorithms :

(1) Hydro-Estimator (HE); which was developed in response to the need to eliminate the dependence on radar that the Auto-Estimator (AE) had. This was done by considering the conditions of the surrounding pixels, rather than only of the pixel itself, when determining the presence and rate of rainfall.

(2) GOES Multi-Spectral Rainfall Algorithm (GMSRA#2); which uses data from all five GOES VIR channels with daytime and nighttime rain/no rain screen developed by Rosenfeld and Lensky (1998) to produce rainfall estimates. The visible data and the difference between T10.7 and T6.9 are used to differentiate cirrus from raining clouds, while a combination of T3.9, T10.7, and T12.0 are used during the daytime to retrieve estimates of cloud particle size.

(3) IR/Microwave Blended Algorithm (Blend); which contains many features of the AE algorithm but instead of a fixed relationship between IR brightness temperature and rain rate, uses microwave-based rain rates from the Special Sensor Microwave/Imager (SSM/I), Advanced Microwave Sounding Unit (AMSU), and Tropical Rainfall Measuring Mission (TRMM) Microwave Imager (TMI) to perform a real-time recalibration of the brightness temperature-rain rate relationship.

In the first phase of this study, an initial validation of each NESDIS rainfall product against ground-based radar measurements has been conducted. The rainfall estimates are then validated against observations from dense networks of rain gauges over a 2° x 2° box with regards to the seasonal and climate variability over the State of Florida. In the second phase, a statistical approach will be developed to compare all possible statistical parameters, simultaneously between the satellite-based rainfall estimates and the ground validation observation data and eventually evaluate the satellite-based retrieval algorithms on real-time precipitation and flood forecasting.

Validation Strategy

The validation process of the pre-mentioned NESDIS satellite based rainfall retrieval algorithms started by testing the quality of the three satellite-based NESDIS rainfall products over Hernando County, FL. for different type of storm events with respect to the seasonal and climate variability against NEXRAD Stage IV estimations as well as hourly and daily rain gauge observations according to the following plan:

-Detailed comparison between rainfall image patterns, spatial comparison, for several storms (explained in details next section) over 2° x 2° study sites in both cold and warm season.

-Comparing all possible statistical parameters as well as the relationship (scatter plots) between the models' output and each of the validation NEXRAD and the rain gauge data over the study sites of interest.

-Analysis and evaluation of each product performance for the different study cases in order to improve its retrieval algorithm.

Results and Discussions

In order to evaluate the performance of the Satellite-Based NESDIS Rainfall products, a detailed study of some cases was performed during cold and warm seasons to see the effect of the seasonal variability on the quality of the models' output. In each season two heavy storms have been selected; all four case studies were evaluated over the same region 2°x 2° box in order to keep the topography factor constant and look only at the effect of seasonal variability on the models' performance at this level of investigation.

Validation During Cold Season

Fig.1 represents the comparison between NEXRAD Stage IV rainfall observations and Hydro-Estimator (HE), GOES Multi-Spectral Rainfall Algorithm (GMSRA#2) and IR/Microwave Blended Algorithm (Blend) rainfall estimates from 1600-1700 of a 6-hr-heavy rainfall event that took place on

02/24/2004 from 1400 UTC – 2000 UTC over Hernando County, FL. (2∞ x 2∞ box, N28 W83).

The statistical comparisons are shown as well in Fig.2 to get a better idea on the degree of agreement between the forecast of interest estimates (rainfall retrieval algorithm) and the relevant ground observation.

Many research studies have been conducted in the past in order to validate different rainfall estimation models, in our current investigation. We are trying to validate all satellite-based NESDIS rainfall products on an hourly basis in order to evaluate the performance of the high-resolution (temporal (hourly) and spatial (4 Km x 4 Km)) rainfall retrieval algorithms over the Continental United States.

From the hourly images of Stage IV and NESDIS rainfall products of two 6-hour heavy rainfall events during cold season over the same validation site, it is obvious that HE is the best forecast model out of all three, but even though HE presents a similar rainfall pattern compared to Stage IV – with a kind of shifting - HE under estimated the rainfall rates in most areas, this is confirmed when we look at the relationship between Stage IV and HE plotted below as well (most the points are above the 45° line) along with the statistical comparison between ground observations and the forecasts' estimates (Mean).

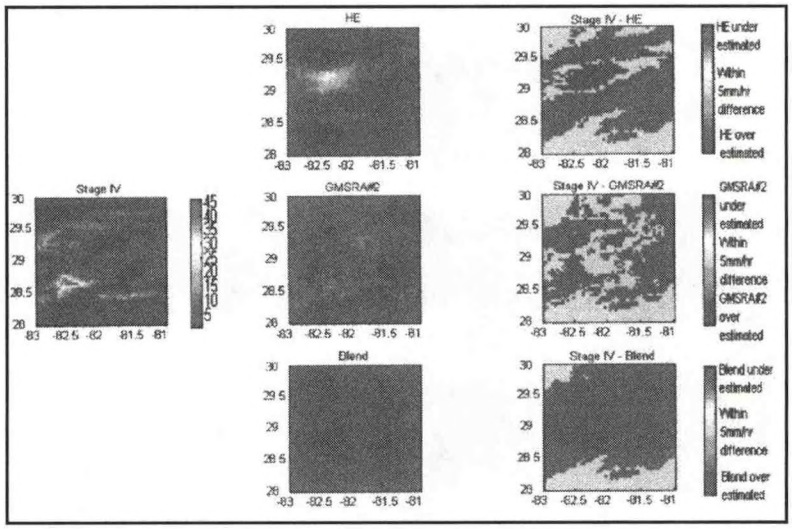

FIG.1.Comparison of NEXRAD Stage IV Rainfall with HE, GMSRA#2 & Blend Rainfall Estimates over a 2° x 2° box, N28 W83, on 02/24/2004, from 1600 -1700 UTC

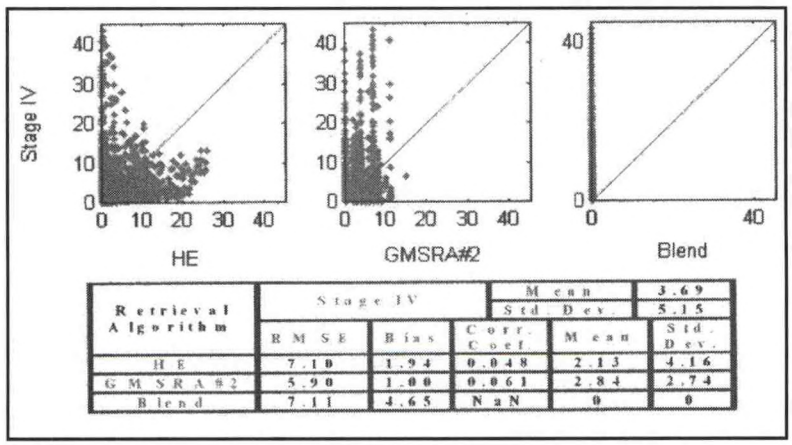

Retrieval Algorithm	Stage IV RMSE	Stage IV Bias	Corr. Coef.	Mean	Std. Dev.
				Mean	3.69
				Std. Dev.	5.15
HE	7.10	1.94	0.048	2.13	4.16
GMSRA#2	5.90	1.00	0.061	2.84	2.74
Blend	7.11	4.65	NaN	0	0

FIG.2. Statistical Comparison between NEXRAD Stage IV Rainfall and HE, GMSRA#2 & Blend Rainfall Estimates over a 2° x 2° box, N28 W83, on 02/24/2004, from 1600 -1700 UTC

From both case studies that we have examined, we have noticed as preliminary conclusions that, most of the retrieval algorithms performed a little better with respect to the ground observations (Stage IV) during the second study case (03/16/2004), our theory is confirmed if we look at the statistical comparison between the models' output and Stage IV for each hour; besides

-HE has shown a substantially improved ability to estimate precipitation compared to GMSRA#2 and Blend algorithms, but performs poorly during cold season as well.

-Blend algorithm shows the lowest performance in the estimation of rainfall, probably because of the use of microwave based rain rates from SSM/I, AMSU for the calibration of the brightness temperature – rain rate relationship (Tb–RR) instead of infra red – brightness temperature and rain rate (IR–RR).

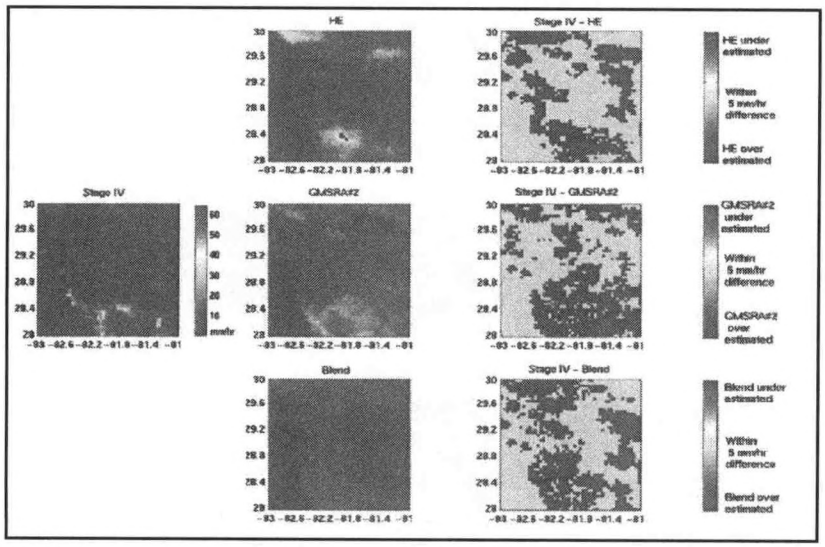

FIG.3.Comparison of NEXRAD Stage IV Rainfall with HE, GMSRA#2 & Blend Rainfall Estimates over a 2° x 2° box, N28 W83, on 08/22/2003, from 2000 -2100 UTC

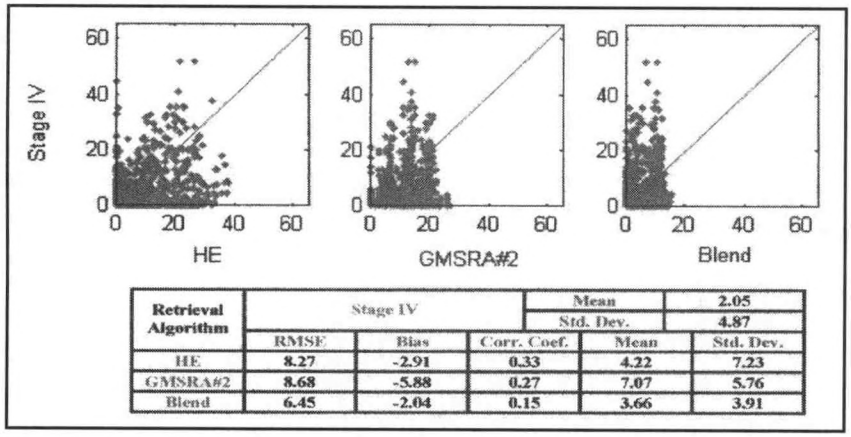

Retrieval Algorithm	Stage IV			Mean	2.05
				Std. Dev.	4.87
	RMSE	Bias	Corr. Coef.	Mean	Std. Dev.
HE	8.27	-2.91	0.33	4.22	7.23
GMSRA#2	8.68	-5.88	0.27	7.07	5.76
Blend	6.45	-2.04	0.15	3.66	3.91

FIG.4. Statistical Comparison between NEXRAD Stage IV Rainfall and HE, GMSRA#2 & Blend Rainfall Estimates over a 2°x 2° box, N28 W83, on 08/22/2003, from 2000 - 2100 UTC

Validation During Warm Season

Fig.3 represents the comparison between NEXRAD Stage IV rainfall observations and Hydro-Estimator (HE), GOES Multi-Spectral Rainfall Algorithm (GMSRA#2) and IR/Microwave Blended Algorithm (Blend) rainfall estimates from 2000-2100 of a 6-hr-heavy rainfall event that took place on 08/22/2003 from 1800 UTC – 2400 UTC over Hernando County, FL. (2∞ x 2∞ box, N28 W83).

The statistical comparisons are shown as well in Fig.4 to illustrate the degree of agreement between the forecast of interest estimates (rainfall retrieval algorithm) and the relevant ground observation.

From the last two study cases during warm season that, we have noticed as preliminary conclusions that, most of the retrieval algorithms performed much better with respect to the ground observations (Stage IV) during the warm season than during the cold season, our theory is confirmed if we look at the statistical comparison between the models' output and Stage IV each hour; besides

-The performance of each retrieval algorithm improves during warm season to a certain level where it starts to overestimate rainfall precipitation with respect to Stage IV observations. (Especially with GMSRA#2 and Blend)

-HE has shown a substantially improved ability to estimate precipitation compared to GMSRA#2 and Blend algorithms, but performs poorly during cold season as well.

-Blend algorithm shows the lowest performance in the estimation of rainfall, most likely because of the use of microwave based rain rates from SSM/I, AMSU and TRMM Microwave Imager (TMI) for the calibration of the Brightness Temperature – Rain Rate relationship instead of Infra Red – Brightness Temperature and Rain Rate.

Validation of HE against Rain Gauge Observations

Given the poor quality of both NESDIS rainfall products GMSRA#2 and Blend when validated against NEXRAD Stage IV during different seasons and for different storms, and given the relatively

improved quality of Hydro-Estimator, we decided to validate HE as well as NEXRAD Stage IV against Rain Gauge observations in order to confirm and emphasize the theory based on the fact that HE under-estimates rainfall, compared to ground-based measurements. In the following section, we presented the comparison of HE with daily rain gauge (due to unavailability of hourly data) measurements for all case studies mentioned earlier in this paper.

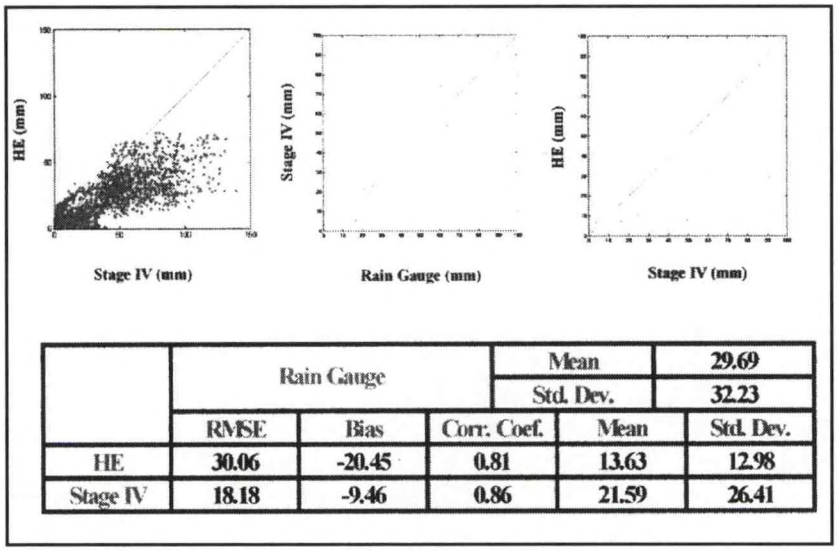

	Rain Gauge		Mean	29.69
			Std. Dev.	32.23
	RMSE	Bias	Corr. Coef.	Mean	Std. Dev.
HE	30.06	-20.45	0.81	13.63	12.98
Stage IV	18.18	-9.46	0.86	21.59	26.41

FIG.5. Validation of NEXRAD Stage IV Rainfall and HE Rainfall Estimates against Rain Gauge observations during 24 hr- Cumulative Rainfall from 03/15/2004 1300 UTC till 03/16/2004 1300 UTC over Hernando County, FL. (N28 W82)

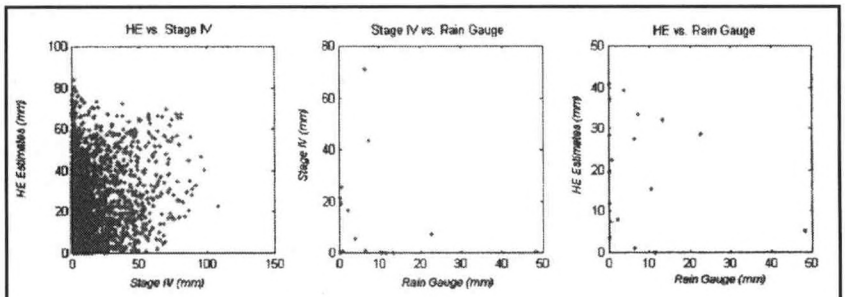

	Rain Gauge		Mean	7.41
			Std. Dev.	11.92
	RMSE	Bias	Corr. Coef.	Mean	Std. Dev.
HE	23.25	12.73	-0.21	20.13	13.82
Stage IV	23.85	-9.66	0.19	12.05	16.61

FIG.6.Validation of NEXRAD Stage IV Rainfall and HE Rainfall Estimates against Rain Gauge observations during 24 hr- Cumulative Rainfall from 09/03/2003 1300 UTC till 09/04/2003 1300 UTC over Hernando County, FL. (N28 W83)

Preliminary Conclusions

The study of four different cases over the same study site in the state of Florida has shown that:

-The performance of each retrieval algorithm improves during warm season to a certain level where it starts to overestimate rainfall precipitation with respect to Stage IV observations. (Especially with GMSRA#2 and Blend).

-Hydro-Estimator (HE) has shown a substantially improved ability to estimate precipitation compared to GMSRA#2 and Blend algorithms, but performs poorly during cold season as well.

-Blend algorithm shows the lowest performance in the estimation of rainfall, probably because of the use of microwave based rain rates from SSM/I, AMSU and TRMM Microwave Imager (TMI) for the calibration of the Brightness Temperature – Rain Rate relationship instead of Infra Red – Brightness Temperature and Rain Rate.(Tb–RR instead of IR–RR relationship)

In fact, methods which employ the Infra Red region of the Electromagnetic spectrum infer rainfall from the cloud top brightness temperature, cloud brightness or other cloud characteristics, whereas methods which utilize radiation in the microwave region directly calculates rainfall rates which can be determined with regards to brightness temperature measurements: scattering and absorption (the more dominant process for liquid drops). It is expected to see a higher rainfall rate than the real one (reported

ground true value) as some ambiguity arises due to absorption by cloud particles and gases in the atmosphere.

It is well known that absorption techniques work poorly over land but perform well over the oceans, that might explains why Blend algorithm performance was so poor.

REFERENCES

Collier, C.G., 2000: Remote Sensing in Hydrology and Water Management. Chapter 6 in Passive microwave estimates of rainfall from space. Springer, Berlin, pp 111-132.

Davenport, J.C., R.J. Kuligowski, and R. A. Scofield 2003: The Hydro-Estimator technique for high-resolution geostationary satellite rainfall estimates. Submitted to Mon. Wea. Rev.

Mahani, S., 1997: Advanced Hydrologic Modeling – Seminar Course, Measurement and Simulation of Rainfall. Chapter 2 in Precipitation Estimation.

Raghavan, R. and S. Goodman, Composite radar data analysis 1993: Implications for hydrometeorology and climatology, International Conference on Radar Meteorology, 765-767.

Sharma, V. 1997: Advanced Hydrologic Modeling – Seminar Course, Measurement and Simulation of Rainfall. Chapter 4 in Microwave Spectrum.

Shultz, G. A. and E. T. Engman, 2000: Remote Sensing in Hydrology and Water Management, Springer, New York.

Vicente, G.A., R.A. Scofield, and W. P. Menzel, 1998: The operational GOES infrared rainfall estimation technique. Bull.Amer.Meteor.Soc. 79, 1883 – 1898.

DEVELOPMENT OF A REAL-TIME ESTIMATION ALGORITHM FOR THE MOUNTAINOUS REGIONS OF THE WESTERN U.S.

(A procedure for Sampling Error Minimization and Cloud Classification Scheme)

Ali Amirrezvani[1,2], Shayesteh Mahani[2], and Reza Khanbilvardi[2]

[1]Department of Earth and Environmental Sciences of the Graduate Center of the City University of New York, 365 Fifth Avenue, New York, NY 10016, United States. (*aamirrezvani@gc.cuny.edu*)

[1]National Oceanic and Atmospheric Administration Cooperative Remote Sensing Science and Technology center, NOAA-CREST Center, Steinman Hall, T-521, 140th Street at Convent Avenue, New York, NY 10031, United States. (212-650-8099; *aamirrezvani@gc.cuny.edu*)

Abstract

The goal of this research is to fill the gaps in the NEXRAD scanning coverage using high-resolution satellite-based precipitation products. The gaps are due to the lack of data in mountainous regions not only because rain-gauge networks and radar not being able to cover everywhere because of high mountains, but also there are sparse or no real-time rain gauge networks. There are several uncertainties that need to be minimized. The PERSIANN (Precipitation Estimation from Remotely Sensed Information using an Artificial Neural Network) is integrated here to minimize following two uncertainties: sampling error and cloud type classification to improve and categorize cloud-top brightness temperature and rainfall (Tb-R) relationship.

As Tb decreases the more chance to have heavy rainfall and vice versa. By further minimizing the sampling error it would reduce the high number of lower rainfall pixels. The search for an optimal gridding approach with precise thresholds for Tb and R (rainfall) for each grid is in progress. As a result, the gridding approach would alleviate the effect of sampling error due to lower rainfall pixels. It would be more representative of the observed data of heavier rainfall. Also, a more adequate evaluation of relationship would exist between input and output data before and after the gridding and an improvement in model rainfall estimates. Each cloud type has a specific Tb-R relationship. The more knowledge and comprehension of these phenomena would aid in developing a cloud classification scheme that would portion clouds into specific categories. It would facilitate the analyses and inferences on those cloud categories and progression towards the other uncertainties. Lessening the other uncertainties (future work) would enhance the accuracy of high temporal, hourly, resolution of model rainfall estimates.

Background

According to Hsu et al. (1996), effective observations of the global distribution of rainfall are necessary for monitoring the variability of weather and climate. Those observations are also significant to the comprehension of the hydrological cycle as it goes throughout the atmosphere, land, and ocean. Rain gauge methods are only good in a relatively sparse sampling of rainfall over the land. Also,

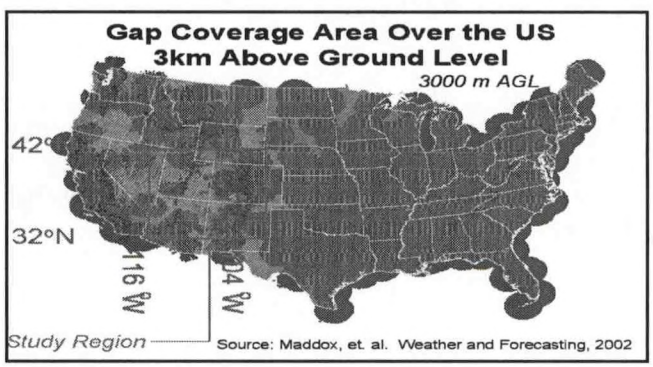

Fig.1 – Study area located on a radar coverage map, over the US, demonstrates the gap coverage areas. This map shows the scan coverage of radar beam 3km above the ground level, which has the maximum coverage.

ground-based radar methods are good for measuring rainfall over significantly large areas, but only over land and oceanic regions along coastlines. Since the 1960's, multi-source channel visible (VIS) and infrared (IR) imagery have been collected by the Geostationary Operational Environmental Satellites (GOES). VIS and IR are techniques being used to estimate surface rainfall. Those two methods attempt to correlate the surface precipitation rate with cloud top brightness temperatures collected by the satellite. Input GOES is chosen because it is 36000km above ground, high temporal (1/2 hourly), high altitude, and has information about neighboring pixels and covers all USA; compared to Polar Orbiting Environmental Satellites (POES), which is at lower altitude and at lower temp resolution, twice a day.

Even though, VIS and IR imagery methods are capable of providing important information on the spatial distribution and temporal variability of rainfall, they are only at lower spatial and temporal resolutions (Lee et al. 1991; Petty, 1995). GOES IR images being half-hourly sampling rate, it is possible to see the diurnal variations of the cloud development but the image is associated with the cloud top temperatures. Those temperatures are only indirectly related to intensify rainfall. As a result, a high uncertainty between the IR signal at the image pixel and the associated precipitation rate underneath the cloud is created. This relationship is non-linear. A more precise method that could justify the non-linearity of the IR-RR relationship is essential for providing precise rainfall rate products. Also, the pixel by pixel mapping of the IR-RR relationship could be regionally and seasonally dependent; one case cannot explain another case. Then, a relationship characterized by extreme transience, heterogeneity, and variability has to be modeled (Hsu et al., 1996).

Studies of satellite imagery in precipitation estimations in the past have been performed. Adler et al. (1993) and others have incorporated IR with microwave information; Xie and Arkin (1996) incorporated GOES, microwave, and rain gauge measurements; Negri et al. (1993) merged IR and numerical cloud model together. Scofield (1987), Grassoti and Garand (1994) have merged sounding measurements, physical fields calculated by numerical weather forecast models into the IR algorithms. The methods used by those researchers had for purpose to enhance the input system to alleviate the rainfall mapping uncertainties for different clouds. Rainfall estimation is very complicated because the relationship between meteorological, geological and other environmental conditions varies with rainfall rates and is also nonlinear and spatially variable (Hsu et al., 1996).

Objective

The goal of this research is to improve an algorithm, to combine multi-sources radar and satellite-based data of rainfall estimates because of blockage of lack of data in the mountainous regions of the western US, for two purposes. The first purpose is to extend the spatial coverage of NEXRAD data, such as to produce continuous gridded high-resolution precipitation estimates. The second purpose is to alleviate errors such as noise and uncertainties in high resolution merged rainfall data sets (4km by 4km resolution) because of errors, cloud tops cover spatial displacement and some errors affecting lower resolution; such as distinguishing rainy clouds from non-rainy clouds, spatial displacement of satellite Infrared image, and limb darkening, to improve rainfall estimates. Another goal is to implement the algorithm in for hydrological operational predictions and flash flood fare.

Datat Used & Study Area

There are three different sources of datasets used in this research:

- Geostationary Infrared half-hourly 4km x 4km resolution, stage 4, 12 mm wavelength.
- Ground-based radar rainfall (NEXRAD) at hourly 4km x 4km resolution.
- Rain Gauge hourly data.

The gap coverage area is in the Western U.S. The study area is of 10o lat by 12 o lon. The latitude range is between 32 o N and 42 o N and the longitude range is between 104 o W and 116 o W. Figure 1 illustrates the NEXRAD coverage area over the U.S., 3km above ground level. The green circles show the coverage area of NEXRAD. It is well distributed over the U.S. but not the Western United States, especially in the mountainous regions (in red/orange).

Methods

To improve the temporal resolution of the model output, time relevant errors, input-output relationship errors, and model structure error have to be minimized. An Artificial Neural Networks (ANN) could be used to improve the model if the following criteria could be met.

1. Increasing the quality of input variables by lowering the associated error sources.

2. Diminishing sampling error could improve hourly rainfall estimates. Classifying cloud types to be able to remove non-rainy clouds and specifying Tb IR-RR relationship for each cloud type. Minimizing other error sources, all possible uncertainties would improve accuracy of hourly temporal and spatial resolutions of model estimates.

3. Improving the connection weight factors between input and hidden layer (Wij) and also between hidden and output layer (Vjk).

The Self-Organizing Feature Map (SOFM) gives the relationship between the input and the hidden layer. The effective input is related to the original output and Wij. The effective input is integrated into the hidden layer. The Self-Organizing Feature Map Linear Output (SOLO) gives the relationship between the hidden and the output layer. The output is related to the effective input and Vjk (Zurada, J.M., 1992).

The quality of pixel-based GOES IR cloud-top Tb at hourly 24km by 24km resolutions used as input variable to improve by adding more Tb information from the neighboring pixels. Also, in addition to the brightness temperature for every pixel, average Tb and standard deviation of Tb for pixels inside a 3 by 3 and also a 5 by 5 windows, centered at the selected pixel, used as extra input variables. Adding information about the values and also the variability of cloud-top brightness temperature on the neighboring pixels would increase the accuracy of the input by reducing some of the error sources.

Model

A rainfall-retrieval algorithm based on an ANN system is selected to be improved and incorporated for fine time and space scale estimates from satellite infrared (IR) cloud-top temperature (Tb). IR-based models, currently, produce rainfall with few-hours temporal and greater than 10-km spatial. PERSIANN, the selected model for improvement, currently produces global 6-hourly 0.25o by 0.25o lat/lon resolutions precipitation. In this part of the project, the goal is to improve the model to estimate higher temporal up to hourly resolution IR-based PERSIANN model will be improved, spatially, in the part of the project, to generate high resolution up to 4km by 4km space scale precipitation. Accuracy and resolutions of the model output can be improved by minimizing the relevant uncertainties.

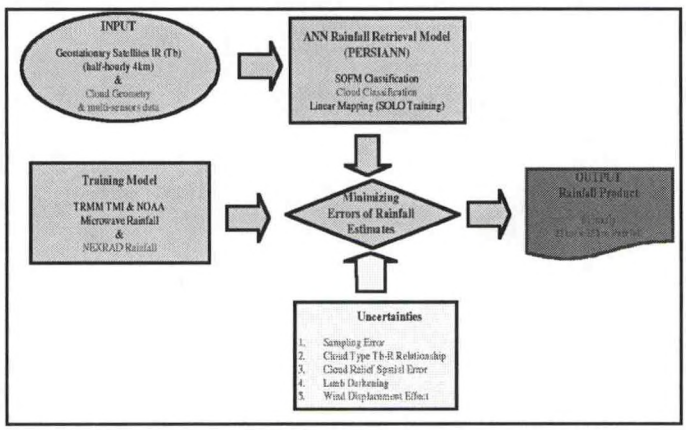

Fig. 2 – Flowchart of the improved-model structure.

In figure 2, the flowchart illustrates the required data, model procedures, and error sources associated to rainfall that need to be taken into account for improving accuracy and resolution of model output. Adding extra cloud information (in red) to model input variables, useful for cloud-type detection and classification, is required for improving Tb-R relationship, and as a result, accuracy of the cloud-top Tb-based model estimates.

Uncertainties

There are five uncertainties that have to be optimized. Those uncertainties are linked to using high-resolution remote sensing data for high-resolution precipitation studies. The optimization of these uncertainties could improve the accuracy of precipitation estimates. Here the first two are studied.

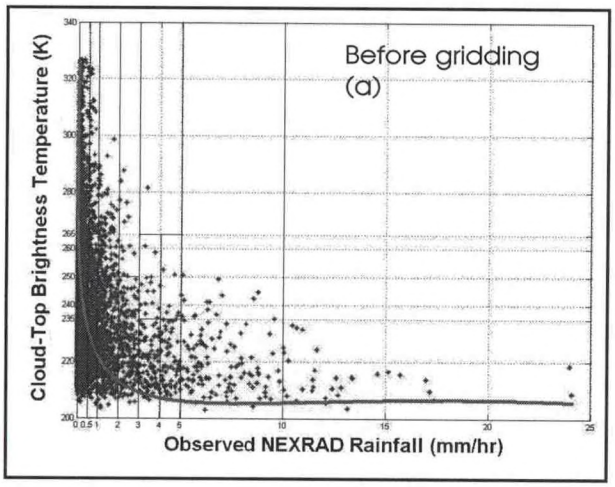

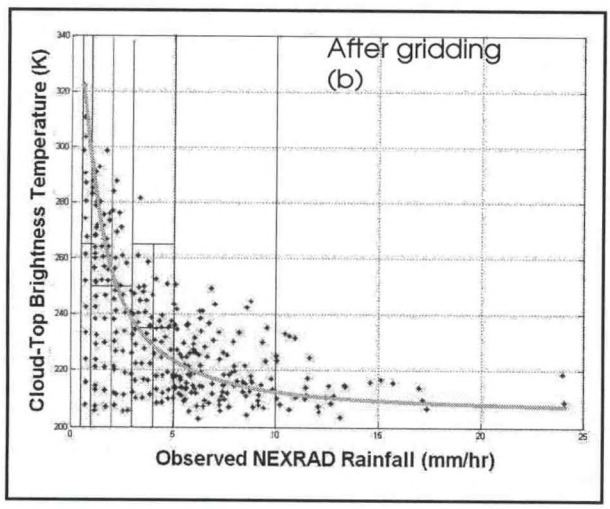

Fig.3 a, b – Illustrates the cloud-top infrared Tb and NEXRAD rainfall observation before (a) and after (b) the gridding approach for several hours of data files on July 10 2002.

Minimizing sampling error would reduce the effect of low rainfall values on Tb-RR relationship to improve model rainfall estimates. A cloud classification scheme has to be developed for portioning clouds into different categories to be able to derive more accurate Tb-R relationship for each cloud type.

Sampling Error Minimization

As the brightness temperature of a cloud-top decreases (get colder), the more chance to produce heavier rainfalls than light rainfalls and vice versa as the temperature of a cloud increases (gets warmer).

The number of pixels with very small rainfall rates are much greater than the number of pixels with higher rainfall rates (fig.3 a). There are a large number of sample pixels with lighter rainfall. They are predominant in the Tb IR-RR relationship. Those pixels create a sampling disproportion in the sampling of the data. A gridding approach is used to diminish the effect of sampling error, by lowering the number of lighter rainfalls so that the rainfall estimates would be more representative of the heavier rainfalls, which are more significant to the forecasting flashfloods. This gridding approach consists of designing several grid sizes with specific parameters of Tb and RR. Figure 3.b illustrates the Tb IR-RR relationship after applying the gridding method.

Results

The model rainfall estimates compared with radar-based observed rainfall for calibration case and also for validation case are displayed below. The scatter-plot of the PERSIAN-based model estimates for several hours of data files for July 10 2002 of the calibration case, model rainfall estimate versus ground-based NEXRAD rainfall observations is illustrated in figure 4. It shows also the model rainfall estimates from Tb IR before and after the gridding method with radar-based rainfall. There is a considerable improvement on the model rainfall estimates after using data from the gridding method, due to the increase in correlation coefficient from 0.2955 to 0.5199.

To evaluate the model output, the derived input-output relationship is used to retrieve rainfall for 24 hours of the rainy day, July 23 2002, validation case. Estimated rainfall using the trained PERSIANN model compared with the radar-based observed rainfall is illustrated in the figures below (5). There is a not a considerable improvement on the model rainfall estimates after using data from the gridding method, due to the increase in correlation coefficient from 0.4289 to 0.5717.

Primary Conclusions

The primary results, only for two days, are not enough for giving certain conclusions. However, there are several results that can be concluded from this test. PERSIANN can be improved and can produce high-resolution rainfall estimates from satellite IR imagery. Also, reducing sampling-error could improve Tb-R relationship and too improve model rainfall estimates (figure 7). The results of the test achieved to evaluate the trained-model output for 24 sample hours, validation case, illustrated in figure 5,

are reasonable. Thereof, improving sampling-error optimization can ameliorate the quality of hourly and fine space scale model rainfall estimates.

Future Work

In the future, the reduction of the other uncertainties to enhancing accuracy of high temporal, hourly, resolution of model rainfall estimates and the blending of high-resolution satellite IR-based estimates with the fine scale NEXRAD Rainfall estimates using successive correction method (SCM) will be performed.

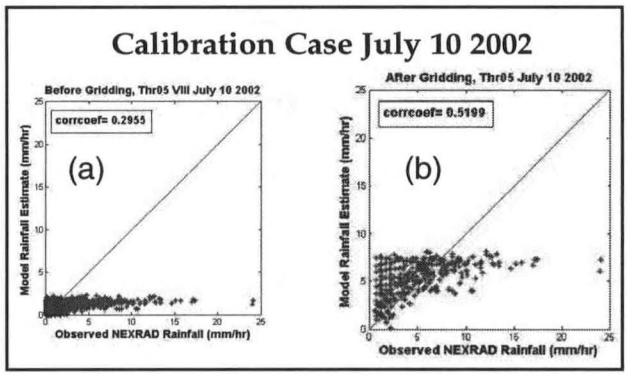

Fig 4 a, b – Model rainfall estimates versus NEXRAD rainfall observations for several hours' data files, from day July 10 2002, before (a) and after (b) using data from the gridding method.

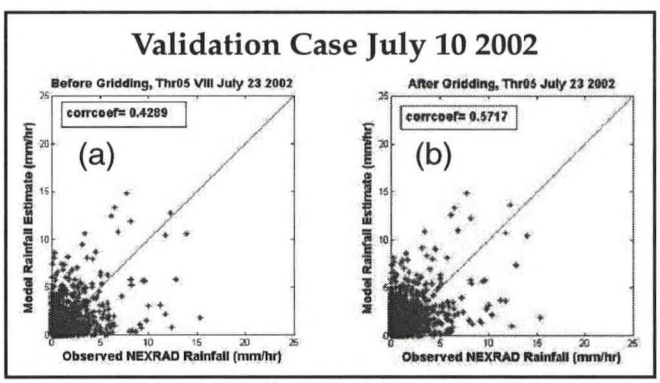

Fig 5 a, b – Illustrates model rainfall estimates versus ground-based radar rainfall observations for 24 hours of the day July 23, 2002.

REFERENCES

Adler, R. F., A. J. Negri, P. R. Keehn and I. M. Hakkarinen, 1993. Estimation of monthly rainfall over Japan and surrounding waters from combination of low-orbit microwave and geosynchronous IR data. J. Appl. Meteor., 32, 335-356.

Grassoti, C. and L. Garand, 1994: Classification-based rainfall estimation using satellite data and numerical forecast model fields. J. of Applied Meteorology, 33, 159-178.

Hsu, K., H., Gupta, S., Sorooshian, and X., Gao, Oct 16-18 1996: An artificial neural network model for rainfall estimation from satellite infrared imagery. Application of Remote Sensing in Hydrology, Proceedings of the Third International Workshop, Greenbelt, MD, USA, NASA Goddard Space Flight Center.

Lee, T. H., J. E. Janowiak, and P. A, Arkin, 1991: Atlas of products from the algorithm intercomparison project 1. Japan and surrounding oceanic regions June-August 1989, Boulder, CO, University Corporation for Atmospheric Research.

Negri, A. J., R. F., Adler, 1993: An intercomparison of three satellite infrared rainfall techniques over Japan and surrounding waters. J. of Applied Meteoro., 32, 357-373.

Petty, G. W., 1995: The status of satellite-based rainfall estimation over land. Remote Sensing of the Environment, 51, 125-137.

Scofield, R. A. 1987: The NESDIS operational convective precipitation technique. Monthly Weather Review, 115, 1773-1792.

Xie, P., and P. A. Arkin, 1996: Analyses of global monthly precipitation using gauge observations, satellite estimates, and model predictions, Journal of Climate, 9, 840-858.

Zurada, J.M., 1992: Introduction to Artificial Neural Systems, West Publishing, St. Paul, MN.

MONITORING REMOTELY SENSED RAINFALL ESTIMATES OVER TROPICAL REGION

Jose Fernandez, Shayesteh Mahani, and Reza Khanbilvardi°Atmospheric Sciences,, Howard National Oceanic and Atmospheric Administration Cooperative Remote Sensing Science and Technology Center, NOAA-CREST Center, Civil Engineering Department, City College of New York, Steinman Hall, T-107 140th Street at Convent Avenue, New York, NY 10031, United States. (212-650-8099; *jf@ce.ccny.cuny.edu*)

Abstract

This is a project, started about one month ago, focuses on monitoring the quality of satellite-based tropical rainfall estimates over tropical regions. A study site is selected over LLORO (5∞ 30′ N, 76∞ 32′ W, and 33 m elevation) located in the CHOCO area in the Colombia country next to the Pacific ocean, because of having significant amount of rainfall, experimentally about 8000 to 13000 (mm/yr) average annual precipitation. Deep convection developed from low-level moisture convergence combined with orographic lifting on the western Andes is very effective on producing heavy storms over this region.

In this study, two satellite-based rainfall products: (1) hourly 0.25∞ x 0.25∞ resolution rainfall product from PERSIANN (Precipitation Estimation from Remotely Sensed Information using an Artificial Neural Networks) model, and (2) daily 1∞ x 1∞ resolution GPCP (Global Precipitation Climatology Project) rainfall product are selected. Accurate hourly and daily rain gauges observations are expected to be used for evaluating the quality of the satellite-based precipitation estimates. Daily PERSIANN and gauge rainfall have been compared for a few days, with heavy storms, in July 2003. The primary results of this test demonstrate satellite-based rainfall products are over estimated with compare to the rain gauge observations. This primary conclusion will be examined by evaluating more daily- and hourly-based remotely sensed rainfall in future work.

Introduction

Despite the traditional ground-based radar and gauge rainfall observation technique, remote sensing is the new and only method that can provide required information over large and continuous spatial and temporal coverage. Rainfall is a one of the products from satellite-based cloud information. Accurate remotely sensed rainfall estimates are very important to be available to water related communities, such as hydrologists, water resources managers, NWS, and hydro-climatologists, for flood forecasting, wet/drought prediction, and so on. In this study, quality of tropical rainfall estimates, from satellite IR imagery, are examined over a tropical region. Satellite-based rainfall products from PERSIANN (Precipitation Estimation from Remotely Sensed Information using neural Networks), developed by Hsu, (1997) in the University of Arizona, in both daily and hourly resolutions and daily GPCP (Global Precipitation Climatology Project) are selected to be evaluated versus daily and hourly ground-based gauge rainfall observations.

A tropical study site with high amounts of precipitation as well as the density of gauges has been selected over LLORO (5° 30′ N, 76° 32′ W) in the region of CHOCO in Colombia Country. This region is mostly covered by tropical rain forest with average air temperature (26-28) °C and mean relative humidity (90 %) throughout the year. The selected study site is mostly covered by tropical rain forest and it is one of the rainiest regions in the world, Poveda and Mesa, (2000). Regarding to the size of tropical storms and topography, the study region is a 12∞ x 12∞ degrees area, in latitude-longitude directions, from 0° to 12° North and from 68° to 80° West, with 48 x 48 pixels. Study site includes mountainous and costal regions. Figure 1, shows the map of study area and rain gauges located over this site.

Rainfall patterns, spatially, and also time series from satellite- and gauge-based rainfall are compared and analyzed over the selected study area. Several particular cases for specific storms in different seasons (warm and cold seasons) at least in two years will be studied. In the first case study three day storms selected July 2003. Daily PERSIANN with 0.25° x 0.25° resolutions is validated versus daily ground-based rain gauge observations

from 30 gauges. Daily rain gauge data are used in this project, have been downloaded from NCDC (National Climatic Data Center). Daily-based rainfall is selected to be evaluated because of not having access to the hourly rain gauge observations. Therefore, hourly-based evaluation will be the time resolution of the next study cases.

The objective of this study is to evaluate the quality of satellite-based tropical rainfall estimates in two: daily and hourly resolution rainfall from PERSIANN model, and daily resolution GPCP, with compare to the rain gauge observations, over the selected tropical area.

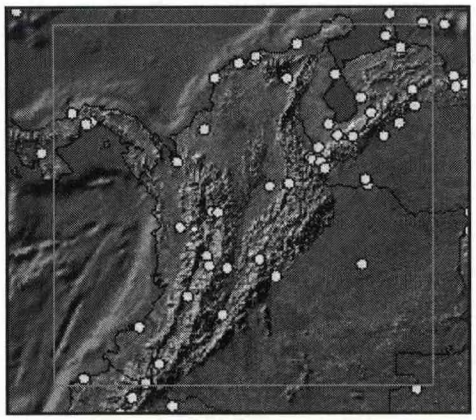

Figure 1: The map of study area and rain gauges.

Methodology

In order to accomplish with the mentioned objective, it is necessary to organize the data to the selected study site. The patterns and amounts of satellite-based rainfall estimates are compared spatially with the rain gauge observations. These data will be compared and analyzed based on time variability (time series) in different clod and warm seasons, as well. In the fist case study, daily PERSIANN rainfall estimated from satellite-based infrared cloud-top brightness temperature for three rainy days in July 2003 have been compared with daily rain gauge data over the selected study area. Figure 2 demonstrates the comparison between the mentioned from two different: satellite and ground sources. The obtained primary results cannot help to give a certain conclusion. Quality of satellite-based rainfall estimates over tropical regions must be tested for more and different types of storms, longer study time in different seasons, with higher time and space resolutions, and from different rainfall retrieval algorithms.

Discussion

Comparison of the daily rain gauge observations with the daily PERSIANN product at 0.25° x 0.25° lat-lon resolution, for the first case study, is illustrated in the Figure 2. Following scatter-plot shows the relationship between satellite- and gauge-based rainfall measurements. The primary conclusion from this figure is that the output of PERSIANN model, satellite IR-Tb based rainfall, is over estimated with compare to the ground-based rain gauge observations at daily-based resolution.

Future Work

Evaluating satellite-based daily tropical rainfall products, in space and time, for more storms based on seasonal variability. Hourly-based remotely sensed rainfall estimates will also be compared, both spatially and temporarily, with the hourly rain gauge observations. Analyzing the results based on the topography and climate conditions over the selected tropical study region.

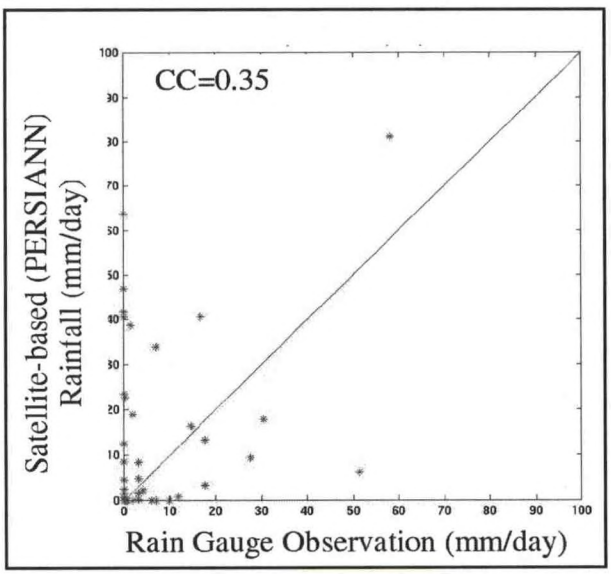

Figure 2: Satellite-based rainfall estimates (using PERSIANN model) vs ground-based rain gauge observations.

REFERENCES

Hsu, K., X. Gao, S. Sorooshian, and H. Gupta, 1997: Pricipitation Estimation from Remotely Sensed Information using Artificial Neural Networks, J. Appl. Meteo., V. 36 (9).

Poveda, G., and O.J. Mesa, 2000: On the Existence of Lloro (the Rainiest Locality on Earth): Enhanced Ocean-Land-Atmosphere Interaction by a Law-Level Jet. Geo. Reas.Letters, V. 27 (11), 1675-1678

A Study of Coupled MM5/WRF Model in Simulation of Landfalling Hurrican Isidore Over the Gulf of Mexico

Alexander Schwartz, Markeitta D. Benjamin and R. Suseela Reddy
Jackson State University, Jackson, Mississippi

Abstract

Tropical Cyclone/Hurricane is nature's catastrophe. As a result, the Gulf costal states region is prone to the highest national frequency to severe weather accompanied by huge economic loss. Understanding of modeling and predicting the coastal processes and dynamics over the region are important in improving weather forecasting of landfalling hurricanes. A mesoscale modeling investigation of tropical cyclone/hurricane forecast over the Gulf of Mexico has been undertaken pertaining to NOAA's interest to assess and predict tropical cyclone intensity, track and environmental changes. The goal is to provide decision makers with reliable scientific information to protect life and property.

Previous studies (Reddy and Schwartz 2004) have established the relationship between ocean-atmospheric interactions and tropical cyclones/hurricanes over the Gulf of Mexico. They identified that ocean-atmospheric interactions play a prevalent role in exchanging heat, momentum and moisture fluxes and associated tropical cyclones/hurricanes using numerical modeling and data assimilation techniques over the Gulf of Mexico. In the present study we have developed a Weather Research and Forecasting (WRF) model run on a high performance computing environment using non-conventional datasets. Data from the PennState\/NCAR MM5 v.3 model is fed into the WRF v.1.3 model as initial and lateral boundary conditions to simulate the surface features of a case oriented 2002 landfalling hurricane Isidore, September 14-22. Simulation parameters include sea level pressures, surface fluxes, sea surface temperature, wind direction and magnitude, and precipitation. The results will be compared with aircraft observations taken by the National Hurricane Center. This model output is then incorporated into a decision support matrix. The results of the model simulations will be presented and discussed. The work is supported by NOAA Howard project at Jackson State University.

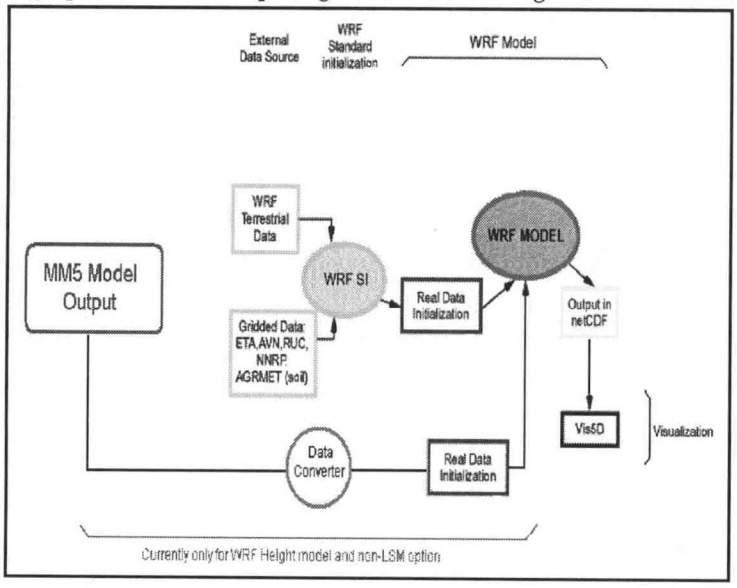

Figure 1: WRF/MM5 Coupling

Introduction

From Maine to Texas, several million people spend their lives without knowing the colossal effects of a hurricane. Hurricanes,

* Corresponding authors address:
R. Suseela Reddy, Jackson State University, Dept. of Physics, Atmospheric Science and General Science, Jackson, MS 39217; e-mail: rsreddy@ccaix.jsums.edu.
Alexander Schwartz, Graduate Research Assistant, Jackson State University, Dept. of Physics, Atmospheric Science and General Science, Jackson, MS 39217; e-mail: alex@msp.jsums.edu.

one of the most feared and respected natural phenomena obliterate life and property in an ambush. Deadly winds, storm surges, and floods are all natural foes of human inhabitation. The Atlantic hurricane season begins 1st June until the end of November. Low air pressure, tropical rainfall patterns, and warm ocean waters all contribute to a hurricane's development and intensification. Although modern technology has been a great helping-hand in tracking hurricanes, predicting the formation, movement, and strength of a hurricane has never been an easy task. Several computation models have been developed for this reason, yet it is merely a guess. Meteorologists rely on models to simulate and predict the weather circulation patterns as close to reality as possible, and along the way corroborate with time and space efficiency issues.

Previous studies (Reddy et.al, 2004) show that air sea interactions play a vital role in the birth and growth of hurricanes. In this study, we investigate the air-sea interactions for a selected cyclone/hurricane over the Gulf of Mexico during the hurricane season 2002 using Penn State/NCAR MM5 and Weather Research and Forecasting (WRFV2) models. These modeling system are useful research tools used for weather diagnostics and prediction. We present the results of the above investigations for Hurricane Isidore 14-26, 2002.

Dynamics	***Non-hydrostatic***		
High resolution	*30 km*		
Vertical Layers	*23*		
Simulation Period	*2 days*		
Initialization	*NCEP Global Analysis*	*2-way*	*2-way*
Radiation Scheme	*Dudhia Simple*		
Microphysics	*Simple*		
Cumulus Scheme	*Grell*		
PBL Scheme	*Blackadar*		

Table 1: MM5 Configuration

Dynamics	***Non-hydrostatic***		
High resolution	*30 km*		
Vertical Layers	*23*		
Simulation Period	*2 days*		
Initialization	*NCEP Global Analysis*	*2-way*	*2-way*
Radiation Scheme	*Dudhia Simple*		
Microphysics	*Simple*		
Cumulus Scheme	*Grell*		

Table 2: WRF Configuration

History

On the 18th, Tropical Depression Ten became Tropical Storm Isidore with a wind speed of 35 knots and central pressure of 1006mb. As Isidore continued to strengthen it reached category two hurricane status as it approached Cuba on the 19th with a minimum pressure of 984mb and wind speed of 70 knots. Isidore crossed the western portion of Cuba on the night of 20 September with a minimum pressure of 961mb right before it made landfall. Isidore continued to move westward leading into the Southeastern portion of the Gulf of Mexico on the 21st and hit Northern Yucatan peninsula as a category three hurricane on the 22nd.

As convection decreased, Hurricane Isidore was downgraded to Tropical Storm Isidore on 23 September as it moved farther into the Gulf of Mexico. As Isidore continued to move towards the United States rain and high wind speeds of 70 mph stretched across most of the Gulf of Mexico. Isidore made landfall on the Louisiana coast early 26 September. It continued to move northeastward as it passed through Louisiana, Mississippi and parts of Alabama as show in Figure 2. Tropical Storm Isidore weakened as it continued to move across land and dissipated on 26 September. Isidore brought on about 13 inches of rain in Louisiana and Mississippi after it made landfall and extensive damage to western Cuba. On the whole Hurricane Isidore had a life span of 12 days with a minimum pressure of 934mb and maximum winds of 125 mph.

Methodology

Upon applying the initialization schemes to atmospheric data within a mesoscale domain, 84 hour forecasts/simulations were made using WRF model at high resolution. Comparisons of the model performance based on the differing initializations are conducted with emphasis primarily on surface or near-surface quantities (Cox et. al. 1998). Parameters considered which include precipitation, surface fluxes, sea level pressure, surface temperature and wind magnitude. Observed data sets used in simulations include observations from FAA/NWS sites and other applicable surface observing networks in order to maximize the ability to detect

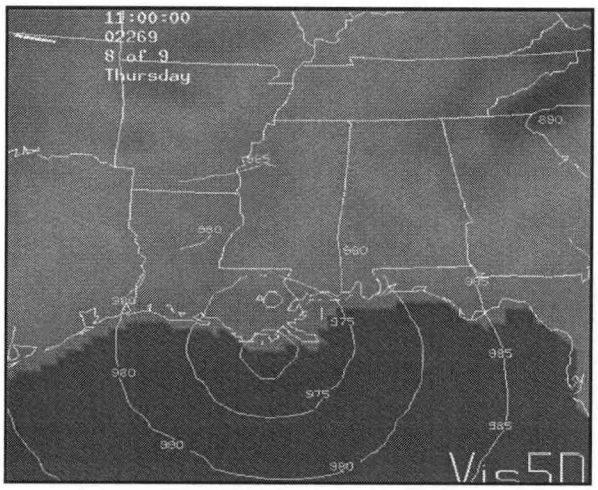

Figure 2 (a) – Sea Level Pressure (mb)

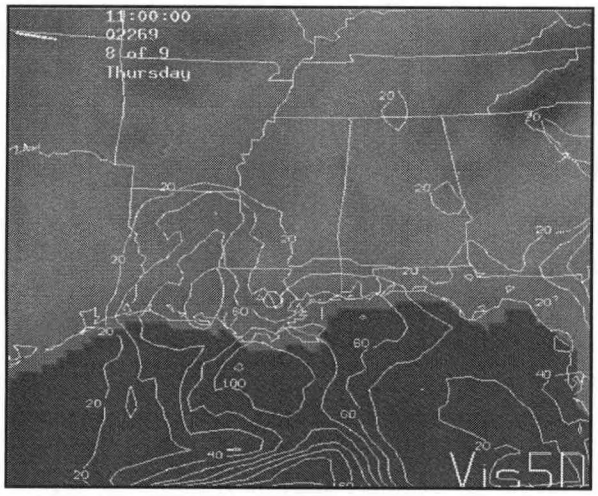

Figure 2 (b) – Precipitation (mm)

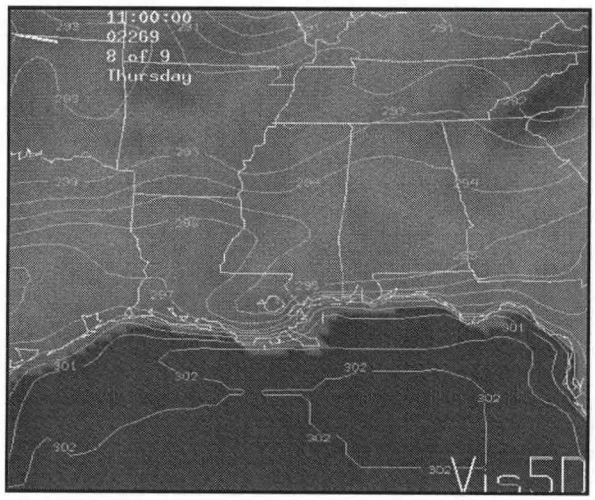

Figure 2 (c) – SST (°K)

mesoscale features.

NCEP Global Analyses containing surface, tropospheric, tropopause and lower stratospheric analyses are used to initialize MM5 run. Objective analysis in MM5 is done using NCEP ADP global upper air observations which are synoptically sorted. Since NCEP uses this dataset in its models there are many quality controls applied to it.

Configuration

4.1. MM5

The area of interest in this setup is also over the Gulf of Mexico region where only a single domain of 30 km horizontal grid distance was fixed with a central of Lat/Lon of 31.5N and 89.4W. Domain grid dimension is 49¥52.

Model initial and lateral boundary conditions were obtained from the NCEP Final Analyses (FNL), currently same as the AVN global analysis, gridded meteorological pressure-level data on a 1¥1 degree Lat/Lon resolution available four times daily. Observational analysis was not performed in this run. The model was run for two days when the storm was approaching the coast on 25 – 26, September 2002.

4.2. WRF

The MM5 model output is then used to construct initial and lateral boundary conditions for the WRF run. WRF (Klemp 2004) is run on height coordinate (Reddy et. al. 2004). A simple flowchart of the working is shown in Figure 1.

Results

For Hurricane Isidore we have provided results shown in Figures 2 (a-) of WRF/MM5 simulation of sea level pressure, surface fluxes, precipitation and wind magnitude at 1100Z on 26 during landfall.

The model is capable to capture predictions close to the actual observations made by NOAA National Hurricane Center. The observed vs. predicted readings are shown in Table 1-4.

We developed this model to understand the formation, development and dynamics by studying the fluxes generated by these powerful storms. The model run for a tropical storm could be compared with the model run for a hurricane to show the intensity differences between them and what caused Hurricane Isidore to build up from a storm to a hurricane. We have discussed our investigation in the following section.

Conclusion

- The WRF model simulations for 48-hr period simula-

tion have been improved by ingesting MM5 output for initial and lateral boundary conditions.

• The maximum values predicted at the center of the storm for hurricane Isidore during the hurricane to tropical storm weakening stage were 240 Watts/m2 (heat flux), 700 Watts/m2 (latent flux), and 48 cm (accumulated convective precipitation).

• The fluxes, precipitation and wind were observed and simulated mostly south, northeast and eastern sectors of the storm.

• The average sea surface temperature of 28∞C was observed over the Gulf of Mexico.

• WRF predicted central pressure, wind speed, and precipitation close to the observations.

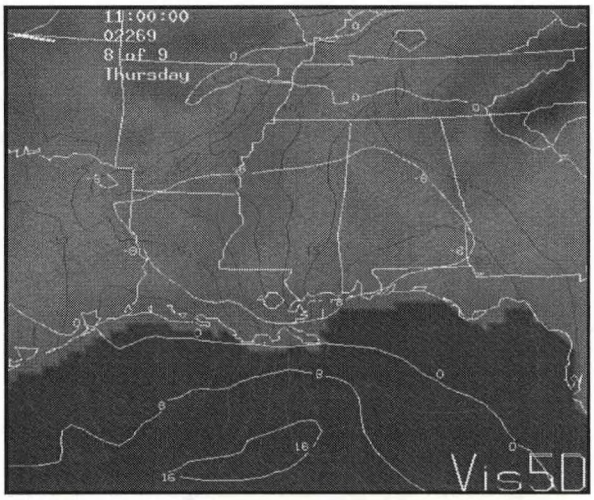

Figure 2 (d) – u,v Wind Magnitude (m/s)

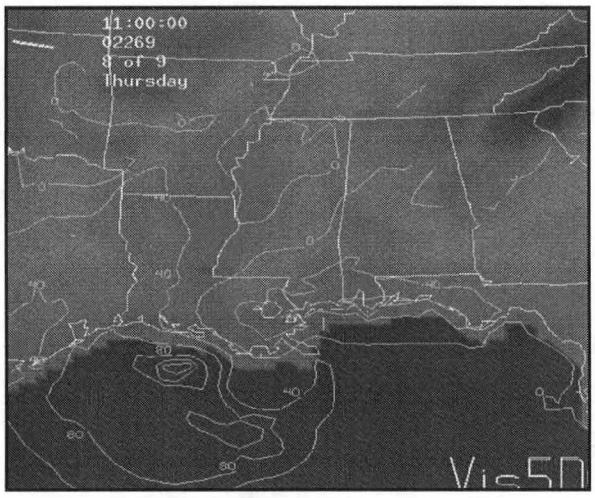

Figure 2 (e) – Heat Flux (W/m2)

Before weakening into a tropical storm, hurricane Isidore contained very strong fluxes, which showed the intensity of a category three hurricane. These flux patterns could also help study the air-sea interactions difference between a tropical storm and a hurricane. Also, by analyzing the structure and dynamics configuration of various cases of tropical cyclones with the help of a numerical model we could more certainly predict the track and intensity change of the storm.

H. Isidore	Observed	Simulated	
		MM5	MM5 /WRF
Central Pressure (mb)	988.7	984	970
Rainfall (cm)	28.7	20.32	18
Wind Speed (m/s)	32.3	20	21

Table 4 – Comparison Table

ACKNOWLEDGEMENTS

The research is supported by NOAA Center for Atmospheric Sciences (NCAS) at Howard University, and Grant No. 634499 at Jackson State University.

REFERENCES

Grell, G., 1993: Prognostic evaluation of assumptions used by cumulus parameterizations. Mon. Wea. Rev., vol. 121, 764-787.

Klemp, J. B., 2004: Next-Generation Mesoscale Modeling: "A technical overview of WRF" Presentation at the 20th Conference on Weather Analysis and Forecasting and 16th Conference on Numerical Weather Prediction. Seattle, Washington, 11-15 January 2004.

Kain, J. S., and J. M., Fritsch, 1993: The representation of cumulus convection in Numerical Models, Meteor. Monger., No. 46, AMS, 165-177.

Reddy, R. S., A. Schwartz, M. A. Askelson, and L. Osborne, 2004: "Data Assimilation using Weather Research and Forecasting Model: An Effort to Improve Fine Scale Modeling", Proc. of the 20th Conference on Weather Analysis and Forecasting/16th Conference on Numerical Weather Prediction, American Meteorological Society, Seattle, Washington, 11-15 January 2004. 46, American Meteorological Society, 165-177.

EFFECT OF GEOMAGNETIC STORMS ON OCEAN-ATMOSPHERIC INTERACTIONS OVER THE GULF OF MEXICO

R. Suseela Reddy, Arundhati Surakanti and Rezwanul Karim

Department of Physics, Atmospheric Sciences and General Science, Jackson State University, Jackson, Mississippi 39217

E-mail: *rsreddy@ccaix.jsums.edu, arundhati.r.surakanti@ccaix.jsums.edu, rkarim@ccaix.jsums.edu*

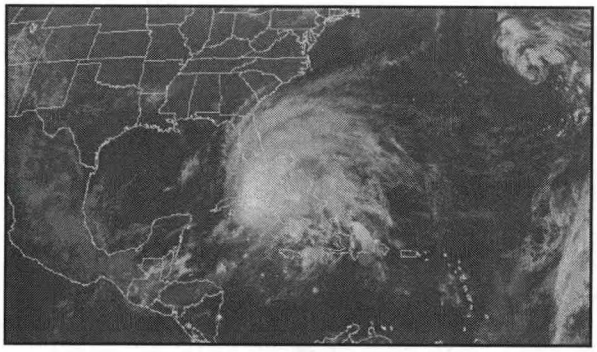

Figure 1: GOES 8 IR 5 NOV 2001 AT 00:15 UTC

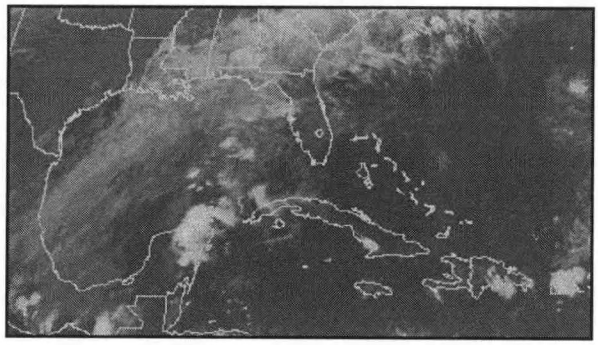

Figure 2: GOES 12 IR 28 OCT 2003 AT 00:15 UTC

Abstract

We investigate the relationship between major geomagnetic storms and ocean-atmospheric interactions including heat, momentum and latent heat fluxes over the Gulf of Mexico during winter months (Oct-Dec) for the years 2001 and 2003.The data used in this study include (i) Geomagnetic storms, and (ii) Buoy data (sea surface temperature, air temperature, sea level pressure and wind speed) obtained from National Data Buoy Center (NDBC). The fluxes were computed using standard bulk formulae. The statistical techniques used for data analysis include superposed epoch analysis and student t-test. The results of the study have pointed out a significant increase in the fluxes during the development of the storm and 0-2 days on and before the storm occurrence using superposed epoch analysis. The effect of these fluxes on Gulf coast weather is noticed. The study is important for further understanding the climate variability of large-scale circulations including ElNino/ Southern Oscillation (ENSO).

There is accumulated evidence from recent past literature to show the possible relation between solar and geomagnetic activity, and meteorological parameters (Reddy et.al., 1978; Bhalme et.al., 1981; Reddy and Karim, 2003). Not many studies have been reported on the relationship between geomagnetic activity and terrestrial weather including ocean-atmospheric interactions that have significant impacts over the large-scale atmospheric circulations.

* Corresponding authors address:
R. Suseela Reddy, Jackson State University, Dept. of Physics, Atmospheric Science and General Science, Jackson, MS 39217; e-mail: rsreddy@ccaix.jsums.edu.
Arundhati Surakanti, Graduate Research Assistant, Jackson State University, Dept. of Physics, Atmospheric Science and General Science, Jackson, MS 39217; e-mail: arundhati.r.surakanti@ccaix.jsums.edu.

Between the ocean surface and the atmosphere, there is an exchange of heat and moisture that depend in part, on temperature differences between water and air. In winter, when air-water temperature contrasts are greatest, there is a substantial transfer of sensible and latent heat from the ocean surface into the atmosphere. This energy helps to maintain the global airflow.

In the present study, we investigate the relationship between the major Geomagnetic storms and Ocean-atmospheric interactions including heat, momentum and moisture fluxes.

Data and Analysis

The data for (i) geomagnetic storms were obtained from NOAA National Geophysical Data Center (NGDC) and (ii) meteorological surface observations were obtained from National Buoy Data Center (NBDC). The fluxes for heat, momentum and latent heat were computed using standard "bulk" formulae. The values for fluxes so obtained were analyzed using superposed epoch analysis and student t-test during the geomagnetic storm activity.

Computations

In the context of large-scale ocean-atmospheric interactions, exchanges can be conveniently represented in terms of 'bulk' parameters of the sea-air interface. Thus, the heat flux (H) from the ocean to the atmosphere, the momentum flux (_) from atmosphere into the ocean and latent heat flux (LH) are given by:

Heat Flux, $H = \_ C_p C_h (T_s - T_a) u_a$, (1)

Momentum Flux, $\_ = \_ C_D u_a^2$, (2)

Latent Heat Flux, $LH = \_ L_v C_E (q_s - q_a) u_a$, (3)

Specific Humidity, $q = \_ e/p$ (4)

Where, _ is the density of air and C_p is specific heat, $(T_s - T_a)$ and $(q_s - q_a)$ are sea-air differences of temperature and specific humidity, u_a is the wind speed near the surface, e is the vapor pressure and p is the total pressure at the surface, and C_D, C_h, C_E are non-dimensional bulk transfer coefficients for momentum, heat and water vapor, and L_v is Latent Heat of Vaporization.

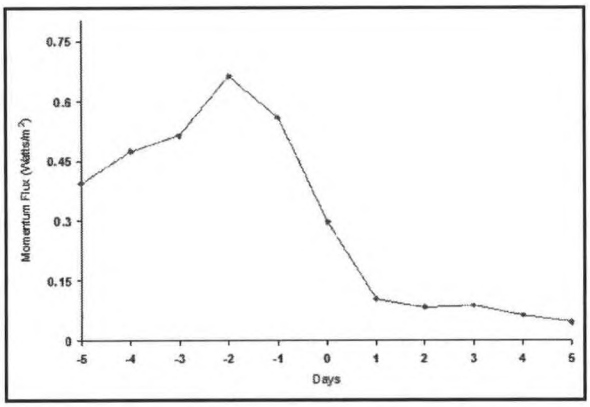

Figure 3: Superposed epoch analysis of Heat Flux followed by the Geomagnetic Storm (Nov 06, 2001 zero day).

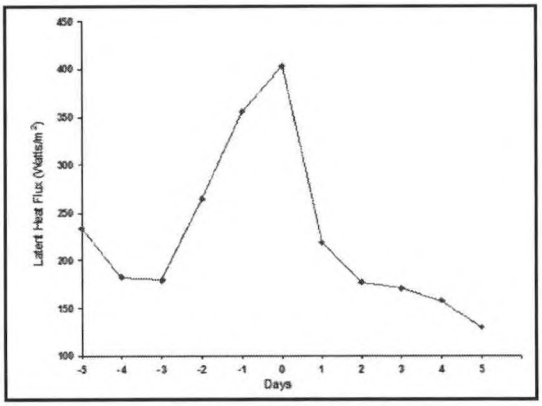

Figure 4: Superposed epoch analysis of Momentum Flux followed by the Geomagnetic Storm (Nov 06, 2001 zero day).

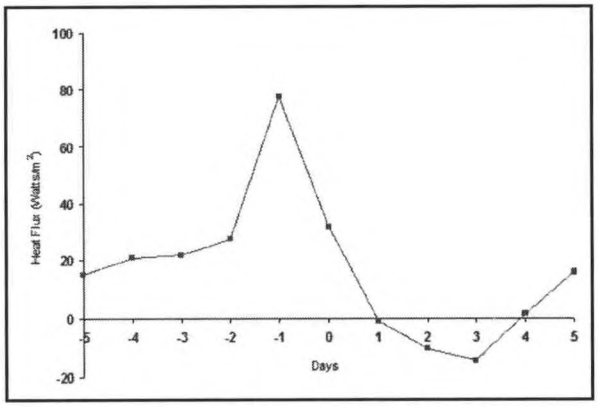

Figure 5: Superposed epoch analysis of Latent Heat Flux followed by the Geomagnetic Storm (Nov 06, 2001 zero day).

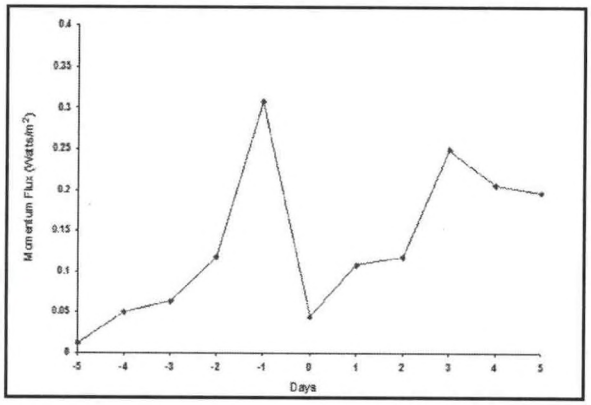

Figure 6: Superposed epoch analysis of Heat Flux followed by the Geomagnetic Storm (Oct 29, 2003 zero day).

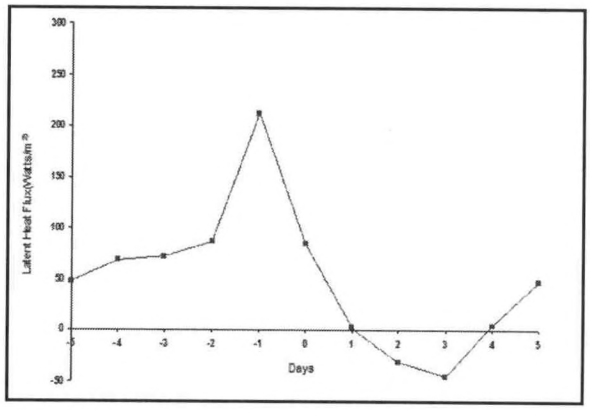

Figure 7: Superposed epoch analysis of Momentum Flux followed by the Geomagnetic Storm (Oct 29, 2003 zero day)

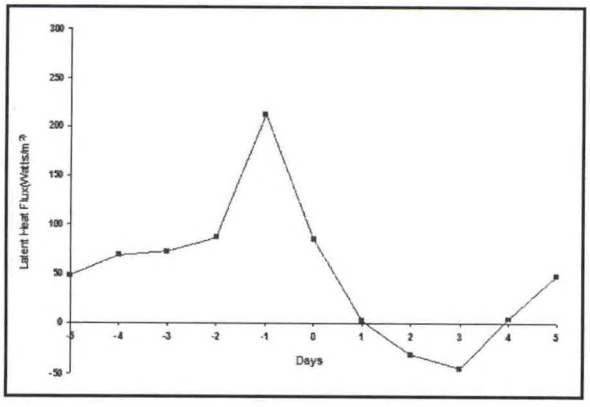

Figure 8: Superposed epoch analysis of Latent Heat Flux followed by the Geomagnetic Storm (Oct 29, 2003 zero day).

Figures 1 and 2 show satellite images over the Gulf of Mexico during the following days: 5 November 2001 and 28 October 2003.

Observations of meteorological parameters during geomagnetic activity are shown below in Table 1.

Date	Wind Speed (m/s)	Water Temp (°C)	Air Temp (°C)	Sea Level Pressure (mb)	Air-Sea Interface (°C)
27	5.40	28.10	27.30	1011	0.80
28	5.00	27.90	26.60	1010	1.30
29	4.00	28.10	24.90	1006	3.30
30	6.40	28.00	26.10	1016	2.10
31	10.70	27.90	26.20	1017	1.70
01	8.10	27.60	25.70	1016	1.90
02	8.20	27.70	26.80	1016	2.00
03	8.90	27.80	26.20	1013	1.60

Results and Discussion

The results of the study have pointed out the following:

- A significant increase in the fluxes (heat, momentum and latent heat) during the development of the geomagnetic storm on and 2 days before the storm occurrence was observed (Figures 3 – 8).
- A decrease in sea level pressure following the geomagnetic storm.
- GOES Satellite IR images show a strong convection during development of the storm (Figures 1 – 2).

At times when air-water temperature contrasts are greatest there is a substantial transfer of sensible and latent heat from the ocean surface into the atmosphere.

Cooling of the air temperature during the development of the storm is important for further understanding the observed relationships.

The study is important for further understanding the climate variability of large-scale circulations including ElNino/Southern Oscillation (ENSO).

ACKNOWLEDGEMENTS

The research is supported by the NOAA/Howard University National Center for Atmospheric Sciences (NCAS) Grant # 634499 at Jackson State University.

REFERENCES

Reddy, R. S., S. S.Paranis and Bh. V. Ramana Murthy., 1978: Geomagnetic activity and rainfall during the northeast monsoon. Indian J. Radio and Space Physics, Vol. 8.

Bhalme, H. N., R. S. Reddy, D.A. Mooley and Bh. V. Ramana Murty., 1981: Solar activity and Indian Weather/climate; Proc. of the Indian Academy of Sciences. Vol.90, pp.245-262.

Reddy R. S. and R. Karim., Effect of Geomagnetic Storms on Ocean Atmospheric Interactions over the Gulf of Mexico. Extended Abstracts, 35th COSPAR Scientific Assembly, PARIS, FRANCE, 18-25 July 2004.

Possible Hailstorm Observed by Mesonet Station

Dr. Loren White and Dr. James Finney
Jackson State University

On July 16 at approximately 11:00 AM CST a strong thunderstorm passed over the Newton County, MS, mesonet station. Although only 0.41 inches of rain were recorded at the observing site, local reports indicated hail in the area. The first precipitation was measured at 10:52, six minutes after the air temperature began rapidly dropping (as fast as 1.8 C or 3.2 F per minute). A three-second wind gust over 48 mph was observed at 10 m, along with rapid variations in station pressure. The presence of small melting hail at the site is hypothesized based on soil temperature response and near-surface lapse rate. Until the precipitation began (or at least began to be measured by the tipping bucket raingage), the soil temperature at a depth of 5 cm was dropping at a rate of only about 0.1 C (or 0.2 F) per minute. However between 10:53 and 10:54 the soil temperature dropped from 32.2 C (90.0 F) to 30.5 C (86.9 F), continuing to cool over the next several minutes down to 27.4 C (81.2 F). A very impressive drop in 10 cm soil temperature began just one minute later. This is strongly indicative of the rapid percolation of unusually cold rainwater or melted hail into the soil. Other evidence is that a very rare daytime surface inversion began within a few minutes of the first reported precipitation, and lasted for about 45 minutes. Temperatures were as much as 1.7 C (or 3.1 F) cooler at 1.5 m than at 10 m, indicating significant cooling coming from the ground.

A Multiseason Comparison of the Forecast Skills among Three Numerical Models over South-central United States

Lu, D; White, L J; Reddy, S R; Karim, R
Jackson State University

Abstract

Three numerical weather forecast models, the WRF, MM5, and COAMPS, operating with a joint effort of NOAA HU-NCAS and Jackson State University (JSU) during summer 2003 and winter 2003~2004 have been chosen to study their forecast skills against observations. The models forecast over the same region with the same initialization, boundary condition, forecast length and spatial resolution. The AVN global dataset have been ingested as initial conditions. The grid resolution of 27 km has been chosen to represent the current mesoscale model. The forecasts with the length of 36h are performed to output the result with 12h interval. The key parameters used to evaluate the forecast skill include 12h accumulated precipitation, sea level pressure, surface wind speed, and surface temperature. Precipitation is evaluated statistically using conventional skill scores, Threat Score (TS), Bias Score (BS), False Alarm Ratio (FAR), Probability Of Detection (POD) and Kuilers Skill Score(KSS), for different threshold values based on 12h rainfall observations whereas other variables were studied using statistical methods such as Mean Error (ME), Mean Absolute Error (MAE) and Root Mean Square Error (RMSE).

Introduction

Recent advances in computer power have significantly decreased the computational time and increased the memory capacity so that real-time numerical weather prediction has spread rapidly from operational center such as NCEP to universities, government agencies, and private industry. However, objective model verification is not always completed for these real-time modeling systems, and many forecasters have little understanding of how these modeling systems perform

Recently, many studies have been focused on the model forecast comparison between MM5 and/or NCEP Eta. Oncley and Dudhia (1995) documented that the daytime cool bias of model simulation can be exacerbated by excessive soil moisture availability in the model, which provides excessive latent heat flux (evaporative cooling) and less sensible heating. Mannin and Davis (1997) showed that the daytime low-level cool bias in the MM5 was also enhanced by too much ice initiation (clouds) aloft. They also found that the forecasted winds over the central United States are too fast near the surface and too slow aloft during cool season. Colle et al. (2003) showed that, during the cool season, both the MM5 and Eta have a low-level cool and moist bias over land, a significant surface warm bias over water and surface winds that are too strong over land to the east of Rockies and too weak over water. During the warm season, the MM5 and Eta have little temperature bias over water, a negative wind speed bias over Rockies and a surface dry and warm bias over land.

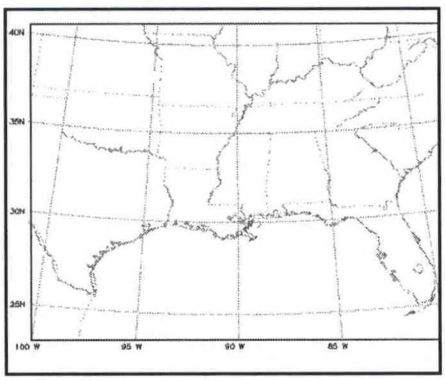

Fig.1 Forecast domain for three models.

On the other hand, model forecast skill of precipitation has not increased as rapidly as other variables in recent years. The errors in quantitative precipitation forecasts (QPF) can result primarily from initial condition uncertainties, insufficient horizontal

resolution, and deficiencies in model microphysics and convective parameterizations. Colle et al. (2003) studied multiseason verification of the MM5 precipitation forecasts over the northeastern United States. They found that, during warm season, both 36- and 12-km grid spacings overpredict precipitation just inland of the coast due to an overactive Kain-Fritsch convective parameterization and significantly underpredict farther inland over the Appalachians due to a low-level dry bias. During cool season, the 12-km MM5 model produces excessive precipitation immediately downwind of the Great Lakes and over the windward slopes of the Appalachians and too little precipitation in the lee of the barrier. Most of the 12-km overprediction occurs at the light to moderate thresholds.

The most previous studies have focused either on one particular model, on several cases or on over the north and central United States. There has been limited documentation about multimodel error comparison for a long-term period across the Southeastern-central United States. Therefore, the purpose of this paper is to evaluate three-model forecast skills during warm and cool seasons

Models, Data and Method

Since the beginning of 2003, Jackson State University (JSU) has been running three mesoscale models operationally, the MM5, Navy's Coupled Ocean/Atmospheric Mesoscale Prediction System (COAMPS) and the Weather Research and Forecasting (WRF) model. Three models were run twice daily (0000 and 1200 UTC) over the same domain (Fig. 1) that covers most southeastern-central United States and The Gulf of Mexico, with the same horizontal resolution of 27-km and with the same horizontal dimension by 79x73 and for the same forecast length that lasts 36-h. The NCEP Aviation Model (AVN) forecast cycle at 0000 and 1200 UTC were used to initialize three models as well as to provide lateral boundary conditions. The detailed description of the MM5 can be available from Colle et al. (2003), COAMPS from Hodur (1997) and WRF from Skamarock et al. (2001).

The observational datasets in two seasons, 2003 summer (July–Sept. 2003) and winter 2003~2004 (Dec. 2003 – Feb. 2004), have been obtained to against the three-model forecasts within 36-h at 12-h interval. The observed 12h precipitation was derived from the NCEP/Office of Hydrology (OH) hourly, multisensor National Precipitation Analysis (NPA). Surface wind, sea level pressure and surface temperature observations were acquired from NCAR DS464 Mass Storage System that provides 6-h land surface observations as well as 6-h ship observations.

Verification statistics were calculated by interpolating model forecasts to the observation sites. The model forecast data at grid points are interpolated to the observation sites by averaging the surrounding four grids. The accuracy of the model forecasts is quantified using the mean error (ME) and root-mean-square error (RMSE), which are defined as followings:

$$ME = \frac{\sum_{n=1}^{N}(F_n - O_n)}{N} \qquad (1)$$

$$RMSE = \sqrt{\frac{\sum_{n=1}^{N}(F_n - O_n)^2}{N}} \qquad (2)$$

where F is the forecast value , O is the observed, and N is the number of forecast-observation pairs that were compared. For precipitation evaluation, a number of scores were computed from the elements of a rain-no rain contingency table (table 1). Each element of the table holds the number of the occurrences where the observed and the forecast precipitation did or did not exceed the specific threshold value.

Table 1. A 2 x 2 contingency table structure. Shaded boxes denote correct forecasts.

		Observed	
		Yes	**No**
Forecast	**Yes**	*A*	*B*
	No	*C*	*D*

Where A = both observed and forecast, B = forecast but not observed, C = observed but not forecast, and D = neither observed nor forecast. The statistical measures used in here: probability of detection (POD), false alarm ratio (FAR), Bias, threat score (TS) and the Kuilers skill score (KSS).

$$Bias = \frac{A+B}{A+C} \tag{3}$$

$$FAR = \frac{B}{A+B} \tag{4}$$

$$TS = \frac{A}{A+B+C} \tag{5}$$

$$POD = \frac{A}{A+C} \tag{6}$$

$$KSS = \frac{AD-BC}{(A+C)(B+D)} = \frac{A}{A+C} + \frac{D}{B+D} - 1 \tag{7}$$

The model forecast skill of precipitation was also illustrated with root-mean-square error (RMSE) by using formula (2). In this case, F^n is the model precipitation, O^n is the observed and N is the number of observations and model forecasts reaching a given threshold.

Surface Verification

To compare the model's forecast capabilities at 12, 24 and 36h, the mean errors of surface temperature, sea level pressure and surface wind speed at 12, 24 and 36h were output for two seasons. From 12 to 36h, it was noted that the distribution and strength of these parameters mean from each model do not have a significant temporal variation. Therefore, the averaged mean errors at 12, 24 and 36h from three models are showed.

Temperature

During the warm season, the MM5 provided a warm bias over the land (Fig. 2a), with the ranging from 1.5°C to 3.0 °C. For both the COAMPS (Fig. 2b) and WRF (Fig. 2c) models, there is a weak warm bias existed over the southeast-central plains with the bias ranging from 0 °C to 0.5 °C whereas a weak cool bias located over the region from the western plains to the southern Texas.

During the cool season, the MM5 (Fig. 2d) and COAMPS (Fig. 2e) shared the similar distribution and magnitude of ME bias where a weak cool bias over the regions from south-central Texas to central plains with ranging –1.0°C to –0.5°C. There are warm biases over southeastern United States, the Gulf streams, and over the western plains. In contrast, the WRF (Fig. 2f) provides a cool bias over land. The largest cool biases (<-2.0°C) are located over the southern Texas and central Apppalachians.

Sea level pressure

During the warm season, both the MM5 (not shown) and WRF (not shown) provided negative biases over the most part of domain with a stronger bias over southeastern US from the WRF. The MM5 and WRF shared the same positive biases over western plains. The COAMPS also underpredicted sea level pressure over eastern plains while it overpredicted over the northwestern plains (not shown).

In contrast, during the cool season (not shown), the positive sea level pressure biases dominated over domain with the larger bias (>1.6 mb) located over western plains through southern Texas for three models. A negative bias (<-0.8 mb) was located over the region from eastern plains to the windward side of the Appalachians for the WRF while the COAMPS yielded an expanded negative bias area from eastern plains to the eastern coasts with a stronger strength (<-1.2 mb).

Wind speed

During the warm season (not shown), an evident high wind speed bias appeared across the

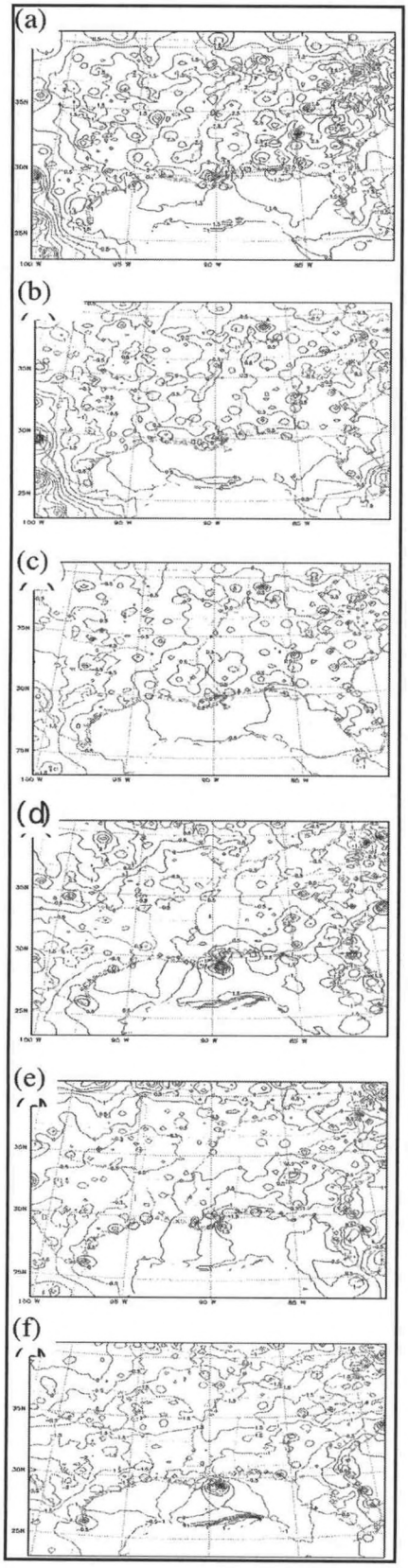

Fig. 2 Average ME biases of surface temperatures at 12, 24 and h for (a) MM5 summer, (b) COAMPS summer, (c) WRF summer, (d) MM5 winter, (e) COAMPS winter, and (f) WRF winter.

domain of the MM5 with the magnitude ranging from 0.5 to 2.5 m/s. The COAMPS and WRF shared the common distribution of mean errors with a low wind speed bias (-0.5 ~ -1.5 m/s) located over the western plains and the southeastern Rockies, and a weaker positive bias (0.5 ~ 1.0 m/s) situated over the southeastern United States and Apppalachians.

For three models, the distributions of the surface wind speed mean error during the cool season are similar to those during the warm season. The MM5 provided a slightly higher bias (10~15% higher) in the winter comparison with that in the summer. So did the COAMPS. In contrast, the WRF provided the comparable surface wind speed biases during the cool season compared with its performance during the warm season.

Temporal variation of skill

To investigate the model's performance at different forecast time, the RMSEs of surface temperature, sea level pressure and surface wind speed at 12, 24 and 36h are analyzed for three models (not shown). It was noticed that, for all three models, the RMSE values of surface temperature, sea level pressure and surface wind speed increased as the forecast time increased, implying the forecast skill deteriorate with the forecast length lasting. The RMSE of sea level pressure possessed the largest temporal variation compared to surface temperature and wind speed. A significant increase of sea level pressure RMSE was observed, especially during cool season. In addition, three models provide slightly larger RMSE values during in cool season than those during warm season. For example, surface temperature RMSE increase by 0.3 - 0.5C, sea level pressure by 0.2 - 0.4mb and surface wind speed by 0.1-0.2m/s.

The more detailed analyses for precipitation will be presented during conference.

Conclusion and Discussion

The performances of three-model (MM5, COAMPS and WRF) forecast skills were evaluated during 2003 warm season and 2003-2004 cool seasons over southeastern-central United States and Gulf coastal areas. The results revealed that, for each model, the temporal variation of ME biases at 12, 24 and 36h were rather little for surface temperature, sea level pressure and surface wind speed. For each model, a warm bias of surface temperature forecast dominated over land during warm season whereas during cool season a weak cool bias existed over the central domain for the MM5 and COAMPS, and the most WRF domain areas was prevailed with an evident cool bias. The insufficient description of soil moisture may be attributed to the surface temperature bias.

The MM5 and WRF yielded the negative biases of sea level pressure during summer while during winter both models produced the positive biases over most domain areas except the weak negative pressure bias over the windward slopes of Appalachians. On the other hand, the COAMPS produced a similar distribu-

tion of sea level pressure biases during two seasons: positive bias over western domain and negative over eastern. During two seasons, the similar surface wind speed bias was produced by each model, where the MM5 gave the evidently high wind speed while the COAMPS and WRF yielded the slightly low surface wind over western plains and slightly high surface wind over eastern plains.

During conference, we will show you that the MM5 yielded a uniform underprediction occurred for all rainfall events, in which a more significant underestimate of precipitation was provided for heavier rainfall. During summer, the MM5 remained its forecast skill with the increase in forecast time at the lighter threshold. But for moderate to heavier thresholds, the model had higher skills during 0-12h and 12-24h than during the periods of 24-36h. During summer, the COAMPS over simulated precipitation at lighter thresholds while under simulated at heavier rainfall. In contrast, the COAMPS provided an overestimate of rainfall for all thresholds during cool season. Compared to the MM5 and COMAPS, the WRF produced much more significant overprediction during two seasons for lighter to moderate precipitation thresholds. On the other hand, it underpredicted the heavier rainfall events.

ACKNOWLEDGMENTS

This research was supported by the NOAA Center for Atmospheric Sciences (NCAS) through Grant NA17AE1623.

REFERENCES

Colle, B. A., J. Olson, and J. S. Tongue, 2003: Multiseason Verification of the MM5. Part I: Comparison with Eta Model over the Central and Eastern United States and Impact of MM5 Resolution. Wea. Forecasting, 18, 431-457.

Gell, G. A., J. Dudhia, and D. R. Stauffer, 1994: A description of the fifth generation Penn State/NCAR Mesoscale Model (MM5). NCAR Tech. Note NCAR/TN-398+1A, National Center for Atmospheric Research, Boulder, CO, 107 pp.

Hodur, R.M., 1997: The navy research laboratory's coupled ocean/atmosphere mesoscale prediction system(COAMPS). Mon. Wea. Rev., 125, 1414-1430.

Manning, K. W., and C. A. Davis, 1997: Verification and sensitivity experiment for the WISP94 MM5 forecasts. Wea. Forecasting, 12, 719-735.

Oncley, S. P., and J. Dudhia, 1995: Evaluation of surface fluxes from MM5 using observations. Mon. Wea. Rev., 125, 3344-3357.

Skamarock, W. C., J. B. Klemp, and J. Dudhia, 2001: Prototypes for the WRF (Weather Research and Forecasting) model. reprints, Ninth Conf. on Me-soscale Processes, Fort Lauderdale, FL, Amer. Meteor. Soc., J11–J15.

SNOWFALL ESTIMATION USING REMOTELY SENSED INFORMATION

Yajaira A. Mejia, Shayesteh Mahani and Reza Khanbilvardi

National Oceanic and Atmospheric Administration Cooperative Remote Sensing Science and Technology Center, Department of Civil Engineering of the City College of New York, Steinman Hall, T-107 140th Street at Convent avenue, New York, NY 10031, United States. (212-650-8099; *yajaira@ce.ccny.cuny.edu*)

ABSTRACT

This project is to develop an artificial neural network algorithm for snowfall estimation, using satellite based cloud information. Multi-spectral data uses infrared (IR) from the Geostationary Operational Environmental Satellites (GOES) and microwave spectral bands from SSM/I and AMSU are used in this study. The calibration of this algorithm is based on rainfall estimates from the Tropical Rainfall Measuring Mission (TRMM) using microwave spectral bands (TMI) and ground-based SNOTEL-ΔSWE (Snow Water Equivalent) observations. Validation is performed through comparison of snowfall estimates with high resolution MODIS snow product. In addition to remotely sensed cloud information, ground surface information (e.g. topography and temperature) and some meteorological air information (e.g. temperature, humidity, and wind) are used to improve snowfall estimates.

In this study an artificial neural network (ANN) based rainfall retrieval model, PERSIANN (Precipitation Estimation from Remotely Sensed Information using Artificial Neural Networks), is selected to be improved for estimating winter precipitation (snowfall) as well as summer convective rainfall. The goal of this study is to: (a) distinguish snowfall from rainfall; and (b) investigate the most effective combination of different variables from cloud, ground surface, and air information for snowfall depth estimation. Snowfall coverage is distinguished using ground surface temperature (Ts), when maximum daily Ts is less than 0° Celsius. A capable ANN-based algorithm is created to estimate snowfall depth using multi-sources snow-related information. The primary results demonstrate adding ground surface and atmospheric information, such as topography, temperature and humidity can improve the snowfall estimates.

INTRODUCTION

Snow is the major source of water supply in the most parts of the world such as: the Western US region. Precipitation, particularly snowfall, is a key parameter and very important information required for hydrological, hydro-climatological and meteorological models applied for flood and weather forecasting, climate change predicting, water resource management and many other applications.

This study is to develop an artificial neural network-based algorithm for estimating solid snowfall from satellite-based cloud observations. Satellite observation became a very important and useful parameter for different applications due to the coverage of large areas, in the last three decades where traditional ground-based techniques cannot cover. In this research, Geostationary Operational Environmental Satellite (GOES) imagers are used because of their high temporal and spatial resolutions.

To improve snowfall estimates, more relevant information from different sources such as: ground observations and meteorological model estimates are added to the satellite-based measurements. Ground surface information such as topography (DEM) and temperature vary the depth of snowfall on the ground. Snowfall amount also depend on the temperature of the air, cloud physics, humidity and wind direction and speed.

In this project three different data categories: input, calibration and validation

are used. The data used for input of the models is from three sources satellite, ground, and atmospheric model, satellite, which mentioned above.

Real time snowfall estimation will allow us to improve runoff predicting and flash flood forecasting.

Study Area & Time:

The study area is selected over the western Unites States (Figure 1), with longitude from 104.5W to 115.25W and latitude from 32.5N to 44.5N, because snow is the major source of water supply in this area. More accurate snowfall information is very important for the most water related applications.

In this study snowfall estimation is examinated only for snowy days (where the maximum daily temperature is less than 0°C), at least, in two winter seasons, and over only snowy pixels.

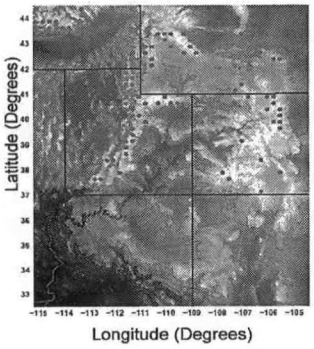

Figure 1. Study area

Data used:

Multi sources data from satellite, ground, and mesoscale models are used in this study.

- Satellite-based information:
  - GOES (Geostationary Operational Environmental Satellites) infrared spectral band observation that is cloud top brightness temperature (Tb).
  - SSM/I and/or AMSU microwave data that provides more information from a cloud because it can penetrate inside clouds.
- Ground-based observations:
  Important information is the topography of the terrain because the snowfall amount varies for different surface temperature that depends on the surface elevation. Hence, ground surface topography (DEM) and temperature are used in this study.
- Air-climate information:
  Snowfall changes for various climate conditions. Therefore, air information such as: temperature, wind direction and speed, humidity, pressure, etc, is required to be used for more accurate snowfall estimates. In this study air information at 700 mb level has been used to improve snowfall coverage and depth estimation as following:
  - Daily minimum and maximum temperature
  - Daily minimum and maximum relative humidity.
  - Daily maximum wind speed

METHODOLOGY

In order to estimate snowfall depth from satellite IR imagery it is necessary to apply two following steps:

First Step: Snowfall detection

The fist step is to distinguish snowfall from rainfall. In this study ground surface temperature is used for recognition of snowfall coverage. If the maximum daily temperature is less than zero degree Celsius then the pixel is classified as only snowy pixel, but if the maximum daily temperature is above zero then the pixel is classified as rainy or mixed snow-rain pixel. Figure 2 shows the snow level (frozen layer), which distinguishes the snowy from the rainy pixels. The frozen layer is located at maximum surface temperature which is equal to zero degree Celsius (max(Ts) = 0°C).

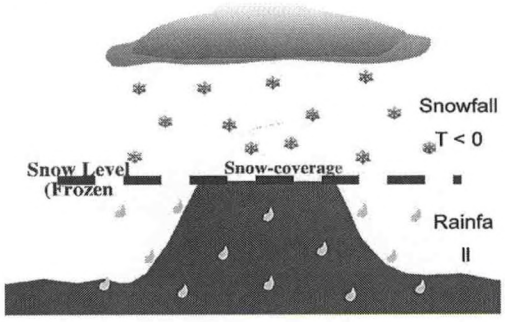

Figure 2. Snowfall Detection (frozen layer)

Model Structure

An ANN rainfall retrieval model, PERSIANN, is selected to estimate snowfall depth only for snowy area. Data used and procedures are illustrated in figure 3.

This model runs in two steps; the first step is to run SOFM, (Self Organizing Feature Map) which specifies the connection weights between the input layer and the hidden layer. The input data set includes several variables, which are data for every pixel and also from its neighboring pixels (3x3 and 5x5 pixels windows) to reduce noises and some errors by using more information. Running SOFM scheme on the input variables classifies the data and calculate the weights that specify the relationship between input and hidden layer for every variable. The second step is to run SOLO, which is the connection between the hidden layer and the output data. Running SOLO identifies the connection weights between effective input (weighted input) and observation. These optimized connection weights specify the best input – output relationship.

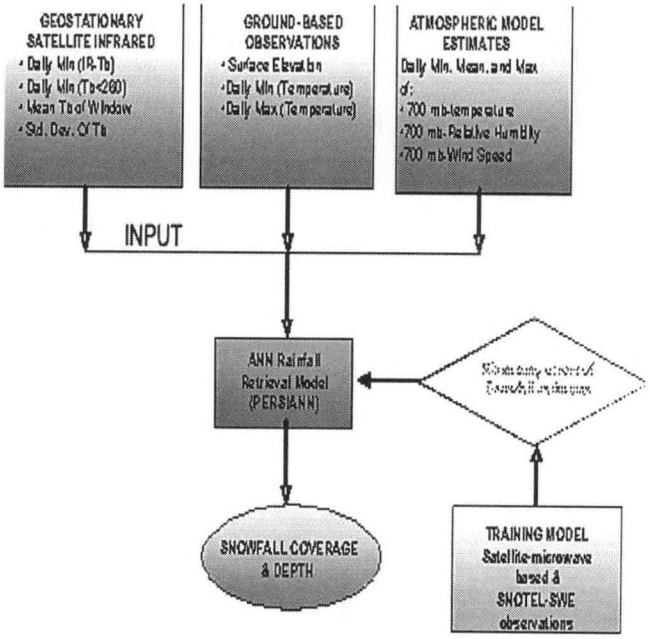

Figure 3. Flowchart of the developed ANN rainfall retrieval model.

Calibration (model training) and validation

Linear least square method is used for error optimization. Satellite-microwave TMI and SNOTEL-ΔSWE observations are used for training the model, by running SOLO scheme to optimize the errors. Ground-based daily snowfall depth observation are also used for calibration. Snowfall depth is equivalent to the difference between observed SWE for every day from the previous day only for the pixels where maximum daily temperature is less than 0°C. Validation data is based on high resolution MODIS snow product.

RESULTS

Three differents tests were applied with different combinations of input variables.

Test (A)

In the 1st test (A), 7 variables were used, which are:

- Minimum daily cloud-top brightness temperature (Tb, Kelvin) for any given pixel;
- Average of minimum daily Tb over nine pixels in 3x3 window, includes the given pixel and its eight neighboring pixels;
- Standard deviation of minimum daily Tb of nine pixels in the 3x3 window;
- average of cloud-top brightness temperature if Tb<260°K for the given pixel;
- Average of the average Tb <260°K over nine pixels in the 3x3 window;
- Standard deviation of the average Tb<260°K over the 3x3 window;
- Ground surface elevation (DEM).

The Figure 4 shows the scatterplot for the 1st test to compare the model estimates with observations. Snowfall esimates using the seven varibles are very poor, because the correlation coeficient is about 0.30.

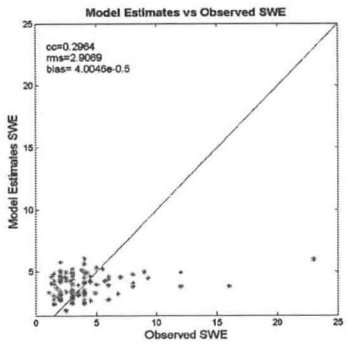

using
7 variables

Test (B)

Three more variables were added to the 7 variables of 1st test.

- minimum daily surface temperature (Celsius),
- maximum daily surface temperature (Celsius),
- maximum air temperature (Celsius) at 700 mb.

Following figure (5), shows small improvement on using snowfall estimation 10 variables. Model estimates still poor but but better than the 1st test. Therefore ground surface and air temperatures can improve snowfall depth retrieval.

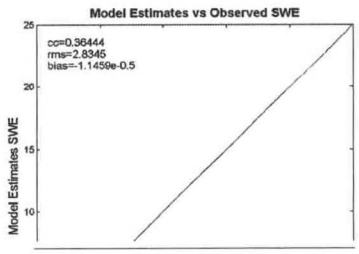

Figure 5. Results of test (B), obtanied using 10 variables

Test (C)

In this test study 6 more variables were added to the ten variables of the 2nd test, which are:

- Average and minimum daily air temperature (Celsius) at 700 mb level,
- Average and maximum daily relative humidity (%) at 700 mb level,
- Average and maximum daily wind speed at 700 mb level.

Figure 6, demostrates no improvement on model estimates using the above extra information, with compare to the 2nd test.

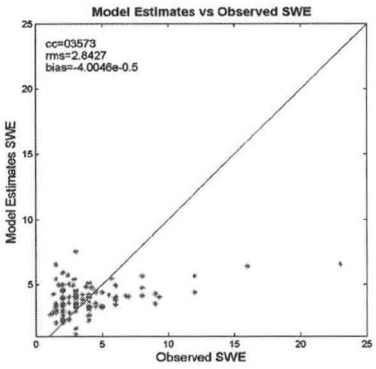

g
16 variables

CONCLUSIONS

Following primary conclusions are from the results of 3 tests for only one day (January 2, 2000). These conclusions may be changed in future after running model for longer time study and also other combination of variables. These given conclusions are based on the statistical analysis, demonstrated in the following table (1), to compare snowfall model estimates with SNOTEL-SWE observations, for all 3 tests, using 7, 10 and 16 variables.

- Using more information as input can improve snowfall estimates.
- Correlation coefficient of the test (B) is greater than correlation coefficient of the test (A) and bias of the test (B) is less than the bias of test (A). This means, adding the daily minimum and maximum surface temperature and maximum air temperature at 700 mb level can improve snowfall estimates.
- Correlation coefficient of the test (C) is about the correlation coefficient of the test (B). Then, the daily minimum and maximum air temperature, relative humidity and wind speed at 700 mb level are not strong parameters in order to improve the snowfall depth.

TESTS	CC	RMS (mm)	BIAS (mm)
A (7variables)	0.2964	2.9069	4.0046e-0.5
B (10variables)	0.3644	2.8345	1.1459e-0.5
C (16variables)	0.3573	2.8427	4.0046e-0.5

Table 1. Statistical analysis for comparing model estimates with observations.

FUTURE WORK

In the future work the PERSIANN model will be run for longer time period, adding more meteorological information as input and using different combination of variables.
Microwave (AMSU and SSMI) and Infrared data will be compared, this way it will be possible to evaluate which channels can improve the results of snowfall estimation.

REFERENCES:

k.-L Hsu, H.V.Gupta, X Gao, and S. Sorooshian: Rainfall estimation from satellite imagery, Department of Hydrology and Water Resources.

Hoshin V. Gupta, Kuo-lin Hsu, and Soroosh Sorooshian, 1997: Superior training of Artificial Neural Networks using Weight-space partioning, Department of Hydrology and water resources.

Roger C. Bales and Robert F. Harrington, 1995: Recent progress in snow hydrology, Department of Hydrology and water resources.

Kuo-lin Hsu, Hoshin V. Gupta, Xiaogang Gao, Soroosh Sorooshioan and Bisher Imam, 2002: Self-organizing linear output map(SOLO): An artificial neural network suitable for hydrologic modeling and analysis.

New Strategies to Predict Hurricane Tracks and Hurricane Intensity

Student: Joan Manuel Castro Sanchez, Advisor: Nazario D. Ramirez
University of Puerto Rico at Mayaguez

Scientists, mathematicians and engineers have studied the evolution of the hurricane for a long time. Two of the most interesting aspects that the hurricane researchers take in consideration are hurricane displacement and hurricane intensification in the North Atlantic Ocean. People who work in the meteorology field have developed a lot of tools and methods to analyze, predict and forecast hurricane intensity and hurricane displacement. Actually, Hurricane experts are using Dynamic Models, for example Geophysical Fluid Dynamics Laboratory Model (GFDL) to predict hurricane tracks and Statistical Models like Statistical Hurricane Intensity Prediction Scheme (SHIPS) to forecast Hurricane Intensity. Our proposed method was developed to predict twelve (12) and twenty-four (24) hours as lead time. Intensity and Tracking models will be based on statistics concepts, because we have found that synoptical variables obtained by aircraft and radiosonde, including Relative Humidity, Geopotential Height, Upper Air Winds and Temperature have high correlation with hurricane tracking and hurricane intensity. Moreover, we observed that satellite information obtained from AMSU, AVHRR, and MODIS sensors estimate surface and upper-air conditions like Sea Surface Temperature and Vertical Wind Sheer that can help to explain hurricane's evolution.

Some elements are important to develop a good statistical model to predict intensity and displacement. One of the elements is to identify the appropriate observations to initialize hurricane tracks and intensity models. Another important element to consider is to obtain enough observations to model a hurricane when it is under development.

In this work, we want to show some strategies to forecast hurricane tracks and hurricane intensity. To do this, we will use statistics tools, for example, develop a selection variables method to calculate the best correlation index, and estimate the minimum prediction error. This method will select the best meteorological variables that can explain the displacement and the intensification of the hurricanes in the North Atlantic Basin for the present, twelve and twenty-four hours in advance.

HAWAII SAR DEMONSTRATION AND QUIKSCAT VALIDATION

Justin Stopa
2004 NY Science Forum

Climate and Geology of Hawaiian Islands

Hawaii has a mild climate throughout the year, mediated by the Pacific as well as the constant trade winds. Since water gains and loses heat slowly, the largest ocean in the world, the Pacific, protects Hawaii's weather from extremes. The islands disrupt the mean wind flow in this region and cause fluctuations in the large-scale ocean currents. The main Hawaiian Islands are located from 19° to 22° north latitude and 154° to 160° west longitude. The northern part of the island chain is called the Emperor's Seamounts and can be traced as far north as the Aleutian Islands. These mainly consist of atolls and underwater seamounts.

Air over the Equator is heated more than the poles because it receives more solar radiation. This warm moist air over the Equator rises and moves northward descending around 30° N: this system is called the Hadley Cell (see figure 1) (Schroeder 13). The air then flows back to the Equator, but is reflected to the "right in the northern hemisphere" because of the rotation of the Earth. This is called the Coriolis affect. The deflection to the right causes the North East (NE) trade winds, which greatly affect the climate of Hawaii.

The year-round NE trade winds act as an air-conditioner to moderate the climate of the Hawaiian Islands. In January, the average climate conditions are affected by, "the subtropical high pressure which lies near 32°N, 130°W and has the central pressure of 1,021 millibars", (Schroeder 14). Although, in July, the center is near 38°N, 150°W and the central pressure is 1,025 millibars, (see figures 2,3) (Schroeder 14). The high pressure (anticyclone) that sits north of the Islands is strengthened by the increase of solar energy into the Hadley cycle. This in turn causes stronger trade winds in the summer season, which runs from May-September. The pressure system is also well north of the Islands and produces steady NE trade winds, which make the climate constant. In January the center of the high pressure system moves southeast and is much weaker. This causes intermittent trade winds, which have a greater variability on the climate. This variability in the climate allows for winter low pressure systems formed in the North Pacific to extend further south. Another type of storm, the Kona Low, is formed west of the Islands. It is a "low-pressure system, which develops in the upper troposphere, and gradually extends to lower altitudes" (Schroeder 19). They are usually accompanied with southerly winds, which blow from the "Kona" side (or leeward side) of the Islands. These storms can bring excessive wind, rain, and surf to the islands for more than a week (Schroeder 19). The strong low-pressure systems and Kona Lows give Hawaii a winter maximum rainfall, which is unlike other locations in the tropics, since most locations in the tropics have a precipitation maximum in the summer season.

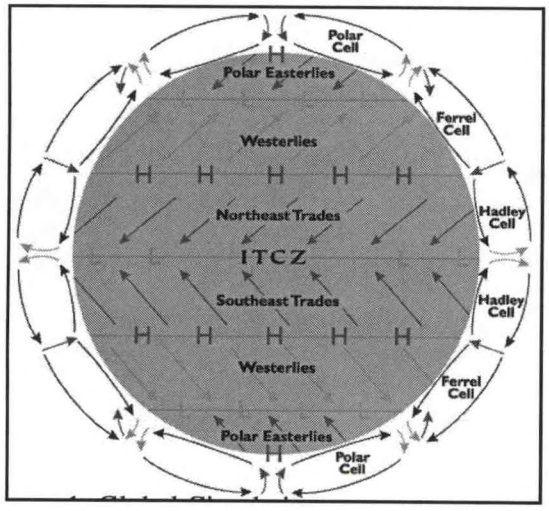

Figure 1: Global Circulation

The trade winds affect each island differently due to their different geological characteristics, with height being the most important. Kauai is the northernmost island and the oldest. The islands were created from a hotspot deep within the Earth's surface. As the Pacific plate moves across the hotspot, new islands are

formed. Kauai was created about 4.5 to 5.6 million years old ago, and for all those years it has been susceptible to erosion. In the south lies the island of Hawaii or the Big Island, and is the geologically the youngest island, which is only 1 to _ million years old. Geologically speaking, 1 to _ million years is very young. Therefore, it has not been exposed to wind and weather that will erode its tall mountain peaks. For example, Kauai's highest mountain peak Kawaikini is 5,243 feet when the Big Island's Mauna Kea and Mauna Loa each raise 13,000 feet or more above the sea level (Sanderson, 3).

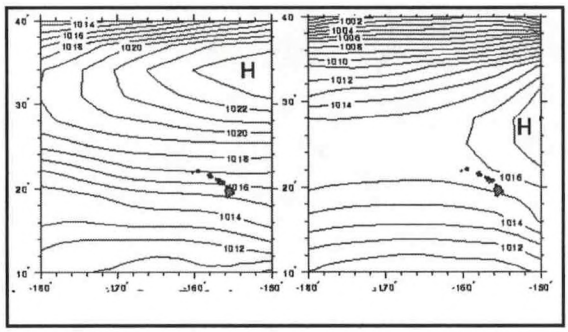

Figure 2 (left): July's average climate
Figure 3 (right): January's average climate

An important feature in regions with trade winds is the trade wind inversion. The dry descending air in the Hadley Cell warms due to adiabatic compression, and forms a warm layer over the cooler rising surface air (Sanderson 13). The average trade wind inversion level is 6,560 feet, but on any given day, the inversion may lie in the range from 4,000 feet to 8,000 feet (Schroeder 14: "Climate of Hawaii"). The trade wind inversion acts as a "lid" on the clouds, which is why they usually appear flat when seen from above. As the moist air from the Pacific is cooled, it condenses and releases its rainfall on the windward sides of the islands. Therefore, during the summer months, the NE sides of all islands receive the most rain, while the leeward sides stay dry. Islands like Kauai, Oahu, and Molokai are not tall enough to be affected by the trade wind inversion, so the rainfall maxima occur on the highest mountain peaks in the center of the islands. Kauai is one of the wettest places in the world with an average annual rainfall maximum of 450 inches (Sanderson 5). However, on the Big Island and Maui most of the precipitation occurs on the windward slopes, while the other areas are very dry. Kawaihae on the Big Island can be considered a desert because it may receive less than ten inches of rain a year (5).

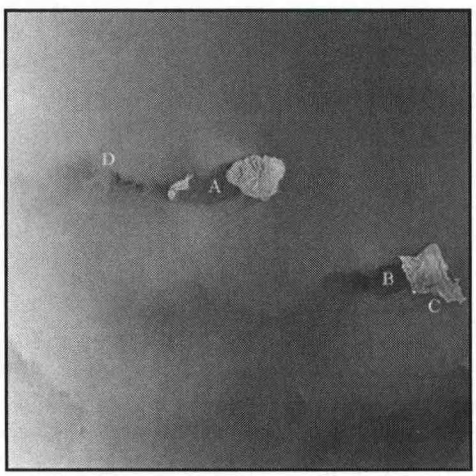

Figure 5: SAR image from RADARSAT-1 © CSA 2001

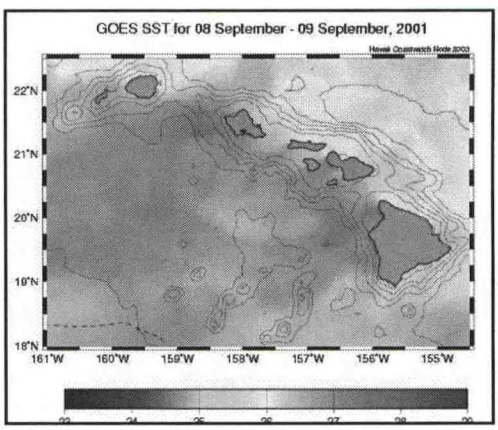

Figure 6: GOES derived SSTs

Understanding the winds are also important to Hawaii because they affect the upper ocean currents, which in turn affect the upwelling of cold water which then affects the sea surface temperatures (SSTs), which may change the thermocline level, which finally affects rainfall – thus creating a continuous cycle. The trade winds affect how much mixing of ocean water occurs. Recall that in the Northern Hemisphere, objects are deflected to the right, because of the Coriolis Effect. The slower an object (or currents, which can move very slowly) moves, the more the Coriolis force affects it. Consequently, to compensate for the diverging surface currents, water from beneath up wells to replace it. The trade winds also affect the wave height, primarily on the Eastern and Northern shores. These wave events have a smaller period and significant wave height than the large NW swells that the Arctic Lows produce in the NW Pacific. The strength of the wind and the fetch (distance the waves travel) affect the significant wave heights.

In conclusion, the trade winds affect Hawaii to a vast extent. They affect the ocean currents, which in turn can influence the SSTs. A strong wind may cause a strong upward nutrient transport, which will result in increased biological productivity. Also, a strong event in trade winds can cause high waves, which result in loss

Figure 7: Point C enlarged from figure 5

of life or property. Trade winds can cause excessive rainfall amounts on the windward sides of the Islands, which may lead to flooding. Therefore, the ability to understand and predict the winds around the Hawaiian Island chain has many useful applications.

Synthetic Aperture Radar (SAR)

Synthetic aperture radar (SAR) is an active sensor that uses pulses of microwaves as its electromagnetic radiation. Microwaves are not susceptible to atmospheric scattering because they can penetrate through clouds, haze, dust, and light rainfall. Some examples of SAR applications are detection of glacier movement and icebergs, flood detection, currents, internal waves, winds, ship detection, phytoplankton detection, shallow bathymetry, and oil slick detection. SAR images are very high-resolution images that can be used day and night, regardless of cloud cover. In certain applications such as slick detection, SAR is best used in combination with other sources of data.

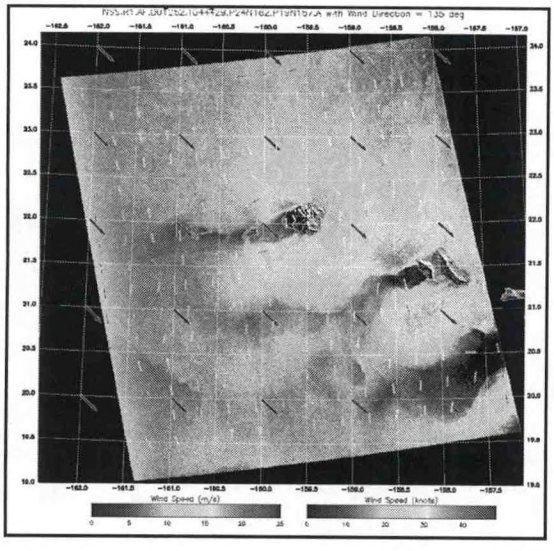

Figure 8: JHU/APL SAR derived wind speeds

SAR's sensor measures backscatter, this means it records the amount of radiation that returns back towards the platform. This will show how rough the ocean surface is by the amount of returned energy. It is important to note that the terms smooth and rough are relative to the wavelength used.

QuikSCAT (Quick Scatterometer)

This satellite operates very similar to SAR by measuring how much the radiation scatters once it reflects from the target. QuikSCAT also uses microwaves therefore this sensor can be used any time of day. The small irregularities in the ocean's surface are created by winds; QuikSCAT then derives wind speeds from the ocean surface roughness. Moderate to heavy rain over the ocean will affect the oceans surface by dampening it. Therefore, QuikSCAT uses an algorithm to "rainflag" possible areas that may be raining. These areas show up as black regions to warn of possible contamination.

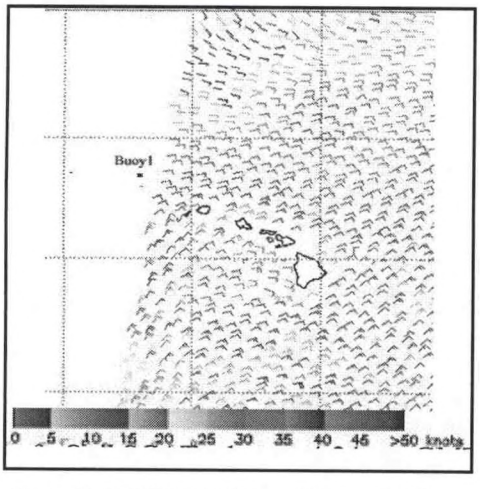

Figure 9: QuikSCAT taken at 4:24 pm GMT

Case Studies

Case 1

Julian Day: 252 Yr: 2001 Time: 4:44:29

Greenwich Mean Time (GMT)

Local time: September 8, 2001 6:44:29 PM

Pacific Standard Time (PST)

In figure 5, the lighter regions return a stronger signal to the sensor. These correlate to areas with higher sea-surface roughness. Inversely, darker regions return a weaker signal because most of the microwave is being reflected forward away from the sensor that measures backscatter. Sea-surface roughness is caused by the wind's magnitude. Notice in figure 5 there is a gradual lightening on the left side of the image. This is because the data is not processed to remove the falloff towards the far-range. The wind may be coming from the NE, due to the wind shadow effect behind the south western shores of Kauai and Oahu (points A and B

respectively). The wind pushes the ocean surface along with it; therefore, the SSTs should be warmer in the darker areas at points A and B.

The white specks in figure 7 are vessels which have a high backscatter, making them easy to distinguish. Honolulu is also recognizable in a strip of white specs along the south shore. The bright white spot in the southwest corner is Barbers Point, which is a military base and highly developed. Point D (Fig. 5) shows a possible convective cloud over the ocean. Convective clouds usually appear as rounded ovals with a dark portion on the windward side because of the winds associated with them. Downdrafts in the convective cell will dampen the ocean surface especially in the areas that are moving towards the active wind flow. The darker region appears on the NE side of the convective cell, consistent with the NE winds. As the wind exits the convective cell, it is accelerated due to the downdraft winds now moving with the active wind; therefore, showing up as a lighter region on the leeward sides of it.

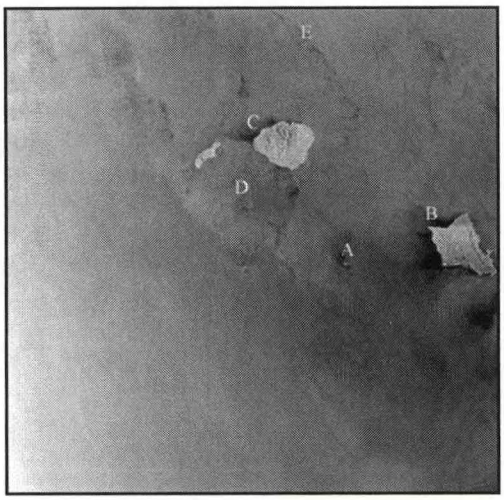

Figure 10: SAR image from RADARSAT-1 © CSA 2002

As the wind moves from the NE direction and encounters the islands, it is forced up and/or around the islands. This may funnel the winds around the corners of the islands, thus creating higher winds speeds. In figure 5, the lighter regions on the leeward side of Kauai and Oahu both may represent this.

Figure 8 shows wind speeds derived from the original SAR image in figure 5 with an algorithm developed by the Johns Hopkins University Applied Research Lab (JHU/APL). Recall, the ocean surface roughness is a, "function of wind speed and direction" (Clemente-Colon, Pichel 54). The large arrows are from the Navy Operational Global Atmospheric Prediction System (NOGAPS) model. Notice that these arrows are inconsistent with the other information. The smaller arrows are part of another algorithm by General Dynamics that estimates the wind direction, using wind features in the image. Prior knowledge of the wind direction is needed to make the JHU/APL product, as opposed to the General Dynamics product. Also note the General Dynamics arrows have a 180° ambiguity. Some of the arrows seem like they are correct with the original hypothesis of Northeasterly winds. SAR wind measurements are very high resolution (25 to 100m) in the absence of noise (Clemente-Colon, Pichel 54). Normal scatterometers have the spatial resolution of 25 to 50km. This allows SAR to be able to make wind estimations very close to the coastlines, "without suffering land contamination evident in other scatterometers" (Clemente-Colon, Pichel 54). Figure 8 agrees with the fact that the wind is accelerated around the corners of the islands.

The QuikSCAT data in figure 9 are very close to the time of our original SAR image in figure 5. Figure 9 shows the winds from the NE, which is consistent with the original hypothesis. Notice the difference in the spatial resolution between the SAR image and the QuikSCAT image. QuikSCAT's spatial resolution is 25km by 25 km, and SAR's spatial resolution is 100m by 100 m. The black wind barbs represent the rain-flagged regions where there could be possible rain. Between the Islands of Oahu and Kauai is a wind barb of higher wind speeds than on windward sides. This could represent the accelerated winds due to Hawaii's topography. Around the island of Hawaii, on the southern point there are also accelerated winds due to Hawaii's massive Mauna Loa, which stands 13,000 feet tall.

Case 2

Julian Day: 030 Yr: 2002 Time: 4:44:51

GMT

Local time: January 30, 2002 6:44:51 PM

PST

In figure 10, it is more difficult to distinguish the direction of the wind. On the South Western side of Oahu there is a large dark area, reflective of reduced wind speeds. On the Northwestern side of Kauai and

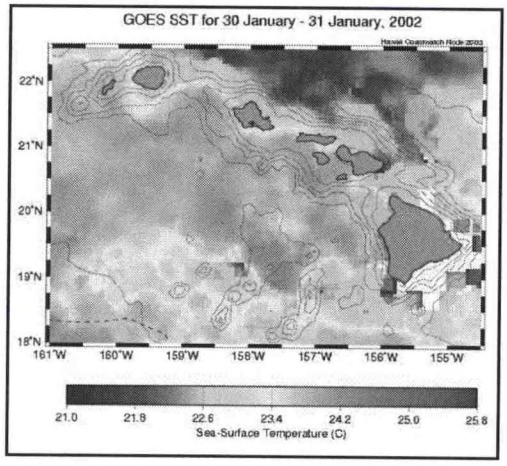

Figure 11: GOES derived SSTs

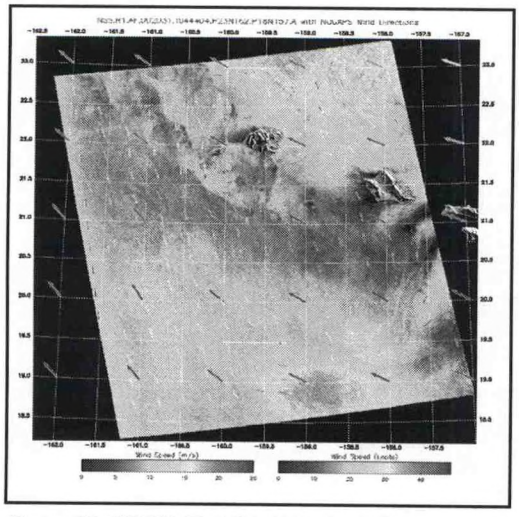

Figure 12: JHU/APL SAR derived wind speeds

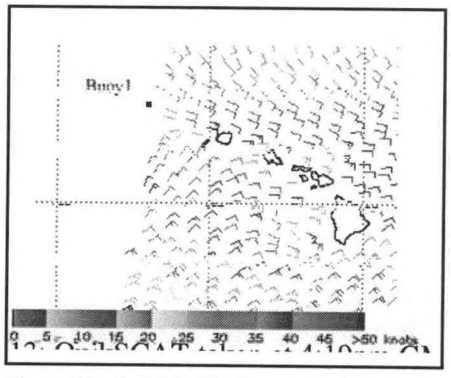

Figure 13: QuikSCAT taken at 4:19pm GMT

Oahu at points C and B there are also darker areas. These wind shadow features are more subtle than the other cases which could be reflective of the wind's speed. Points B and C could represent a wind from the East but with a slight South component. In the lower left-hand corner of figure 10 shows there are stronger winds than the rest of the image. At point A shows a very bright spot in relation to the surrounding area. This could be a strong convective cloud producing an ice cloud which is highly reflective to the microwave energy. Similar to figure 5 point D shows a convection cloud/downdraft that is much larger. This convective cell also appears in a circular shape with a darker side to the East and a lighter side to the West. This means the wind is flowing from the East. Point E could also be another atmospheric front due to convection occurring in the bands north of Kauai.

Figure 11 shows the SSTs are warmer on the western shores than the eastern, with a difference of about 2° C. Comparing this with figure 6 shows there is generally cooler water around the Islands due to the seasonality. Also notice, there are warmer areas to the northwest ends of the islands; which could mean that the wind has a South component to it. The white areas in figure 11 are areas with cloud cover since GOES uses infrared and visible wavelengths to obtain its information.

The NOGAPS model arrows in figure 12 are consistent with an ESE wind direction. In the bottom middle of figure 12 there are strong winds with speeds of 40 knots. In the upper right-hand corner there are also strong winds. The areas on the southwestern shores of Oahu could be areas where it may be raining due to convection.

The QuikSCAT image in figure 13 is very close to the time of our original SAR image. Figure 13 shows a wind primarily from the East with a hint of South around Oahu and Kauai, which is consistent with the original hypothesis.

In figure 14 there is a Kona-Low affecting the Islands' weather. The winds do have a slight south component as hypothesized. Possibly 24 hours prior to this map the low-pressure system may have been closer to the Islands, which would result in a more direct Southward flow. This forecast shows the low-pressure system moving to the southwest.

Analysis

In graph 1, QuikSCAT is accurate in measuring the wind speeds over the ocean at the buoys but not over locations on land. Buoys 2, 3, 4 were all underestimated but were very close to the recorded wind speed. This time, in graph 2 QuikSCAT overestimated the wind speeds. Therefore, QuikSCAT does not estimate wind speed over land very well. Both Honolulu and Lihue are located along the coastlines, which should give better wind estimates than an inland location. As shown earlier, wind is accelerated around the corners of the Islands due to the Islands elevation and sometimes QuikSCAT could be reading this as the closest point. This is not an error of QuikSCAT, but a limitation of its spatial resolution. QuikSCAT was designed to produce ocean surface winds as close to "real time" as possible. This is the reason for its spatial resolution being large, so it can reduce the amount of

data to be processed.

The closest QuikSCAT recorded point sometimes exceeds spatial resolution of 25km because of a land point or the swath widths. The next QuikSCAT pass over the area will be 12 hours later than this time and that pass may not be reflective of these particular SAR cases studies. There is little temporal difference for September 8, 2001 between the QuikSCAT pass taken at 4:20 GMT and the recorded points were recorded at 4:20 GMT. Similarly for January 30, 2002 between the QuikSCAT pass taken at 4:52 GMT and the recorded points were recorded at 4:50 GMT.

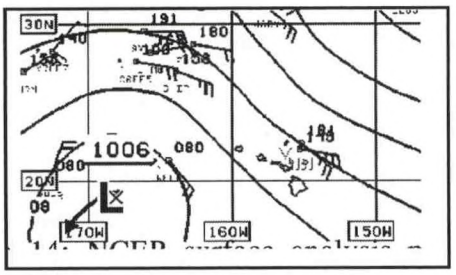

Figure 14: NCEP surface analysis map for 1/30/02, 6 GMT

Conclusion

In conclusion, the case studies shown represent much of the factors that contribute to the Hawaiian Islands' climate. The first case, September 8, represented a "normal" trade wind event, representative of a typical summer day. The second case, January 30 is a good example of a Kona storm that would bring much rain to the Islands. For example on January 29, 2.10 inches of precipitation was measured in Honolulu. On January 28 in Lihue, 1.95 inches were measured, and then on January 30, 1.71 inches were measured. This was the same system that contributed to these two amounts. The average rainfall in Honolulu in January is 3.55 inches and the average rainfall in Lihue is 5.89 inches in January (Schroeder 50). So these totals are "normal" for this time of year.

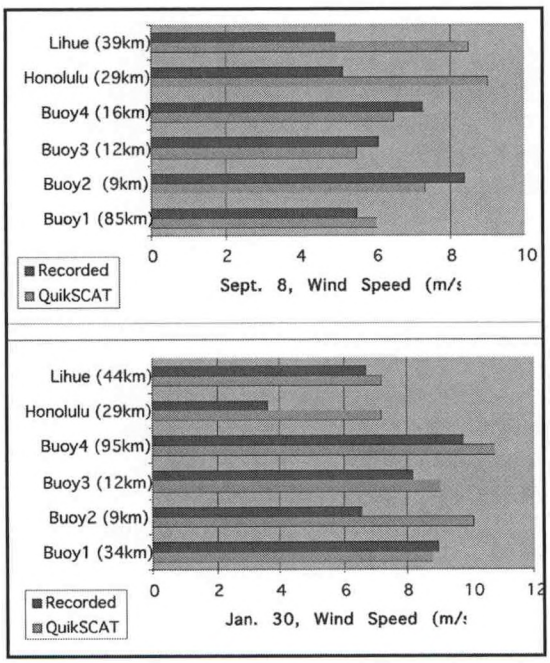

Graphs 1,2 respectively
Note: the number in kilometers is the closest recorded QuikSCAT point to the location.

WORKS CITED

Clemente-Colon, Pablo & Pichel, William. "NOAA CoastWatch SAR Applications and Demonstration." Johns Hopkins APL Technical Digest Vol. 21.1 (2000): 49-57.

Sanderson, Marie. Prevailing Trade Winds, Weather and Climate in Hawaii: Introduction. Honolulu: University of Hawaii Press, 1993.

Schroeder, Thomas. Prevailing Trade Winds, Weather and Climate in Hawaii: Climate Controls. Honolulu: University of Hawaii Press, 1993.

WORKS CONSULTED

Chang, Paul. "Ocean Surface Winds Derived from the SeaWinds Scatterometer." 25 July, 2004<http://manati.wwb.noaa.gov/quikscat/>

"Climate of Hawaii" 2 July, 2004 http://www.wrcc.dri.edu/narratives/HAWAII.htm

Falcon, Peter. "SeaWinds on QuikSCAT" 20 July, 2004 <http://winds.jpl.nasa.gov/missions/quikscat/index.cfm>

Flament, P., Kennan, S., Lumpkin R., Sawyer M., and Stroup, E. D. "The Ocean Atlas of Hawaii." 28 June, 2004 <http://radlab.soest. hawaii.edu/atlas/>

Friedman, Karen. "Alaska SAR Imagery Manual." 20 June, 2004 <http://www.orbit.nesdis.noaa.gov/sod/mecb/sar/ sar_manual.PDF>

"Unedited Local Climatological Data." 16 July, 2004 <http://www.ncdc.noaa.gov/servlets/ULCD>

Wackerman, Chris. "Introduction to SAR." 20 June, 2004 <http://www.orbit.nesdis.noaa.gov/sod/mceb/sar/IntroSAR_ERIM.pdf>

MesoBLAST: The Mesoscale Boundary Layer Atmospheric System of Tall Towers

Dr. James Finney and Dr. Loren White
Jackson State University

The Jackson State University Meteorology Program is planning an ambitious project named MesoBLAST, the Mesoscale Boundary Layer Atmospheric System of Tall Towers. The primary objective of MesoBLAST is to provide real-time measurement of meteorological conditions in the boundary layer throughout the state of Mississippi with high temporal resolution. This observational capability will improve the availability of research quality weather data for the region and complement related efforts at developing a statewide surface mesonet. Important features of the tall tower observing network will include sensors to measure atmospheric variables (air temperature, humidity, wind speed and direction, solar radiation) at a minimum of three heights on eight public television transmission towers (each at least 1000 feet tall) and capability for instantaneous data access through the internet. Current research projects in the JSU Meteorology Program focus primarily on mesoscale numerical modeling. The mesonet will greatly enhance the local data available to be assimilated into numerical models and for model verification efforts. Undergraduate research and education will benefit not only from the data, but also from the opportunity for students to be involved in the installation and calibration of automated meteorological sensors. Research issues that will be addressed using the tall tower network data include: characterization of thunderstorm environments, vertical structure of near-surface frontal features, boundary layer contributions to evolution of frozen precipitation events, and surface roughness effects. Unique applications of the data to wind energy feasibility studies are expected.

Nocturnal Warming Events in Mississippi

Loren White and James Finney
Jackson State University Meteorology Program

At the Newton, MS mesonet site operated by Jackson State University, occasional cases of sudden warming have been observed on several occasions during night-time hours. Typically these events have occurred under stable (non-convective) conditions without any known frontal boundaries nearby. During the warming events, dewpoint temperature also drops sharply. However, winds usually only increase moderately. Likely explanations are that the warming is associated with trapping of infrared radiation by passing cloud cover, or that a slight increase in wind speed is resulting in sudden mixing of a surface temperature inversion. Nocturnal warming events may be significant for forecasting of daily minimum temperature.

THE URBAN HEAT ISLAND OF JACKSON, MS

Loren White and James Finney
Jackson State University Meteorology Program

Using automated portable weather stations received from private donations, the Jackson State University Meteorology Program has incorporated observation of the urban heat island effect into student instruction and research. So far stations have been placed in three locations representing: 1) the core residential area of Jackson (on the JSU campus); 2) a rural environment (at an agricultural research farm); and 3) a suburban environment near a major reservoir (at a private home). Results show the expected warmer temperatures within the urbanized areas, particularly at night under light winds. Comparison with nearby permanent weather stations and, where appropriate, satellite infrared imagery is planned.

Validation of MM5 for Evolution of Cold Fronts Approaching the Gulf of Mexico

Loren D. White

Jackson State University, Jackson, MS

A preliminary validation study has been performed of the twice-daily operational runs of the MM5 mesoscale meteorological model over Mississippi and Louisiana for a few cases of cold fronts. To examine how well the model simulates the structure and evolution of cold fronts as they approach the northern Gulf of Mexico, time series of surface meteorological parameters are compared from the model output and observations taken at select stations. In particular, the one-minute resolution meteorological observations of the Louisiana Agriclimatic Information System (LAIS) are used for comparison. Results reveal impressive model performance on timing and magnitude of temperature and dewpoint changes, but less favorable agreement on wind evolution during frontal passages. Significant differences are noted between frontal cases and at stations at varying distances from the Gulf of Mexico (as the fronts are modified by interaction with the warm, moist surface).

VALIDATION OF ONE-MINUTE DATA IN AN OPERATIONAL MESONET

Dr. James Finney and Dr. Loren White
Jackson State University

Since 2001, one-minute resolution weather data have been available from over 20 stations of the Louisiana Agriclimatic Information System (LAIS), a network managed by the Louisiana State University Agricultural Center. Jackson State University is in the initial phases of developing a similar mesonet consisting of more than 100 stations within Mississippi, building upon the experiences from LAIS. Example data will be shown where one-minute meteorological observations have been crucial for describing events observed by the Louisiana and Mississippi stations. Such valuable information is lost to networks with poorer temporal resolution.

The Effect of the Vegetation Cover Category on Spatial and Temporal Soil Moisture Variation

Nasim Jahan (M.Sc. student), Hosni Ghedira (Assistant Professor), and Reza Khanbilvardi (Professor)

NOAA-CREST, City University of New York

Soil moisture is an important component of the hydrological cycle. The capability to observe soil moisture frequently and over large regions could significantly improve our ability to estimate some hydrological parameters such as infiltration, runoff, and soil wetness, which are very useful in hydrological modeling, real-time flooding forecast and irrigation management.

The primary intent of this project was to map the spatial variability of soil moisture and to assess the effect of the land cover and meteorological conditions (precipitation, temperatures...etc) on this variability. The outcome of this project will be used to identify the optimal remote sensing data to be used for soil moisture mapping and to reduce the negative effects of the vegetation cover on classification accuracy

The soil moisture data were collected at L band wavelength over a 10,000 km2 using ESTAR Instrument (Electronically Scanned Thinned Array Radiometer) during the SGP97 campaign (operated by NASA). The SFP97 was a large, interdisciplinary experiment carried out over a month period in 1997 in Oklahoma (97d35'W, 36d15'N). The derived soil moisture from different dates was analyzed in conjunction with meteorological and vegetation data to understand the effect of vegetation cover and meteorological conditions on the soil moisture variation.

Evaluation of SSM/I Filtering Algorithm for Snow Cover Identification in Northern New York State

Juan Carlos Arevalo, Hosni Ghedira, and Reza Khanbilvardi

NOAA-CREST, City University Of New York, Convent Ave. At 138th Street, New York, NY 10031. Telephone: (212) 650 8536, Facsimile: (212) 650 6965.

Abstract

Snow-cover parameters are being increasingly used as input to hydrological models. An accurate knowledge of the onset of snow melts and snow water equivalent values are important variables in different hydrological applications such as flooding prediction, reservoir management and agricultural activities. However, the traditional field sampling methods and the ground-based data collection are often very sparse, time consuming, and expensive compared to the coverage provided by remote sensing techniques. Microwave remote sensing techniques have been investigated by numerous researchers using various sensors and have been demonstrated to be effective for monitoring snow pack parameters such as spatial and temporal distribution, snow water equivalent, depth, and snow condition (wet/dry state). Those researches have resulted that the microwave brightness temperature and the microwave backscattering are related to the snow cover structure with different correlation degrees.

The primary objective of this research is to produce a spatial estimation of snow water equivalent in a timely fashion with sufficient spatial and temporal resolution using multi-source microwave and optical data. The final product of this project will be an additional tool for flood warning and water resource forecasts, which can be an additional input to the actual hydrological models. The contribution of remote sensing snow related information into the advanced hydrologic prediction system (AHPS) operated by NWS/NOAA (with 4 km grid resolution) will be also evaluated. The focus of this paper is to investigate the performance of filtering algorithm for global snow cover identification developed by NESDIS (NOAA) in northern New York State.

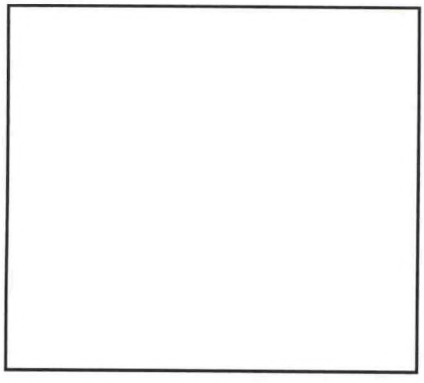

Figure 1. Study area.

Introduction

Snow coverage and depth are two key parameters that are essential to be estimated and applied in a wide range of hydrological applications. Currently, most of snow data used in hydrological applications is obtained through the use of standard and recording rain gauges, seasonal storage precipitation gauges, snow boards, and snow stakes. Direct measurements of snow depth at a single station are generally not very useful in making estimates of distribution over large areas, since the measured depth may be highly unrepresentative because of drifting or blowing [1].

Visible satellite sensors can detect snow cover only during daylight, cloud-free condition and without providing any information of snow depth. In addition, the traditional procedures used to distinguish between clouds and snow cover, require an intensive manual work and continuous human interaction [2].

In addition to penetrating through clouds, microwaves can penetrate the snow cover and provide information about snowpack properties since the scattered emission due to the penetration is very sensitive to variation in the physical characteristics within the snow cover and snow-ground interface.

Furthermore, it has been shown that snow scattering emissions are results of three major components, surface scattering, volume scattering and, subsurface or snow-ground interface scattering [3]. In dry and shallow snow the major effect comes from snow-ground interface [4]. However, in wet and deep snow surface scattering and volume scattering play the major role consecutively.

The focus of this paper is to investigate the performance of filtering algorithm for global snow cover identification developed in 1996 by Grody and Basist [2].

Data Set and Study Area

The study area is located in the north of the state of New York between 71°50'W - 76°25'W (Longitude) and 41°00'N - 44°50'N (Latitude), as seen in figure 1.

Brightness temperature data from the current SSM/I (Special Sensor Microwave Imager) sensors on board the DMSP F13 and F14 satellites are used in both ascending and descending orbits. These images provide (twice-a-day) measurements of the brightness temperature (Tb) in different frequencies and polarizations (19 V, 19 H, 22 V, 37V, 37 H, 85 V, and 85 H).

Five snow days have selected during 2001/2002 winter (12/21 to 12/25) and a total of 301 ground stations covering the study area have been identified for this experiment. Snow depth measurements have been collected from the National Climatic Data Center (NCDC) through the Cooperative Observer Network for the U.S. snow Monitoring. The snow depths measured during this 5-days period have been compiled and gridded into 25 km x 25 km grid. Additional data from stations located outside the study area have been selected to avoid any extrapolation during the gridding process.

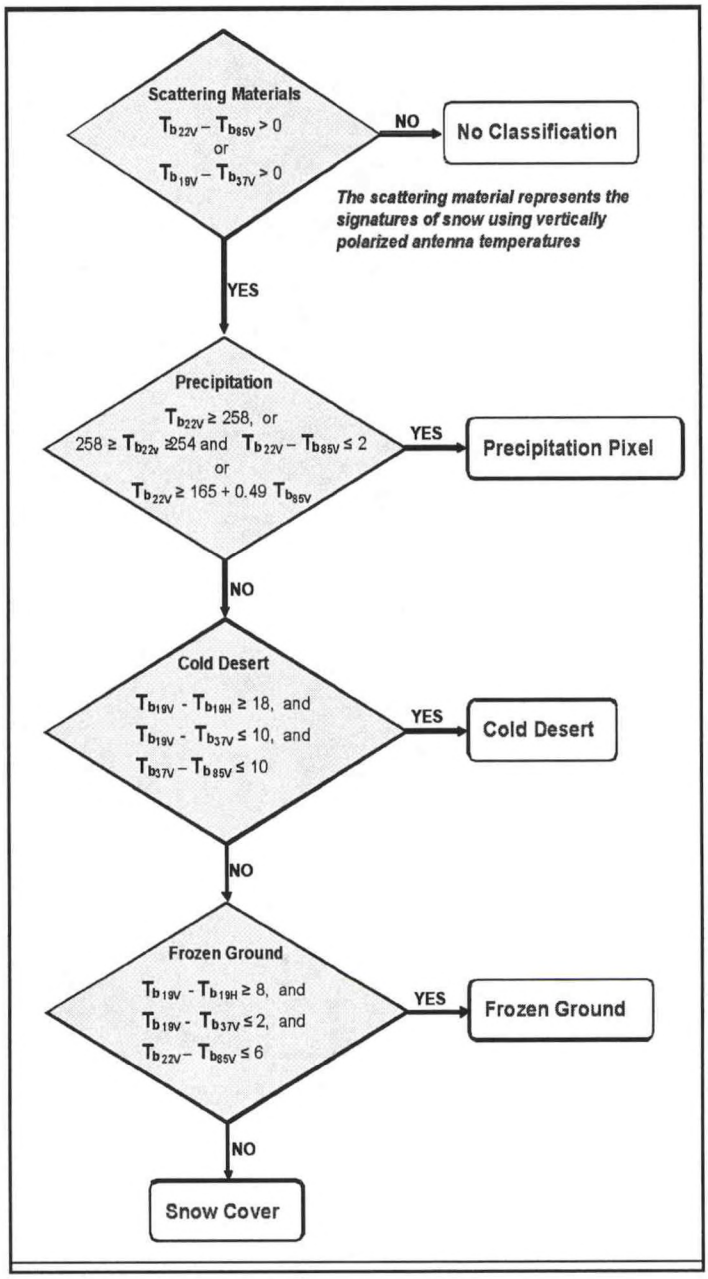

Figure 2. Decision Tree (Adapted from Grody and Basist, 1996 [2]).

The final study area contains 15 x 12 pixels with spatial resolution of 25 km x 25 km. Only pixels having more than one inch of snow are considered as snow pixels. This information are considered as truth data on validating the decision tree algorithm.

Methodology

A filtering algorithm for global snow cover identification was applied and evaluated over the study area. The algorithm consists of a decision tree (Fig 2) which establishes sensitive thresholds to filter

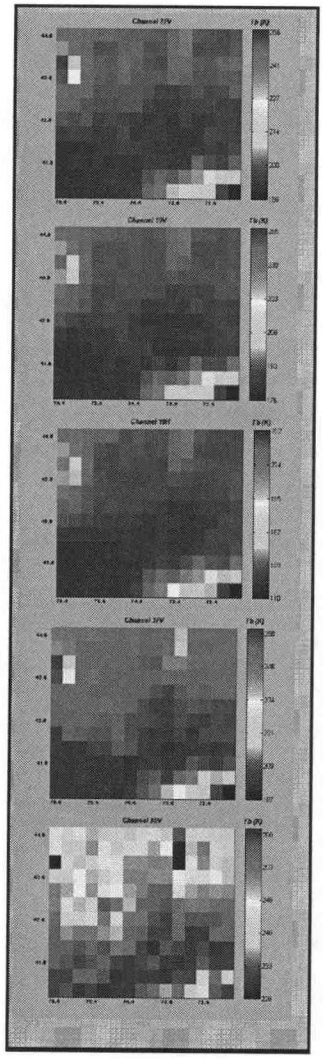

Figure 3. Five channels of SSM/I, December 28, 2001.

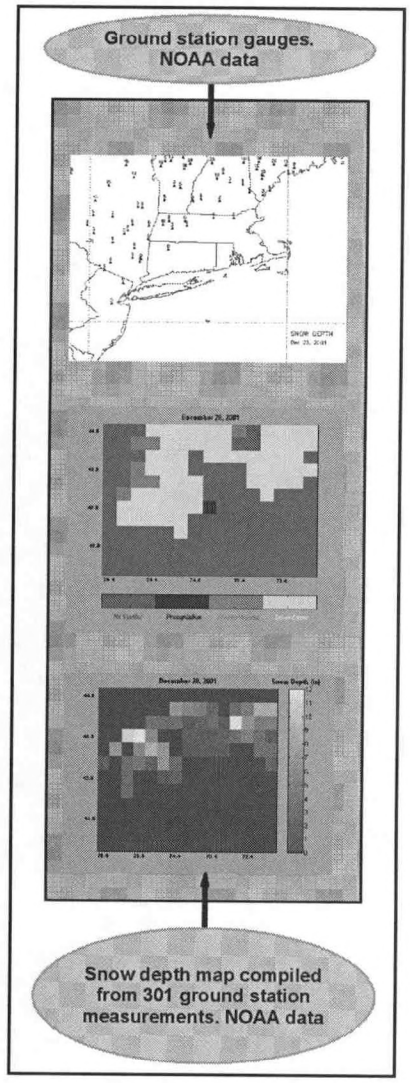

Figure 4. Comparison of snow-cover map for December 28, 2001

out precipitation, warm desert, cold desert and frozen surfaces. This filtering algorithm uses five of the seven channels of SSM/I (19V, 19H, 22V, 37V, and 85H). Fig 3 illustrates the five SSM/I channels collected over the study area on December 28, 2001.

The comparison between the decision tree output and the snow-cover map generated from the ground station gauges measurements (collected for December 28, 2001) is illustrated in Fig 4.

Five consecutive days for the winter season of 2001 - 2002 were selected to assess the accuracy of the decision tree algorithm. For the same days, five snow-cover maps have been generated from the ground station gauges covering the study area. The comparisons between the decision tree results and the gridded data are illustrated in Fig 5.

In order to assess the performance of the decision tree in identifying snow pixels, confusion matrices were calculated for each day (2 images per day on ascending and descending orbits).

Results

TABLE 1: CONFUSION MATRICES

	Dec 21, 2001			Dec 22, 2001			Dec 23, 2001			Dec 24, 2001			Dec 25, 2001		
		S	NS		S	NS		S	NS		S	NS		S	NS
Ascending Orbit	S	**0.29**	0.07	S	**0.43**	0.21	S	**0.02**	0.01	S	**0.38**	0.15	S	**0.68**	0.19
	NS	0.71	**0.93**	NS	0.57	**0.79**	NS	0.98	**0.99**	NS	0.62	**0.85**	NS	0.32	**0.81**
		Accuracy = **73**			Accuracy = **66**			Accuracy = **71**			Accuracy = **71**			Accuracy = **78**	
Descending Orbit		S	NS		S	NS		S	NS		S	NS		S	NS
	S	**0.29**	0.11	S	**0.49**	0.21	S	**0.45**	0.14	S	**0.21**	0.10	S	**0.56**	0.22
	NS	0.71	**0.89**	NS	0.51	**0.79**	NS	0.55	**0.86**	NS	0.79	**0.90**	NS	0.44	**0.78**
		Accuracy = **70**			Accuracy = **67**			Accuracy = **74**			Accuracy = **69**			Accuracy = **73**	

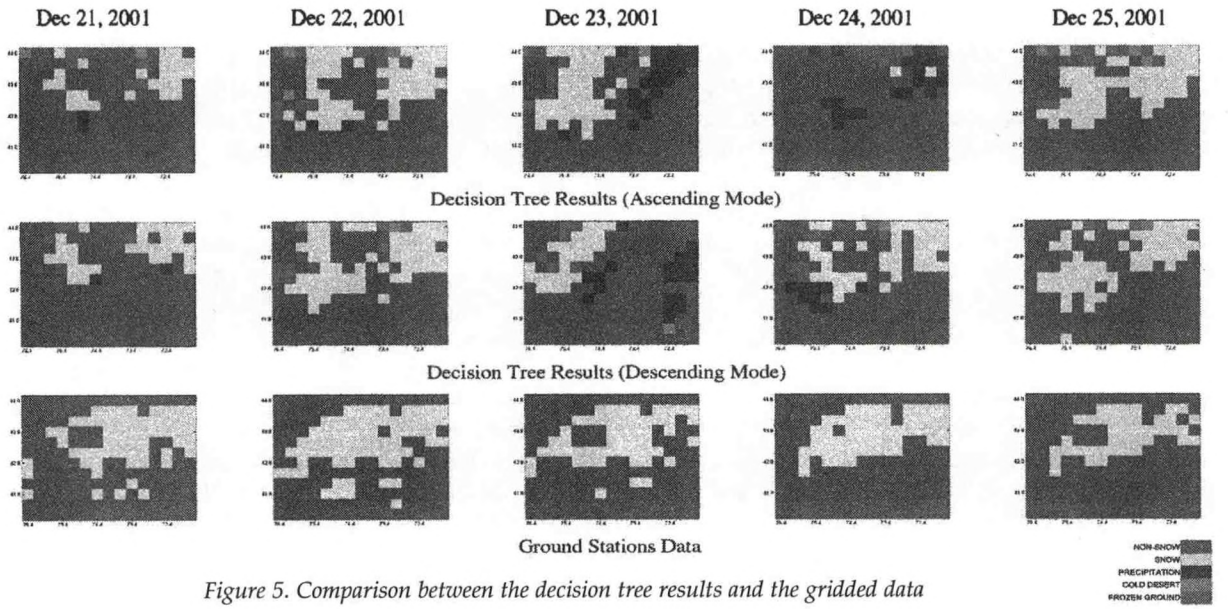

Figure 5. Comparison between the decision tree results and the gridded data

The confusion matrix shown in Table 1 illustrates clearly the well performance of the decision tree algorithm in identifying the non-snow pixels where the accuracy was varying between 79% and 99% for both ascending and descending modes. However, the performance in identifying snow pixels was very poor with an accuracy of 2% for December 23rd.

REFERENCES

[1] Viessman, W., and G. Lewis, 1995: Introduction to hydrology. Forth edition, Harper Collins.

[2] Grody, N., and N. Basist., 1996: Global identification of snowcover using SSM/I measurements. IEEE Transaction on Geosciences and Remote Sensing., 34, No. 1,.

[3] Ulaby, F., R. Moore., and A. Fung, 1981: Microwave remote sensing active and passive. Vol 1, Artech House.

[4] De Sève, D., M. Bernier, J.-P. Fortin, and A. Walker., 1997: Preliminary analysis of snow microwave radiometry using the SSM/I passive-microwave data: the case of La Grande River watershed (Quebec). Ann. Glaciol., 25, 353-361.

[5] Wang, James R., A. Chang., and A. K. Charma., 1992: On the estimation of snow depth from microwave radiometric measurements. IEEE Transaction on Geosciences and Remote Sensing., 30, No. 4,.

[6] Wilson L., L. Tsang., J. Hwang., and C. Chen., 1999: Mapping snow water equivalent by combining a spatially distributed snow hydrology model with passive microwave remote sensing data. IEEE Transaction on Geosciences and Remote Sensing., 37, No. 2,.

WINTERTIME AEROSOL PARTICLE NUCLEATION EVENTS IN THE NORTHERN COLORADO ROCKIES, USA

Wee, M.[1]; Hindman, E. [1]; Borys, R. [2]

[1]Earth and Atmospheric Sciences Department, The City College of New York, NYC, NY 10031
[2]Desert Research Institute and the University of Nevada, Reno, NV, 89512 USA

Storm Peak Laboratory (SPL, 3210 m MSL) is at the crest of the N-S oriented Park Range in the northern Colorado Rockies. During the wintertime, the range and the surrounding valleys are snow-covered producing extremely stable boundary layers during storm-free periods. Thus, it is expected that mid-troposphere aerosol measurements can be obtained from the site especially during such periods. However, condensation nucleus (CN) measurements made during these periods at SPL and SPLM (mid-mountain) often reveal significantly elevated CN concentrations in the afternoon. Similar CN "storms" have been detected in the Alps and in the Himalayas. These "storms" have been explained by transport of CN-rich boundary-layer air in day-time up-slope flows. This hypothesis has been tested at SPL in the following manner. CN transport in up-slope flows has been estimated by filtering the CN data collected at SPLM with the wind-direction data into up-slope and down-slope populations. Surprisingly, significant transport of CN did not always occur in up-slope flows. CN transport in boundary-layer convection has been investigated using atmospheric soundings produced from temperature measurements at SPL, SPLM and SPLB (valley station) and from a high-resolution numerical atmospheric model (MM5). The measured and simulated surface temperature inversion weakened in the afternoon indicating some vertical mixing. This mixing combined with weak up-slope flows indicates boundary-layer CN can be transported to SPL. Finally, in situ ultra-fine CN production at SPL occurs at a rate of approximately 0.6 cm-3s-1 at about 7 nmh-1 for particles between 3 and 10 nm in diameter. Thus, aerosol nucleation events plus the transport of boundary-layer CN can explain the CN "storms" at SPL.

Presented at 8th Intl. Global Atmospheric Chemistry Conference, Christchurch, NZ, 4-9 September 2004

Discrimination of Rock Types Using a Combined ASTER/SSMI Algorithm

Marco Vargas, Nick Steiner, Dinorah Hudson and Jeff Steiner

Rainfall measurements for western Washington and northern Oregon are correlated with a time series wetness 'decay' function to differentiate the Grande Ronde Basalt of the Columbia River Basalt Plateau series from Quaternary Alluvium and members of the Picture Gorge basalt. The discrimination uses library values for the basalt and surface alluvium spectra and creates image segmentation of ASTER satellite images based on the ENVI pre-programmed decision structure. Soil moisture and rock information for image analysis are provided using the SSM/I, a passive microwave sensor aboard the Defense Meteorological Satellite Program (DMSP) platform. The SSM/I spectra are incorporated into the ENVI package using a presently organized subroutine, SSMI-ADJ, written in the Interactive Digital Language (IDL) format. The calibration of each SSM/I channel in the SSMI-ADJ program initially involves converting the raw data in Degrees Kelvin –70 to antenna temperatures. Antenna temperature is converted to brightness temperature using standard Naval Research Laboratory (NRL) algorithms. A subsequent surface classification subroutine in SSMI-ADJ differentiates land, water and other bodies. Specific soil moisture output and the proposed rock categories are then generated using the McFarland/Neale algorithm for soil moisture and a modified algorithm for rock formations.

THE NATIONAL OCEANIC AND ATMOSPHERIC ADMINISTRATION (NOAA) conducts research and gathers data about the global oceans, atmosphere, space, and sun, and applies this knowledge to science and service that touch the lives of all Americans.

NOAA warns of dangerous weather, charts our seas and skies, guides our use and protection of ocean and coastal resources, and conducts research to improve our understanding and stewardship of the environment, which sustains us all.

A Commerce Department agency, NOAA provides these services through five major organizations: the National Weather Service, the National Ocean Service, the National Marine Fisheries Service, the National Environmental Satellite, Data and Information Service, and NOAA Research; and numerous special program units. In addition, NOAA research and operational activities are supported by the Nation's seventh uniformed service, the NOAA Corps, a commissioned officer corps of men and women who operate NOAA ships and aircraft, and serve in scientific and administrative posts.

NOAA'S EDUCATIONAL PARTNERSHIP PROGRAM is designed to provide financial assistance to minority serving academic institutions to support collaborative research and training of students in NOAA-related sciences through competitive processes. The program's goal is to increase the number of students who are trained and graduate in sciences directly related to NOAA's mission. It also seeks to increase collaborative research efforts between NOAA scientists and researchers at minority serving academic institutions, as defined by the Department of Education. Financial assistance is provided through four program components, they include: the Cooperative Science Centers; the Environmental Entrepreneurship Program; the Graduate Sciences Program; and, the Undergraduate Scholarship Program.

NOAA-COOPERATIVE REMOTE SENSING SCIENCE & TECHNOLOGY (CREST) is a multi-disciplinary and multi-institutional center at City College of City University of New York since 2001, funded by NOAA. The Center brings together the City College of New York (lead Institution), Lehman College and Bronx Community College from City University of New York; along with Hampton University; University of Puerto Rico at Mayaguez; Bowie State University; University of Maryland, Baltimore County and Columbia University. NOAA-CREST forms a broad-based research team in Remote Sensing with applied research in Earth Atmospheric, Hydro climate, and Coastal Sciences. NOAA-CREST conducts research that is consistent with NOAA's mission and provides excellent opportunities through scholarships for undergraduate and graduate students for career opportunities with NOAA and other Federal Agencies like NASA and Industries like Raytheon.

The Education and Science Forum, 2004 held in City College of New York, October 21-23, 2004 was designed to bring together representatives from the government, research, academic and private sector communities who are engaged academic and private sector communities in activities that support NOAA's mission, and who have an interest in providing training and career opportunities for students.

Participants including scientists, faculties and students attended the two and a half day forum, which covered five plenary sessions. There were four break-out sessions with 3 to 4 concurrent sessions within each session. Out of 206 papers, 74 were selected for oral presentations, and 132 for poster presentations.

The topics of the sessions reflected NOAA's research: Atmospheric Science; Marine & Fisheries Sciences; Environmental Sciences; Climate & Weather; Satellite Remote Sensing and Education & Outreach.

NOAA-CREST Center

Steinman Hall, T-107
140th St. @ Convent Avenue
City College of City University of New York
New York, NY 10031
Phone: 212-650-5465
Fax: 212-650-8097
Email: noaa-crest@ccny.cuny.edu
Wesbite: www.ccny.cuny.edu/noaa-crest